



CENTRAL LIBRARY

# SCHOLARLY ARTICLES

*A CURRENT AWARENESS BULLETIN  
OF ARTICLES BY  
FACULTY, STUDENTS AND ALUMNI*

~ JULY 2013 ~

DELHI TECHNOLOGICAL UNIVERSITY

(FORMERLY DELHI COLLEGE OF ENGINEERING)

GOVT. OF N.C.T. OF DELHI

SHAHBAD DAULATPUR, MAIN BAWANA ROAD

DELHI 110042

# PREFACE

This is the Seventh Issue of Current Awareness Bulletin for the year 2013, started by Delhi Technological University Library. The aim of the bulletin is to compile, preserve and disseminate information published by the Faculty, Students and Alumni for mutual benefits. The bulletin also aims to propagate the intellectual contribution of DTU as a whole to the academia. It contains information resources available in the internet in the form of articles, reports, presentation published in international journals, websites, etc. by the faculty and students of Delhi Technological University in the field of science and technology. The publication of Faculty and Students, which are not covered in this bulletin, may be because of the reason that the full text either was not accessible or could not be searched by the search engine used by the library for this purpose. To make the bulletin more comprehensive, the learned faculty and Students may provide their uncovered publication to the library either through email or in CD, etc.

This issue contains the information published during July 2013. The arrangement of the contents is alphabetical wise starting from A-Z. The Full text of the article, which is either subscribed by the University or available in the web, is provided in this Bulletin.

# CONTENTS

1. A Compact Efficient MIMO Antenna with EBG Structure Arun Kumara and **\*Taimoor Khanb** Department of ECE
2. A Compact Efficient Yagi-Uda Patch Antenna with EBG Structure **\*Taimoor Khanb** Department of ECE
3. A Compact MIMO Antenna with DGS Structure Prabhat Sharmaa and **\*Taimoor Khanb** Department of ECE
4. Biogeography and geo-sciences based land cover feature extraction **\*Lavika Goela** **\*Daya Guptaa**, V.K. Panchal, Computer Engineering Department
5. Cellular Automata Based Test Data Generation **\*Harsh Bhasin** Neha Singla Shruti Sharma, Department of Computer Science
6. Comparison of Shear Strength of Silty Sand from Ottawa and Yamuna River Basin using Relative Compaction **@Sadanand Ojha** and **\*Ashutosh Trivedi**, Department of Civil Engineering
7. Database optimization of News articles through Indexing **@Shweta Taneja** Computer Engineering Department
8. EFFECT OF WELDING PARAMETER ON MICRO HARDNESS OF SYNERGIC MIG WELDING OF 304L AUSTENITIC STAINLESS STEEL **\$Ravi Butola**, Shanti Lal Meena, **\$Jitendra Kumar** 1,3PG Scholar, Mechanical Department
9. Energy and Exergy Analyses of a New Triple-Stage Refrigeration Cycle Using Solar Heat Source **\*Abdul Khaliq** and **\*Rajesh Kumar** Department of Mechanical Engineering
10. Fault Ride Through Analysis Of Wind Farm In Low Voltage Distribution System Manju Aggarwal, S. K. Gupta, **\*Madhusudan Singh**

11. Fekete-Szegő problem for a class of analytic functions **\*Virendra Kumar and \*S. Sivaprasad** Kumar Department of Applied Mathematics
  
12. General Robust Stability Analysis of Uncertain system Shyama Kant Jha, A.K. Yadav **\$Prerna Gaur**, J.R. P. Gupta
  
13. Impact of Geometry on Photonic Bandgaps for TE polarization in Two Dimensional Photonic Crystals with Triangular Lattice **\*Vinita and \*A. Kumar** Department of Applied Physics
  
14. Influence on ferromagnetic resonance signal of perpendicular magnetic anisotropic Co/Pt bilayer thin film due to microwave induced spin-Hall effect Saood Ahmad, Jyoti Shah, **\*Nitin K. Puri**, P. S. Negi, and R. K. Kotnala, Department of Applied Physics
  
15. Magnesium oxide grafted carbon nanotubes based Impedimetric genosensor for biomedical application Manoj Kumar Patela, Md. Azahar Alia, Saurabh Srivastavaa, Ved Varun Agrawala, S. G. Ansarib, **\*Bansi D. Malhotrac**, Department of Biotechnology
  
16. Modified Multi-Chaotic Systems that are Based on Pixel Shuffle for Image Encryption Om Prakash Verma, **\*Munazza Nizam\*** and Musheer Ahmad Dept. of Information Technology
  
17. Multiband Microstrip Patch Antenna for Wireless Communication Systems **\*Amit Kumar, Sachin Kumar and Prof.P.R .CHADHA** Dept.of ECE
  
18. Parametric sensitivity analysis of factors affecting sound insulation of double glazing using Taguchi method **\*Naveen Garg**, Anil Kumar and **\*Sagar Maj** Department of Mechanical and Production Engineering
  
19. Performance and Emission Study of Linseed Oil as a Fuel for CI Engine **@Ashutosh Kumar Rai, \*Naveen Kumar and \*Bhupendra Singh Chauhan** Department of Mechanical Engineering



20. Prevention Of DOS & DDOS Attack Using Count Based Filtering Method In Cloud Computing **\*R. K. Yadav, \*Daya Gupta and \*Devendra Dadoriya** Computer Engineering Department
21. Privacy & Security of Mobile Cloud Computing **#Manmohan Chaturvedi**, Sapna Malik, Preeti Aggarwal and Shilpa Bahl
22. Reddish-Orange emission from Pr<sup>3+</sup> doped Zinc Alumino Bismuth Borate Glasses Sk.Mahamuda<sup>1</sup>, K.Swapna, **\*A.Srinivasa Rao**, T.Sasikala and L.Rama Moorthy Department of Applied Physics
23. Significance and implications of airborne sound insulation criteria in building elements for traffic noise abatement **\*Naveen Garg**, Anil Kumar, **\*Sagar Maji** Department of Mechanical and Production & Industrial Engineering
24. Sol-gel derived nanostructured zirconia for cholesterol detection Ajeet Kaushika, Pratima R. Solankia, Pandurang M. Chavhana, Shekhar Bhansalib, **\*Bansi D. Malhotra** Department of Biotechnology
25. Use of Biodiesel in CI Engines: A Review **\$Saurabh Singh**, Manish Jain and **\*Amit Pal** Department of Mechanical Engineering

**\* Faculty**  
**# Alumni**  
**\$ PG Scholar**  
**@ Research Scholar**

# Comparison of Shear Strength of Silty Sand from Ottawa and Yamuna River Basin using Relative Compaction

**Sadanand Ojha**

*Research Scholar, Department of Civil Engineering  
Faculty of Technology, University of Delhi  
(Delhi Technological University Campus)  
Bawana Road, Delhi-110042, India  
e-mail: [sadanand\\_ojha@yahoo.com](mailto:sadanand_ojha@yahoo.com)*

**Ashutosh Trivedi**

*Professor, Department of Civil Engineering  
Delhi Technological University  
Bawana Road, Delhi-110042, India  
e-mail: [prof.trivedi@yahoo.com](mailto:prof.trivedi@yahoo.com)*

## ABSTRACT

Shear strength of silty sand depends not only on silt percentage but also on other factors like its source, gradation and hydrological parameters (difference in altitude of origin and fall of river, length of traverse, mean discharge, catchment area and basin characteristics etc.). Other parameters affecting the strength characteristics are methods of testing, sample preparation, confining pressure, the state of denseness or overburden pressure and the critical angle of internal friction. In the present work the values of shear strength parameters  $Q_{af}$  and  $R_{af}$  obtained from triaxial test results of silty sand obtained from Yamuna river basin and Ottawa river basin has been compared. Triaxial tests on silty sand were carried out in the lab at different relative density and confining pressure. The review of past works on silty sand indicates that strength parameter of clean sand and silty sands often evaluated corresponding to relative density containing significant percentage of fines often leads to experimental error due to the uncertainty involved in estimation of the relative density. Therefore the authors in their previous work introduced a term relative compaction to interpret the strength parameter of the soil containing fines and the same has also been reproduced here after ignoring the scattered data of triaxial test with deviation exceeding more than twice the standard deviation. Also the triaxial data of Ottawa sand was re-evaluated in terms of relative compaction to compare the shear strength characteristics of silty sand from obtained from Yamuna and Ottawa River basin. The results indicates that the values of  $Q_{af}$  and  $R_{af}$  evaluated based on relative compaction for both Yamuna sand and Ottawa sand shows lesser variation as compared to values of  $Q_b$  and  $R_b$  calculated based on relative density. The large variation in the results of  $Q_b$  and  $R_b$  for Yamuna sand and Ottawa sand is due to the uncertainty involved in estimation of the relative density for silty sands when fine contents is more than a certain limit.

**KEYWORDS:** silty sand, relative compaction, relative density, strength parameters.

## INTRODUCTION

In the present work shear strength properties of silty sand obtained from the basin of river Ottawa and Yamuna has been compared. The shear strength of silty sand depends upon inter particle cohesion and its friction angle [1, 2]. The cohesion between sand particles apart from various other factors

depends upon the presence of silt and or clay [4, 6, 7, 8, 9]. Grain size distribution of silty sand depends upon the source from which it has been obtained. Hence variation in the origin and destination of the source river (length of river), difference in the elevation of origin and mouth fall, discharge, location (altitude and longitude), average temperature over length of flow directly affects the strength properties of silty sand. It has been observed that the percentage of silt present in the silty sand greatly influence the shear strength characteristics of silty sand [3, 5, 10, 13, 14, 15, 16, 17, 18]. It is observed that upto a certain low percentage of silt (less than 10 percent) the silt particles occupies the voids between the sand particles and when the percentage of silt is more than 15 percent, silt particles tries to align along the surface of sand particles [10, 11]. The behavior of the soil is now inclined towards plastic silt and thereby a sudden reduction in the shear strength of soil.



**Figure 1:** Ottawa River Drainage Basin (source : [http://en.wikipedia.org/wiki/Ottawa\\_River](http://en.wikipedia.org/wiki/Ottawa_River))

In the present study the various parameters for Ottawa River and Yamuna River are taken into account to evaluate the strength properties of silty sand obtained from the catchment area of respective river basin. Various tests were performed as per Codal provision [12]. The Ottawa River flows in the Canadian provinces of Ontario and Quebec. The river defines the border between these two provinces along most part of its length. The river originates from its source in Lake Capimitchigama, in the Laurentian Mountains of central Quebec, and flows west to Lake Timiskaming. From Lake Timiskaming, the river flows southeast to Ottawa and Gatineau, where it tumbles over the Chaudière Falls and further takes in the Rideau and Gatineau rivers.. The river flows through large areas of deciduous and coniferous forest. Most part of the river flows through the Canadian Shield, although lower areas flow through Lime stone plains and glacial deposits. The

drainage basin of Ottawa River is shown in Fig.1. Yamuna River is the largest tributary of the Ganges River Ganga in northern India. Its source is at Yamunotri, in the Uttarakhand Himalaya, in the Himalayan Mountains. It flows through the states of Delhi, Haryana and Uttar Pradesh, before merging with the Ganges at Allahabad. Originating in the Yamunotri glacier in the Himalayas, Yamuna covers a distance of over 1300 km, before merging with the Ganga in Allahabad. Fig.2 and fig.3 shows the drainage basin of Yamuna River and its origin at Yamunotri. Topographical data for Ottawa and Yamuna River is given in Table1. The data given in Table 1 gives its total length, drainage area and the mean discharge along with other hydrological data.

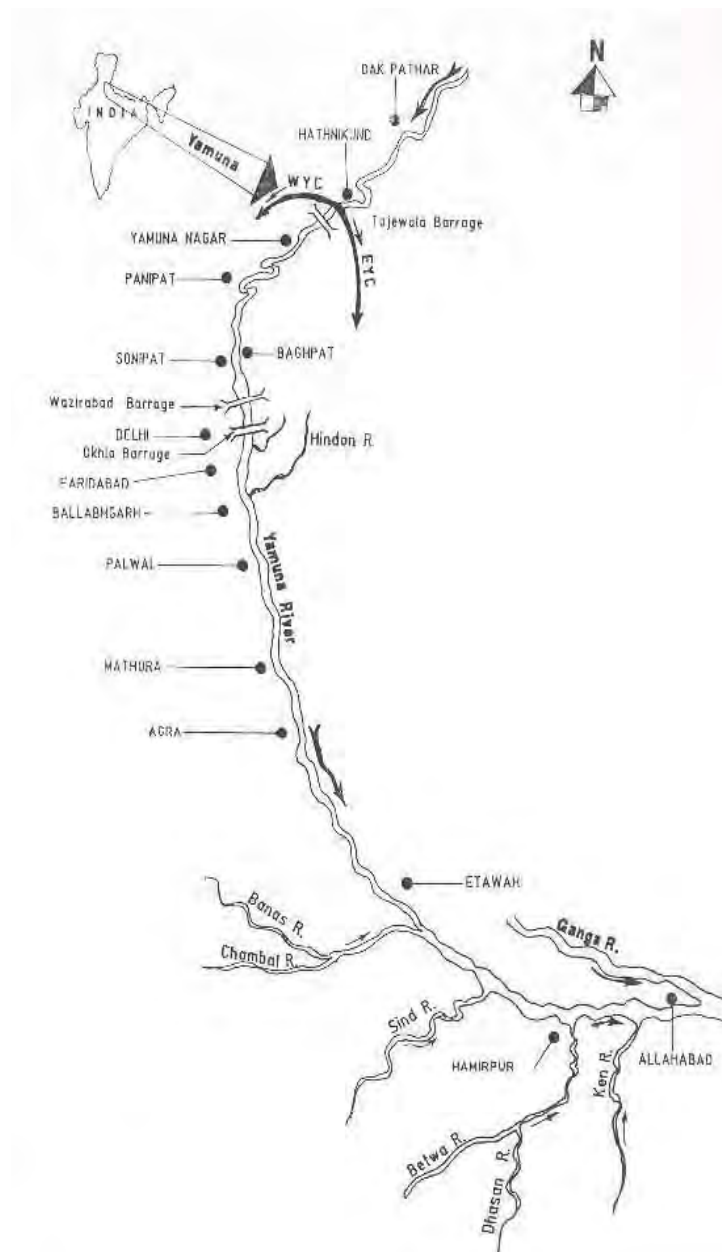


**Figure 2:** Yamuna River drainage basin



**Figure 3:** Yamuna at Yamunotri

**Table 1:** Hydro and Geological data for Yamuna and Ottawa River

S. No.	Description	Yamuna River	Ottawa River
1.	Country	India	Canada
2.	Source	Yamunotri	Lake Capimitchigama
3.	Mouth	Ganga	St. Lawrence River
3.	Co-ordinates	31°01'0.12"N 78°27'0"E / 31.0167°N 78.45°E /	45°27'N 74°05'W 45.45°N 74.083°W
4.	Elevation at Source	3293m	430m
5.	Elevation at Mouth	74m	20m
6.	Approximate Length	1376 km	1271 km
7.	Catchment Area	219663 km <sup>2</sup>	146300 km <sup>2</sup>
8.	Discharge	317097 m <sup>3</sup> /s	5351 m <sup>3</sup> /s

## SHEAR STRENGTH-DILATANCY RELATION

Mohr was the first to present a generalised form of the theory around the end of the 19th century for the evaluation of the shear strength of the granular sand. Mohr theory of failure states that the failure of soil due to shear stress depends upon normal stresses on the potential failure plane and the failure is caused by a critical combination of normal and shear stresses. Mohr proposed that shear strength of soil at failure is a unique function of normal stress acting on that plane and is represented by following expression,

$$\tau_f = f(\sigma) \quad (1)$$

A plot drawn between normal stress and shear stress at failure using Eq. (1) is called Mohr envelope and there is unique failure envelope for each soil. Using the concept of Coulomb [19] which

developed a more general relation considering cohesion between soil particle ( $c$ ) and angle of internal friction ( $\phi$ ). It was later known as Mohr–Coulomb failure criterion. This relation is expressed as

$$\tau = c + \sigma \tan \phi \quad (2)$$

For cohesionless soil the Eq. (2) reduces to

$$\tau = \sigma \tan \phi \quad (3)$$

This is a form of Eq. (1). The failure occurs when the stresses are such that the Mohr circle just touches the failure envelope as shown in fig. (1). It is clear that the failure occurs if the stresses  $\sigma$  and  $\tau$  on failure plane either touches it at point B or above the failure line. Point lying below failure envelope represents a stable and non-failure condition.

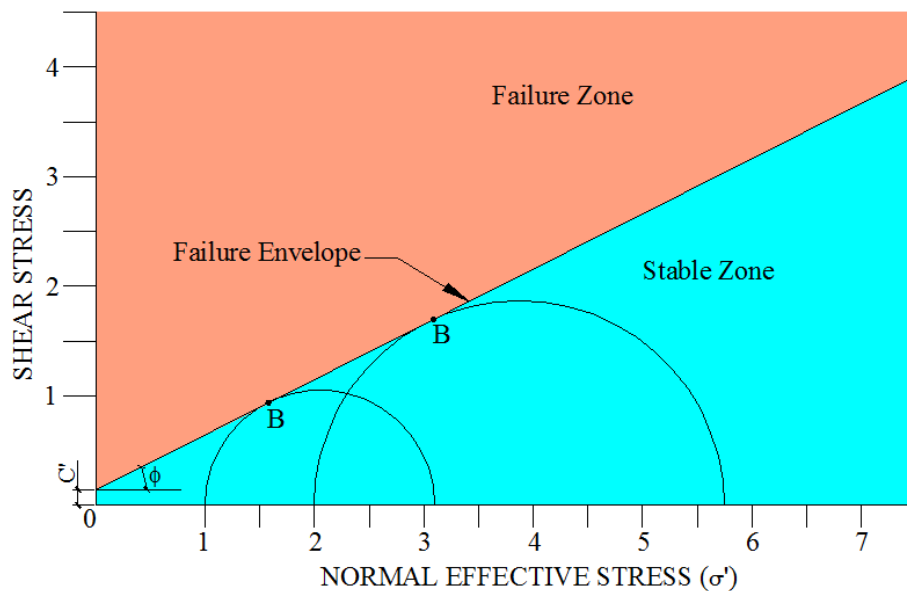


**Figure 4:** Shear stress and normal stress plot showing failure envelope.

**Table 2:** Test Data for Silty Sand [16, 17]

S. No.	Description	Yamuna	Ottawa
1.	Number of Test	75	70
2.	Testing Techniques	Triaxial Dry Pulverization	Bender Element
3.	Range of Pressure (kPa)	100, 200 & 400	100-400
4.	Range of Relative Density	60, 65, 70, 75 & 80	14-100
5.	Range of Relative Compaction	0.92, 0.93, 0.94, 0.95 & 0.96	0.86-0.96
6.	Plasticity	NP & P	NP

Later research done by various investigator showed that the parameter  $c$  and  $\phi$  depends upon number of factors such as water content, drainage conditions, and methods of testing and is not necessarily the fundamental properties of soil. Terzaghi [19] established that the normal stresses that controls the shear strength of the soil are effective stresses and not normal stresses, and modified the Eq. (2) as

$$\tau = c' + \sigma' \tan \phi' \quad (4)$$

Here  $c'$  and  $\phi'$  are the cohesion intercept and angle of internal friction in terms of effective stresses. Eq. (4) is known as revised Mohr-Coulomb equation for shear strength of soil. With the further advancement of research on granular sand Bolton [3] studied the behavior of 17 nos. of different sand in axisymmetric or plane strain at different densities and confining pressures and established a relation between strength and dilatancy given by expression

$$\Phi = \Phi_c + 0.8\psi \quad (5)$$

However, not much work was done to assess the effect of fine content on the strength behavior of clean sand in the past. Salgado [17] has calculated the values of shear strength parameter ( $Q$  and  $R$ ) for clean and silty Ottawa sand for different silt percentage and found that a value of  $R = 0.5$  works well for all gradation and within the limited range of relative density. He gave a relationship between the peak friction angle  $\Phi_p$  and the critical-state friction angle  $\Phi_c$  in terms of dilatancy index  $I_R$ , for tri-axial conditions as

$$I_R = [\Phi_p - \Phi_c]/3 \quad (6)$$

$$\text{where } I_R = D_r(Q - \ln 100 p_p^*/P_A) - R \quad (7)$$

where,  $D_r$  is relative density expressed as a number between 0 and 1,  $p_p^*$  is mean effective stress at peak strength in kPa,  $P_A$  is reference stress (100 kPa) in the same units as  $p_p^*$ ,  $Q$  and  $R$  are fitting parameters.

From Eq. (7) and (8)

$$[\Phi_p - \Phi_c]/3 = D_r Q - D_r \ln 100 (p_p^*/P_A) - R$$

$$[\Phi_p - \Phi_c]/3 + D_r \ln 100 (p_p^*/P_A) = D_r Q - R \quad (9)$$

Further we define  $I_N$  as

$$I_N = [\Phi_p - \Phi_c]/3 + D_r \ln 100 (p_p^*/P_A)$$

Eq. (9) can be expressed as

$$I_N = D_r Q - R \quad (10)$$

Bolton [3] found that values  $Q = 10$  and  $R = 1$  created a definition for a relative dilatancy index which apparently offered a unique set of correlations for the dilatancy-related behaviour of each of the sands in laboratory element tests. The values of “ $Q$ ” and “ $R$ ” are highly dependent on range of relative density, confining pressure, hydro-geology, catchment area, basin characteristics, and plasticity of silt and gradation of soil.

Ojha and Trivedi [16] observed that there are serious problem associated with the estimation of relative density of the soil containing significant percentage of plastic and non plastic silt. This relative density assumption for the soil containing significant percentage of fines often leads to significant error in overall estimation of strength and deformation properties of silty sands. Therefore the authors used relative compaction of the soil instead of relative density to interpret the strength parameter of the soil containing fines and modified the Eq. (10) by replacing the term relative density ( $D_r$ ) with relative compaction ( $R_c$ ) as given below:

$$I_{Na} = R_c Q_f - R_{af} \quad (11)$$



$Q_{af}$  and  $R_{af}$  are shear strength parameters for plastic silt. It has been established that the shear strength parameter calculated based on relative compaction over come the difficulty and the error involved in estimation of relative density.

## RESULTS AND DISCUSSION

Based on Eq. (11), findings of Salgado [17] on silty Ottawa sand was re-evaluated in terms of relative compaction and the results were compared with that of Yamuna sand [16]. The sequential comparison with discussion of results is presented here.

Plot between maximum and minimum void ratio for Yamuna sand and Ottawa sand has been plotted based on laboratory test as shown in figure 5. It is observed that both maximum and minimum void ratio decreases with increase in fines for both sand but the total voids for the same percent fines are more in Yamuna sand than for Ottawa sand. This is due to the fact that fines used in the analysis of Ottawa sand was non-plastic and for Yamuna sand plastic fines were used.

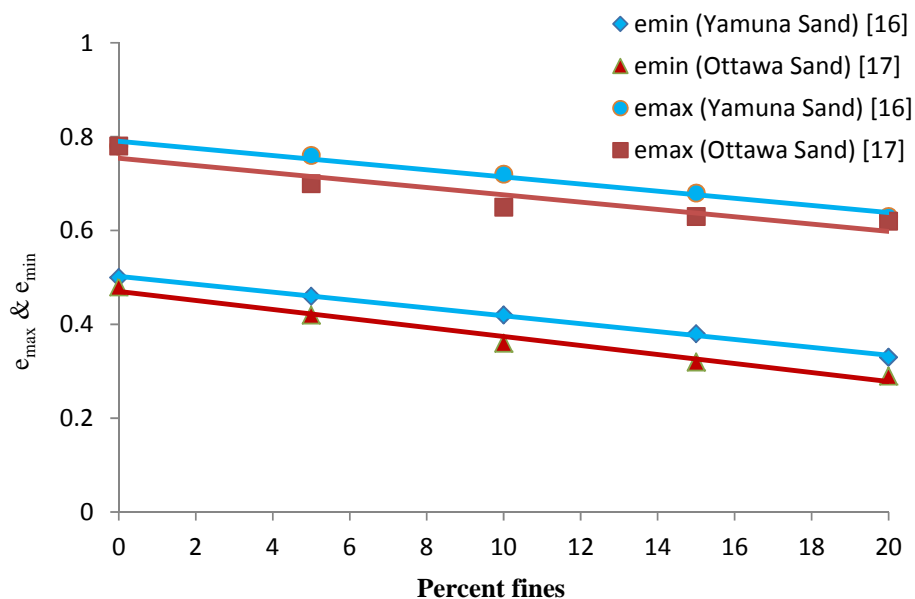


**Figure 5:**  $e_{max}$  &  $e_{min}$  vs. Percent fines

The plot between critical state friction angle and percent fine were also drawn for Ottawa and Yamuna sand as shown in Fig.6. It has been found that the Yamuna sand reaches its peak much earlier than Ottawa sand for the same percent fines due to presence of plastic fines which slips easily under the same normal and confining stress. The plot shown ignores the scattered data falling beyond the range of twice the standard deviation.



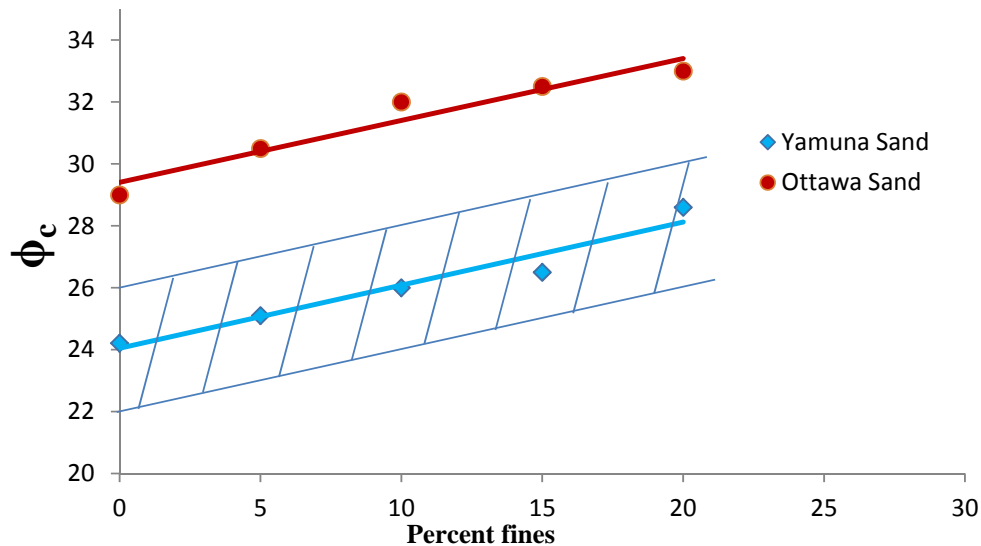


**Figure 6:** Critical Friction Angle vs. Percent Fines

Based on the test results data obtained from triaxial test of Ottawa sand by Salgado [17] for maximum and minimum proctor density, relative density has been converted into relative compaction and the plot between  $D_r$  and  $R_c$  at different percent fine has been drawn as shown in fig. 7(a) -7(e). The same plot for Yamuna sand based on the work done by Ojha and Trivedi [16] was also superimposed with that of Ottawa sand and an empirical relation between  $R_c$  and  $R_d$  has been found which is validated theoretically by substituting in Bolton's equation. From the plot it is clear that Ottawa sand is more compressible for fines percent up to 10% and the rate of compression decreases when percent fine increases above 10%.

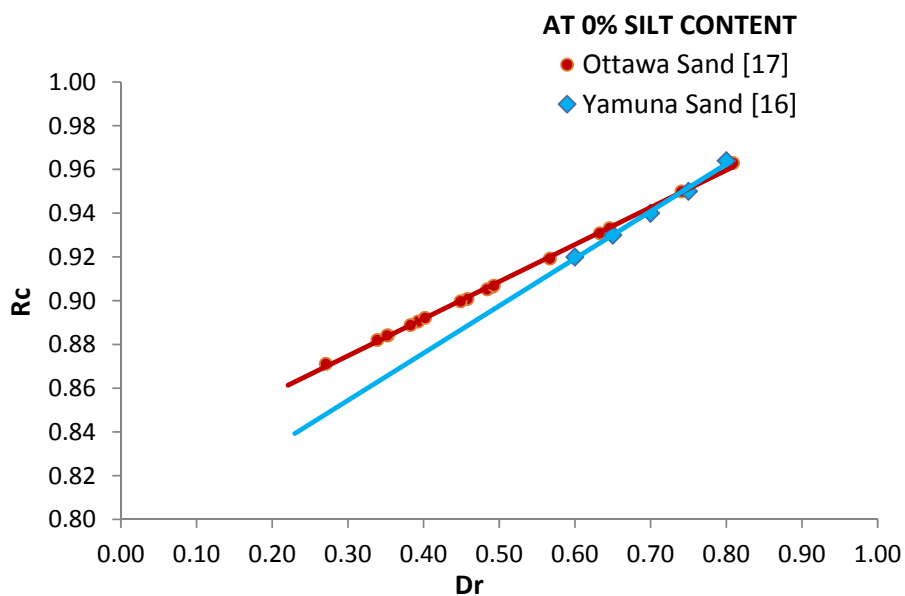


**Figure 7 (a):**  $R_c$  v/s.  $D_r$  (At 0% Silt Content)

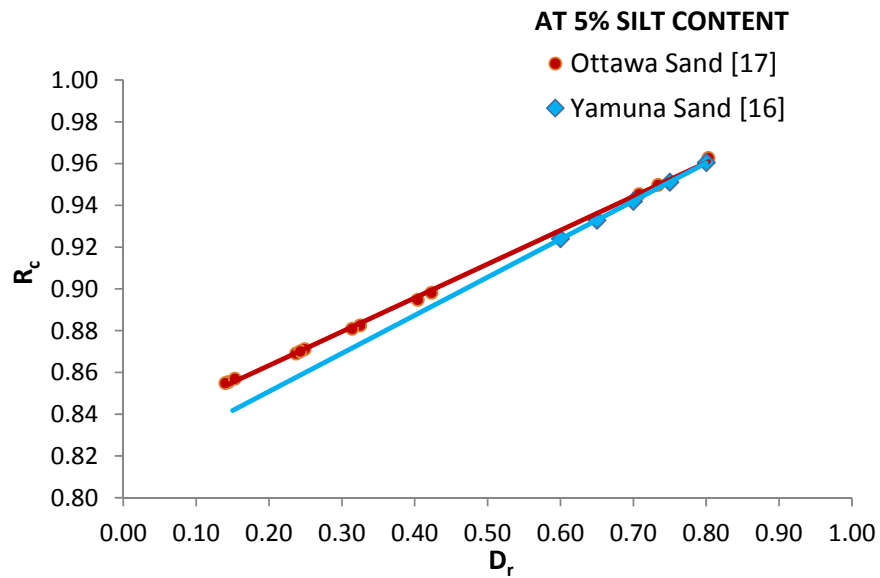


**Figure 7 (b):  $R_c$  v/s.  $D_r$  (At 5% Silt Content)**

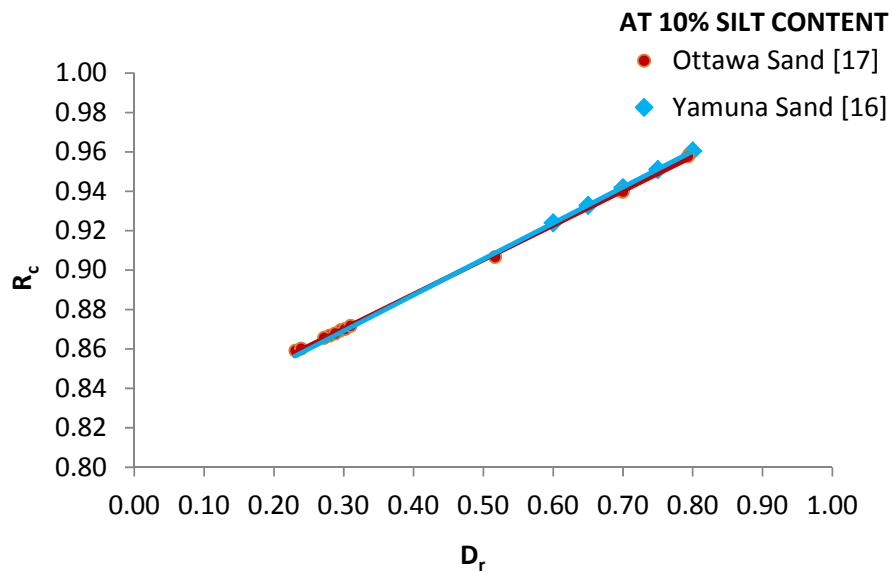
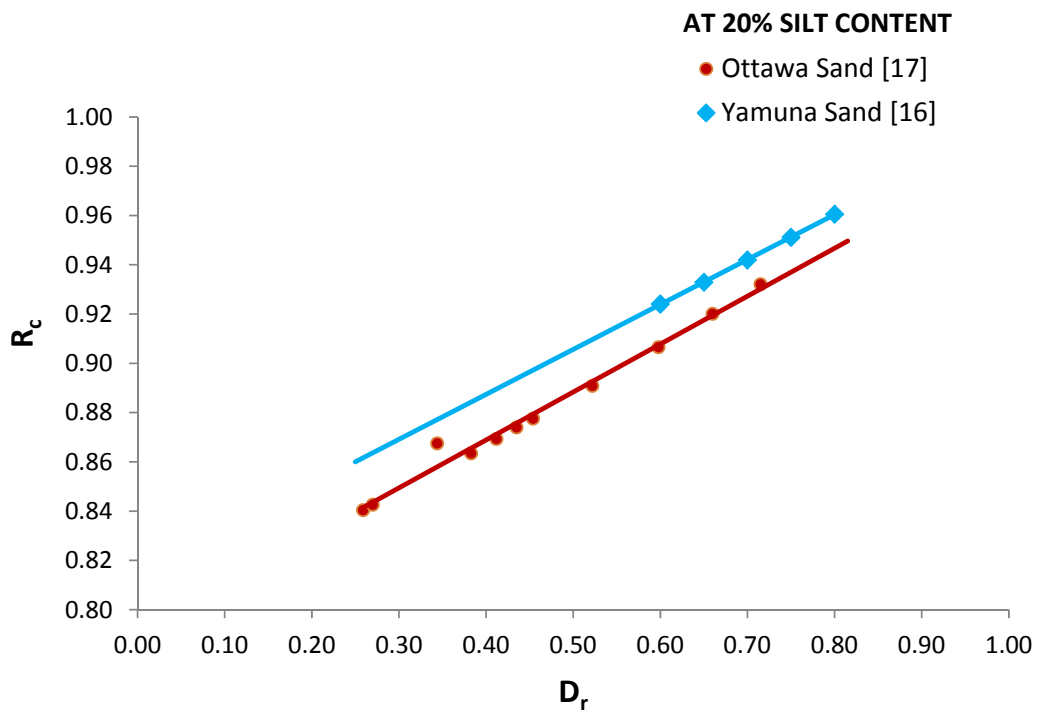
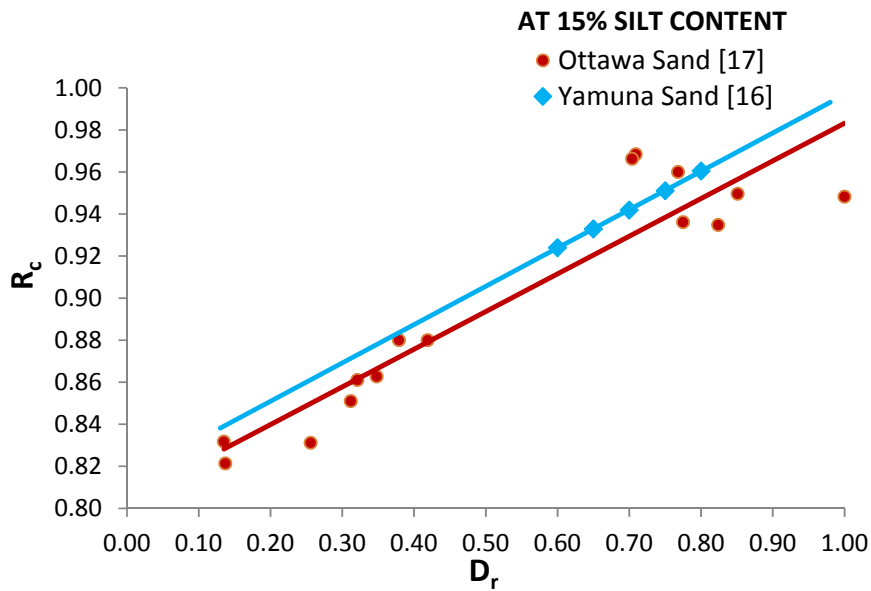


**Figure 7 (c):  $R_c$  v/s.  $D_r$  (At 10% Silt Content)**



A typical variation of  $I_N$  with relative compaction is shown in Fig. 8(a) -8(e) Table 3 shows the values of  $Q_s, R_s$  and  $Q_a, R_a$  based on relative density using Eq. (10). Using the relationships of Eqs (11), we obtained the values of  $Q_{sf}, R_{sf}$  and  $Q_{af}, R_{af}$  and are tabulated in table 4. From the table 3 and 4 It is

clear that coefficient of correlation is much better for silty sand with silt percentage up to 15% when evaluated based on relative compaction as compared to that calculated based on relative density.

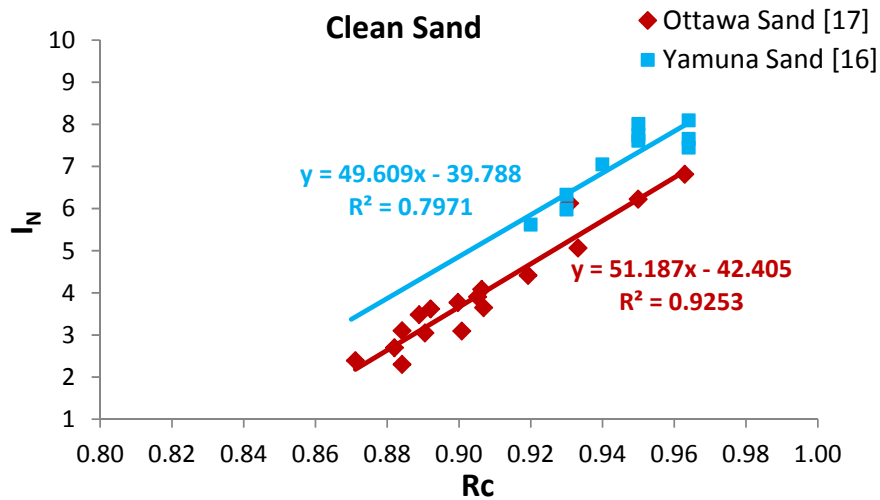


Figure 8 (a):  $I_N$  v/s.  $R_c$  (At 0% Silt Content)

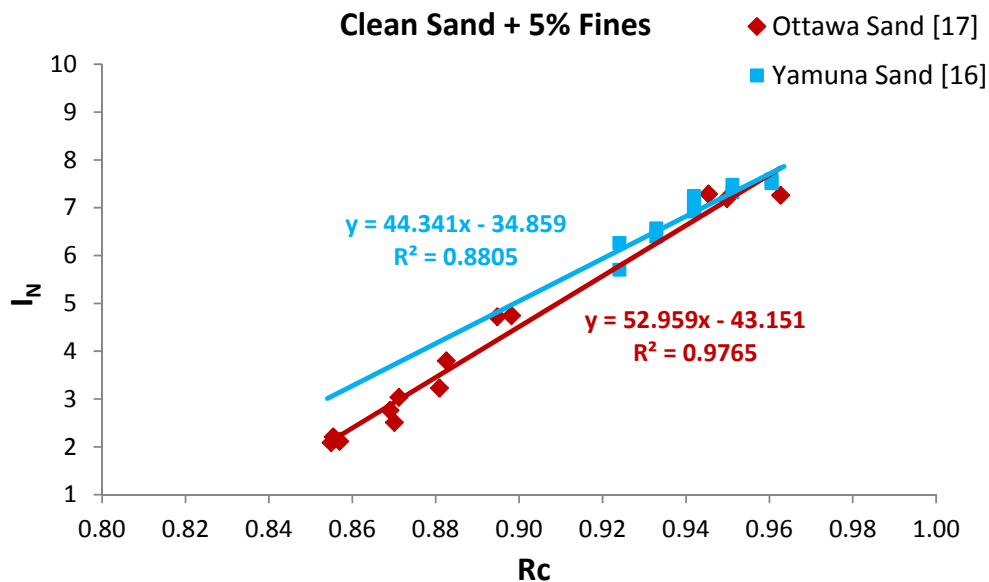


Figure 8 (b):  $I_N$  v/s.  $R_c$  (At 5% Silt)

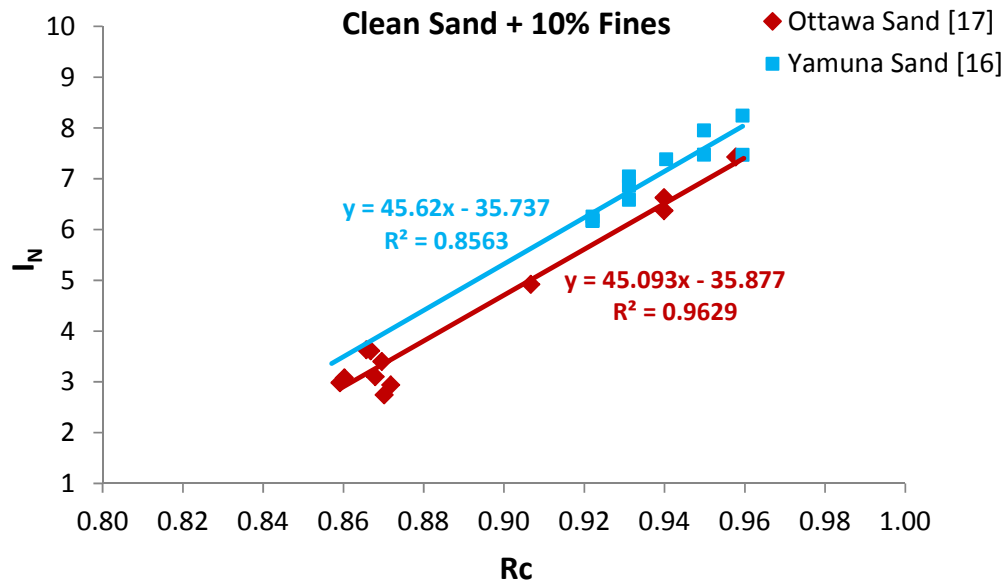


Figure 8 (c):  $I_N$  v/s.  $R_C$  (At 10% Silt Content)

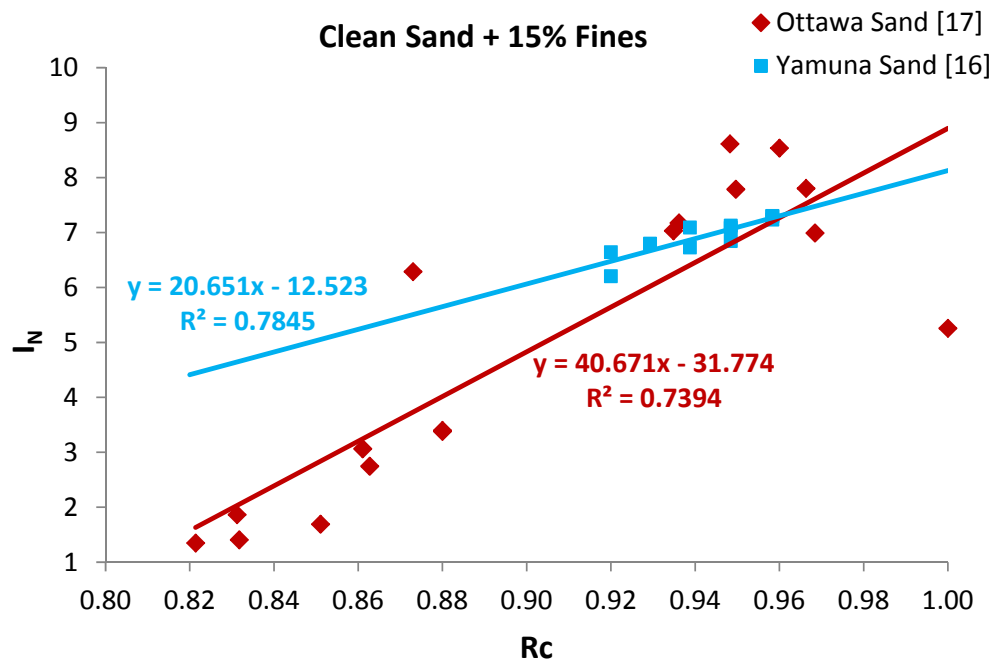
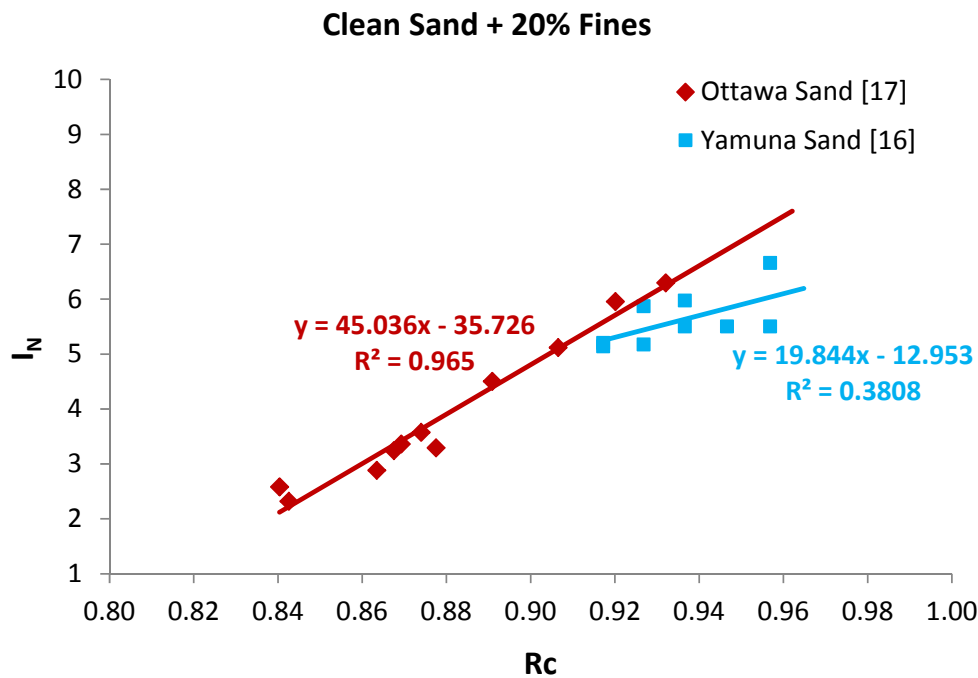


Figure 8 (d)  $I_N$  v/s.  $R_C$  (At 15% Silt Content)

**Table 3:** Comparison of Shear strength parameter based on relative density for silty Sand

Silt (%)	Yamuna Sand [16]		Ottawa Sand [17]		Tread line with $R_a = 0.5$ Yamuna Sand [16]		Tread line with $R_s = 0.5$ Ottawa Sand [17]	
	$Q_a$	$r^2$	$Q_s$	$r^2$	$Q_a$	$r^2$	$Q_s$	$r^2$
0	11.674	0.721	9	0.93	7.096	0.502	9	0.93
5	11.397	0.79	9	0.98	7.047	0.673	11	0.92
10	10.934	0.705	8.3	0.97	7.433	0.632	10.6	0.87
15	11.041	0.553	11.4	0.97	6.817	0.471	10.3	0.96
20	5.435	0.356	10.1	0.95	5.426	0.332	9.5	0.95

**Table 4:** Comparison of Shear strength parameter based on relative compaction for silty Sand

Silt (%)	Yamuna Sand [16]		Ottawa Sand [17]		Tread line with $R_{af} = 40$ Yamuna Sand [16]		Tread line with $R_{sf} = 40$ Ottawa Sand [17]	
	$Q_{af}$	$r^2$	$Q_{sf}$	$r^2$	$Q_{af}$	$r^2$	$Q_{sf}$	$r^2$
0	49.609	0.7971	51.187	0.9253	49.833	0.7970	48.53	0.9229
5	44.341	0.8805	52.959	0.9765	49.797	0.8671	49.43	0.9722
10	45.620	0.8563	45.093	0.9629	50.163	0.8478	49.72	0.9527
15	20.651	0.7845	40.671	0.7394	49.800	0.7790	49.74	0.7025
20	19.844	0.3808	45.036	0.9650	48.742	0.4270	49.88	0.9538

## CONCLUSIONS

In the present work, the shear strength parameter ( $Q_a$ ,  $Q_s$ ,  $Q_{af}$ ,  $Q_{sf}$ ) of silty sand based on relative compaction is compared for Ottawa and Yamuna sand. The values of shear strength parameters ( $Q_{af}$  and  $R_{af}$ ) of silty sand calculated based on the concept of relative compaction is more appropriate as compared to that based on relative density due to the inherent limitation associated with the correct determination of relative density for silty soils. The values thus obtained for  $Q_{af}$  and  $R_{af}$  are comparable with that calculated by Salgado upto 15% of fine ( $Q_{as}$  and  $R_{as}$ ). Based on the above results and discussions the following conclusion can be drawn.

1. The outcome of present study indicates that the strength characteristics of silty sand containing non-plastic fine (Ottawa sand) and plastic fines (Yamuna sand) is different though showing the similar trend.
2. The mean size of particle depends on the difference in elevation of origin and fall of river. The Yamuna river carries plastic fines due to its origin at very high altitude in hilly region as compared to Ottawa river which mostly flows in plains.
3. Coefficient of co-relation is higher for shear strength parameter when calculated based on relative compaction than when calculated based on relative density due to the error involved in estimation of relative density.
4. Values of  $Q_{af}$  &  $R_{af}$  are sensitive to the range of mean sizes, relative compaction and extent of confinement.
5. Ottawa sand is more compressible for fines percent upto 10% and the rate of compression decreases when percent fine increases above 10%.
6. Yamuna sand reaches its peak much earlier than Ottawa sand for the same percent fines due to presence of plastic fines which slips easily under the same normal and confining stress.

## LIST OF SYMBOLS

$\tau_f$	Shear strength at failure
$\sigma$	Normal stress on the plane of shearing
$C$	Cohesion
$\sigma'$	Effective normal stress
$\sigma_1$	Principal stress
$\sigma_3$	Confining stress
$\Phi$	Friction angle
$\Phi_p$	Peak friction angle
$\Phi_c$	Critical friction angle
$\Psi$	Dilatancy angle
$G_s$	Specific gravity
$\sigma_d$	Deviator stress
$e_{max}$ and $e_{min}$	Maximum and minimum void ratio
$\gamma_w$	Unit weight of water
$\gamma_{min}$ and $\gamma_{max}$	Minimum and maximum dry density
$Dr$	Relative density
$P_p$	Mean effective stress at peak strength
$P_A$	Reference stress
$Q, R, Q_a, R_a, Q_s, R_s, Q_{af}, R_{af}, Q_{sf}, R_{sf}$	Fitting parameters
$r^2$	Coefficient of co-relation
$R_c$	Degree of compaction
$D_m$	Mean diameter of particles
$I_R$	Dilatancy index

## REFERENCES

1. Ayadat, T, Hanna, A. (2007) Prediction of collapse behaviour in soil, *Revue Europeans de Genie Civil*, 11 (5), 603-619.
2. Been, K., Jefferies, M. G., and Hachey, J.(1991). "The critical state of sands." *Geotechnique*, 41(3), 365–381.
3. Bolton, M. D. (1986). "The strength and dilatancy." *Geotechnique*, 36(1), 55–78.
4. Bui, M. and Priest, J. (2007). "Discussion of "Particle Shape Effects on Packing Density, Stiffness, and Strength: Natural and Crushed Sands" by Gye-Chun Cho, Jake Dodds, and J. Carlos Santamarina." *J. Geo-tech. Geo-environ. Eng.*, 133(11), 1473–1474.
5. Chakraborty T. and Salgado R. (2010). "Dilatancy and Shear strength of sand at low Confining Pressure", *Journal of Geotechnical and Geo-Environmental Engineering*, ASCE, 136(3), 527-534.
6. Chen, Y. C., and Liao, T. S. (1999). "Studies of the state parameter and liquefaction resistance of sands." *Earthquake Geotechnical Engineering: Proc., 2nd Int. Conf.*, Lisbon, Portugal, [P. S. Seco e Pinto, ed.].
7. ChoG, Dodds J, and SantamarinaJ., (2006) "Particle Shape Effects on Packing density, Stiffness, and Strength: Natural and Crushed Sands", *Journal of Geotechnical and Geo-environmental Engineering*, ASCE, 132, (5), 591-602
8. Chu, J., and Lo, S. C. R. (1993). "On the measurement of critical state parameters of dense granular soils." *Geo-tech. Test. J.*, 16(1), 27–35.
9. Diego C.F. Lo Presti, Pedroni S. and Crippa V. (1992). "Maximum dry density of cohesion less soil by pluviation and by ASTM D 4253-83: A comparative study." *Geotech. Testing J.*, 15(2), 180–189.
10. Gupta R. and Trivedi A. (2009). "Effects of non-plastic fines on the behaviour of loose sand an experimental study", *Electronic Journal of Geotechnical Engineering*, 14, (B), 1-14.
11. Gupta, R., and Trivedi, A. (2009). "Bearing Capacity and Settlement of Footing Resting on Confined Loose Silty Sands." *Electronic Journal of Geotechnical Engineering*, 14, (B).
12. IS: 2720 (Part3/Sec2)-1980 Methods of tests for soils: Part 3 Determination of specific gravity, Section 2 Fine, medium and coarse grained soils.
13. Konrad, J. M. (1990). "Minimum undrained strength versus steady-state strength of sands." *J. Geotech. Eng.*, 116(6), 948–963.
14. Lee, C. J. (1995). "Static shear and liquefaction potential of sand." *Proc., 3rd Int. Conf. on Recent Advances in Geotechnical Earthquake Engineering and Soil Dynamics*, St. Louis, Vol. 1, 115–118.
15. Ojha S., Goyal P., Trivedi A., (2012) "Non linear behaviour of silty sand from catchment area of Yamuna river" *Proceeding of IGC conference Dec 2012 Delhi*, paper no. B211, 277-280.
16. Ojha, S. (2013). "Shear Strength Parameters for Silty- Sand Using Relative Compaction." *Electronic Journal of Geotechnical Engineering*, 18(1), 81–99.
17. Salgado R., Bandini P. and Karim A. (2000). "Shear Strength and Stiffness of Silty Sand", *Journal of Geotechnical and Geo-environmental Engineering*, ASCE, 126(5), 451–462.
18. Trivedi A. (2010). "Strength and dilatancy of jointed rocks with granular fill", *ActaGeotechnica*, 5(1), 15-31.
19. Terzaghi, K. (1942), *Theoretical Soil Mechanics*, New York: Wiley, ISBN 978-0-471-85305-3





## Research Article

## A Compact Efficient MIMO Antenna with EBG Structure

Arun Kumar<sup>a\*</sup> and Taimoor Khan<sup>b</sup><sup>a</sup>Department of ECE, Trident ET Group of Institutions, Ghaziabad-201003<sup>b</sup>Department of ECE, Delhi Technological University, Delhi

Accepted 5 July 2013, Available online 01 August 2013, Vol.3, No.3 (August 2013)

### Abstract

A compact efficient multiple-input- multiple-output (MIMO) antenna with EBG structure is presented. The MIMO antenna consists of two symmetric monopoles and an EBG (electromagnetic band gap) plane which is present at an air gap of 0.4 mm above the ground plane. This EBG surfaces offer a mechanism to improve antenna performance, reduce antenna size and reduce antenna to antenna coupling on platforms. In this paper, we also introduced the comparison of performance parameters of the proposed MIMO antenna with EBG structure and referred MIMO antenna. The concept of air gap is also used with EBG and to collectively enhance the impedance bandwidth, increases the gain, increases the efficiency and reduces the effective size of the antenna. A high bandwidth with  $S_{11} \leq -10$  dB and  $S_{21} \leq -18$  dB from 2.303 - 6.738 GHz is achieved. The analysis has been done by using IE3D software based on method of moments (MOM).

**Keywords:** Multiple-input multiple-output (MIMO) antenna, S-parameter ( $S_{11}$  &  $S_{21}$ ), Directivity, Gain, Antenna Efficiency, Radiation Efficiency, EBG and Air gap.

### 1. Introduction

Now-a- days, there is a demand to increase the data rate of existing wireless communication systems. The application of diversity techniques, most commonly assuming two antennas (commonly known as MIMO antenna (Qing-Xin Chu *et al*, 2012) ) in a mobile terminal , can enhance the data rate and reliability without sacrificing additional spectrum or transmitted power in rich scattering environments (T. Bolin *et al*, 2005). When these two or more antennas can be used at both transmitter and receiver are called Multiple-input and multiple-output (MIMO) antenna or system. Theoretical and experimental investigations have revealed substantial improvements in channel capacity and reliability when multiple transmitter and receiver antennas are deployed. A critical point is to arrange, these compact MIMO antenna elements without impairing antenna performance and system requirements (Youngki Lee *et al*, 2012). When a multiple-input multiple-output (MIMO) antenna is applied in a multifunctional portable device, good performance parameters are demanded. As we know that the MIMO systems which consists of two or more monopole antennas have the advantages of low cost, easy fabrication, and good performance (Cheng Yang, *et al*, 2012). But these performance parameters of MIMO antenna are not good enough to increase the performance of the portable device. However, the design of a compact efficient MIMO

antenna with good performance parameters is an open issue.

In this paper, a compact efficient MIMO antenna with EBG structure is proposed. The electromagnetic band gap (EBG) structures between the substrate and the ground plane of referred MIMO antenna is inserted and its effect on the performance parameters of the MIMO antenna are studied . These structures (EBG) consist of uniformly distributed periodic metallic, dielectric or composite structures that exhibit pass and stop bands in their frequency response. Essentially the behaviour of the EBG structure is based on the interactions between adjacent cells and therefore the larger the number of cells, the more effective the structure (R.B. Waterhouse , *et al*, 2000). When these structures are introduced at the ground level some radiation will occur in the reverse side of MIMO antenna also. This creates back lobe in the opposite side. This EBG plane is used at the distance from the ground plane, which creates an air gap between the substrate and ground plane. When this EBG plane is placed at an air gap of 0.4 mm above the ground plane, all the parameters of the MIMO antennas have been increased much further (N. S. Raghava , *et al*, 2006). Hence, the MIMO antenna performance parameters such as radiation efficiency, antenna efficiency, directive gain (K. Payandehjoo , *et al*, 2009) are improved. As we have discussed above how EBG structure is used to enhance the performance of referred MIMO antenna. In this proposed paper the effect of air-gap with reference to EBG on the performance parameters of the MIMO antenna are also

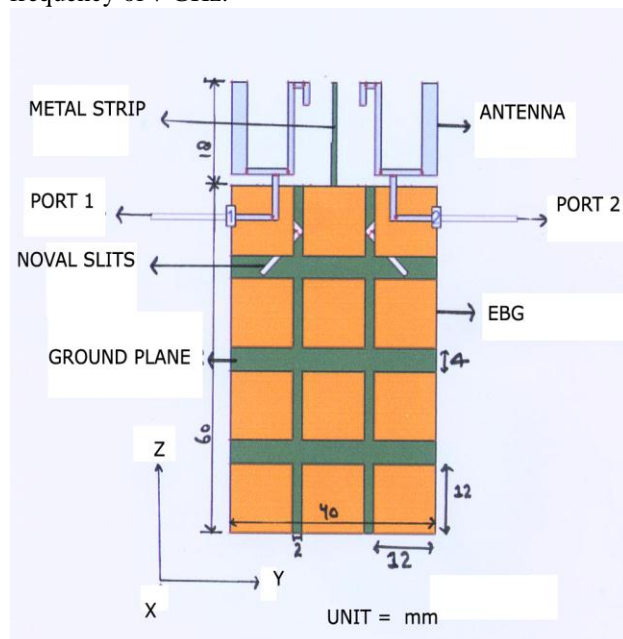
\*Corresponding author: Arun Kumar

studied. This air-gap technique collectively enhances the impedance bandwidth, increases the gain, increases the efficiency and reduces the effective size of the antenna. This air-gap helps in order to achieve tunable resonant frequency characteristics.

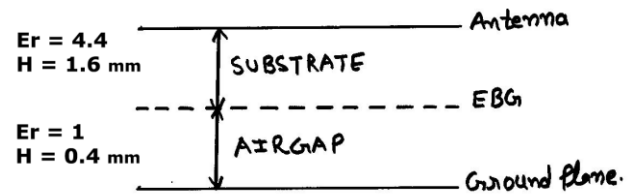
The proposed Compact Efficient MIMO antenna with EBG structure consist of two dual-branch monopoles and an EBG surface which at an air gap of 0.4 mm above the ground plane and the compact sizes of the monopole, the ground plane ( $L \times W$ ), EBG cells, gap between EBG cells on width sides and gap between EBG cells on length sides are 18mm\* 15 mm, 60mm\* 40 mm, 12mm\*12 mm, 2 mm and 4 mm, respectively. A high bandwidth with  $S_{11} \leq -10$  dB and  $S_{21} \leq -18$  dB from 2.303 to 6.738 GHz is achieved, which covers 2.4/5.2/5.8-GHz WLAN, 2.5/3.5/5.5-GHz Wi-MAX and the lower UWB band (3.1–4.8 GHz) operation.

## 2. Proposed MIMO Antenna With EBG Structure

The geometry of the proposed MIMO antenna with EBG is designed by using IE3D software (Zeland), which is illustrated in Fig. 1. The MIMO antenna is printed on the upper part of a partially grounded FR4 substrate with dimensions 78mm\*40mm\*1.6mm<sup>3</sup> and relative permittivity 4.4. And an EBG structure is inserted at an air-gap of 0.4mm above the ground plane. On the back surface of the substrate, the main rectangular ground plane of 40 mm in width and 60 mm in length is printed. The compact sizes of the monopole, the ground plane ( $L \times W$ ), EBG cells, gap between EBG patches on width sides and gap between EBG patches on length sides are 18mm\* 15 mm, 60mm\* 40 mm, 12mm\*12 mm, 2 mm and 4 mm, respectively. EBG is of like Mushroom-type and each slit is coupled fed by a 50 ohm microstrip line. The geometry of proposed antenna is simulated on the meshing frequency of 7 GHz.



(a) Top-view



(b) Side-view

Fig 1: MIMO Antenna with EBG structure.

## 3. Working Mechanism of Proposed Antenna

The proposed MIMO antenna with EBG structure shown in Fig. 1 has been simulated and studied to a good agreement using IE3D software. From the calculated graphs and tables we can say that the performance parameters of MIMO with EBG structure shows much improvement as compare to refer MIMO antenna. Between 3-3.5 GHz and above 6 GHz frequency, the performance parameters of proposed antenna show great improvement.

## 4. Simulated Results and Comparison

### Performance Parameters of Proposed Antenna

(i) **S-parameters** – As we know that it describe the input-output relationship between ports (or terminals) in an electrical system. If  $S_{11} = -10$  dB, this implies that if 3 dB of power is delivered to the antenna, -7 dB is the reflected power. Fig 2 depicts the return loss ( $S_{11}$ ) and ( $S_{21}$ ) characteristics of the proposed antenna and the referred MIMO antenna with frequency respectively. It also shows a high bandwidth with  $S_{11} \leq -10$  dB and  $S_{21} \leq -18$  dB from 2.303 to 6.738 GHz covering the following bands: 2.4/5.2/5.8-GHz WLAN, 2.5/3.5/5.5-GHz Wi-MAX and the lower UWB band (3.1–4.8 GHz) operation.

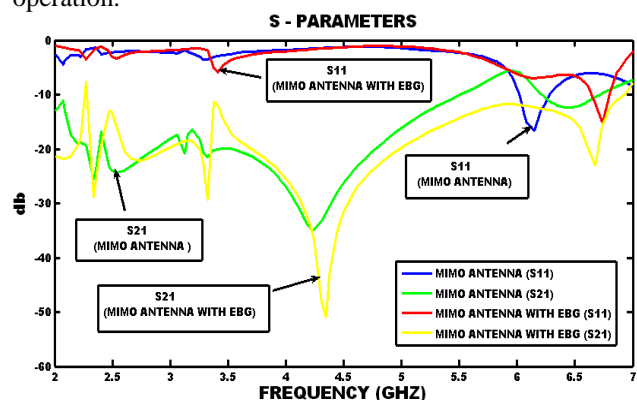


Fig 2: S-parameters ( $S_{11}$  and  $S_{21}$ ) vs. Frequency

The above graph shows the comparison of  $S_{11}$  and  $S_{21}$  characteristics of MIMO antenna with EBG and the referred MIMO antenna (Qing-Xin Chu *et al*, 2012). The proposed antenna worked in various frequency bands which is shown by fine frequency dips in the above

graphs. The values of  $S_{11}$  and  $S_{21}$  characteristics against these frequencies dip are shown in the below table.

**(ii) Directivity** - As we know that it is the ability of an antenna to focus energy in a particular direction when transmitting, or to receive energy better from a particular direction. Fig. 3 depicts the variations of antenna directivity characteristics of the proposed antenna and the referred MIMO antenna with frequency respectively.

From the below graph, it is calculated that the directivity of the proposed antenna is above 6.6 dBi over a frequency band 3-3.5 GHz and 6 GHz, respectively. Also the Directivity (D) of proposed MIMO antenna with EBG structure is increased by 0.487% against the referred MIMO antenna and by 0.487 % against the MIMO antenna with Air gap respectively over a frequency band of 3-3.5 GHz.

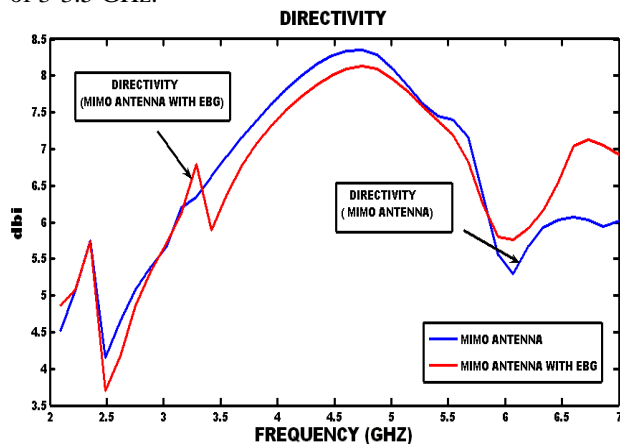


Fig 3: Directivity vs. Frequency

**(iii) Gain** - The gain is an actual quantity, which is always less than the directivity. We are only interested in the maximum gain, which is the gain in the direction in which the antenna is radiating most of the power. Fig 4 depicts the variations of antenna gain characteristics of the proposed antenna and the referred MIMO antenna with frequency respectively.

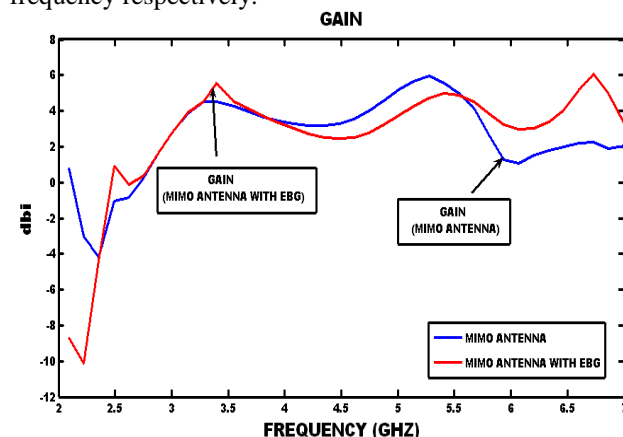


Fig 4: Gain vs. Frequency

The proposed antenna has a gain above 5 dBi over a frequency band 3-3.5 GHz and 6.5 GHz respectively which we have calculated from the above graph. And also the Gain (G) of proposed antenna is increased by 12.88%

against the referred MIMO antenna and by 5.583 % against the MIMO antenna with Air gap respectively over a frequency band of 3-3.5 GHz.

**(iv) Efficiency** - The antenna efficiency (or radiation efficiency) can be written as the ratio of the radiated power to the input power of the antenna. Fig 5(a) depicts the variations of antenna efficiency characteristics of the proposed antenna and the referred MIMO antenna with frequency respectively. The proposed antenna has an antenna efficiency of 83.16 % and 74.92 % over a frequency band 3-3.5GHz and 6 GHz, respectively which is calculated from the below graph.

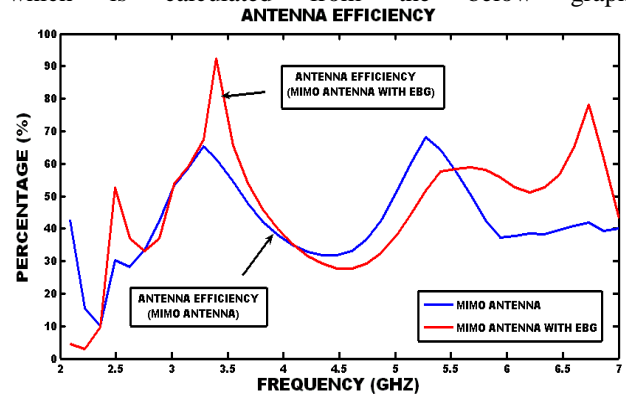


Fig 5(a) Antenna Efficiency vs. Frequency

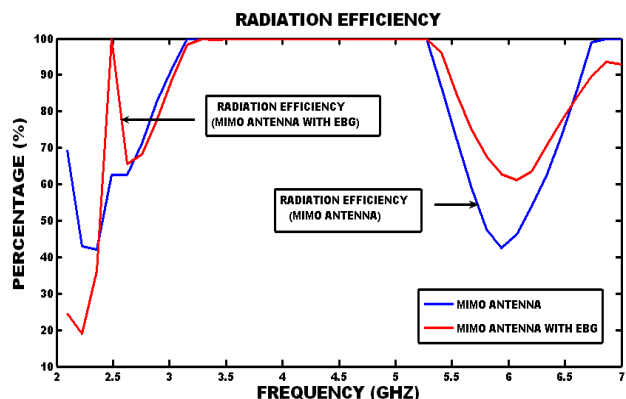


Fig 5(b) Radiation Efficiency vs. Frequency

Fig 5(b) depicts variations of radiation efficiency characteristics with frequency. The proposed antenna has a radiation efficiency of 100% over both frequency band 3-3.5 GHz and 6 GHz, respectively which cover 2.5/3.5/5.5-GHz Wi-MAX and the lower UWB band (3.1–4.8 GHz) operation. And in reference to the other antenna's ( MIMO antenna and MIMO antenna with Air gap) the radiation efficiency (RE) of proposed antenna is same ( 100 % ) over a frequency band of 3- 3.5 GHz.

#### (A) MIMO Antenna with EBG Structure

Table 1 show the variations of different performance parameters (directivity, gain, antenna efficiency, radiation efficiency) with respect to frequency and we have noted these variations from the above graphs.

Table 1: MIMO Antenna with EBG Structure

S. No.	f (GHz)	S <sub>11</sub> (dB)	D (dBi)	G (dBi)	AE (%)	RE (%)
1	2.303	-3.096	5.215	-3.115	15.04	34.91
2	2.504	-3.294	3.750	1.218	57.63	86.34
<b>3</b>	<b>3.388</b>	<b>-5.785</b>	<b>6.596</b>	<b>5.125</b>	<b>83.16</b>	<b>100</b>
4	6.137	-6.948	5.839	2.981	51.78	61.99
<b>5</b>	<b>6.738</b>	<b>-14.246</b>	<b>7.187</b>	<b>5.936</b>	<b>74.92</b>	<b>81.15</b>

The above table of proposed antenna shows a high bandwidth with  $S_{11} \leq -10$  dB and  $S_{21} \leq -18$  dB from 2.303-6.738 GHz covering the following bands: 2.4/5.2/5.8-GHz WLAN, 2.5/3.5/5.5-GHz Wi-MAX and the lower UWB band (3.1–4.8 GHz) operation. In above table the bold portion shows much improvement in performance parameters over frequency band 3 – 3.5 GHz and above 6 GHz when compared to the referred MIMO antenna and the MIMO antenna with air gap.

#### (B) MIMO Antenna with Air-Gap OF 0.01 mm from Ground Plate

This table show the readings or variations of different performance parameters (directivity, gain, antenna efficiency, radiation efficiency) with respect to frequency and we have noted these variations from the graphs for our own interest which we get after simulation of MIMO antenna with air gap ( 0.01mm ) geometry. This geometry is simulated to check whether the performance parameters of referred MIMO antenna are increased or not. The results shows slight improvements in all the parameters.

Table2: MIMO Antenna with Air-gap

S. No.	f(GHz)	S <sub>11</sub> (dB)	D(dBi)	G(dBi)	AE (%)	RE (%)
1	2.11	-4.981	4.637	2.923	55.14	68.78
2	2.249	-3.424	5.129	-2.906	15.96	42.48
3	2.431	-2.471	4.758	-2.206	44.9	88.62
4	3.154	-2.536	5.857	3.61	60.61	96.45
<b>5</b>	<b>3.326</b>	<b>-3.306</b>	<b>6.564</b>	<b>4.854</b>	<b>64.7</b>	<b>100</b>
6	6.143	-14.991	5.457	1.341	38.9	51.48

The above table of MIMO antenna with air gap shows a high bandwidth with  $S_{11} \leq -10$ dB and  $S_{21} \leq -18$  dB from 2.110 to 6.143 GHz covering the following bands: 2.4/5.2/5.8-GHz WLAN, 2.5/3.5/5.5-GHz Wi-MAX and the lower UWB band (3.1–4.8 GHz) operation. In above table the bold portion shows the improvement in performance parameters of the MIMO antenna with air gap over frequency band 3-3.5 GHZ when compared to the referred MIMO antenna.

#### (C) MIMO Antenna

Table 3 show the readings or variations of different performance parameters with respect to frequency and we have noted these variations from the above graphs.

The below table of MIMO antenna shows a high bandwidth with  $S_{11} \leq -10$  dB and  $S_{21} \leq -18$  dB from 2.114 to 6.137 GHz covering the following bands: 2.4/5.2/5.8-GHz WLAN, 2.5/3.5/5.5-GHz Wi-MAX and the lower UWB band (3.1–4.8 GHz) operation. In above table the bold portion shows the best performance parameters over frequency band 3-3.5 GHz.

Antenna efficiency (AE) of MIMO antenna with EBG is increased by 28.61% against the referred MIMO antenna and 28.53 % against the MIMO antenna with Air gap respectively over a frequency band of 3-3.5 GHz.

Table3: MIMO Antenna

S. No.	f (GHz)	S <sub>11</sub> (dB)	D (dBi)	G (dBi)	AE (%)	RE (%)
1	2.114	-11.430	4.733	-2.301	23.43	54.25
2	2.249	-3.389	5.288	-3.118	14.68	41.77
3	2.413	-2.481	3.847	0.887	51.25	96.51
4	3.099	-2.361	6.034	3.077	51.06	97.81
<b>5</b>	<b>3.321</b>	<b>-3.479</b>	<b>6.423</b>	<b>4.540</b>	<b>64.66</b>	<b>100</b>
6	6.137	-16.834	5.449	1.270	38.20	49.73

From the above tables we can say that between 3 to 3.5 GHz and above 6 GHz frequency, the performance parameters of MIMO with EBG show great improvement compare to the other two antennas (MIMO antenna with air-gap and referred MIMO antenna).

#### Conclusion

A compact efficient MIMO antenna with EBG structure has been investigated and also the comparison of performance parameters of the proposed antenna with the MIMO antenna with Air gap and the MIMO antenna (Qing-Xin Chu *et al*, 2012) are studied. A high bandwidth with  $S_{11} \leq -10$ dB and  $S_{21} \leq -18$ dB from 2.303 to 6.738 GHz is achieved, which covers 2.4/5.2/5.8-GHz WLAN, 2.5/3.5/5.5-GHz Wi-MAX and the lower UWB band (3.1–4.8GHz) operation. The comparison of calculated results from the graphs and tables shows that the performance parameters of the proposed antenna are increasing to a great extent. The MIMO antenna with air gap shows slight improvement in the performance parameters when compared to the referred MIMO antenna. As we have also seen in this paper that EBG techniques are used to enhance the impedance bandwidth, increase gain, increase efficiency and reduces the effective size of the antenna.

#### References

Qing-Xin Chu, Tian-Gui Huang, Jian-Feng Li (2012), Compact wideband MIMO antenna with two novel bent slits, *IEEE Trans on Antennas and Propag*, Vol. 60, No. 2.

- T. Bolin, A. Derneryd, G. Kristensson, V. Plicanic, and Z. Ying (2005), Two-antenna receive diversity performance in indoor environment, *Electron Lett*, Vol. 41, No. 2, pp. 1205–1206.
- Youngki Lee, Deukhyeon Ga and Jaehoon Choi (2012), Design of a MIMO Antenna with Improved Isolation Using MNG Metamaterial, *International Journal of Antennas and Propagation*, Article ID 864306, 7 pages, doi:10.1155/2012/864306.
- Cheng Yang, Yuan Yao, Junsheng Yu and Xiaodong Chen (2012), Novel Compact Multiband MIMO Antenna for Mobile Terminal, *International Journal of Antennas and Propagation*, Article ID 691681, 9 pages, doi:10.1155/2012/691681.
- R.B. Waterhouse and D. Novak (June 2000), A Small Electromagnetic Band-gap Structure, *IEEE Proceedings-International Microwave Symposium*.
- N. S. Raghava and Asok De (2006), Photonic Band-gap Stacked Rectangular Microstrip Antenna for Road Vehicle Communication, *IEEE Antennas and Wireless Propagation Letters*, Vol. 5, pp. 421–423.
- K. Payandehjoo and R. Abhari (2009), Employing EBG Structures in Multiantenna Systems for Improving Isolation and Diversity Gain, *IEEE Antennas and Wireless Propagation Letters*, Vol. 8, pp. 1162–1165.
- Zeland IE3D 14.1 software which work on method of moments (MOM).

## Research Article

## A Compact Efficient Yagi-Uda Patch Antenna with EBG Structure

Arjun Singh<sup>a\*</sup> and Taimoor Khan<sup>b</sup><sup>a</sup>Department of ECE, ABSS Institute of Technology, Meerut-250001<sup>b</sup>Department of ECE, Delhi Technological University, Delhi

Accepted 5 July 2013, Available online 01 August 2013, Vol.3, No.3 (August 2013)

### Abstract

The paper describes a design of planar three-element Yagi-Uda antenna for 1-3 GHz band. The structure has been optimized for a maximum directivity and maximum gain and other performance parameter by include the air gap of 1.5cm and simulated by IE3D Software. This Yagi antenna consisted of the driven element, a reflecting element and a directing element. We measured the gain of the purposed antenna is 5.8dB.

**Keywords:** Yagi-Uda antenna, Directivity, Gain, Antenna Efficiency, Radiation Efficiency.

### 1. Introduction

Antennas are devices that transmit or receive electromagnetic waves. If an antenna is receiving a signal it converts the incident electromagnetic waves into electrical currents; if it is transmitting it does the opposite. Antennas are designed to radiate (or receive) electromagnetic energy with particular radiation and polarization properties suited for its specific application. The Yagi-Uda antenna is basically an arrangement of dipoles in such a way that the whole system provides a directional antenna beam in desired direction. That's why some times it is called a directional antenna system. The Yagi antenna's overall basic design consists of a resonant fed dipole (John D. Kraus et al,1997) (the fed dipole is the driven element). The Yagi-Uda antennas are directional along the axis perpendicular to the dipole in the plane of the elements, from the reflector toward the driven element and the director(s). Typical spacing's between elements vary from about 1/10 to 1/4 of a wavelength, depending on the specific design. The lengths of the directors are smaller than that of the driven element, which is smaller than that of the reflector(s) according to an elaborate design procedure. These elements are usually parallel in one plane, supported on a single crossbar known as a boom. The Yagi antenna is a directional antenna which consists of a dipole and several parasitic elements. The parasitic elements in a Yagi antenna are the reflectors and the directors. A Yagi antenna typically has only one reflector which is slightly longer than the driving element (dipole) and several directors, which are slightly shorter than the driving element. The Yagi antenna is said to be directional because it radiates power in one direction allowing it to

transmit and receive signals with less interference in that particular direction. Figure 1 is a diagram of the general configuration of a Yagi antenna.

**The driven element** of a Yagi-Uda patch is the feed point where the feed line is attached from the transmitter to the Yagi to perform the transfer the power from the transmitter to the antenna. A dipole driven element will be resonant when its electrical length is  $\frac{1}{2}$  of the wavelength of the frequency applied to its feed point (Sun, B.H et al,2009). The feed point is on the center of the driven element. **The directors** are the shortest of the parasitic element and this end of the Yagi is aimed at the receiving station. It is resonant slightly higher in frequency than the driven element, and its length will be about 5% shorter, progressively than the driven element. The length of directors can vary depending upon the director spacing. The numbers of directors that can (length) of the supporting boom needed by the used are determined by the physical size design. The directors are used to provide the antenna directional pattern with gain. The amount of gain is directly proportional to the length of the antenna array not by the number of directors used. The spacing of the directors can range from 0.1 to 0.5 wavelengths or more and will depend largely up on the design specification of the antenna (Balanis, C.A et al,1997). **The reflector** is the element that is placed at the rear of the driven element (The dipole). Its resonant frequency is lower, and its length is approximately 5% longer than the driven element. Its length will vary depending on the spacing and the element diameter. The spacing of the reflector will be between 0.1 wavelengths and 0.25 wavelengths (H. Yagi et al,1928). Its spacing will depend upon the gain, bandwidth forward/backward ratio, and side lobe pattern requirements of the final antenna design. The length and

\*Corresponding author: Arjun Singh



spacing between the elements which we are taken to design the antenna are shown in the Table 1.

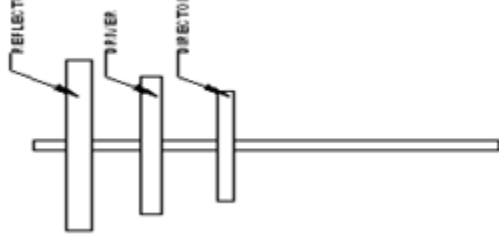


Figure 1: Proposed Yagi-Uda Patch Antenna

## 2. Proposed YAGI-UDA Patch Antenna

Table 1: Length and spacing between the elements

Element	Length	Separation
Reflector	$0.55\lambda$	$0.1\lambda$
Driver	$0.50\lambda$	$0.1\lambda$
Directors	$0.45\lambda, 0.40\lambda, 0.35\lambda$	$0.1\lambda$

The dimensions of the purposed Yagi antenna are illustrated in Figure 2. First we design the ground plane. The dimension of is (14.15\*14.15 cm). Then above the ground plane we include 1.5cm air gap and above the air gap we design EBG (electromagnetic band gap). EBG is of mushroom-type. Dielectric layer (3.27) is positioned between the lower surface of the antenna and upper part of the EBG. The thickness of the EBG plane is 0.77 cm. The three compact Yagi-Uda antenna is designed first for 1.6 GHz in free space. A driver is fitted on the centre of the patch. The distance between the driver and the director is 0.61 cm and the distance between the driver and the reflector is 0.54 cm. The EBG ground plane is designed with procedure similar to (J. M. Bell et al,2004). Both Yagi and EBG structure, including patches, columns, and the bottom ground plane, are made of copper.

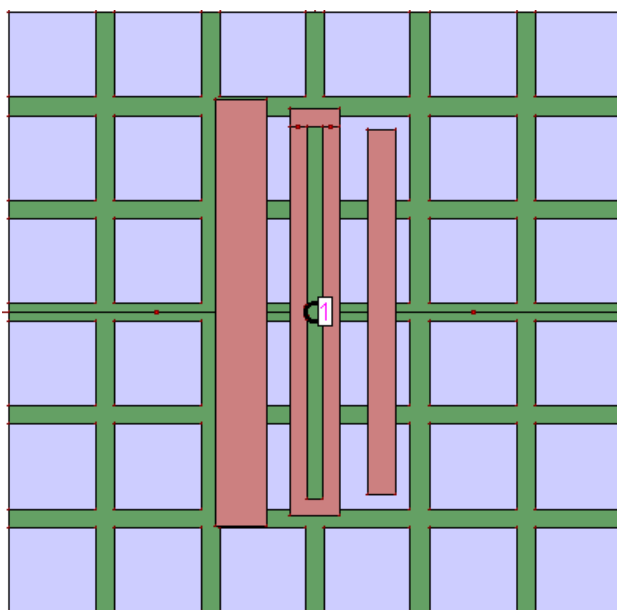


Figure 2(a): Compact-Efficient Yagi-Uda Antenna

The dimensions of three elements of compact Yagi-Uda antenna are shown in the above Figure2 (b).

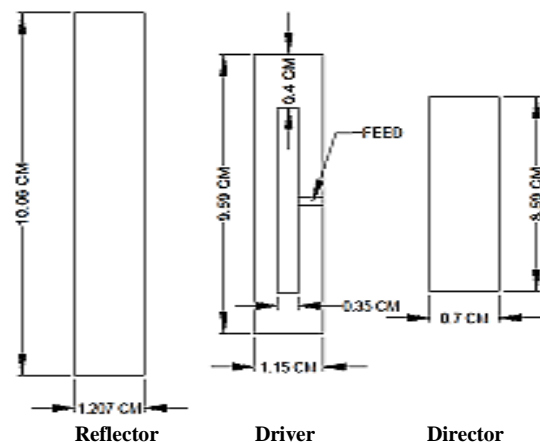


Figure 2(b) Elements of Yagi Antenna

## 3. Simulated Results and Comparisons

The proposed Yagi-Uda antenna with EBG and with air gap structure shown in Fig. 2 and it has been studied and simulated. Similarly other geometries with difference air gap simulated and we get best results in 1.5cm air gap. The results show that the performance parameters of Yagi-Uda antenna with EBG with air gap structure is better include air gap. The  $S_{11} < -20\text{dB}$  from 2-3 GHz.

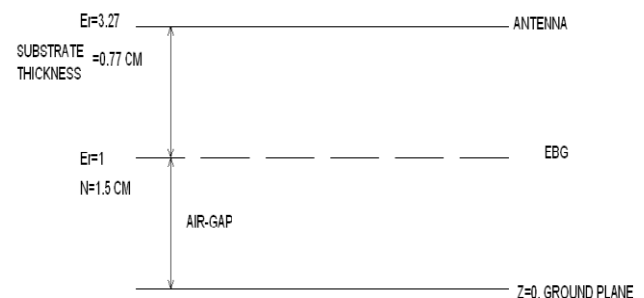


Figure 2 (c): Side View of antennal layer

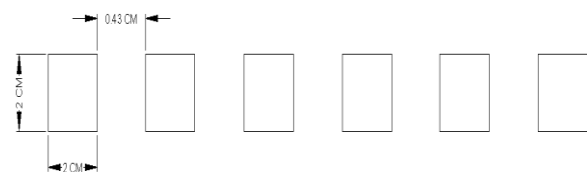


Figure 2(d) Side view of EBG

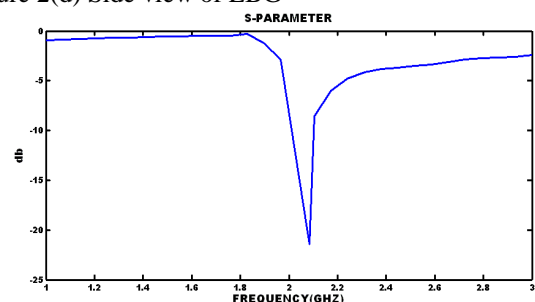


Figure 3: Frequency vs  $S_{11}$  Parameter.

**(i) S-parameters-** S-parameters describe the input-output relationship between ports (or terminals) in an electrical system. For instance, if we have a communication system with two radios (radio 1 and radio 2), then the radio terminals (which deliver power to the two antennas) would be the two ports.  $S_{11}$  then would be the reflected power radio 1 is trying to deliver to antenna 1.  $S_{22}$  would be the reflected power radio 2 is attempting to deliver to antenna 2. And  $S_{12}$  is the power from radio 2 that is delivered through antenna 1 to radio 1. Note that in general S-parameters are a function of frequency (i.e. vary with frequency).  $S_{21}$  represents the power received at antenna 2 relative to the power input to antenna 1. The most commonly quoted parameter in regards to antennas is  $S_{11}$ .  $S_{11}$  represents how much power is reflected from the antenna, and hence is known as the **reflection coefficient** (sometimes written as gamma or return loss). If  $S_{11} = 0$  dB, then all the power is reflected from the antenna and nothing is radiated. If  $S_{11} = -10$  dB, this implies that if 3 dB of power is delivered to the antenna, -7 dB is the reflected power.

**(ii) Directivity:** The **directivity** is a fundamental antenna parameter. It is a measure of how 'directional' an antenna's radiation pattern is. An antenna that radiates equally in all directions would have effectively zero directionality, and the directivity of this type of antenna would be 1 (or 0 dB). Directivity is the ability of an antenna to focus energy in a particular direction when transmitting, or to receive energy better from a particular direction when receiving. In a static situation, it is possible to use the antenna directivity to concentrate the radiation beam in the wanted direction. However in a dynamic system where the transceiver is not fixed, the antenna should radiate equally in all directions, and this is known as an Omni-directional antenna.

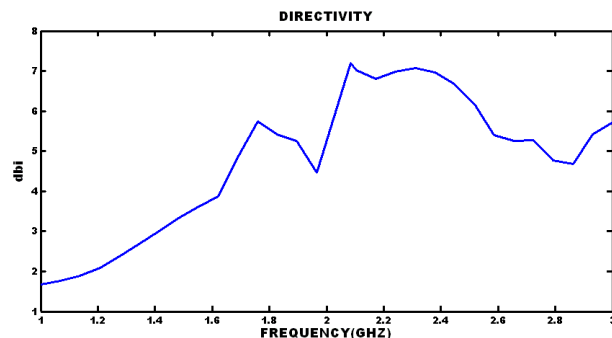


Figure 4: Field directivity vs frequency.

**(iii) Gain:** Gain is not a quantity which can be defined in terms of a physical quantity such as the Watt or the Ohm, but it is a dimensionless ratio. Gain is given in reference to a standard antenna. The gain of an antenna in a given direction is the amount of energy radiated in that direction compared to the energy an isotropic antenna would radiate in the same direction when driven with the same input power. Usually we are only interested in the maximum gain, which is the gain in the direction in which the antenna is radiating most of the power. An antenna gain of 3 dB compared to an isotropic antenna would be written as 3 dBi. The method of measuring gain by comparing the

antenna under test against a known standard antenna (isotropic antenna), which has a calibrated gain.

**(iv) Efficiency:** The **efficiency** of an antenna relates the power delivered to the antenna and the power radiated or dissipated within the antenna. A high efficiency antenna has most of the power present at the antenna's input radiated away. A low efficiency antenna has most of the power absorbed as losses within the antenna, or reflected away due to impedance mismatch.

**Conclusion:** The paper describes a design of planar three-element Yagi-Uda antenna for 1-3 GHz band. The structure has been optimized for a maximum directivity and maximum gain and other performance parameter by include the air gap of 1.5cm and simulated by IE3D Software. This Yagi antenna consisted of the driven element, a reflecting element and a directing element. We simulated the gain of the purposed antenna is 5.8dB.

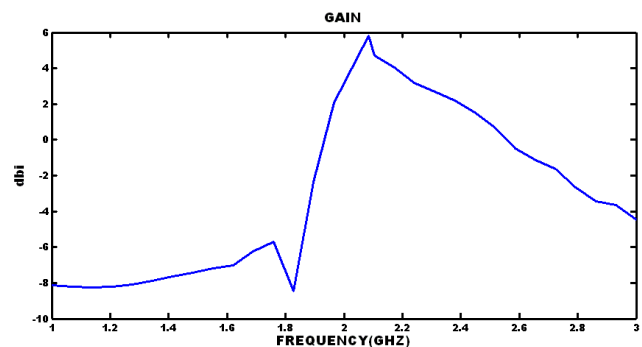


Figure 5: Total Field gain vs. Frequency

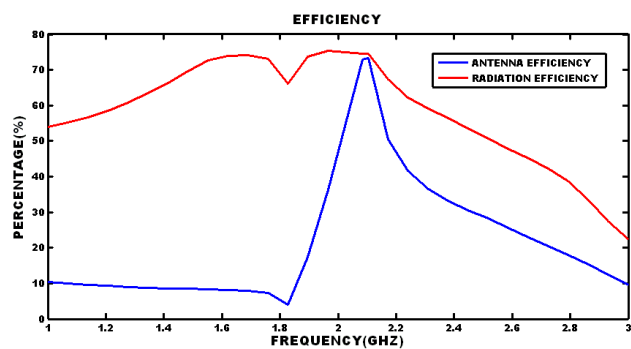


Figure 6: Efficiency vs. Frequency

This table show the variations of different performance parameters (directivity, gain, antenna efficiency, radiation efficiency) with respect to frequency and we have noted these variations from the above graphs

Table 2: Performance parameter

Parameter	Simulated Results
Frequency (GHz)	2.083
$ S_{11} $ (dB)	-21.42
Directivity (dBi)	7.19
Gain (dBi)	5.8
Antenna efficiency (%)	72.92
Radiation efficiency (%)	74



The above table of proposed antenna shows a bandwidth of 96 % with  $S_{11} \leq -21$  dB from 1 to 3 GHz. In above table shows much improvement in performance parameters over frequency band 1 – 3 GHz. In the table shows the best results of proposed antenna at frequency of 2.083GHz.

## References

- John D. Kraus(1997), Yagi-Uda Antennas, Second Edition, pp. 621, 1997.
- Sun, B.H., S.G Zhou, Y. Fwei, and Q.-Z Liu (2009), Modified two elements and Yagi-uda-antenna with tunable beams with tunable beams progress, *Progress in Electromagnetic Research*, Vol. 16, pp.406-419.
- Balanis, C.A. (June 1928), Antenna Theory, Analysis and Design, 2<sup>nd</sup> edition, *John Wiley & Sons, Inc.*, pp. 468.
- H. Yagi (June 1928), Beam Transmission of ultra short waves *proceeding of the IRE* vol. 16, pp. 715-740.
- J. M. Bell and M. F. Iskander (2004), A low-profile Archimedean spiral antenna using an EBG ground plane, *IEEE Antennas Wireless Propag. Lett.*, Vol. 3, pp. 223-226.

## Research Article

# A Compact MIMO Antenna with DGS Structure

Prabhat Sharma<sup>a\*</sup> and Taimoor Khan<sup>b</sup>
<sup>a</sup>Department of ECE, Asian institute of Management & Technology, Yamuna Nagar

<sup>b</sup>Department of ECE, Delhi Technological University, Delhi

Accepted 5 July 2013, Available online 01 August 2013, Vol.3, No.3 (August 2013)

## Abstract

In this paper, a compact MIMO antenna with DGS (defective ground surface) is proposed. The proposed DGS of Rectangular shape is placed in ground plane. It's offer a mechanism to improve antenna performance, reduce antenna size and reduce antenna to antenna coupling on platforms. In this way, the performance parameters of MIMO antennas can be further improved. The concept of DGS is also used to collectively enhance the impedance bandwidth of antenna. A high bandwidth is achieved with  $S_{11} \leq -10\text{dB}$  and  $S_{21} \leq -18\text{dB}$  from 2.057 to 6.140 GHz is achieved. The analysis has been done by using IE3D software based on method of moments (MOM). In this paper we also introduced the comparison of performance parameters of two antennas proposed MIMO antenna with DGS structure with MIMO antenna using IE3D software.

**Keywords:** Defective ground structure (DGS), MIMO Antenna, Directivity, Gain, Antenna Efficiency, Radiation Efficiency.

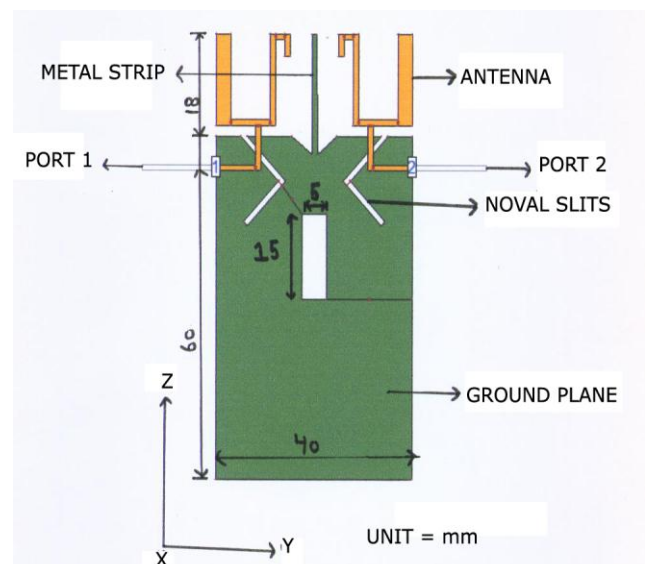
## 1. Introduction

Multiple-input-multiple-output (MIMO) technology has attracted attention in modern wireless communication systems. A significant increase in channel capacity is achieved without the need of additional bandwidth or transmits power by deploying multiple antennas for transmission to achieve an array gain and diversity gain, thereby improving the spectral efficiency and reliability. MIMO antenna (Qing-Xin Chu *et al*, 2012) systems require high decoupling between antenna ports and a compact size for application in portable devices. Many methods have been proposed for reducing mutual coupling between the antennas. Various structures are introduced in the ground plane to achieve low mutual coupling. Low mutual coupling can also be achieved it has been found that mushroom-like EBG structures reduce the mutual coupling by suppressing surface wave propagations.

Recently, **Defected Ground Structures** (DGS) (Ashwini K. Arya *et al*, 2010) are introduced to improve antenna performance characteristics like size reduction, gain and bandwidth enhancement, and it is also used in reduction of mutual coupling between antenna elements. In this paper, a single rectangular-shaped DGS (L. H. Weng *et al*, 2008) is introduced in the ground plane of a compact MIMO antenna system; the rectangular shape enhances the isolation and improves the antenna parameters. The Directivity, Gain, Antenna Efficiency and Radiation Efficiency are calculated to evaluate the

performance parameters of the proposed MIMO antenna with DGS structure. In this paper comparison of performance parameters of the MIMO Antenna (referred) and the MIMO antenna with DGS structure are discussed.

## 2. Proposed MIMO Antenna with DGS Structure

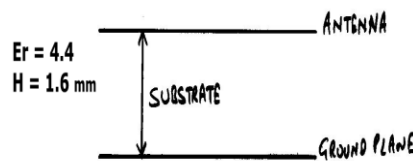


(a) Top-view

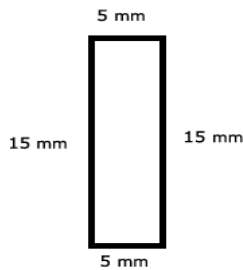
The geometry of the proposed MIMO antenna with DGS is illustrated in Fig.1. The MIMO antenna with DGS consists of two symmetric dual-branch monopoles. A DGS

\*Corresponding author: Prabhat Sharma

is printed on the upper part of a partially grounded FR4 substrate with dimensions 78mm\*40mm\* 1.6mm and relative permittivity 4.4 and there is also an air gap of 0.4 between ground plane and DGS. Here we inserted a rectangular shape DGS in length and width (5mm\*15mm)



(b) Side-view



(c) DGS of rectangle shape

Fig 1: Proposed MIMO Antenna with DGS

is illustrated in fig c. On the back surface of the substrate, the main rectangular ground plane of 40 mm in width and 60 mm in length is printed. Here we try the many shapes of DGS i.e. circle, triangle in the mid of ground plane but we get the best result in rectangular shape.

### 3. Working Mechanism of Proposed Antenna

The proposed MIMO antenna with DGS structure as shown in Fig1 has been simulated and studied to a good agreement using IE3D software. From the calculated graphs and tables we can say that the performance parameters of MIMO with DGS structure shows much improvement as compare to MIMO antenna. Between 3 to 3.5 GHz and above 6 GHz frequency, the performance parameters of proposed antenna shows great improvement which are as follows.

#### Performance Parameters of MIMO Antenna with DGS Structure

(i) **S-parameters**-S-parameters describe the input-output relationship between ports (or terminals) in an electrical system.  $S_{11}$  represents how much power is reflected from the antenna, and hence is known as the **reflection coefficient** (sometimes written as gamma or **return loss**). If  $S_{11} = -10$  dB, this implies that if 3 dB of power is delivered to the antenna, -7 dB is the reflected power.

Fig 2 depicts the return loss ( $S_{11}$ ) characteristics of the proposed antenna and also shows a high bandwidth with  $S_{11} \leq -10$  dB and  $S_{21} \leq -18$  dB from 2.057 to 6.140 GHz.

(ii) **Directivity**- Directivity is the ability of an antenna to focus energy in a particular direction when transmitting, or

to receive energy better from a particular direction. It is defined as a ratio of the max. Radiation intensity in a given direction from the antenna to the radiation intensity averaged over all directions.

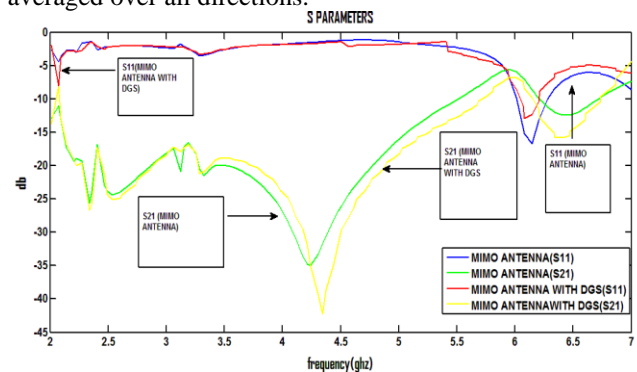


Fig 2: S parameters Graph

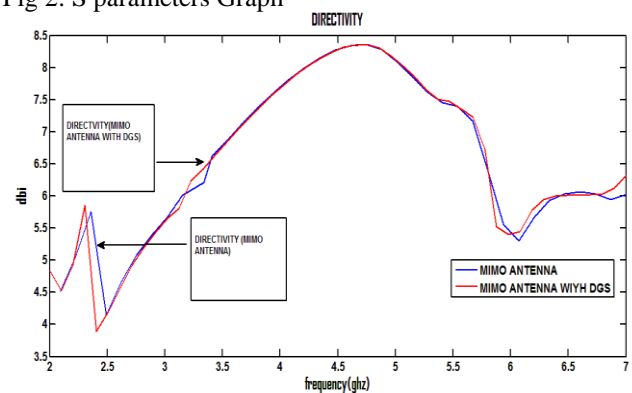


Fig 3: Directivity Graph

Fig. 3 depicts variations of antenna directivity characteristics with frequency. The proposed antenna has a directivity of 6.427 dBi over a frequency band 3.33-3.5 GHz which covers the lower UWB band (3.1-4.8 GHz) operation. Also the Directivity of proposed MIMO antenna with DGS structure is increased by 0.4% against the MIMO Antenna.

(iii) **Gain**- The gain of an antenna in a given direction is the amount of energy radiated in that direction compared to the energy an isotropic antenna would radiate in the same direction when driven with the same input power. An antenna gain of 3 dB compared to an isotropic antenna would be written as 3 dBi.

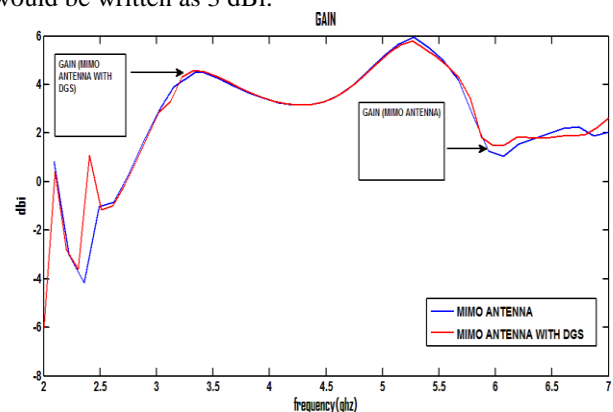


Fig 4: Gain Graph

Fig.4 depicts variations of antenna gain characteristics with frequency. The proposed antenna has a gain of 4.583dBi over a frequency band 3-3.5 GHz which covers the lower UWB band (3.1-4.8 GHz) operation, also the GAIN of proposed MIMO Antenna with DGS structure is increased by 4.3% against the MIMO Antenna.

(iv) **Efficiency**- The efficiency of an antenna relates the power delivered to the antenna and the power radiated or dissipated within the antenna.

Figs. 5 & 6, depict variations of efficiency (antenna efficiency, radiation efficiency) characteristics with frequency. The proposed antenna has an antenna efficiency of 64.68 % and 100 % over a frequency band 3-3.5 GHz, Also the Antenna efficiency of proposed MIMO antenna with DGS structure is increased by 28% against the MIMO Antenna and radiation efficiency is same as of MIMO Antenna.

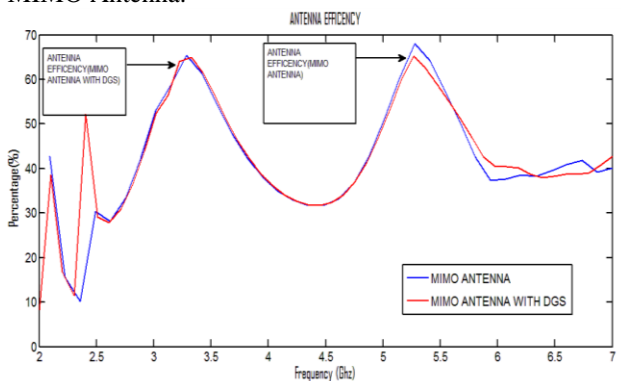


Fig 5: Antenna Efficiency Graph

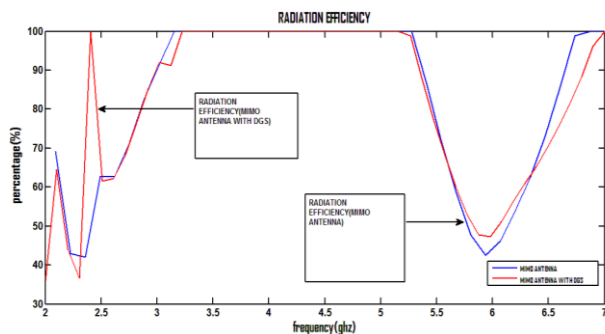


Fig 6: Radiation Efficiency Graph

#### 4. Simulated Result and Comparison

Table 1 show the readings or variations of different performance parameters (directivity, gain, antenna efficiency, radiation efficiency) with respect to frequency and we have noted these variations from the above graphs.

The below table of proposed antenna shows a high bandwidth with  $S_{11} \leq -10$  dB and  $S_{21} \leq -18$  dB from 2.057 to 6.140 GHz. In above table the bold portion shows good

improvement in performance parameters of MIMO Antenna with DGS as compare to MIMO Antenna over frequency band 3-3.5 GHz and above 6 GHz when compared to the MIMO Antenna.

Table 1: MIMO Antenna with DGS

f(GHz)	$S_{11}$ (dB)	G(dBi)	D(dBi)	A (%)	R (%)
2.057	-7.942	-2.437	4.66	25.20	51.90
2.25	-3.516	-3.191	5.37	14.17	40.36
2.40	-2.458	1.050	4.026	52.051	99.62
3.17	-1.976	3.253	6.005	60.56	95.36
3.30	-3.416	4.47	6.38	64.73	100
<b>3.33</b>	<b>-3.429</b>	<b>4.583</b>	<b>6.427</b>	<b>64.68</b>	<b>100</b>
5.960	-6.894	1.33	5.417	40.46	47.37
6.140	-14.37	1.59	5.66	39.97	54.136

#### 5. Conclusion

A compact MIMO antenna with DGS structure has been investigated and also the comparison of performance parameters of the proposed antenna with the MIMO antenna (referred) is studied. This comparison of calculated results of all geometries shows that the performance parameters of proposed antenna are much better than the MIMO antenna (Qing-Xin Chu *et al*, 2012). DGS geometry is used to increase the directivity gain by preventing coupling between two antennas. Defected Ground Structures (DGS) are introduced to improve antenna performance characteristics like size reduction, gain and bandwidth enhancement, and it is also used in reduction of mutual coupling between antenna elements. In this proposed paper we enhanced all the performance parameters (directivity, gain, antenna efficiency, radiation efficiency) of MIMO antenna by using a DGS structure of rectangular shape. As we have seen in this paper that DGS technique is used to enhance the bandwidth, increase gain, increase efficiency and reduces the effective size of the antenna.

#### References:

- Qing-Xin Chu , Tian - Gui Huang , Jian - Feng Li (Feb 2012) Compact Wideband MIMO Antenna with two novel bent slits *IEEE Trans. on Antennas and Propag*, vol. 60, no. 2.
- Ashwini K. Arya, M. V. Kartikeyan, A. Patnaik (Oct 2010), Defected Ground Structure in the perspective of Microstrip antenna, *Frequenz*, Vol.64, Issue5-6, pp.79-84.
- L. H. Weng, . C. Guo, X.W. Shi , X. Q. Chen (July 2008), An overview on defected ground structure, *Progress in electromagnetic Research B*, Vol.7, pp.173-189.
- W. L. Stutz man and G. A. Thiele (1998), Antenna Theory and design , second edition *John Wiley & Sons*, pp.172-173.
- C. A. Balanis (1997), Antenna Theory: Analysis and Synthesis, Second Edition, *John Wiley & Sons*.



Contents lists available at SciVerse ScienceDirect

Applied Soft Computing

journal homepage: [www.elsevier.com/locate/asoc](http://www.elsevier.com/locate/asoc)



# Biogeography and geo-sciences based land cover feature extraction

q1 Lavika Goel<sup>a,\*</sup>, Daya Gupta<sup>a</sup>, V.K. Panchal<sup>b</sup>

<sup>a</sup> Delhi Technological University (DTU), Computer Engineering Department, Delhi 110042, India

<sup>b</sup> Defense & Terrain Research Laboratory, DRDO, Delhi, India

## ARTICLE INFO

### Article history:

Received 16 December 2012

Received in revised form 3 June 2013

Accepted 22 June 2013

Available online xxx

### Keywords:

Remote sensing

Geo-sciences

Biogeography

Entropy

## ABSTRACT

This work proposes a biogeography and geo-sciences based soft computing technique which is an extension of original biogeography based feature extraction algorithm using the concept of entropy inspired from the geo-sciences phenomenon of mantle convection and dynamics of the earth. This algorithm uses surface entropy in the relevant band of multi-spectral images as the basis of calculating the habitat suitability index which in turn forms the basis of identifying different terrain features in the satellite image. The proposed work has been primarily developed for the purpose of finding the applications of geo-sciences in developing computationally intelligent models. This may lead to another concept of process randomization, generation of virtual scenarios, etc. which are important ingredients in battlefield assessment. The proposed feature extractor algorithm has been applied on the datasets of Alwar region in Rajasthan and Patalganga area in Shivalik ranges. The results indicate that our proposed geo-sciences based classifier is highly efficient in extracting land cover features. Further when integrated with hybrid bio-inspired intelligent classifier proposed in our previous work, it improves its classification efficiency and outperforms the earlier probabilistic classifiers, recent soft computing classifiers such as membrane computing, hybrid FPAB/BBO, extended non-linear BBO, etc. and the very recent hybrid ACO2/PSO/BBO classifier proposed by us [19,24]. In order to explore the benefits of modifying the original BBO by incorporating the geo-sciences concepts, we compare the performance of our proposed biogeography and geo-sciences model with the original BBO and seven other population-based optimization methods of ACO, DE, ES, GA, PBIL, PSO and SGA on the set of 14 standard benchmark functions that are generally used to test the effectiveness of an evolutionary algorithm [30,33,53]. Our results conclude that the classifier based on our proposed model is the best known classifier developed till date. The proposed model is flexible and can adapt itself to suit to a large number of classification problems including mixed pixel resolution, face recognition, pattern recognition, etc. whereby entropy can be simply calculated in any other band or according to its standard definition and hence feature extraction can be made.

© 2013 Published by Elsevier B.V.

## 1. Introduction

Currently, many soft computing techniques like fuzzy sets, artificial neural network, rough set theory, ant colony optimization, particle swarm optimization, genetic algorithms, membrane

computing and biogeography based optimization are being used for feature extraction or image classification, ground water detection, etc. [38,39] for which satellite remote sensing has been recognized as a valuable tool that views, analyzes, characterizes and makes decisions about the environment [51,58]. Artificial neural networks can handle non-convex decisions. The use of textural features in ANN helps to resolve misclassification [2]. The rough sets were basically designed for synthesis of approximation of concepts from the acquired data [49,50]. The genetic algorithm searches a space of image processing operations for a set that can produce suitable feature planes, and a more conventional classifier which uses those feature planes to output a final classification. Fuzzy measures show the detection of textures by analyzing the image by stochastic properties. The fundamental stochastic properties of the image are isolated by different kinds of stochastic methods, by non-linear filtering and by non-parametric methods [45]. The swarm intelligence techniques of ACO [7], PSO [9] and BBO [53] and membrane computing [28] are based on the concepts of image

**Abbreviations:** ACO, ant colony optimization; BBO, biogeography based optimization; PSO, particle swarm optimization; LISS, linear imaging self scanning; RS1, Radarsat-1; RS2, Radarsat-2; DN, digital number; I, maximum immigration rate; HSI, habitat suitability index; SIV, suitability index variables; NIR, near infra red; MIR, middle infrared; DEM, digital elevation model; E, maximum emigration rate; ANN, artificial neural networks; EA, evolutionary algorithm; GA, genetic algorithm; BBO-GS, biogeography and geo-sciences based optimization; IEPPO, immunity enhanced particle swarm optimization; RCGA, real coded genetic algorithm; DE, differential evolution; PBIL, probability based incremental learning; SGA, stud genetic algorithms; ES, evolutionary strategy.

\* Corresponding author at: S-E-142A Shastri-Nagar, Ghaziabad, U.P. 201001, India. Tel.: +91 9899973105/11052141.

E-mail address: [goel.lavika@gmail.com](mailto:goel.lavika@gmail.com) (L. Goel).

1568-4946/\$ – see front matter © 2013 Published by Elsevier B.V.  
<http://dx.doi.org/10.1016/j.asoc.2013.06.015>

Please cite this article in press as: L. Goel, et al., Biogeography and geo-sciences based land cover feature extraction, Appl. Soft Comput. J. (2013), <http://dx.doi.org/10.1016/j.asoc.2013.06.015>



clustering and heuristic method implementation and are more accurate when working with low spatial resolution images. Enhanced versions of these techniques have also been used for solving various engineering problems such as the improved PSO called as the immunity enhanced particle swarm optimization (IEPSO) for damage detection [31] wherein a damage detection method based on combined data of static and modal tests using particle swarm optimization (PSO) is discussed. To improve the performance of PSO, some immune properties such as selection, receptor editing and vaccination are introduced into the basic PSO and an improved PSO algorithm is formed. The BBO technique has been adapted and modified for economic load dispatch analysis [6] to solve both convex and non-convex economic load dispatch (ELD) problems of thermal plants involving constraints such as transmission losses, ramp rate limits, valve point loading, multi-fuel options and prohibited operating zones. The GA has been modified in the form of the real coded genetic algorithm for target sensing [47] wherein an evolutionary soft-computing technique of real coded genetic algorithm is applied to solve the system of linear equations. This paper demonstrates the evolution of a new soft computing paradigm for satellite image classification using the concept of entropy inspired from the geo-sciences phenomenon of mantle convection and dynamics of the earth thereby presenting the modified version of the original biogeography based land cover feature extraction technique [46].

Our motivation is the absence of geo-sciences based approaches as contributory domains to computational intelligence. Till now, the domains like philosophy, psychology, cognition, logic and bio-sciences all have been used as contributory domains for the development of computational intelligence techniques, however, geo-sciences have never been used as applied sciences for developing a computational model. Also, the computational intelligence techniques [2] can be divided into techniques based on modelization of human mind and nature inspired intelligent techniques as the techniques that have been used till date for solving the problem of land cover feature extraction. However, it has been observed that geo-sciences which fall under the category of nature inspired intelligent techniques have never been used for the purpose. Hence, we propose a computational model inspired from the earth's dynamics as a geo-sciences based nature inspired intelligent technique which can be used to improve the original BBO technique [53] and develop an enhanced algorithm for land cover feature extraction. The proposed model is flexible to be applicable to a large number of classification problems wherein entropy can be calculated in any other band in case of applications where the dataset is terrain multi-spectral images for example, mixed pixel resolution, design of hybrid classifiers, etc. or simply formulating the entropy function according to its standard definition and evaluating the fitness function for applications where the dataset are normal images, for example, in case of face recognition application, pattern recognition, etc. Below, we summarize the main contributions of the paper:

- [1] The proposed biogeography and geo-sciences based hybrid intelligent classifier, the hybrid (BBO-GS)/ACO2/PSO, extends the taxonomy of soft computing feature extraction techniques and improves the intelligent hybrid bio-inspired classifier, the hybrid ACO2/PSO/BBO classifier, demonstrated in our previous paper [22,24] wherein the strengths of the ACO2/PSO technique were combined with the characteristic strengths of BBO.
- [2] Our proposed model uses surface entropy in DEM band as the measure for designing the fitness function. This entropy is the driving force leading to the formation of heterogeneous regions called as plates (texture analysis), similar to the convection forces in the mantle of the Earth. Hence, our classifier is able to classify the homogeneous regions (the regions with the lower entropy), more efficiently than the other hybrid classifiers

presented in our previous works [20,24]. This also validates the theory established in our paper [22] which states that the classification efficiency of biogeography based extractor on a given land cover feature is proportional to the degree of entropy for that feature.

- [3] We explore the benefits of the BBO-GS model by comparing its performance with the original BBO and seven other population-based optimization methods of ACO, DE, ES, GA, PBIL, PSO and SGA on the set of 14 standard benchmark functions wherein it is observed that the BBO-GS outperforms the standard BBO on all the benchmark functions.

The paper is organized into six sections, the section following the introduction illustrates the concepts of biogeography and geo-sciences. The third section describes the parameter settings, the hypotheses development and the proposed methodology of the biogeography and geo-sciences based feature extraction algorithm. The fourth section presents the implementation results and discussion for two different datasets. The fifth section presents the classification comparison of the results of the other recent soft computing classifiers with the proposed classifier on a standard dataset and also demonstrates the performance of our algorithm on benchmark functions to prove its effectiveness. The last section concludes and summarizes the future work.

## 2. Basics of biogeography and geo-sciences

This section presents the concepts of geo-sciences which can be adaptively applied for building the modified version of the original BBO for solving the problem of land cover feature extraction more efficiently [8,40,46].

### 2.1. Biogeography based land cover feature extraction

BBO is a population based algorithm motivated by the migration mechanisms of ecosystems. It is based on the mathematics of biogeography. In BBO, problem solutions are represented as islands, and the sharing of features between solutions is represented as emigration and immigration [53]. In BBO, each individual is considered as a habitat with a HSI [40,53], which is analogous to the fitness function of other conventional algorithms, to measure the individual fitness. Also, an SIV which characterizes the habitability of an island is used. A good solution is analogous to an island with a high HSI, and a poor solution indicates an island with a low HSI. High HSI solutions tend to share their features with low HSI solutions. Low HSI solutions accept a lot of new features from high HSI solutions [10,53]. Thus, BBO is a swarm intelligence technique based on the concept of information sharing as discussed in our paper [23]. From our paper, we know that the concepts of sharing information in BBO can be adapted to suit to the problem of land cover feature extraction where it has been mentioned that BBO is well suited for natural terrain feature elicitation application and hence we modify the original BBO and adapt it to the problem of feature extraction. Fig. 1 presents the algorithm for biogeography based land cover feature extraction [46].

### 2.2. Geo-sciences

There are two underlying concepts which form the base of the geo-sciences phenomenon, the first being the dynamics of the movement of earth's plates and the second is the crust formation [10,26,41]. We consider that it is the entropy or the degree of disorder of the earth's mantle convection which is the driving force of the mechanism of plate dynamics. Fig. 2 shows that the plate dynamics is considered as analogous to the clustering of similar pixels which is accomplished through texture analysis using rough sets

Input – Multi-spectral satellite image  
Output – Classified image  
Classify image in elementary classes using fuzzy c- means and consider them as species of the universal habitat. Consider each feature as one habitat.  
Ecosystem = Total No. of Habitats = Universal Habitat + Feature Habitat  
Define HSI,  $S_{max}$ ,  $S_{min}$ , immigration rate and emigration rate.  
Calculate HSI for each feature habitat.  
Select species from universal habitat and migrate it to one of the other habitat and recalculate HSI.  
If recalculated HSI is within threshold then absorb the species to that habitat else.  
Check for the other habitats and recalculate the HSI.  
If all species in universal habitat are checked then stop else go to step 4.

Fig. 1. Algorithm for biogeography based land cover feature extraction.

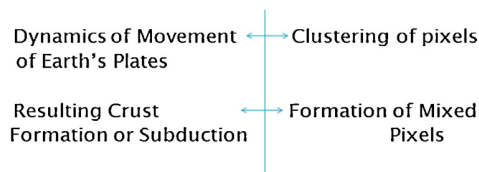


Fig. 2. Adapting the geo-sciences phenomenon of earth's dynamics for land cover feature extraction.

in our proposed algorithm and resulting crust formation is considered as analogous to the presence of mixed pixels in an input plate. Hence, the underlying concepts of geo-sciences can be adapted to integrate with the original BBO technique for feature extraction in the satellite image. This paper is an attempt to modify the original biogeography based feature extraction technique using an analogy between biogeography and geo-sciences phenomenon of earth's dynamics as shown in Fig. 3 and some of the ideas of which were first presented in our paper [21].

### 3. Biogeography and geo-sciences based land cover feature extraction

This section discusses the parameter settings, our proposed methodology and the framework of biogeography based feature extraction technique inspired from the geo-sciences concepts.

#### 3.1. Parameter settings and procedures

We in this section identify some important parameter settings and procedures adopted which comprise the preprocessing steps of the biogeography and geo-sciences based land cover feature extraction algorithm [4,24]. For a better understanding of the definitions discussed, we discuss these with reference to the dataset of Alwar image for demonstration and include pointers to the corresponding settings for the second dataset of Patalganga region.

- Plates  $plate(j)$  refer to the image  $I$  consisting of a set of plates which correspond to the image pixels. A 7-band satellite image of Alwar region of size  $472 \times 546$  is taken as an input image for biogeography and geo-sciences based feature extraction. The image has 257,712 pixels and each pixel is of 25 m by 25 m spatial



Fig. 3. Our attempt at a new AI technique.

resolution. For Patalganga image, a 4-band image of size  $508 \times 744$  is taken as input which has about 3,77,952 pixels.

- An eco-system is comprised of a universal habitat which hosts all the individual plates generated through texture analysis. The plates in the feature habitat are nothing but the labeled dataset/training dataset generated by the expert. Five types of feature plates are considered here for Alwar region, namely: water, vegetation, rocky, urban and barren. For Patalganga dataset, we consider only 3 feature plates that of vegetation, snow and rocky. Therefore, the ecosystem H6 is a group of 6 habitats (one universal habitat and five Feature habitats). In case of Patalganga, the ecosystem H4 will be a group of 4 habitats.
- Each of the multispectral bands of the image represents one SIV of the habitat. Further, image in each band is a gray image; therefore,  $SIV \in C$  is an integer and  $C \subseteq [0,255]$ .
- A habitat  $H \in SIV^m$  where,  $m$  is 7 = total image bands. For Patalganga image,  $m = 4$  bands.
- The image is subjected to unsupervised clustering using the concept of rough sets thus generating equivalence classes or plates. The preference to the rough sets is given because the equivalence classes generate clusters based on the criteria of indiscernibility and also, we do not need to know the number of clusters required beforehand [49,50]. In the resulting data, digital number value of each pixel is replaced by the discretized interval. Each row in the resulting data represents the  $x, y$  coordinates and the digital number values in the red, green, NIR, MIR, RS1, RS2 and DEM bands respectively of each pixel in the image (for patalganga image, the bands are red, green, NIR and MIR bands). This discretized data is further partitioned on the basis of NIR and MIR band which contain a good amount of geo-spatial information [38,45] to obtain the final classes.
- Inspired from the concepts of geo-sciences, we use the surface entropy of the plates calculated in the DEM band as the habitat suitability index. For the calculation of entropy ( $\varphi$ ), we follow the procedure below [22]. We copy the pixels of the input plate in  $H_u$  for which the entropy has to be calculated, in an excel sheet and then divide the digital number values in the DEM band into ' $m$ ' intervals. Next, we calculate the no. of pixels of the entire plate  $plate(j)$  falling in each of the ' $m$ ' ranges obtained above and hence, calculate the entropy of the particular plate,  $\varphi(plate(j))$  by using the equation below.

$$\text{Entropy}(\varphi(plate(j))) = - \sum_{k=1}^m P_k \log(P_k)$$

where,  $P_k = m_k/N$  where  $m_k$  is the no. of pixels in the  $k$ th interval and  $N$  is the total no. of pixels in the input plate  $plate(j)$ . For both the datasets of Alwar and Patalganga, we calculated the entropy values deciding upon a uniform interval count of 10 for all features after testing with smaller/greater interval counts both in order to maintain the tradeoff between the preciseness

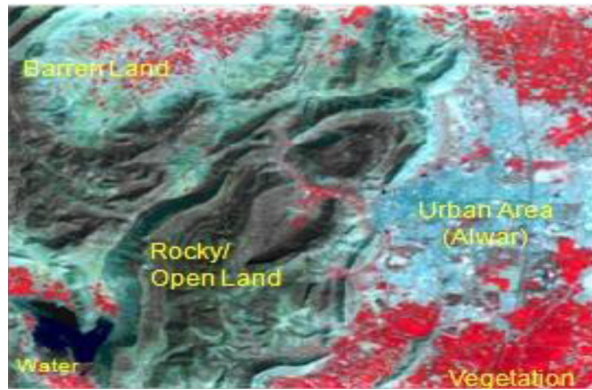


**Fig. 4.** Surface topography demarcates the different land use types in the Alwar image.

in entropy provided and the computational complexity of the entropy calculation module for the given dataset.

- g. Number of similarity classes 'c' formed are equal to the no. of land cover feature plates feature(k) for each dataset. Since the maximum value of  $k=5$  and 3 for Alwar and Patalganga datasets respectively, c is assigned the values of 5 and 3. Thus, if 'count(sim(k))' is the no. of elements in the similarity class corresponding to feature k, and n is the total number of plates in  $H_u$ , then, the following equation holds,

$$\bigcup_{k=1}^d \bigcup_{l=1}^{\text{count}(\text{sim}(k))} \text{plate}(l) = \bigcup_{j=1}^n \text{plate}(j)$$

- h. We assign a significance level ( $S_l$ ) of 0.1, i.e.  $-0.05 \leq S_l \leq +0.05$ . This is the value within which the plate similarity factor should lie so that the two plates can be categorized as similar plates leading to the formation of similarity classes. After careful observations, this value was chosen as the measure based upon which we can optimally categorize two plates as similar.
- i. The heuristic function makes use of a specific threshold value. A standard threshold value  $\delta$ , where  $\delta$  ranges from  $-0.05$  to  $+0.05$ , is assigned for classification of the plates in each similarity class. The classification is done by comparing the HSI (plate similarity factor with the feature plates) with this value defined for classifying an input plate into the feature 'k'. This number can be increased or decreased depending upon the precision in the classification results required. If we decrease the threshold value, a larger number of iterations will be required to completely classify the image, however, the results will be more accurate.

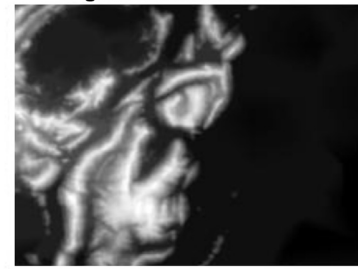
### 3.2. BBO-GS methodology

This section presents the proposed hypotheses for classification based on biogeography and geo-sciences [36,42,55]. Alwar area in Rajasthan, illustrated in Fig. 4, is taken as a case study to develop the hypothesis, that may be generalized in future developments. The area is selected as it contains hilly track, water, agriculture land, urban zone, barren lands.

**Step I.** Remote Sensing images, the actual data we have to work on, is reflectance values of solar radiation of the surface objects [1,51,57]. This phenomena may be represented through Texture analysis.

**Step II.** Generate heterogeneous regions called plates through texture analysis of the region under consideration. We use rough sets theory for texture analysis (unsupervised clustering).

**Digital Elevation Model**



**Hill Shading Model**

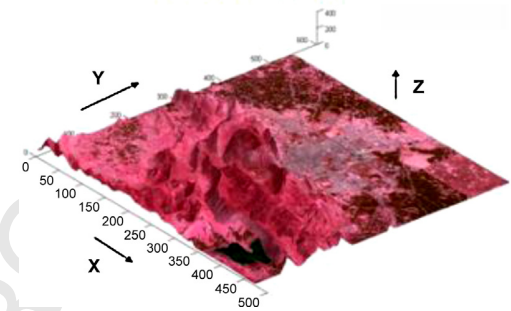


**Fig. 5.** DEM & Hill Shading of Alwar.

**Step III.** In the initial state of the ecosystem required to initialize our geo-sciences based biogeographical classifier, we consider each of the individual plates obtained through texture analysis as a member of the Universal habitat.

**Step IV.** The surface topography well represents visible perceptions of the plate concepts. Surface Topography is an indirect manifestation of the plate tectonic mechanism. This may be represented nicely through Digital Elevation Model (DEM) or slope map or hill shading.

**Step V.** Based on this, different areas may be delineated. DEM & Hill Shading of Alwar region are shown below in Fig. 5.

**Step VI.** Our major assumption is that it is the entropy which is the driving force of these regions, similar to the convection force in the mantle of the Earth.

**Step VII.** Hence, we use the surface entropy in the DEM band of each of the plates of the Universal habitat to generate the clusters of similar plates. For the purpose, we compare the differences in the surface entropies in DEM band of each of the plates in the Universal habitat with the feature habitat plates by migration. This value is called the plate similarity factor. The feature habitat contains the plates representing the training data set of Human Expert's knowledge used for supervised clustering for each of the land cover features that need to be extracted. Hence, we categorize the input plate as similar to a feature habitat plate or homogeneous if their plate similarity factor lies below the significance level ' $S_f$ ' else they are considered as heterogeneous plates. The significance level marks a threshold for identifying two plates as similar. Hence, we obtain a similarity class 'c' (where 'c' ranges from 1 to 'd') containing the group of similar plates for each of the land cover feature plates 'k' where 'k' ranges from 1 to 'd'.

For verification, the average entropy in the DEM band for the similarity class 'c' corresponding to the land cover feature plate 'k' containing the group of similar plates is calculated. Also, the entropy of the training data set in DEM band for each of the land cover feature plates 'k' is calculated. Next, we calculate the difference in the average entropy of the similarity class 'c' with the entropy of each of the land cover feature plates ranging from 1 to 'd'. This difference in entropy will be the minimum and within the



1. Generate individual plates through texture analysis.
2. In the initial state of the ecosystem, consider each of these individual plates as a member of the Universal habitat.
3. Represent the surface entropy through the Digital Elevation Model (DEM).
4. Calculate the surface entropy in the DEM band of each of the plates of the Universal habitat.
5. Generate the similarity classes 'c' for each of the land cover feature plates 'k' by comparing the plate similarity factor with the significance level 'Sf' for each plate.
6. Verify the formation of similarity classes by comparing the average entropy of the similarity classes 'c' and the entropy of each of the land cover features 'k'.
7. Proceed for classification of the plates in each similarity class by comparing the HSI (plate similarity factor) with the standard threshold value 'δ' defined for classifying an input plate into the feature 'k'.
8. Initialize a new ecosystem for the classification of the remaining unclassified plates in the universal habitat and repeat the above steps.

**Fig. 6.** Summary of the steps followed for developing the hypotheses for biogeography and geo-sciences based feature extraction.

significance level for the feature 'k' to which the class 'c' corresponds to.

**Step VIII.** Once we have similarity classes 'c' for each of the land cover features 'k', we proceed for the classification of the plates by taking into account the standard threshold 'δ' defined for classifying an input plate into the feature 'k'.

We classify each of the input plates in the similarity class 'c' by migrating the input plate from the universal habitat to the feature habitat and calculating the HSI [1,4] after migration. We take HSI as the plate similarity factor calculated by finding the difference in the entropy of the input plate and the entropy of the feature habitat or the land cover feature plate 'k'. If the HSI calculated is within the threshold 'δ', then, the input plate in the similarity class 'c' is classified into the feature 'k' otherwise, we further split the input plate which remained in the Universal habitat (since it could not be classified) through texture analysis. It can also be noted that using entropy as the basis of the HSI function will improve the classification accuracy of the original biogeography based land cover feature extractor which uses standard deviation as the HSI function as was demonstrated in the analytical study of the performance governing factors of biogeography based feature extractor that we carried out in our paper [22].

**Step IX.** Also, we then initialize a new ecosystem which follows a similar procedure for a more refined classification of the remaining unclassified plates in the universal habitat. The above framework for biogeography and geo-sciences inspired feature extraction is summarized in Fig. 6.

### 3.3. Functional architecture

The proposed functional framework for our biogeography and geo-sciences based feature extractor is presented in the form of algorithm in Fig. 7 below and explained next. The input to the algorithm is the multi-spectral satellite image.

a. The algorithm begins by the initialization of the ecosystem which generates the input plates to initialize our biogeography and geo-sciences based classifier. The input plates are generated by means of texture analysis wherein we use the rough sets part of the biogeography based land cover feature extraction algorithm [46]. The rough sets generator uses multiple bands of the image (which represent the texture of each of the land cover features in the image clearly, hence, clustering is based on texture analysis) during the discretization and partitioning step [24,46]

to generate the unsupervised clusters called the equivalence classes.

- b. In the initial state of the ecosystem required to initialize our biogeography and geo-sciences based classifier, we consider each of these equivalence classes as individual plates,  $plate(j)$ , each of which is considered as a member of the Universal habitat,  $H_u$ , where  $j$  ranges from 1 to  $n$  where  $n$  is the total no. of members in  $H_u$ . Depending on our application, in other words depending on which feature we want to extract from the image most efficiently, we can choose the band for partitioning as described in [44–46]. For our illustration, we have chosen the NIR and MIR band of the 7-band image since we want to extract the water pixels effectively and clearly identify the water body in the image and these are the bands in which the water feature is particularly more highlighted and best viewed. Therefore, we use the NIR and the MIR bands for discretization and partitioning step in the semi-naïve algorithm used for creating rough set equivalence classes for each of the clusters. Each of these resultant classes are put in the universal habitat.
- c. Since we know that the surface topography is an indirect manifestation of the geo-sciences phenomenon of plate tectonics, we can represent it nicely through the Digital Elevation Model (DEM) or *slope map* or *hill shading model*. Using entropy as the basis of the HSI function will improve the classification accuracy of the original biogeography based land cover feature extractor as was demonstrated in the analytical study of the performance governing factors of biogeography based feature extractor that we carried out in our paper [22].
- d. For the calculation of entropy, we follow the procedure described in 3(a) above. The procedure followed for calculation of the entropies of each of the land cover features is the same. Based on the results, we delineate each of the input plates of  $H_u$  into homogeneous and heterogeneous plates using the concept of  $entropy(\varphi)$ , similar to the convection forces in the mantle of the earth.
- e. Next, we generate the set of similarity classes  $c$  where  $c$  ranges from 1 to  $d$  and  $d$  is the no. of similarity classes obtained (equal to the no. of land cover features).
  - i. All the input plates are kept in the universal habitat where the no. of species (or input plates) in the universal habitat is  $n$ . Let  $\varphi(plate(j))$  represent entropy of each of the input plates,  $plate(j)$ , of  $H_u$  in the DEM band.
  - ii. We assign a plate similarity factor,  $S_f$  to each plate based on the difference between the entropy in the DEM band of the input plate  $plate(j)$  in the universal habitat  $H_u$  and the entropy in DEM band of the land cover feature plate  $feature(k)$  in the feature habitat  $H_f$  to which the input plate is migrated to.
  - iii. Feature habitat  $H_f$  is the training data set representing human expert's knowledge and used for supervised clustering of these plates. We consider  $k$  land cover features where  $k$  ranges from 1 to  $d$  which are considered as the feature habitat. Here, we have 5 feature habitats each for water, urban, rocky, barren and vegetation features, having members produced by experts.
  - iv. Hence, plate similarity factor,  $S_f = |\varphi(plate(j)) - \varphi(feature(k))|$ . We assign a significance level in order to infer if two plates are similar or different. We assign a significance level ( $S_l$ ) of 0.1, i.e.  $0.05 \leq S_l \leq +0.05$ .
  - v. Next, we generate the clusters of similar plates called the similarity classes  $c$

$$\bigcup_{l=1}^{count(sim(k))} plate(l)$$

where  $sim(k)$  is the set of plates similar to  $feature(k)$  by comparing the plate similarity factor  $S_f$  with the significance level  $S_l$  for each plate in  $H_u$ . For each  $plate(j)$  in  $H_u$ , we migrate the

Algorithm for biogeography\_and\_geo-sciences\_based\_feature\_extraction

```

{
  while (no. of unclassified plates in  $H_u \neq \text{NULL}$ )
  {
    a. Generate individual plates,  $\text{plate}(j)$ , through texture analysis.
    b. In the initial state of the ecosystem, consider each of these individual plates,
        $\sum_{j=1}^n \text{plate}(j)$  as a member of the universal habitat,  $H_u$ . //  $n$  is the total no. of plates in  $H_u$ 
    c. Represent the surface entropy,  $\varphi(\text{plate}(j))$ , through DEM.
    d. Calculate  $\varphi(\text{plate}(j))$  in the DEM band of each of the plates of  $H_u$ .
    e. Generate the clusters of similar plates,  $\text{sim}(k)$  for each land cover feature  $k$  called the similarity classes  $c$  by
       comparing the plate similarity factor  $S_f$ , with the significance level  $S_l$  for each plate in  $H_u$ 
       // plate similarity factor of two plates  $a$  and  $b$ ,  $S_f(a, b) = |\varphi(\text{plate}(a)) - \varphi(\text{plate}(b))|$ 
       For each plate  $j$  in  $H_u$ 
       Migrate  $\text{plate}(j)$  to each of the feature plates  $(k)$  in  $H_f$ 
       /*  $k$  ranges from 1 -  $d$  and  $d$  is the no. of land cover features to be extracted */
       if  $|\varphi(\text{plate}(j), \text{feature}(k))| \leq S_l$ 
       similar plates  $(k) = \{\text{similar plates}(k), \text{plate}(j)\}$ ;
       End For
    f. Verify the similarity classes formed by using the following inequality:
       
$$\frac{d}{k=1} \sum_{i=1}^{\text{count}(\text{sim}(k))} \frac{1}{\text{count}(\text{sim}(k))} (\varphi(\text{plate}(l)) - \varphi(\text{feature}(k)) < S_f$$

       for each  $c$  corresponding to feature  $k$ .
    g. // Proceed for final classification step.
       For each similarity class  $c$  in  $H_u$  corresponding to feature  $k$ 
       For each  $\text{plate}(l)$  in  $c$ 
       //  $l$  ranges from 1 to  $\text{count}(\text{sim}(k))$ .
       
$$\text{HSI} = |\varphi(\text{plate}(l)) - \varphi(\text{feature}(k))|$$

       If  $(\text{HSI} < \delta)$ 
        $\text{plate}(l) = \text{feature}(k)$ ;
        $H_u = H_u - \text{plate}(l)$ ;
       End For
       End For
    h. Initialize a new ecosystem for the classification of the remaining unclassified plates in  $H_u$ .
  } //  $H_u$  is empty since no unclassified plates remain in  $H_u$ .
End.

```

Fig. 7. Biogeography and geo-sciences based land cover feature extraction.

$\text{plate}(j)$  to each of the feature plates  $\text{feature}(k)$  in  $H_f$  where  $k$  ranges from 1 to  $d$ . Now, we calculate the plate similarity factor value after migration of  $\text{plate}(j)$  to  $\text{feature}(k)$ . If  $S_f$  or surface entropy  $|\varphi(\text{plate}(j)) - \varphi(\text{feature}(k))| \leq S_l$ , it represents an insignificant difference and thus a homogeneous region (similar plate) else a heterogeneous region (different plate).

vi. Here, we group all the similar plates to  $\text{feature}(k)$  in one similarity class and thus obtain a similarity class, leading to a set of similarity classes  $c$ .

f. We verify the similarity classes formed.

i. For the purpose, we start by taking the average of the entropies in the DEM band for each of the similarity classes  $c$  corresponding to the land cover feature plate  $k$  containing the group of similar plates, according to

$$\text{Avg}_c = \frac{d}{k=1} \left( \frac{1}{\text{count}(\text{sim}(k))} \right) \sum_{l=1}^{\text{count}(\text{sim}(k))} \varphi(\text{plate}(l))$$

where 'count(sim(k))' is the no. of elements in the similarity class corresponding to feature  $k$ .

ii. Next, we calculate the difference in the average entropy of the similarity class  $c$  corresponding to feature  $k$  with the entropy of each of the land cover feature plates  $k$ , i.e.

$$\frac{d}{k=1} \sum_{i=1}^{\text{count}(\text{sim}(k))} \frac{1}{\text{count}(\text{sim}(k))} (\varphi(\text{plate}(l)) - (\varphi(\text{feature}(k))) < S_f$$

for each  $c$  corresponding to feature  $k$ .

iii. If this difference in entropy is the minimum and within the significance level for the feature  $k$ , the plate is verified to belong to the class  $c$  to which it corresponds to.

g. Next, we proceed with the final classification step taking into account the standard threshold value  $\delta$  for classifying an input plate into the  $\text{feature}(k)$ .

i. We classify each of the input plates in the similarity class  $c$  by migrating the input plate from the universal habitat to the feature habitat and calculating the HSI [40,53] after migration.  $\delta$  is the standard value against which the HSI of all the input plates will be compared. HSI is taken as the plate similarity

$$U_{k=1}^d U_{l=1}^{\text{count}(\text{sim}(k))} \left( \min_{k=1}^d \left( \varphi(\text{plate}(l)) - \varphi(\text{feature}(k)) \right) \right) < \text{Threshold}(\delta)_{-0.05 < \tau < +0.05}$$

Iterate the whole process until no unclassified plate is left in  $H_u$

Fig. 8. Mathematical formulation of the biogeography and geo-sciences based feature extraction algorithm.

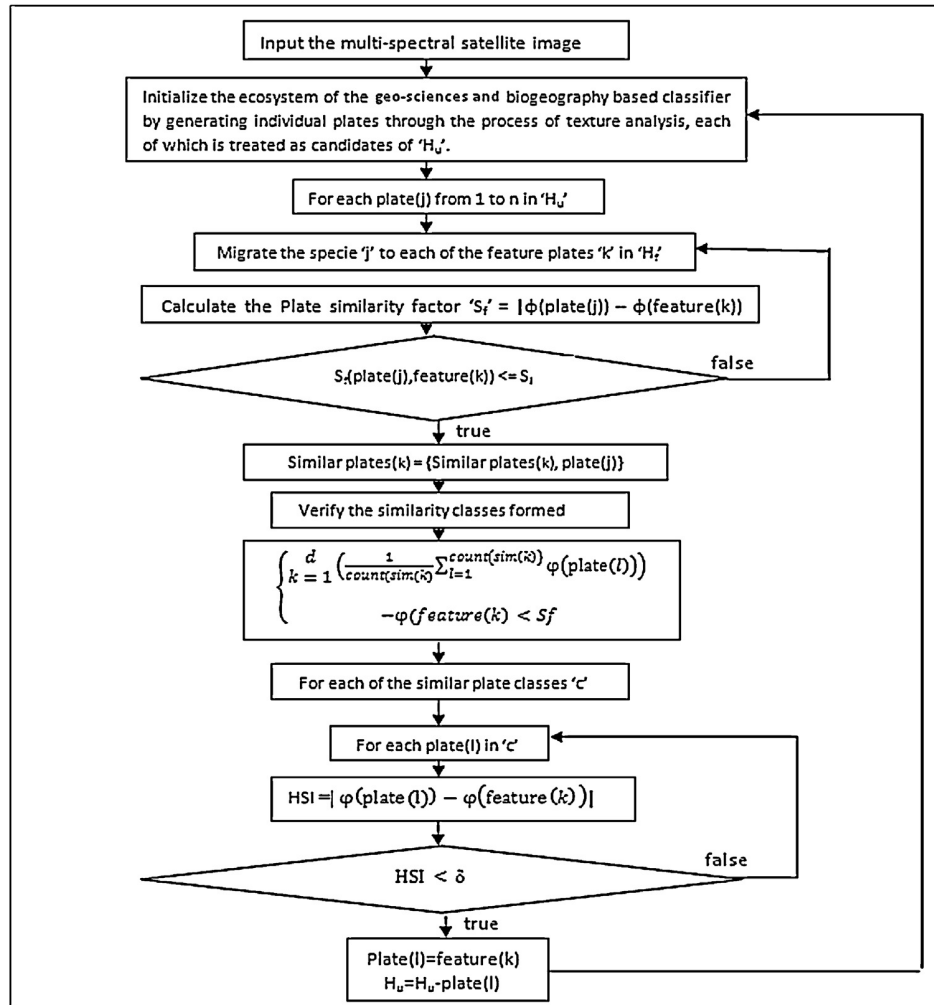


Fig. 9. Flowchart representing the biogeography and geo-sciences based land cover feature extraction.

factor. For each of the input plates in the similarity class  $c$  corresponding to feature  $k$ , we calculate the difference  $HSI =$

$$d \left| \left( \frac{count(sim(k))}{l=1} (\varphi(plate(l)) - (\varphi(feature(k)))) \right) \right|$$

where  $k$  is the feature to which the similarity class  $c$  is mapped to, and  $c$  is the similarity class to which  $plate(l)$  belongs to.

- ii. If  $(HSI < \delta)$ , then we classify the input plate  $plate(j)$  in the similarity class  $c$  into the  $feature(k)$ , else we further split the input plate  $plate(j)$  (which remained in the Universal habitat since it could not be classified) through texture analysis as described above and repeat the above procedure for the input plate  $l$  left in the Universal habitat.

- h. Initialize a new ecosystem for the classification of the remaining unclassified plates in the universal habitat  $H_u$  and repeat the above procedure.

where,

$$sim(k) = \{sim(k), plate(j)\},$$

If  $(S_f(plate(j)), feature(k)) \leq S_l$  and  $j$  ranges from 1 to the number of plates  $n$  in  $H_u$ .

For our biogeography and geo-sciences based feature extractor, we proceed in the following manner, i.e. for the DEM band, we calculate the difference in the surface entropy of each input plate of the similarity class of the Universal Habitat and each feature plate of the Feature Habitat containing the expert generated training set of each land cover feature of the image. If this difference is the minimum for the feature 'k' and also less than the pre-specified threshold value of  $-0.05 < t < +0.05$ , then that particular plate is classified as the feature 'k' else it is left as unclassified. The process is repeated for each feature's similarity class plate until there is no similarity class left in the universal habitat and the whole process is iterated till there is no unclassified plate left. The detailed internal architecture of our biogeography and geo-sciences based feature extractor is demonstrated by means of a flowchart in Fig. 9.

### 3.4. Mathematical formulation of biogeography and geo-sciences based feature extractor

Therefore, the working of our proposed algorithm can be summarized in the form of the following equation based on HSI which is analogous to the fitness function in other conventional algorithms (Fig. 8).

## 4. Results and analysis

This section presents the results obtained after applying the biogeography and geo-sciences based land cover feature extractor on

**Table 1**

Error matrix of BBO-GS based extractor on Alwar region (kappa coefficient = 0.7440).

	Vegetation	Urban	Rocky	Water	Barren	Total
Vegetation	142	0	0	0	1	143
Urban	3	66	8	0	4	81
Rocky	0	14	185	1	4	204
Water	0	0	0	69	0	69
Barren	5	111	6	0	161	283
Total	150	190	200	70	170	780

two different datasets for verification of the results. The datasets chosen are of Alwar region in Rajasthan and Patalganga region in Shivalik ranges. We The results and analysis for each of the case studies are described in the sections below.

#### 4.1. Case study: Alwar region in Rajasthan

This section demonstrates the applicability of our proposed classifier by applying it on the Alwar image of Rajasthan. The dataset used is the 7-band multi-spectral, multi resolution and multi sensor image of Alwar area in Rajasthan with dimensions  $472 \times 576$  and is the same dataset as was used in our previous paper [24].

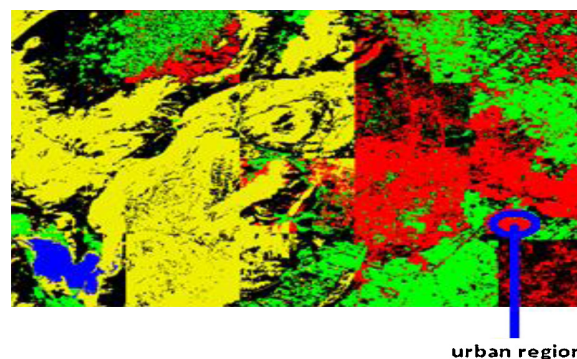
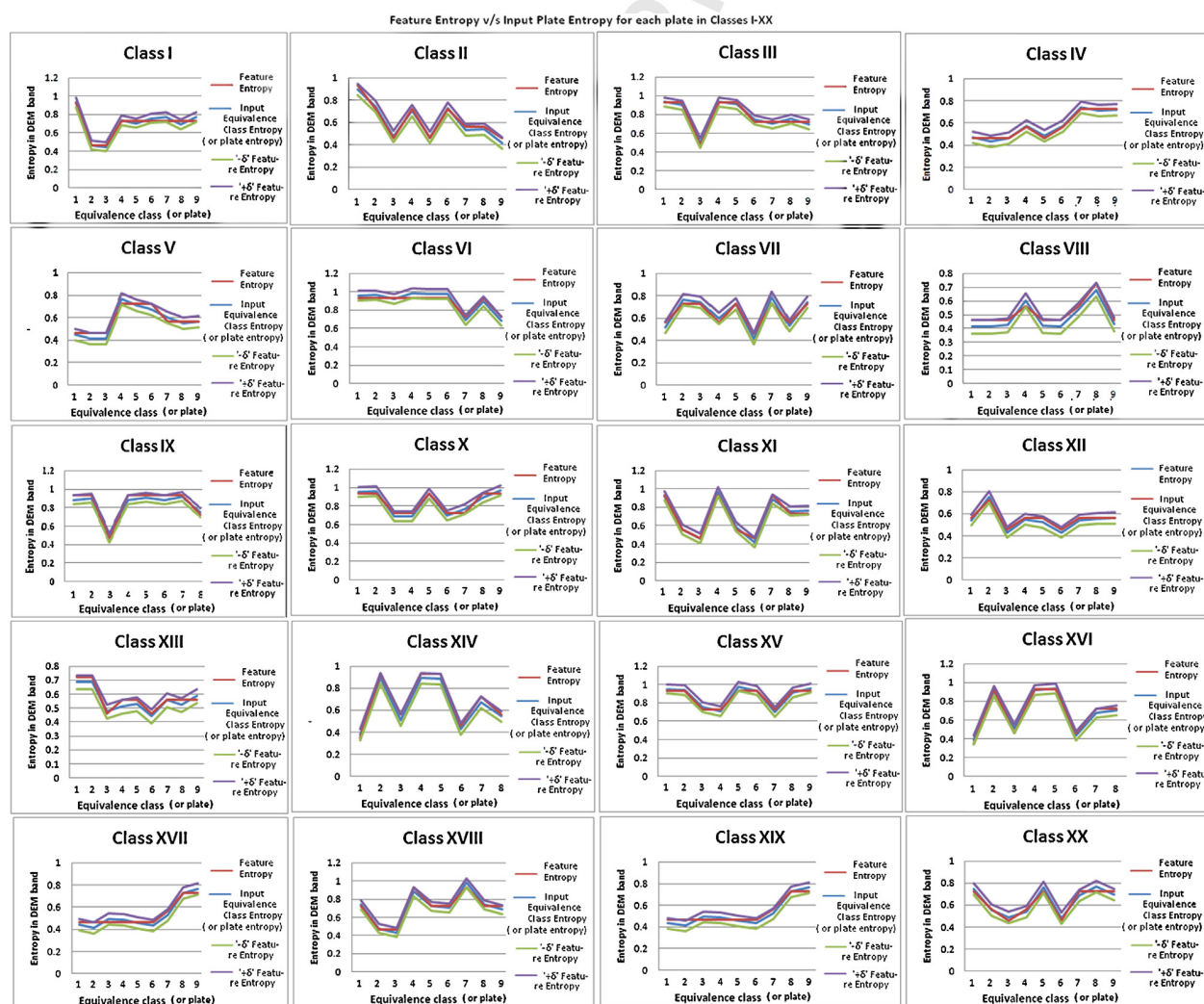
**Fig. 10.** Biogeography and geo-sciences based feature extractor (kappa coefficient = 0.7440).

Table 2 represents the calculations of the entropies in the DEM band for each plate (equivalence class) obtained through texture analysis on the Alwar image. The image is subjected to 'n' (here, we take  $n = 20$  however this number can be varied to any value depending upon the image size) simple partitions, for the sake of simplicity. The calculations are represented in a tabular form which summarizes the DEM entropies calculated for each of the equivalence class

**Fig. 11.** Feature entropy vs plate entropy for each plate in classes 1–XX.



**Table 2**  
HSI calculations and the corresponding classified feature for the first iteration.

Similarity class for 'Water' feature entropy = 0.3486		Similarity class for 'Rocky' feature entropy = 0.9316		Similarity class for 'Barren' feature entropy = 0.7249		Similarity class for 'Vegetation' feature entropy = 0.4619		Similarity class for 'Urban' feature entropy = 0.5631	
Plate entropy	HSI	Plate entropy	HSI	Plate entropy	HSI	Plate entropy	HSI	Plate entropy	HSI
0.3886	0.0400	0.9319	0.0003	0.7375	0.0126	0.4671	0.0052	0.5405	0.0226
		0.8944	0.0372	0.7040	0.0209	0.4474	0.0145	0.5708	0.0077
		0.9332	0.0016	0.7597	0.0348	0.4736	0.0117	0.5706	0.0075
		0.8996	0.032	0.7693	0.0444	0.4651	0.0032	0.6028	0.0397
		0.9038	0.0278	0.6938	0.0311	0.4155	0.0464	0.5552	0.0079
		0.9616	0.03	0.7701	0.0452	0.4932	0.0313	0.5663	0.0032
		0.9619	0.0303	0.7418	0.0169	0.4749	0.013	0.5132	0.0499
		0.9191	0.0125	0.7039	0.021	0.4348	0.0271	0.5979	0.0348
		0.9840	0.0524	0.7248	1E–04	0.4640	0.0021	0.5305	0.0326
		0.9784	0.0468	0.7428	0.0179	0.4829	0.021	0.6037	0.0406
		0.9747	0.0431	0.7000	0.0249	0.4513	0.0106	0.5364	0.0267
		0.8981	0.0335	0.7526	0.0277	0.4156	0.0463	0.5610	0.0021
		0.8867	0.0449	0.6945	0.0304	0.4168	0.0451	0.5913	0.0282
		0.8890	0.0426	0.7424	0.0175	0.5115	0.0496	0.5438	0.0193
		0.9422	0.0106	0.7164	0.0085	0.4485	0.0134	0.5493	0.0138
		0.9481	0.0165	0.7218	0.0031	0.4137	0.0482	0.5249	0.0382
		0.9330	0.0014	0.7673	0.0424	0.4123	0.0496	0.5408	0.0223
		0.8861	0.0455	0.7131	0.0118	0.4130	0.0489	0.5554	0.0077
		0.8967	0.0349	0.6762	0.0487	0.4255	0.0364	0.5623	0.0008
		0.8848	0.0468	0.6930	0.0319	0.4168	0.0451	0.5109	0.0522
		0.9086	0.023	0.6798	0.0451	0.4142	0.0477	0.5287	0.0344
		0.8852	0.0464	0.7590	0.0341	0.4722	0.0103	0.5573	0.0058
		0.9185	0.0131	0.6812	0.0437	0.4628	0.0009	0.5223	0.0408
		0.9459	0.0143	0.7699	0.045	0.4181	0.0438	0.5873	0.0242
		0.9541	0.0225	0.7743	0.0494	0.4325	0.0294	0.5139	0.0498
		0.9331	0.0015	0.7671	0.0422	0.4314	0.0305	0.5257	0.0374
		0.8913	0.0403	0.7663	0.0414	0.4750	0.0131	0.5543	0.0088
		0.9668	0.0352	0.7399	0.015	0.5109	0.049	0.5437	0.0194
		0.9096	0.0220	0.7255	0.0006	0.4402	0.0217		
		0.9194	0.0122	0.7847	0.0598	0.5119	0.05		
		0.9374	0.0058	0.7377	0.0128	0.4319	0.03		
		0.9532	0.0216	0.6814	0.0435	0.4728	0.0109		
		0.9371	0.0055	0.7473	0.0224	0.4318	0.0301		
		0.9767	0.0451	0.6884	0.0365	0.4365	0.0254		
		0.9309	0.0007	0.6863	0.0386	0.4107	0.0512		
		0.9098	0.0218	0.6911	0.0338	0.4944	0.0325		
		0.9613	0.0297	0.7659	0.041	0.4872	0.0253		
		0.8855	0.0461	0.7570	0.0321	0.4531	0.0088		
		0.9812	0.0496	0.7647	0.0398	0.4317	0.0302		
				0.7539	0.029	0.4873	0.0254		
				0.6749	0.05	0.4819	0.02		
				0.7052	0.0197				
				0.7497	0.0248				
				0.7068	0.0181				
				0.7000	0.0249				
				0.7378	0.0129				
				0.7245	0.0004				
				0.7034	0.0215				
				0.7378	0.0129				
				0.6872	0.0377				
				0.7231	0.0018				
				0.7621	0.0372				
				0.7437	0.0188				
				0.7637	0.0388				
				0.6918	0.0331				
				0.7694	0.0445				
				0.6931	0.0318				

in each of the ' $n$ ' partitions. The plates are categorized into similarity classes for each land cover feature based on the entropies calculated in the DEM band with the significance level ' $S_f$ ' of  $-0.05$  to  $+0.05$ . We classify each of the input  $plate(j)$  by taking into account the standard threshold ' $\delta$ ' of  $-0.05$  to  $+0.05$  we defined for classifying an input plate into the feature ' $k$ '. In our case, the plates get classified in the first iteration only, however, if we decrease the threshold, more iterations will be required to fully classify all the plates in the Universal habitat. The feature entropies are calculated preliminarily and summarized in Table 2. The HSI calculations and the feature classification can also be deduced graphically (see

Fig. 11). The graph can be plotted between the feature entropy vs the plate entropy for each plate in the DEM band for each partition of the image (referred to as class). The graph plot will plot each input  $plate(j)$ 's entropy in DEM band in ' $H_u$ ', the entropy of the land cover feature ' $k$ ' to which the  $plate(j)$  belongs to, in the DEM band, and the ' $-\delta$ ' and ' $+\delta$ ' threshold graphs representing the area within which the feature entropy of feature plate ' $k$ ' should lie for the input  $plate(j)$  to be classified in the feature ' $k$ '. For the plates to be classified into the corresponding mapped land cover features, they should lie within this interval. The classified image is obtained in Fig. 10 which clearly shows the extraction of land cover features of

**Table 3**

Error matrix of BBO-GS based extractor on Patalganga region (kappa coefficient = 0.7870).

	Rocky	Snow	Vegetation	Total
Rocky	197,630	22,572	0	220,202
Snow	18,330	121,008	0	139,338
Vegetation	0	0	16,412	16,412
Total	215,960	143,580	16,412	375,952

water, urban, rocky, vegetation and barren. The yellow color represents rocky area, green color represents vegetation area, black color represents barren area and red color represents the urban area. The kappa coefficient for the classified image is obtained as 0.7440 (explained in later sections). From our previous works, we know that the classified image obtained through the application of original biogeography based land cover feature extractor has a kappa coefficient of 0.6715 [19,23,46]. Comparing the results, it can be seen that the encircled region has been correctly classified as urban region by our geo-sciences based classifier (which was wrongly classified by the original BBO as barren [1,18,24]. Table 1 shows the classification accuracy of our proposed algorithm using the classification error matrix. We took 150 vegetation pixels, 190 urban pixels, 200 rocky pixels, 70 water pixels, 170 barren pixels from the training set and the error matrix obtained is shown in Table 1. The error matrix for the original BBO classifier can be held from our paper [24] wherein it is observed that our proposed classifier performs much better than the original BBO for example, if we see the first column, here, out of total 150 vegetation pixels, 142 pixels were correctly classified as vegetation and only 3 and 5 pixels were wrongly classified as urban and barren respectively, a total of only 8 misclassified pixels which is much better than the original BBO classification which classified 127 vegetation pixels correctly and produced a total of 23 wrongly classified pixels [1,18,24]. Hence the KHAT statistics of the proposed biogeography and geo-sciences based land cover feature extractor is 0.7440. This value is a substantial agreement between the ideal classifier and the proposed algorithm. The kappa (K) coefficient of the Alwar image is 0.7440 which indicates that an observed classification is 74.40% better than one resulting from chance (Tables 2 and 3; Fig. 11).

#### 4.2. Case study: Patalganga region in Shivalik ranges

This section demonstrates the applicability of our proposed classifier by applying it on the Patalganga image of Shivalik ranges. For Patalganga, area in Shivalik mountainous ranges is undertaken. We have used 4 band images of Patalganga taken from Landsat-I satellite with dimensions  $508 \times 744$ . The bands are Red, Green, Near Infra-Red (NIR) and Middle Infra-Red (MIR). (For details about the dataset used, please see our paper [22]. We calculate the feature entropies and the entropies calculated in the DEM band for each plate (equivalence class) obtained through texture analysis on the Patalganga image with the threshold ' $\delta$ ' of  $-0.05$  to  $+0.05$  as shown in Table 4. We can also display the feature entropy vs the plate entropy plotted for each plate in the DEM band for each partition of the image graphically (see Fig. 13). The classified image is obtained in Fig. 12 which clearly shows the extraction of land cover features of snow, vegetation and rocky area and has a kappa coefficient of 0.7248. The yellow color represents rocky area, green color represents vegetation area, and red color represents the snowy area. The original BBO classified image of Patalganga displayed a kappa coefficient of 0.7870 [23]. The efficiency of our proposed classifier is reflected from the classification of the encircled region which has been correctly classified as rocky region in Fig. 12 (which was wrongly classified as snowy region by the original BBO based feature extractor as is reflected in our work [22]. Table 3 displays the

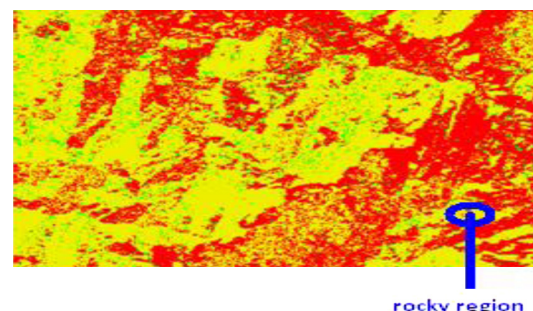


**Fig. 12.** Final classified image of patalganga region after applying biogeography and geo-sciences based land cover feature extraction. (kappa coefficient = 0.7870).

classification accuracy of our proposed algorithm by means of the classification error matrix. (For the error matrix for the original biogeography based classifier, please refer our paper [24]). Hence the KHAT statistics of the proposed biogeography and geo-sciences based land cover feature extractor is 0.7870 (Fig. 13).

#### 5. Application of biogeography and geo-sciences based algorithm for feature extraction applications

In this section, we test the concepts proposed in our BBO-GS algorithm on standard benchmark functions that are generally used for testing the effectiveness of an evolutionary algorithm [30,32,33]. Our proposed algorithm based on the concept of using entropy as an indicator of the goodness of a solution is basically a modification of the original BBO algorithm and hence we incorporate the above concept for comparison of HSI values and identification of best solution. We therefore present the performance results of the proposed BBO-GS algorithm on a set of commonly used benchmark functions [3,5,11]. We next demonstrate the effectiveness and applicability of our BBO-GS based classifier for improving our hybrid bio-inspired classifier [19,24].

The choice of DEM band for evaluating the entropy in our designed BBO-GS based hybrid classifier is in accordance with the proposed algorithm which states that the texture analysis is done in the DEM band since this band well represents the surface topography however, the choice of the band for evaluating the entropy depends upon the application on which feature extraction is performed and the nature and characteristics of dataset. Thus, depending upon the features which we want to extract from the image, the band used for calculating the entropy values may be chosen. For optimal band selection for application of our proposed BBO-GS method, the reader is referred to our paper [20] which discusses the optimal choice of bands depending upon the features contained in the input image or which we want to extract from the image. The presented application takes as input satellite multi-spectral images of natural terrain for which the DEM band is a good indicator of identifying different land cover features however, for other multi-spectral datasets, other bands may be more appropriate. For example, yet another application of mixed pixel resolution in satellite multi-spectral imagery of natural terrain which has been discussed in our paper [13,54] also requires to calculate entropy in DEM band, however, for mixed pixel resolution in magnetic resonance imaging for disease diagnosis, where the sensors detect signals from blood vessels, the entropy is not calculated in DEM band. Further, the proposed algorithm can also be applied for face recognition application by modifying the HSI function definition in our paper [12] in terms of surface entropy of the digital number values of the image pixels of the face dataset. In fact, the proposed BBO-GS based algorithm can be applied for various feature extraction applications by modifying the fitness function

**Table 4**

HSI Calculations and the corresponding classified feature for the first iteration.

Similarity Class for 'Vegetation' feature entropy = 0.8570		Similarity Class for 'Snow' feature entropy = 0.7361				Similarity Class for 'Rocky' feature entropy = 0.6094			
Plate entropy	HSI	Plate entropy	HSI	Plate entropy	HSI	Plate entropy	HSI	Plate entropy	HSI
0.8296	0.0274	0.6893	0.0468	0.7162	0.0199	0.5790	0.0304	0.5738	0.0356
0.8498	0.0072	0.7507	0.0146	0.7721	0.036	0.5959	0.0135	0.6262	0.0168
0.8730	0.016	0.7720	0.0359	0.7402	0.0041	0.6014	0.008	0.5660	0.0434
0.8578	0.0008	0.7192	0.0169	0.7847	0.0486	0.5627	0.0467	0.5680	0.0414
0.8439	0.0131	0.7244	0.0117	0.7674	0.0313	0.5996	0.0098	0.5712	0.0382
0.8261	0.0309	0.7654	0.0293	0.7831	0.047	0.5765	0.0329	0.6527	0.0433
0.8082	0.0488	0.7376	0.0015	0.7812	0.0451	0.5621	0.0473	0.5598	0.0496
		0.6854	0.0507	0.7851	0.049	0.6500	0.0406	0.6161	0.0067
		0.7073	0.0288	0.7581	0.022	0.6478	0.0384	0.5773	0.0321
		0.6960	0.0401	0.7072	0.0289	0.5984	0.011	0.6154	0.006
		0.7592	0.0231	0.7816	0.0455	0.6328	0.0234	0.6239	0.0145
		0.7691	0.033	0.7818	0.0457	0.6180	0.0086	0.5974	0.012
		0.6953	0.0408	0.7261	0.01	0.5672	0.0422	0.5851	0.0243
		0.7819	0.0458	0.7059	0.0302	0.5656	0.0438	0.6369	0.0275
		0.7597	0.0236	0.7227	0.0134	0.5856	0.0238	0.5597	0.0497
		0.7798	0.0437	0.7146	0.0215	0.5906	0.0188		
		0.7377	0.0016	0.7360	1E–04	0.5793	0.0301		
		0.7609	0.0248	0.7536	0.0175	0.6022	0.0072		
		0.6976	0.0385	0.7031	0.033	0.6062	0.0032		
		0.7807	0.0446	0.7245	0.0116	0.6101	0.0007		
		0.7859	0.0498			0.6467	0.0373		
		0.7063	0.0298			0.6000	0.0094		
		0.7628	0.0267			0.6031	0.0063		
		0.7263	0.0098			0.5971	0.0123		
		0.7774	0.0413			0.5614	0.048		
		0.7586	0.0225			0.6541	0.0447		
		0.7130	0.0231			0.5954	0.014		
		0.6863	0.0498			0.5682	0.0412		
		0.7528	0.0167			0.5849	0.0245		
		0.7069	0.0292			0.5829	0.0265		
		0.7771	0.041			0.5899	0.0195		
		0.7133	0.0228			0.5680	0.0414		
		0.7779	0.0418			0.5902	0.0192		
		0.7336	0.0025			0.5752	0.0342		
		0.7762	0.0401			0.5868	0.0226		
		0.7806	0.0445			0.6136	0.0042		
		0.7375	0.0014			0.6036	0.0058		
		0.7818	0.0457			0.5974	0.012		
		0.7507	0.0146			0.5632	0.0462		
		0.7837	0.0476			0.5855	0.0239		
		0.7256	0.0105			0.5839	0.0255		
		0.6985	0.0376			0.6405	0.0311		
		0.7838	0.0477			0.5944	0.015		
		0.7623	0.0262			0.5958	0.0136		
		0.7580	0.0219			0.5640	0.0454		
		0.7747	0.0386			0.5702	0.0392		
		0.7815	0.0454			0.5753	0.0341		
		0.7574	0.0213			0.5716	0.0378		
		0.7703	0.0342			0.5881	0.0213		
		0.7826	0.0465			0.5880	0.0214		
		0.7553	0.0192			0.6002	0.0092		
		0.7071	0.029			0.5637	0.0457		
		0.7043	0.0318			0.5614	0.048		
		0.6936	0.0425			0.6581	0.0487		

to use surface entropy (or surface entropy in the appropriate band in case of multi-spectral images) of the digital number values of the image pixels as the measure of comparison and classification of features in the input image dataset.

#### 5.1. Performance analysis on benchmark functions

In order to explore the benefits of the BBO-GS model, we compare its performance with the original BBO and seven other population-based optimization methods of ACO, DE, ES, GA, PBIL, PSO and SGA on the set of 14 standard benchmark functions [30,33,53]. The benchmarks that we minimize are functions that are representative of those used in the literature for comparison

of optimization methods [48]. The benchmarks were compared by implementing integer versions of all the optimization algorithms in Matlab [30,33]. Each algorithm had a population size of 50, an elitism parameter of 2, and ran for 50 generations. We ran 50 Monte Carlo simulations of each algorithm on each benchmark to get representative performances [30,53]. The parameter settings that were used are: For BBO-GS, the habitat entropy = 0, immigration entropy bounds per gene = [0,1], step size for numerical integration of entropies = 1, maximum immigration and migration rates for each island = 1, and mutation entropy = 1 [40,53]. For ACO, the initial pheromone value was taken as  $1E-6$ , pheromone update constant as 20, global pheromone decay rate as 0.9, exploration constant as 1, local pheromone decay rate as 0.5, pheromone



Feature Entropy v/s Input Plate Entropy for each plate in Classes I–XV

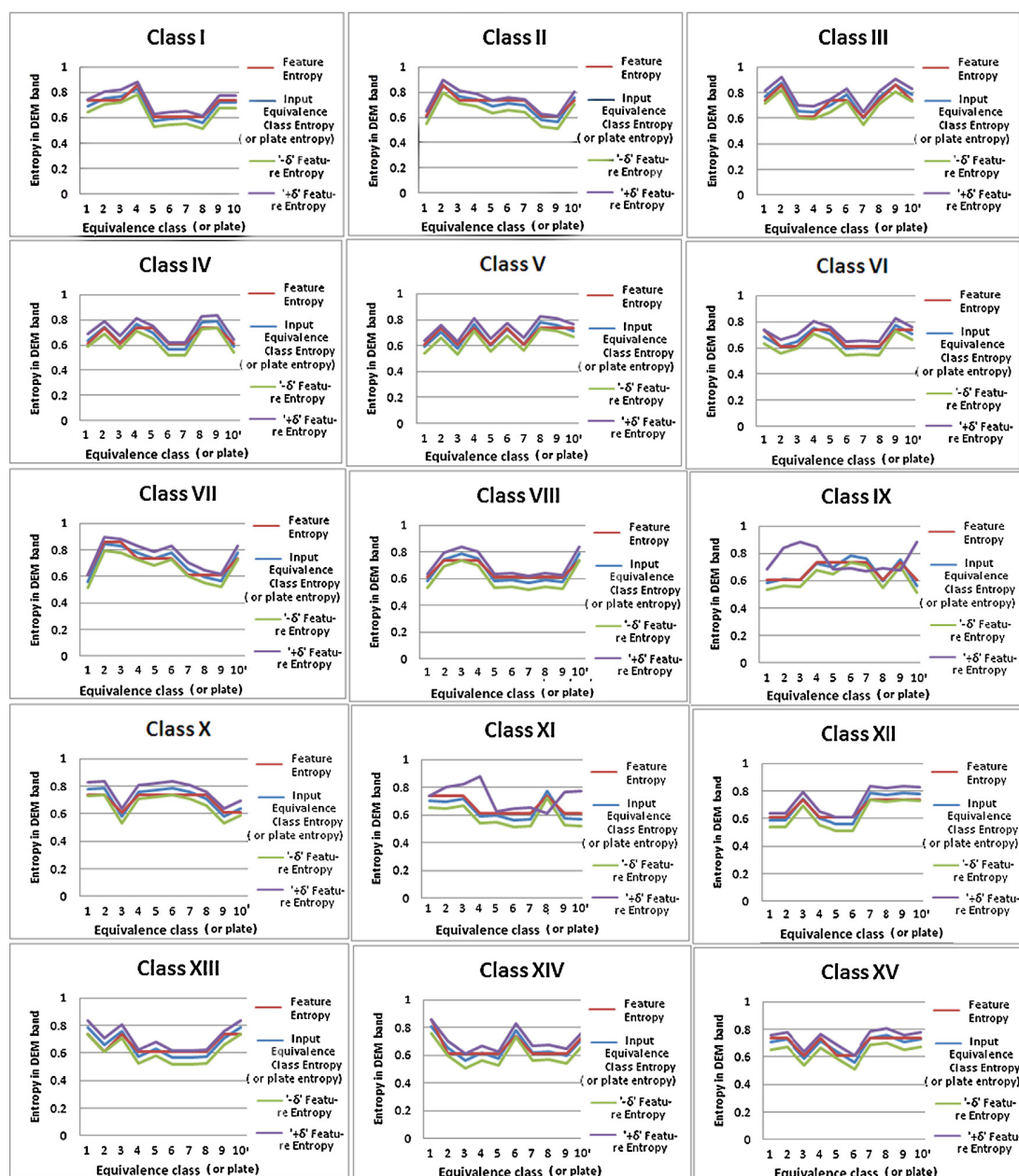


Fig. 13. Feature entropy vs plate entropy for each plate in classes 1–XV.

sensitivity as 1, and visibility sensitivity as 5 [7,15]. For BBO, the habitat modification probability = 1, immigration probability bounds per gene = [0,1], step size for numerical integration of probabilities = 1, maximum immigration and migration rates for each island = 1, and mutation probability = 0 [40,53]. For DE, we used a weighting factor of 0.5 and a crossover constant equal to 0.5. For the ES, we produced  $\lambda = 10$  offspring each generation, and standard deviation  $\sigma = 1$  for changing solutions [52,56]. For the GA, a single point crossover with a crossover probability of 1, and a mutation probability of 0.01 was used [25]. For PBIL, we used a learning rate of 0.05, 1 good population member and 0 bad population members, an elitism parameter of 1, and a 0 probability vector mutation rate [53]. For SGA, a single point crossover with a crossover probability of 1, and a mutation probability of 0.01 was used [35]. For PSO, we used an inertial constant = 0.3, a cognitive constant = 1, and a social

constant for swarm interaction = 1 [9,17]. As in [30,53] we consider each algorithm to have a population size of 50, an elitism parameter of 2, and ran for 50 generations.

Table 5 shows the results of the simulations. Table 5 shows the mean (average) minima found by each algorithm, respectively, over 50 Monte Carlo runs on standard benchmark functions. (Since the normalizations in the tables are based on different scales, so numbers cannot be compared between the two tables). From Table 5, we see that the BBO-GS performed the best (on average) on eight of the 14 benchmarks followed by SGA which performs the best on seven of the standard benchmark functions. From the table, it is observed that the BBO-GS outperforms the standard BBO on all the benchmark functions which is evident from the fact that the average minimal value found by BBO-GS is much lower than that found by the original BBO model for all the 14 benchmark functions. From

**Table 5**

Mean normalized optimization results and CPU times on benchmark functions. The numbers shown are the minimum function values found by the algorithms, averaged over 50 Monte Carlo simulations, and normalized so that the smallest number in each row is 100.

	BBO-GS	BBO	ACO	DE	ES	GA	PBIL	PSO	SGA
Ackley	<b>100</b>	102	193	132	187	244	345	175	120
Fletcher	<b>100</b>	117	802	366	425	400	918	723	178
Griewank	115	135	177	214	636	560	3319	1750	<b>100</b>
Penalty #1	1321	1.16E4	2.33E7	1.399E4	1.29E7	3.11E5	3.818E7	1.275E6	<b>100</b>
Penalty #2	206	701	5.44E5	5171	4.59E4	1.34E4	7.89E5	5.299E4	<b>100</b>
Quartic	<b>100</b>	265	2722	2043	63,231	2073	5.69E4	7623	165
Rastrigin	<b>100</b>	105	539	252	478	348	620	747	121
Rosenbrock	105	109	1389	266	1326	490	1766	430	<b>100</b>
Schwefel 1.2	<b>100</b>	115	102	301	402	103	601	502	151
Schwefel 2.21	<b>100</b>	115	156	223	263	253	345	124	190
Schwefel 2.24	<b>100</b>	111	399	245	1004	500	820	542	219
Schwefel 2.26	176	242	283	117	145	179	179	198	<b>100</b>
Sphere	<b>100</b>	103	1412	286	925	983	2960	1520	112
Step	116	145	210	300	899	632	3697	1771	<b>100</b>

**Table 6**

Comparison of kappa coefficient of Hybrid ACO<sub>2</sub>/PSO/(BBO-GS) based classifier with the recent soft computing classifiers.

Extended (non-linear) biogeography based feature extractor	Membrane computing based classifier	Hybrid FPAB classifier	Hybrid ACO <sub>2</sub> /PSO/BBO classifier	Hybrid ACO <sub>2</sub> /PSO/(BBO-GS) based feature extractor
0.6912	0.6818	0.6790	0.98182	0.9870

the above discussion, we can conclude that the proposed BBO-GS far outperforms the standard BBO and the other algorithms as well and hence proposes an advanced algorithm.

## 5.2. Application of biogeography and geo-sciences based extractor for the design of hybrid classifier

Next, we apply our proposed biogeography and geo-sciences based feature extractor for the improvement of the hybrid classifier that we developed in our previous paper [24]. We next present the results of classification of the BBO-GS based hybrid ACO<sub>2</sub>/PSO/(BBO-GS) classifier since the hybrid ACO<sub>2</sub>/PSO/BBO classifier is the best known classifier developed till date [24,46] and hence we study the result of substituting the original BBO with our proposed BBO-GS in the design of this hybrid bio-inspired intelligent classifier. Since we know from our previous work [24] that our hybrid ACO<sub>2</sub>/PSO/BBO based hybrid classifier produced the best results and had outperformed the other recent soft computing classifiers and the traditional hard computing classifiers, on the Alwar dataset, hence, we compare our results with our benchmark hybrid classifier and only those feature extractors which have been developed thereafter on the 7-band cartosat satellite image of Alwar region in Rajasthan, India. These classifiers which were compared and tested in our previous paper were the hard computing classifiers (traditional probabilistic classifiers such as the Minimum Distance to Mean Classification (MDMC) and the Maximum Likelihood Classifier (MLC) [39] which had kappa coefficients of 0.7364 and 0.7525 respectively, the fuzzy and the integrated rough-fuzzy classifiers which achieved the kappa-coefficients of 0.9134 and 0.9700 respectively [45,49], the cAntMiner classifier (kappa coefficient = 0.964) [4,7,14,15], hybrid ACO-BBO technique from our papers [4,19] and the hybrid ACO<sub>2</sub>/PSO technique [4,9] which achieved kappa-coefficients of 0.96699 and 0.975 respectively, and the semantic web based classifier with a kappa coefficient of 0.9861 [37]. The hybrid ACO<sub>2</sub>/PSO/BBO classifier had the highest kappa coefficient of 0.9818 [15,17,24] and is shown in Fig. 14(d). Fig. 14 also presents the satellite image classification results of the other very recent feature extractors. Fig. 14(a) presents the results of the extended biogeography based feature extractor (with non-linear immigration and emigration rates) on the image which has

**Table 7**  
Error matrix of hybrid ACO<sub>2</sub>/PSO/(BBO-GS) on Alwar region (kappa coefficient = 0.9870).

	Vegetation	Urban	Rocky	Water	Barren	Total
Vegetation	140	0	0	0	0	140
Urban	2	190	0	1	1	194
Rocky	0	0	198	0	2	200
Water	0	0	0	69	0	69
Barren	1	0	1	0	162	164
Total	143	190	199	70	165	767

a kappa coefficient of 0.6912 [27]. Fig. 14(b) and (c) are the result of applying the membrane computing and the bacterial foraging algorithms (hybrid FPAB/BBO) and achieve accuracy of 0.6818 and 0.6970 respectively [28,34]. Fig. 14(e) presents the results after applying the proposed hybrid ACO<sub>2</sub>/PSO/(BBO-GS) classifier which achieves the classification efficiency of 0.9870 and hence enhances the accuracy provided by the original hybrid ACO<sub>2</sub>/PSO/BBO classifier (which had a kappa coefficient of 0.9818). In fact, the hybrid ACO<sub>2</sub>/PSO/(BBO-GS) based on the proposed concept of using surface entropy in DEM band in BBO achieves the highest classification efficiency of 98.7% and hence outperforms all the above recent soft and the hard computing classifiers developed and adapted till date for geo-spatial feature extraction. Also, the proposed classifier is an addition to the taxonomy of soft computing techniques that we proposed in our papers [19,24].

Table 6 below summarizes and compares the kappa coefficients of the proposed hybrid ACO<sub>2</sub>/PSO/(BBO-GS) classifier with these very recent feature extractors and the benchmark hybrid ACO<sub>2</sub>/PSO/BBO classifier. Now we proceed to calculate the classification accuracy of our proposed algorithm using the classification error matrix. The error matrix for the original hybrid ACO<sub>2</sub>/PSO/BBO based classifier can be held from our paper [24] and that of the proposed hybrid ACO<sub>2</sub>/PSO/BBO-GS based classifier is shown in Table 7. From the tables, it is evident that the proposed hybrid ACO<sub>2</sub>/PSO/BBO-GS based classifier outperforms the original one. Hence the KHAT statistics of the proposed biogeography and geo-sciences based land cover feature extractor is 0.9870. The kappa (K) coefficient of the Alwar image is 0.9870 which indicates that

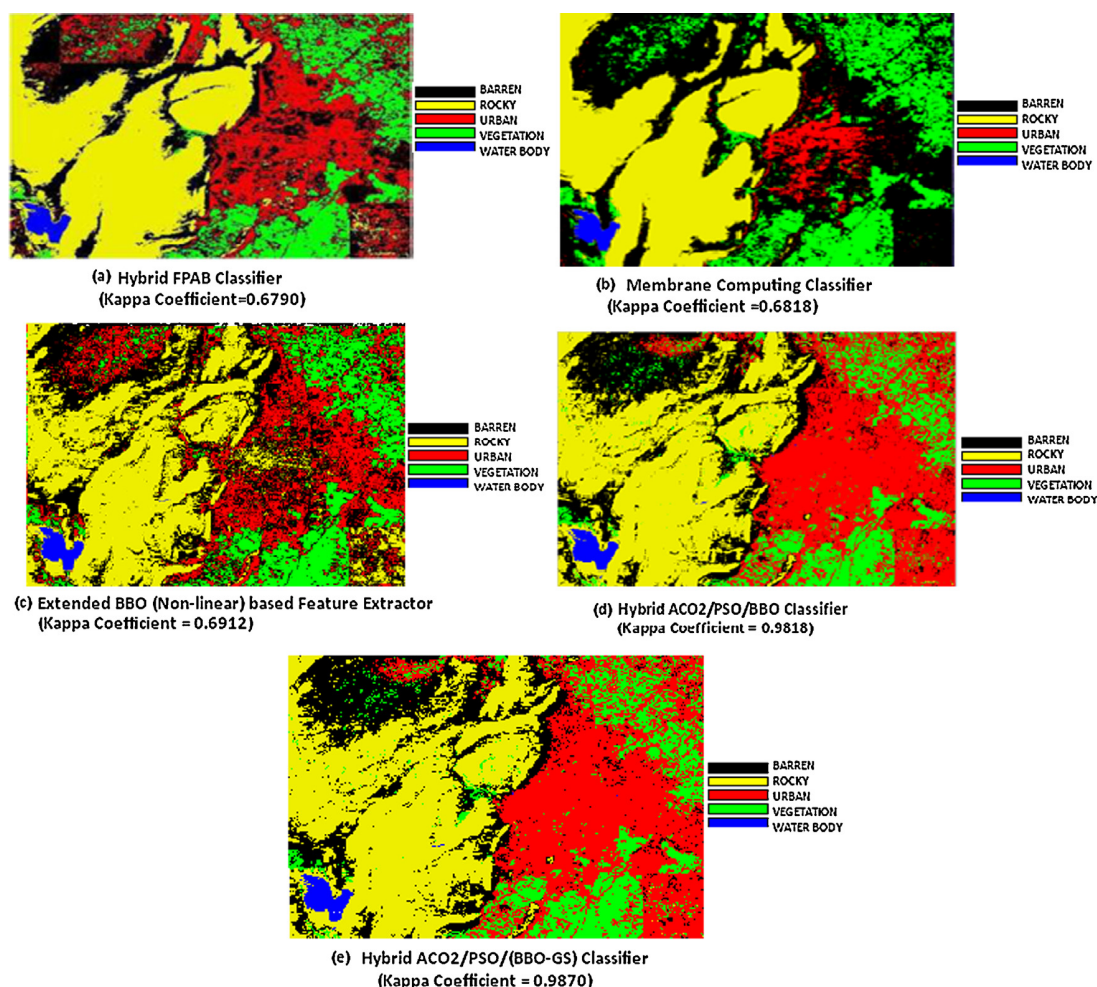


**Fig. 14.** Comparison of feature extraction results of hybrid ACO2/PSO/BBO-GS based classifier with the other recent computational intelligence based classifiers on the dataset of Alwar Region. (a) Hybrid FPAB classifier (kappa coefficient = 0.6790), (b) membrane computing classifier (kappa coefficient = 0.6818), (c) extended BBO (non-linear) based feature extractor (kappa coefficient = 0.6912), (d) hybrid ACO2/BBO classifier (kappa coefficient = 0.9818) and (e) hybrid ACO2/(BBO-GS) classifier (kappa coefficient = 0.9870).

**Table 8**  
Producer's accuracy.

Feature	Accuracy calculation	Producer's accuracy
Vegetation	140/143	97.9%
Urban	190/190	100.0%
Rocky	198/199	99.5%
Water	69/70	99.0%
Barren	162/165	98.2%

an observed classification is 98.70% better than one resulting from chance. Tables 8 and 9 depict the producer's and the user's accuracies which indicate how well the training pixels of a given cover type are classified. The results in Table 8 show that urban pixels

have been extracted most efficiently followed by rocky and water pixels, respectively. User's Accuracies which indicates the probability that a pixel classified into a given category actually represents that category on the ground is shown in Table 9. From the table, it can be observed that water and vegetation features show 100% accuracy of classification followed by rocky pixels.

**Table 9**  
User's accuracy.

Feature	Accuracy calculation	User's accuracy
Vegetation	140/140	100.0%
Urban	190/194	97.9%
Rocky	198/200	99.0%
Water	69/69	100%
Barren	162/164	98.8%

## 6. Conclusion and future directions of the work

The paper is an evolution of a new paradigm, the development of a new biogeography based classification algorithm inspired from the concepts of geo-sciences for land cover feature extraction. The main argument in the paper is finding a novel mechanism of



classification of images based on purely geo-sciences process. This may lead to another concept of process randomization, generation of virtual scenario, etc. which are important ingredients in battlefield assessment. The proposed classifier has been applied to two different datasets of Alwar region in Rajasthan and Patalganga area in Shivalik ranges. The results indicate that our proposed geo-sciences based classifier is highly effective in extracting land cover features and proves itself to be a better classifier than the traditional probabilistic classifiers as well as the original BBO classifier [46] as reflected by Table 9. On replacing the original BBO with the proposed BBO-GS, in the hybrid bio-inspired intelligent classifier that we proposed in our previous paper [22,24], the obtained hybrid ACO2/PSO/BBO-GS classifier achieves the highest classification efficiency amongst the other recent soft computing classifiers and hence proves to be the best known classifier developed till date for geo-spatial feature extraction.

The proposed model is however, flexible and can be made applicable to a large number of classification problems wherein entropy can be calculated in any other band in case of applications where the dataset is terrain multi-spectral images for example, mixed pixel resolution [54], design of hybrid classifiers, etc. For example, for the application of mixed pixel resolution in satellite multi-spectral imagery of natural terrain which has been discussed in our paper [13], the algorithm requires to calculate entropy in DEM band, however, for mixed pixel resolution in magnetic resonance imaging for disease diagnosis, the entropy is not calculated in DEM band. In case of applications where the dataset are normal images, for example, in case of face recognition application [12], pattern recognition, etc., we can simply formulate the entropy function according to its standard definition and evaluate the fitness function. In fact, the proposed BBO-GS based algorithm can be applied for various feature extraction applications by modifying the fitness function to use surface entropy (or surface entropy in the appropriate band in case of multi-spectral images) of the digital number values of the image pixels as the measure of comparison and classification of features in the input image dataset. The future scope of the research can be modeling other aspects of geo-sciences such as the details of mechanism of earth's dynamics and plate motion, etc. for proposing certain modification to the BBO-GS algorithm so that the classification mechanism can be refined further and hence can be adapted for further more feature extraction applications. Also, we can further divide the image into more plates so that a more accurate comparison can be made and the classification efficiency can be further increased by more accurate categorization of mixed pixels [29].

#### Uncited references

[16,43].

#### References

- [1] A. Accad, D.T. Neil, Lowland rainforest structural vegetation communities of Northeastern Australia: spatial response to predicted climate change, in: Proceedings of the 18th World IMACS/MODSIM Congress, Cairns, Australia, 2009, pp. 2028–2034.
- [2] E. Alpaydin, Introduction to Machine Learning, MIT Press, United States of America, 2004.
- [3] T. Back, Evolutionary Algorithms in Theory and Practice, Oxford Univ. Press, Oxford, UK, 1996.
- [4] S. Bansal, D. Gupta, V.K. Panchal, S. Kumar, Swarm Intelligence Inspired Classifiers in Comparison with Fuzzy and Rough Classifiers: A Remote Sensing Approach, Contemporary Computing, Communications in Computer and Information Science, vol. 40, Springer, USA, 2009.
- [5] H. Beyer, The Theory of Evolution Strategies, Springer, New York, 2001.
- [6] A. Bhattacharya, P.P. Chattopadhyay, Application of biogeography-based optimization for solving multi-objective economic emission load dispatch problems, Electric Power Components and Systems 38 (3) (2010) 340–365.
- [7] C. Blum, Ant colony optimization: introduction and recent trends, Physics of Life Reviews 2 (2005) 353–373.
- [8] J.C. Briggs, Biogeography & Plate Tectonics, Elsevier Publications, New York, 1987.
- [9] M. Clerc, Particle Swarm Optimization, ISTE Publishing, Amsterdam, The Netherlands, 2006.
- [10] D.J. Currie, Global Ecology and Biogeography, Blackwell Publishing Ltd., UK, 2012.
- [11] D. Dasgupta, Z. Michalewicz (Eds.), Evolutionary Algorithms in Engineering Applications, Springer, New York, 2001.
- [12] D. Gupta, L. Goel, Abhishek, An Efficient Biogeography Based Face Recognition Algorithm, CSE, 2013 (accepted for publication).
- [13] D. Gupta, L. Goel, T. Varshney, V.K. Panchal, Efficient mixed pixel resolution using bio-inspired heuristics, GCIS 2013. (communicated).
- [14] M. Dorigo, L. Gambardella, M. Middendorf, T. Stutzle, Special section on 'ant colony optimization', IEEE Transactions on Evolutionary Computation 6 (4) (2002) 317–365.
- [15] M. Dorigo, T. Stutzle, Ant Colony Optimization, MIT Press, Cambridge, MA, 2004.
- [16] R. Eberhart, Y. Shi, J. Kennedy, Swarm Intelligence, Morgan Kaufmann, San Mateo, CA, 2001.
- [17] R. Eberhart, Y. Shi, Special issue on particle swarm optimization, IEEE Transactions on Evolutionary Computation 8 (3) (2004) 201–228.
- [18] J. Franklin, Predictive vegetation mapping: geographic modelling of biospatial patterns in relation to environmental gradients, Progress in Physical Geography 19 (4) (1995) 474–499.
- [19] L. Goel, Land cover feature extraction using hybrid swarm intelligence techniques—a remote sensing perspective, ACEEE International Journal on Signal & Image Processing 1 (3) (2010) 1–3.
- [20] L. Goel, V.K. Panchal, D. Gupta, Embedding expert knowledge to hybrid bio-inspired techniques—an adaptive strategy towards focussed land cover feature extraction, International Journal of Computer Science and Information Security 8 (2) (2010) 244–253.
- [21] L. Goel, D. Gupta, V.K. Panchal, Biogeography and plate tectonics based optimization for water body extraction in satellite images, in: International Conference on Soft Computing and Pattern Recognition (SocProS), Advances in Soft Computing series of Springer, vol. 131, Springer, Roorkee, India, 2011, pp. 1–10.
- [22] L. Goel, D. Gupta, V.K. Panchal, Performance governing factors of BBO for land cover feature extraction: an analytical study, in: World Congress on Information and Communication Technologies (WICT), IEEE Publications, Mumbai, India, 2011, pp. 165–170.
- [23] L. Goel, D. Gupta, V.K. Panchal, Information sharing in swarm intelligence techniques: a perspective application for natural terrain feature elicitation, International Journal of Computer Applications 32 (2) (2011) 34–40.
- [24] L. Goel, D. Gupta, V.K. Panchal, Hybrid bio-inspired techniques for land cover feature extraction: a remote sensing perspective, Applied Soft Computing Journal of Elsevier Publications 12 (2) (2012) 832–849.
- [25] D. Goldberg, Genetic Algorithms in Search, Optimization, and Machine Learning, Addison-Wesley, Reading, MA, 1989.
- [26] V.I. Gornyi, The mantle convection and the drift of Euro-Asian plate (according the remote geothermal method data), in: IEEE International Geoscience and Remote Sensing Symposium (IGARSS), vol. 4, IEEE, St. Petersburg, Russia, 2002, pp. 2029–2035.
- [27] S. Gupta, V.K. Panchal, S. Goel, Extended biogeography based optimization for natural terrain feature classification from satellite remote sensing images, Communications in Computer and Information Science (LNCS) 168 (2011) 262–269.
- [28] D. Gupta, B. Das, V.K. Panchal, A methodical study for the extraction of landscape traits using membrane computing technique, in: WORLDCOMP, Las Vegas, USA, 2011.
- [29] N. Gupta, V.K. Panchal, Swarm Intelligence for mixed pixel resolution, in: Computers & Simulations in Modern Science, vol. 5, WSEAS Press, USA, 2011, pp. 190–194.
- [30] F. Kang, J. Li, Z. Ma, Rosenbrock artificial bee colony algorithm for accurate global optimization of numerical functions, Information Sciences 181 (16) (2011) 3508–3531.
- [31] F. Kang, J. Li, Q. Xu, Damage detection based on improved particle swarm optimization using vibration data, Applied Soft Computing 12 (8) (2012) 2329–2335.
- [32] F. Kang, J. Li, H. Li, Artificial bee colony algorithm and pattern search hybridized for global optimization, Applied Soft Computing 13 (4) (2013) 1781–1791.
- [33] F. Kang, J. Li, Z. Ma, An artificial bee colony algorithm for locating the critical slip surface in slope stability analysis, Engineering Optimization 45 (2) (2013) 207–223.
- [34] N.K. Johal, S. Singh, H. Kundra, A hybrid FPAB/BBO algorithm for satellite image classification, International Journal of Computer Applications 6 (5) (2010) 31–36.
- [35] W. Khatib, P. Fleming, The stud GA: a mini revolution? in: A. Eiben, T. Back, M. Schoenauer, H. Schwefel (Eds.), Parallel Problem Solving from Nature, Springer, New York, 1998.
- [36] K.J. Williams, et al., Which environmental variables should I use in my biodiversity model? International Journal of Geographical Information Sciences, Special Issue: Second Special Issue on Spatial Ecology 26 (11) (2012) 2009–2047.
- [37] S. Kumar, D. Gupta, V.K. Panchal, S. Kumar, Enabling web services for classification of satellite images, in: International Conference on Semantic Web and Web Services (SWWS'09), Nevada, USA, 2009.
- [38] T.M. Lillesand, R. Kiefer, Remote Sensing and Image Interpretation, third ed., John Wiley, New York, 1993.

- [39] W. Long III, S. Srihann, Unsupervised and supervised classifications: land cover classification of SSC image: unsupervised and supervised classification using ERDAS Imagine, in: IGARSS '04 Proceedings, vol. 4, 2004, pp. 20–24.
- [40] H. Ma, An analysis of the equilibrium of migration models for biogeography-based optimization, *Information Sciences* 180 (18) (2010) 3444–3464.
- [41] L. Moresi, M. Gurnis, M. Shijie Zhong, Plate tectonics and convection in the earth's mantle: toward a numerical simulation, *International Journal of Computing in Science and Engineering* 2 (3) (2000) 22–23.
- [42] N.E. Zimmermann, T.C. Edwards Jr., C.H. Graham, P.B. Pearman, J.-C. Svenning, New trends in species distribution modelling, *Ecography, Special issue on Species Distribution Modelling* 33 (6) (2010) 985–989.
- [43] A. Øhrn, Komorowski, J. ROSSETA, A rough set tool kit for analysis of data, in: Proc. 3rd International Joint Conference on information Sciences, Durham, NC, 1997, pp. 403–407.
- [44] V.K. Panchal, P.C. Saxena, S. Deshmukh, Resolving spectrally similar landuse/landcover class conflict in remote sensing images using rough sets, in: IEEE Computer Society International Conference on Hybrid Information Technology (ICHIT), vol. 2, Korea, 2006, pp. 460–466.
- [45] V.K. Panchal, N. Singhal, S. Kumar, S. Bhakna, Rough-fuzzy sets tie-up for geospatial information, in: ISRO's International Conference on Emerging Scenario in Space Technology & Applications (ESSTA' 2008), vol. 1, Chennai, India, 2008.
- [46] V.K. Panchal, P. Singh, N. Kaur, H. Kundra, Biogeography based satellite image classification, *International Journal of Computer Science and Information Security* 6 (2) (2009) 269–274.
- [47] L. Pappula, Application of real coded genetic algorithm for target sensing, in: Sixth International Conference on Sensing Technology (ICST), Kolkata, India, 2012, pp. 69–72.
- [48] I. Parmee, *Evolutionary and Adaptive Computing in Engineering Design*, Springer, New York, 2001.
- [49] Z. Pawlak, Rough sets, *International Journal of Computer and Information Science* 11 (5) (1982) 341–356.
- [50] Z. Pawlak, Rough set theory and its applications to data analysis, *Cybernetics and Systems* 29 (7) (1998) 661–688.
- [51] D.R. Peddle, H. Peter White, R.J. Soffer, J.R. Miller, E.F. LeDrew, Reflectance processing of remote sensing spectroradiometer data, *Computers & Geo-sciences* 27 (2001) 203–213.
- [52] K. Price, R. Storn, Differential evolution, *Dr. Dobb's Journal* 22, 24, 78 (1997) 18–20.
- [53] D. Simon, Biogeography based optimization, *IEEE Transactions on Evolutionary Computation* 12 (6) (2008) 702–713.
- [54] S. Sinha, A. Bhola, V.K. Panchal, S. Singhal, A. Abraham, Resolving mixed pixels by hybridization of biogeography based optimization and ant colony optimization, in: WCCI 2012 IEEE World Congress on Computational Intelligence, Brisbane, Australia, 2012, pp. 126–131.
- [55] S.Z. Dobrowski, H.D. Safford, Y.B. Cheng, S.L. Ustin, Mapping mountain vegetation using species distribution modeling, image-based texture analysis, and object-based classification, *Applied Vegetation Science* 11 (4) (2008) 499–508.
- [56] R. Storn, System design by constraint adaptation and differential evolution, *IEEE Transactions on Evolutionary Computation* 3 (1999) 22–34.

- [57] Y. Li, B. Cheng, An improved k-nearest neighbor algorithm and its application to high resolution remote sensing image classification, in: 17th International Conference on Geoinformatics, IEEE, Beijing, China, 2009, pp. 1–4.
- [58] Z. Wei, Survey and analysis of land satellite remote sensing applied in highway transportations infrastructure and system engineering, in: IGARSS, vol. 4, IEEE, Boston, MA, 2008, pp. 479–482.



in these courses.

**Lavika Goel** is a research scholar in the Department of Computer Engineering at Delhi Technological University (DTU), Delhi, India. She worked at Oracle India Private Ltd. for six months through campus recruitment and then left it to pursue research in the field of Nature Inspired Intelligence, her interest area. Securing a GATE percentile of 98.7%, she did her M.E. (Master of Engineering with *Distinction*) in Computer Technology & Applications from Delhi Technological University (formerly Delhi College of Engineering), Delhi and B-Tech (with Honors) in Computer Science & Engineering from JSS Academy of Technical Education, U.P. Technical University and has always been among the top rank-holders of the university



**Dr. Daya Gupta** is a Professor in the Department of Computer Engineering, Delhi Technological University, Delhi and is currently the head of the department there. She has done Ph.D. in Computer Engineering from University of Delhi and M.Sc. (Maths), Post M.Sc. in Computer Science from IIT, Delhi. She is a senior member of IEEE and a life member of CSI. Her research interests are in the field of requirement engineering, network security, adhoc networks and image classification in remote sensing. She has published several research papers in international journals and conferences and has chaired sessions and delivered invited talks at many national and international conferences.



and delivered invited talks at many national and international conferences.

**Dr. V.K. Panchal** is the Associate Director at Defense Terrain & Research Lab, Defense and Research Development Organization (DRDO), New Delhi, India. He is an Associate Member of IEEE (Computer Society) and Life Member of Indian Society of Remote Sensing. He is also the Vice-Chairman of the Indian Society of Remote Sensing, Delhi Chapter. He has done Ph.D. in Computational Intelligence from Jawaharlal Nehru University, Delhi and M.S. in Information Systems from BITS, Pilani and is currently working as Scientist 'G' at DRDO, Delhi. His research interests are in the synthesis of terrain understanding model based on incomplete information set using bio-inspired intelligence and remote sensing. He has chaired many sessions

# Cellular Automata Based Test Data Generation

Harsh Bhasin

Department of Computer Science  
Delhi Technological University  
Delhi, India  
+91-9818730508

i\_harsh\_bhasin@yahoo.com

Neha Singla

M. Tech Scholar, CE Department  
YMCAUST  
Sec 6, Faridabad, India  
+91-9999929738

nehasingla2815@gmail.com

Shruti Sharma

Assistant Professor, CE Department  
YMCAUST  
Sec 6, Faridabad, India  
+91-9958993483

shruti.mattu@gmail.com

## ABSTRACT

Manual Test Data Generation is an expensive, error prone and tedious task. Therefore, there is an immediate need to make the automation of this process as efficient and effective as possible. The work presented intends to automate the process of Test Data Generation with a goal of attaining maximum coverage. A Cellular Automata system is discrete in space and time. Cellular Automata have been applied to things like designing water distribution systems and studying the patterns of migration. This fascinating technique has been amalgamated with standard test data generation techniques to give rise to a technique which generates better test cases than the existing techniques. The approach has been verified on programs selected in accordance with their Lines of Code and utility. The results obtained have been verified. The proposed work is a part of a larger system being developed, which takes into account both black box and white box testing.

## Categories and Subject Descriptors

D.2.5 [Software Engineering]: Testing and Debugging – *Testing Tools* (e.g., data generators, coverage testing)

## General Terms

Algorithms, Reliability, Verification.

## Keywords

Testing, Test Data Generation, Cellular Automata, Path Coverage, Autocorrelation.

## 1. INTRODUCTION

Manual test data generation is tedious and it accounts for a considerable percentage of time and cost. So, there is a need to make Automatic Test Data Generation (ATDG) more efficient, both in terms of time and coverage. This will enhance the reliability of testing and the quality of the product being tested. As per the literature, the best test case suite is the one that maximizes the coverage of code and at the same time minimizes the Oracle cost. Oracle cost is the combination of the cost of executing the entire test suite and the cost of checking the system behavior as the whole [10]. The coverage is maximum when there is at least one test case in the suite for each independent path of the Program under Test (PUT). To minimize the Oracle cost, the number of test cases to be executed must be reduced.

The work being carried out takes into account the coverage criteria and minimization of the oracle cost. These bi-objective optimization criteria can be achieved by taking the best possible test case, from amongst the set of test cases generated, for each individual path. In order to do so, just one test case would be considered for a path, so the need of minimizing the oracle cost is eliminated. The task of generating paths is accomplished using the concept of Cellular Automata (CA) and the test data generation is done by considering the variables defined and variables used in each path. The procedure also considers programs having many modules and thus paves the way for its applicability to component based programming as well. This is necessary as most of the existing test data generators fail to consider the interaction between modules.

So let's have a look at the proposed cellular test data generator. The following sections give insights into our work and its importance to the discipline. "I heard that there was a secret cord, that David played and it pleased our lord". The task intends to find the secret cord that can please the lord of Software Engineering. The primary contributions of the paper are as follows:

1. CA has been used for test case generation, thus paving way for the use of other artificial life approaches in the discipline.
2. The selection of patterns of CA has been done in a novel way, which is statistically sound and uses autocorrelation as its base, thus making sure that requisite patterns are selected from CA.
3. Test case generation follows path coverage hence a time tested technique instills confidence in the proposed work.
4. The technique is a part of a bigger system being developed, which proposes using module state diagrams to analyze the interactions between the modules as per the design specifications.

The rest of the paper is organized as follows. Section 2 presents a literature review. Section 3 gives an overview of CA. Section 4 provides an insight into the problem discussed, ATDG. The work proposed has been explained in the section 5, followed by the conclusion and future scope in section 6.

## 2. LITERATURE REVIEW

In order to state "Baby I've been here before. I know this room I've walked this floor." an extensive review has been conducted to study the techniques proposed until now. This is done to find the gaps in the existing works and propose a new technique. The seed of 'Automated Test Data Generation' (ATDG) was sowed by Ramamoorthy et al. [27] and Miller and Spooner, in 1976 [32]. The work proposed by Ramamoorthy [27] had a Source code evaluator, a constraint generator and a test data generator. The Fortran Source Code Processor evaluates the source code and generates a program graph. The source code is also converted into its internal representation, which helps in generating path constraints at a later stage. The program graph generated earlier helps the path generator to test the paths. Test data is generated with the help of the program graph generator, the constraint generator and the symbol table. The symbol table plays a vital role in the generation of test data. The technique proposed by Ramamoorthy, handles the constraints that were there in the earlier techniques. One of the problems that were faced by the above technique was the index of an array being an array itself. The concept was tested by about the 1000 FORTRAN programs ranging from 30 statements to 150 statements and it was observed that processing time was half a second per constraint. It was also observed that most of the time was utilized in backtracking. The work had its own limitations but at least it was successful in demonstrating the feasibility of the technique and the advantages of symbolic execution. The Test Data Generation used the following technique: the constraints were converted into Conjunctive Normal Form (CNF) and all the input variables were arranged in a sequence. The constraints were observed and a new value was generated for every variable. In the paper,

equations were formed with the help of constraints and those equations were solved to get the values for test data.

Miller and Spooner used the concept of numerical maximization instead of symbolic execution to generate test data for numerical programs or programs with floating point data [22].

Clarke gave an algorithm for test data generation in 1976 that uses the concept of symbolic execution of the given path and creates a set of constraints on the program's input variables. The symbolic execution phase uses path descriptions and information about the program unit. An inequality solver solves the set of constraints generated and test data is obtained. The technique proposed was verified on programs written in ANSI Fortran [5].

Various Techniques have been proposed to automate the process of Test Data Generation in which many techniques are based on Evolutionary Algorithms.

A systematic survey was conducted by McMinn in 2004, on Search based software Test Data Generation [19]. Various papers related to these techniques have been studied and thoroughly analyzed. Most of the researchers used Genetic Algorithms (GAs) to solve the problem of ATDG [35, 31, 21, 30, 16, 29, 20, 25, 33, 12, 13, 28].

In the work proposed by Xanthakis et al. in 1992, variable length genetic algorithms were deployed to optimize and select the software path clusters which were weighted in accordance with criticality of the path. More critical paths were executed first [35].

Miller et al. proposed a technique which utilizes program dependence graph and GAs to generate test data. It works on branch coverage criteria [21]. The technique proposed deals with Boolean variables or enumerated types. The proposed system was named TDGen. The proposed technique was compared with GADGET on the basis of various metrics, such as Ease-of-Execution, Improved-Ease-Set, Path coverage, Statement coverage, Branch coverage and Condition-Decision coverage. The approach was verified by applying it on various standard programs and then comparing it with the existing tool GADGET.

GAs have been considered for automatic generation of test data for different coverage criteria, such as path coverage [30], Branch coverage [16, 29], loop coverage [29] and Condition – decision coverage [20].

Pargas. et al. in 1999, proposed the use of GAs to generate data that causes execution of a given statement, branch, path, or definition-use pair. Parallel processing was used to improve the performance of the search. The tool developed was named TGen [25]. The proposed work was verified using six C programs and was compared with the Random Test Data Generation approach. The metrics used for comparison were statement coverage and branch coverage.

In the work proposed by Wegner et al., an evolutionary test environment was developed that performs fully automatic test data generation for most structural test methods [33]. The developed test environment supports all common control-flow and data-flow oriented test methods, such as Node-oriented, Path-oriented, Node-path-oriented and Node-node-oriented. For each method, a separate Fitness function was evaluated. The approach was verified using 6 test objects (programs) in C language. Results were compared with Random test data generation approach.

Girgis in 2005, presented an approach for data flow coverage criterion using GAs [12]. The proposed GA accepts an instrumented version of the program to be tested, the list of def-use associations to be covered, the number of input variables, and the domain and precision of each input variable as input. The algorithm produces a set of test cases, the set of def-use associations covered by each test case, and a list of uncovered def-use associations, if any. A new selection operator was proposed known as random selection method and was compared with

the existing Roulette Wheel selection method. New test data was constructed from the previously generated test data.

Gong et al. in 2011, uses GAs for many paths coverage based on grouping [13]. First, target paths were divided into several groups according to their similarities, and each group forms a sub-optimization problem, which transformed a complicated optimization problem into several simpler sub-optimization problems; then a domain-based fitness function was designed. Finally, these sub-optimization problems were simplified along with the process of generating test data, hence improving the efficiency of generating test data.

Sofokleous and Andreou in 2008, proposed a dynamic test data generation framework that makes use of two optimization algorithms: Batch-Optimistic (BO) and Close-Up (CU) algorithms based on the principle of edge/condition coverage criteria. These algorithms make use of GAs. Authors have used weights  $w_1$  and  $w_2$ , to calculate the fitness function, where,  $w_1$  and  $w_2$  are weights that define the significance of edges or/and predicates in the overall execution. But, in the review it was observed that they have not proposed any way to decide the weights. Ideally the weights cannot be chosen randomly as this would lead to meaningless fitness function evaluation [28].

Lin and Yeh proposed a technique based on GAs for path testing. Test cases for a selected path were generated and then evolved to obtain a better test case. The proposed fitness function evaluates the best test case out of all the existing test cases and also deals with the loops if present in the path [17].

In a work proposed by Ruchika Malhotra et al. GAs have been used along with the adequacy based testing criteria [18]. They used mutation analysis for adequacy based testing criteria and GAs was applied to obtain near-global optimum solutions.

Besides GAs, other evolutionary techniques have also been proposed such as Scatter Search approach proposed by Blanco et al. in 2008 [4]. The technique makes use of the branch coverage adequacy criterion.

Another Evolutionary algorithm was given by Ferrer et al. for prioritized pairwise test data generation [9]. The authors used Combinatorial Interaction Testing (CIT). It is a black box sampling technique, which discovers faults caused by parameter interactions in highly configurable systems. Prioritization with interaction coverage was used.

Abreu et al. proposed an alternative approach for Test Data Generation which is based on Generalized Extremal Optimization (GEO) and a variation of GEO ( $GEO_{var}$ ) [1]. They considered the programs that had loops for the test data generation. The technique assumes that the paths had already been generated using some criteria and focuses on generating test data for the given paths. They compared their technique with Standard Genetic Algorithm (SGA). Results show that the coverage obtained by GEO and  $GEO_{var}$  is not better than SGA, rather, it takes less time to generate the test cases. But time taken to generate the test cases does not matter in real time software, where, reliability of the software is more crucial factor than few more minutes or hours of testing.

Evolutionary Algorithms are also used in multi-objective test data generation. In these algorithms minimizing oracle cost and maximizing the coverage are the two objectives. Lakhota et al. reformulated the problem of ATDG into MOTDGP (Multi-Objective Test Data Generation Problem) for the first time [14] and then modified by Harman et al. in 2010 [15]. Various Multi-Objective algorithms have been proposed such as NSGA-II, MOCeII, SPEA2, PEAS, etc. K. Deb et al. proposed an algorithm named NSGA-II based on GAs [6]. The MOCeII (Multi-Objective Cellular Genetic Algorithm) technique was proposed by Nebro et al. It is an algorithm which is a combination of Cellular approach and Genetic Algorithms [23]. It takes the concept of neighborhood from Cellular Automata and amalgamates it with GAs. SPEA2 (Strength Pareto Evolutionary Algorithm) is an algorithm



proposed by Zitler et al. [37]. Knowles and Corne proposed a metaheuristic approach PAES that found the diverse solutions in the Pareto Optimal set [2]. The algorithm does not make use of crossover operator, but instead finds the solution by just modifying the current solution. Ferrer et al. in 2010, compared the techniques for MOTDGP [10].

### 3. CELLULAR AUTOMATA

A Cellular Automata (CA) is a dynamical system that is discrete in space and time, and operates on a regular lattice. They are characterized by local interactions. A CA is a system that generates patterns that have the capacity of replicating themselves [24]. These patterns are generated by simple rules. They have been successfully used to reproduce any machine described in the program, including a copy of the program itself [24]. Von Neumann created a theoretical universal constructor using a CA [26].

The following are the characteristics of a CA.

#### 3.1 Cellular Space

Cellular Space is the type of grid on which CA is computed. In 1D automata, we can have consecutive cells in linear fashion, 2D automata can have triangles, squares, hexagons etc., as their basic building blocks. 3D automata can resemble a hyperbolic structure [34].

#### 3.2 Neighborhood

The neighborhood is the set of cells by which the state of the current cell is affected. Various types of neighborhoods have been defined. The simplest choice is "nearest neighbors," in which only cells directly adjacent to a given cell may be affected at each time step. In case of a one-dimensional CA, cells on the left and right of a cell act as the neighborhood. Two common neighborhoods in the case of a two-dimensional cellular automaton on a square grid are the Moore neighborhood (a square neighborhood) and the Von Neumann neighborhood (a diamond-shaped neighborhood) [32].

#### 3.3 States of the Cell

The number of states that each cell can take must be specified and limited. An Automaton can have any number of states, depending on the application. The Von Neumann CA had 29 states [3].

#### 3.4 Transition Rule

Over time, the cells can change their states. The change is governed by the cellular automaton's rules and information of the neighbors' states.

#### 3.5 Boundary Conditions

The boundary cells of a cellular space do not have same number of neighbors as the other cells. So, a rule or condition is required to complete the neighborhood of the boundary cells [11].

#### 3.6 Initial Conditions

In order to start the system in a controlled way, an initial state is defined [11].

The above discussion leads to the following definition of cellular automata.

A CA is composed of a number of identical cells; each can take a finite number of states. The state of a cell changes with time and a rule is used to update the state of all the cells at discrete time steps and synchronously for all the cells of the automaton. Thus, a CA is an  $N - \text{dimensional}$  lattice.

Let,  $S_i$  be the state of cell  $i$ .

$S_i(t)$  be the state of cell  $i$  at time  $t$ .

$N_i$  be the set of neighbors of cell  $i$ .

$\Phi$  be the transition function or transition rule.

The state of cell at time  $(t + 1)$  is a function of both the state of the neighborhood cells at time  $t$  and the state of itself at time  $t$ .

$$S_i(t + 1) = \Phi(S_j(t), S_i(t)), j \in N_i \quad [11]$$

The type of CA used in the work is Elementary Cellular Automata.

Elementary CA has cells which can have 0 and 1 as their values. The configuration of a cell is determined by its neighbors. Since, there are 2 neighbors therefore, the 3 adjacent cells can have 8 states. Therefore,  $2^8$  i.e. 256 rules can be formed resulting in different patterns.

### 4. AUTOMATED TEST DATA GENERATION

Coming back to "Hallelujah", the next line of the song asks if we care for the music? The answer is yes. The Cellular Automata provides music to the ATDG that is crucial for testing because test data is one of the key factors that determines the quality of a software test [7]. "There was a time you let me know, what's really going on below", in our case it is the long term cost of testing. The Core Test data Generator has the following components.

#### 4.1 Architecture of Test Data Generation

The process of ATDG consists of 3 components:

##### 4.1.1 Program Analyzer

Program Analyzer takes source code as input and performs static analysis giving the Control Flow Graph, Data Dependence Graph, etc. as the output. The produced output is used by the other two components.

##### 4.1.2 Path Selector

Based on the code coverage criterion opted, the path selector evaluates the paths for which test data is to be generated. A good test suite depends on the paths that it covers, that further depend on the coverage criteria selected. There are various types of coverage criteria that can be used in isolation or in combination with other criteria to obtain better results. Coverage criteria includes criteria such as Function coverage, Statement coverage, Branch coverage, Decision coverage, Condition coverage, Multiple-Condition coverage, Path coverage, Parameter Value coverage, etc.

##### 4.1.3 Test Data Generation

The paths generated by path selector acts as input for the test data generator. The main task of the Test Data Generator (TDG) is to generate test cases for the paths generated. A test case is a set of all the variables used in the program with their definite values, and the output obtained after executing the test case on the program. The TDG can also provide feedback to the Path Selector to provide additional information such as information regarding infeasible paths which help to generate paths more effectively and efficiently.

Adequate test data can never be created if performance at any of the steps is poor or the execution is incorrectly performed. The proposed work takes into account the analysis of the program, selection of appropriate paths and generation of best possible test cases as per the bi-objective optimization criteria.

### 5. PROPOSED WORK

The work uses a Control Flow Graph (CFG) as its base. Independent paths are then generated for the Program under Test (PUT). For each independent path, test cases are to be defined. It may be noted that, test cases should cover all independent paths. The aim of this step is to attain maximum coverage. In each path, the variables that are defined and used are stored in a data structure; henceforth called  $var[]$ , which is a 2D array. The design specifications are then used to find out the legal range of variables. Test cases are generated by seeing the above constraints and the range of values that are assigned to the variables. There can be many such paths. So the question is to select a path out of these paths and make sure that the path selected satisfies the criteria of maximum coverage.

Let there be ‘m’ modules and each module has at most ‘n’ decision nodes. Each path followed by true evaluation is denoted by ‘1’ and with false evaluation is denoted by ‘0’. To generate the paths, for which test cases need to be generated, the approach of Cellular Automata (CA) has been used. Out of 256 rules of CA, few rules have been selected via statistical analysis.

Out of the above rules, a rule is selected randomly. From the pattern generated by the selected rule, a local region is selected. This local region generates ‘n’ values. The generated values can be either 0 or 1. An array of  $1 \times n$  is obtained, where  $i^{th}$  value of array depicts whether the  $i^{th}$  decision node will be evaluated to true or false. If the value is ‘0’ then the condition of the node will be evaluated to false, otherwise it will be evaluated to true.

The values for the decision nodes generated above will decide the path generated for which test case is to be crafted. It may be noted that many such test cases can be crafted in accordance with the path.

The above procedure can be repeated as many times as the number of test cases required for that particular module. After generating paths, redundant paths are removed to minimize oracle cost.

After the generation of paths, the next step is to generate test cases for the paths. To generate the test cases, information obtained from the definition and use of the variables is used as already discussed above. From the legal values obtained, a value is selected using a Pseudo Random Number Generator (PRNG) for each variable and with the combination of these values, a test case is obtained.

The same procedure is followed for the remaining modules. The algorithm is stated in Figure 1.

**Algorithm: TestDataGeneration**

```

1.  cfg ← ConstructCFG(pgm);
2.  for each module do
3.      m ← ModuleSelection(pgm);
4.      repeat
5.          r ← RuleSelection(rule);
6.          p[,] ← PatternGeneration(r);
7.          l[,] ← LocalRegionSelection(p);
8.          v[,] ← SelectValue(l);
9.          paths[,] ← GeneratePath(cfg,v);
10.     until no more path required
11.     finalPaths[,] ← RemoveRedundant(paths);
12. For each path do
13.     path[] ← PathSelection(finalPaths);
14.     var[,] ← VarDefUse(path);
15.     for each variable do
16.         variable ← VariableSelection(var);
17.         range ← ExtractRange(variable);
18.         value ← Pick(range);
19.     testCase ← GenCumulativeTestCase(value);
```

**Figure 1. Algorithm for Automatic Test Data Generation**

The methods and data structures used in the proposed algorithm are as follows:

### 5.1 pgm Data Structure

‘pgm’ is a data structure in which the program under test is stored.

### 5.2 rule Data Structure

‘rule’ is an array containing the rule numbers, selected for generating binary numbers.

### 5.3 ConstructCFG()

This function generates the CFG of the PUT.

### 5.4 ModuleSelection()

This function selects the module for which test cases have not been generated as yet.

### 5.5 RuleSelector()

This function randomly selects the rule from the numbers stored in ‘rule’.

### 5.6 PatternGenerator()

This function generates the pattern for the selected rule.

### 5.7 LocalRegionSelector()

This function selects a Local Region from the generated pattern.

### 5.8 SelectValue()

This function selects ‘n’ values from the local region obtained in the above step.

### 5.9 PathGenerator()

This function generates paths by using the values obtained in the above step. If the value ‘0’ is generated then the decision node is evaluated to false. If the value ‘1’ is generated then the decision node is evaluated to true.

### 5.10 RemoveRedundant()

The above steps may generate a single path more than once. So there is a need to remove the redundant paths. This function accomplishes the above task.

### 5.11 PathSelector()

This function selects the path for which test cases have not been generated yet.

### 5.12 VarDefUse()

This function identifies the variables defined and used in the selected path.

### 5.13 VariableSelector()

This function selects a variable whose value is to be generated from the above variables.

### 5.14 ExtractRange()

This function extracts the range of the selected variable from the design specifications.

### 5.15 Pick()

This function selects a value from the range obtained in the above step.

### 5.16 GenCumulativeTestCase()

Values of all the variables in a path are collected and a test case is generated for the selected path.

The above procedure has been depicted in Figure 2. The figure has been divided into two parts, Figure 2A and Figure 2B, connected by the connector ‘C’.

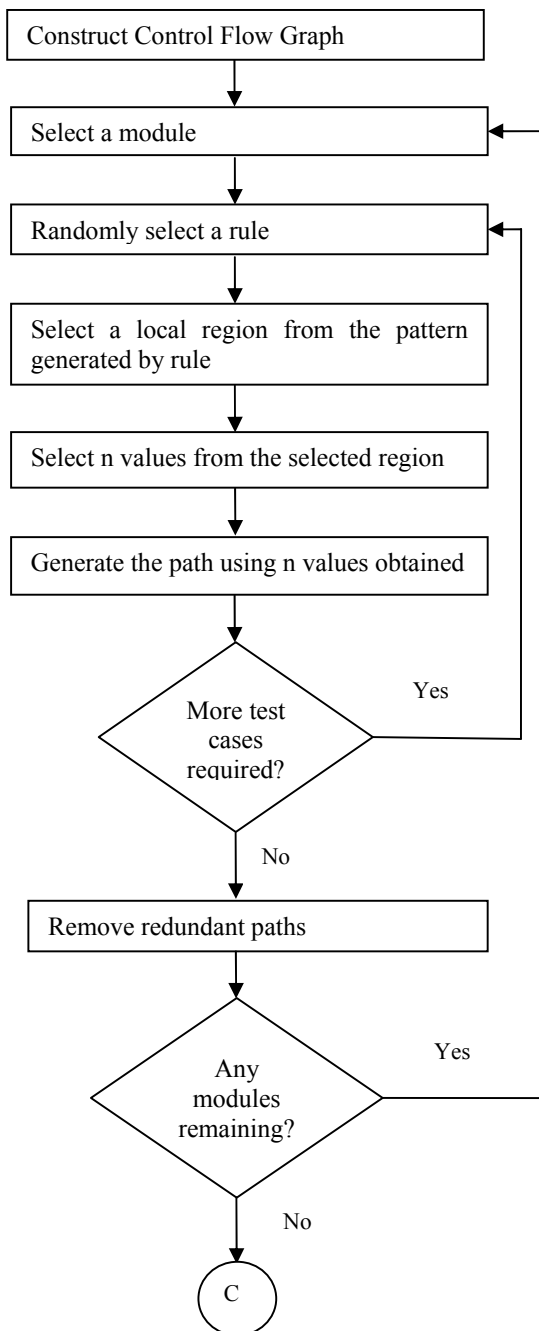


Figure 2A. Flow Diagram of the Proposed technique

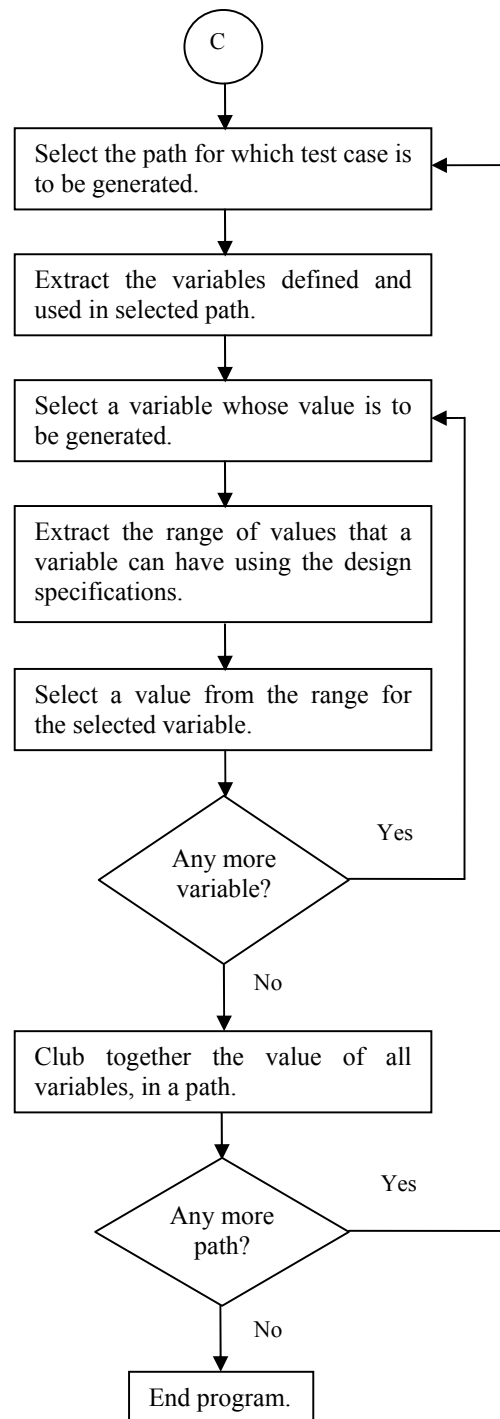


Figure 2B. Flow Diagram of the Proposed Technique

For the purpose of Selection of a local region, initially a rule is randomly selected and then a pattern corresponding to that rule is generated. Initially a 1D CA system was used, constituting 100 cells. Cells have been updated for 100 discrete time steps. Thus, a pattern of  $100 \times 100$  is obtained.

From this pattern, a local region of  $20 \times 20$  is to be selected. A randomness criterion has been used to select the pattern. In order to accomplish this task deviation is calculated for each region.

$$\text{Deviation} = \text{abs}(n_1 - n_0)$$

$n_1$  = number of 1's in selected region

$n_0$  = number of 0's in selected region

From the deviations obtained, the minimum deviation is calculated and all the regions having the value obtained above as its deviation are considered as local regions.

But, the results obtained are not encouraging and do not support the criteria of randomness. So, an alternative approach for the selection of local regions has been considered which calculates the Coefficient of Autocorrelation for each possible region.

$$r_k = \frac{\sum_{i=1}^{N-k} (Y_i - \bar{Y})(Y_{i+k} - \bar{Y})}{\sum_{i=1}^N (Y_i - \bar{Y})^2}$$

Where, value of k is assumed as 1,

$N = 20$ , as there are 20 rows in the region which represents the state of cells at 20 discrete time steps.

$Y_i$  = Value of  $i^{\text{th}}$  row, which is calculated by multiplying the individual values in the respective row by  $2^{-10}$  to  $2^9$ .

$\bar{Y}$  = mean of all the  $Y_i$  values obtained.

$$\bar{Y} = \frac{\sum_{j=1}^N Y_j}{N}$$

Where, j varies from 1 to 20.

The work presented above is a part of a comprehensive system. The second component of the system has also been developed. The second component is based on the interaction between the modules via Module State Diagram (MST). The technique presented above generates test cases for each module and the second component being developed in parallel relies on the design specification and the interaction between the modules. The overall system will fill the gaps in the existing methodologies and instil confidence in the robustness of the test suite developed.

The technique proposed is intended to be applied to other procedural paradigms such as nested blocks, switch case, loops, etc.

## 6. CONCLUSION AND RESULTS

“Chaos was the law of nature; order was the dream of man”. The above work intends to apply the order of nature in order to achieve dream of man. The patterns generated by a CA system are chaotic but the task accomplished by them in the Cellular Test Data Generator brings order to the discipline of software testing. Software engineering principles would not work without a good test case generator. The above work finds the gaps in the existing techniques and proposes a novel algorithm, which fills the above gaps.

“Your faith was strong but you needed proof”, the proof here is the results of verification after applying the proposed technique on 20 programs. The programs have been selected considering the lines of code and their importance. The programs are diverse, both in terms of size and in terms of applicability. The system is also being tested by taking an example of an Enterprise Resource Planning (ERP) system developed for a paint company by “Sahib Soft”. The technique will take the discipline of test case generation to a new level, owing to its applicability to Component Based Programming. The above technique uses cellular automata as its premise.

Two important secondary studies by Yoo[36] and Emilie[8] point to the fact that techniques like regression testing will become more relevant, if they are amalgamated with an Automated Test Data Generator. The above work will therefore be combined with regression testing, so as to generate a system that will be independent and robust.

## 7. REFERENCES

- [1] Abreu, B. T. D., Martins, E., Sousa, F. L. D. 2007. Generalized extremal optimization: an attractive alternative for test data generation. *GECCO 2007*. 1138.
- [2] Angeline, P. J., Michalewicz, Z., Schoenauer, M., Yao, X., Zalzal, A. 1999. The Pareto Archived Evolution Strategy: A New Baseline Algorithm for Pareto Multiobjective Optimisation, *IEEE Press: Mayflower Hotel, Washington D.C., USA*. Vol.1.
- [3] Bhasin, H., Singla, N. 2012. Harnessing Cellular Automata and Genetic Algorithms To Solve Travelling Salesman Problem. *International Conference on Information, Computing and Telecommunications, (ICICT -2012)*. 72 – 77.
- [4] Blanco, R., Tuya, J., Adenso-Díaz, B. 2009. Automated test data generation using a scatter search approach. *Information and Software Technology*, 51, 4, 708-720.
- [5] Clarke, L. A. 1976. A system to generate test data and symbolically execute programs. *IEEE Trans. Software Eng.* SE-2, 3, 215-222.
- [6] Deb, K., Pratap, A., Agarwal, S., Meyarivan, T. 2002. A fast and elitist multiobjective genetic algorithm : NSGA-II. *IEEE Transactions on Evolutionary Computation*. 6, 2, 182–197.
- [7] Edvardsson, J. 1999. A Survey on Automatic Test Data Generation. In *Proceedings of the Second Conference on Computer Science and Engineering in Linköping*. 21-28.
- [8] Engström, E., Runeson, P., Skoglund, M. 2010. A systematic review on regression test selection techniques. *Information and Software Technology*.
- [9] Ferrer, J., Kruse, P., Chicano, F., Alba, E. 2012. Evolutionary algorithm for prioritized pairwise test data generation. *GECCO 2012*. 1213-1220.
- [10] Ferrer, J., Chicano, F. and Alba, E. 2012. Evolutionary algorithms for the multi-objective test data generation problem. *Softw: Pract. Exper.* 42, 1331–1362.
- [11] Floreano, D., Mattiussi, C. 2008. Bio – Inspired Artificial Intelligence: Theories, Methods, and Technologies. *MIT Press*.
- [12] Girgis, M.R. 2005. Automatic test data generation for data flow testing using a genetic algorithm. *Journal of Universal Computer Science*. 11, 5, 898–915.
- [13] Gong, D., Zhang, W., Yao, Y. 2011. Evolutionary generation of test data for many paths coverage based on grouping. *Journal of Systems and Software*. 84, 12, 2222-2233.
- [14] Harman, M., Lakhotia, K., McMinn, P. 2007. A multi-objective approach to search-based test data generation. *GECCO '07: Proceedings of the 9th annual conference on Genetic and evolutionary computation*, ACM: New York, NY, USA. 1098–1105.
- [15] Harman, M., Kim, S. G., Lakhotia, K., McMinn, P., Yoo, S. 2010. Optimizing for the number of tests generated in search based test data generation with an application to the oracle cost problem. *Proceedings of the 3rd International Workshop on Search-Based Software Testing (SBST) in conjunction with ICST 2010, IEEE: Paris, France*. 182–191.
- [16] Jones, B., Sthamer, H., Eyres, D. 1996. Automatic structural testing using genetic algorithms. *Software Engineering Journal*. 11, 5, 299–306.
- [17] Lin, J., Yeh, P. 2001. Automatic test data generation for path testing using GAs. *Information Sciences: an International Journal*. 131, 1-4, 47-64.

- [18] Malhotra, R., Garg, M. 2011. An Adequacy Based Test Data Generation Technique Using Genetic Algorithms. *Journal of Information Processing System (JIPS)*, 7, 2, 363-384.
- [19] McMinn, P. 2004. Search-based software test data generation: a survey. *Research Articles, Software Testing, Verification & Reliability*. 14, 2, 105-156.
- [20] Michael, C.C., McGraw, G.E., Schatz, M.A. 2001. Generating software test data by evolution. *IEEE Transactions on Software Engineering*. 27, 12, 1085-1110.
- [21] Miller, J., Reformat, M., Zhang, H. 2006. Automatic test data generation using genetic algorithm and program dependence graphs. *Information and Software Technology*. 48, 7, 586-605.
- [22] Miller, W. and Spooner, D. L. 1976. Automatic generation of floating-point test data. *IEEE Trans. Software Eng.* SE-2, 3, 223-226.
- [23] Nebro, A. J., Durillo, J. J., Luna, F., Dorronsoro, B., Alba, E. 2009. MOCeL: A cellular genetic algorithm for multiobjective optimization. *Int. J. Intell. Syst.* 24, 7, 726-746.
- [24] Neumann, J. V. 1996. Theory of Self-Reproducing Automata. *University of Illinois Press*, Champaign, IL.
- [25] Pargas, R.P., Harrold, M.J., Peck, R.R. 1999. Test data generation using genetic algorithms. *Journal of Software Testing, Verification and Reliability*. 9, 4, 263-282.
- [26] Pesavento, U. 1995. An implementation of von Neumann's self-reproducing machine. *Artificial Life*, 2, 4, 337-354.
- [27] Ramamoorthy, C. V., Ho, S. and Chen, W. T. 1976. On the automated generation of program test data. *IEEE Trans. Software Eng.* SE-2, 4, 293-300.
- [28] Sofokleous, A. A., Andreou, A. S. 2008. Automatic, evolutionary test data generation for dynamic software testing. *Journal of Systems and Software*. 81, 11, 1883-1898.
- [29] Sthamer, H. 1996. The automatic generation of software test data using genetic algorithms. Ph.D. Thesis, *University of Glamorgan*, Pontypridd, Wales, UK.
- [30] Watkins, A. 1995. The automatic generation of test data using genetic algorithms. *Proceedings of the 4th Software Quality Conference*, 300-309.
- [31] Watkins, A., Hufnagel, E.M. 2006. Evolutionary test data generation: a comparison of fitness functions. *Software Practice and Experience*. 36, 95-116.
- [32] Weisstein, Eric W. "Cellular Automaton." From MathWorld--A Wolfram Web Resource. <http://mathworld.wolfram.com/CellularAutomaton.html>.
- [33] Wegener, J., Baresel, A., Sthamer, H. 2001. Evolutionary test environment for automatic structural testing. *Journal of Information and Software Technology*. 43, 14, 841-854.
- [34] Wolfram, S. 1994. Cellular Automata and Complexity: Collected Papers, ISBN 0-201-62716-7.
- [35] Xanthakis, S., Ellis, C., Skourlas, C., Le Gall, A., Katsikas, S. 1992. Application of genetic algorithms to software testing. *5th International Conference on Software Engineering and its Applications*, Toulouse, France. 625-636.
- [36] Yoo, S., Harman, M. 2012. Regression testing minimization, selection and prioritization: a survey. *Softw. Test., Verif. Reliab.* 22, 2, 67-120.
- [37] Zitzler, E., Laumanns, M., Thiele, L., 2001. SPEA2: Improving the strength pareto evolutionary algorithm. Technical Report 103, Gloriestrasse 35, CH-8092 Zurich, Switzerland.

# Fekete-Szegő problem for a class of analytic functions

S. Sivaprasad Kumar and Virendra Kumar

**Abstract.** In the present investigation, by taking  $\phi(z)$  as an analytic function, sharp upper bounds of the Fekete-Szegő functional  $|a_3 - \mu a_2^2|$  for functions belonging to the class  $\mathcal{M}_{g,h}^\alpha(\phi)$  are obtained. A few applications of our main result are also discussed.

**Mathematics Subject Classification (2010):** 30C45, 30C80.

**Keywords:** Analytic functions, convex functions, Fekete-Szegő inequality, starlike functions, subordination.

## 1. Introduction

Let  $\mathcal{A}$  be the class of analytic functions  $f$  defined on the unit disk  $\Delta := \{z \in \mathbb{C} : |z| < 1\}$  of the form

$$f(z) = z + \sum_{n=2}^{\infty} a_n z^n. \quad (1.1)$$

Let  $\mathcal{S}$  be the subclass of  $\mathcal{A}$  consisting of univalent functions. For two functions  $f$  and  $g$  analytic in  $\Delta$  we say that  $f$  is *subordinate* to  $g$  or  $g$  is *superordinate* to  $f$ , denoted by  $f \prec g$ , if there is an analytic function  $w$  with  $|w(z)| \leq |z|$  such that  $f(z) = g(w(z))$ . If  $g$  is univalent, then  $f \prec g$  if and only if  $f(0) = g(0)$  and  $f(\Delta) \subseteq g(\Delta)$ .

A function  $p(z) = 1 + p_1 z + p_2 z^2 + \dots$  is said to be in the class  $\mathcal{P}$  if  $\operatorname{Re} p(z) > 0$ . Let  $\phi$  be an analytic univalent function in  $\Delta$  with positive real part and  $\phi(\Delta)$  be symmetric with respect to the real axis, starlike with respect to  $\phi(0) = 1$  and  $\phi'(0) > 0$ . Ma and Minda [6] gave a unified presentation of various subclasses of starlike and convex functions by introducing the classes  $\mathcal{S}^*(\phi)$  and  $\mathcal{C}(\phi)$  satisfying  $zf'(z)/f(z) \prec \phi(z)$  and  $1 + zf''(z)/f'(z) \prec \phi(z)$  respectively, which includes several well-known classes as special case. For example, when  $\phi(z) = (1 + Az)/(1 + Bz)$  ( $-1 \leq B < A \leq 1$ ) the class  $\mathcal{S}^*(\phi)$  reduces to the class  $\mathcal{S}^*[A, B]$  introduced by Janowski [3].

Ali *et al.* [1] introduced the class  $\mathcal{M}(\alpha, \phi)$  of  $\alpha$ -convex functions with respect to  $\phi$  consisting of functions  $f$  in  $\mathcal{A}$ , satisfying

$$(1 - \alpha) \frac{zf'(z)}{f(z)} + \alpha \left( 1 + \frac{zf''(z)}{f'(z)} \right) \prec \phi(z).$$

The class  $\mathcal{M}(\alpha, \phi)$  includes several known classes namely  $\mathcal{S}^*(\phi)$ ,  $\mathcal{C}(\phi)$  and  $\mathcal{M}(\alpha, (1 + (1 - 2\alpha)z)/(1 - z)) =: \mathcal{M}(\alpha)$ . The class  $\mathcal{M}(\alpha)$  is the class of  $\alpha$ -convex functions, introduced and studied by Miller and Mocanu [7]. Several coefficient problems for  $p$ -valent analytic functions were considered by Ali *et al.* [2].

In 1933, Fekete and Szegő proved that

$$|a_2^2 - \mu a_3| \leq \begin{cases} 4\mu - 3 & (\mu \geq 1), \\ 1 + \exp(-\frac{2\mu}{1-\mu}) & (0 \leq \mu \leq 1), \\ 3 - 4\mu, & (\mu \leq 0) \end{cases}$$

holds for the functions  $f \in \mathcal{S}$  and the result is sharp. The problem of finding the sharp bounds for the non-linear functional  $|a_3 - \mu a_2^2|$  of any compact family of functions is popularly known as the Fekete-Szegő problem. Keogh and Merkes [4], in 1969, obtained the sharp upper bound of the Fekete-Szegő functional  $|a_2^2 - \mu a_3|$  for functions in some subclasses of  $\mathcal{S}$ . For many results on Fekete-Szegő problems see [1, 2, 9, 10, 12, 13, 14].

The Hadamard product (or convolution) of  $f(z)$ , given by (1.1) and  $g(z) = z + \sum_{n=2}^{\infty} g_n z^n$  is defined by

$$(f * g)(z) := z + \sum_{n=2}^{\infty} a_n g_n z^n =: (g * f)(z).$$

Recently, using the Hadamard product Murugusundaramoorthy *et al.* [8] introduced a new class  $M_{g,h}(\phi)$  of functions  $f \in \mathcal{A}$  satisfying

$$\frac{(f * g)(z)}{(f * h)(z)} \prec \phi(z) \quad (g_n > 0, h_n > 0, g_n - h_n > 0),$$

where  $g, h \in \mathcal{A}$  and are given by

$$g(z) = z + \sum_{n=2}^{\infty} g_n z^n \quad \text{and} \quad h(z) = z + \sum_{n=2}^{\infty} h_n z^n. \quad (1.2)$$

Motivated by the work of Ma and Minda [6] and others [1, 2, 4, 8], in the present paper, we introduce a more general class  $M_{g,h}^{\alpha}(\phi)$  defined using convolution and subordination and deduce Fekete-Szegő inequality for this class. Certain applications of our results are also discussed. In fact our results extend several earlier known works in [4, 6, 8].

**Definition 1.1.** Let  $g$  and  $h$  are given by (1.2) with  $g_n > 0, h_n > 0$  and  $g_n - h_n > 0$ . A function  $f \in \mathcal{A}$  given by (1.1) is said to be in the class  $M_{g,h}^{\alpha}(\phi)$ , if it satisfies

$$(1 - \alpha) \frac{(f * g)(z)}{(f * h)(z)} + \alpha \frac{(f * g)'(z)}{(f * h)'(z)} \prec \phi(z) \quad (\alpha \geq 0), \quad (1.3)$$

where  $\phi$  is an analytic function with  $\phi(0) = 1$  and  $\phi'(0) > 0$ .



Note that in Definition 1.1, we are not assuming  $\phi(\Delta)$  to be symmetric with respect to the real axis and starlike with respect to  $\phi(0) = 1$ . In order to prove the class  $M_{g,h}^\alpha(\phi)$  is non empty, consider the function  $f(z) = z/(1-z)$ . Assuming

$$\Phi(z) = (1-\alpha) \frac{(f * g)(z)}{(f * h)(z)} + \alpha \frac{(f * g)'(z)}{(f * h)'(z)},$$

we have  $\Phi(z) = 1 + (1+\alpha)(g_2 - h_2)z + \dots$ . Clearly  $\Phi(0) = 1$  and  $\Phi'(0) = (1+\alpha)(g_2 - h_2) > 0$ , thus  $f(z) = z/(1-z) \in M_{g,h}^\alpha(\phi)$ .

**Remark 1.2.** For various choices of the functions  $g$ ,  $h$ ,  $\phi$  and the real number  $\alpha$ , the class  $M_{g,h}^\alpha(\phi)$  reduces to several known classes, we enlist a few of them below:

1. The class  $M_{g,h}^0(\phi) =: M_{g,h}(\phi)$ , introduced and studied by Murugusundaramoorthy *et al.* [8].
2. If we set

$$g(z) = \frac{z}{(1-z)^2}, \quad h(z) = \frac{z}{(1-z)} \quad (1.4)$$

and  $\phi(z) = (1+z)/(1-z)$ , then the class  $M_{g,h}^\alpha(\phi)$  reduces to the class of  $\alpha$ -convex functions.

3.  $M_{\frac{z}{(1-z)^2}, \frac{z}{(1-z)}}^\alpha(\phi) =: \mathcal{M}(\alpha, \phi)$ .
4. For the functions  $g$  and  $h$  given by (1.4),  $M_{g,h}^\alpha((1+z)/(1-z)) =: \mathcal{M}(\alpha)$  is the class of  $\alpha$ -convex functions.
5.  $M_{\frac{z}{(1-z)^2}, \frac{z}{(1-z)}}^0(\phi) =: \mathcal{S}^*(\phi)$  and  $M_{\frac{z}{(1-z)^2}, \frac{z}{(1-z)}}^1(\phi) =: \mathcal{C}(\phi)$  are the well known classes of  $\phi$ -starlike and  $\phi$ -convex functions respectively.

The following lemmas are required in order to prove our main results. Lemma 1.3 of Ali *et al.* [2], is a reformulation of the corresponding result for functions with positive real part due to Ma and Minda [6].

Let  $\Omega$  be the class of analytic functions  $w$ , normalized by the condition  $w(0) = 0$ , satisfying  $|w(z)| < 1$ .

**Lemma 1.3.** [2] If  $w \in \Omega$  and  $w(z) := w_1 z + w_2 z^2 + \dots (z \in \Delta)$ , then

$$|w_2 - tw_1^2| \leq \begin{cases} -t & (t \leq -1), \\ 1 & (-1 \leq t \leq 1), \\ t & (t \geq 1). \end{cases}$$

For  $t < -1$  or  $t > 1$ , equality holds if and only if  $w(z) = z$  or one of its rotations. For  $-1 < t < 1$ , equality holds if and only if  $w(z) = z^2$  or one of its rotations. Equality holds for  $t = -1$  if and only if  $w(z) = z(\lambda + z)/(1 + \lambda z)$  ( $0 \leq \lambda \leq 1$ ) or one of its rotations, while for  $t = 1$ , equality holds if and only if  $w(z) = -z(\lambda + z)/(1 + \lambda z)$  ( $0 \leq \lambda \leq 1$ ) or one of its rotations.

**Lemma 1.4.** [4] (see also [11]) If  $w \in \Omega$ , then, for any complex number  $t$ ,

$$|w_2 - tw_1^2| \leq \max\{1, |t|\}$$

and the result is sharp for the functions given by  $w(z) = z^2$  or  $w(z) = z$ .

## 2. Fekete-Szegő problem

We begin with the following result:

**Theorem 2.1.** *Let  $\phi(z) = 1 + B_1z + B_2z^2 + \dots$ . If  $f(z)$  given by (1.1) belongs to the class  $M_{g,h}^\alpha(\phi)$ , then, for any real number  $\mu$ ,*

$$|a_3 - \mu a_2^2| \leq \begin{cases} \frac{B_1 A}{(1+2\alpha)(g_3-h_3)} & (\mu \leq \sigma_1), \\ \frac{B_1}{(1+2\alpha)(g_3-h_3)} & (\sigma_1 \leq \mu \leq \sigma_2), \\ \frac{B_1 A}{(1+2\alpha)(h_3-g_3)} & (\mu \geq \sigma_2), \end{cases} \quad (2.1)$$

where

$$A = \frac{B_2}{B_1} - \frac{[(1+3\alpha)(h_2^2 - h_2g_2) + \mu(1+2\alpha)(g_3 - h_3)]B_1}{(1+\alpha)^2(g_2 - h_2)^2},$$

$$\sigma_1 := \frac{(B_2 - B_1)(1+\alpha)^2(g_2 - h_2)^2 - (1+3\alpha)(h_2^2 - h_2g_2)B_1^2}{(1+2\alpha)(g_3 - h_3)B_1^2}$$

and

$$\sigma_2 := \frac{(B_2 + B_1)(1+\alpha)^2(g_2 - h_2)^2 - (1+3\alpha)(h_2^2 - h_2g_2)B_1^2}{(1+2\alpha)(g_3 - h_3)B_1^2},$$

and for any complex number  $\mu$

$$|a_3 - \mu a_2^2| \leq \frac{B_1}{2(1+2\alpha)(g_3 - h_3)} \max\{1; |t|\}, \quad (2.2)$$

where

$$t := \frac{[(1+3\alpha)(h_2^2 - h_2g_2) + \mu(1+2\alpha)(g_3 - h_3)]B_1^2 - B_2(1+\alpha)^2(g_2 - h_2)^2}{(1+\alpha)^2(g_2 - h_2)^2B_1}.$$

*Proof.* If  $f \in \mathcal{M}_{g,h}^\alpha(\phi)$ , then there exists an analytic function  $w(z) = w_1z + w_2z^2 + \dots \in \Omega$  such that

$$(1-\alpha)\frac{(f*g)(z)}{(f*h)(z)} + \alpha\frac{(f*g)'(z)}{(f*h)'(z)} = \phi(w(z)). \quad (2.3)$$

A computation shows that

$$\frac{(f*g)(z)}{(f*h)(z)} = 1 + a_2(g_2 - h_2)z + [a_3(g_3 - h_3) + a_2^2(h_2^2 - h_2g_2)]z^2 + \dots, \quad (2.4)$$

$$\frac{(f*g)'(z)}{(f*h)'(z)} = 1 + 2a_2(g_2 - h_2)z + [3a_3(g_3 - h_3) + 4a_2^2(h_2^2 - h_2g_2)]z^2 + \dots \quad (2.5)$$

and

$$\phi(w(z)) = 1 + B_1w_1z + (B_1w_2 + B_2w_1^2)z^2. \quad (2.6)$$

From (2.3), (2.4), (2.5) and (2.6), we have

$$(1+\alpha)(g_2 - h_2)a_2 = B_1w_1 \quad (2.7)$$

and

$$(1+2\alpha)(g_3 - h_3)a_3 + (1+3\alpha)(h_2^2 - h_2g_2)a_2^2 = B_1w_2 + B_2w_1^2. \quad (2.8)$$

A computation using (2.7) and (2.8) give

$$|a_3 - \mu a_2^2| = \frac{B_1}{(1+2\alpha)(g_2 - h_2)} [w_2 - tw_1^2], \quad (2.9)$$

where

$$t := -\frac{B_2}{B_1} + \frac{[(1+3\alpha)(h_2^2 - h_2g_2) + \mu(1+2\alpha)(g_3 - h_3)]B_1}{(1+\alpha)^2(g_2 - h_2)^2}. \quad (2.10)$$

Now the first inequality (1.3) is established as follows by an application of Lemma 1.3.

If

$$-\frac{B_2}{B_1} + \frac{[(1+3\alpha)(h_2^2 - h_2g_2) + \mu(1+2\alpha)(g_3 - h_3)]B_1}{(1+\alpha)^2(g_2 - h_2)^2} \leq -1,$$

then

$$\mu \leq \frac{(B_2 - B_1)(1+\alpha)^2(g_2 - h_2)^2 - (1+3\alpha)(h_2^2 - h_2g_2)B_1}{(1+2\alpha)(g_3 - h_3)B_1^2} := \sigma_1$$

and Lemma 1.3, gives

$$|a_3 - \mu a_2^2| \leq \frac{B_1 A}{(1+2\alpha)(g_3 - h_3)}.$$

For

$$-1 \leq -\frac{B_2}{B_1} + \frac{[(1+3\alpha)(h_2^2 - h_2g_2) + \mu(1+2\alpha)(g_3 - h_3)]B_1}{(1+\alpha)^2(g_2 - h_2)^2} \leq 1,$$

we have  $\sigma_1 \leq \mu \leq \sigma_2$ , where  $\sigma_1$  and  $\sigma_2$  are as given in the statement of theorem. Now an application of Lemma 1.3 yields

$$|a_3 - \mu a_2^2| \leq \frac{B_1}{(1+2\alpha)(g_3 - h_3)}.$$

For

$$-\frac{B_2}{B_1} + \frac{[(1+3\alpha)(h_2^2 - h_2g_2) + \mu(1+2\alpha)(g_3 - h_3)]B_1}{(1+\alpha)^2(g_2 - h_2)^2} \geq 1,$$

we have  $\mu \geq \sigma_2$  and it follows from Lemma 1.3 that

$$|a_3 - \mu a_2^2| \leq \frac{B_1 A}{(1+2\alpha)(h_3 - g_3)}.$$

Now the second inequality (2.2) follows by an application of Lemma 1.4 as follows:

$$\begin{aligned} |a_3 - \mu a_2^2| &= \frac{B_1}{(1+2\alpha)(g_2 - h_2)} [w_2 - tw_1^2] \\ &\leq \frac{B_1}{(1+2\alpha)(g_3 - h_3)} \max \{1; |t|\}, \end{aligned}$$

where  $t$  is given by (2.10). □

**Remark 2.2.** If we set  $\alpha = 1$ ,  $g$  and  $h$  are as given by (1.4), then Theorem 2.1 reduces to the result [6, Theorem 3] of Ma and Minda. When  $\alpha = 0$ , Theorem 2.1 reduces to the result [8, Theorem 2.1], proved by Murugusundaramoorthy *et al.* Note that there were few typographical errors in the assertion of the result [8, Theorem 2.1] and it is rectified in the following corollary:

**Corollary 2.3.** [8, Theorem 2.1] *Let  $\phi(z) = 1 + B_1z + B_2z^2 + \dots$ . If  $f(z)$  given by (1.1) belongs to the class  $M_{g,h}(\phi)$ , then for any real number  $\mu$ ,*

$$|a_3 - \mu a_2^2| \leq \begin{cases} \frac{B_1}{g_3 - h_3} \left( \frac{B_2}{B_1} - \frac{[(h_2^2 - h_2g_2) + \mu(g_3 - h_3)]B_1}{(g_2 - h_2)^2} \right) & (\mu \leq \sigma_1), \\ \frac{B_1}{g_3 - h_3} & (\sigma_1 \leq \mu \leq \sigma_2), \\ \frac{B_1}{g_3 - h_3} \left( \frac{[(h_2^2 - h_2g_2) + \mu(g_3 - h_3)]B_1}{(g_2 - h_2)^2} - \frac{B_2}{B_1} \right) & (\mu \geq \sigma_2), \end{cases}$$

where

$$\sigma_1 := \frac{(B_2 - B_1)(g_2 - h_2)^2 - (h_2^2 - h_2g_2)B_1^2}{(g_3 - h_3)B_1^2}$$

and

$$\sigma_2 := \frac{(B_2 + B_1)(g_2 - h_2)^2 - (h_2^2 - h_2g_2)B_1^2}{(g_3 - h_3)B_1^2}.$$

Here below, we discuss some applications of Theorem 2.1:

**Corollary 2.4.** *Let  $\phi(z) = 1 + B_1z + B_2z^2 + \dots$ . Assume that*

$$g(z) = z + \sum_{n=2}^{\infty} \frac{n\Gamma(n+1)\Gamma(2-\delta)}{\Gamma(n-\delta+1)} z^n \quad \text{and} \quad h(z) = z + \sum_{n=2}^{\infty} \frac{\Gamma(n+1)\Gamma(2-\delta)}{\Gamma(n-\delta+1)} z^n.$$

*If  $f(z)$  given by (1.1) belongs to the class  $M_{g,h}^{\alpha}(\phi)$ , then for any real number  $\mu$ ,*

$$|a_3 - \mu a_2^2| \leq \begin{cases} \frac{(2-\delta)(3-\delta)B_1}{12(1+2\alpha)} \left( \frac{B_2}{B_1} - \frac{[12\mu(1+2\alpha)(2-\delta) - 4(3-\delta)(1+3\alpha)]B_1}{4(3-\delta)(1+\alpha)^2} \right) & (\mu \leq \sigma_1), \\ \frac{(2-\delta)(3-\delta)B_1}{12(1+2\alpha)} & (\sigma_1 \leq \mu \leq \sigma_2), \\ \frac{(2-\delta)(3-\delta)B_1}{12(1+2\alpha)} \left( \frac{[12\mu(1+2\alpha)(2-\delta) - 4(3-\delta)(1+3\alpha)]B_1}{4(3-\delta)(1+\alpha)^2} - \frac{B_2}{B_1} \right) & (\mu \geq \sigma_2), \end{cases}$$

where

$$\sigma_1 := \frac{(3-\delta)[(B_1 - B_2)(1+\alpha)^2 + (1+3\alpha)B_1^2]}{3(2-\delta)(1+2\alpha)B_1^2}$$

and

$$\sigma_2 := \frac{(3-\delta)[(B_1 + B_2)(1+\alpha)^2 + (1+3\alpha)B_1^2]}{3(2-\delta)(1+2\alpha)B_1^2}.$$

**Remark 2.5.** Taking  $\alpha = 8/\pi^2$ ,  $B_2 = 16/3\pi^2$  and  $\delta = 1$  in Corollary 2.4, we have the result of Ma and Minda [5, Theorem 2]. When  $\alpha = 0$ , the above Corollary 2.4 reduces to [8, Corollary 3.2] of Murugusundaramoorthy *et al.* Note that there were few typographical errors in the assertion of [8, Corollary 3.2] and the following result is the corrected one:

**Corollary 2.6.** [8, Corollary 3.2] *Let  $\phi(z) = 1 + B_1z + B_2z^2 + \dots$ . If  $f(z)$  given by (1.1) belongs to the class  $M_{g,h}(\phi)$ , then, for any real number  $\mu$ ,*

$$|a_3 - \mu a_2^2| \leq \begin{cases} \frac{(2-\delta)(3-\delta)B_1}{12} \left( \frac{B_2}{B_1} - \frac{[12\mu(2-\delta) - 4(3-\delta)]B_1}{4(3-\delta)} \right) & (\mu \leq \sigma_1), \\ \frac{(2-\delta)(3-\delta)B_1}{12} & (\sigma_1 \leq \mu \leq \sigma_2), \\ \frac{(2-\delta)(3-\delta)B_1}{12} \left( \frac{[12\mu(2-\delta) - 4(3-\delta)]B_1}{4(3-\delta)} - \frac{B_2}{B_1} \right) & (\mu \geq \sigma_2), \end{cases}$$

where

$$\sigma_1 := \frac{(3 - \delta)[B_1 - B_2 + B_1^2]}{3(2 - \delta)B_1^2}$$

and

$$\sigma_2 := \frac{(3 - \delta)[B_1 + B_2 + B_1^2]}{3(2 - \delta)B_1^2}.$$

Putting  $\phi(z) = (1 + z)/(1 - z)$ ,  $g$  and  $h$  are as given by (1.4) in Theorem 2.1, we deduce the following result:

**Corollary 2.7.** *Let  $f(z)$  is given by (1.1) belongs to the class  $\mathcal{M}(\alpha)$ , then, for any real number  $\mu$ ,*

$$|a_3 - \mu a_2^2| \leq \begin{cases} \frac{(\alpha^2 + 8\alpha + 3) - 4\mu(1 + 2\alpha)}{(1 + \alpha)^2(1 + 2\alpha)} & (\mu \leq \sigma_1), \\ \frac{1}{(1 + 2\alpha)} & (\sigma_1 \leq \mu \leq \sigma_2), \\ \frac{4\mu(1 + 2\alpha) - (\alpha^2 + 8\alpha + 3)}{(1 + \alpha)^2(1 + 2\alpha)} & (\mu \geq \sigma_2), \end{cases}$$

where  $\sigma_1 := \frac{1 + 3\alpha}{2(1 + 2\alpha)}$  and  $\sigma_2 := \frac{\alpha^2 + 5\alpha + 2}{2(1 + 2\alpha)}$ .

Note that for  $\alpha = 0$ , Corollary 2.7 reduces to a result in [4] (see also [14]). By taking  $\phi(z) = (1 + z)/(1 - z)$ ,  $g$  and  $h$ , given by (1.4) in second result of Theorem 1.3, we have the following result:

**Corollary 2.8.** *Let  $f(z)$  is given by (1.1) belongs to the class  $\mathcal{M}(\alpha)$ , then for any complex number  $\mu$*

$$|a_3 - \mu a_2^2| \leq \frac{1}{1 + 2\alpha} \max \left\{ 1; \left| \frac{4\mu(1 + 2\alpha) - (\alpha^2 + 8\alpha + 3)}{(1 + \alpha)^2} \right| \right\}.$$

**Remark 2.9.** For  $\alpha = 1$ , the above Corollary 2.8 reduces to the result [4, Corollary 1] of Keogh and Merkes.

## References

- [1] Ali, R. M., Lee, S. K., Ravichandran, V. and Subramaniam, S., *The Fekete-Szegő coefficient functional for transforms of analytic functions*, Bull. Iranian Math. Soc., **35**(2009), no. 2, 119-142.
- [2] Ali, R.M., Ravichandran, V. and Seenivasagan, N., *Coefficient bounds for  $p$ -valent functions*, Appl. Math. Comput., **187**(2007), no. 1, 35-46.
- [3] Janowski, W., *Extremal problems for a family of functions with positive real part and for some related families*, Ann. Polon. Math., **23**(1970/1971), 159-177.
- [4] Keogh, F.R. and Merkes, E.P., *A coefficient inequality for certain classes of analytic functions*, Proc. Amer. Math. Soc., **20**(1969), 8-12.
- [5] Ma, W.C. and Minda, D., *Uniformly convex functions. II*, Ann. Polon. Math., **58**(1993), no. 3, 275-285.
- [6] Ma, W.C. and Minda, D., *A unified treatment of some special classes of univalent functions*, in: Proceedings of the Conference on Complex Analysis (Tianjin, 1992), 157-169, Conf. Proc. Lecture Notes Anal., I Int. Press, Cambridge, MA.

- [7] Miller, S.S. and Mocanu, P.T., *Differential subordinations*, Monographs and Text Books in Pure and Applied Mathematics, 225, Dekker, New York, 2000.
- [8] Murugusundaramoorthy, G., Kavitha, S. and Rosy T., *On the Fekete-Szegő problem for some subclasses of analytic functions defined by convolution*, Proc. Pakistan Acad. Sci., **44**(2007), no. 4, 249-254.
- [9] Ravichandran, V., Gangadharan, A. and Darus, M., *Fekete-Szegő inequality for certain class of Bazilevic functions*, Far East J. Math. Sci. (FJMS), **15**(2004), no. 2, 171-180.
- [10] Ravichandran, V., Darus, M., Khan, M.H. and Subramanian, K.G., *Fekete-Szegő inequality for certain class of analytic functions*, Aust. J. Math. Anal. Appl., **1**(2004), no. 2, Art. 4, 7 pp.
- [11] Ravichandran, V., Polatoglu, Y., Bolcal, M. and Sen, A., *Certain subclasses of starlike and convex functions of complex order*, Hacet. J. Math. Stat. Hacet. J. Math. Stat., **34**(2005), 9-15.
- [12] Sivaprasad Kumar, S. and Virendra Kumar, *Fekete-Szegő problem for a class of analytic functions defined by convolution*, Tamkang J. Math., **44**(2013), no. 2, 187-195.
- [13] Sivaprasad Kumar, S. and Virendra Kumar, *On the Fekete-Szegő inequality for certain class of analytic functions*, submitted.
- [14] Srivastava, H.M., Mishra, A.K. and Das, M.K., *The Fekete-Szegő problem for a subclass of close-to-convex functions*, Complex Variables Theory Appl., **44**(2001), no. 2, 145-163.

S. Sivaprasad Kumar  
 "Delhi Technological" University  
 Department of Applied Mathematics  
 Delhi-110042, India  
 e-mail: [spkumar@dce.ac.in](mailto:spkumar@dce.ac.in)

Virendra Kumar  
 "Delhi Technological" University  
 Department of Applied Mathematics  
 Delhi-110042, India  
 e-mail: [vktmaths@yahoo.in](mailto:vktmaths@yahoo.in)

# Comparison of Shear Strength of Silty Sand from Ottawa and Yamuna River Basin using Relative Compaction

**Sadanand Ojha**

*Research Scholar, Department of Civil Engineering  
Faculty of Technology, University of Delhi  
(Delhi Technological University Campus)  
Bawana Road, Delhi-110042, India  
e-mail: [sadanand\\_ojha@yahoo.com](mailto:sadanand_ojha@yahoo.com)*

**Ashutosh Trivedi**

*Professor, Department of Civil Engineering  
Delhi Technological University  
Bawana Road, Delhi-110042, India  
e-mail: [prof.trivedi@yahoo.com](mailto:prof.trivedi@yahoo.com)*

## ABSTRACT

Shear strength of silty sand depends not only on silt percentage but also on other factors like its source, gradation and hydrological parameters (difference in altitude of origin and fall of river, length of traverse, mean discharge, catchment area and basin characteristics etc.). Other parameters affecting the strength characteristics are methods of testing, sample preparation, confining pressure, the state of denseness or overburden pressure and the critical angle of internal friction. In the present work the values of shear strength parameters  $Q_{af}$  and  $R_{af}$  obtained from triaxial test results of silty sand obtained from Yamuna river basin and Ottawa river basin has been compared. Triaxial tests on silty sand were carried out in the lab at different relative density and confining pressure. The review of past works on silty sand indicates that strength parameter of clean sand and silty sands often evaluated corresponding to relative density containing significant percentage of fines often leads to experimental error due to the uncertainty involved in estimation of the relative density. Therefore the authors in their previous work introduced a term relative compaction to interpret the strength parameter of the soil containing fines and the same has also been reproduced here after ignoring the scattered data of triaxial test with deviation exceeding more than twice the standard deviation. Also the triaxial data of Ottawa sand was re-evaluated in terms of relative compaction to compare the shear strength characteristics of silty sand from obtained from Yamuna and Ottawa River basin. The results indicates that the values of  $Q_{af}$  and  $R_{af}$  evaluated based on relative compaction for both Yamuna sand and Ottawa sand shows lesser variation as compared to values of  $Q_b$  and  $R_b$  calculated based on relative density. The large variation in the results of  $Q_b$  and  $R_b$  for Yamuna sand and Ottawa sand is due to the uncertainty involved in estimation of the relative density for silty sands when fine contents is more than a certain limit.

**KEYWORDS:** silty sand, relative compaction, relative density, strength parameters.

## INTRODUCTION

In the present work shear strength properties of silty sand obtained from the basin of river Ottawa and Yamuna has been compared. The shear strength of silty sand depends upon inter particle cohesion and its friction angle [1, 2]. The cohesion between sand particles apart from various other factors



depends upon the presence of silt and or clay [4, 6, 7, 8, 9]. Grain size distribution of silty sand depends upon the source from which it has been obtained. Hence variation in the origin and destination of the source river (length of river), difference in the elevation of origin and mouth fall, discharge, location (altitude and longitude), average temperature over length of flow directly affects the strength properties of silty sand. It has been observed that the percentage of silt present in the silty sand greatly influence the shear strength characteristics of silty sand [3, 5, 10, 13, 14, 15, 16, 17, 18]. It is observed that upto a certain low percentage of silt (less than 10 percent) the silt particles occupies the voids between the sand particles and when the percentage of silt is more than 15 percent, silt particles tries to align along the surface of sand particles [10, 11]. The behavior of the soil is now inclined towards plastic silt and thereby a sudden reduction in the shear strength of soil.



**Figure 1:** Ottawa River Drainage Basin (source : [http://en.wikipedia.org/wiki/Ottawa\\_River](http://en.wikipedia.org/wiki/Ottawa_River))

In the present study the various parameters for Ottawa River and Yamuna River are taken into account to evaluate the strength properties of silty sand obtained from the catchment area of respective river basin. Various tests were performed as per Codal provision [12]. The Ottawa River flows in the Canadian provinces of Ontario and Quebec. The river defines the border between these two provinces along most part of its length. The river originates from its source in Lake Capimitchigama, in the Laurentian Mountains of central Quebec, and flows west to Lake Timiskaming. From Lake Timiskaming, the river flows southeast to Ottawa and Gatineau, where it tumbles over the Chaudière Falls and further takes in the Rideau and Gatineau rivers.. The river flows through large areas of deciduous and coniferous forest. Most part of the river flows through the Canadian Shield, although lower areas flow through Lime stone plains and glacial deposits. The

drainage basin of Ottawa River is shown in Fig.1. Yamuna River is the largest tributary of the Ganges River Ganga in northern India. Its source is at Yamunotri, in the Uttarakhand Himalaya, in the Himalayan Mountains. It flows through the states of Delhi, Haryana and Uttar Pradesh, before merging with the Ganges at Allahabad. Originating in the Yamunotri glacier in the Himalayas, Yamuna covers a distance of over 1300 km, before merging with the Ganga in Allahabad. Fig.2 and fig.3 shows the drainage basin of Yamuna River and its origin at Yamunotri. Topographical data for Ottawa and Yamuna River is given in Table1. The data given in Table 1 gives its total length, drainage area and the mean discharge along with other hydrological data.

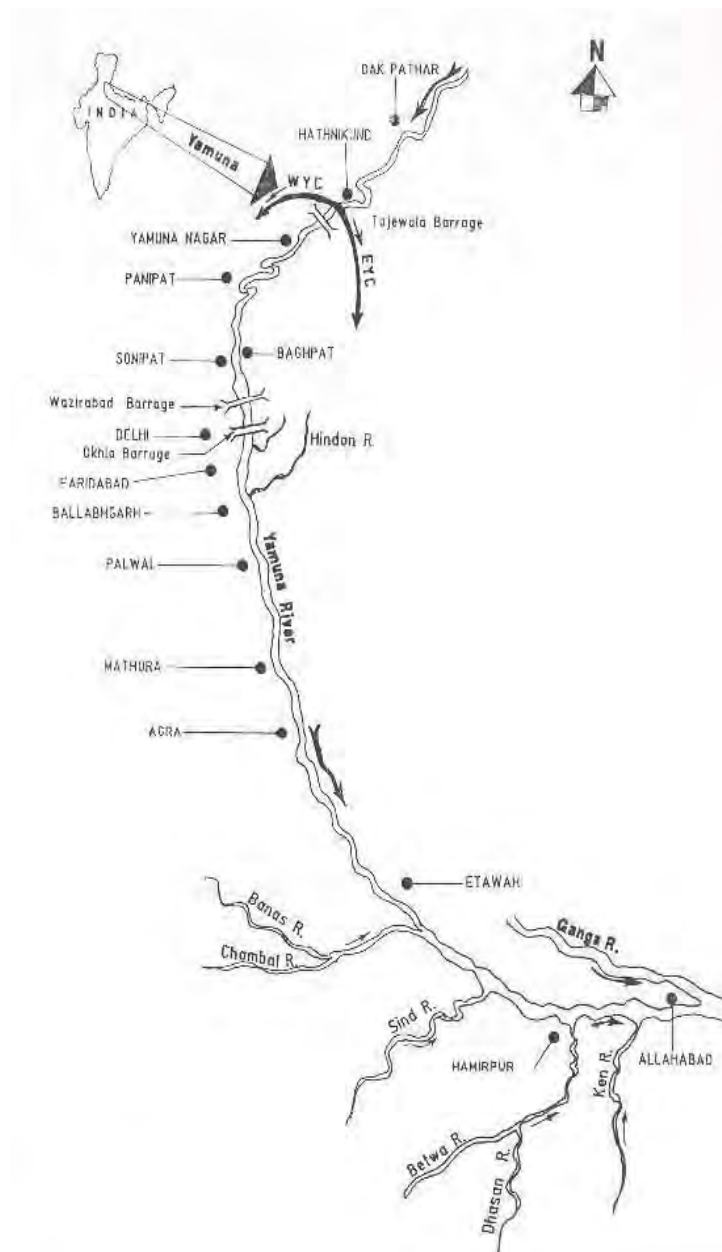


**Figure 2:** Yamuna River drainage basin



**Figure 3:** Yamuna at Yamunotri

**Table 1:** Hydro and Geological data for Yamuna and Ottawa River

S. No.	Description	Yamuna River	Ottawa River
1.	Country	India	Canada
2.	Source	Yamunotri	Lake Capimitchigama
3.	Mouth	Ganga	St. Lawrence River
3.	Co-ordinates	31°01'0.12"N 78°27'0"E / 31.0167°N 78.45°E /	45°27'N 74°05'W 45.45°N 74.083°W
4.	Elevation at Source	3293m	430m
5.	Elevation at Mouth	74m	20m
6.	Approximate Length	1376 km	1271 km
7.	Catchment Area	219663 km <sup>2</sup>	146300 km <sup>2</sup>
8.	Discharge	317097 m <sup>3</sup> /s	5351 m <sup>3</sup> /s

## SHEAR STRENGTH-DILATANCY RELATION

Mohr was the first to present a generalised form of the theory around the end of the 19th century for the evaluation of the shear strength of the granular sand. Mohr theory of failure states that the failure of soil due to shear stress depends upon normal stresses on the potential failure plane and the failure is caused by a critical combination of normal and shear stresses. Mohr proposed that shear strength of soil at failure is a unique function of normal stress acting on that plane and is represented by following expression,

$$\tau_f = f(\sigma) \quad (1)$$

A plot drawn between normal stress and shear stress at failure using Eq. (1) is called Mohr envelope and there is unique failure envelope for each soil. Using the concept of Coulomb [19] which

developed a more general relation considering cohesion between soil particle ( $c$ ) and angle of internal friction ( $\phi$ ). It was later known as Mohr–Coulomb failure criterion. This relation is expressed as

$$\tau = c + \sigma \tan \phi \quad (2)$$

For cohesionless soil the Eq. (2) reduces to

$$\tau = \sigma \tan \phi \quad (3)$$

This is a form of Eq. (1). The failure occurs when the stresses are such that the Mohr circle just touches the failure envelope as shown in fig. (1). It is clear that the failure occurs if the stresses  $\sigma$  and  $\tau$  on failure plane either touches it at point B or above the failure line. Point lying below failure envelope represents a stable and non-failure condition.

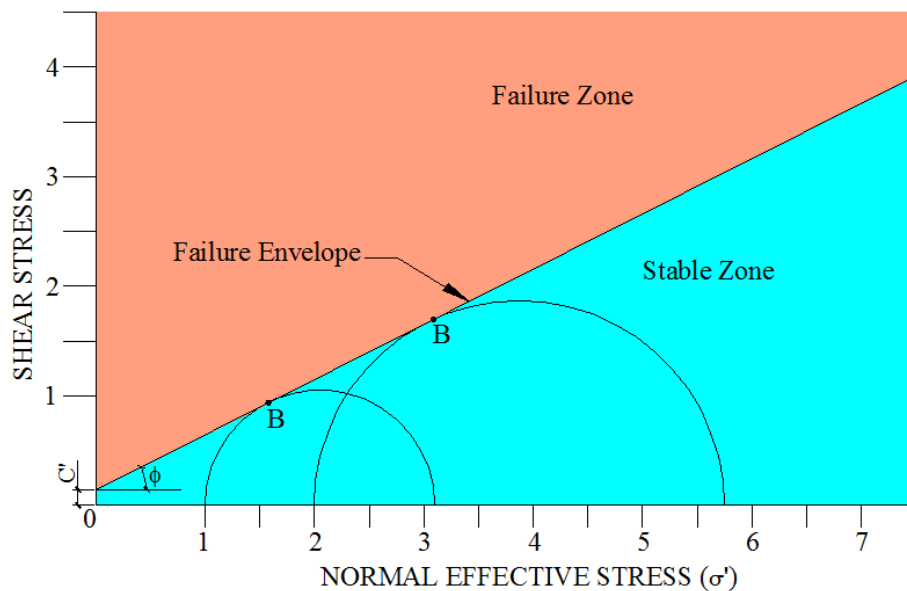


**Figure 4:** Shear stress and normal stress plot showing failure envelope.

**Table 2:** Test Data for Silty Sand [16, 17]

S. No.	Description	Yamuna	Ottawa
1.	Number of Test	75	70
2.	Testing Techniques	Triaxial Dry Pulverization	Bender Element
3.	Range of Pressure (kPa)	100, 200 & 400	100-400
4.	Range of Relative Density	60, 65, 70, 75 & 80	14-100
5.	Range of Relative Compaction	0.92, 0.93, 0.94, 0.95 & 0.96	0.86-0.96
6.	Plasticity	NP & P	NP

Later research done by various investigator showed that the parameter  $c$  and  $\phi$  depends upon number of factors such as water content, drainage conditions, and methods of testing and is not necessarily the fundamental properties of soil. Terzaghi [19] established that the normal stresses that controls the shear strength of the soil are effective stresses and not normal stresses, and modified the Eq. (2) as

$$\tau = c' + \sigma' \tan \phi' \quad (4)$$

Here  $c'$  and  $\phi'$  are the cohesion intercept and angle of internal friction in terms of effective stresses. Eq. (4) is known as revised Mohr-Coulomb equation for shear strength of soil. With the further advancement of research on granular sand Bolton [3] studied the behavior of 17 nos. of different sand in axisymmetric or plane strain at different densities and confining pressures and established a relation between strength and dilatancy given by expression

$$\Phi = \Phi_c + 0.8\psi \quad (5)$$

However, not much work was done to assess the effect of fine content on the strength behavior of clean sand in the past. Salgado [17] has calculated the values of shear strength parameter ( $Q$  and  $R$ ) for clean and silty Ottawa sand for different silt percentage and found that a value of  $R = 0.5$  works well for all gradation and within the limited range of relative density. He gave a relationship between the peak friction angle  $\Phi_p$  and the critical-state friction angle  $\Phi_c$  in terms of dilatancy index  $I_R$ , for tri-axial conditions as

$$I_R = [\Phi_p - \Phi_c]/3 \quad (6)$$

$$\text{where } I_R = D_r(Q - \ln 100 p_p^*/P_A) - R \quad (7)$$

where,  $D_r$  is relative density expressed as a number between 0 and 1,  $p_p^*$  is mean effective stress at peak strength in kPa,  $P_A$  is reference stress (100 kPa) in the same units as  $p_p^*$ ,  $Q$  and  $R$  are fitting parameters.

From Eq. (7) and (8)

$$[\Phi_p - \Phi_c]/3 = D_r Q - D_r \ln 100 (p_p^*/P_A) - R$$

$$[\Phi_p - \Phi_c]/3 + D_r \ln 100 (p_p^*/P_A) = D_r Q - R \quad (9)$$

Further we define  $I_N$  as

$$I_N = [\Phi_p - \Phi_c]/3 + D_r \ln 100 (p_p^*/P_A)$$

Eq. (9) can be expressed as

$$I_N = D_r Q - R \quad (10)$$

Bolton [3] found that values  $Q = 10$  and  $R = 1$  created a definition for a relative dilatancy index which apparently offered a unique set of correlations for the dilatancy-related behaviour of each of the sands in laboratory element tests. The values of “ $Q$ ” and “ $R$ ” are highly dependent on range of relative density, confining pressure, hydro-geology, catchment area, basin characteristics, and plasticity of silt and gradation of soil.

Ojha and Trivedi [16] observed that there are serious problem associated with the estimation of relative density of the soil containing significant percentage of plastic and non plastic silt. This relative density assumption for the soil containing significant percentage of fines often leads to significant error in overall estimation of strength and deformation properties of silty sands. Therefore the authors used relative compaction of the soil instead of relative density to interpret the strength parameter of the soil containing fines and modified the Eq. (10) by replacing the term relative density ( $D_r$ ) with relative compaction ( $R_c$ ) as given below:

$$I_{Na} = R_c Q_f - R_{af} \quad (11)$$

$Q_{af}$  and  $R_{af}$  are shear strength parameters for plastic silt. It has been established that the shear strength parameter calculated based on relative compaction over come the difficulty and the error involved in estimation of relative density.

## RESULTS AND DISCUSSION

Based on Eq. (11), findings of Salgado [17] on silty Ottawa sand was re-evaluated in terms of relative compaction and the results were compared with that of Yamuna sand [16]. The sequential comparison with discussion of results is presented here.

Plot between maximum and minimum void ratio for Yamuna sand and Ottawa sand has been plotted based on laboratory test as shown in figure 5. It is observed that both maximum and minimum void ratio decreases with increase in fines for both sand but the total voids for the same percent fines are more in Yamuna sand than for Ottawa sand. This is due to the fact that fines used in the analysis of Ottawa sand was non-plastic and for Yamuna sand plastic fines were used.

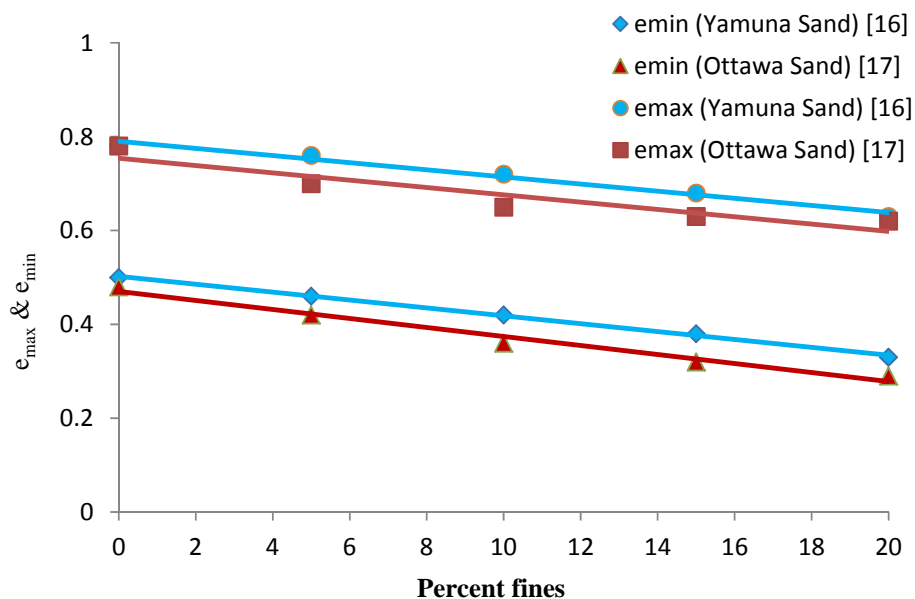


**Figure 5:**  $e_{max}$  &  $e_{min}$  vs. Percent fines

The plot between critical state friction angle and percent fine were also drawn for Ottawa and Yamuna sand as shown in Fig.6. It has been found that the Yamuna sand reaches its peak much earlier than Ottawa sand for the same percent fines due to presence of plastic fines which slips easily under the same normal and confining stress. The plot shown ignores the scattered data falling beyond the range of twice the standard deviation.

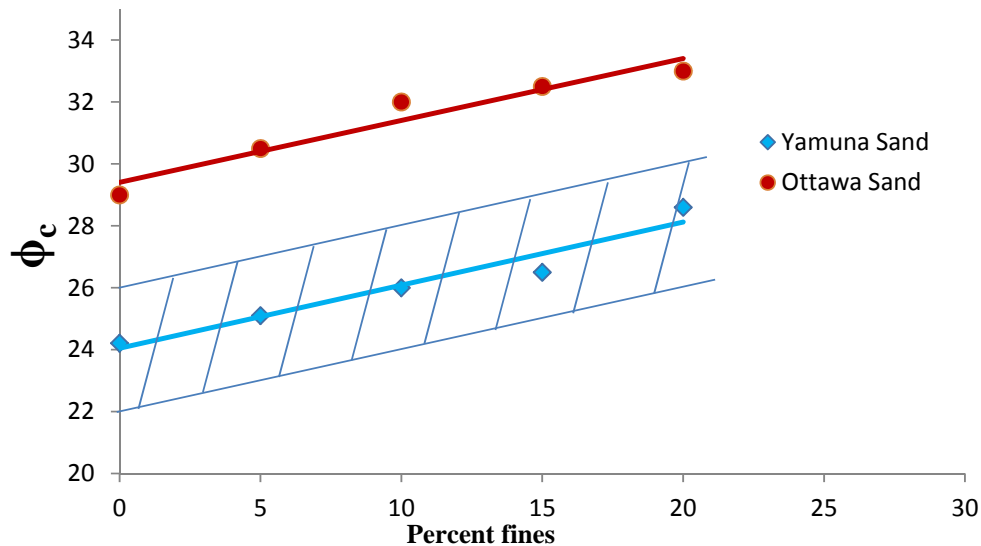


**Figure 6:** Critical Friction Angle vs. Percent Fines

Based on the test results data obtained from triaxial test of Ottawa sand by Salgado [17] for maximum and minimum proctor density, relative density has been converted into relative compaction and the plot between  $D_r$  and  $R_c$  at different percent fine has been drawn as shown in fig. 7(a) -7(e). The same plot for Yamuna sand based on the work done by Ojha and Trivedi [16] was also superimposed with that of Ottawa sand and an empirical relation between  $R_c$  and  $R_d$  has been found which is validated theoretically by substituting in Bolton's equation. From the plot it is clear that Ottawa sand is more compressible for fines percent up to 10% and the rate of compression decreases when percent fine increases above 10%.

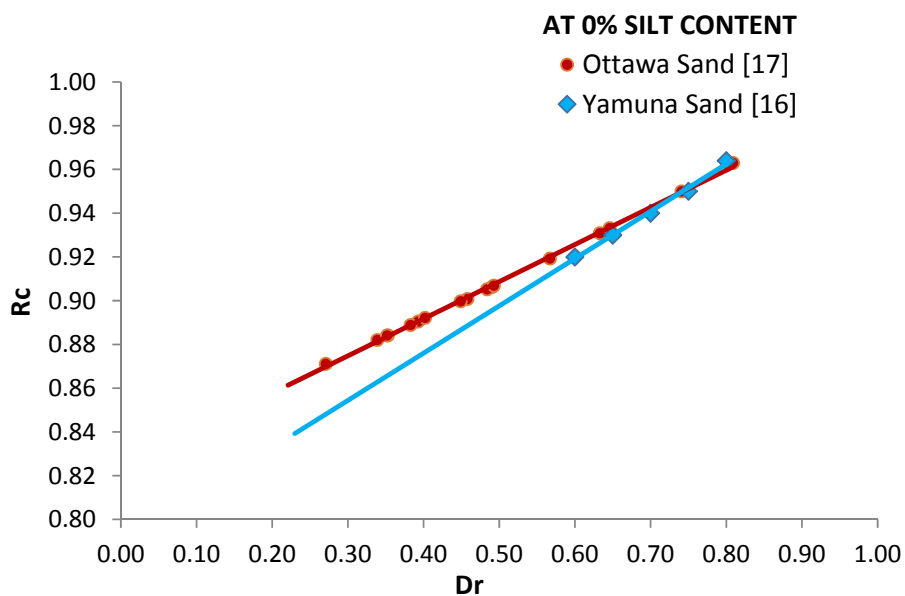


**Figure 7 (a):**  $R_c$  v/s.  $D_r$  (At 0% Silt Content)



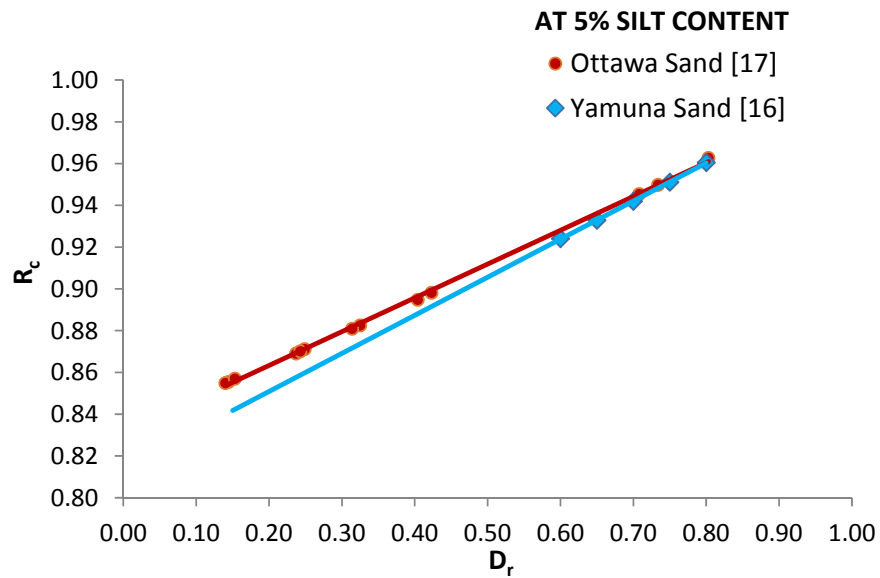


**Figure 7 (b):  $R_c$  v/s.  $D_r$  (At 5% Silt Content)**

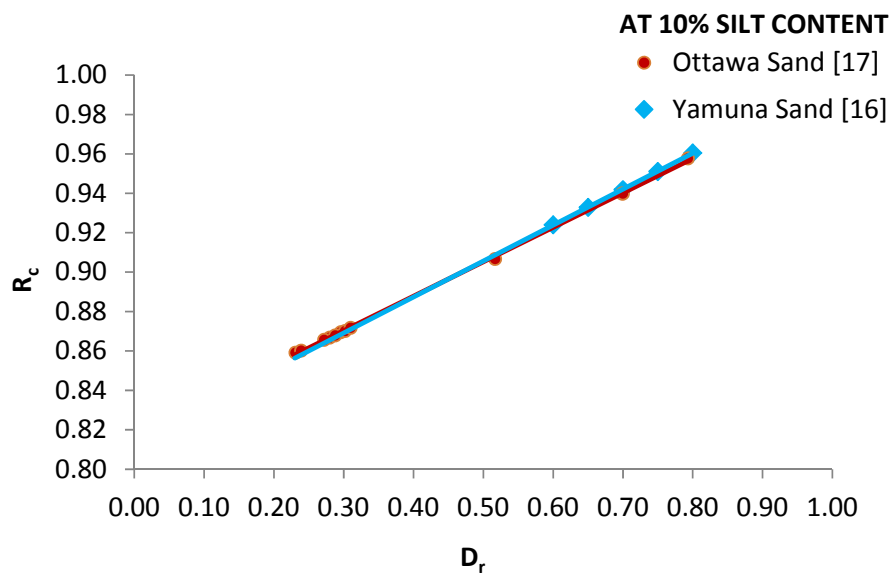
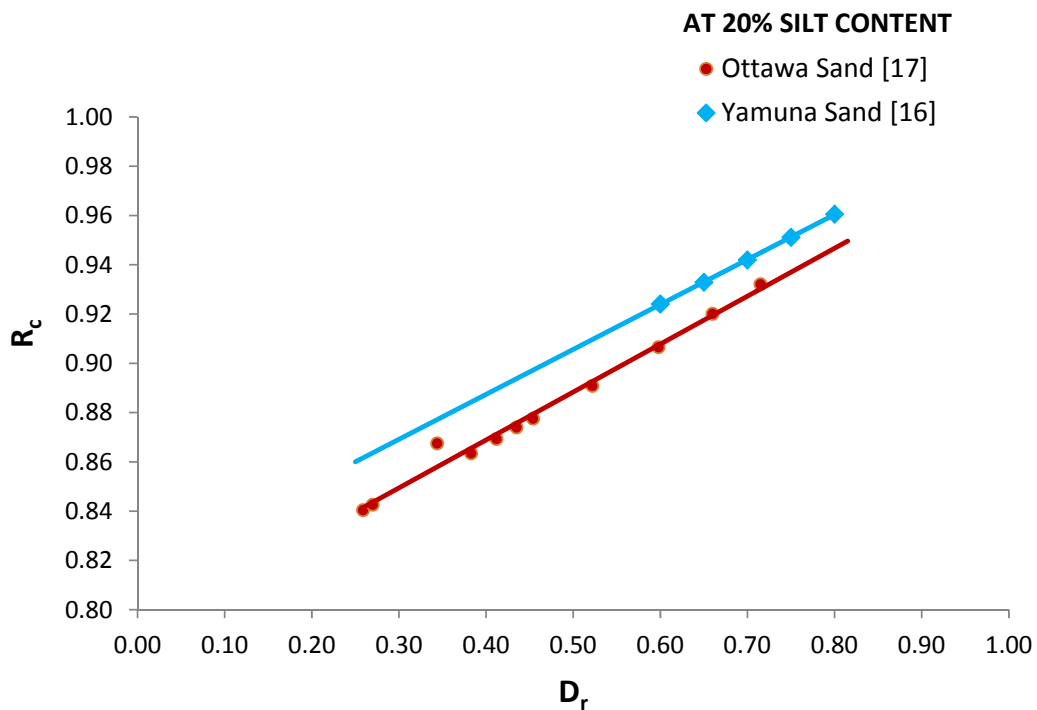
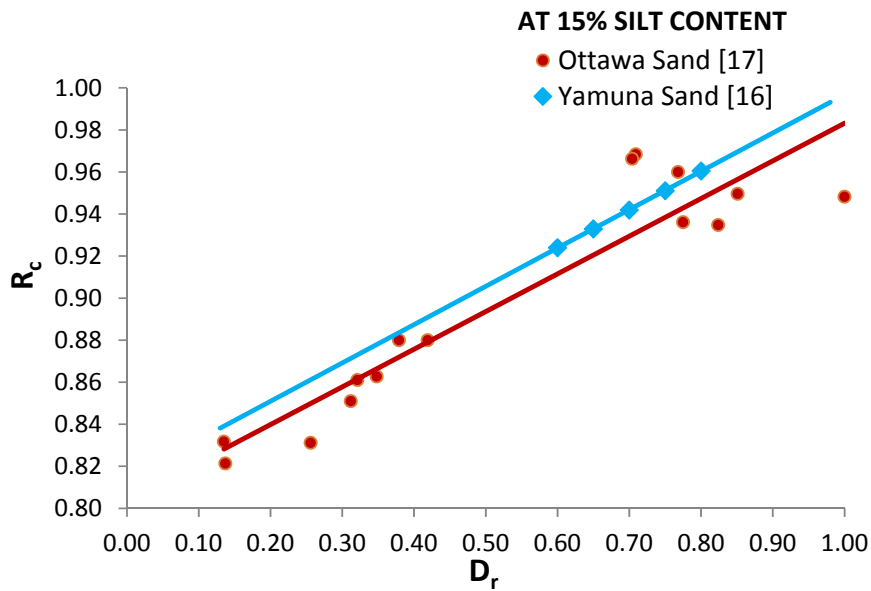


**Figure 7 (c):  $R_c$  v/s.  $D_r$  (At 10% Silt Content)**



A typical variation of  $I_N$  with relative compaction is shown in Fig. 8(a) -8(e) Table 3 shows the values of  $Q_s, R_s$  and  $Q_a, R_a$  based on relative density using Eq. (10). Using the relationships of Eqs (11), we obtained the values of  $Q_{sf}, R_{sf}$  and  $Q_{af}, R_{af}$  and are tabulated in table 4. From the table 3 and 4 It is

clear that coefficient of correlation is much better for silty sand with silt percentage up to 15% when evaluated based on relative compaction as compared to that calculated based on relative density.

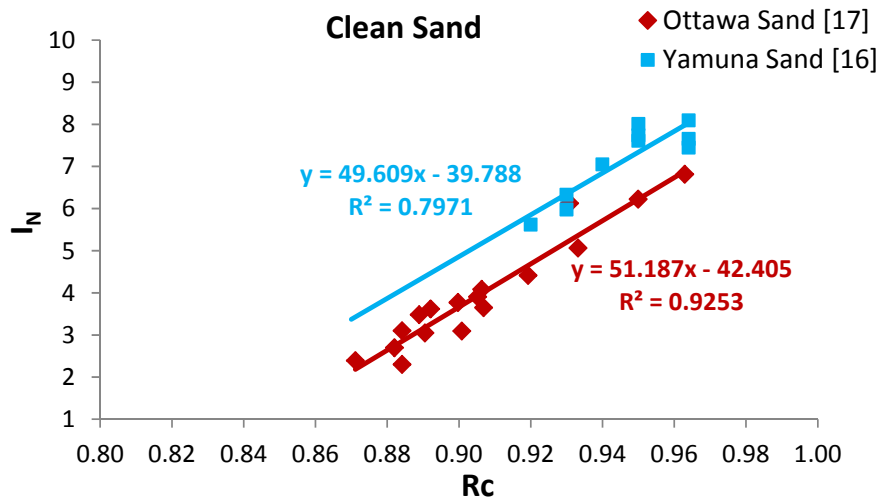


Figure 8 (a):  $I_N$  v/s.  $R_c$  (At 0% Silt Content)

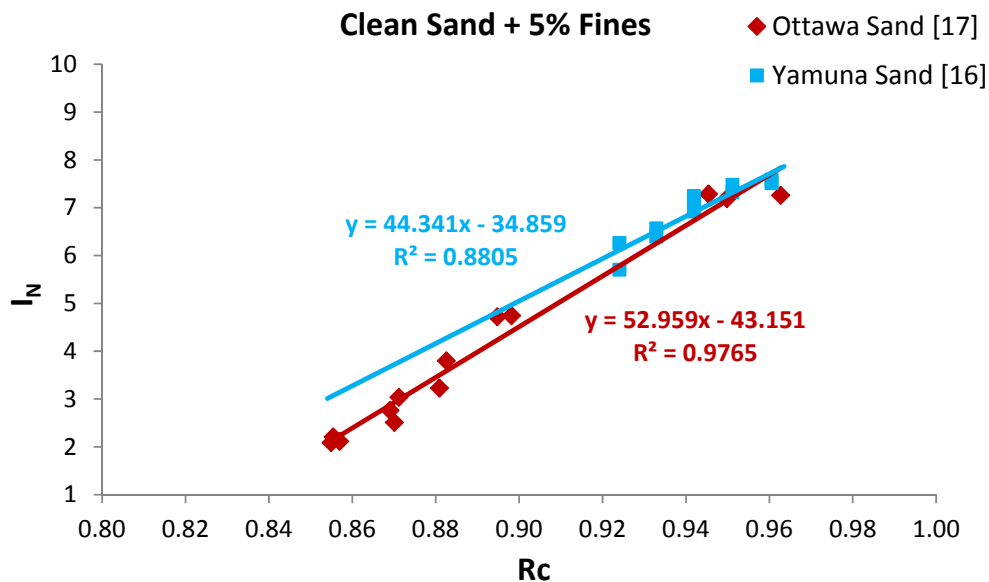
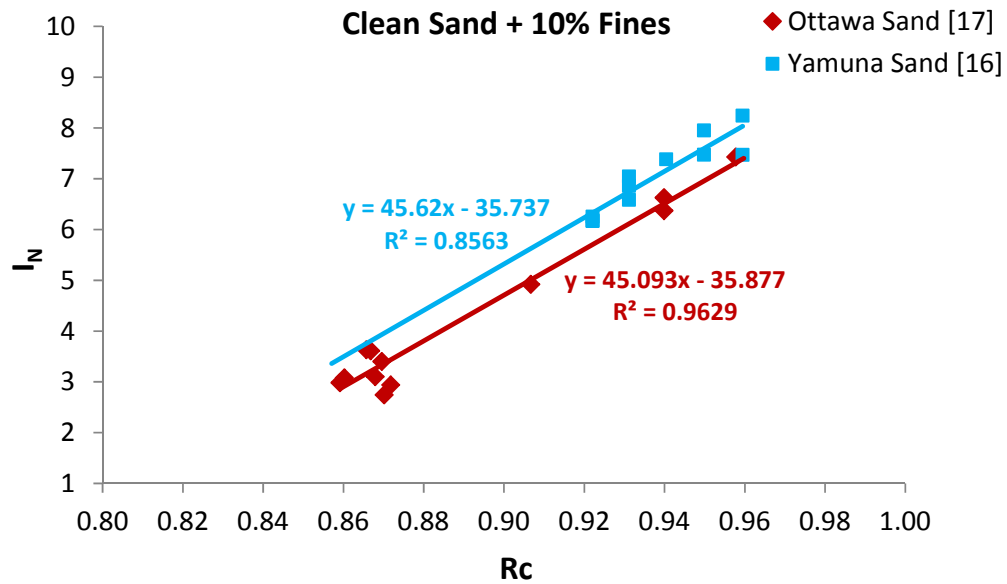
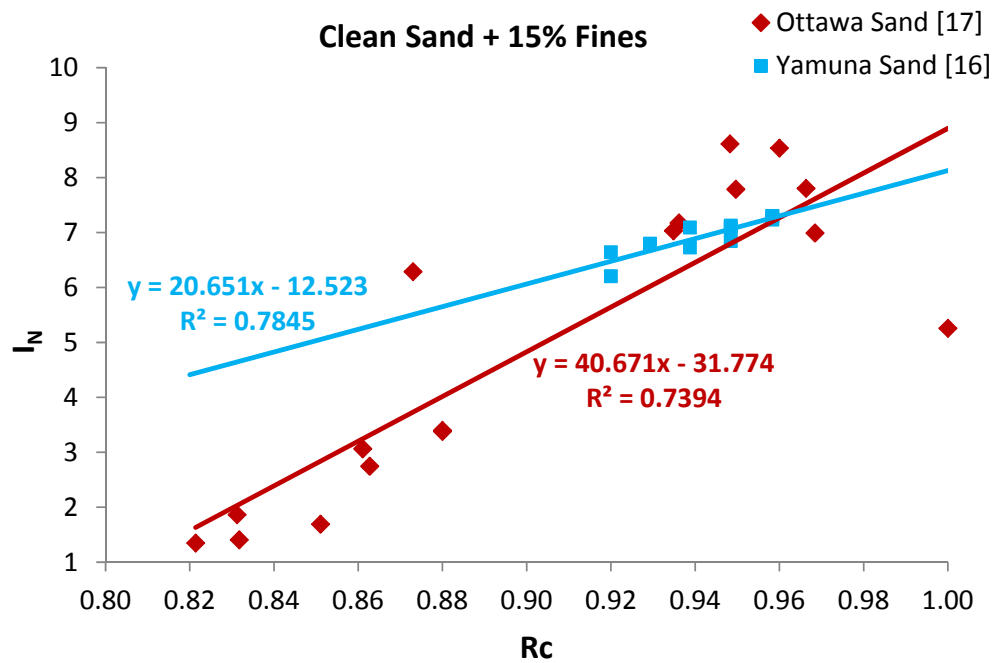
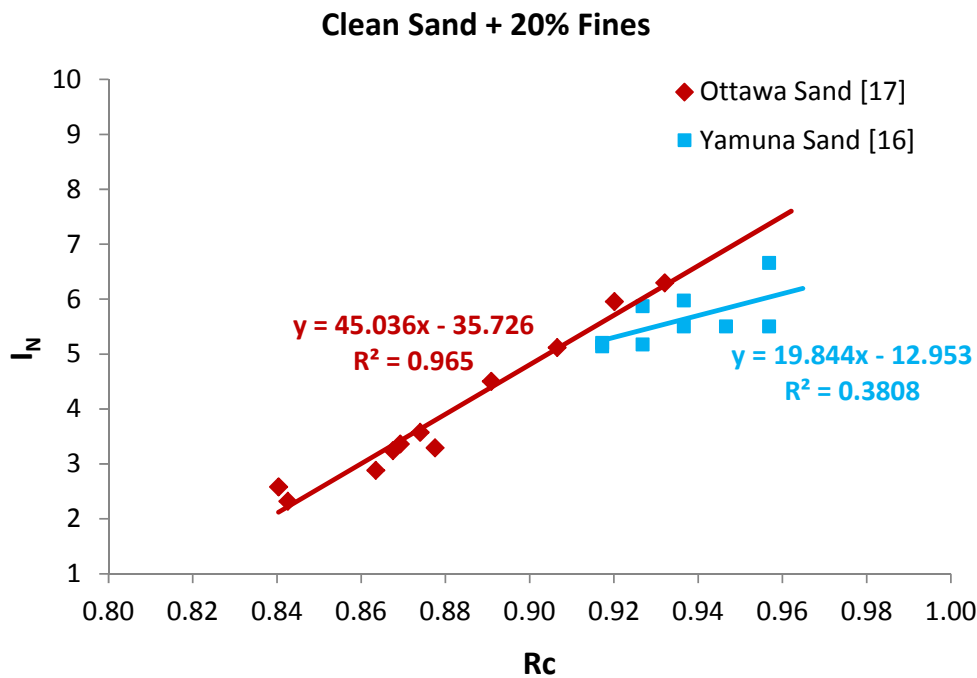


Figure 8 (b):  $I_N$  v/s.  $R_c$  (At 5% Silt)

Figure 8 (c):  $I_N$  v/s.  $R_C$  (At 10% Silt Content)Figure 8 (d)  $I_N$  v/s.  $R_C$  (At 15% Silt Content)

**Table 3:** Comparison of Shear strength parameter based on relative density for silty Sand

Silt (%)	Yamuna Sand [16]		Ottawa Sand [17]		Tread line with $R_a = 0.5$ Yamuna Sand [16]		Tread line with $R_s = 0.5$ Ottawa Sand [17]	
	$Q_a$	$r^2$	$Q_s$	$r^2$	$Q_a$	$r^2$	$Q_s$	$r^2$
0	11.674	0.721	9	0.93	7.096	0.502	9	0.93
5	11.397	0.79	9	0.98	7.047	0.673	11	0.92
10	10.934	0.705	8.3	0.97	7.433	0.632	10.6	0.87
15	11.041	0.553	11.4	0.97	6.817	0.471	10.3	0.96
20	5.435	0.356	10.1	0.95	5.426	0.332	9.5	0.95

**Table 4:** Comparison of Shear strength parameter based on relative compaction for silty Sand

Silt (%)	Yamuna Sand [16]		Ottawa Sand [17]		Tread line with $R_{af} = 40$ Yamuna Sand [16]		Tread line with $R_{sf} = 40$ Ottawa Sand [17]	
	$Q_{af}$	$r^2$	$Q_{sf}$	$r^2$	$Q_{af}$	$r^2$	$Q_{sf}$	$r^2$
0	49.609	0.7971	51.187	0.9253	49.833	0.7970	48.53	0.9229
5	44.341	0.8805	52.959	0.9765	49.797	0.8671	49.43	0.9722
10	45.620	0.8563	45.093	0.9629	50.163	0.8478	49.72	0.9527
15	20.651	0.7845	40.671	0.7394	49.800	0.7790	49.74	0.7025
20	19.844	0.3808	45.036	0.9650	48.742	0.4270	49.88	0.9538

## CONCLUSIONS

In the present work, the shear strength parameter ( $Q_a$ ,  $Q_s$ ,  $Q_{af}$ ,  $Q_{sf}$ ) of silty sand based on relative compaction is compared for Ottawa and Yamuna sand. The values of shear strength parameters ( $Q_{af}$  and  $R_{af}$ ) of silty sand calculated based on the concept of relative compaction is more appropriate as compared to that based on relative density due to the inherent limitation associated with the correct determination of relative density for silty soils. The values thus obtained for  $Q_{af}$  and  $R_{af}$  are comparable with that calculated by Salgado upto 15% of fine ( $Q_{as}$  and  $R_{as}$ ). Based on the above results and discussions the following conclusion can be drawn.

1. The outcome of present study indicates that the strength characteristics of silty sand containing non-plastic fine (Ottawa sand) and plastic fines (Yamuna sand) is different though showing the similar trend.
2. The mean size of particle depends on the difference in elevation of origin and fall of river. The Yamuna river carries plastic fines due to its origin at very high altitude in hilly region as compared to Ottawa river which mostly flows in plains.
3. Coefficient of co-relation is higher for shear strength parameter when calculated based on relative compaction than when calculated based on relative density due to the error involved in estimation of relative density.
4. Values of  $Q_{af}$  &  $R_{af}$  are sensitive to the range of mean sizes, relative compaction and extent of confinement.
5. Ottawa sand is more compressible for fines percent upto 10% and the rate of compression decreases when percent fine increases above 10%.
6. Yamuna sand reaches its peak much earlier than Ottawa sand for the same percent fines due to presence of plastic fines which slips easily under the same normal and confining stress.

## LIST OF SYMBOLS

$\tau_f$	Shear strength at failure
$\sigma$	Normal stress on the plane of shearing
$C$	Cohesion
$\sigma'$	Effective normal stress
$\sigma_1$	Principal stress
$\sigma_3$	Confining stress
$\Phi$	Friction angle
$\Phi_p$	Peak friction angle
$\Phi_c$	Critical friction angle
$\Psi$	Dilatancy angle
$G_s$	Specific gravity
$\sigma_d$	Deviator stress
$e_{max}$ and $e_{min}$	Maximum and minimum void ratio
$\gamma_w$	Unit weight of water
$\gamma_{min}$ and $\gamma_{max}$	Minimum and maximum dry density
$D_r$	Relative density
$P_p$	Mean effective stress at peak strength
$P_A$	Reference stress
$Q, R, Q_a, R_a, Q_s, R_s, Q_{af}, R_{af}, Q_{sf}, R_{sf}$	Fitting parameters
$r^2$	Coefficient of co-relation
$R_c$	Degree of compaction
$D_m$	Mean diameter of particles
$I_R$	Dilatancy index

## REFERENCES

1. Ayadat, T, Hanna, A. (2007) Prediction of collapse behaviour in soil, *Revue Europeans de Genie Civil*, 11 (5), 603-619.
2. Been, K., Jefferies, M. G., and Hachey, J.(1991). "The critical state of sands." *Geotechnique*, 41(3), 365–381.
3. Bolton, M. D. (1986). "The strength and dilatancy." *Geotechnique*, 36(1), 55–78.
4. Bui, M. and Priest, J. (2007). "Discussion of "Particle Shape Effects on Packing Density, Stiffness, and Strength: Natural and Crushed Sands" by Gye-Chun Cho, Jake Dodds, and J. Carlos Santamarina." *J. Geo-tech. Geo-environ. Eng.*, 133(11), 1473–1474.
5. Chakraborty T. and Salgado R. (2010). "Dilatancy and Shear strength of sand at low Confining Pressure", *Journal of Geotechnical and Geo-Environmental Engineering*, ASCE, 136(3), 527-534.
6. Chen, Y. C., and Liao, T. S. (1999). "Studies of the state parameter and liquefaction resistance of sands." *Earthquake Geotechnical Engineering: Proc., 2nd Int. Conf.*, Lisbon, Portugal, [P. S. Seco e Pinto, ed.].
7. ChoG, Dodds J, and SantamarinaJ., (2006) "Particle Shape Effects on Packing density, Stiffness, and Strength: Natural and Crushed Sands", *Journal of Geotechnical and Geo-environmental Engineering*, ASCE, 132, (5), 591-602
8. Chu, J., and Lo, S. C. R. (1993). "On the measurement of critical state parameters of dense granular soils." *Geo-tech. Test. J.*, 16(1), 27–35.
9. Diego C.F. Lo Presti, Pedroni S. and Crippa V. (1992). "Maximum dry density of cohesion less soil by pluviation and by ASTM D 4253-83: A comparative study." *Geotech. Testing J.*, 15(2), 180–189.
10. Gupta R. and Trivedi A. (2009). "Effects of non-plastic fines on the behaviour of loose sand an experimental study", *Electronic Journal of Geotechnical Engineering*, 14, (B), 1-14.
11. Gupta, R., and Trivedi, A. (2009). "Bearing Capacity and Settlement of Footing Resting on Confined Loose Silty Sands." *Electronic Journal of Geotechnical Engineering*, 14, (B).
12. IS: 2720 (Part3/Sec2)-1980 Methods of tests for soils: Part 3 Determination of specific gravity, Section 2 Fine, medium and coarse grained soils.
13. Konrad, J. M. (1990). "Minimum undrained strength versus steady-state strength of sands." *J. Geotech. Eng.*, 116(6), 948–963.
14. Lee, C. J. (1995). "Static shear and liquefaction potential of sand." *Proc., 3rd Int. Conf. on Recent Advances in Geotechnical Earthquake Engineering and Soil Dynamics*, St. Louis, Vol. 1, 115–118.
15. Ojha S., Goyal P., Trivedi A., (2012) "Non linear behaviour of silty sand from catchment area of Yamuna river" *Proceeding of IGC conference Dec 2012 Delhi*, paper no. B211, 277-280.
16. Ojha, S. (2013). "Shear Strength Parameters for Silty- Sand Using Relative Compaction." *Electronic Journal of Geotechnical Engineering*, 18(1), 81–99.
17. Salgado R., Bandini P. and Karim A. (2000). "Shear Strength and Stiffness of Silty Sand", *Journal of Geotechnical and Geo-environmental Engineering*, ASCE, 126(5), 451–462.
18. Trivedi A. (2010). "Strength and dilatancy of jointed rocks with granular fill", *ActaGeotechnica*, 5(1), 15-31.
19. Terzaghi, K. (1942), *Theoretical Soil Mechanics*, New York: Wiley, ISBN 978-0-471-85305-3





## Database optimization of News articles through Indexing

Shweta Taneja  
Assistant Professor  
Deptt. Of CSE  
BPIT, Delhi, India

Charu Gupta  
Assistant Professor  
Deptt. Of CSE  
BPIT, Delhi, India

Ankita Mohan Saxena, Jatin Rijhwani, Sanya  
Malhotra  
Deptt. Of CSE  
BPIT, Delhi, India

**Abstract—** With rapid advances in information technology, there is a plethora of information available. Out of this huge amount of data, a user (in need of information) requests the system in the form of a query. Normally the systems are not expected to return the actual information but only documents containing that information. In order to retrieve relevant information out of this huge database, the database has to be optimized in order to process the query efficiently. In this paper, indexing as a database optimization technique has been implemented on news articles. With the present work, a structured database has been created which is then optimized. A performance evaluation has been done on numerous parameters with normal execution, execution with clustered index and non-clustered index. The results show that it can significantly improve the performance which in turn will help in improving the performance of novelty mining system.

**Keywords-** Database optimization, Preprocessing, Information retrieval, Indexing.

### I. INTRODUCTION

In today's information age, it is easy to store large amounts of data. However, although the amount of data available to us is continuously growing, our ability to gather this information and use it remains constant. Imagine the time savings if we are only presented with novel information to read, while the old or redundant information is filtered out. Thus, novelty mining [1] can help to single out novel information out of a massive set of text documents. The term novelty (derived from Latin word Novus for "new") is the quality of being new, or following from that, of being striking, original or unusual. In novelty mining, users are able to send different documents to be tested for its relevance and novelty. Due to the millions of data in the database, the insertion and selection of data have to be kept at optimum. Therefore, for that we require database optimization techniques. Database optimization is a technique to improve the query performance with indexing and statistics.

Database optimization techniques like Indexing can separate data structures that allow DBMS to locate particular records in the file of base table more quickly. Optimizing data types for a particular column in a table can reduce the CPU workload. This reduces time needed to retrieve and insert data into the database. Research of optimizing database systems has been an ongoing process where Database Management Systems (DBMS) have been evolving rapidly. Also, as lifestyles are becoming fast paced, slow and inefficient database applications are unacceptable. One of the key challenges and motivations is to pre-process the dataset. This paper includes techniques like Database Indexing that can be employed for optimization of database. A database index is a method to improve the speed of data recovery operations on a database table. It helps by reducing the

time spent in database search as well as making it more efficient. The software tool used is SQL SERVER 2005, open source database software. The contributions of this paper are thus twofold. Firstly, to design and develop the optimizing techniques for SQL SERVER 2005 database for retrieval of relevant information, which has not been well-studied before, and secondly, to study the novelty mining system which involves pre-processing as its first phase followed by classification and novelty mining techniques to detect novel data from a dataset. This paper spans across the three major emerging research areas of databases that include database indexing and information retrieval by query processing, pre-processing of dataset and knowledge management.

This paper is organized as follows. In the first section, brief introduction about the motivations for the research and development of database optimization is presented. In the second section literature review of optimization as well as indexing is shown. The third section comprises of the framework that we have proposed for our entire Novelty Mining system. In sections four details about the dataset used i.e. Reuters 21578 is explained. In section five and six the experiments conducted and subsequent performance evaluation is shown. Finally, at the end of this paper we conclude and give suggestions for future work in this field.

### II. RELATED WORK

The major contribution in the field of optimization and novelty mining is by Flora S. Tsai. Other authors have also contributed in this area. In [1], authors have explored the feasibility and performance of novelty mining and database optimization technique on a dataset of business blogs, with a very high accuracy. Previous researches on novelty detection have focused mainly on the task of finding novel material, given a set or stream of documents on a certain topic. Authors in [2] investigated the more difficult two part task defined by TREC 2002 novelty track that is firstly, finding the relevant sentences from the documents and then finding the novel sentences from the collection of relevant sentences. The research here shows that the former step appears to be more difficult part of the task, and the performance of novelty measures is very sensitive to the presence of non relevant sentences. In [3], authors have analyzed web logs posts for various categories of cyber security threats related to detection of cyber attacks, cyber crime and terrorism, they have used Latent Semantic models such as Latent Semantic Analysis (LSA) and Probabilistic LSA, to detect keywords from cyber security web logs. LSA is also discussed in another paper [6], where a new method for automatic indexing and retrieval is demonstrated. This approach takes the advantage of implicit higher order structure in

the association of terms with documents (“semantic structure”) in order to improve the detection of relevant documents on the basis of terms found in queries. In another work [5], authors have proposed experimental results on APWSJ data set. They have shown that Document-2-Sentence framework outperforms standard document level novelty detection in terms of redundancy-precision (RP) and redundancy-recall (RR). However they have suggested that D2S shows a strong capability to detect redundant information regardless of the percentage of novelty in the document. Also, in [8] authors aim to explore the performance of redundancy and novelty mining in the business blogosphere. They have adopted the mixed metric approach which combines symmetric and asymmetric metrics.

Different researchers have contributed in the area of database optimization, but either they have focused on B-Trees or indexing techniques by LSA method. None has given attention to pre processing and optimization using indexes. In our paper, we have proposed a framework which converts unstructured data of news articles to a structured form (tables) and there after indexing is performed and performance comparison is observed. This will also form basis for our future work of novelty mining, keeping in mind the constraints and challenges in natural text.

### III. PROPOSED FRAMEWORK

The framework of Novelty Mining system is shown in figure 1. It is divided into three phases:-A. Pre-processing

B. Database Optimization C. Novelty Mining. The detailed explanation of these phases is given below.

#### A. PRE- PROCESSING

There are various pre-processing techniques that infer or extract structured representations from raw unstructured data sources. In pre processing, there are different operations carried out like stop word removal and word stemming. Stop word removal aims to remove stop words like ‘is’, ‘an’, ‘the’ etc. Word stemming is the process of reducing inflected (or sometimes derived) words to their stem, basic root form- generally a written word form. E.g. running-> run, Drinks-> drink, Mangoes-> mango

##### 1.) ALGORITHM USED FOR WORD STEMMING

We have used a modified form of Porter Stemmer Algorithm [10]. The Porter stemming algorithm (or ‘Porter stemmer’) is a process for performing stemming i.e., reducing the word to its root form. It is mainly used as a part of term pre-processing, that is usually done when setting up Information Retrieval systems. The algorithm stems the data using a set of rules. There are 60 rules in 6 steps of porter stemmer algorithm. These steps are:-

1. Removes plurals of the words.
2. Turns terminal y to i when there is another vowel in the stem. Maps double suffixes to single ones, eg-‘ization’, ‘ational’ etc
3. Deals with suffixes -full, -ness etc.
4. Takes off -ant, -ence etc.
5. Removes a final -e.

In our modified porter stemmer algorithm, we remove stop words like ‘is’, ‘an’, ‘the’ etc along with above suffix removal. We have used java as a programming language for implementing our algorithm. The benefit of implementing porter stemmer is to enhance search process in the large pool of data and moreover to increase the efficiency of the entire system.

#### B. DATABASE OPTIMIZATION

Database optimization is a technique to improve the query performance with indexing and statistics. It can be defined as the optimization of resources used to increase throughput and minimize contention, enabling the largest possible CPU workload to be processed. In our paper we have used indexing to optimize the dataset.

There are two types of indexes that have been built on the data namely clustered index and non clustered index. The two types of indexes are as explained below:

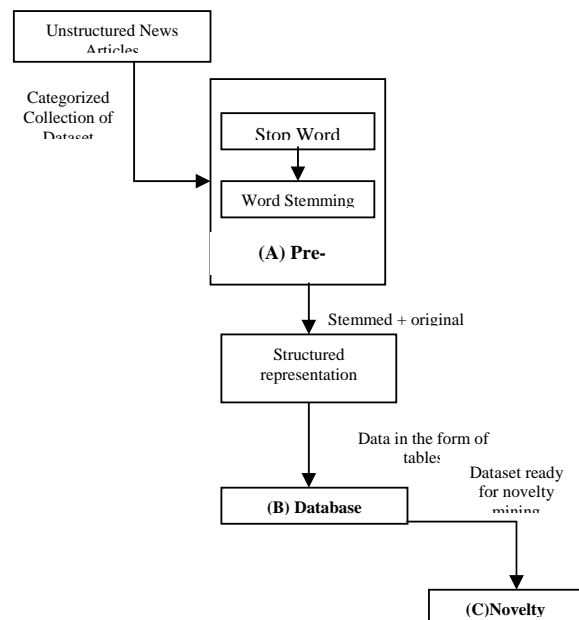


Figure 1: Proposed Framework

##### 1) NON-CLUSTERED INDEX

The data is present in arbitrary order [12], but the logical ordering is specified by the index. The data rows may be spread throughout the table regardless of the value of the indexed column or expression. The non-clustered index tree contains the index keys in sorted order, with the leaf level of the index containing the pointer to the record (page and the row number in the data page in page-organized engines; row offset in file-organized engines). In a non-clustered index: The physical order of the rows is not the same as the index order. Typically created on non-primary key columns used in JOIN, and WHERE. There can be more than one non-clustered index on a database table. Non-Clustered indexes have structures that are different from the data rows. A non clustered index key value is used to point to data rows that contain the key value. This value is known as row locator. The structure of the row locator is determined on the basis of the type of storage of the data

pages. A heap table [11] by definition is a table that doesn't have any clustered indexes. Different pages of the heap-based table occupy different non-contiguous areas on a disk, and they are not linked together in any way.

Another case arises when there is no index defined for a table at all. In that case the address of the first IAM page of the heap table itself is stored in the sysindexes table with indid = 0 as shown in figure 3. In that respect, the abbreviation IAM is a little misleading; it would be better called as SAM (Storage Allocation Map or Space Allocation Map).

## 2) CLUSTERED INDEX

Clustering alters the data block [12] into a certain distinct order to match the index, resulting in the row data being stored in order. Therefore, only one clustered index can be created on a given database table. Clustered indices can greatly increase overall speed of retrieval, but usually only where the data is accessed sequentially in the same or reverse order of the clustered index, or when a range of items is selected.

Since the physical records are in this sort order on disk, the next row item in the sequence is immediately before or after the last one, and so fewer data block reads are required. The primary feature of a clustered index is therefore the ordering of the physical data rows in accordance with the index blocks that point to them. Some databases separate the data and index blocks into separate files, others put two completely different data blocks within the same physical file(s). An object is created where the physical order of rows is the same as the index order of the rows and the bottom (leaf) level of clustered index contains the actual data rows.

## C. NOVELTY MINING

Novelty mining is the identification of new or unknown information from a given set of text documents. It is useful in personal newsfeeds, information filtering, as well as many other fields where duplicate information may be returned to the users. The major components of novelty mining are Novelty scoring, Novelty decision making and Performance evaluation [2].

A novelty score is a calculated value that determines the novelty of a document and depends largely on the novelty metric that is selected. For comparison of a relevant document to its history documents following two standard forms of comparisons are used

- one-to-one comparison :

Where the current sentence is compared with each of the previous sentences, then, the maximum of the redundancy scores obtained is compared against a threshold (a) to finally decide whether the current sentence is redundant. If the maximum redundancy score exceeds a, the current sentence is detected as redundant.

- all-to-one comparison:

Where the current sentence is compared to the pool of all the previous sentences, in order to generate the redundancy score

Novelty decision setting: after obtaining the novelty score of the incoming document, the system will make a final decision on whether a document is novel or not based on the novelty decision point.

Performance evaluation: the F-score is a popular evaluation measure that is used for evaluating the results of novelty mining as well as information retrieval for measuring search, blog classification and query classification performance.

## IV. DATASET

### A. REUTERS 21578

We have used Reuters 21578 dataset [9] in our work. The documents in the Reuters-21578 collection appeared on the Reuters newswire in 1987. The documents were assembled and indexed with categories by personnel from Reuters Ltd. (Sam Dobbins, Mike Topliss, Steve Weinstein) and Carnegie Group, Inc. (Peggy Andersen, Monica Cellio, Phil Hayes, Laura Knecht, Irene Nirenburg) in 1987. We have used a subset of this complete dataset for our study. The dataset is divided into six categories namely companies, exchanges, organizations, people, exchanges and topics.

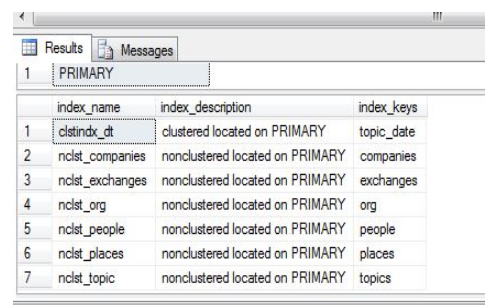
### B. TOOL USED

The database software that we have used is MICROSOFT SQL SERVER 2005. Microsoft SQL Server 2005 is a relational database management system developed by Microsoft. As a database, it is a software product whose primary function is to store and retrieve data as requested by other software applications, be it those on the same computer or those running on another computer across a network (including the Internet). SQL Server 2005 (formerly codenamed "Yukon") was released in October 2005. It included native support for managing XML data, in addition to relational data.

## V. PERFORMANCE EVALUATION

Performance evaluation is the key aspect of undertaking any research work. So we have evaluated our work and finally concluded by elaborating the efficiency of our work. But before discussing the various cases of execution, we first give an overview of the work done and then its relevant efficiency.

Following figure 2 is the list of indexes that we have created on our database:-



	index_name	index_description	index_keys
1	PRIMARY	clustered located on PRIMARY	topic_date
2	ncst_companies	nonclustered located on PRIMARY	companies
3	ncst_exchanges	nonclustered located on PRIMARY	exchanges
4	ncst_org	nonclustered located on PRIMARY	org
5	ncst_people	nonclustered located on PRIMARY	people
6	ncst_places	nonclustered located on PRIMARY	places
7	ncst_topic	nonclustered located on PRIMARY	topics

Figure 2: list of indexes on the table

As it can be seen from the above figure, we have made a total of 7 indexes on our dataset (table). One of them is a clustered index while all the others are non clustered index. The significance of using such indexes has already been discussed.

Let us now look at the various aspects of query processing in the project and thus determine optimization efficiency.

#### CASE 1: WHEN THERE ARE NO INDEXES ON THE TABLE.

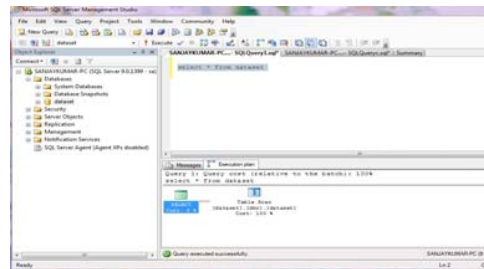


Figure 3(a): query execution plan when no indexes are present

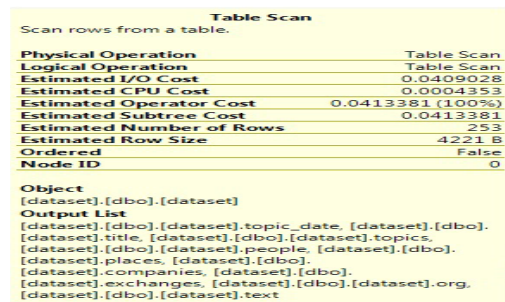


Figure 3(b): query execution plan when no indexes are present

The above mentioned figures 3 and 4 give the detailed execution plan of the query being processed by the tool with various cost factors included, which can be used to evaluate the difference between the optimized and non-optimized database.

#### CASE 2: WHEN THERE IS NO INDEX ON THE TABLE (STILL USING WHERE CLAUSE)

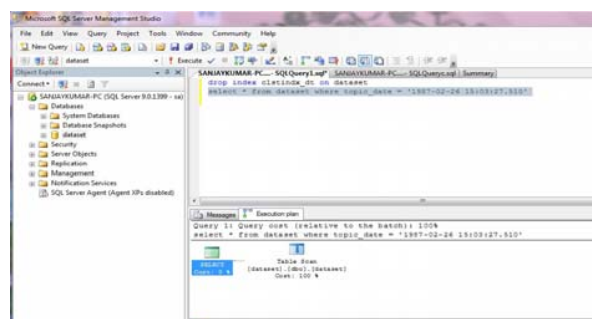


Figure 4(a): query execution plan using where clause, still no indexes on the table

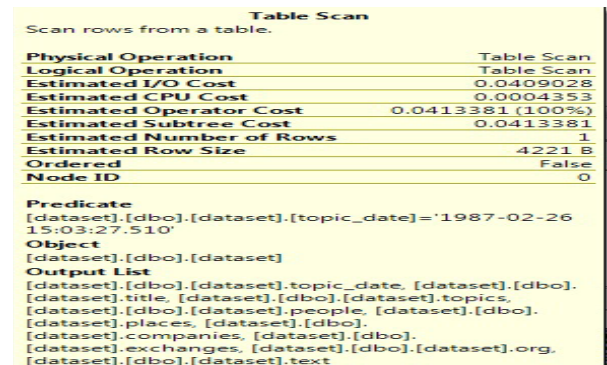


Figure 4(b): query execution plan using where clause, still no indexes on the table

#### CASE 3: WHEN THERE IS A CLUSTERED INDEX ON THE TABLE, BUT IT IS NOT USED.

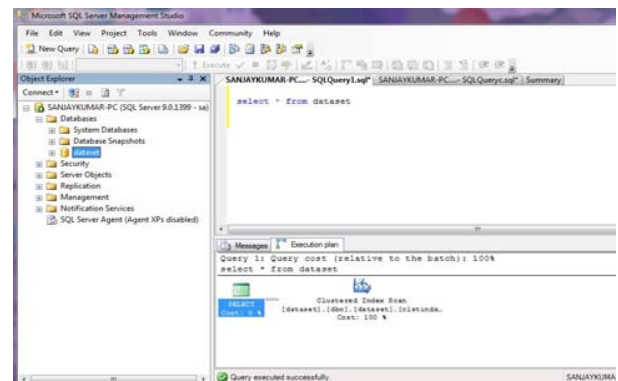


Figure 5(a): query execution plan with indexes applied, but not used

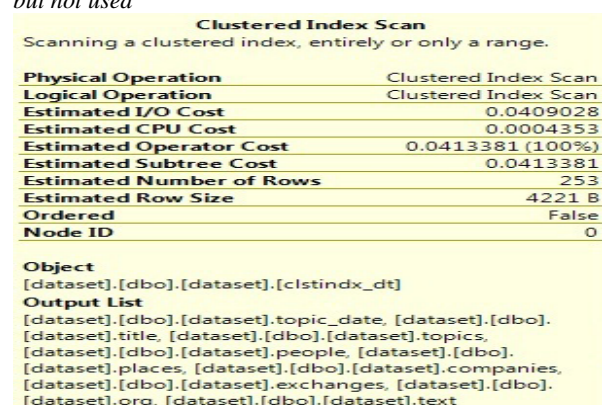


Figure 5(b): query execution plan with indexes applied, but not used.

Here as shown by figure 5 we can see that in place of using the "table scan" here "clustered index scan" is used, which improves the query processing even though the index is still not used optimally here, as the time required to fetch the values from the table is still the same.

CASE 4: WHEN THERE IS A CLUSTERED INDEX ON THE TABLE AND IT IS USED AS WELL.

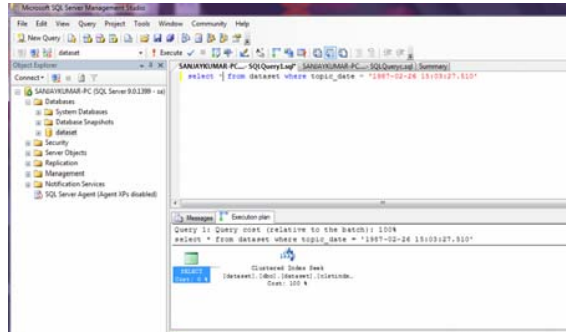


Figure 6(a): query execution plan using clustered index

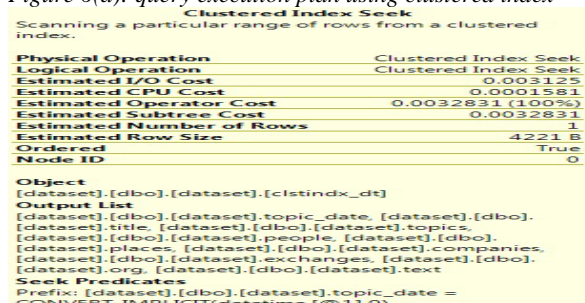


Figure 6(b): query execution plan using clustered index

As we can now notice from the above figure 6 that in place of “table scan” and “clustered index scan”, here “clustered index seek” is used. Hence there is optimal use of index present on the database and which is also reflected in the cost of overall query execution.

CASE 5: QUERY EXECUTION USING NON CLUSTERED INDEX.

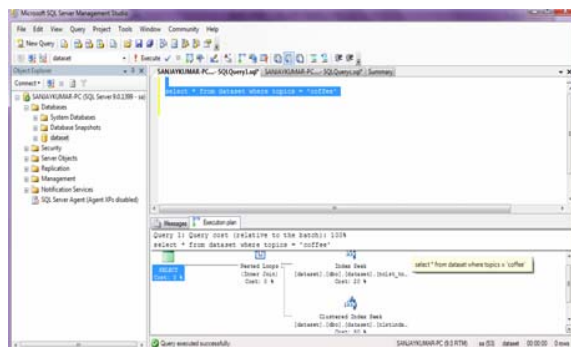


Figure 7(a): Query execution plan with non clustered indexes

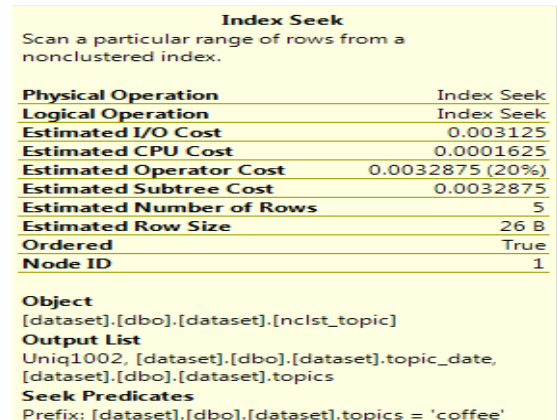


Figure 7(b): Query execution plan with non clustered indexes

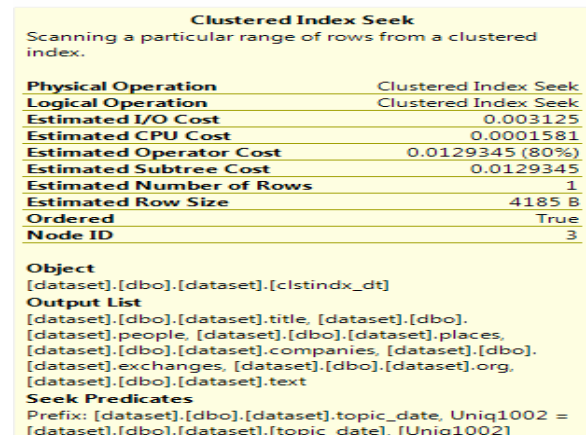


Figure 7(c): Query execution plan with non clustered indexes

As it can be observed from figures 7 (a),(b) and (c), in the case of non clustered index, the entire query is split into two parts and thus it uses two techniques “index seek” and “clustered index seek” both in the single query and thus leading to query optimization.

## VI. PERFORMANCE COMPARISON

Now the comparison between the various execution plans is given in a tabular form for easy understanding and comparison. The numerical values depicted in the table are in the form of CPU cycles required to perform the task. As can be noticed from table 1, the execution times in case of “clustered index seek” are lowest. The query execution is optimum in this case. Also the values for “index seek” and “table scan” are similar, this is due to the fact that in both the cases the indexes are not used.



TABLE I PERFORMANCE COMPARISON TABLE

PARAMETER	Normal execution	Normal execution on clustered attribute before indexing	Normal execution on non clustered attribute before indexing	Execution without using clustered index after indexing	Execution with clustered index	Execution with non Clustered index
Physical Operation	Table scan	Table scan	Table scan	Clustered index scan	Clustered index seek	Index seek, Clustered index seek
Logical Operation	Table scan	Table scan	Table scan	Clustered index scan	Clustered index seek	Index seek, Clustered index seek
Estimated I/O Cost	0.0409028	0.0409028	0.0409028	0.0409028	0.003125	0.003125, 0.003125
Estimated CPU Cost	0.0004353	0.0004353	0.0004353	0.0004353	0.0001581	0.001625, 0.0001581
Estimated Operator Cost	0.0413381	0.0413381	0.0413381	0.0413381	0.0032831	0.0032875, 0.0129345
Estimated Subtree Cost	0.0413381	0.0413381	0.0413381	0.0413381	0.0032831	0.0032875, 0.0129345
Estimated number of rows	253	1	5	253	1	5,1

## CONCLUSION AND FUTURE WORK

In this paper, an efficient way to optimize database has been proposed with indexing technique. The proposed work uses a large dataset of news articles. The experimental results obtained in Table I show that the proposed work optimizes the database with the execution time in clustered index seek. The execution time, as can be noticed is lowest out of all other attributes. Also the value of Index seeks and Table scan are similar, as both do not consider indexes. With the proposed work the effectiveness of optimization has been studied carefully. Further investigation to the topic reveals that novelty mining with database optimization can give good results. The concept has been worked out and can be used in future with novelty mining.

## ACKNOWLEDGMENT

We take this opportunity to express our sincere thanks and deep gratitude to all those who extended their wholehearted co-operation and have helped us in completing this work successfully. We express our sincere thanks to Mr. Suyash Gupta, DBA (HCL Technologies) for his encouragement and valuable suggestions.

## REFERENCES

- [1] A. T. Kwee, and F. S. Tsai, "Database Optimization for Novelty Mining of business blogs", Elsevier Expert Systems with Applications 38 (2011) 11040–11047.
- [2] J. Allan, C. Wade, and A. Bolivar, "Retrieval and Novelty Detection at the Sentence Level", SIGIR'03, ACM 1-58113-646-3/03/0007., Toronto, Canada, July 28–August 1, 2003
- [3] F. S. Tsai and K. L. Chan "Detecting Cyber Security Threats in Weblogs Using Probabilistic Models", Springer – Verlag Berlin Heidelberg, LNCS 4430, pp. 46-57, 2007.

- [4] H. Cui , M.Y. Kan and T.S. Chua, "Unsupervised Learning Of Soft Patterns For Generating Definitions From Online News", ACM 1-58113-844-X/04/0005, WWW 2004, May 17–22, 2004.
- [5] Flora S. Tsai · Yi Zhang, "D2S: Document-to-sentence framework for novelty detection", Received: 18 June 2009 / Revised: 22 July 2010 / Accepted: 11 December 2010© Springer-Verlag London Limited 2010
- [6] Scott Deerwester, Susan T. Dumais, Richard Harshman, "Indexing by latent semantic analysis", Journal of the American Society for Information Science (1986-1998); Sep1990; 41,6; ABI/INFORM Global Pg.391.
- [7] F. S. Tsai and K. L. Chan, "Redundancy and novelty mining in the business blogosphere". The Learning Organization, Vol. 17 Iss: 6 pp. 490 – 499, Emerald Article,2010..
- [8] The Text Mining Handbook Advanced Approaches in Analyzing Unstructured Data, Ronen Feldman, Bar-Ilan University, Israel James Sanger ABS Ventures, Waltham, Massachusetts.
- [9] The dataset source: [http://kdd.ics.uci.edu/databases/reuters21578 [Accessed on: January 2013]
- [10] Porter-Stemmer algorithm for preprocessing of dataset http://tartarus.org/martin/PorterStemmer [Accessed on: January 2013].
- [11] http://msdn.microsoft.com/enus/library/aa964133(v=SQL.90).aspx [Accessed on: February 2013]
- [12] http://en.m.wikipedia.org/wiki/Database\_index [Accessed on: February 2013 ]

## AUTHORS PROFILE

**Shweta Taneja** was born in 1981 in India. She completed her B.E. Computer Science and Engineering in 2003 and M. Tech in Computer Science and Engineering in 2009 from NSIT, Delhi in 2009. She is currently pursuing Ph.D from Delhi Technological University, Delhi. She is working as Assistant Professor in Computer Science Department at Bhagwan Parshuram Institute of Technology, Affiliated to GGSIPU, Delhi. Her areas of interest include Data Warehousing, Data Mining and Database Management Systems, Information Retrieval, Text Mining.

**Charu Gupta** was born in 1987 in Delhi, India. She completed her B.E. in Computer Science & Engineering in 2009 and M.Tech in Computer Science and Engineering in 2011 from JSS Academy of Technical Education, Noida. She is working as Assistant Professor in Computer

Science Department at Bhagwan Parshuram Institute of Technology, Affiliated to GGSIPU, Delhi. Her areas of interest include Database Management Systems, Data Mining, Information Reterival, Fuzzy Logic, Evolutionary algorithms and applications of Evolutionary Algorithms.

**Ankita Mohan Saxena** was born in 1991 in New Delhi, India. She has completed her B.Tech in Computer Science and Engineering from Bhagwan Parshuram Institute of Technology, IP University, Delhi, India. Her areas of interests include Data Mining, Information Reterival and Java Programming.

**Jatin Rijhwani** was born in 1990 in New Delhi, India. He has completed his B.Tech in Computer Science and Engineering from Bhagwan

Parshuram Institute of Technology, IP University, Delhi, India. His areas of interests include Data Mining, Information Reterival and Java Programming.

**Sanya Malhotra** was born in 1991 in New Delhi, India. She has completed her B.Tech in Computer Science and Engineering from Bhagwan Parshuram Institute of Technology, IP University, Delhi, India. Her areas of interests include Data Mining, Information Reterival and Java Programming.



# INTERNATIONAL JOURNAL OF MECHANICAL ENGINEERING AND TECHNOLOGY (IJMET)

ISSN 0976 – 6340 (Print)

ISSN 0976 – 6359 (Online)

Volume 4, Issue 3, May - June (2013), pp. 337-343

© IAEME: [www.iaeme.com/ijmet.asp](http://www.iaeme.com/ijmet.asp)

Journal Impact Factor (2013): 5.7731 (Calculated by GISI)

[www.jifactor.com](http://www.jifactor.com)



.....

## EFFECT OF WELDING PARAMETER ON MICRO HARDNESS OF SYNERGIC MIG WELDING OF 304L AUSTENITIC STAINLESS STEEL

Ravi Butola<sup>1</sup>, Shanti Lal Meena<sup>2</sup>, Jitendra Kumar<sup>3</sup>

<sup>1,3</sup>PG Scholar, Mechanical Department, Delhi Technological University, Bawana Road,  
Delhi-110042, India

<sup>2</sup>Assistant. Prof. in Mechanical Department, Galgotias University, Greater Noida, Gautam  
Budh Nagar, UP India

### ABSTRACT

In the present work, bead-on -plate welds were carried out on 304L austenitic stainless steel using Synergic MIG process. In this present investigation 304L having 1.2 mm diameter was used as an electrode with direct current electrode positive polarity. Argon and CO<sub>2</sub> was employed for shielding purposes. The fusion zone is generally characterized by a few geometrical features namely bead width, bead height and depth of penetration. The shape of the fusion zone depends upon a number of parameters such as gas flow rate, voltage, travel speed and wire feed rate. In order to understand the Knoop micro hardness measurements were taken across the weld bead base material.

**Keywords:** austenitic stainless steel, bead geometry, Knoop Hardness.

### 1. INTRODUCTION

Initially GMAW was called as MIG Welding because only inert gasses were used to protect the molten puddle. The application of this process was restricted to aluminum, deoxidized copper and silicon bronze. Later it was used to weld ferrite and austenitic steels, and mild steel successfully by using active gasses in place of inert gasses and hence was term MAG (Metal Active Gas) welding [2]. All the major commercial metals can be welded by GMAW (MIG/CO<sub>2</sub>) process, including carbon steels, low alloy and high alloy steels, stainless, aluminum, and copper titanium, zirconium and nickel alloys. [3]. by suitable adjusting the process parameters, it is possible to weld joints in

the thickness range of 1-13 mm in all welding position. Several researchers have attempted to investigate the effects of various process variables on the weld bead geometry and metal transfer. The quality of any weld process is characterized by the weld distortion, mechanical

Properties and weld bead geometry. Out of these factors, the weld bead geometry is the easiest to measure and control. The synergic capability enabled all of the welding parameters to be controlled from a signal dial control which optimized the current peak pulse and background values, the voltage, wire feed speed.

## **2. LITERATURE REVIEW**

The studies of the effects of various welding process parameters on the formation of bead and bead geometry have attracted the attention of many researchers to carry out further investigations. **Kim I.S. et al.** [4] studied the effect of welding process parameters on weld bead penetration Gas Metal Arc Welding (GMAW) process. Welding process parameters included wire diameter, gas flow rate, welding speed, arc current and arc voltage. The experiment results revealed that weld bead penetration increased as wire diameter, arc current and voltage increased. **Ganjigatti J.P. et al** [5] studied global versus cluster-wise regression analyses for prediction of bead geometry in MIG Welding process. They observed that the cluster-wise regression analyses perform slightly better than the global approach in predicting weld bead geometric parameters. **Erdal Karadeniz et al** [6] in their study, the effects of various welding parameters on welding penetration in Erdemir 6842 steel having 2.5 mm thickness welded by robotic gas metal arc welding were investigated. The welding current, arc voltage and welding speed were chosen as variable parameters. The depths of penetration were measured for each specimen after the welding operations and the effects of these parameters on penetration were researched. The study revealed that increasing welding current increased the depth of penetration. In addition, arc voltage is another parameter in incrimination of penetration. **Pires RM et al.** [7] describes the influences of the gases on the stability of the joining process and of the melted metal transfer through the electric arc. The influence of the type of the gas and welding speed, as well as other process parameters are addressed. The bead appearance and shape are analyzed, mainly underscoring the gases influences on the convexity of the bead, its colour, brightness, smoothness and surface pores formation. **Murugan N et al.** [8] used response surface methodology to established quadratic relations between welding parameters and bead geometry for depositing stainless steel into structure steel, using automated submerged arc welding.

## **3. SELECTIONS AND DESIGN OF WELDS**

In the design process, the goal is to produce a product that satisfies all requirements at the lowest cost. Welding is a vital approach in design because it is arguably the best joining process. The main processes for joining materials are fastening, welding, and casting. However, welding is still less expensive than casting and it is a more flexible. Welding is 3 to 4 times stronger than other processes so much less total material is required. It is also stiffer, has greater ductility, and is less likely to crack than castings. Lastly, welding resists impact loads better than castings.

#### 4. SELECTION OF DESIGN PARAMETERS

Trial runs were conducted by varying the process parameters at a time. The working range was fixed by previous research papers. The upper and lower limits were coded as +2 and –2, respectively. The coded values for intermediate values can be calculated from the relationship:

$$X_i = \frac{2[2X - (X_{\max} + X_{\min})]}{(X_{\max} - X_{\min})}$$

Where,  $X_i$  is the required coded value of a variable  $X$ , when  $X$  is any value of the variable from  $X_{\min}$  to  $X_{\max}$ ;  $X_{\max}$  and  $X_{\min}$  are the maximum and minimum levels of the variables. The selected process parameters and their upper and lower limits together with notations and units are given in Table 4.1

**TABLE 4.1: DESIGN PARAMETERS AND THEIR LIMIT**

PARAMETERS USED	LEVELS				
	1 (-2)	2 (-1)	3 (0)	4 (1)	5 (2)
Plate thickness(mm)	3	5	7	11	14
Gas flow rate (lit/min.)	6	8	10	14	18
Current(A)	160	190	230	270	310
Travel speed (cm/min.)	25	30	35	40	45

#### 5. EXPERIMENTAL PROCEDURE

Bead on plate technique was employed for depositing the weld beads on stainless steel plate (304L) using semi mechanized welding station. For the experiment, five different parameters were taken; they are plate thickness, gas flow rate, Travel speed, and current. Correspondingly 30 plates were cut each of dimensions 6 inch in length of five different thicknesses:

**TABLE 5.1; DISTRIBUTION OF PLATE THICKNESS**

Thickness (mm)	No. of plates
3	01
6	08
8	13
12	07
15	01



**Fig.5.1** welded plates

After cutting all plates, welding was carried out as per specified parameters for all plates individually. In the welding experiment, a 304L filler wire with a 1.2 mm diameter was used. All experiments were carried out with a contact-tip to work distance of 20 mm using the mixture of Argon and CO<sub>2</sub> as shielded gas at five different flow rates. A Direct current power source was used to perform the bead on plate by means of synergic MIG process. The welded pieces are shown in figure 3.10.

## 6. SYNERGIC MIG WELDING

Synergic MIG/MAG is an advanced welding system which incorporates both spray and pulse transfer. Optimum conditions can be established for a range of applications which are readily reproduced by the welder. The synergic capability enabled all of the welding parameters to be controlled from a signal dial control which optimized the current peak pulse and background values, the voltage, wire feed speed.

## 7. SAMPLE PREPARATION FOR BEAD MEASUREMENT

This procedure of preparation of a specimen involves the method of preparing the samples cut out from the plates fit for viewing under a metallurgical microscope. The ultimate objective is to produce a flat, scratch free, mirror like surface.



**Fig. 3.11** samples after etching

## 8. MICRO HARDNESS

Variation of micro hardness was observed at the various points. To measure the micro hardness, Omnitech MVH Auto Micro Hardness tester was used with 100 gram load and dwell time of 20 seconds.

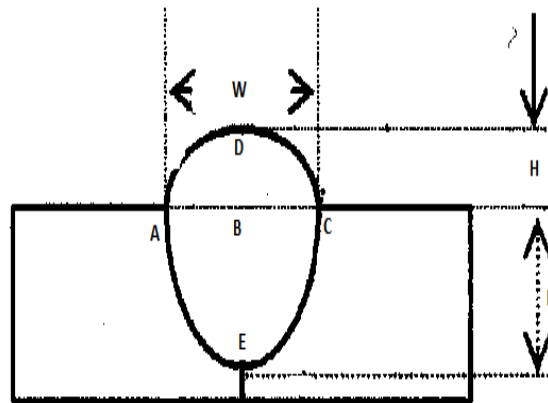


**Figure 8.1** Varies points on bead to measure the micro hardness

The micro hardness values were calculated at various points. These points are at different -2 regions, starting from point A to point E. The points are shown in figure 5.14. The values reported are for Koop's Micro hardness. A pyramidal diamond point is pressed into the polished surface of the test material with a known force, for a specified dwell time, and the resulting indentation is measured using a microscope. The calculated values of micro hardness are shown in table 8.1

**TABLE 8.1; KNOOP MICRO HARDNESS NO**

Sample no	A	B	C	D	E
2	1428	1402	1426	1348	1488
5	1298	1261	1302	1236	1312
19	1750	1662	1705	1455	1782
24	1625	1520	1675	1605	1807
30	1385	1312	1402	1289	1439

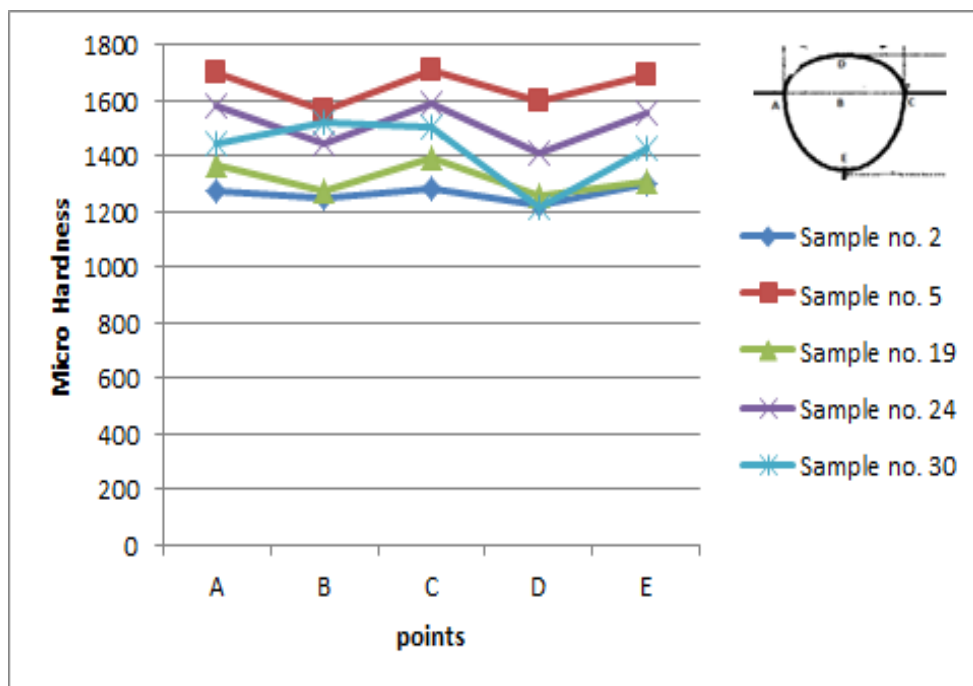


**Figure 8.2:** Variation of micro hardness at different regions

The micro hardness values at different point are obtained. For base metal the micro hardness value is measured as 1125KHN. The graphs are plotted between micro hardness and various points. The hardness measurements were carried out at a depth of 2 mm from the base metal surface. From above table we see that the KHN value for the weld zone and the base metal are comparable while maximum hardness is observed at point A, C and E. These points are in the heat affected zone (HAZ). So the maximum micro hardness value is observed in HAZ. This observation can be attributed to pearlite content and the size range of the micro structure. The pearlite content and the range of size distribution for the base metal and the weld zone are almost same. While the pearlite content for the HAZ is

higher and greater numbers of grains are in the lower range, indicating finer microstructure; as compared to weld zone and base metal. The increased pearlite content combined with finer microstructure results in greater micro hardness in the HAZ. Also it can be observed that the micro hardness is greatest in the grain refined region, having the highest Pearlite content and where the grains are finest.

## **9. CONCLUSION**

High welding current and high welding voltage produced the mixed mode but predominantly axial spray and occasional short circuiting transfer between. The weld bead ripple were fairly uniform and the general appearances of the bead were very good. Micro hardness value is maximum in HAZ. This results that the grain sizes are finest in the HAZ. The micro hardness value increases from base metal to HAZ.

## **10. REFERENCES**

- [1]. E. Karadeniz, Ozsarac, U. and Yildiz, C. 2007. The effect of process parameters on penetration in gas metal arc welding process, *Materials and Design*. Vol 28 , Issue 2 , pp. 649-656.
- [2]. M. Suban and J. Tusek, 2003. Methods for the determination of arc stability, *Journal of Materials Processing Technology*, pp. 430-437.
- [3]. Johnson J, Murphy PG, Zeckely AB. 1995 Influence of oxygen additions on argon shielded gas metal arc welding processes. *Weld J*;74(2):48s–58s.
- [4]. Kim I.S., Basu A. and Siores E., 1996 Mathematical models for control of weld bead penetration in GMAW process. *International journal of advanced manufacturing technology*, vol 12, pp 393-401.
- [5]. Ganjigatti J.P., Pratihari D.K. Roychoudhury A. 2007 Global versus cluster-wise regression analysis for prediction of bead geometry in MIG welding process. *Journal of materials processing technology*, vol 189, pp 352-366.
- [6]. Karadeniz E , Ozsarac U, Yildiz C, 2007, The effect of process parameters on penetration in gas metal arc welding processes *Materials and Design*; 28: 649–656.
- [7]. Pires RM, Quintino I and Miranda L. 2006 Analysis of the influence of shielding gas mixtures on the gas metal arc welding metal transfer modes and fume formation rate. *Material and Design J*; 28(5):1623–31.
- [8]. Murugan N. Parmar R.S and Sud S.K, 1999, Effect of submerged arc process variables on dilution and bead geometry in single wire surfacing. *Journal of Material Processing and Technology*, vol371, pp 767-780.
- [9]. Harshal K. Chavan, Gunwant D. Shelake and Dr. M. S. Kadam, “Finite Element Model To Predict Residual Stresses in MIG Welding”, *International Journal of Mechanical Engineering & Technology (IJMET)*, Volume 3, Issue 3, 2012, pp. 350 - 361, ISSN Print: 0976 – 6340, ISSN Online: 0976 – 6359.
- [10] Harshal K. Chavan, Gunwant D. Shelake and Dr. M. S. Kadam, “Impact of Voltage on Austenitic Stainless Steel for the Process of TIG and MIG Welding”, *International Journal of Mechanical Engineering & Technology (IJMET)*, Volume 1, Issue 1, 2010, pp. 60 - 75, ISSN Print: 0976 – 6340, ISSN Online: 0976 – 6359.



**Abdul Khaliq<sup>1</sup>**

e-mail: khaliqsb@gmail.com

**Rajesh Kumar**

Department of Mechanical Engineering,  
Delhi Technological University,  
Government of NCT of Delhi,  
Bawana Road,  
Delhi 110042, India

**Ibrahim Dincer**

Faculty of Engineering and Applied Science,  
University of Ontario Institute of Technology,  
2000 Simcoe Street North,  
Oshawa, L1H7K4 ON, Canada

**Farrukh Khalid**

Department of Mechanical Engineering,  
Aligarh Muslim University,  
Aligarh 202002,  
Uttar Pradesh, India

# Energy and Exergy Analyses of a New Triple-Staged Refrigeration Cycle Using Solar Heat Source

*In this paper, energy and exergy analyses of a new solar-driven triple-staged refrigeration cycle using Duratherm 600 oil as the heat transfer fluid are performed. The proposed cycle is an integration of absorption refrigeration cycle (ARC), ejector (EJE) refrigeration cycle (ERC), and ejector expansion Joule–Thomson (EJT) refrigeration cryogenic cycles which could produce refrigeration output of different magnitude at different temperature simultaneously. Both exergy destruction and losses in each component and hence in the overall system are determined to identify the causes and locations of the thermodynamic imperfection. Several design parameters, including the hot oil outlet temperature, refrigerant turbine inlet pressure, and the evaporator temperature of ERC and EJT cycle are also tested to evaluate their effects on energy and exergy performance. It is observed that largest contribution to cycle irreversibility comes from the central receiver and heliostat field with the heat recovery vapor generator (HRVG), condenser, and ejector of ERC itself also contributing considerably. The exergy efficiency of the solar-driven triple-staged refrigeration cycle is 4% which is much lower than its energy efficiency of 10%, respectively. The results clearly reveal that thermodynamic investigations based on energy analysis alone cannot legitimately be complete unless the exergy concept becomes a part of the analysis. [DOI: 10.1115/1.4024126]*

**Keywords:** solar energy, triple-effect refrigeration, ejector, absorption, Joule–Thomson cryogenic cycle, exergy, efficiency

## 1 Introduction

For the last few years much research is devoted to the development of technologies that can offer reductions in energy consumption, peak electrical demand, and energy costs without lowering the desired level of comfort conditions. Solar energy refrigeration technologies have the advantage of removing the majority of harmful effects of traditional refrigeration machines and that the peaks of requirements in cold coincide most of the time with the availability of solar radiation. The development of solar refrigeration technologies became the worldwide focal point for concern again [1].

In order to utilize the solar energy for its potential in reducing fossil fuel consumption and alleviating environmental problem, more interests have been paid to the solar thermal-driven refrigeration technologies like solar ejector cooling, solar powered absorption refrigeration, and solar energy driven combined ejector-absorption cooling cycles. Detailed discussion on the thermodynamic performance of these refrigeration cycles is recently published. Priasawas and Lundqvist [2] studied the solar-driven ejector system and calculated the irreversibilities in each component of the system to find the optimum operating conditions. Their results indicate that most significant destruction/losses occur in the solar collector and ejector. Hernandez et al. [3] showed that for an evaporator temperature of  $-10^{\circ}\text{C}$ , an ejector refrigeration

system employing R134a can operate at a generator temperature of  $85^{\circ}\text{C}$  with average energy efficiencies between 21% and 58%, depending on the condenser temperature. Alexis and Katsanis [4] obtained similar results for methanol. Varga et al. [5] carried out a theoretical study to assess system and refrigeration efficiencies of a solar-assisted ejector cycle using water as the operating fluid. Their analysis indicated that in order to achieve an acceptable coefficient of performance, generator temperatures should not fall below  $90^{\circ}\text{C}$ . Evaporator temperatures below  $10^{\circ}\text{C}$  and condenser temperatures over  $35^{\circ}\text{C}$  resulted in a significant drop in system efficiency. Solar-driven absorption refrigeration systems are suitable for use with solar energy and existing absorption system show limitations in the evaporator range  $-20^{\circ}\text{C}$  to  $+10^{\circ}\text{C}$ . It is widely realized that now refrigerant-absorbent combinations may be more suitable than the most commonly used solutions (LiBr- $\text{H}_2\text{O}$  and  $\text{NH}_3$ - $\text{H}_2\text{O}$  solutions). In this context, Pierres et al. [6] examined the possibility to design a new deep freezing process to produce cold at low temperature ( $-40^{\circ}\text{C}$ ) from low grade heat source ( $80^{\circ}\text{C}$ ) using absorption thermochemical technology. They reported that the exergies involved in thermochemical process for cold production distinguish between the quantity and quality of the inlet and outlet energies. Dincer et al. [7] used a mixture of R-22 and dimethyl ether tetra ethylene glycol as the working fluid. The coefficient of performance (COP) for theory and experiment was found to be 0.6 and 0.4, respectively, at a generator temperature of  $90^{\circ}\text{C}$ . Das and Mani [8] recommended the use of R22-N,N-dimethyl formamide. Another attempt towards the improving of the performance of solar-driven absorption cycle is to improve the performance of the solar collection by using glazed collectors/generators [9]. Atmaca and Yigit [10] carried out a thermodynamic optimization of solar powered absorption cycle using  $\text{NH}_3$ - $\text{H}_2\text{O}$  mixture as a working fluid. Ziegler et al. [11] introduced the

<sup>1</sup>Corresponding author.

Contributed by the Solar Energy Division of ASME for publication in the JOURNAL OF SOLAR ENERGY ENGINEERING. Manuscript received March 8, 2013; final manuscript received March 14, 2013; published online July 2, 2013. Editor: Gilles Flamant.

multieffect absorption cycles to yield better cooling performances using low grade heat. Sozen et al. [12] highlighted the prospects for utilization of solar-driven ejector-absorption cooling system and reported that there is a great potential for utilization of solar cooling system for domestic heating/cooling applications in Turkey. Wang et al. [13] dealt with a solar-driven ejector-absorption refrigeration cycle with re-absorption of the strong solution and pressure boost of the weak solution ( $\text{NH}_3\text{-LiNO}_3$ ). It is demonstrated that the cycle has obvious advantages as compared with the conventional absorption refrigeration cycle. Fan et al. [14] shows that solar power ejector-absorption technologies are attractive alternatives that not only can serve the needs of air conditioning and refrigeration purposes but also can meet demand for energy conservation and environmental protection. Solar operated ejector and absorption refrigeration systems are limited in their ability to produce cooling in the range of 250 K–290 K. These systems were found suitable for refrigeration and air conditioning purpose. There are many applications, where cooling in the cryogenic range (80 K–220 K) is needed, like infrared detector, gas chillers or liquefaction, cryosurgery, cryopreservation, water vapor cryotrapping, and astronautical application, etc. To meet out such a cooling demand, the EJT cryogenic cycle has been explored and various investigations related to this cycle are reported in the literature. At this onset, Naer and Rozhentsev [15] conducted the experimental investigation with Joule–Thomson microcoolers in the range of 90–200 K for hydrocarbon mixtures. Yu et al. [16] performed a component level exergy analysis, for the ejector Joule–Thomson cycle using the two component refrigerant mixture  $\text{N}_2\text{-CH}_4$  and showed that the ejector Joule–Thomson cycle exhibits a clear increase in exergetic efficiency compared to the basic Joule–Thomson refrigeration cycle. Recently, Rashidi et al. [17] applied the first-law and second-law approach to study an ejector Joule–Thomson cryogenic refrigeration cycle. Their investigations show that COP and exergy efficiency increase with increasing evaporator temperature and ejector pressure. More recently, Gong et al. [18] developed the dual mixed gases Joule–Thomson refrigeration system for  $-186^\circ\text{C}$  cryogenic preservation. Their investigations show that the dual mixture refrigeration cycle has a good performance for low temperature applications. For the effective exploitation of solar energy and to provide cooling for refrigeration and space conditioning in various ranges of operating temperature for domestic, commercial, and industrial applications, an emergence of hybrid cycle combining the various solar powered refrigeration cycles has become an imperative need to overcome with the twin menace of increasing energy demand and environmental degradation through fossil fuel consumption for cooling applications.

The literature review indicates that the energy and exergy analyses of solar energy driven hybrid cycle for triple-staged refrigeration, which use heliostat field and central receiver as the concentrator-receiver system, have not been reported till now. In this regard, the objective of this article is to construct a theoretical framework for the energy and exergy analysis of solar powered triple-staged refrigeration cycle using *Duratherm* 600 oil as the heat transfer fluid. The proposed cycle is the integration of  $\text{LiBr-H}_2\text{O}$  ARC which may be used for space conditioning of  $4^\circ\text{C}$  to  $10^\circ\text{C}$ , ERC which provides cooling for refrigeration in the range of  $-9^\circ\text{C}$  to  $-1^\circ\text{C}$  (264 K–272 K), and EJT cryogenic cycle which is effectively applicable for cryogenic cooling in the range of  $-193^\circ\text{C}$  to  $-143^\circ\text{C}$  (80 K–130 K). The proposed cycle is an effort for the effective exploitation of solar energy to meet out the cooling demands of various industries like space conditioning, cold storages, pharmaceuticals, infrared detectors, cryosurgical probes, and vaccine preservation, etc. Parallel to the advancement in refrigeration systems for the effective exploitation of waste heat, second law of thermodynamics along with the traditional first law approach, is highly desirable in order to make the theoretical treatment of the proposed cycle in general and to identify and quantify the sources of losses for evaluating its true efficiency in particular. A reduction in thermodynamic losses in its various

components will lead to its effective exploitation through efficient and environmentally benign operation. The effect of most influenced parameters has been observed on the energy and exergy efficiency of the proposed cycle along with the exergy destruction in its various components. Numerical results are graphed and commented upon.

## 2 Description of the Proposed Cycle

The proposed system consists of Rankine cycle (RC), ERC, ARC, and EJT cycle with only solar heat source. Figure 1 shows the simplified RC, ERC, ARC, and EJT cycle, while Fig. 1(a) depicts the corresponding T-s diagram. Solar energy falls on the heliostat field and reflected on the aperture area of central receiver which is located at the top of the tower. The concentrated rays, which fall onto the receiver results in high temperature of the central receiver is used to heat the oil (*Duratherm* 600). The oil is flowing through the pipes which transfer the thermal energy from central receiver to the HRVG (1–2) and generator (2–12). Superheated vapor of R141b (4) is expanded in a turbine to generate work. The turbine exhaust (5) passes through converging diverging supersonic nozzle of EJE1. The very high velocity refrigerant vapor at the exit of the nozzle creates a very high vacuum at the inlet of the mixing chamber and extract secondary vapor (11) into the chamber from the evaporator-1 (E1) of ERC and this causes cooling effect at E1 of ERC. The primary vapor (5) and secondary vapor (11) are mixed in the mixing chamber. The mixed stream (6) is cooled in condenser-1 (C1). The saturated liquid (7) is divided into two parts (8, 9), one part (9) is passed through throttling valve-1 (TV1) where pressure is reduced to evaporator pressure (10) and feed to E1, and second part (8) is pumped by pump-1 (P1) to the HRVG of RC cycle. The solar thermal energy (2) coming out from HRVG passes through the generator of ARC and finally recirculated to the central receiver. The saturated pure water vapor (13) coming from generator is cooled in C2. Saturated liquid (14) at condenser pressure passes through TV2 to generate saturated liquid (15) at reduced pressure, i.e., evaporator pressure. Saturated vapor (16) after receiving heat from E2 enters the absorber (A). Solution (20) which is a mixture of  $\text{LiBr-H}_2\text{O}$  passes through solution heat exchanger (SHX) and cooled to (21) and then passes through throttle valve to reduce its pressure, i.e., absorber pressure. Absorber is maintained at  $35^\circ\text{C}$  at E2 pressure. Two streams (16, 22) mixed at absorber (A) and form a new mixture (17), which passes through P2 and SHX and then finally enters to the generator (G).

The work output from turbine is fed as input to the compressor of EJT cycle. The working fluid (propane) compressed from state 23 to 24 isothermally. Next, the high-pressure vapor enters the heat exchanger-1 (HX1) and cooled to 25. Subsequently, the flow is divided into two streams; one stream leaves the HX1 and enters the EJE2, the other stream enters the HX2 and is further subcooled to 26. The vapor in HX1 and HX2 is subcooled (25–26) by the returning low-pressure gas stream from the EJE2. The subcooled refrigerant transforms to two-phase flow after the TV4 at state 27. The low pressure and temperature flow that enter the E3 are vaporized by absorbing heat from cooling media and produces the necessary cooling effect and exits the evaporator in a two-phase flow at state 28.

The extracted vapor (25) from the HX1 enters the nozzle of the EJE2 as the primary fluid. The very high velocity vapor at the exit of the nozzle produces vacuum at the inlet of mixing chamber and entrains the two-phase flow (secondary fluid) from the E3. The two streams are mixed in the mixing chamber and the mixed stream discharges from the EJE2 to the HX2 at state 29. The temperature of vapor increases while passing through HX1 and HX2 and in due course superheated vapor enters the compressor at state 23.

The following assumptions are made for the analysis of the proposed cycle:



- only physical exergies are used for the industrial waste heat source and vapor flows
- kinetic, potential, and chemical exergies of the substances are neglected
- lithium bromide solutions in the generator and absorber are in equilibrium state at their respective temperature and pressure

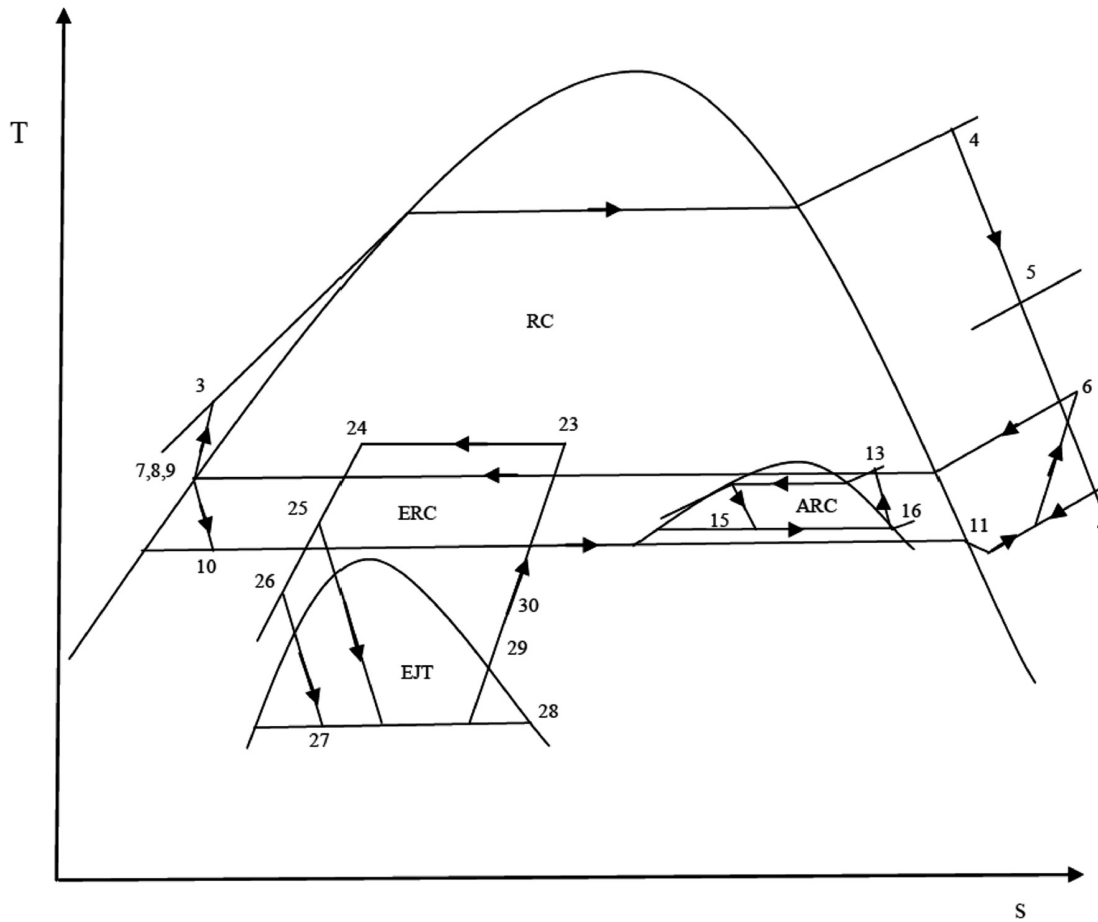


Fig. 1 (a) T-s diagram of solar operated triple-staged refrigeration cycle

- the water refrigerant at condenser and evaporator exit is at saturated state
- the strong solution leaving the absorber and the weak solution leaving the generator are saturated
- to avoid crystallization of the solution in ARC, the temperature of the solution entering the TV3 should be at least 7 °C–8 °C above the crystallization temperature
- amount of power consumed by refrigerant pump and solution pump is found to be negligible, hence it is assumed to be zero

For the analysis, the specifications of the combined RC, ERC, ARC and EJT cycle are given in Table 1.

The key component of this combined cycle is ejector and its performance is dependent upon entrainment ratio which determines the magnitude of mass flow rate of secondary refrigerant in terms of mass flow rate of primary refrigerant coming out from the turbine. The basic principle of the model was introduced by Keenan et al. [19] based on gas dynamics and formulated by Huang et al. [20] and Ouzzane and Aidoun [21]. The formulation and assumption of entrainment ratio are based on mass, momentum, and energy equations which is recently developed by Dai et al. [22] and may be reported as

$$\mu = \sqrt{\eta_n \eta_m \eta_d (h_{pf,n1} - h_{pf,n2,s}) / (h_{mf,d,s} - h_{mf,m})} - 1 \quad (1)$$

Note that, the properties of the heliostat, central receiver, nozzle, mixing chamber, and diffuser are reported in Table 1 and the required enthalpy values at various state points of the ejector cycle for a given refrigerant are taken from REFPROP 6.01 [23]

The ejector mainly consists of three sections, that is, nozzle, mixing, and diffuser section. In the nozzle section, the energy con-

servation equation for the adiabatic and steady primary flow is given as

$$\dot{m}_{pf} h_{pf,n2} + \frac{\dot{m}_{pf} u_{pf,n2}^2}{2} = \dot{m}_{pf} h_{pf,n1} + \frac{\dot{m}_{pf} u_{pf,n1}^2}{2} \quad (2)$$

The nozzle efficiency may be defined as

$$\eta_n = \frac{h_{pf,n1} - h_{pf,n2}}{h_{pf,n1} - h_{pf,n2,s}} \quad (3)$$

In the mixing section, the momentum conservation equation is given as

$$\dot{m}_{pf} u_{pf,n2} + \dot{m}_{sf} u_{sf,n2} = (\dot{m}_{pf} + \dot{m}_{sf}) u_{mf,m,s} \quad (4)$$

In the diffuser section, the energy equation is given as

$$\frac{1}{2} (u_{mf,m}^2 - u_{mf,d,s}^2) = h_{mf,d,s} - h_{mf,m} \quad (5)$$

The diffuser efficiency is given as

$$\eta_d = \frac{h_{mf,d,s} - h_{mf,m}}{h_{mf,d} - h_{mf,m}} \quad (6)$$

### 3 Thermodynamic Analysis

A thermodynamic analysis considering both the first and the second laws of thermodynamics provide an opportunity to

**Table 1 Main parameters considered for the analysis [22,25]**

Environment temperature (°C)	15
Environment pressure (MPa)	0.10135
Turbine inlet pressure range (MPa)	0.9–1.7
Hot oil outlet temperature (°C)	160–180
Hot oil inlet temperature (°C)	85
Solar radiation received per unit area ( $\text{W m}^{-2}$ )	850
Apparent sun temperature (K)	4500
Heliostat aperture area ( $\text{m}^2$ )	3000
Turbine back pressure range (MPa)	0.22–0.3
Turbine isentropic efficiency (%)	85
Isothermal efficiency of compressor (%)	55
ARC evaporator temperature (°C)	5
ERC evaporator temperature range (°C)	(−1 to −9) or (264 K–272 K)
EJT evaporator temperature range (°C)	(−193 to −143) or (80 K–130 K)
Condenser-2 temperature (°C)	35
Hot oil mass flow rate ( $\text{kg s}^{-1}$ )	8.0
Pump isentropic efficiency (%)	70
HRVG efficiency (%)	100
Pinch point temperature difference (°C)	10.0
Nozzle efficiency (%)	90
Mixing chamber efficiency (%)	85
Diffuser efficiency (%)	85
Energy efficiency of heliostat field (%)	75
Energy efficiency of central receiver (%)	90
Exergy efficiency of heliostat field (%)	75
Exergy efficiency of central receiver (%)	30
View factor of central receiver	0.8
Emissivity of central receiver	0.8
Reflectivity of central receiver	0.04

evaluate the theoretical performance of the proposed cycle. The model based on thermodynamic analysis able to predict the cycle performance, efficiency, and emissions. Theoretical analysis minimize the number of experimental tests that have conducted, which are usually costly and time consuming when new thermodynamic cycle technologically advanced are appraised. Exergy analysis which is the combined application of both first and second laws of thermodynamics determines the system performance based on exergy which is defined as the maximum amount of work produced during the reversible transition of a stream of matter from its given thermodynamic state to the restricted dead state where the stream of matter will only be in thermal and mechanical equilibrium with the environment not in chemical equilibrium, hence the exergy obtained during this process will be the physical exergy.

Mathematically

$$\dot{E} = \dot{m}[(h - h_0) - T_0(s - s_0)] \quad (7)$$

According to Bejan [24], the entropy generation over a control volume is given by

$$\dot{S}_{\text{gen}} = \frac{dS}{dt} - \sum_{i=0}^n \frac{\dot{Q}_i}{T_i} - \sum_{\text{in}} \dot{m} s + \sum_{\text{out}} \dot{m} s \geq 0 \quad (8)$$

The exergy destruction and entropy generation are related as

$$\dot{E}_D = T_0 \dot{S}_{\text{gen}} \quad (9)$$

**3.1 Energy Efficiency ( $\eta_{\text{energy}}$ ).** It can be defined as the ratio of the desired effect ( $\dot{Q}_{E1}, \dot{Q}_{E2}, \dot{Q}_{E3}$ ) to the thermal energy of solar input ( $\dot{Q}_{\text{Solar}}$ ). The energy efficiency of the triple-staged refrigeration cycle is then given by

$$\eta_{\text{energy}} = \frac{\dot{Q}_{E1} + \dot{Q}_{E2} + \dot{Q}_{E3}}{\dot{Q}_{\text{Solar}}} \quad (10)$$

Note that the basic equations obtained from the law of conservation of energy in the components of RC, ERC, ARC, and EJT may be written as follows:

For heliostat: A part of thermal energy received by heliostat is delivered to the central receiver and rest is lost to the environment [25]

$$\dot{Q}_{\text{Solar}} = A_h q \quad (11)$$

where  $A_h$  and  $q$  are the aperture area and solar radiation per unit area

$$\dot{Q}_{\text{Solar}} = \dot{Q}_{\text{CR}} + \dot{Q}_{\text{lost, heliostat}} \quad (12)$$

So,

$$\eta_{\text{energy, heliostat}} = \frac{\dot{Q}_{\text{CR}}}{\dot{Q}_{\text{Solar}}}$$

**3.2 Exergy Efficiency ( $\eta_{\text{exergy}}$ ).** Since exergy is more valuable than energy according to the second law of thermodynamics, it is useful to consider both output and input in terms of exergy. The amount of exergy supplied in the product to the amount of exergy associated with the fuel is more accurate measure of the thermodynamic performance of the system which is defined as the ratio of exergy contained in the product to the exergy associated with the fuel input and the exergy efficiency of combined cycle may be reported as

$$\eta_{\text{exergy}} = \frac{\Delta \dot{E}_{E1} + \Delta \dot{E}_{E2} + \Delta \dot{E}_{E3}}{\dot{E}_{\text{Solar}}} \quad (13)$$

where  $\Delta \dot{E}_{E1}$  is the change in exergy at evaporator of ERC,  $\Delta \dot{E}_{E2}$  is the change in exergy at evaporator of ARC,  $\Delta \dot{E}_{E3}$  is the change in exergy at evaporator of EJT cycles, and  $\dot{E}_{\text{Solar}}$  is the exergy associated with solar radiation falling on heliostat.

Equations (7)–(9) have been applied to evaluate the energy and exergy balances and hence the equations for exergy destruction in each component of the proposed solar-driven triple-staged refrigeration cycle are provided in the Appendix.

## 4 Results and Discussion

A parametric study is carried out to identify the effect of various parameters on the performance of the solar-driven triple-staged refrigeration system. Following parameters have been chosen in the typical range of its operation: hot oil temperature at the exit of central receiver, turbine inlet pressure (0.9–1.7 MPa), evaporator temperature of ERC (264 K–272 K), and evaporator temperature of EJT cycle (80 K–130 K). The parameter under consideration is varied over a given typical range while values of other parameters are kept constant at the level of base case values.

The energy efficiency and energy distribution of solar heat source are obtained by energy balance approach or first law analysis of the cycle. However, the exergy destruction or irreversibility in each component, and the exergy efficiency are investigated under the exergy balance approach or second-law analysis of the cycle. The exergy destruction in each component of the cycle as a whole is nondimensional by expressing it as a percentage of the exergy of solar heat source. The distribution of heat source exergy among the components, exergy destruction due to irreversibility of the components of the cycle, useful energy output (refrigeration capacity of ERC, ARC, and EJT cycle) is clearly depicted. Inclusion of losses in an irreversibility analysis approaches the performance of real cycle. The thermodynamic properties of R141b of ERC, refrigerant of EJT cycle (Propane) were calculated by REFPROP 6.01 (1998) and thermodynamic properties of



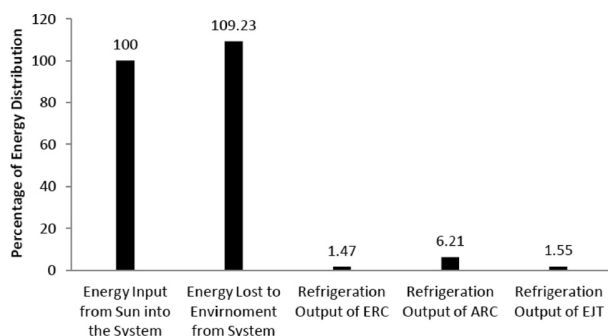


**Fig. 2 Percentage (%) of Sun's energy distribution for triple-staged refrigeration cycle**

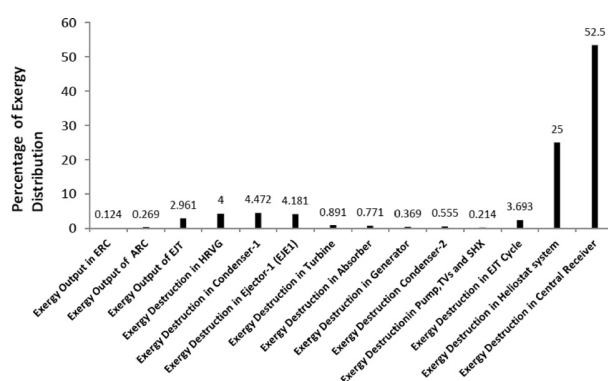


**Fig. 3 Percentage (%) of Sun's exergy distribution in output and destruction for triple-staged refrigeration cycle**

LiBr/H<sub>2</sub>O mixture for the operation of ARC are taken from Chua et al. [26]. First law analysis simply provides the overall performance of the cycle. On the other hand, second-law analysis identifies and quantifies the sources of losses in the system and hence helps in to gain an insight into the system performance, therefore, both energy and exergy distribution of proposed cycle are shown in Figs. 2 and 3.

Figure 2 indicates that out of 100% solar energy supplied to the system, around 9.23% is available as useful energy output (refrigeration capacity of ARC, ERC, and EJT cycle), 109.23% is lost to the environment via thermal energy exhaust from the system. Application of second-law analysis to the proposed cycle leads to the exergy distribution in the system. It is found that around 3.5% of the total input exergy is available as an exergy output (amount of exergy associated with the cooling produced at the evaporator of ARC, exergy associated with the cooling effect at the evaporator of ERC, and amount of exergy associated at the evaporator of EJT cycle) and 96.5% of the input (solar heat) exergy is destructed and lost due to irreversibilities occurred in various components of the proposed cycle and exergy carried away by the cooling water at absorber and condensers as shown in Fig. 3.

The energy and exergy efficiency of the heliostat field are 75% which indicates 25% loss at the heliostat. The exergy efficiency of central receiver is 30% which is much lower than its energy efficiency which is around 90%. This is an evidence of the deeper insight provided from second-law analysis compared to the performance obtained from first law. Therefore, performance evaluation of solar-driven refrigeration system based on first-law analysis is inadequate and hence more meaningful evaluation must include second-law analysis. The second-law analysis aids to pinpoint the cycle component of maximum irreversibility. It is observed that percentage of exergy destruction is highest in central receiver which is around 52.5%. The next largest exergy

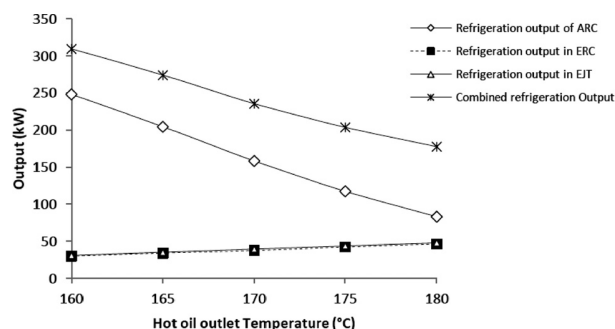


**Fig. 4 Variation of individual refrigeration output and combined refrigeration output for triple-staged refrigeration cycle with hot oil outlet temperature**

destruction was observed in the C1 of the ERC, heat recovery vapor generator, and ejector of ERC which were in the range of (4–5%) as shown in Fig. 3. Less than 1% exergy destructions were observed in other components of the cycle in question. Exergy destruction of 3.7% is observed in the EJT cycle. This is because the ejector of both ERC and EJT cycle comprises the various processes of entropy generation like mixing, normal shock formation, and friction which are the main sources of entropy generation. Therefore, from second-law point of view central receiver, heliostat, HRVG, ejector, condenser of the ERC, and EJT cycle need special attention in order to improve the overall performance of the proposed solar-driven triple-staged refrigeration cycle.

Figure 4 shows the variation of the refrigeration output of three refrigeration cycles individually as well as its combined refrigeration output of the proposed triple-staged refrigeration cycle. It is observed that output of ERC and EJT cycle increases with the increase in hot oil outlet temperature. This is due to the fact that the quality of vaporized refrigerant at the turbine inlet which is a prime mover for both the ejector cycles will be improved with the increase in hot oil outlet temperature. When refrigerant at significant pressure and temperature passes through the nozzle section of the ejector, it will increase mass flow rate of the secondary refrigerant which will result in larger refrigerating effect at the evaporator of the EJT cycle because increase in turbine power output due to increased hot oil outlet temperature enhances mass flow rate of refrigerant (propane) across the compressor which indirectly results in larger cooling effect produced at the evaporator of EJT cycle. It is further observed that increase in hot oil outlet temperature causes a lower refrigerating effect at the evaporator of ARC. This is due to the reason that increase in hot oil outlet temperature results in lower temperature at the exit of HRVG which causes a low mass flow rate of water refrigerant goes to the C2, and hence a lower refrigerating effect at the evaporator of ARC. Since the refrigeration output of ARC is much higher than the refrigeration output of ERC and EJT cycle, therefore the total refrigeration output is also showing the same trend of decreasing with the increase in hot oil outlet temperature.

In order to observe a complete thermodynamic view of proposed cooling cycle, energy efficiency based on first law and exergy efficiency based on second law is also evaluated and their representation against the hot oil outlet temperature is shown in Fig. 5. Energy analysis of the cycle reveals that the refrigeration capacity of ARC decreases significantly with increase in oil temperature, while the refrigeration capacity of ERC and EJT cycle increases marginally with the same. Since the refrigeration capacity of ARC dominates over refrigeration capacity of other two cycles, therefore, the energy efficiency of proposed triple-effect refrigeration cycle decreases considerably with the increase in oil temperature. On the other hand, the exergy efficiency which is defined as the ratio of amount of exergy associated with the refrigeration capacity to the amount of exergy associated with the

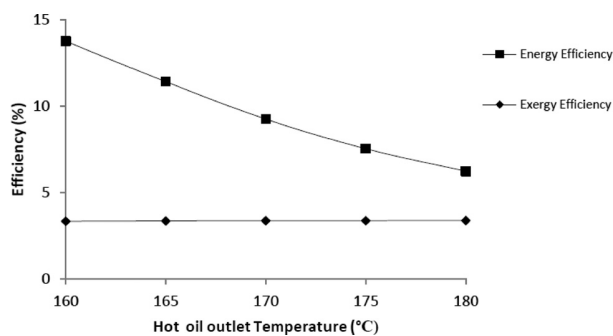


Fig. 5 Variation of energy and exergy efficiency for triple-staged refrigeration system with hot oil outlet temperature

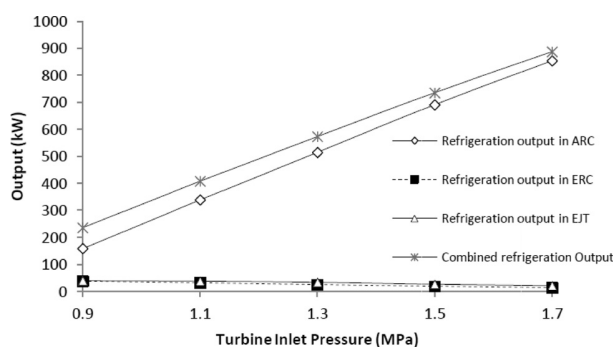


Fig. 6 Variation of individual refrigeration output and total refrigeration output for triple-staged refrigeration cycle with turbine inlet pressure

solar heat input. Exergy associated with refrigeration capacity is the ratio of refrigeration capacity to the Carnot COP of a refrigerator operates between the evaporator temperature and ambient. Since the evaporator temperature of ARC is closer to the ambient temperature, therefore, the exergy output of ARC decreases considerably similar to its refrigeration capacity. The exergy associated with the ERC increases marginally while the exergy associated with the EJT cycle increases significantly due to the fact that the difference of temperature between the evaporator of ERC and ambient is not of larger magnitude but the difference of temperature between the evaporator of EJT cycle and ambient is very large. Due to these reasons, the exergy output of ERC cycle increases marginally while the exergy output of EJT cycle increases significantly. Overall, the exergy output of triple-staged refrigeration cycle increases marginally with the increase in hot oil outlet temperature which results in the marginal overall increase in its exergy efficiency.

Figure 6 shows the effect of refrigerant turbine inlet pressure on the individual as well as combined output of proposed triple-staged refrigeration cycle. It is observed that refrigeration capacity of ERC and EJT cycle decreases with the increase in turbine inlet pressure while the refrigeration capacity of ARC increases significantly with the same. The reason for this is that increase in turbine inlet pressure results in lower mass flow of refrigerant vapor produced in the HRVG and a lower turbine exit temperature which further results in reduction of velocity at the ejector nozzle which causes a reduced mass flow rate of secondary refrigerant through ejector evaporator. Refrigeration capacity of ARC increases significantly due to fact that increase in turbine inlet pressure which lowers the mass flow rate of refrigerant vapor will result in a reduced absorption of heat from the exhaust gases through the HRVG which leads to the higher value of HRVG exit temperature. This higher temperature at the inlet of generator causes a significant increase in the capacity of ARC due to increased mass

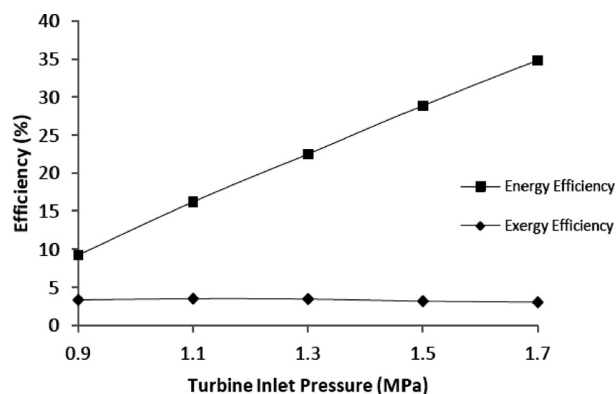


Fig. 7 Variation of energy and exergy efficiency for triple-staged refrigeration cycle with turbine inlet pressure

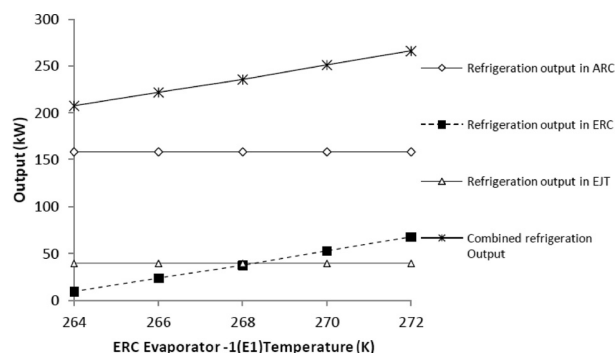


Fig. 8 Variation of individual refrigeration and total refrigeration output for triple-staged refrigeration cycle with ERC E1 temperature

flow rate of water refrigerant. The decrease in refrigerating capacity of EJT cycle is observed due to the reduced mass flow rate of refrigerant (propane) across the compressor which is caused because of reduced mass flow rate of R141b across the turbine. The reduced mass flow rate will decrease the refrigerating capacity of EJT cycle due to overall reduced mass flow rate across the cycle. The effect of change in turbine inlet pressure on energy and exergy efficiency of triple-staged refrigeration cycle is clearly shown in Fig. 7. The energy efficiency found to be increased significantly with the increase in turbine inlet pressure while its exergy efficiency decreases with the same. This is due to the reason that increase in turbine inlet pressure causes a significant improvement in refrigeration output of ARC and reduction in refrigeration output of ERC and EJT cycle. Since the rate of enhancement in the refrigeration capacity of ARC is much greater than the rate of reduction in the refrigerating capacity of ERC and EJT cycle, therefore, the overall energy efficiency of triple-staged refrigeration cycle increases with the increase in turbine inlet pressure. The exergy efficiency of the proposed triple-staged refrigeration cycle shows the trend of increasing with increase in turbine inlet pressure to some extent and then it starts decreasing with the same. This is because initially the rate of increase in exergy output of ARC is greater than the rate of decrease in exergy output of ERC and EJT cycle becomes greater than the rate of increase in exergy output of ARC.

In order to highlight the importance of employment of EJT cycle, the effects of change in the evaporator temperature of ERC and evaporator temperature of EJT cycle are observed on the refrigeration capacity of individual refrigeration cycles and combined triple-staged refrigeration cycle. It is shown that refrigeration capacity of ERC and combined refrigeration cycle increases



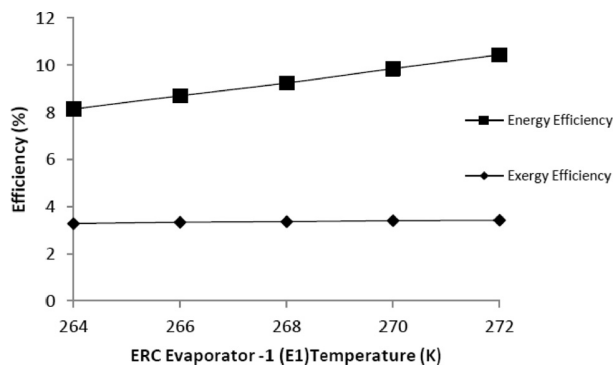


Fig. 9 Variation of energy and exergy efficiency for triple-staged refrigeration cycle with ERC E1 temperature

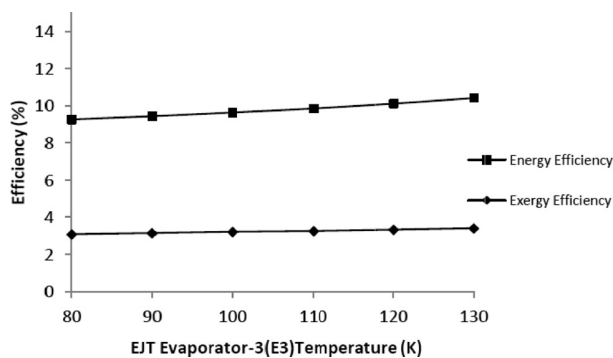


Fig. 10 Variation of energy and exergy efficiency for triple-staged refrigeration cycle with EJT E3 temperature

considerably with the increase in evaporator temperature of ERC while insignificant variation is observed in the refrigeration capacity of EJT cycle and ARC, respectively, as shown in Fig. 8. The effect of change in evaporator temperature of ERC on energy and exergy efficiency of the triple-staged refrigeration cycle is shown in Fig. 9 and it is found that energy efficiency increases significantly with the increase in evaporator temperature of ERC while the exergy efficiency of the combined refrigeration cycle increases marginally with the same. It is further observed that increase in evaporator temperature of EJT cycle causes a marginal increase in the energy and exergy efficiency of combined triple-staged refrigeration cycle as shown in Fig. 10.

## 5 Conclusion

A new solar-driven triple-staged refrigeration cycle is proposed for the production of cooling from air conditioning to cryogenic range. Energy and exergy methods are employed which enable us to develop a systematic approach that can be used to identify the sites of the real destructions/losses of valuable energy in thermal devices. The effect of several design parameters was observed on energy and exergy performance of the proposed cycle. The conclusions of the present analysis can be summarized as follows:

- Out of 100% energy (solar heat source) supplied to the system around 9.23% is produced as refrigeration capacity and 109.23% is lost to the environment.
- About 3.5% of the input exergy is available as exergetic refrigeration output and 96.5% is lost due to irreversibilities in the components and via thermal lost to the ambient.
- For a given solar heat source, the exergy output of EJT cycle is around 2.96% which is significantly higher than the exergy outputs of ARC and ERC of 0.27% and 0.124%, respectively.

- The largest contribution to cycle irreversibility comes from central receiver and heliostat field of 52.5% and 25%, respectively.
- The irreversibility of the order of 4–5% is observed in the HRVG, ejector and condenser of the ERC.
- The exergy efficiency of around 4% for solar-driven triple-effect cycle is obtained which is much lower than its energy efficiency of 10%.

This comprehensive thermodynamic analysis provides a powerful and systematic tool for identifying the sources of real losses in solar-driven triple-staged refrigeration cycle and guided for the effective exploitation of solar thermal energy using an integrated refrigeration system.

## Nomenclature

$A_h$	= aperture area of heliostat ( $\text{m}^2$ )
ARC	= absorption refrigeration cycle
COMP	= compressor
$\dot{E}$	= exergy rate ( $\text{kJ s}^{-1}$ )
$\Delta \dot{E}$	= exergy change ( $\text{kJ s}^{-1}$ )
EJT	= ejector expansion Joule–Thomson cryogenic
ERC	= ejector refrigeration cycle
LiBr–H <sub>2</sub> O	= lithium bromide–water
$\dot{Q}$	= energy rate ( $\text{kJ s}^{-1}$ )
R141b	= 1,1-dichloro-1-fluoroethane
RC	= Rankine cycle
$T$	= absolute temperature (K), Turbine
$\dot{W}$	= work output ( $\text{kJ s}^{-1}$ )
$h$	= enthalpy ( $\text{kJ kg}^{-1}$ )
$\dot{m}$	= mass flow rate ( $\text{kg s}^{-1}$ )
$q$	= solar radiation received per unit area ( $\text{W m}^{-2}$ )
$s$	= entropy ( $\text{kJ kg}^{-1} \text{K}^{-1}$ )
$u$	= velocity of flow in nozzle and diffuser ( $\text{m s}^{-1}$ )

## Greek Symbols

$\mu$	= entrainment ratio
$\eta$	= efficiency (%)

## Subscript

A	= absorber
C1	= condenser-1
C2	= condenser-2
CR	= central receiver
D	= destruction
E	= evaporator
E1	= evaporator-1
E2	= evaporator-2
E3	= evaporator-3
EJE1	= ejector-1
EJE2	= ejector-2
G	= generator
HRVG	= heat recovery vapor generator
HX1	= heat exchanger-1
HX2	= heat exchanger-2
P1	= pump-1
P2	= pump-2
SHX	= solution heat exchanger
T	= turbine
TV1	= throttle valve-1
TV2	= throttle valve-2
TV3	= throttle valve-3
TV4	= throttle valve-4
d	= diffuser
ejt	= ejector expansion Joule–Thomson cryogenic
f	= refrigerant fluid

h = heliostat field  
m = mixing chamber  
n = nozzle  
n1 = inlet of nozzle  
n2 = outlet of nozzle  
oil = hot oil (Duratherm 600)  
pf = primary flow  
r = water refrigerant  
s = solution mixture of LiBr/H<sub>2</sub>O, isentropic  
sf = secondary flow

1, 2, 3... a, b, c... = state points in Fig. 1

## Appendix

**Energy Balance Equations.** For central receiver (CR): A part of thermal energy received by central receiver is absorbed by oil (Duratherm 600) and rest is lost to the environment

$$\dot{Q}_{CR} = \dot{Q}_{oil} + \dot{Q}_{lost,CR} = \dot{m}_{oil}(h_1 - h_{12}) + \dot{Q}_{lost,CR} \quad (A1)$$

and

$$\eta_{energy,CR} = \frac{\dot{Q}_{oil}}{\dot{Q}_{CR}}$$

For HRVG

$$\dot{m}_{oil}(h_1 - h_2) = \dot{m}_{pf}(h_4 - h_3) \quad (A2)$$

For turbine

$$\dot{W}_T = \dot{m}_{pf}(h_4 - h_5) \quad (A3)$$

For pump-1

$$\dot{W}_{P1} = \dot{m}_{pf}(h_3 - h_8) \quad (A4)$$

For ejector-1

$$\dot{m}_{pf}h_5 + \dot{m}_{sf}h_{11} = h_6(\dot{m}_{pf} + \dot{m}_{sf}) \quad (A5)$$

For condenser-1

$$\dot{Q}_{C1} = \dot{m}_{C1}(h_d - h_c) = (\dot{m}_{pf} + \dot{m}_{sf})(h_6 - h_7) \quad (A6)$$

For throttle valve-1

$$h_9 = h_{10} \quad (A7)$$

For evaporator-1

$$\dot{Q}_{E1} = \dot{m}_{E1}(h_a - h_b) = \dot{m}_{sf}(h_{11} - h_{10}) \quad (A8)$$

For generator

$$\dot{Q}_G = \dot{m}_{oil}(h_2 - h_{12}) = (\dot{m}_s - \dot{m}_r)h_{20} + \dot{m}_r h_{13} - \dot{m}_s h_{19} \quad (A9)$$

For condenser-2

$$\dot{Q}_{C2} = \dot{m}_{C2}(h_f - h_e) = \dot{m}_r(h_{13} - h_{14}) \quad (A10)$$

For throttle valve-2

$$h_{14} = h_{15} \quad (A11)$$

For evaporator-2

$$\dot{Q}_{E2} = \dot{m}_{E2}(h_i - h_j) = \dot{m}_r(h_{16} - h_{15}) \quad (A12)$$

For absorber

$$\dot{Q}_A = \dot{m}_A(h_h - h_g) = (\dot{m}_s - \dot{m}_r)h_{22} + \dot{m}_r h_{16} - \dot{m}_s h_{17} \quad (A13)$$

For pump-2

$$\dot{W}_{P2} = \dot{m}_s(h_{18} - h_{17}) \quad (A14)$$

For solution heat exchanger

$$\dot{m}_s h_{18} + (\dot{m}_s - \dot{m}_r)h_{20} = \dot{m}_s h_{19} + (\dot{m}_s - \dot{m}_r)h_{21} \quad (A15)$$

For throttle valve-3

$$h_{21} = h_{22} \quad (A16)$$

For compressor:

$$\dot{W}_{comp} = \dot{W}_T = \dot{m}_{ejt}[(h_{24} - h_{23}) - T_{23}(s_{24} - s_{23})]/\eta_c \quad (A17)$$

For heat exchanger-1

$$\dot{m}_{ejt}(h_{24} - h_{25}) = \dot{m}_{ejt}(h_{23} - h_{30}) \quad (A18)$$

For heat exchanger-2

$$\dot{m}_{ejt,sf}(h_{25} - h_{26}) = \dot{m}_{ejt}(h_{30} - h_{29}) \quad (A19)$$

For throttle valve-4

$$h_{26} = h_{27} \quad (A20)$$

For evaporator-3

$$\dot{Q}_{E3} = \dot{m}_{E3}(h_k - h_l) = \dot{m}_{ejt,sf}(h_{28} - h_{27}) \quad (A21)$$

For ejector-2

$$\dot{m}_{ejt,pf}h_{25} + \dot{m}_{ejt,sf}h_{28} = \dot{m}_{ejt}h_{29} \quad (A22)$$

## Exergy Destruction Equations

$$\Delta \dot{E}_{E1} = \dot{m}_{sf}[(h_{10} - h_{11}) - T_0(s_{10} - s_{11})] \quad (A23)$$

$$\Delta \dot{E}_{E2} = \dot{m}_r[(h_{15} - h_{16}) - T_0(s_{15} - s_{16})] \quad (A24)$$

$$\Delta \dot{E}_{E3} = \dot{m}_{ejt,sf}[(h_{27} - h_{28}) - T_0(s_{27} - s_{28})] \quad (A25)$$

$$\dot{E}_{Solar} = \dot{Q}_{Solar} \left( 1 - \frac{T_0}{T_s} \right)$$

where  $T_s$  is the apparent sun temperature taken as 4500 K.

$$\dot{E}_1 = \dot{m}_{oil}[(h_1 - h_0) - T_0(s_1 - s_0)] \quad (A26)$$

$$\dot{E}_{12} = \dot{m}_{oil}[(h_{12} - h_0) - T_0(s_{12} - s_0)] \quad (A27)$$

$\dot{E}_1$  is the exergy associated with incoming hot oil from receiver while  $\dot{E}_{12}$  is the exergy associated with outgoing hot oil to the receiver.

The basic equations of exergy destruction rate in the components of RC, ERC, ARC, and EJT are written as follows:

For heliostat: A part of exergy received by heliostat is delivered to the central receiver and rest is destroyed (irreversibility)

$$E_{\text{Solar}} = \dot{E}_{\text{CR}} + E_{\text{lost,heliostat}} \quad (\text{A28})$$

and

$$\eta_{\text{exergy,heliostat}} = \frac{\dot{E}_{\text{CR}}}{\dot{E}_{\text{Solar}}}$$

For CR: A part of exergy received by central receiver is absorbed by oil (Duratherm 600) and rest is lost to the environment (irreversibility)

$$\begin{aligned} \dot{E}_{\text{CR}} &= \dot{E}_{\text{oil}} + \dot{E}_{\text{lost,CR}} \\ &= \dot{m}_{\text{oil}} c_{p,\text{oil}} \left[ T_1 - T_{12} - T_0 \ln \left( \frac{T_1}{T_{12}} \right) \right] + \dot{E}_{\text{lost,CR}} \end{aligned} \quad (\text{A29})$$

and

$$\eta_{\text{exergy,CR}} = \frac{\dot{E}_{\text{oil}}}{\dot{E}_{\text{CR}}}$$

For HRVG

$$\dot{E}_{\text{D,HRVG}} = T_0 [\dot{m}_{\text{oil}}(s_2 - s_1) + \dot{m}_{\text{pf}}(s_4 - s_3)] \quad (\text{A30})$$

For turbine

$$\dot{E}_{\text{D,T}} = T_0 [\dot{m}_{\text{pf}}(s_5 - s_4)] \quad (\text{A31})$$

For ejector-1

$$\dot{E}_{\text{D,EJE1}} = T_0 [(\dot{m}_{\text{pf}} + \dot{m}_{\text{sf}})s_6 - \dot{m}_{\text{pf}}s_5 - \dot{m}_{\text{sf}}s_{11}] \quad (\text{A32})$$

For condenser-1

$$\dot{E}_{\text{D,C1}} = T_0 (\dot{m}_{\text{pf}} + \dot{m}_{\text{sf}})(s_7 - s_6) \quad (\text{A33})$$

For throttle valve-1

$$\dot{E}_{\text{D,TV1}} = T_0 \dot{m}_{\text{sf}}(s_{10} - s_9) \quad (\text{A34})$$

For generator

$$\dot{E}_{\text{D,G}} = T_0 [\dot{m}_{\text{r}}(s_{13} - s_{20}) + \dot{m}_{\text{s}}(s_{20} - s_{19}) + \dot{m}_{\text{oil}}(s_{12} - s_2)] \quad (\text{A35})$$

For solution heat exchanger

$$\dot{E}_{\text{D,SHX}} = T_0 [\dot{m}_{\text{s}}(s_{19} - s_{18}) + (\dot{m}_{\text{s}} - \dot{m}_{\text{r}})(s_{21} - s_{20})] \quad (\text{A36})$$

For pump-2

$$\dot{E}_{\text{D,P2}} = T_0 [\dot{m}_{\text{s}}(s_{18} - s_{17})] \quad (\text{A37})$$

For throttle valve-3

$$\dot{E}_{\text{D,TV3}} = T_0 [(\dot{m}_{\text{s}} - \dot{m}_{\text{r}})(s_{22} - s_{21})] \quad (\text{A38})$$

For absorber

$$\dot{E}_{\text{D,A}} = T_0 [\dot{m}_{\text{r}}(s_{22} - s_{16}) + \dot{m}_{\text{s}}(s_{17} - s_{22}) + \dot{m}_{\text{A}}(s_{\text{h}} - s_{\text{g}})] \quad (\text{A39})$$

For condenser-2

$$\dot{E}_{\text{D,C2}} = T_0 [\dot{m}_{\text{r}}(s_{14} - s_{13}) + \dot{m}_{\text{C2}}(s_{\text{f}} - s_{\text{e}})] \quad (\text{A40})$$

For throttle valve-2

$$\dot{E}_{\text{D,TV2}} = T_0 [\dot{m}_{\text{r}}(s_{15} - s_{14})] \quad (\text{A41})$$

For compressor

$$\dot{E}_{\text{D,comp}} = \dot{m}_{\text{ejt}} \left[ (h_{23} - h_{24}) \left( 1 - \frac{1}{\eta_{\text{c}}} \right) + (s_{23} - s_{24}) \left( \frac{T_{23}}{\eta_{\text{c}}} - T_0 \right) \right] \quad (\text{A42})$$

For ejector-2

$$\dot{E}_{\text{D,EJE2}} = T_0 [\dot{m}_{\text{ejt}}(s_{29}) - \dot{m}_{\text{ejt,pf}}(s_{25}) - \dot{m}_{\text{ejt,sf}}(s_{28})] \quad (\text{A43})$$

For throttle valve-4

$$\dot{E}_{\text{D,TV4}} = T_0 [\dot{m}_{\text{ejt,sf}}(s_{27} - s_{26})] \quad (\text{A44})$$

For heat exchanger-1

$$\dot{E}_{\text{D,HX1}} = \dot{m}_{\text{ejt}} T_0 [(s_{25} - s_{24}) + (s_{23} - s_{30})] \quad (\text{A45})$$

For heat exchanger-2

$$\dot{E}_{\text{D,HX2}} = T_0 [\dot{m}_{\text{ejt,sf}}(s_{26} - s_{25}) + \dot{m}_{\text{ejt}}(s_{30} - s_{29})] \quad (\text{A46})$$

## References

- [1] Kalogirou, S. A., 2004, "Solar Thermal Collectors and Applications," *Prog. Energy Combust. Sci.*, **30**, pp. 231–295.
- [2] Priasawas, W., and Lundqvist, P., 2004, "An Exergy Analysis of a Solar Driven Ejector Refrigeration System," *Sol. Energy*, **76**, pp. 369–379.
- [3] Hernandez, J. I., Best, R., Dorantes, R. J., and Estrada, C. A., 2005, "Study of a Solar Booster Assisted Ejector Refrigeration System With R134a," *ASME J. Sol. Energy Eng.*, **127**, pp. 53–59.
- [4] Alexis, G. K., and Katsanis, J. S., 2004, "Performance Characteristics of a Methanol Ejector Refrigeration Unit," *Energy Convers. Manage.*, **45**, pp. 2729–2744.
- [5] Varga, S., Oliveira, A. C., and Diaconu, B., 2009, "Analysis of a Solar Assisted Ejector Cooling System for Air Conditioning," *Int. J. Low Carbon Technol.*, **4**, pp. 2–8.
- [6] Pierres, N. L., Stitou, D., and Mazet, N., 2007, "New Deep-Freezing Process Using Renewable Low-Grade Heat: From the Conceptual Design to Experimental Results," *Energy*, **32**(4), pp. 600–608.
- [7] Dincer, I., Edin, M., and Ture, I. E., 1996, "Investigation of Thermal Performance of a Solar Powered Absorption Refrigeration System," *Energy Convers. Manage.*, **37**, pp. 51–58.
- [8] Das, K., and Mani, A., 1996, "Comparative Study of Cycle Performance for a Two Stage Intermittent Solar Refrigerator Working With R22-Absorbent Combinations," *Energy Convers. Manage.*, **37**, pp. 87–93.
- [9] Yang, R., and Wang, P. L., 2001, "A Simulation Study of Performance Evaluation of Single-Glazed and Double-Glazed Collectors for an Open Cycle Absorption Solar Cooling System," *Sol. Energy*, **71**, pp. 263–268.
- [10] Atmaca, I., and Yigit, A., 2003, "Simulation of Solar Powered Absorption Cooling System," *Renewable Energy*, **28**, pp. 1277–1293.
- [11] Ziegler, F., Kahn, R., Summerer, F., and Alefeld, G., 1993, "Multieffect Absorption Chillers," *Int. J. Refrigeration*, **16**(5), pp. 301–311.
- [12] Sozen, A., Ozalp, M., and Arcaklioglu, E., 2004, "Prospects for Utilization of Solar Driven Ejector-Absorption Cooling System in Turkey," *Appl. Therm. Eng.*, **24**, pp. 1019–1035.
- [13] Wang, J., Chen, G., and Jiang, H., 1998, "Study on a Solar Driven Ejection Absorption Refrigeration Cycle," *Int. J. Energy Res.*, **22**, pp. 733–739.
- [14] Fan, Y., Luo, L., and Souyri, B., 2007, "Review of Solar Sorption Refrigeration Technologies: Development and Applications," *Renewable Sustainable Energy Rev.*, **11**, pp. 1758–1775.
- [15] Naer, V., and Rozhentsev, A., 2002, "Application of Hydrocarbon Mixtures in Small Refrigerating and Cryogenic Machines," *Int. J. Refrigeration*, **25**, pp. 836–847.
- [16] Yu, J., Tia, G., and Xu, Z., 2009, "Exergy Analysis of Joule Thomson Cryogenic Refrigeration Cycle With an Ejector," *Energy*, **34**(11), pp. 1864–1869.
- [17] Rashidi, M. M., Beg, O. A., and Habibzadeh, A., 2010, "First and Second Law Analysis of an Ejector Expansion Joule Thomson Cryogenic Refrigeration Cycle," *Int. J. Energy Res.*, **36**(2), pp. 231–240.
- [18] Gong, M., Wu, J., Cheng, Q., Sun, Z., Liu, J., and Hu, Q., 2012, "Development of a –186 °C Cryogenic Preservation Chamber Based on a Dual Mixed-Gases Joule-Thomson Refrigeration Cycle," *Appl. Therm. Eng.*, **36**, pp. 188–192.

- [19] Keenan, H., Neumann, E. P., and Lustwerk, F., 1950, "An Investigation of Ejector Design by Analysis and Experiment," *ASME J. Appl. Mech.*, **72**, pp. 299–309.
- [20] Huang, B. J., Chang, J. M., Wang, C. P., and Petronko, V. A., 1999, "A 1-D Analysis of Ejector Performance," *Int. J. Refrigeration*, **22**, pp. 354–364.
- [21] Ouzzane, M., and Aidoun, Z., 2003, "Model Development and Numerical Procedure for Detailed Ejector Analysis and Design," *Appl. Therm. Eng.*, **23**, pp. 2337–2351.
- [22] Dai, Y., Wang, J., and Gao, L., 2009, "Exergy Analysis, Parametric Analysis and Optimization for a Novel Combined Power and Ejector Refrigeration Cycle," *Appl. Therm. Eng.*, **29**, pp. 1983–1990.
- [23] NIST Standard Reference Database 23, 1998, "NIST Thermodynamic and Transport Properties of Refrigerants and Refrigerant Mixtures REFPROP," Version 6.01.
- [24] Bejan, A., 2002, "Fundamentals of Exergy Analysis, Entropy Generation Minimization, and the Generation of Flow Architecture," *Int. J. Energy Res.*, **26**, pp. 545–565.
- [25] Xu, C., Wang, Z., Li, X., and Sun, F., 2011, "Energy and Exergy Analysis of Solar Power Tower Plants," *Appl. Therm. Eng.*, **31**, pp. 3904–3913.
- [26] Chua, H. T., Toh, H. K., Malek, A., Ng, K. C., and Srinivasan, K., 2000, "Improved Thermodynamic Property Fields of LiBr-H<sub>2</sub>O Solutions," *Int. J. Refrigeration*, **23**, pp. 412–429.

## Fault Ride Through Analysis Of Wind Farm In Low Voltage Distribution System

Manju Aggarwal, S. K. Gupta, Madhusudan Singh

*Apeejay Styta University, Sohna, Haryana, India, DCRUST, Murthal, Haryana, India*

*Delhi Technological University, Delhi, India*

### Abstract

*In this paper, a wind farm comprising of squirrel cage induction generators (SCIG) is described and impact of different types of faults, balanced and unbalanced, at different locations in low voltage distribution system has been analyzed. A distribution Static Compensator (DSTATCOM) is being used for Fault Ride through (FRT) analysis of wind farm in low voltage distribution system. The role of a DSTATCOM is to enhance the capability of wind farm as required by grid code for grid below 100kV.*

### 1. Introduction

Today, modern energy industry faces a growing awareness regarding the impact of conventional power generation on the environment. Issues such as limited fossil fuel reserves, climate change due to CO<sub>2</sub> emissions, brings to attention alternative technologies [1-2] to generate electricity in a more sustainable manner. Wind power is the world's rapid growing source of energy. The penetration of wind power in the electrical grids increases steadily in many European countries, with highest percentage found in Denmark (28%). Increasing penetration of wind turbines into grid system has led system operator to develop new grid codes. Grid code describes the connection condition of wind turbines to grid. The grid codes are mainly related to fault ride through (FRT) capability, power quality issues, grid stability, and reactive power control of wind turbines. Connection requirements of wind power generating units have been explained in [3-7]. Six Grid Codes are selected for the analysis of a generic Grid Code. Among the chosen Grid Codes is Denmark due to the high penetration of wind power. Ireland, EON [8] (a German transmission system Operator (TSO)),

Scotland and the UK. The Grid Code of Germany is chosen due to the important wind power market and due to detailed technical descriptions in the Grid Code of EON. The squirrel cage induction generators (SCIG) which typically employ a conventional induction machine, is simpler in design and do not incorporate power electronics and thus do not have issues related to harmonic injection into the system. However, the wind turbines drain large amount of reactive power from the grid which causes low voltage. Reactive power capacity of SCIG [9-14] can be controlled by using shunt capacitors during steady state operation. However, reactive power injection capability decreases during fault conditions therefore, these devices require some additional power electronic compensation devices to fulfil FRT capability. Among other devices DSTATCOM is best suited for such applications as DSTATCOMs are faster, smaller and have better performances at reduced voltages.

This paper explains the analysis of different types of faults i.e. unbalanced and balanced, at different location in low voltage distribution system. The role of DSTATCOM [15-20] is to enhance the FRT capability of wind farm as required by grid code. The fault ride through (FRT) capability, which is one of the most demanding requirement that have been included in the grid codes and shown in Fig.1. The wind turbine should remain stable and connected during the fault while voltage at the PCC drop to 15% of the nominal value i.e. drops of 85% for the part of 150 msec. Only when the grid voltage falls below the curve, the turbine is allowed to disconnect from the grid.

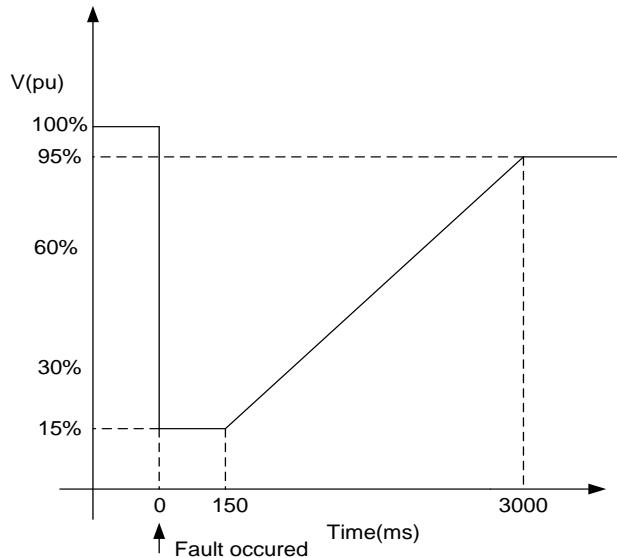


Fig. 1. Fault Ride Through (FRT) capability

## 2. System Configuration

The proposed system consists of 11kV, 450kVA, 50Hz low voltage distribution system along with a wind energy conversion system (WECS) connected directly to the grid and DSTATCOM as shown in Fig.2. The distribution system consists of a 11kV/415V transformer and a feeder. Voltage at the point of common coupling (PCC) is 415V. Wind farm comprising of three 7.5kW Squirrel Cage Induction Generators (SCIG) driven by fixed speed wind turbines. A DSTATCOM supplies the lagging or leading current to manage the constant terminal voltage at PCC during fault conditions.

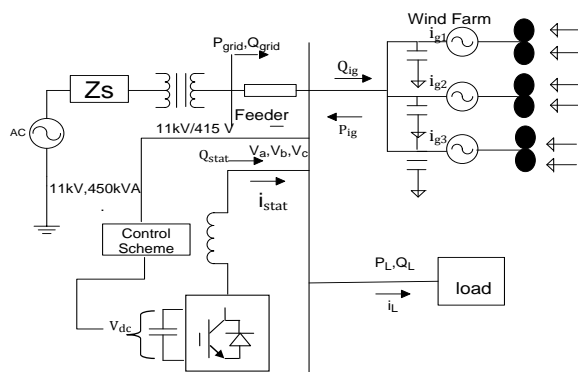


Fig. 2. Basic Structure of Test System

## 3. System modelling

### 3.1. Model equations of wind turbine

A wind farm consists of several wind generators connected to the grid system through a single bus. Equivalent model of wind farm [21-22] can be built by combining all wind turbines into single equivalent turbine. By Betz theory, power extracted from air through wind turbine is given by

$$P_{wind} = \rho \frac{\pi R^2}{2} v_{wind}^3 \quad (2)$$

$$P_m = C_p(\lambda, \beta) P_{wind} \quad (3)$$

Where  $P_{wind}$  is the power absorbed,  $P_m$  is the mechanical output power of the turbine and  $C_p$  is the performance coefficient of the turbine,  $\lambda$  is the ratio of the rotor blade tip speed to wind speed,  $\rho$  is the air density (Kg/ m<sup>3</sup>) and  $\beta$  is the blade pitch angle in radian, R is turbine radius in meters,  $v_{wind}$  is the wind speed in m/s. The equation for  $C_p(\lambda, \beta)$  is given by

$$C_p(\lambda, \beta) = C_1 \left( \frac{C_2}{\lambda_i} - C_3 \beta - C_4 \right) \exp \left( -\frac{C_5}{\lambda_i} \right) + C_6 \lambda \quad (4)$$

$$\text{With } \frac{1}{\lambda_i} = \frac{1}{\lambda + 0.08\beta} - \frac{0.035}{\beta^2 + 1} \quad (5)$$

Power coefficient  $C_p$  is the function of tip speed ratio and blade pitch angle. In order to achieve high  $C_p$ , ( $C_{pmax}$ ) optimal value of tip speed ratio and blade pitch angle is required and therefore giving the maximum power output at all available wind speed.

Optimal value of  $C_p$  can be achieved at one optimal value of tip speed ratio i.e.  $\lambda_{nom}$ . So it is required to control tip speed ratio according to wind speed which is known as maximum power point tracking. Active pitch control is used mainly for high wind speed. In the present analysis pitch angle is zero which is a valid assumption for low to medium wind speed. In this analysis the system maximum value of power coefficient ( $C_{pmax}$ ) is 0.48 when  $\beta = 0$ .



### 3.2. DSTATCOM Control algorithm

Basic working principle of DSTATCOM is described by the following equations. The instantaneous value of current are written using Kirchoff's current law's as

$$i_{grid}(t) = i_L(t) - i_{stat}(t) - i_g(t) \quad (6)$$

$$i_g(t) = i_{g1}(t) + i_{g2}(t) + i_{g3}(t) \quad (7)$$

Where  $i_{grid}, i_L, i_{stat}, i_g$  are the grid current, load current, compensator current and wind farm current respectively.  $i_{g1}(t), i_{g2}(t), i_{g3}(t)$  current supplied by each wind generator

Compensating currents provided by DSTATCOM to make utility voltage purely sinusoidal are given as

$$i_{stat}(t) = i_L(t) - i_{grid}(t) - i_g(t) \quad (8)$$

The main current needs to be sinusoidal for ideal compensation; irrespective of the nature of the load based on the generation of source currents components.

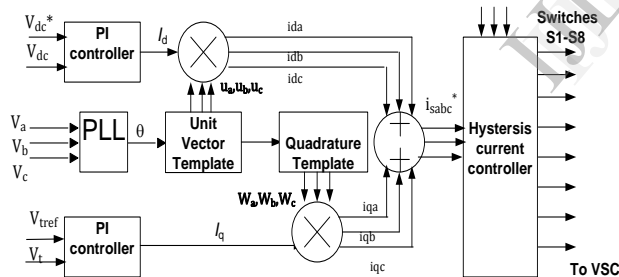


Fig. 3. Control scheme of DSTATCOM

Control scheme of DSTATCOM is shown in Fig.3. Reference source currents are the sum of direct and quadrature axis currents. Direct axis currents ( $i_{dabc}$ ) are derived by first calculating unit vector template from a phase locked loop (PLL) by generating angle  $\theta$  as

$$u_a = \sin(\theta) \quad (9)$$

$$u_b = \sin\left(\theta - \frac{2\pi}{3}\right) \quad (10)$$

$$u_c = \sin\left(\theta + \frac{2\pi}{3}\right) \quad (11)$$

The in phase component of reference currents are derived using in phase unit vector template as

$$i_{da} = I_d * u_a \quad (12)$$

$$i_{db} = I_d * u_b \quad (13)$$

$$i_{dc} = I_d * u_c \quad (14)$$

Where  $I_d$  is the output of PI controller regulating dc bus voltage of DSTATCOM. Quadrature components of reference current are obtained as follows

$$w_a = -u_b/\sqrt{3} + u_c/\sqrt{3} \quad (15)$$

$$w_b = \sqrt{3}u_a/2 + (u_b - u_c)/2\sqrt{3} \quad (16)$$

$$w_c = -\sqrt{3}u_a/2 + (u_b - u_c)/2\sqrt{3} \quad (17)$$

Quadrature component of reference source current ( $i_{qabc}$ ) is calculated by

$$i_{qa} = I_q * w_a \quad (18)$$

$$i_{qb} = I_q * w_b \quad (19)$$

$$i_{qc} = I_q * w_c \quad (20)$$

Where ( $I_q$ ) is obtained by comparing it with the reference voltage i.e. maximum value of desired A.C voltage ( $V_{tref}$ ) at PCC. PI controller processes the voltage error. The amplitude of reactive current to be produced by the STATCOM is decided by the output of the PI controller in AC voltage control loop. In inner current loop hysteresis current controller is used, where source currents are compared with reference current derived from outer loop. This enables the source current controlling to be sinusoidal. This method is simple, robust and favorable as compared with other methods.



#### 4. Simulation results and discussion

Fault ride through analysis of wind farm with and without static compensator is analyzed for various types of faults, at different location in low voltage distribution system. The proposed scheme is modeled and simulated in MATLAB/simulink. The r.m.s value of voltage at point of common coupling ( $V_{pcc}$ ), rms voltages of each phase ( $V_{abc}$ ), rotor speed ( $w$ ), and reactive power of wind generators ( $Q_{ig}$ ) are presented with and without controller. Positive values of active / reactive power of wind generator and DSTATCOM imply that these powers flow towards PCC.

##### 4.1. Analysis of low voltage distribution system with Line to line fault near grid without/with controller

In order to analyze the behavior of the 11kV, 450kVA, and 50Hz low voltage distribution system following unbalanced fault, a line to line fault has been simulated near grid. Line to line fault is applied at  $t = 1.0s$  and clearance time is 150ms. Fig.4 presents the voltage at the point of common coupling ( $V_{pcc}$ ), rms voltages of each phase ( $V_{abc}$ ), speed of rotor ( $w$ ), reactive powers absorbed by the generators ( $Q_{ig}$ ) and Fig.5 presents reactive power injected by DSTATCOM and dc link voltage ( $V_{dc}$ ) in addition to waveforms of Fig.3.

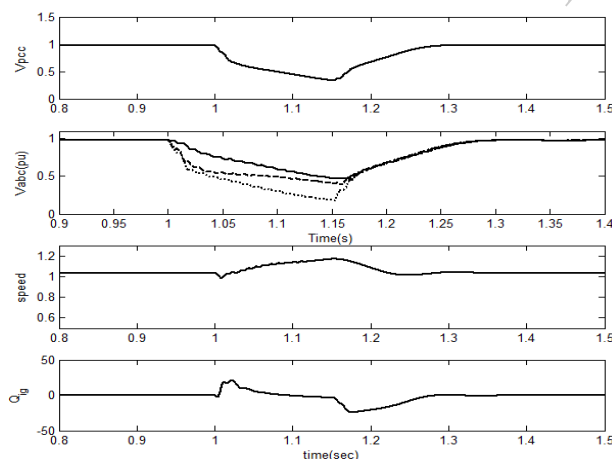


Fig. 4. R.m.s.voltage at the point of common coupling( $V_{pcc}$ ), rms voltages of each phase at pcc( $V_{abc}$ ), speed ( $w$ ), reactive power absorbed by wind farm( $Q_{ig}$ ), without DSTATCOM

It has been observed from that DSTATCOM helps in reducing the voltage dip and time to clear fault by supplying reactive power during fault. Frequency increases to 1.2pu without controller but with DSTATCOM it is within range i.e. 1.05pu. The values of voltage at point of common coupling and time to clear the fault for different types of fault at different location has been given in Table1.

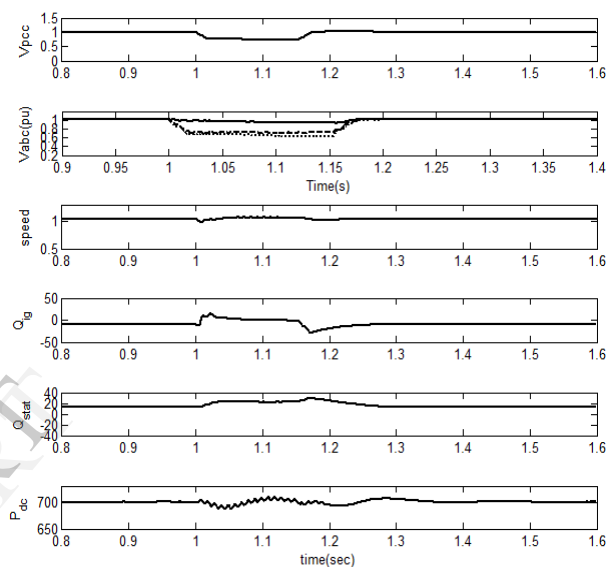


Fig. 5. R.m.s.voltage at the point of common coupling( $V_{pcc}$ ), rms voltage aof each phase at pcc, speed ( $w$ ), reactive power absorbed by wind farm( $Q_{ig}$ ), reactive power injected by DSTATCOM( $Q_{stat}$ ),dc link voltage( $V_{dc}$ )

##### 4.2. Analysis of low voltage distribution system with three phase fault near grid without/with controller

To analyze the behavior of the system with balanced fault, three phase fault has been simulated near grid. Fig.6 shows that the voltage at the point of common coupling drops below 0.15pu during fault occurrence which leads to disconnection of wind turbine from the grid as depicted in Fig1. DSTATCOM helps to avoid such situation by supplying reactive power as observed from Fig.7 hence, contributing to FRT enhancement

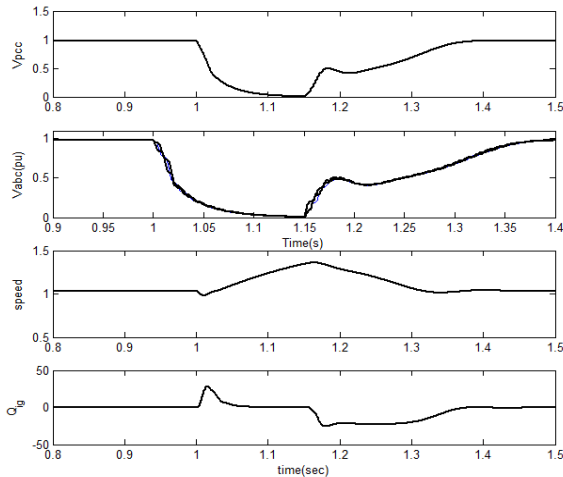


Fig. 6. R.m.s.voltage at the point of common coupling( $V_{pcc}$ ), rms voltage aof each phase at pcc, speed (w ), reactive power absorbed by wind farm( $Q_{ig}$ ), without DSTATCOM

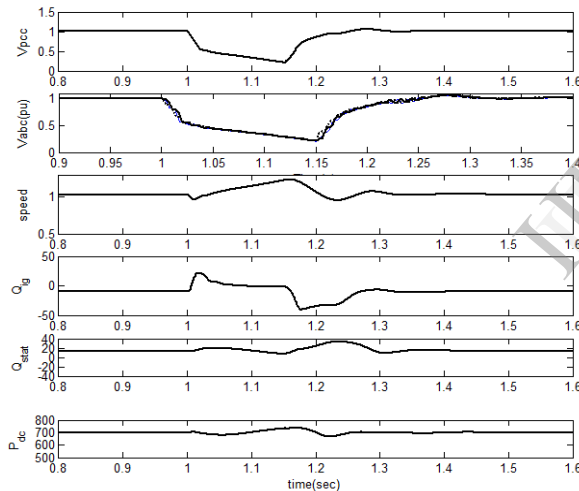


Fig. 7. R.m.s.voltage at the point of common coupling( $V_{pcc}$ ), rms voltage aof each phase at pcc, speed (w ), reactive power absorbed by wind farm( $Q_{ig}$ ), reactive power injected by DSTATCOM( $Q_{stat}$ ),dc link voltage( $V_{dc}$ )

#### 4.3. Analysis of low voltage distribution system with Line to line fault at pcc without controller

Now, the system is analyzed with same type of faults i.e. balanced and unbalanced. However, the location is weakest point i.e. point of common coupling because at this point where the wind turbine is connected to low voltage distribution system and from this point the wind

turbine takes its reactive power and sends its generated power to the grid.

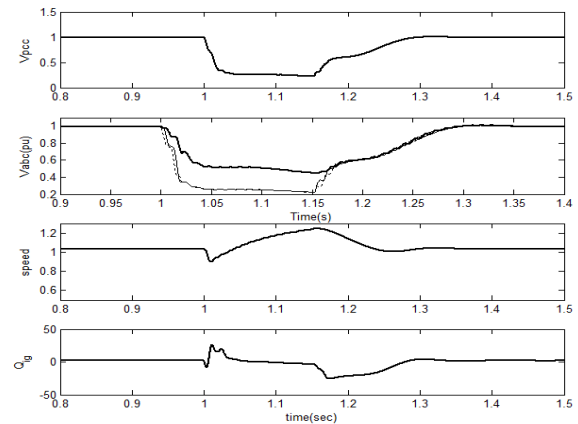


Fig. 8. R.m.s.voltage at the point of common coupling( $V_{pcc}$ ), rms voltage aof each phase at pcc, speed (w ), reactive power absorbed by wind farm( $Q_{ig}$ ), without DSTATCOM

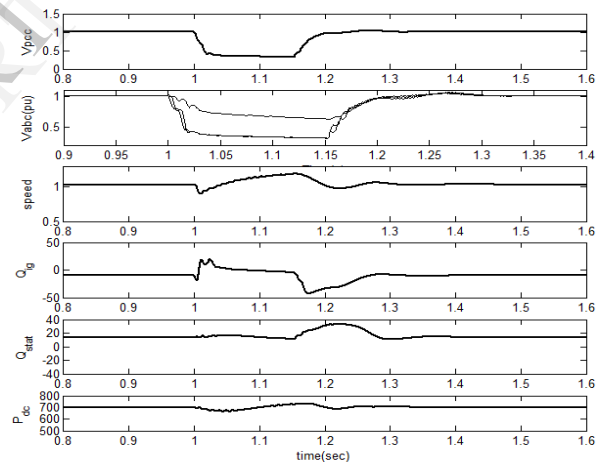


Fig. 9. R.m.s.voltage at the point of common coupling( $V_{pcc}$ ), rms voltage aof each phase at pcc, speed (w ), reactive power absorbed by wind farm( $Q_{ig}$ ), reactive power injected by DSTATCOM( $Q_{stat}$ ),dc link voltage( $V_{dc}$ )

Line to line fault is applied between phase a and phase b. The contribution of DSTATCOM is very little in case of a fault as the voltage drop in fault condition is major, hence reactive power injection is limited. Instead, DSTATCOM plays a vital role in post fault clearance scenario when it injects reactive power as per its rated capacity to help recover the voltage faster and hence improving the system stability

#### 4.4. Analysis of low voltage distribution system with three phase fault at pcc without controller

For the three phase balanced fault at pcc, the DSTATCOM do not have the ability to let the wind turbine ride through this type of fault because voltage on its terminal will be zero. After the fault clearance DSTATCOM helps in reducing the time to clear the fault.

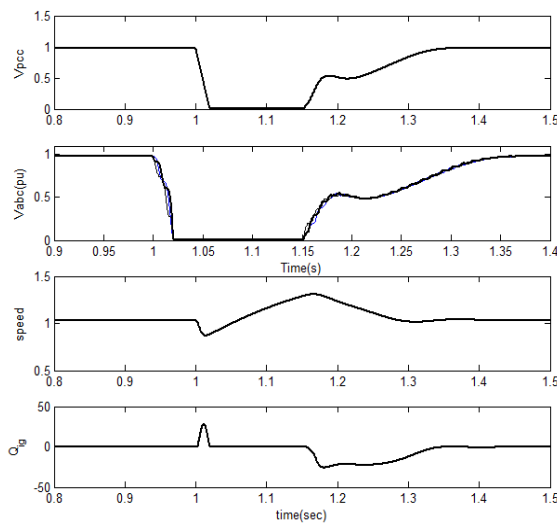


Fig. 10. R.m.s.voltage at the point of common coupling( $V_{pcc}$ ), rms voltage aof each phase at pcc, speed (w ), reactive power absorbed by wind farm( $Q_g$ ), without DSTATCOM

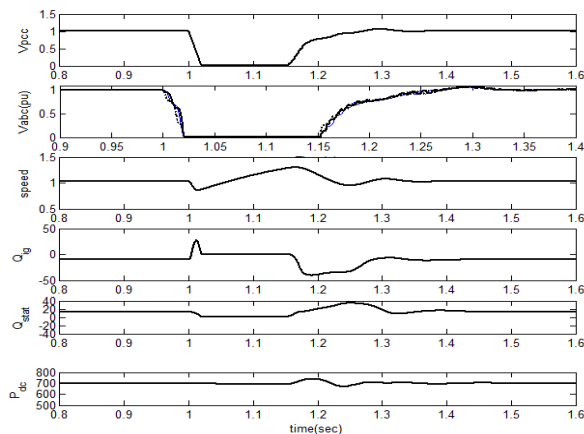


Fig. 11. R.m.s.voltage at the point of common coupling( $V_{pcc}$ ), rms voltage aof each phase at pcc, speed (w ), reactive power absorbed by wind farm( $Q_g$ ),a active power injected by DSTATCOM( $Q_{stat}$ ),dc link voltage( $V_{dc}$ )

TABLE 1. rms voltages at pcc and time to clear fault for different types of fault at different location

Location of fault	Type of fault		$V_{pcc}$ $t=1s$ $t=1.15$	Time to clear fault
Near Grid	Three phase fault	Without controller	0	0.24s
		With controller	0.2pu	0.1s
Near Grid	L-L Fault	Without controller	0.22pu	0.15s
		With controller	0.54pu	0.02s
At point of common coupling	Three phase fault	Without controller	0	0.25s
		With controller	0	0.11s
At point of common coupling	L-L Fault	Without controller	0.22pu	0.15s
		With controller	0.32pu	0.05s
		Without controller	0.32pu	0.05s
		With controller	0.32pu	0.05s

TABLE 2. rms voltages at pcc and time to clear fault for different types of fault at different location

Location of fault	Rms voltage of each phase	Without controller	With controller
Near grid	Va	0.19pu	0.62pu
	Vb	0.44pu	0.74pu
	Vc	0.45pu	0.93pu
At pcc	Va	0.22pu	0.32pu
	Vb	0.22pu	0.33pu
	Vc	0.45pu	0.63pu

## 5. Conclusion

This paper analyzes the impact of different types of faults at different location, in low voltage distribution system with and without DSTATCOM. Results shows that DSTATCOM helps in providing voltage support following voltage dips that arise from external short-circuits occurrence. DSTATCOM is considered as an effective means of enhancing the FRT capability of wind farm.

## 6. Appendix

The parameters of 11kV, 450kVA, and 50 Hz low voltage distribution system are given below:

SCC=450kVA,  $X/R = 7$

Feeder parameters:

$R = 0.2 \Omega$ ,  $L = 4.4\text{mH}$

Following are the parameters of 7.5kW, 415V, 50Hz, 4-pole Y - connected induction machine:

$R_r = 0.03\text{pu}$ ,  $R_s = 0.035\text{pu}$ ,  $X_{lr} = X_{ls} = 0.062\text{pu}$ ,  $J = 0.1384 \text{ kg-m}^2$

DSTATCOM Parameters:

$L_f = 5\text{mH}$ ,  $R_f = 0.01\Omega$ ,  $V_{dc} = 700\text{volts}$  and  $C_{dc} = 8000\mu\text{F}$

Parameters of AC voltage regulator

$K_{iq} = 0.008$ ,  $K_{pq} = 0.5$

Parameters of DC voltage regulator

$K_{id} = 10$ ,  $K_{pd} = 0.6$

Wind turbine Characteristics:

Three turbines of rating 7.5kW

$C_p = 0.48$ ,  $\mu = 8.1$

$c_1 = 0.5176$ ,  $c_2 = 116$ ,  $c_3 = 0.4$ ,  $c_4 = 5$ ,  $c_5 = 21$  and  $c_6 = 0.006$

## 7. References

- [1]. M. Liserre, T. Sauter, and J. Y. Hung, "Future energy systems," IEEE Ind. Electron. Mag., vol. 4, pp. 18–37, Mar. 2010.
- [2]. Tzanakis, M. Hadfield, B. Thomas, S.M. Noya, I. Henshaw, S. Austen, "Future perspectives on sustainable tribology," Renewable and Sustainable Energy Reviews 16 (2012) 4126– 4140
- [3]. ARULAMPALAM, A., RAMTHARAN, G., JENKINS, N., RAMACHANDARAMURTHY, V. K., EKANAYAKE, J. B., and STRBAC, G., "Trends in wind power technology and grid code requirements", proc. International Conference on Industrial and Information Systems, no. pp.129-134, Aug.2007
- [4]. EL-HELW, H. M., TENNAKOON, and S. B., "Evaluation of the suitability of a fixed speed wind turbine for large scale wind farms considering the new UK grid code", Renewable Energy 33 (2008) 1-12.
- [5]. Sharad W. Mohod, and Mohan V. Aware, "A Statcom Control Scheme for Grid Connected Wind Energy System for Power Quality Improvement," IEEE Transaction on System Journal, Vol. 4, No. 3, pp. 346-352, Sept. 2010
- [6]. Arulampalam, M. Barnes, N. Jenkins, and J. B. Ekanayake, "Power quality and stability improvement of a wind farm using STATCOM supported with hybrid battery energy storage," IEE Proc. Generation, Transmission and Distribution, vol. 153, no. 6, pp.701-710, Nov. 2006
- [7]. M. Tsili and S. Papathanassiou, "A review of grid code technology

- requirements for wind turbine," *Proc. IET Renew. power gen.*, vol. 3, pp. 308–332, 2009
- [8]. I. Erlich, W. Winter, and A. Dittrich, "Advanced grid requirements for the integration of wind turbines into the German transmission system," in *Power Engineering Society General Meeting*, 2006. IEEE, 18-22 June 2006, p. 7pp.
- [9]. S. M. Alghuwainem, R. A. Hammouda, and A.-R. M. Al-Farhan, "Transient analysis of a wind-driven induction generator," in *Proc. Canadian Conf. Electrical Computer Engineering*, vol. 2, 2001, pp. 13–16.
- [10]. D.J. Trudnowski, A. Gentile, M. Khan and E.M. Petritz, "Fixed-Speed Wind-Generator and Wind-Park Modeling for Transient Stability Studies," *IEEE Trans. Power Syst.*, Vol. 19, No. 4, November, 2004
- [11]. L. M. Fernandez, J. R. Saenz, and F. Jurado, "Dynamic models of wind farms with fixed speed wind turbines," *Renewable Energy*, vol. 31, pp.1203 -1230, 2006.
- [12]. Y. Uctug and M. Demirekler, "Modeling, Analysis and Control of a Wind-Turbine Driven Self-Excited Induction generator," *IEE Proceedings Generation, Transmission and Distribution*, Vol. 135, No. 4, July 1988.
- [13]. L. Holdsworth, X.G.Wu, J.B.Ekanayak and Jenkins, "Comparison of Fixed-speed and doubly-fed Induction Generator Wind Turbines during Power System Disturbances," *IEE proceedings C- Gener. Transm., Distrib.* vol.150, no.3, pp.343-352, July 2003
- [14]. L. Holdsworth, X. G. Wu, J. B. Ekanayake, and N. Jenkins, "Comparison of fixed speed and doubly-fed induction wind turbines during power system disturbances," *Proc. Inst. Elect. Eng., Commun.*, vol. 150, no. 3, pp. 343–352, May 2003
- [15]. Gaztañaga, I. Etxeberria-Otadui, D. Ocasu, and S. Bacha, "Real-time analysis of the transient response improvement of fixed-speed wind farms by using a reduced-scale STATCOM prototype," *IEEE Trans Power Syst.*, vol. 22, no. 2, pp. 658–666, May 2007.
- [16]. M. Molinas, J. A. Suul, and T. Undeland, "Wind farms with increased transient stability margin provided by a STATCOM," in *Proc. Int Power Electron. Motion Contr. Conf. (IPEMC'06)*, Shanghai, China, Aug. 16, 2006, vol. 1, pp. 63–69.
- [17]. M. Molinas, J. Kondoh, J. A. Suul, and T. Undeland, "Reactive support for wind and wave farms with a STATCOM for integration into the power system," in *Proc. Renewable Energy Conf.*, Makuhari, Japan, Oct. 9–13, 2006, pp. 1665–1668.
- [18]. G. Chicco, M. Molinas, T. Undeland, and G. Viglietti, "Improvement of the transient stability margin in wind systems with a STATCOM," in *Proc. VI World Energy Syst. Conf.*, Torino, Italy, Jul. 12, 2006, pp. 371–376.
- [19]. W. Xueguang, A. Atputharajah, Z. Changjiang, and N. Jenkins, "Application of a static reactive power compensator (STATCOM) and a dynamic braking resistor (DBR) for the stability enhancement of a large wind farm," *Wind Eng.*, vol. 27, no. 2, 2003
- [20]. Alex Q. Huang, Mesut E. Baran, Subhashish Bhattacharya, Wanye Litzenberger, Loren Anderson, Anders L. Johnson and Abdel-Aty Edris, "STATCOM Impact Study on the Integration of a Large Wind Farm into Weak Loop Power System," *IEEE Transaction on Energy Conversion*, Vol. 23, No. 1, pp. 226-233, March 2008.
- [21]. L. M. Fernandez, J. R. Saenz, and F. Jurado, "Dynamic models of wind farms with fixed speed wind turbines," *Renewable Energy*, vol. 31, pp.1203 -1230, 2006.
- [22]. Z. Saad-Sauoud and N. Jenkins, "Simple wind farm dynamic model," *IEE Proc. Generation, Transmission, and Distribution*, vol. 142, no. 5, pp. 545-548, Sept. 1995.

# Performance and Emission Study of Linseed Oil as a Fuel for CI Engine

Ashutosh Kumar Rai, Naveen Kumar, and Bhupendra Singh Chauhan

**Abstract**—Increased energy demand and the concern about environment friendly technology, renewable bio-fuels are better alternative to petroleum products. In the present study linseed oil was used as alternative source for diesel engine fuel and the results were compared with baseline data of neat diesel. Performance parameters such as brake thermal efficiency (BTE) and brake specific fuel consumption (BSFC) and emissions parameters such as CO, unburned hydro carbon (UBHC), NO<sub>x</sub>, CO<sub>2</sub> and exhaust temperature were compared. BTE of the engine was lower and BSFC was higher when the engine was fueled with Linseed oil compared to diesel fuel. Emission characteristics are better than diesel fuel. NO<sub>x</sub> formation by using linseed oil during the experiment was lower than diesel fuel. Linseed oil is non edible oil, so it can be used as an extender of diesel fuel energy source for small and medium energy needs.

**Keywords**—Bio-fuel, exhaust emission, linseed oil, triglyceride.

## I. INTRODUCTION

THE world is moving towards a sustainable energy era with major emphasis on energy efficiency and use of renewable energy sources. Growing concerns on the long-term availability of diesel and its environmental disadvantage have necessitated the search for a renewable alternative to diesel fuel. Bio-fuels can provide a feasible solution to these problems; known liquid bio-fuels are fuels derived from alcohol and vegetable oils. However, modification, handling and transportation, ease of production, and investment cost are some of the important parameters that should be considered before using an alternative fuel in an existing diesel engine. The modification required in the engine design should be very minor to minimize the investment in engine modification [1]-[4]. Diesel engines are major source of energy for agricultural need. Linseed oil is a better option for small and medium capacity energy needs.

Oil seed crops can provide a fuel grade product using relatively simple extraction and processing technology which could be performed on individual farms. Vegetable oils are promising fuels, particularly for diesel engines. The practicality of vegetable oils as diesel fuels has been sufficiently demonstrated to warrant further investigation of

their effectiveness and to develop techniques that will permit their incorporation into agricultural operations, particularly in times of energy shortfall. The present work aims at comparative assessment of performance evaluation exhaust emissions of neat linseed oil with diesel fuel in a single cylinder diesel engine. Due to high viscosity and slight lower calorific value of Linseed oil it can be used with or without blending in diesel.

## II. LINSEED OIL AS A POTENTIAL FUEL FOR DIESEL ENGINE

Identification of alternative fuels for use in IC engines has been subjected to studies throughout the globe. Performance tests have shown suitability of variety of alternative fuels such as hydrogen, alcohols, biogas, producer gas and various types of edible and non edible oils. However, in Indian context, the bio-origin fuels like alcohols, vegetable oils, and biogas can contribute significantly towards the problems related to fuel crises. Petroleum based diesel fuels have different chemical structure than vegetable oil. The former contain only carbon and hydrogen atoms which are arranged in normal (straight chain) or branched chain structures as well as aromatic configurations. The normal structure is preferred for better ignition quality. Diesel fuel can contain both saturated and straight or unbranched chain unsaturated hydrocarbons, but the later are not present in large amounts to make oxidation a problem [5]-[7]. Vegetable oils consist of triglycerides to about 97%; the other 3% distribute among di and mono glycerides and further more 3 fatty acids and the fat accompanying which are mostly removed with refining [8]. Structurally, a triglyceride is a reaction product of one molecule of glycerol with three fatty acid molecules to yield three molecules of water and one molecule of triglyceride [9].

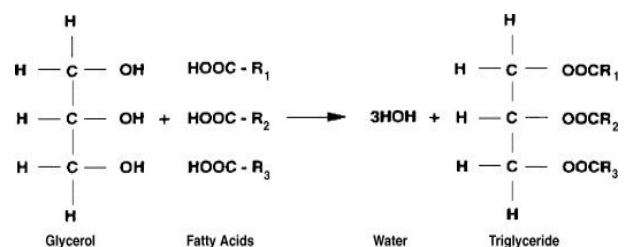


Fig. 1 Chemical structure of vegetable oils

where R<sub>1</sub>, R<sub>2</sub> and R<sub>3</sub> are the alkyl groups of different carbon chain lengths (varying between 12-18), and -COO- is an carboxyl group. Vegetable oils have different chemical structure as shown [10].

Ashutosh Kumar Rai is research scholar with the Department of Mechanical Engineering, Delhi Technological University, Delhi, India (phone: +91-9891161172; e-mail: ashu22sep@gmail.com).

Naveen Kumar is with the Department of Mechanical Engineering, Delhi Technological University, Delhi, India. (e-mail: naveenkumardce@gmail.com).

Bhupendra Singh Chauhan is with the Department of Mechanical Engineering, Delhi Technological University Delhi, India. (e-mail: bhupendradce@gmail.com).

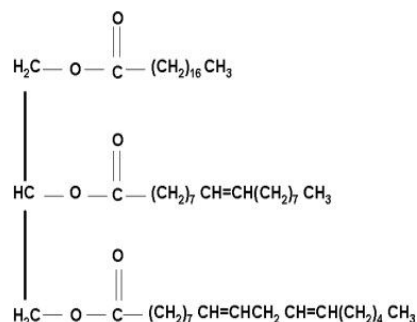


Fig. 2 Structure of a typical triglyceride molecule

The large size of the vegetable oil molecules and the presence of oxygen in the molecules suggest that some fuel properties of the vegetable oils would differ markedly from those of hydrocarbon fuels [8]. Linseed oil consists of primarily of the mixed glycerides of Oleic acid, Linoleic acid and Linolenic acid. The kinematic viscosity of Linseed oils varies in the range of 26-30 mm<sup>2</sup>/s at 40°C. The high viscosity is due to their larger molecular mass and chemical structure. Vegetable oils have high molecular weights of 600-900, which are three or more times higher than that of diesel fuel. The flash point of linseed oil is also very high (about 222°C). The auto-ignition temperature is about 343°C. Specific gravity is 0.93 and density 931 kg/m<sup>3</sup>. Calorific value is about 40 MJ/kg, comparatively lower than that of diesel fuels (about 45 MJ/kg). This is because the presence of chemically bonded oxygen in vegetable oils lowers the heating value by about 10%. The cetane number is in the range of 32-40, while the iodine value ranges from 0-200, depending on unsaturation. The cloud and pour point of vegetable oils is higher than that of diesel fuel [11]-[14].

### III. EXPERIMENTAL SETUP

A Kirloskar make, single cylinder, constant speed, air cooled, direct injection, CAF 8 model diesel engine was selected for the present research work, which is primarily used for agricultural activities and household electricity generations. It is a single cylinder, naturally aspirated, four stroke, vertical, air-cooled engine. It has a provision of loading electrically since it is coupled with single phase alternator through flexible coupling. The engine can be hand started using decompression lever and is provided with centrifugal speed governor. The lubrication system used in this engine is of wet sump type, and oil is delivered to the crankshaft and the big end by means of a pump mounted on the front cover of the engine and driven from the crankshaft. The inlet and exhaust valves are operated by an overhead camshaft driven from the crankshaft through two pairs of bevel gears. The fuel pump is driven from the end of camshaft.

A voltmeter, ammeter and wattmeter were connected between alternator and load bank. The thermocouples were mounted in the exhaust manifold to measure the exhaust temperature. The AVL 437 smoke meter and AVL Di-Gas Analyzer were also kept in proximity for the measurements

of various exhaust gas parameters. The engine was started at no load by pressing the exhaust valve with decompression lever and it was released suddenly when the engine was hand cranked at sufficient speed. Then feed control was adjusted so that engine attains rated speed and was allowed to run about half hour till the steady state condition was reached. With the fuel measuring unit and stop watch, the time elapsed for the consumption of 20cc of fuel was measured. Fuel consumption, RPM, exhaust temperature, smoke density, CO, NO<sub>x</sub>, HC, CO<sub>2</sub> and power output were also measured. The engine was loaded gradually keeping the speed within the permissible range and the observations of different parameters were evaluated. Short term performance tests were carried out on the engine with diesel to generate the base line data and subsequently Linseed Oil and Diesel was used to evaluate its suitability as a fuel. The performance and emission characteristics of Linseed Oil was evaluated and compared with diesel fuel.

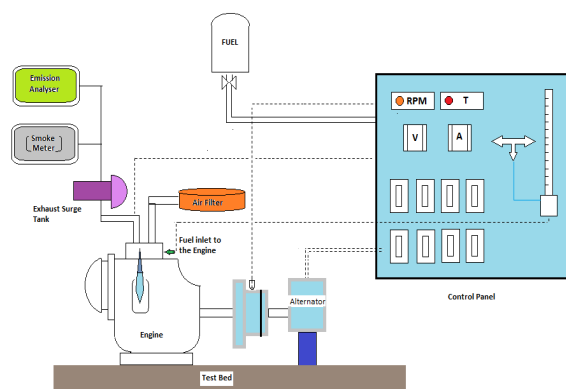


Fig. 3 Schematic diagram of experimental test rig

### IV. RESULT & DISCUSSION

The variation of the brake thermal efficiency (BTE) of the engine with linseed oil and diesel is shown in Fig. 4. With increasing brake power, the BTEs of vegetable oils and diesel also increased; however, they tended to decrease when further increase in brake power was observed. The BTEs of the linseed oil are lower than those of diesel fuel throughout the entire range, possibly due to the lower calorific value and the high viscosity of linseed oil compared with diesel fuel.

The brake-specific fuel consumptions (BSFC) were also higher in the case of linseed oil than in diesel fuel, as evident in Fig. 5. This is mainly due to the combined effects of the relative fuel density, viscosity, and heating value.

Within the experimental range, the CO emission from linseed oil is higher than neat diesel fuel, as seen in Fig. 6. This is possible due to the high viscosity of vegetable oils; the higher the viscosity, the more difficult it is to atomize vegetable oils. This resulted in locally rich mixtures in the engine.



The  $\text{CO}_2$  emissions are shown in Fig. 7. In the range of the whole engine load, the  $\text{CO}_2$  emissions of diesel fuel are higher than that of the other fuels because vegetable oil contains oxygen element. The carbon content is relatively lower in the same volume of fuel consumed at the same engine load, and consequently, the  $\text{CO}_2$  emissions from the vegetable oil and its blends are lower.

The value of unburned HC emission from the diesel engine in the case of straight vegetable oil is higher than that of diesel fuel, as seen in Fig. 8. HC emissions are lower at partial loads but tend to increase at higher loads for both fuels. This is due to the lack of oxygen, which is caused by engine operation at a higher equivalence ratio.

The  $\text{NO}_x$  emissions, shown in Fig. 9, increase along with the increasing engine load due to the higher combustion temperature. This proves that the most important factor for the emissions of  $\text{NO}_x$  is the combustion temperature in the engine cylinder and the local stoichiometry of the mixture. Within the  $\text{NO}_x$  emissions were reduced at full load, possibly due to the smaller calorific value of vegetable oils.

Fig. 10 shows that the exhaust gas temperature increases with the increase in brake power in all cases. This is due to the poor combustion characteristics of the linseed oil because of its high viscosity.

#### V. CONCLUSIONS

The results of the experiment showed that the performance of the engine on Linseed oil was slightly inferior to that on diesel fuel. The thermal efficiency of the engine was lower and the brake specific energy consumption of the engine was higher when the engine was fueled with Linseed oil compared to diesel fuel. The oxides of nitrogen from during the whole range of experiment were lower than diesel fuel. The Carbon monoxide, unburned hydrocarbon from the fuel was found higher than diesel fuel during the whole experimental range. The results from the experiments suggest that linseed oil is potentially good substitute fuel for diesel engine and performance and emissions characteristics were found to be comparable to diesel fuel.

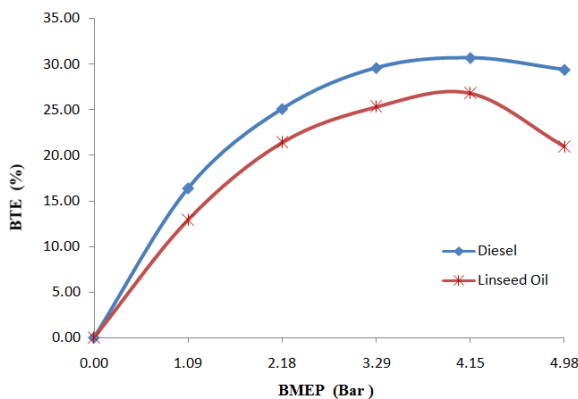


Fig. 4 Variation of brake thermal efficiency with brake means effective pressure

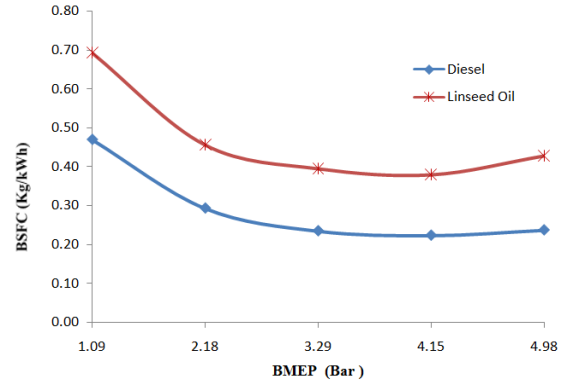


Fig. 5 Variation of brake specific fuel consumption with brake means effective pressure

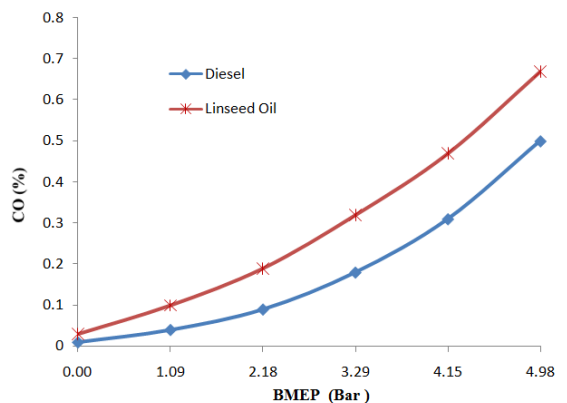


Fig. 6 Variation of carbon monoxide with brake means effective pressure

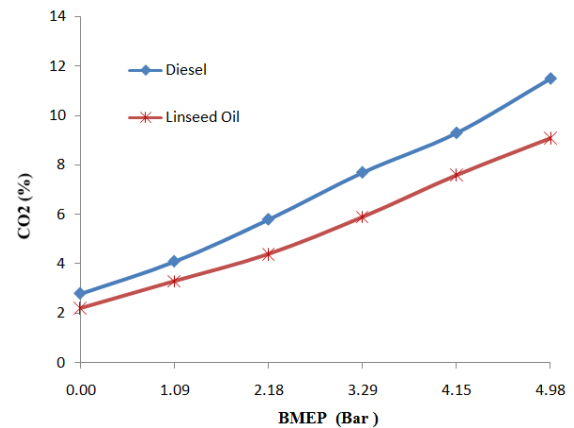


Fig. 7 Variation of carbon dioxide with brake means effective pressure

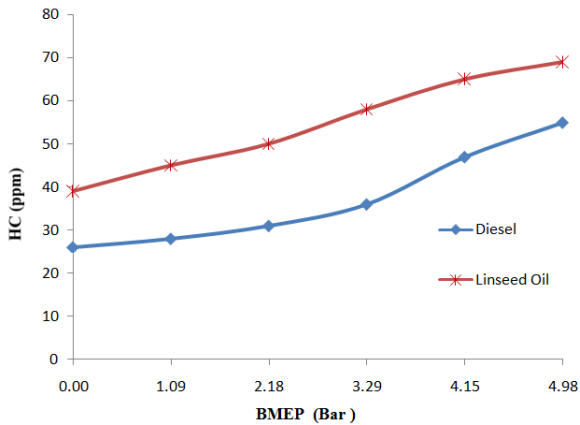


Fig. 8 Variation of unburned hydrocarbon with brake means effective pressure

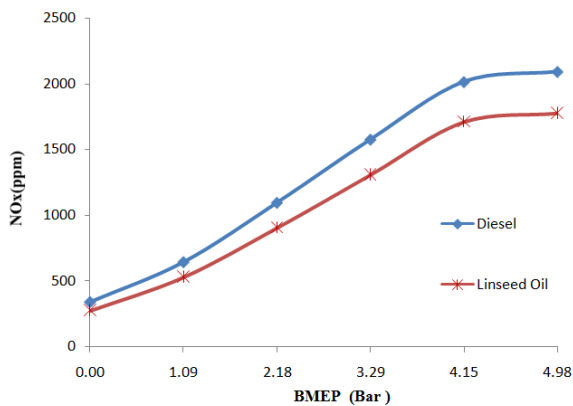


Fig. 9 Variation of oxides of nitrogen with brake means effective pressure

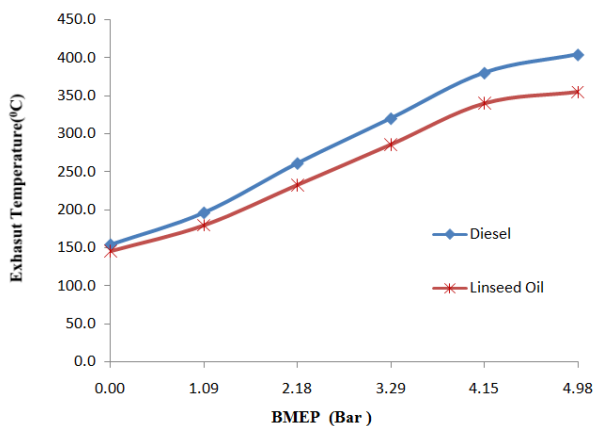


Fig. 10 Variation exhaust temperature with brake means effective pressure

#### REFERENCES

- [1] BS Chauhan, N Kumar, HM Cho. "A study on the performance and emission of a diesel engine fueled with Jatropha biodiesel oil and its blends," *Energy*; Vol. 37, pp. 616-622, 2012
- [2] BS Chauhan, N Kumar, YD Jun, KB Lee, "Performance and emission study of preheated Jatropha oil on medium capacity diesel engine," *Energy*, vol. 35, pp. 2484-92, 2010;
- [3] BS Chauhan, N Kumar, SS Pal, YD Jun, "Experimental studies on fumigation of ethanol in a small capacity diesel engine," *Energy*, vol. 36pp.1030-8, 2011.
- [4] BS Chauhan, N Kumar, HM Cho, "Performance and emission studies on an agriculture engine on neat Jatropha oil, *JMST* vol. 24(2), pp. 529-35, 2010.
- [5] A Srivastava, R Prasad, "Triglycerides-based diesel fuels" *Renewable and Sustainable Energy Reviews* vol. 4, pp.111-133, 2000.
- [6] JN Reddy, A Ramesh, "Parametric studies for improving the performance of a Jatropha oil-fuelled CI engine," *Renewable Energy* vol. 31, pp. 1994-2016, 2006.
- [7] BK Barnwal, MP Sharma, Prospects of biodiesel production from vegetable oils in India, *Renewable and Sustainable Energy Reviews*, vol. 9 pp. 363-378, 2005.
- [8] R. Narayan, "Biomass (renewable) resources for production of material," *Chemicals and Fuels*, vol 476 pp. 1-10, 1992.
- [9] A. Farsaie, J. V. Debarhte and W. J. Kenworthy, "Analysis of producing the vegetable oil as an alternate fuel" *Energy in Agriculture*, vol. 4, pp. 189-205, 1985.
- [10] Kemal, Yunus, Elcin, "Some Physical Properties of Linseed," *Biosystems Engineering* vol. 95 (4), pp. 607-612, 2006.
- [11] C. J. Abraham, "A solution to spontaneous combustion in linseed oil formulations," *Polymer Degradation and Stability*, vol. 5 4, pp.157-166, 1996.
- [12] Jutia et al, Oxidation reactions and spontaneous ignition of linseed oil, *Proceedings of the Combustion Institute* vol. 33 pp. 2625-2632, 2011.
- [13] V. Sharma et al, Spectroscopic characterization of linseed oil based polymer nano-composites, *Polymer Testing* vol. 27, pp. 916-923, 2008.
- [14] Sukumar et al, "Effect of injection pressure on performance, emission and combustion characteristics of high linolenic linseed oil methyl ester in a DI diesel engine," *Renewable Energy* vol. 34, pp. 1227-1233, 2009.

## **General Robust Stability Analysis of Uncertain system**

**Shyama Kant Jha, A.K. Yadav  
Prerna Gaur, J.R. P. Gupta**

Division of Instrumentation and Control Engineering,  
NSIT, Dwarka, New Delhi, India  
*jhask271@gmail.com, anilei007@gmail.com,  
prernagaur@yahoo.com, jrpg83@yahoo.com*

### **Abstract**

The main objective of this paper is to investigate the robust control aspect of chaotic and uncertain system. The robust stability analysis of closed loop attitude control system of an aircraft is presented using the Kharitonov theorem. The proposed technique for examining the robust stability of chaotic polynomial is efficient and expeditious one as the onerous application of Routh stability criterion for infinite no of interval polynomials of the perturbed system can be completely dispensed with.

**Keywords-** Robust control, Kharitonov's theorem, Routh criterion, Interval systems

### **Introduction**

Study and design of robust system has been a matter of concern and drawn the attention of many authors in recent years [1-3]. The designed system is said to be robust if it remains insensitive to the presence of parametric uncertainties. Incorporation of robust features in the modern control design is indispensably necessary. Here, in this paper we take into consideration the example of the precise attitude control of an aircraft which is variedly used in aerospace application. For the precise attitude control of an aircraft we need to control the positions of the fins of a modern aircraft. Fins are mostly the flattened part that projects from an aircraft for providing stability. Owing to the requirement of improved response and reliability, modern aircraft are controlled by electric actuators and electronic control [1]. Initially in order to check the stability of characteristic polynomial by Routh criterion it was assumed that the coefficient of characteristic polynomial are constant but practically it

does not happen. The coefficients are bound to change under extraneous circumstances in certain range and thus lead to the formation of interval polynomial.

The stability of such kind of polynomials where coefficients are varying in nature has attracted the attention of many researchers. These systems are not immune and insensitive to parameter variation. When we envisage the design of attitude control aircraft under parametric variation, the robust stability analysis seems to be extremely important [7, 8]. This analysis is done using Kharitonov theorem which entails formations of four polynomials (from the parameter variation within some extremes) and application of Routh criterion to these four polynomials only to determine the system stability under perturbation [2]. Earlier, in [3-6], [9, 10], the robust stability analysis was carried out by determining all the uncertain values within some defined extremes as dictated by Kharitonov's theorem. Here we have proposed the method shown by [2] for the robust stability analysis of attitude control system of an aircraft. The main objective of this paper is to present an analysis of the robust stability of attitude control of an aircraft under variations in circuit parameters. The proposed method is found to be efficient and computationally simpler for an infinite no of interval polynomials of the perturbed system.

### Mathematical Preliminaries

In classical control the coefficient of the characteristic equation was assumed to be constant. Practically the coefficients are the functions of energy storing or dissipating elements which may change its value due to external conditions. So the same characteristic equation will now represent an infinite family of characteristic polynomial when the components are subjected to uncertainties. Robust control design necessitates the study and formulation of interval polynomial. The concept of interval analysis is useful in the study of robust control of systems with parametric uncertainty within known bounds. The uncertain parameter is incorporated in terms of interval entity and the robust stability is analysed here by Kharitonov's theorem.

#### Kharitonov's Theorem [2]

When we deal with the robust stability of interval polynomial i.e., when the coefficients of characteristics equation are no longer constant, Kharitonov theorem come to a great rescue. Suppose that a family of polynomials is given by

$$s^n + a_1 s^{n-1} + a_2 s^{n-2} + \dots + a_{n-1} s + a_n \quad (1)$$

where  $\alpha_i \leq a_i \leq \beta_i$  ,  $1 \leq i \leq n$ .

According to Kharitonov's theorem, the family of polynomials (1) are said to be stable if and only if the following four polynomials are stable:

$$s^n + \alpha_1 s^{n-1} + \alpha_2 s^{n-2} + \beta_3 s^{n-3} + \beta_4 s^{n-4} + \dots \quad (2)$$

$$s^n + \alpha_1 s^{n-1} + \beta_2 s^{n-2} + \beta_3 s^{n-3} + \alpha_4 s^{n-4} + \dots (3)$$

$$s^n + \beta_1 s^{n-1} + \beta_2 s^{n-2} + \alpha_3 s^{n-3} + \alpha_4 s^{n-4} + \dots (4)$$

$$s^n + \beta_1 s^{n-1} + \alpha_2 s^{n-2} + \alpha_3 s^{n-3} + \beta_4 s^{n-4} + \dots (5)$$

### Attitude Control System Of An Aircraft

In order to have the precise attitude control of an aircraft one need to control the positions of the fins of a modern aircraft. Fins are mostly the flattened part that projects from an aircraft for providing stability. Owing to the requirement of improved response and reliability, modern aircraft are controlled by electric actuators and electronic control.

Figure 1 and figure 2 shows the controlled surfaces and simplified block diagram of one axis of such a position control or attitude control system. Figure 3 shows the analytical block diagram of the same system using expanded model of dc motor. The system considered here is simplified to the extent that saturation of the amplifier gain and gear backlash etc has been neglected.  $\Theta_r$  is the desired output (desired position of control surface) and  $\Theta_y$  is the actual output (actual position of control surface) to the system.

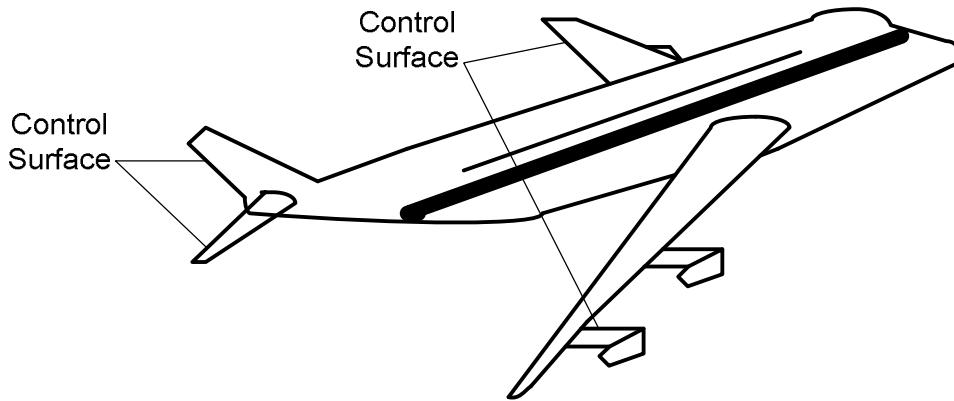


Fig.1 Schematic diagram of control surfaces of Aircraft

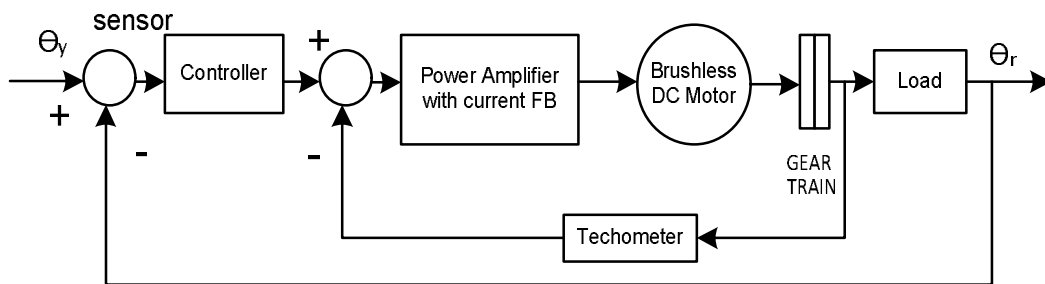


Fig.2 Block diagram of an attitude control system of an aircraft

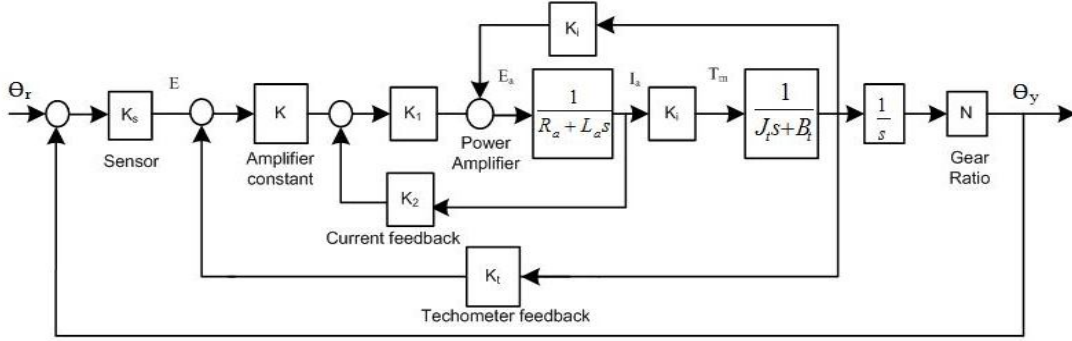


Fig.3 Analytical block diagram of an attitude control system using expanded model of DC motor.

The open-loop transfer function of an attitude control system of aircraft is given as [1]

$$G(s) = \frac{K_s K_1 K_i K N}{s[L_a J_t s^2 + (R_a J_t + L_a B_t + K_1 K_2 J_t)s + R_a B_t + K_1 K_2 B_t + K_i K_b + K K_1 K_t K_i]} \quad (6)$$

where  $J_t = J_m + N^2 J_L$  and  $B_t = B_m + N^2 B_L$ . The implications of other symbols used in (6) are given and illustrated in appendix. In this section we presume that the components and parameters used in (6) are constant and in the next section, realistic uncertainty in parameter variation is taken into consideration for analysis of robust aspect of control design.

If  $K_s = 1$ ,  $K = \text{adjustable}$ ,  $K_1 = 10$ ,  $K_2 = 0.5$ ,  $K_t = 0$ ,  $R_a = 5$ ,  $L_a = 0.003$ ,  $K_i = 9$ ,  $K_b = 0.0636$ ,  $J_m = 0.0001$ ,  $J_L = 0.001$ ,  $B_m = 0.005$ ,  $B_L = 1$ ,  $N = 0.1$

Using (6), the open loop transfer function of attitude control system becomes:

$$G(s) = \frac{1.5 \times 10^7 K}{s(s^2 + 3408.3s + 1204000)} = \frac{1.5 \times 10^7 K}{s(s + 400.26)(s + 3008)} \quad (7)$$

The closed loop transfer function is

$$\frac{\theta_y(s)}{\theta_r(s)} = \frac{1.5 \times 10^7 K}{s^3 + 3408.3s^2 + 1204000s + 1.5 \times 10^7 K} \quad (8)$$

### Robust Stability Of Attitude Control System

In terms of the components and parameters of attitude control system in fig. 2, the characteristic polynomial of the closed loop system is given as

$$s^3 + \frac{R_a J_t + L_a B_t + K_1 K_2 J_t}{L_a J_t} s^2 + \frac{R_a B_t + K_1 K_2 B_t + K_i K_b + K K_1 K_t K_i}{L_a J_t} s + \frac{K_s K_1 K_i K N}{L_a J_t} \quad (9)$$

This is nothing but a polynomial having variable coefficients. The stability of such kind of polynomials where coefficients are varying in nature is ubiquitously present and has attracted the attention of many researchers. These systems are not immune and insensitive to parameter variation. Hence robust stability analyses of such systems seem to be indispensable one because these are variedly used in aerospace application. In practice the parameters of (9) are not constant, because armature resistance of motor  $R_a$  and armature inductance of motor  $L_a$ , change with time because of aging effects. In a similar fashion, other parameter such as load inertia  $J_L$ , inertia of motor rotor  $J_m$ , back emf constant of motor  $K_b$ , gain of preamplifier  $K$ , etc are also not constant and may vary. Therefore presumably it is specified that the different components and feedback gains are subject to the following ranges of uncertainty.

$$\begin{aligned} K_s &= 1 \pm 0.5 \frac{V}{rad}, K = 100 \pm 50, K_1 = 10 \pm 4 \frac{V}{V}, K_2 = 0.5 \pm \frac{0.2V}{A}, K_t = \\ &0, R_a = 5.0 \pm 2.0 \Omega, L_a = 0.003 \pm .001 H, K_i = 9 \pm 4, K_b = 0.0636 \pm \\ &0.0100 V/rad/sec, J_m = 0.0001 \pm 0.00005, J_L = 0.01 \pm 0.005, B_m = \\ &0.005 \pm 0.001, B_L = 1.0 \pm 0.5, N = 0.1 \end{aligned} \quad (10)$$

After taking all these realistic uncertainties into account we examine the robust stability of attitude control system of an aircraft. Robust stability analysis of state feedback control of PWM DC-DC Push-Pull converter using Kharitonov's theorem has been presented in [4]. Here we will apply Kharitonov's theorem to our system.

#### A. Robust Stability Using Kharitonov's Theorem

Here the stability of (9) is investigated by testing the stability of a large set of polynomials using Kharitonov's theorem [2]. Characteristics polynomial (9) may be written in the form given below

$$P(s) = s^3 + a_1 s^2 + a_2 s + a_3 \quad (11)$$

In which the ranges of coefficients between two extremes are  $a_1 \in [\alpha_1, \beta_1]$ ,  $a_2 \in [\alpha_2, \beta_2]$  and  $a_3 \in [\alpha_3, \beta_3]$ . Here we intend to do the robust analysis of characteristic interval polynomial (11) in the following three steps.



*Step 1:* Evaluation of the extremal range of coefficients, i.e.

$$\begin{aligned}
 \alpha_1 &= \min_q \left\{ \frac{R_a J_t + L_a B_t + K_1 K_2 J_t}{L_a J_t} \right\} = 2.4 \times 10^3 \\
 \beta_1 &= \max_q \left\{ \frac{R_a J_t + L_a B_t + K_1 K_2 J_t}{L_a J_t} \right\} = 4.3 \times 10^3 \\
 \alpha_2 &= \max_q \left\{ \frac{R_a B_t + K_1 K_2 B_t + K_i K_b + K K_1 K_t K_i}{L_a J_t} \right\} = 10.9 \times 10^5 \quad (12) \\
 \beta_2 &= \min_q \left\{ \frac{R_a B_t + K_1 K_2 B_t + K_i K_b + K K_1 K_t K_i}{L_a J_t} \right\} = 15.1 \times 10^5 \\
 \alpha_3 &= \min_q \left\{ \frac{K_s K_1 K_i K N}{L_a J_t} \right\} = 3.7 \times 10^7 \\
 \beta_3 &= \max_q \left\{ \frac{K_s K_1 K_i K N}{L_a J_t} \right\} = 3.4 \times 10^9
 \end{aligned}$$

The vector  $q$  represents the vector of the uncertain circuit components  $K_s, K, K_1, K_2, K_t, R_a, L_a, K_i, K_b, J_m, J_L, B_m, B_L, N$ . In (12) the min (minimum) and max (maximum) of the coefficient of the characteristic polynomial (9) are computed when the components are subjected to the uncertainties as represented in (10). Now we apply the Kharitonov's theorem [2] to (11) for testing the robust stability as the family of polynomials represented by (11) has infinite coefficients. The four Kharitonov polynomials corresponding to (9) are given in step 2 ahead.

*Step 2:* Formulation of all the four Kharitonov polynomials

$$s^3 + 2.4 \times 10^3 s^2 + 10.9 \times 10^5 s + 3.4 \times 10^9 \quad (13)$$

$$s^3 + 2.4 \times 10^3 s^2 + 15.1 \times 10^5 s + 3.4 \times 10^9 \quad (14)$$

$$s^3 + 4.3 \times 10^3 s^2 + 15.1 \times 10^5 s + 3.7 \times 10^7 \quad (15)$$

$$s^3 + 4.3 \times 10^3 s^2 + 10.9 \times 10^5 s + 3.7 \times 10^7 \quad (16)$$

*Step 3:* Checking for robust stability

Now applying the Routh criterion to (13) through (16) it is found that all the four Kharitonov polynomials satisfy the Hurwitz stability conditions. Hence the chaotic attitude control system represented by (9) is stable.

## Conclusions

In this paper we have proposed Kharitonov's theorem in conjunction with Routh stability criterion for the robust stability analysis of attitude control of an aircraft. Based on this theorem, arrangement of four Kharitonov's polynomial is presented using upper and lower bounds. Here it is observed that the perturbed system is robust stable in the specified range of all the component values. Thus the computational cost can be reduced to a great extent for numerous interval polynomials. Moreover in future similar application of Kharitonov theorem can be developed for the robust stability of digital control system.

## APPENDIX

### Nomenclatures and Abbreviations':

$K_S$  = Gain of encoder

$K$  = Gain of the preamplifier

$K_1$  = Gain of power amplifier

$K_2$  = Gain of current feedback

$K_t$  = Gain of tachometer feedback

$R_a$  = Armature resistance of motor

$L_a$  = Armature inductance of motor

$K_i$  = Torque constant of motor

$K_b$  = Back-emf constant of motor

$J_m$  = Inertia of motor rotor

$J_L$  = Inertia of load

$B_m$  = Viscous-friction coefficient of motor

$B_L$  = Viscous-friction coefficient of load

$N$  = Gear-train ratio between motor and load

$\theta_y$  = Position of control surface

$\theta_r$  = Reference or desired Position of control surface

## References

- [1] B. C. Kuo, F. Golnaraghi, "Automatic Control System," John Wiley & Sons, Eighth Edition, 2003.
- [2] V. L. Kharitonov, "Asymptotic stability of an equilibrium position of a family of systems of linear differential equations," *Differ. Equa.*, vol. 14, pp. 2086-2088, 1978.
- [3] Yogesh V. Hote, D. Roy Choudhary, and J.R.P. Gupta. "On Robust Stability of the Systems," *International Journal of Control, Automation, and Systems*, vol. 7, no.3 .pp. 469-474, Aug. 2009.
- [4] D. Czarkowski, L. R. Pujaria, and M. K. Kazimierczuk, "Robust stability of state-feedback control of PWM DC-DC push-pull converter," *IEEE Trans.*

- IND. Electron.*, vol.42, no.1, pp. 108-111, Feb. 1995.
- [5] L. R. Pujaria, "Robust stability of PWM Buck DC-DC converter," in Proc. 1996 *IEEE INT. Conf. Control Appl.*, Dearbon, MI, pp.632-636.
  - [6] L. R. Pujaria, "On the stability of uncertain polynomials with dependent coefficients," *IEEE Trans. Autom. Control*, vol. 35, no. 6, pp.756-759, Jun 1990.
  - [7] B. L. Stevens and F. L. Lewis, "Aircraft Control and Simulation," Hoboken, New Jersey: John Wiley & Sons, Inc., 2nd ed., 2003.
  - [8] David G. Hull, "Fundamentals of Airplane Flight Mechanics," Springer-Verlog London Limited, 2009.
  - [9] S. P. Bhattacharyya, Aniruddha Datta, and L. H. Keel, "Linear Control Theory: Structure, Robustness and Optimization," CRC Press, Taylor and Francis Group, New York, 2009.
  - [10] T. Meressi, D. Chen, and B. Paden, "Application of Kharitonov's theorem to Mechanical Systems," *IEEE Trans. on Automatic Control*, vol. 38, no.3, pp. 488-491, 1993.

### Biographies:



**S. K. Jha** received his B.Sc. (Engg.) degree in Electrical Engineering from Bhagalpur College of Engineering, Bhagalpur and M.E. degree in Control & Instrumentation from Delhi College of Engineering, Delhi University in 1994 and 2003 respectively. He joined the industry (U.B. Engineering Ltd.) in 1995 and Netaji Subhas Institute of Technology (NSIT) as a Lecturer in 1999. Currently he is holding the post of Assistant Professor in the Instrumentation & Control engineering Department at N.S.I.T, New Delhi. His research interest includes control theory, optimal control, robust control, electric drives, intelligent control etc. He is a Life Member of the Indian Society for Technical Education (ISTE).



**Anil Kumar Yadav** was born in Jalalpur, Pratapgarh, (UP), India. He received his B.Tech in Electronics and Instrumentation Engineering from Hindustan College of Science and Technology Mathura (Uttar Pradesh Technical University Lucknow) (UP) in 2007, M.Tech from Netaji Subhas Institute of Technology, Delhi University, in 2010. He was Lecturer and Senior Lecturer in the Electronics and Instrumentation Engineering Department at Meerut Institute of Engineering and Technology Meerut (UP). He is working as Teaching Cum Research Fellow (TRF) in the Instrumentation and Control Engineering Division at Netaji Subhas Institute of Technology, Delhi University. His research interests are in the areas design of AI based Controllers, Robust and Adaptive Control.



**Prerna Gaur** received her B.Tech and M.E in 1988 and 1996 from G.B. Pant College of Technology, Uttranchal, India and Delhi College of Engineering, Delhi University, respectively. She is PhD in the field of Motion Control of PMSM. She joined the industry in 1989 and Delhi College of Engineering as a Lecturer in 1994. She is a Assistant Professor in the Instrument and Control Engineering Division at Netaji Subhas Institute of Technology, Delhi University since 1998. She is a Life Member of the Indian Society for Technical Education (ISTE) and Senior Member of Institute of Electrical and Electronics Engineers (IEEE). Her research interests includes power electronics, electric drives, artificial intelligence based control etc.



**J. R. P. Gupta** received his B.Sc (Engg.) Degree in Electrical Engineering from Muzaffarpur Institute of Technology, Muzaffarpur and Ph.D from University of Bihar in 1972 and 1983 respectively. After serving Post and Telegraph Department, Government of India for nearly three years, he joined M.I.T. Muzaffarpur as assistant professor in 1976. He then switched over to R.I.T. Jamshedpur in 1986 and then to N.S.I.T New Delhi in 1994 where currently he is holding the post of professor and Head of the Department, Instrumentation and Control Engineering, University of Delhi. His research interest include power electronics, electric drives, control theory, intelligent instrumentations etc. He has been awarded K. S. Krishnan memorial award for the best system oriented paper by Institute of Electronics and Telecommunication Engineers (India), in 2008. He is senior member of IEEE.

# Impact of Geometry on Photonic Bandgaps for TE polarization in Two Dimensional Photonic Crystals with Triangular Lattice

Vinita, Ajeet Kumar and Vipul Rastogi

**Abstract**— In this paper, we have investigated Photonic Band Gap (PBG) of two dimensional Photonic Crystals (PhCs) for TE polarization. Effect of shape, size and orientation of scatterers on PBG in triangular lattice has been investigated. OptiFDTD software has been used to calculate PBG, having simulator, Planewave Band solver, based on plane wave expansion method. The scatterers are air holes in dielectric media. It has been found that PBG can be controlled by changing the scatterer's properties. A triangular lattice with hexagonal air holes is able to show maximum band gap in 2-D PhC. PBG for TE polarization has been calculated for air holes in triangular lattice with background dielectric material, Si and GaAs. It has been found that although the gap mid gap ratio is different in above two materials but band gap behavior is almost similar.

**Index Terms**— Filling fraction, photonic crystal, plane wave expansion method, triangular lattice.

## I. INTRODUCTION

PHOTONIC crystals (PhCs) are materials in which the refractive index is periodically modulated on a length scale comparable to desired operation wavelength [1]-[3]. One of the most striking features of PhCs is associated with the fact that suitably engineered PhCs may exhibit frequency ranges over which ordinary linear propagation is forbidden, irrespective of direction [4]. These photonic band gap (PBG) structures have numerous applications in linear, non-linear and quantum optics. Since PBG is the major feature of a PhC, it is essential to design a structure which possesses a forbidden gap as large as possible. There are countless combinations of lattice symmetry, filling fraction, scattering object shape, and refractive index contrast, but it is impossible to predict which one gives the largest absolute PBG [5], [6]. A systematic algorithm is still lacking, and the PhC design is based on several rules of thumb [7], which help in reducing the dimensionality of the problem. Although three-dimensional PhCs suggest the most interesting ideas for novel applications, two- dimensional (2D) structures also have several important

uses, such as polarization-sensitive PBG devices [8], PhC based semiconductor lasers [9]. In solid state physics there are two fundamental 2D structures: square and hexagonal lattices. There are three variations in the hexagonal lattice: triangular, honeycomb (graphite) and kagome lattices. For dielectric columns in air, bandgaps are most abundant for the TM polarization, as long as columns are not large to touch one another and for air columns, the TE polarization has more bandgaps [1]. In our present work, PhC having triangular lattice with various types of scatterer has been considered and effect of various parameters, like filling fraction and orientation angle of scatterer on bandgap for TE polarization has been investigated. In our calculation, we have taken PhCs having air holes in dielectric substrate, since these are more important from an application point of view than dielectric columns, in particular, because they can be efficiently connected to other optical integrated devices [10]. The dielectric medium used here is Si and GaAs with the relative dielectric constant  $\epsilon=13$  and 11.4 respectively. "PWE band solver" of the optiFDTD™ software package has been used for the band diagram calculation which is based on plane wave expansion method.

## II. NUMERICAL METHODS FOR SIMULATION

The interaction of electromagnetic radiations with PhC can be modeled with the macroscopic Maxwell equations which gives an equation:

$$\nabla \times \left[ \frac{1}{\epsilon(\mathbf{r})} \nabla \times \mathbf{H} \right] = \frac{\omega^2}{c^2} \mathbf{H} \quad (1)$$

This equation is known as master equation, where  $\epsilon(\mathbf{r})$  is a position dependent dielectric constant;  $\mathbf{r}$  lies in the plane normal to the rods;  $\omega$  is frequency and  $c$  is the speed of light in vacuum. PBG can be obtained by solving (1), using various numerical methods like plane wave expansion method (PWEM), finite difference time domain method (FDTD), and finite element method (FEM). In our calculations, we have used PWEM. Expanding the magnetic field  $\mathbf{H}(\mathbf{r})$  and the dielectric function  $\epsilon(\mathbf{r})$  in a series of plane waves [11], we obtain

$$\mathbf{H}(\mathbf{r}) = \sum_{\mathbf{G}} \sum_{j=1,2} \mathbf{H}_{G,j} \hat{\mathbf{e}}_j e^{i(\mathbf{k}+\mathbf{G}) \cdot \mathbf{r}} \quad (2)$$

Vinita is with the Department of Engineering Physics, Delhi Technological University, Delhi-110042, India (e-mail: vinitadce@gmail.com).  
A. Kumar is with the Department of Applied Physics, Delhi Technological University, Delhi-110042, India (e-mail: ajeet.phy@dce.edu).  
V. Rastogi is with the Department of Physics, Indian Institute of Technology, Roorkee-247667, India (e-mail: vipulph@gmail.com).

$$\varepsilon(\mathbf{r}) = \sum_{\mathbf{G}} \varepsilon(\mathbf{G}) e^{i\mathbf{G} \cdot \mathbf{r}} \quad (3)$$

where  $\mathbf{k}$  is the wave vector in the first Brillouin zone;  $\mathbf{G}$  is a reciprocal-lattice vector, and  $\hat{\mathbf{e}}_j$  ( $j=1,2$ ) are unit vectors orthogonal to  $(\mathbf{k}+\mathbf{G})$ . The fourier coefficient  $\varepsilon(\mathbf{G})$  is defined by

$$\varepsilon(\mathbf{G}) = \frac{1}{S} \int_S \varepsilon(\mathbf{r}) e^{-i\mathbf{G} \cdot \mathbf{r}} d\mathbf{r} \quad (4)$$

where the integration is carried out over the area of  $S$  of one unit cell of the lattice. Substituting (2) and (3) into (1), two standard eigenvalues are obtained corresponding to two independent polarisations. The matrix equations obtained for the TE and TM polarisations, respectively, are

$$\sum_{\mathbf{G}'} |\mathbf{K} + \mathbf{G}| |\mathbf{K} + \mathbf{G}'| \varepsilon^{-1}(\mathbf{G} - \mathbf{G}') H_{\mathbf{G}',1} = \frac{\omega^2}{c^2} H_{\mathbf{G},1} \quad (5)$$

$$\sum_{\mathbf{G}'} |\mathbf{K} + \mathbf{G}| |\mathbf{K} + \mathbf{G}'| \varepsilon^{-1}(\mathbf{G} - \mathbf{G}') H_{\mathbf{G}',2} = \frac{\omega^2}{c^2} H_{\mathbf{G},2} \quad (6)$$

where  $\square^{-1}(\mathbf{G}-\mathbf{G}')\square$  represents the inverse of  $\square(\mathbf{G}-\mathbf{G}')$ . In our simulations, we have used software optiFDTD™ having Planewave band solver which is based on PWEM.

### III. DESIGN AND MODELING

#### A. Modeling

In order to investigate complete PBG of PhC in OptiFDTD, following steps are followed in order, as shown in Fig.1:

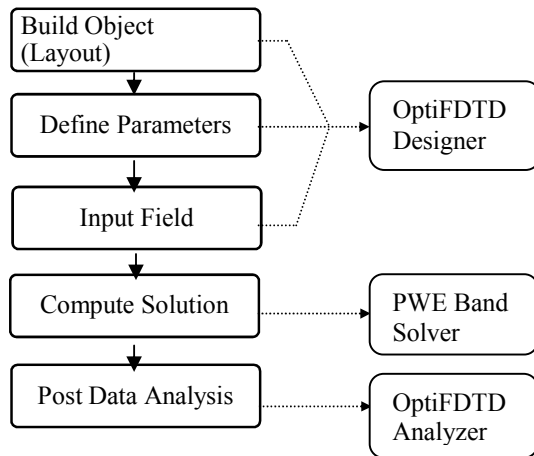


Fig. 1 Flowchart for modeling of PhC Band gap structures in OptiFDTD.

In geometrical modeling, a wafer of appropriate dimension and refractive index is designed. In the next step, PhC having triangular lattice with different shapes of holes, arranged periodically in the dielectric background with appropriate parameters is designed. This is followed by setting of physical parameters, such as wavelength of input light and refractive

index of hole. After GUI modeling, mesh size and k-vector path for first Brillouin zone, number of bands and tolerance are defined for PBG computation. Based on above given parameters, PWE band solver computes the PBG for TE polarization by calculating eigen values of Eq.5. Finally, the results are plotted in PWE Band Solver Simulator.

#### B. Design

In order to make detailed analysis of PBG for TE polarization in triangular lattice, we have designed five types of structures based on different shapes of scatterer, as shown in table 1. We have analyzed air holes of different shapes, circular, elliptical, square, rectangular and hexagonal which are arranged periodically in background dielectric material. This type of arrangement can be defined by two parameters: i) size of scatterers i.e radius in case of circular holes, major and minor radius in elliptical holes, side in hexagonal and square holes, length and breadth in rectangular holes; ii) lattice constant,  $a$  i.e. distance between two consecutive periodic structures (either holes or dielectric rods). The width of PBG can be controlled by changing these parameters along with orientation.

Simulations have been carried out using background material GaAs having relative dielectric constant,  $\varepsilon = 11.4$  and Si,  $\varepsilon = 13$ . Initially, computations have been done for orientation angle,  $\theta = 0^\circ$  and later orientation of holes has been changed. The definition of orientation angle,  $\theta$  for non-circular rods has been mentioned in Fig.2.

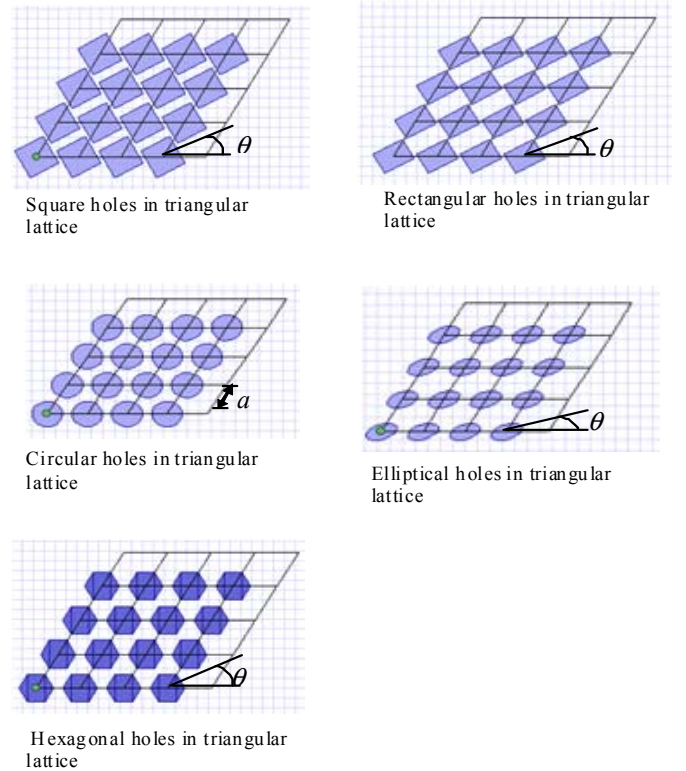


Fig.2 2-D photonic crystal with five different structures along with definition of angle  $\theta$  for non-circular rods

#### IV. NUMERICAL RESULTS AND ANALYSIS

In this simulation, TE polarization has been considered with mesh size,  $32 \times 32$  and tolerance,  $10^{-6}$ . For each structure effect of filling fraction  $f = S_r/S$  (where  $S_r$  is the total cross sectional area of holes within the unit cell of the lattice) and scatterers orientation angle have been observed. Dependency of the band gap width  $\Delta\omega$  with filling fraction for different orientations has been presented. For largest band gap width, gap mid-gap ratio,  $\omega_R = \Delta\omega/\omega_g$  (where  $\omega_g$  is the frequency at the middle of the gap,  $\Delta\omega$  the frequency width of the gap) has been calculated.

##### A. Circular Air Holes in Dielectric Background

For this structure it has been found that for Si, when filling fraction,  $f = 0.702$ , then maximum band gap width,  $(\Delta\omega)_{\max} = 0.1957(2\pi c/a)$  having gap-midgap ratio,  $\omega_R = 46.5\%$  (Fig. 3) while for GaAs the maximum band gap width is,  $(\Delta\omega)_{\max} = 0.187(2\pi c/a)$  with  $\omega_R = 45\%$  at  $f = 0.703$  (Fig. 3).

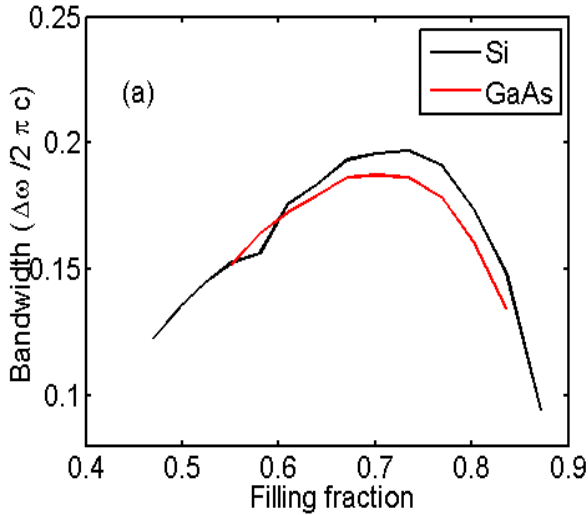


Fig.3 Dependence of band gap width on filling fraction for Si and GaAs having circular air holes in triangular lattice

##### B. Square Air Holes in Dielectric Background

For this structure it has been found that at  $f = 0.649$  and orientation angle,  $\theta = 4^\circ$ , as shown in Fig.4, the maximum band gap width,  $(\Delta\omega)_{\max} = 0.1526(2\pi c/a)$  having gap midgap ratio,  $\omega_R = 39.7\%$  has been obtained in case of GaAs substrate while for Si the maximum band gap width,  $(\Delta\omega)_{\max} = 0.15872(2\pi c/a)$  having gap midgap ratio,  $\omega_R = 42.96\%$  has been obtained at  $f = 0.667$  and  $\theta = 4^\circ$ , as shown in Fig.5.

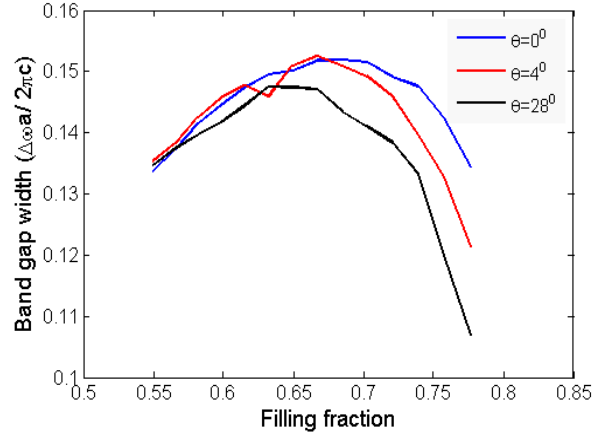


Fig.4 Dependence of band gap width,  $\Delta\omega$  on filling fraction,  $f$  for different orientation,  $\theta = 0^\circ, 4^\circ$  and  $28^\circ$  for square air holes in GaAs.

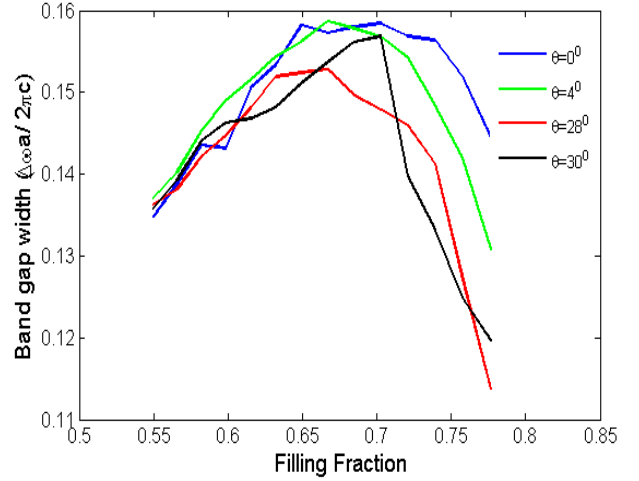


Fig.5 Dependence of band gap width,  $\Delta\omega$  on filling fraction,  $f$  for different orientation,  $\theta = 0^\circ, 4^\circ, 28^\circ$  and  $30^\circ$  for square air holes in Si

##### C. Rectangular Air Holes in Dielectric Background

The minimum band gap has been found in case of rectangular air holes in triangular lattice for both GaAs and Si substrate. At  $f = 0.3547$  and  $\theta = 0^\circ$ , maximum band gap for Si substrate has been obtained. The maximum bandgap width is,  $(\Delta\omega)_{\max} = 0.06134(2\pi c/a)$  and gap-midgap ratio  $\omega_R = 25.2\%$ . In case of GaAs the maximum band gap width,  $(\Delta\omega)_{\max} = 0.0614(2\pi c/a)$  having gap-midgap ratio,  $\omega_R = 24.15\%$  is obtained when filling fraction  $f = 0.312$  and orientation angle  $\theta = 0^\circ$ , as shown in Fig.6.



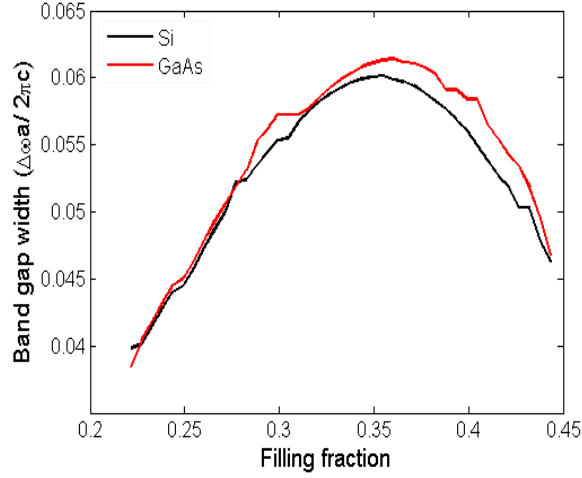


Fig.6 Dependence of band gap width on filling fraction for Si and GaAs having rectangular air holes in triangular lattice, for orientation angle,  $\theta = 0^\circ$

#### D. Elliptical Air Holes in Dielectric Material

In this structure, when both  $f$  and  $\theta$  have been varied, for GaAs the maximum bandgap width  $(\Delta\omega)_{\max} = 0.17779(2\pi c/a)$  and  $\omega_R = 43.47\%$  has been obtained at  $f = 0.731$  and  $\theta = 94^\circ$ , as shown in Fig.7 while for Si the maximum band gap width,  $(\Delta\omega)_{\max} = 0.15813(2\pi c/a)$  and gap-midgap ratio,  $\omega_R = 37.36\%$  have been obtained when  $f = 0.714$  and orientation angle,  $\theta = 94^\circ$ , as shown in Fig.8. In this case, GaAs substrate has maximum band gap width than Si substrate. So elliptical holes are more favoured in GaAs than Si for obtaining maximum band gap.

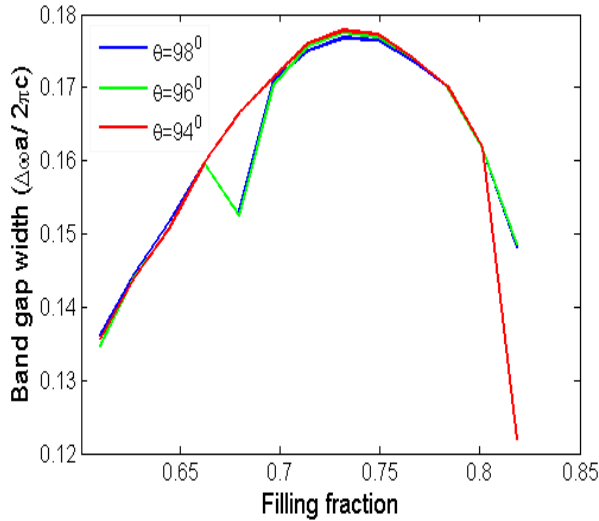


Fig.7 Dependence of band gap width on filling fraction in GaAs having elliptical air holes in triangular lattice, for orientation angle,  $\theta = 94^\circ, 96^\circ$  and  $98^\circ$

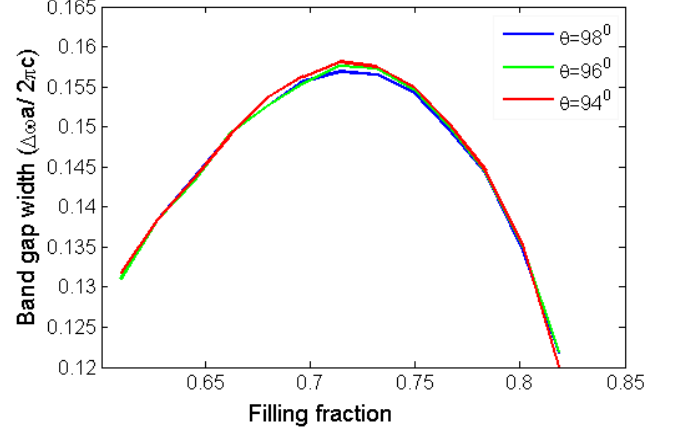


Fig.8 Dependence of band gap width on filling fraction in Si having elliptical air holes in triangular lattice, for orientation angle,  $\theta = 94^\circ, 96^\circ$  and  $98^\circ$

#### E. Hexagonal Air Holes in Dielectric Background

Among all five structures the largest band gap has been found for this structure. For GaAs the maximum band gap width,  $(\Delta\omega)_{\max} = 0.1974(2\pi c/a)$  with gap-midgap ratio,  $\omega_R = 49.37\%$  is obtained at  $f = 0.7203$  and  $\theta = 30^\circ$ , as shown in Fig.9 while for Si when filling fraction is  $f = 0.7203$  and orientation angle,  $\theta = 30^\circ$ , as shown in Fig.10 then there is maximum band gap having band gap width,  $(\Delta\omega)_{\max} = 0.2089(2\pi c/a)$  and gap-midgap ratio,  $\omega_R = 53.75\%$ , as shown in Fig.11. These results have been obtained because PhCs have maximum band gap when symmetry of air holes/dielectric rods is same as the Brillouin Zone (BZ) of the lattice [12]. For triangular lattice the shape of the BZ is hexagonal and hexagonal air holes also have the same symmetry as those of the BZ.

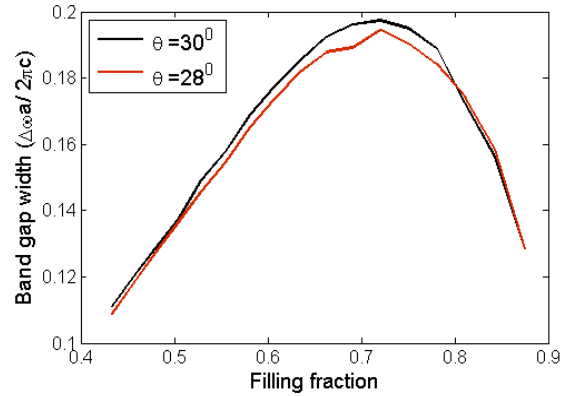


Fig.9 Dependence of band gap width,  $\Delta\omega$  on filling fraction,  $f$  for different orientation,  $\theta = 28^\circ$  and  $\theta = 30^\circ$  for hexagonal holes in GaAs

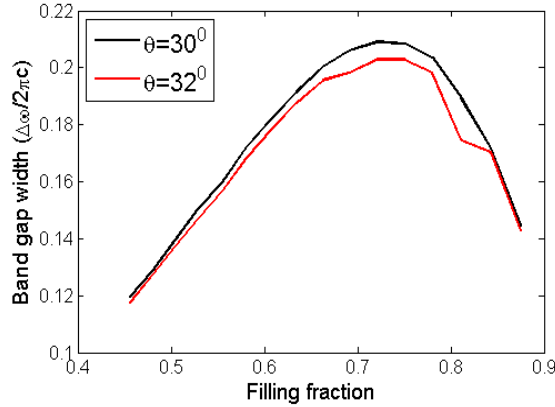


Fig.10 Dependence of band gap width  $\Delta\omega$  on filling fraction  $f$  for different orientation  $\theta = 30^\circ$  and  $\theta = 32^\circ$  for hexagonal holes in Si.

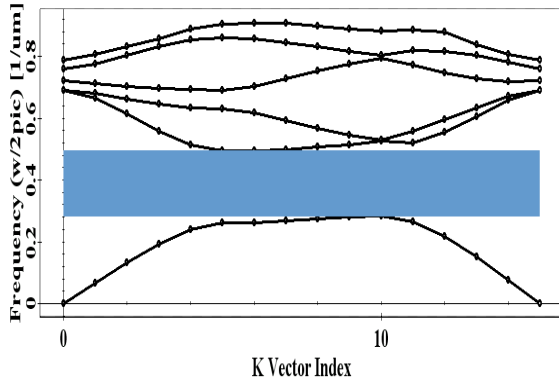


Fig.11 Band structure for TE PBG for filling fraction  $f = 0.7203$  and orientation angle  $\theta=30^\circ$  for hexagonal air holes in Si.

For elliptical air holes, TE bandgap is found to be more in GaAs material as compared to the Si as dielectric substrate. In remaining structures TE bandgap of Si substrate is found to be more than that of GaAs. PhCs with rectangular air holes have the least TE bandgap in both Si and GaAs as compared to the remaining four structures.

## V. CONCLUSIONS

Extensive investigations on the photonic bandgap structures for TE polarization in 2D photonic crystals with triangular lattice for various shapes of holes is performed. It has been found that for TE polarization largest photonic band gap occurs when shape of the Brillouin zone of the triangular

lattice is similar to the shape of the air holes. Therefore, hexagonal holes have the largest photonic band gap. Furthermore, this photonic band gap can be increased by changing the orientation of the holes. Holes having lower symmetry than that of Brillouin zone of triangular lattice exhibits smaller photonic bandgap for TE polarization. These results can prove useful in designing of polarization sensitive photonic bandgap devices. A TE-pass polarization filter can be designed for larger range of wavelengths using above mentioned PhC.

## VI. REFERENCES

- [1] J. D. Joannopolous, S. G. Johnson, J. Winn, and R. Meade, *Photonic Crystals: Molding the Flow of Light*, 4<sup>th</sup> ed, Princeton University Press, New Jersey, 2008.
- [2] H. Benisty, C. Weisbuch, D. Labilloy, M. Rattier, J. M. C. Smith, M. Richard, R. Houdre, U. Oesterle, C. Jouanin and D. Cassagne, "Optical and confinement properties of two dimensional photonic crystals," *J. Lightwave Technol.*, vol. 17, pp. 2063-2077, 1999.
- [3] A. A. Erchak, J. D. Ripin, S. Fan, G. S. I. Etrich, J. D. Joannopoulos, L. A. Kolodziejski and P. Erich, "Increased light extraction from a light-emitting diode using a two-dimensional photonic crystal," *IEEE Tech. digest of Quantum Electronics and Laser Science Conference (QELS-2000)*, pp.43-44, 2000.
- [4] K. Busch, S. Lolkes, R. B. Wehrspohn, and H. Foll, *Photonic Crystals: Advances in Design, Fabrication and Characterization*, 1<sup>st</sup> ed, Wiley-VCH, Weinheim, Germany, 2004.
- [5] M. A. Habib, M. S. Khan, C. G. S. Al-Amin, I. Azad, S. M. Ullah and S. Rafique, "Complete bandgap in two dimensional photonic crystals with square bravais lattice," *IEEE Tech. digest of International Conference on Photonics (ICP)*, pp. 1-5, 2010.
- [6] L. C. Andreani and D. Gerace, "Photonic-crystal slabs with a triangular lattice of triangular holes investigated using a guided-mode expansion method," *Phys. Rev. B*, vol. 73, 235114, 2006.
- [7] J. D. Joannopolous, P. R Villeneuve, and S. Fan, "Photonic Crystals: Putting a new twist on light," *Nature*, vol. 386, pp. 143-149, 1997.
- [8] Y. Kalra and R. K. Sinha, "Photonic bandgap engineering in 2D photonic crystals," *Pramana*, vol. 67, pp. 1157-1164, 2006.
- [9] Y. H.Y. Ryu, G. H. G. Park and H. H. Yong, "Two dimensional photonic crystal semiconductor lasers: computational design, fabrication, and characterization," *IEEE Journal of Selected Topics in Quantum Electronics*, vol. 8, pp. 891-908, 2002.
- [10] A.V. Dyogtyev, I. A. Sukhoivanov, and R. M. De La Rue, "Photonic band-gap maps for different two dimensional periodic photonic crystal structures," *J. Appl. Physics*, vol. 107, pp. 013081-013087, 2010.
- [11] R. Wang, X. H. Wang, B. Y. Gu, G. Z. Yang, "Effect of shapes and orientation of scatterers and lattice symmetries on the photonic bandgap in two dimensional photonic crystals," *J. Appl. physics*, vol. 90, pp. 4307-4313, 2001.
- [12] M. A. Habib, M. Z. U. Suja, S. B. Bhasar and S. M. Ullah, "Bandgap calculation of a 2-D photonic crystal and its application towards a thin film solar cell," *Photonics Letters of Poland*, vol. 3, pp. 162-164, 2011.

## Influence on ferromagnetic resonance signal of perpendicular magnetic anisotropic Co/Pt bilayer thin film due to microwave induced spin-Hall effect

Saood Ahmad, Jyoti Shah, Nitin K. Puri, P. S. Negi, and R. K. Kotnala

Citation: *Appl. Phys. Lett.* **103**, 032405 (2013); doi: 10.1063/1.4813833

View online: <http://dx.doi.org/10.1063/1.4813833>

View Table of Contents: <http://apl.aip.org/resource/1/APPLAB/v103/i3>

Published by the AIP Publishing LLC.

---

### Additional information on *Appl. Phys. Lett.*

Journal Homepage: <http://apl.aip.org/>

Journal Information: [http://apl.aip.org/about/about\\_the\\_journal](http://apl.aip.org/about/about_the_journal)

Top downloads: [http://apl.aip.org/features/most\\_downloaded](http://apl.aip.org/features/most_downloaded)

Information for Authors: <http://apl.aip.org/authors>

## ADVERTISEMENT

The advertisement features a background of dynamic blue water splashes. On the left, the text 'Recirculation Pumps' is written in red, followed by 'with Speed Control' in a smaller black font. Below this, 'Laser Cooling / Chillers' and 'Brushless DC • Magnetic Drive' are listed in black. The website 'www.GRIpumps.com/Integrity' is displayed in black. On the right, there is a black and white image of a small, cylindrical pump unit. In the top right corner, the 'GRI PUMPS' logo is shown in blue, with 'A GORMAN-RUPP COMPANY' written in small black letters underneath.

# Influence on ferromagnetic resonance signal of perpendicular magnetic anisotropic Co/Pt bilayer thin film due to microwave induced spin-Hall effect

Saood Ahmad,<sup>1</sup> Jyoti Shah,<sup>1</sup> Nitin K. Puri,<sup>2</sup> P. S. Negi,<sup>1</sup> and R. K. Kotnala<sup>1,a)</sup>

<sup>1</sup>CSIR-National Physical Laboratory, New Delhi 110012, India

<sup>2</sup>Department of Applied Physics, Delhi Technological University, Delhi, India

(Received 22 May 2013; accepted 28 June 2013; published online 16 July 2013)

Microwave induced spin-Hall effect has been investigated in sputtered Co/Pt bilayer thin film for its application in the field of spintronics. Measurements were carried out in the frequency range from 0.1 to 10.0 GHz at 10 mW power level with a sweeping magnetic field up to 0.2 T. The maximum dc voltage measured was 5.78  $\mu$ V at 0.1 GHz in perpendicular applied magnetic field on the bilayer film. The direction of magnetic field, frequency, and power level influence the ferromagnetic resonance signal. Measurements confirm lower effective spin pumping due to a weak perpendicular anisotropy in the film. © 2013 AIP Publishing LLC. [<http://dx.doi.org/10.1063/1.4813833>]

Spin Hall Effect (SHE) is an important part of spintronics, which was first predicted in 1971 by D'yakonov and Perel.<sup>1</sup> The phenomenological theory with impurity scattering was developed by Hirsch<sup>2</sup> and further extended to the diffusive transport regime by Zhang.<sup>3</sup> Literature survey reveals that progress towards understanding and implementing the SHE in metallic heterostructures is gaining momentum as more researchers globally begin to address the relevant changes of spintronics.<sup>4</sup> Intensive studies on the Co/Pt thin film have been carried out in the recent years. Reported work shows that magnetization of Co/Pt multilayer film decreases with increase in Pt layer thickness.<sup>5,6</sup> Nakayama<sup>7</sup> showed that the maximum microwave energy is absorbed by the Co/Pt with 10 nm thickness, resulting in significant dc voltage output across the bilayer thin film as compared to 75 nm layer thickness. Due to microwave induced SHE in Co/Pt bilayer thin film spin, current is generated in Pt and injected to Co layer, which leads to the oscillation of bilayer resistance.<sup>8–10</sup> In the present work, SHE voltage dependence on microwave frequency, power level, sweeping dc magnetic field, and its direction with respect to film surface have been studied. The experimental results of microwave induced SHE and its frequency and amplitude dependence in Co/Pt bilayer thin film have been reported at room temperature.

Co/Pt film was deposited on a silicon (Si 100) substrate using RF sputtering system with an optimized gas pressure, deposition rates, etc. The platinum layer was first sputtered on silicon substrate, and subsequently cobalt layer was deposited on Pt layer followed by annealing. The layers thicknesses were controlled during deposition, and the sample was cut in a dimension of 1.0 cm  $\times$  0.8 cm. Co/Pt film comprising 50 nm thick magnetic Co layer and a 60 nm thick Pt layer as illustrated in Fig. 1(a). The schematic illustration of film for electrical measurements is shown in Fig. 1(b). In Pt layer, the SHE converts electric current ( $J_c$ ) into spin current ( $J_s$ ), which propagates in to Co through the interface. The generation of dc voltage in magnetic heterostructures

under ferromagnetic resonance (FMR) excitation has been reported.<sup>8–13</sup> The experimental setup we have used to demonstrate microwave induced SHE in Co/Pt film is shown in Fig. 1, which includes microwave source, bias tee, nanovoltmeter, and electromagnet along with measurement jig. The measurements were carried out using R&S SMR-27 microwave source, Keithley 2182A precision nanovoltmeter at 10 mW power level from 0.1 GHz to 10 GHz along with the sweeping dc magnetic field up to 0.2 T. Thin film was mounted on a specially designed measurement jig, which was simulated for S parameters to have a good impedance match. Microwave power was excited using a bias tee in the presence of a magnetic field and measured the FMR voltage spectra across the film. The spin polarization of the spin current was directed along  $J_c \times n$ ,<sup>2</sup> where “n” is the normal vector to the interface plane. During measurements, external magnetic field ( $H_{dc}$ ) was applied along and perpendicular direction separately to the bilayer film. All the measurements were performed at room temperature.

Characterization of the Co/Pt film has been done using X-ray diffraction (XRD) and scanning electron microscopy (SEM). Phase formation of Co/Pt film was investigated by XRD analysis using Bruker AXS D8 Advanced powder X-ray diffractometer at room temperature with Cu K $\alpha$  radiation (40 kV, 35 mA), scanned for  $2\theta$  from 10° to 80° with a step size of 0.001°/s. The XRD data have been shown in Fig. 2(b). Peaks corresponding to  $\sim 38^\circ$  and  $\sim 44^\circ$  are assigned to Pt and Co, respectively. The high intensity peak observed at  $\sim 69^\circ$  has been assigned to Si (100) substrate. XRD measurement has shown that a bilayer film has a well defined crystalline structure. The thin film morphology was characterized by SEM. The SEM image is shown as an inset in Fig. 2, which confirms good quality of film. The saturation magnetization of Co/Pt film was measured as  $0.55 \times 10^3$  emu/cm<sup>3</sup> and  $0.32 \times 10^3$  emu/cm<sup>3</sup> when the applied magnetic field was perpendicular and parallel, respectively, using Vibrating Sample Magnetometer (VSM). Magnetic moment of the film in perpendicular direction with field begins to saturate at 0.2 T. This confirms that the film is perpendicularly magnetic anisotropic as shown in Fig. 3. However, magnetization value for the grown film is less than the bulk Co value. It may be due to magnetic anisotropy and magnetic

<sup>a)</sup>Author to whom correspondence should be addressed. Electronic addresses: rkkotnala@nplindia.org and rkkotnala@gmail.com. Tel.: 011-45608599. Fax: 011-45609310.

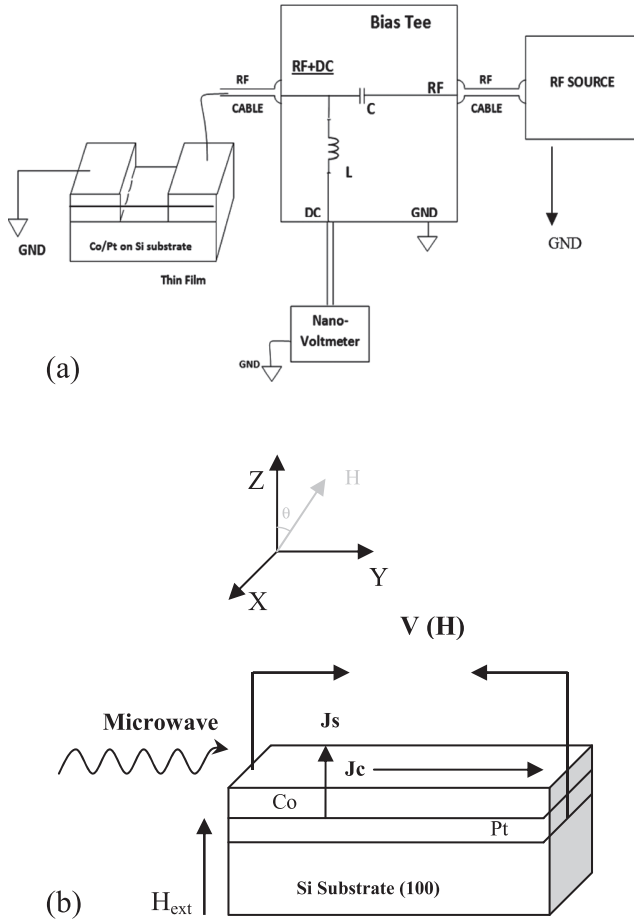


FIG. 1. (a) Schematic of the FMR measurement setup, (b) schematic illustration of bilayer thin film on Si substrate.

inhomogeneity at the interface of bilayer thin film. Cobalt film magnetization in our sample is less than the bulk cobalt, may be due to simultaneous in plane and perpendicular magnetization of the film. Also, an additional orbital magnetic moment is caused by s-d hybridization at Co/Pt interface, which is also responsible for perpendicular anisotropy.<sup>14</sup> The flow of alternating current through a bilayer thin film generates an oscillating transverse spin current in Pt layer, and the

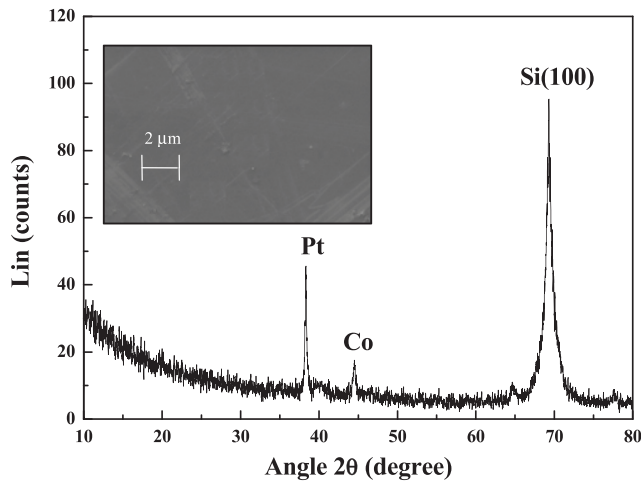


FIG. 2. X-ray diffraction pattern of Co/Pt bilayer thin film deposited on Si (100) substrate and SEM image of Co/Pt bilayer thin film (inset).

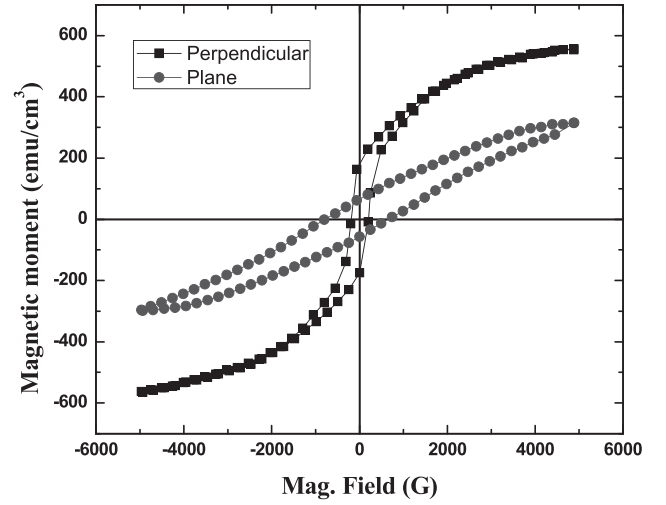


FIG. 3. MH curve of Co/Pt bilayer thin film using VSM when applied magnetic field is along and perpendicular to the sample.

resultant transfer of spin angular momentum to the other layer induces resonance dynamics, which leads to an oscillation of the bilayer resistance. The dc voltage signal developed across the film is due to mixing of microwave power and the oscillating resistance. The injected charge current is converted into spin current, which gives rise to an electrical potential difference across the sample. The dc voltage ( $V$ ) was measured transversely on the edges of the film as a function of dc magnetic field ( $H_{dc}$ ) shown in Fig. 1(b). The magnitude of spin-Hall voltage induced by microwave based ferromagnetic resonance depends on the absorption intensity of the film. Maximum dc voltage generated across the film is at ferromagnetic resonance condition. The model equation for the voltage developed across the thin film as Eq. (1) has been estimated by Lorentzian model.<sup>15</sup> According to this model, there are three important parameters dc magnetic field ( $H_{dc}$ ), resonant field ( $H_r$ ), and the FMR linewidth ( $\Delta H$ ). All measurements  $V(H_{dc})$  were performed under the standard controlled environment

$$V(H_{dc}) = \frac{\sqrt{2}C}{2 \left[ (H_{dc} - H_r)^2 + \left( \frac{\Delta H}{2} \right)^2 \right]^{\frac{1}{2}}}, \quad (1)$$

where  $C$  is a constant at fixed microwave frequency and power level, however, value of  $C$  depends upon applied microwave current ( $I_{rf}$ ), resistance of thin film sample ( $R_s$ ), Oersted field due to charge current density ( $h_{rf}$ ), and magnetic induction in thin film due to rf which is constant for a fixed microwave frequency and power level ( $A$ ), whereas  $C = I_{rf} * R_s * h_{rf} * A$ .

The derivative of Eq. (1) with respect to the dc magnetic field  $H_{dc}$  gives the FMR absorption slope using Eq. (2). The FMR voltage spectra ( $dV/dH_{dc}$ ) assumed to be Lorentzian in form is consistent with our experimental results obtained in Co/Pt film<sup>16</sup>

$$\frac{dV}{dH_{dc}} = C \frac{-(H_{dc} - H_r)}{\left[ (H_{dc} - H_r)^2 + \left( \frac{\Delta H}{2} \right)^2 \right]^{\frac{3}{2}}}. \quad (2)$$



Resonance is the absorption of microwave power by a magnetic film, measured as a function of the applied sweeping dc magnetic field. The FMR curves<sup>17</sup> associated with Eq. (2) at different frequencies are shown in Fig. 4. It is reported that amplitude and shape of FMR voltage spectra with respect to dc magnetic field vary with angle of orientation of magnetic field.<sup>18–22</sup> Microwave induced SHE measurements were investigated on Co/Pt film using measurement setup shown in Fig. 1. The FMR signal was excited by a microwave signal, while applying sweeping dc magnetic field along and perpendicular to the film plane separately. Using Eq. (2), the FMR spectra of Co/Pt film at 0.1, 0.5, and 1.0 GHz has been shown in Fig. 4, which is field derivative of absorbed microwave power. The magnitude of dc voltage generated across bilayer thin film was  $5.78 \mu\text{V}$  at 0.1 GHz,  $1.36 \mu\text{V}$  at 0.5 GHz, and  $0.83 \mu\text{V}$  at 1.0 GHz for an incident microwave power of 10 mW corresponding to sweeping perpendicular magnetic field up to 0.2 T. The SHE voltage obtained is slightly lower than that reported by other groups.<sup>8–11</sup> This may be due to less effective spin pumping by a weak magnetic perpendicular anisotropy present in the film. Spin pumping depends upon the magnetic dynamics of a ferromagnetic film. It would be more efficient provided thin film is highly perpendicularly magnetic anisotropic. Our magnetic measurements exhibit Co film that is not strongly perpendicularly magnetic anisotropic (Fig. 3) as it possesses magnetization along and perpendicular to the film plane. Therefore, a weak perpendicular magnetic anisotropy of film aligns interfacial Pt spin parallel to Co spin by a weak exchange interaction, resulting in low effective spin pumping. Besides this, presence of magnetic inhomogeneity at interface also contributes for weak spin polarization which is

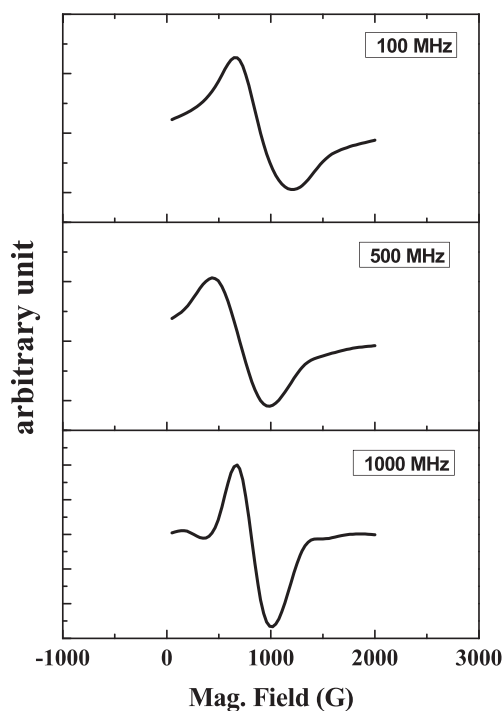


FIG. 4. FMR absorption spectra (derivative) of output voltage signal due to microwave induced SHE in Co/Pt bilayer thin film under 10 mW microwave excitation with respect to dc magnetic field at 0.1 GHz, 0.5 GHz, and 1.0 GHz.

confirmed by broadening of FMR line width as shown in Fig. 4. Spin Hall voltage developed across film is due to spin-orbit interaction arising from relativistic theory of electron positron system. Spin carrying electrons are scattered asymmetrically by a central potential to create a spin polarization in an initially un-polarized beam of electrons. In this, spherically symmetrical impurity conserves orbital and spin angular momentum. The collision of electrons with impurities pumps momentum in transverse direction, and spin electric field is generated due to spin accumulation at the lateral edges of the thin film. Therefore, applied microwave signal to a bilayer thin film generates an oscillating transverse spin current in Pt layer, and resultant transfer of spin angular momentum to Co layer induces resonance dynamics resulting in oscillation of bilayer resistance. The magnitude of FMR field and shape of FMR spectra depend upon the magnetic field direction, magnetic anisotropy, magnetic inhomogeneity, and quality of used thin film. Magnetic inhomogeneity induces FMR line width broadening and magnetic relaxation. In our case, magnetic relaxation might be due to phonon or defect through spin-orbit coupling at Co/Pt interface. Therefore, using Eq. (2), broadening of FMR line width seen in the experimental results (Fig. 4) is due to magnetic inhomogeneity, besides intrinsic Gilbert damping effect. Gilbert damping factor ( $G$ ) has been calculated using the relation  $G = \alpha\gamma M_s$ , where  $\alpha$  is damping constant,  $\gamma$  is gyromagnetic ratio, and  $M_s$  is the saturation magnetization of thin film. We found that in our film the value of Gilbert damping factor ( $G$ ) is  $4.8 \times 10^8 \text{ s}^{-1}$  compared to the reported values of  $4.5 \times 10^8 \text{ s}^{-1}$  (Ref. 23) for Co thin film,  $3.5 \times 10^8 \text{ s}^{-1}$  reported for FeCo film,  $2.4 \times 10^8 \text{ s}^{-1}$  for CoNi film,<sup>24</sup> and  $3.0 \times 10^8 \text{ s}^{-1}$  (Ref. 25) for epitaxial Co film. It has been reported that magnetic damping of conduction electrons in non-magnetic metals is mainly caused by spin-orbit interaction.<sup>26–29</sup> Orientation of film was changed to parallel with respect to magnetic field, and measurements were taken at 1.0 GHz. The intensity of output signal was significant due to magnetization remains in the plane but resonance field and peak to peak line width were difficult to obtain. When external magnetic field was inverted, the generated dc voltage was also reversed. It has been reported that variation in output voltage spectra for a bilayer thin film at FMR condition depends on precision cone angle ( $\theta$ ) and the angle of applied magnetic field ( $\alpha$ ) with respect to the central line of thin film plane ( $V_{\text{SHE}} \propto \sin \alpha \sin^2 \theta$ ). As the applied magnetic field approaches to resonance condition, there is a change in voltage given by  $\Delta V = \Delta R_m * I_{\text{rf}} * \sin^2 \theta$ , where  $\Delta R_m$  is the change in magnetoresistance at the bilayer interface and  $I_{\text{rf}}$  is the applied microwave current.<sup>30</sup> To interpret experimentally observed data as shown in Fig. 4, investigations were carried out to study microwave induced SHE signal as a function of microwave power and frequency in Co/Pt film. For power level dependence, output of microwave source was swept from 1 mW to 10 mW. Experimental results show dc voltage generated due to SHE across the Co/Pt film increases linearly with respect to the microwave power level. The linear fitting of the experimental data is shown in Fig. 5 with red colour. The frequency dependence of SHE voltage was conducted from 0.1 GHz to 10 GHz with respect to applied dc magnetic field at 0.05 T, 0.1 T, and 0.15 T. The output signal was

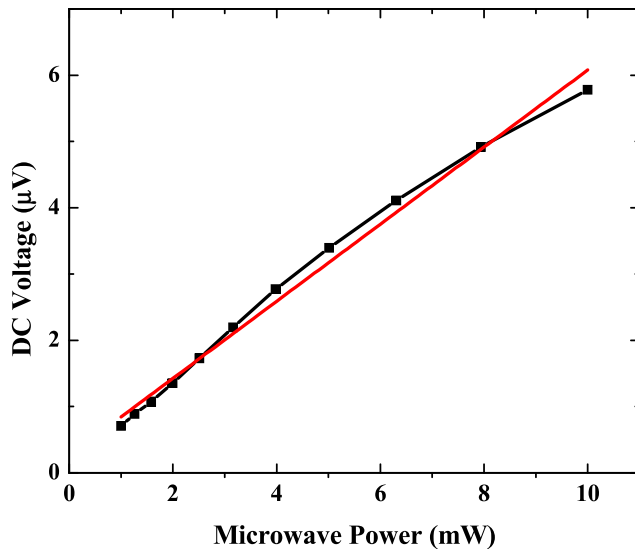


FIG. 5. Linear dependence of output dc voltage as a function of incident microwave power in Co/Pt bilayer thin film.

maximum at 0.1 GHz and then decreases linearly up to 2.0 GHz after which it remains almost constant up to 10 GHz. Fig. 6 confirms that output voltage signal depends on microwave frequency and applied dc magnetic field. The intensity of a microwave signal absorbed by thin film depends upon the power level. As microwave signal increases, there will be more charge current ( $J_c$ ) flowing in thin film, resulting in additional spin current ( $J_s$ ). Their relationship is given by well reported equation  $J_c = \theta_{\text{SHE}} (2e/\hbar) \times J_s$ . It has been reported that with increase in frequency the transverse voltage decreases<sup>8,31</sup> due to phase shift of the reflected signal with respect to applied signal, resulting decrease in oscillating resistance at the interface. It confirms dependence of dc voltage signal generated as a function of microwave signal and applied dc magnetic field. Furthermore, our observed values for output voltage spectra and its shape are in good agreement with reported values.

The study of FMR signals due to microwave induced SHE has paved way to understanding of physical and

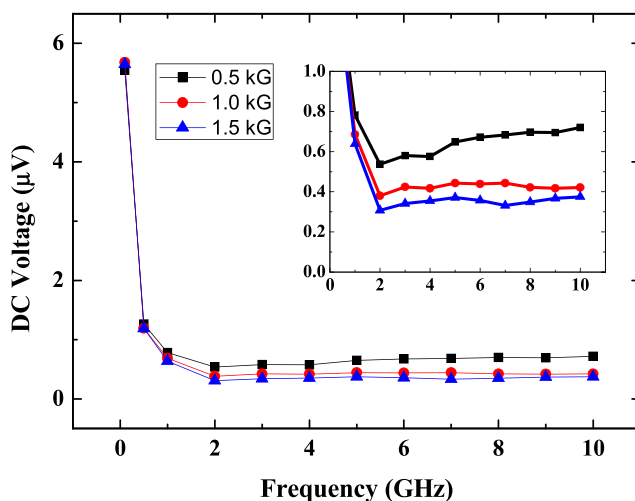


FIG. 6. Microwave frequency dependence of dc voltage output at fixed dc magnetic field of 0.5 kG, 1.0 kG, and 1.5 kG at 10 mW microwave power excitation in Co/Pt bilayer thin film and its zoom part (inset).

electrical mechanisms leading to this effect. It has been observed that FMR signal of perpendicular magnetic anisotropic Co/Pt bilayer thin film increases and attains maximum at resonance followed by decrease with respect to dc magnetic field. The dependence of FMR signal on orientation of film with applied magnetic field indicates that electromotive force is dominated mainly by microwave induced SHE. It has been demonstrated that dc voltage developed across the bilayer thin film along with FMR measurements yields the correlation of spin-Hall voltage signal with microwave frequency, power, and orientation of film with applied dc magnetic field. The maximum value of SHE signal exhibits a linear dependence of incident microwave power and is consistent with spin pumping theory. These results of Co/Pt bilayer thin film will be useful for understanding magnetic dynamics in spintronic devices used for memory and microwave signal applications.

A special thanks to Professor R. C. Budhani, Director-National Physical Laboratory, India, for his kind support and motivation to carry out this work.

<sup>1</sup>M. I. Dyakonov and V. I. Perel, *Phys. Lett.* **35**, 459 (1971).

<sup>2</sup>J. E. Hirsch, *Phys. Rev. Lett.* **83**, 1834 (1999).

<sup>3</sup>S. Zhang, *Phys. Rev. Lett.* **85**, 393 (2000).

<sup>4</sup>S. A. Wolf, D. D. Awschalom, R. A. Buhrman, J. M. Daughton, S. Von Molnar, M. L. Roukes, A. Y. Chtchelkanova, and D. M. Treger, *Science* **294**, 1488 (2001).

<sup>5</sup>F. D. Czeschka, L. Dreher, M. S. Brandt, M. Weiler, M. Weiler, M. Althammer, I.-M. Imort, G. Reiss, A. Thomas, W. Schoch, W. Limmer, H. Huebl, R. Gross, and S. T. B. Goennenwein, *Phys. Rev. Lett.* **107**, 046601 (2011).

<sup>6</sup>T. Yoshino, K. Ando, K. Harii, H. Nakayama, Y. Kajiwara, and E. Saitoh, *Appl. Phys. Lett.* **98**, 132503 (2011).

<sup>7</sup>H. Nakayama, K. Ando, K. Harii, Y. Fujikawa, Y. Kajiwara, T. Yoshino, and E. Saitoh, *J. Phys.: Conf. Ser.* **266**, 012100 (2011).

<sup>8</sup>L. Liu, T. Moriyama, D. C. Ralph, and R. A. Buhrman, *Phys. Rev. Lett.* **106**, 036601 (2011).

<sup>9</sup>O. Mosendz, J. E. Pearson, F. Y. Fradin, G. E. W. Bauer, S. D. Bader, and A. Hoffmann, *Phys. Rev. Lett.* **104**, 046601 (2010).

<sup>10</sup>K. Ando, S. Takahashi, K. Harii, K. Sasage, J. Ieda, S. Maekawa, and E. Saitoh, *Phys. Rev. Lett.* **101**, 036601 (2008).

<sup>11</sup>T. Kimura, Y. Otani, T. Sato, S. Takahashi, and S. Maekawa, *Phys. Rev. Lett.* **98**, 156601 (2007).

<sup>12</sup>K. Harii, T. An, Y. Kajiwara, K. Ando, H. Nakayama, T. Yoshino, and E. Saitoh, *J. Appl. Phys.* **109**, 116105 (2011).

<sup>13</sup>L. H. Vilela-Leão, G. L. da Silva, C. Salvador, S. M. Rezende, and A. Azevedo, *J. Appl. Phys.* **109**, 07C910 (2011).

<sup>14</sup>N. Nakajima, T. Koide, T. Shidara, H. Miyauchi, H. Fukutani, A. Fujimori, K. Iio, T. Katayama, M. Niyvlt, and Y. Suzuki, *Phys. Rev. Lett.* **81**, 5229 (1998).

<sup>15</sup>C. P. Slichter, *Principles of Magnetic Resonance: With Examples from Solid State Physics* (Harper & Row, New York, 1963), Chap. 2.

<sup>16</sup>E. Saitoh, M. Ueda, and H. Miyajima, *Appl. Phys. Lett.* **88**, 182509 (2006).

<sup>17</sup>J. N. Chazalviel and I. Solomon, *Phys. Rev. Lett.* **29**, 1676 (1972).

<sup>18</sup>H. Y. Inoue, K. Harii, K. Ando, K. Sasage, and E. Saitoh, *J. Appl. Phys.* **102**, 083915 (2007).

<sup>19</sup>G. D. Fuchs, J. C. Shankey, V. S. Pribragi, L. Qian, P. M. Braganca, A. G. F. Garcia, E. M. Ryan, Z.-P. Li, O. Ozatay, D. C. Ralph, and R. A. Buhrman, *Appl. Phys. Lett.* **91**, 062507 (2007).

<sup>20</sup>S. O. Valenzuela, *J. Appl. Phys.* **101**, 09B103 (2007).

<sup>21</sup>J. C. Sankey, P. M. Braganca, A. G. F. Garcia, I. N. Krivorotov, R. A. Buhrman, and D. C. Ralph, *Phys. Rev. Lett.* **96**, 227601 (2006).

<sup>22</sup>K. Harii, K. Ando, H. Y. Inoue, K. Sasage, and E. Saitoh, *J. Appl. Phys.* **103**, 07F311 (2008).

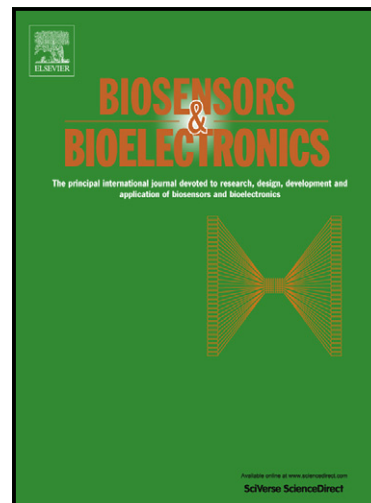
<sup>23</sup>S. J. Lee, C. C. Tsai, H. Cho, M. Seo, T. Eom, W. Nam, Y. P. Lee, and J. B. Ketterson, *J. Appl. Phys.* **106**, 063922 (2009).



- <sup>24</sup>M. Oogane, T. Wakitani, S. Yakata, R. Yilgin, Y. Ando, A. Sakuma, and T. Miyazaki, *Jpn. J. Appl. Phys.* **45**, 3889 (2006).
- <sup>25</sup>J. Pelzl, R. Meckenstock, D. Spoddig, F. Schreiber, J. Pflaum, and Z. Frait, *J. Phys.: Condens. Matter* **15**, S451 (2003).
- <sup>26</sup>S.-J. Yuan, K. Xu, L.-M. Yu, S.-X. Cao, C. Jing, and J.-C. Zhang, *J. Appl. Phys.* **101**, 113915 (2007).
- <sup>27</sup>S. O. Valenzuela and M. Tinkham, *Nature* **442**, 04937 (2006).
- <sup>28</sup>A. Azevedo, L. H. Vilela Leao, R. L. Rodriguez-Suarez, A. B. Oliveira, and S. M. Rezende, *J. Appl. Phys.* **97**, 10C715 (2005).
- <sup>29</sup>Y. Tserkovnyak and A. Brataas, *Phys. Rev. Lett.* **88**, 117601 (2002).
- <sup>30</sup>O. Mosendz, V. Vlaminc, J. E. Pearson, F. Y. Fradin, G. E. W. Bauer, S. D. Bader, and A. Hoffmann, *Phys. Rev. B* **82**, 214403 (2010).
- <sup>31</sup>Y. V. Pershin and M. Di Ventra, *Phys. Rev. B* **79**, 153307 (2009).

Magnesium oxide grafted carbon nanotubes based Impedimetric genosensor for biomedical application

Manoj Kumar Patel, Md.Azahar Ali, Saurabh Srivastava, Ved Varun Agrawal, S.G. Ansari, Banshi D. Malhotra



[www.elsevier.com/locate/bios](http://www.elsevier.com/locate/bios)

PII: S0956-5663(13)00476-4  
DOI: <http://dx.doi.org/10.1016/j.bios.2013.07.006>  
Reference: BIOS6062

To appear in: *Biosensors and Bioelectronics*

Received date: 19 May 2013

Revised date: 2 July 2013

Accepted date: 2 July 2013

Cite this article as: Manoj Kumar Patel, Md.Azahar Ali, Saurabh Srivastava, Ved Varun Agrawal, S.G. Ansari, Banshi D. Malhotra, Magnesium oxide grafted carbon nanotubes based Impedimetric genosensor for biomedical application, *Biosensors and Bioelectronics*, <http://dx.doi.org/10.1016/j.bios.2013.07.006>

This is a PDF file of an unedited manuscript that has been accepted for publication. As a service to our customers we are providing this early version of the manuscript. The manuscript will undergo copyediting, typesetting, and review of the resulting galley proof before it is published in its final citable form. Please note that during the production process errors may be discovered which could affect the content, and all legal disclaimers that apply to the journal pertain.

## Magnesium oxide grafted carbon nanotubes based Impedimetric genosensor for biomedical application

Manoj Kumar Patel<sup>a,b</sup>, Md. Azahar Ali<sup>a</sup>, Saurabh Srivastava<sup>a</sup>, Ved Varun Agrawal<sup>a,\*</sup>, S. G. Ansari<sup>b,\*\*</sup>, Bansi D. Malhotra<sup>c,a,d,\*\*\*</sup>

<sup>a</sup>Department of Science and Technology Centre on Biomolecular Electronics, Biomedical Instrumentation Section, National Physical Laboratory (CSIR), Dr. K. S. Krishnan Marg, New Delhi, 110 012, India

<sup>b</sup>Centre for Interdisciplinary Research in Basic Sciences, Jamia Millia Islamia, New Delhi, 110 025, India

<sup>c</sup>Department of Biotechnology, Delhi Technological University, Main Bawana Road, Delhi, 110 042, India

<sup>d</sup>Centre for NanoBioengineering & Spintronics, Chungnam National University, 220 Gung-Dong, Yuseong-Gu, Daejeon 305-764, Korea.

### ABSTRACT

Nanostructured magnesium oxide (size < 10 nm) grafted carboxyl (COOH) functionalized multi-walled carbon nanotubes (nMgO-cMWCNTs) deposited electrophoretically onto indium tin oxide (ITO) coated glass electrode has been utilized for *Vibrio cholerae* detection. Aminated 23 bases single stranded DNA (NH<sub>2</sub>-ssDNA) probe sequence (O1 gene) of *V. cholerae* has been covalently functionalized onto nMgO-cMWCNTs/ITO electrode surface using EDC-NHS chemistry. This DNA functionalized MgO grafted cMWCNTs electrode has been characterized using X-ray photoelectron (XPS), Fourier transform infrared spectroscopy (FT-IR), scanning electron microscopy (SEM), transmission electron microscopy (TEM) and electrochemical techniques. The results of XPS studies reveal that the sufficient O-C=O groups present in nMgO-cMWCNTs surface are utilized for DNA binding. The results of hybridization studies have been conducted with fragmented target DNA (ftDNA) of *V. cholerae* using electrochemical impedance spectroscopy (EIS) reveal sensitivity as 3.87  $\Omega$  ng<sup>-1</sup> cm<sup>-2</sup> and detection limit of ~21.70 ng  $\mu$ L<sup>-1</sup> in the linear range of 100 to 500 ng  $\mu$ L<sup>-1</sup> and shows the stability of about 120 days. The proposed DNA functionalized nMgO-cMWCNTs nanomatrix provides a novel impedimetric platform for the fabrication of a compact genosensor device for biomedical application.

**Keywords:** DNA Functionalization, Genosensor, Impedance Spectroscopy, Magnesium Oxide, Multiwalled Carbon Nanotubes, *Vibrio cholerae*

Corresponding Authors: E-mail: bansi.malhotra@gmail.com (B.D. Malhotra, Tel: +911127294668, Fax: +911127871023); saansari@jmi.ac.in (S.G.Ansari), ved.varun@gmail.com (Ved Varun Agrawal).

## 1. Introduction

The bio-functionalization of nanostructured metal oxides has been predicted to have a great potential for fabrication of label-free biomedical devices (Abu-Salah et al. 2010). Nanostructured magnesium oxide (nMgO) is known to provide high surface to volume ratio, tunable size, high electron transfer capability, biocompatibility, chemical inertness and affinity groups containing oxygen that can be advantageous for biomedical application (Umar et al., 2009). The small positive electron affinity of 0.85 eV and high isoelectric point (IEP:  $\sim 12$ ) of MgO can be useful for direct immobilization of DNA having low IEP of  $\sim 4.0$  without any chemical modification (Ferrari et al., 2000). However, DNA functionalized MgO has limited conductivity that can affect the biosensor performance. Recently, CNTs have been recognized as a promising template for metal oxides grafting to develop highly sensitive biosensing devices (Gooding, 2005). Therefore, to overcome the limitation of low conductivity of nMgO, it can be grafted onto multi-walled carbon nanotubes (MWCNTs) surface to achieve better conduction path, which may result in increased electron transportation (Liu et al., 2012).

The nucleic acid molecules such as DNA, RNA, PNA and aptamer functionalized CNTs surface can modify the electronic properties of CNTs for genosensor fabrication (Kong et al., 2011). In this context, CNTs can improve electro-activity of biomolecules leading towards fast electron transfer. CNTs are known to be exciting material due to their flexibility, redox mediator and enhanced electrical conduction for desired bio-electrochemical reactions. However, the poor solubility of CNTs in an aqueous media continues to be a concern. The chemical treatment of CNTs sidewalls may perhaps provide an additional impetus towards DNA functionalization. Covalent functionalization using different active moieties, such as hydroxyl and carboxyl groups via chemical treatment or fluorination has been found to result in increased dispersion of CNTs in a

polar solvent; enhancing the activity of the immobilized biomolecules (Shim et al., 2002; Zhao et al., 2004). In addition, 1-D properties of CNTs make them excellent carrier for loading desired biomolecules including nucleic acids for amplification of the electronic signals. In particular, MWCNTs may act as nanoelectrodes that can be integrated with biomolecules to communicate with the outside environment by electron transportation. Thus, electronic properties of CNTs can perhaps be advantageous for chemical functionalization with a moiety and altering the structure whose intrinsic properties are electrically tunable. In this context, nMgO can play an important role to reduce dispersion or agglomeration of MWCNTs.

Recent advances in nucleic acid probe based biosensors have led to the development of genosensor technology for the detection of virulent gene sequence (Yang et al., 1997; Castaneda et al., 2007). There is thus a considerable scope to explore the development of a genosensing device for rapid and sequence specific *V. cholerae* detection. Current diagnostic techniques for cholera are based on immunological detection kits/ELISA and polymerase chain reaction (PCR) etc., which are very expensive, tedious and require at least 3-4 h (Lazcka et al., 2007). Cholera is serious infectious diseases which cause an acute diarrheal infection and lead to death if untreated at earlier stage (Kelly, 2011). Therefore, there is an urgent need to develop a genosensor for rapid detection of cholera. The voltammetry techniques for fabrication of genosensing devices may alter the recognition properties of the DNA functionalized electrode layer due to applied potential. However, the electrochemical impedance spectroscopy (EIS) is a label-free, non-destructive, rapid technique to characterize DNA functionalized electrode (Moisel et al., 2008). In this context, the impedimetric method provide a suitable detection tool for rapid investigation of charge transfer properties, ion exchange and diffusion that occur at the electrode-electrolyte interface (Bonanni and Pumera, 2011).

We report results of the studies relating to the fabrication of nMgO grafted cMWCNTs based impedimetric genosensing platform for selective detection of *V. cholerae*. The designed amine terminated single stranded (NH<sub>2</sub>-ssDNA) probe has been covalently functionalized onto nMgO-cMWCNTs/ITO electrode surface via EDC-NHS chemistry.

## 2. Materials and methods

### 2.1. Chemicals and reagents

Magnesium nitrate [Mg (NO<sub>3</sub>)<sub>2</sub>.6H<sub>2</sub>O], oxalic acid (H<sub>2</sub>C<sub>2</sub>O<sub>7</sub>.2H<sub>2</sub>O) and acetonitrile (CH<sub>3</sub>CN), have been purchased from E. Merck, Mumbai, India. NHS (N-hydroxysuccinimide) and EDC (N-ethyl-N'-(3-dimethylaminopropyl carbodiimide) have been purchased from Sigma-Aldrich, USA. Tris (hydroxymethyl) amino methane, ethylene diamine tetra acetic acid (EDTA), sodium dihydrogen ortho-phosphate (NaH<sub>2</sub>PO<sub>4</sub>), di-sodium hydrogen orthophosphate (Na<sub>2</sub>HPO<sub>4</sub>) and dimethyl sulfoxide (DMSO) have been procured from Qualigens, India. Probe and DNA solutions are prepared in Tris EDTA buffer (TE, 10 mM Tris, 1 mM EDTA, pH 8.0). ITO coated glass (Balzers Ltd., UK, sheet resistance: 15 Ω/sq) have been used as a substrate. Phosphate buffer saline (PBS, 50 mM, pH 7.0 with 0.9 % NaCl) containing [Fe(CN)<sub>6</sub>]<sup>3-/4-</sup> is used for impedimetric measurement. The synthetic oligoneucleotide probe sequences have been procured from Midland certified reagent company, USA.

### 2.2. Probe designing and DNA isolation

The specific virulent gene (O1 gene) sequence of *V. cholerae* has been identified and genomic DNA has been isolated from clinical samples according to previous reported method (Patel et al., 2013b). The concentration of genomic DNA and purity has been measured using Nanodrop spectrophotometer at absorbance 260 and 260/280 nm, respectively. The various designed

oligoneucleotide probe sequences used for DNA hybridization studies are listed in Table S1 (supplementary data).

### 2.3. *Material synthesis and electrode fabrication*

The nMgO have been synthesized as per previously reported protocol after slight modification (Patel et al., 2013a and 2013b). Here, gel is calcined at 900 °C for about 3 h to obtain nMgO powder and further used for electrode fabrication. MWCNTs have been synthesized via catalytic chemical vapor deposition and functionalized with acid treatment (Bhatia and Prasad, 2010). The obtained nMgO powder and carboxyl functionalized (cMWCNTs, 1 mg mL<sup>-1</sup>) are dispersed in acetonitrile solution for stock solution. For electrophoretic deposition (EPD), colloidal solution of nMgO-cMWCNTs (250 µL) has been dispersed in 10 mL of acetonitrile after 2 h sonication. A platinum electrode is kept at a positive potential, whereas the negative potential is applied to the working electrode i.e. ITO (0.25 cm<sup>2</sup>). The potential of 90 V has been applied for about 60 s for fabrication of nMgO-cMWCNTs/ITO electrodes.

### 2.4. *Fabrication of genosensing electrode*

An amine-terminated single stranded probe DNA (NH<sub>2</sub>-ssDNA, 10 pM µL<sup>-1</sup>) is covalently immobilized onto the specified nMgO grafted cMWCNTs surface via carbodiimide coupling chemistry (EDC, 0.4 M as the coupling agent and NHS, 0.1 M as activator). The NH<sub>2</sub>-ssDNA offers an intriguing possibility for carbon nanotubes binding depending on its sequence and structure, aromatic nucleotide bases by forming  $\pi$ -stacking interactions with the sidewall of carbon nanotubes (Hughes et al., 2007). The terminal of the cMWCNTs can be used for covalent coupling of aminated biomolecules (Hu et al., 2005). They attract each other via electrostatic interaction and displace the water molecules between the two components (Lu et al., 2005). The strategy of probe immobilization in better orientation provides highest degree of thermodynamic freedom, which



significantly speeds up the rate of DNA hybridization. The fabricated bioelectrode ( $\text{NH}_2$ -ssDNA/nMgO-cMWCNTs/ITO) is washed twice with tris EDTA buffer (TE, 50 mM, pH 7.0) to remove unbound probe. The longer genomic (target) DNA strands is break into shorter fragments (ftDNA) using ultrasonication for 20 min at 24 KHz (Vibronics, India) followed by heat shock treatment at 95 °C for ~5 min and sudden chilling in ice bath for 1 min to separation of strands (Ermini et al., 2012; Thiruppathiraja et al., 2011). This ftDNA is further used for hybridization onto  $\text{NH}_2$ -ssDNA/nMgO-cMWCNTs/ITO bioelectrode surface. This hybridized bioelectrode (dsDNA/nMgO-cMWCNTs/ITO) is washed twice with TE buffer to remove unspecific hybridization. The proposed mechanisms of impedimetric genosensor fabrication steps have shown in Scheme 1.

### 2.5. Material characterization

Structural information has been obtained by using X-ray diffraction spectroscopy (XRD, Rigaku) with  $\text{Cu-K}\alpha$  ( $\lambda = 1.542 \text{ \AA}$ ) X-ray source, Raman spectroscopy (HR800 LabRam, Horiba/Jobin-Yvon), Fourier transformed infrared spectroscopy (FT-IR, Perkin-Elmer, Model 2000) and X-ray photoelectron spectroscopy (XPS) using S-Probe ESCA model 2803 (Fison Instrument, 10 kV, 20 mA) with  $\text{Al K}\alpha$  as X-rays source. Morphological observations have been carried out using scanning electron microscope (SEM, Zeiss EVO 40), atomic force microscope (AFM, Vicco 440) and high-resolution transmission electron microscope (HR-TEM, JEOL-2100 F, 200 KV). Electrochemical workstation (Model AUT-84275) has been used for electrochemical studies with three-electrode system. Fabricated electrodes act as working electrode,  $\text{Ag/AgCl}$  as reference electrode and platinum wire serve as counter electrode.

### 3. Results and discussions

#### 3.1. Structural characterization

The XRD studies has been carried out to investigate the crystallinity of nMgO powder and shown in Fig. S1 (supplementary data). The presence of diffraction peaks relating to (111), (200), (220), (311) and (222) planes confirmed by JCPDS Card No. 89-7746, reveal the crystalline nature of synthesized MgO nanoparticles (Fig. S1a, i). The highest intensity of (200) reflecting plane with  $d_{200}$  value of 2.1 Å implies that majority of the grains are preferably grown along (200) crystal orientation. For cMWCNTs (Fig. S1a, ii), the wide and shallow diffraction peak at  $2\theta=26^\circ$  with  $d_{002}$  value 3.4 Å corresponding to (002) plane is attributed to hexagonal graphitic structure of cMWCNTs (JCPDS Card No. 89-8487). The peaks seen at  $2\theta = 43^\circ$  and  $54^\circ$  correspond to (100) and (004) graphitic planes, respectively. Fig. S1a (iii) shows the diffraction spectra of nMgO-cMWCNTs. It has been observed that the intensity of (002) graphite plane of cMWCNTs decrease after incorporation of MgO nanoparticles. The peak for the plane (111) in case of nMgO-cMWCNTs has slightly shifted towards higher  $2\theta$  value.

Fig. S1(b) (supplementary data) depicts the Raman spectra of (i) pristine MWCNTs and (ii) carboxyl functionalized MWCNTs. The peak seen at  $1354\text{ cm}^{-1}$  is due to D band of MWCNTs indicating disordered  $sp^3$  hybridized carbon atoms on the inner walls of the nanotubes surface. The peak found at  $1581\text{ cm}^{-1}$  corresponds to G-band due to the tangential stretching of  $sp^2$ -bonded carbon atoms in graphitic structure (Huang et al., 2011). The ratio of D-band to G-band intensities of pristine MWCNTs found to be 0.77 and increases after functionalization of carboxyl group onto MWCNTs. This increase in the  $I_D/I_G$  ratio indicates the generation of defect sites and functional group (COOH) after the acid treatment.

Fig. 1(a) shows the survey scan XPS spectra for various deposited films. The peaks related to C1s, O1s and Mg2p are observed at 284.5 eV, 529 eV, and 49.6 eV, respectively, for all the samples (Fig. 1a: i-iv). The peak related to N1s is observed at 397 eV, clearly indicates that DNA is covalently functionalized onto NH<sub>2</sub>-ssDNA/nMgO-cMWCNTs/ITO surface (Fig. 1a, iv).

Fig. 1(b) reveals the core level XPS spectra of C1s region for cMWCNTs/ITO (Fig. 1b, i), nMgO-cMWCNTs/ITO (Fig. 1b, ii) and dsDNA/nMgO-cMWCNTs/ITO (Fig. 1b, iii) films, which have been deconvoluted into the characteristic peaks using Shirley type baseline and Lorentzian-Doniac-Sunsic curves with Gaussian profile. The peak positions have been referenced with C1s peak (284.5 eV). The binding energy peaks found at 284.5 eV may be assigned to graphitic carbon (sp<sup>2</sup> C=C) while the peak seen at 285.6 eV may be attributed to the defects on the nanotube structure (sp<sup>3</sup> C-C). The other binding energy peaks seen at 286.6, 287.8 and 289.4 eV are assigned to the C-O, C=O (carbonyl) and O-C=O (carboxyl) groups respectively as a results of different oxygenated moieties during chemical functionalization (Datsyuk et al., 2008). The binding energy peaks corresponding to these functional groups are also visible in the nMgO-cMWCNTs/ITO film (Fig. 1b, ii). However, in case of dsDNA/nMgO-cMWCNTs/ITO sample an additional broad peak found at 287.9 eV is attributed to amide bond (N-C=O) formation between carboxyl group present at nMgO-cMWCNTs/ITO electrode surface and the aminated DNA (Fig. 1b, iii). The relative atomic % of carboxyl group has been determined to be 17.6% in nMgO-cMWCNTs/ITO sample, which decreases to 7.3% in dsDNA/nMgO-cMWCNTs/ITO sample indicating that most of the carboxyl groups present in nMgO-cMWCNTs/ITO have been utilized for DNA functionalization via amide bond formation. On the other hand, the relative atomic % of amide peak, which is negligible in the nMgO-cMWCNTs/ITO film, increases to 9.31% in dsDNA/nMgO-cMWCNTs/ITO film. An additional peak seen at around 283 eV in all the spectra can be correlated

to the presence of C-Mg bond because of adsorption of the magnesium ion during EPD (Srivastava et al., 2013).

Fig. 1c shows the core level N1s spectra of nMgO-cMWCNTs and dsDNA/nMgO-cMWCNTs/ITO. The peak is found to be deconvoluted into the characteristic peaks corresponding to -N = at 398.6 eV, -NH- at 399.8 eV, and NH<sub>2</sub> at 402.0 eV (Fig. 1c, ii) (Singh et al., 2010). The peak at 406.7 eV corresponds to 1s-σ\* resonance peak (Rath et al., 2008). However, these peaks are found to be absent in the spectra of nMgO-cMWCNTs/ITO (Fig. 1c, i). The relative atomic % of functional groups for C1s and N1s spectra of various films and their peak fitting parameters have been listed in Table S2, S3 and S4, respectively (supplementary data).

### 3.2. Morphological characterization

Fig. S2 (supplementary data) depicts the set of 2D and 3D AFM images of various films. Prior to ftDNA hybridization, randomly oriented cMWCNTs are of almost uniform diameter with small granules of ~50-51 nm (marked area by square) on the surface is attributed to nMgO (Fig. S2, (i)). From 3D view, the uniform height distribution throughout the surface is seen in Fig. S2 (i). Fig. S2 (ii) shows the AFM image of the nMgO-cMWCNTs/ITO surface obtained after hybridization with ftDNA. In the marked area by circle, the protrusion of DNA is seen belt like structure, which can be due to the agglomeration of the DNA molecules and drying of the solvent exhibiting the high surface roughness. The noise in the image (Fig. S2 (ii)) implies that either the AFM tip is softly touching the DNA hybridized surface or its apex is changed by adsorption of DNA molecules.

SEM images of the nMgO-cMWCNTs/ITO film and after ftDNA hybridization are shown in Fig.2. The cMWCNTs are randomly distributed and forming a network like structure. MgO nanoparticles are grafted onto the surface of cMWCNTs (Fig. 2 (i)). MgO nanoparticles are directly

attached onto the edges of tubular surface of cMWCNTs, which is marked by dotted red circle (Fig. 2(i)). Attachment of nMgO along the tubular edge is due to electrostatic interaction between the negatively charged cMWCNTs and positively charged nMgO under the influence of electric field applied during EPD. There is no significant morphological change noticed after ftDNA hybridization (Fig. 2 (ii)). Energy-dispersive X-ray spectroscopy (EDX) (Fig. 2 (iii)) spectra of nMgO-cMWCNTs have shown in Fig. 2 (i) reveals the peak related to Mg, C, N, Sn, and O, indicating the composition of nMgO and cMWCNTs on ITO substrate. Whereas, after ftDNA hybridization, an additional peak of phosphorus (P) has been observed and the intensity of Mg peak is drastically reduced (Fig. 2(iv)) which confirms the DNA hybridization.

Fig. 3 and Fig. S3 (supplementary data) shows the HR-TEM image of nMgO grafted cMWCNTs. The Fig. S3 (a) (supplementary data) shows the cMWCNTs are well dispersed over a few micrometer lengths with straight and tubular appearance. Fig. 3 (i, iii and iv) reveals the nMgO grafted cMWCNTs, where diameter of cMWCNTs varies from 50 nm to 100 nm. The MgO nanoparticles grafted on sidewalls of cMWCNTs surface have been clearly seen in Fig. 3 (i). Well-distributed spherical nMgO mostly of size 9-10 nm and shown in the histogram plot (Fig. 3 (ii)). At several places the nMgO are agglomerated on the sidewalls of the cMWCNTs (Fig. 3 (iii)), which is more clearly seen in the inset of image (iii). The attachment of nMgO along the sidewalls of cMWCNTs is attributed to the electrostatic interactions as discussed earlier. Fig. 3 (iv and v) are the HR-TEM image reveals the lattice fringe pattern of both nMgO and cMWCNTs. The lattice spacing of 0.35 nm corresponds to  $d_{002}$  graphitic plane of cMWCNTs, whereas the lattice spacing of 0.21 nm is of  $d_{200}$  plane of nMgO. The lattice spacing of both cMWCNTs and nMgO are consistent with values estimated from the XRD patterns. The selected area electron diffraction pattern of nMgO and cMWCNTs are strongly supported to XRD studies (Fig. S5b, i and ii), supplementary data).

### 3.3. Electrochemical characterization

The impedimetric studies have been conducted at constant potential of 25 mV, in the frequency range of 0.1-10<sup>4</sup> Hz (Fig. 4 (a)). The Randles equivalent circuit (inset: Fig. 4(a)) contains solution resistance ( $R_s$ ), charge transfer resistance ( $R_{ct}$ ), constant phase element or double layer capacitance (CPE) and Warburg resistance (W) and listed in Table S5 (supplementary data). This resistance is the characteristic of electron-transfer kinetics of redox species at electrode interface and varies with different substances are adsorbed onto the electrode surface. The  $R_{ct}$  value for bare nMgO/ITO electrode has been increased to 879.8  $\Omega$ ; MgO being insulating  $R_{ct}$  increases (curve iii) as compared to that of cMWCNTs/ITO electrode ( $R_{ct}$  value: 816.1  $\Omega$ ; curve ii) due to cumulative conducting properties of carbon nanotubes resulted due to the presence of defects in cMWCNTs. After grafting of nMgO onto cMWCNTs surface, the effective value of  $R_{ct}$  reduces decreases to 265.3  $\Omega$  (curve i). This suggests that the nMgO-cMWCNTs enhance/facilitate electron transport via establishing conduction path/channels for electron conduction which results in decreased impedance. Curve (iv) depicts increased  $R_{ct}$  value of 970.2  $\Omega$  after immobilization of NH<sub>2</sub>-ssDNA probe onto nMgO-cMWCNTs surface. This increase of  $R_{ct}$  is attributed to intrinsic insulating nature of DNA that impedes electron diffusion towards the electrode. Also, the repulsion between negatively charged NH<sub>2</sub>-ssDNA probe and [Fe(CN)<sub>6</sub>]<sup>3-/4-</sup> redox species perhaps inhibits the interfacial electron transfer resulting in increased impedance (Katz and Willner, 2003). The  $R_{ct}$  value has increased to 1.367 k $\Omega$  after hybridization with ftDNA (curve viii) onto NH<sub>2</sub>-ssDNA/nMgO-cMWCNTs/ITO surface. The ftDNA hybridization results in helix formation that increases the negative charge of the electrode surface resulting in enhanced  $R_{ct}$  value (Hu et al., 2011). The corresponding Bode plots between logarithms of impedance as functions of logarithm of frequencies have shown in Fig. S4 (supplementary data). The impedance decreases with increase

in frequency with a sharp transition around  $\sim 1.5$ , each sample exhibits same trend.

### 3.4. Impedimetric response studies

The impedimetric sensing performance has been carried out by varying ftDNA concentration (100-500 ng  $\mu\text{L}^{-1}$ ). The  $R_{ct}$  in Nyquist plot for the  $\text{NH}_2$ -ssDNA/nMgO-cMWCNTs/ITO bioelectrode increases on addition of ftDNA (Fig. 5(a)). The maximum time is required to complete one EIS measurement is about 4 min for bioelectrode response. It has been observed that the  $R_{ct}$  value increases due to increased negative charge onto the electrode surface arising from ftDNA hybridization and duplex formation with DNA probe ( $\text{NH}_2$ -ssDNA). Also, the negative charge from  $[\text{Fe}(\text{CN})_6]^{3-/4-}$  redox species will contribute to additional charges. With increase in the ftDNA concentration, the  $R_{ct}$  value increases further, indicating that more probe DNA molecules are hybridized with the ftDNA strands, resulting in increased negative charge on the electrode surface and enhance the  $R_{ct}$  value (Table S5, supplementary data). Hybridization with ftDNA facilitates the ion transport onto the electrode surface due to the negatively charged phosphate backbone of DNA oligomer (Park et al., 2012). This may be due to the acute electrical conductance change arises from the modulation of energy level alignment between carbon nanotubes and electrode contact (Tang et al., 2006). The calibration curve between the increments of  $R_{ct}$  values and ftDNA concentration (100-500 ng  $\mu\text{L}^{-1}$ ) is shown in Fig. 5(b).

The dsDNA/nMgO-cMWCNTs/ITO bioelectrode shows high sensitivity of  $3.87 \Omega \text{ ng}^{-1} \text{ cm}^{-2}$  and low detection limit of  $21.70 \text{ ng } \mu\text{L}^{-1}$ . This is because cMWCNTs network facilitates the dispersion of nMgO because of their large surface to volume ratio and provide conduction pathway for the electron transport towards the electrode from bulk solution (Fig. 5(b)) (Zhang et al., 2010). Again, nMgO acts as mediator that facilitates transfer of electrons with favorable integration of cMWCNTs into the matrix that offers a high aspect ratio leading to a noticeable change in mass



transportation or charge transfer. Increase in the charge transfer ( $R_{ct}$ ) with respect to ftDNA concentration follows the Eq. (1).

$$R_{ct} (\Omega) = 1.064 \text{ k}\Omega + 0.969 (\Omega \mu\text{L ng}^{-1}) \times [\text{ftDNA Concentration}] \text{ ng } \mu\text{L}^{-1}; R^2=0.944 \quad \text{Eq. (1)}$$

The control experiment has been performed without using  $\text{NH}_2$ -ssDNA probe onto nMgO-cMWCNTs/ITO surface for ftDNA hybridization by varying concentration (100 to 500  $\text{ng } \mu\text{L}^{-1}$ ) as shown in Fig. S5 (supplementary data). There is negligible change in the response has been observed as compared to that of ftDNA hybridized bioelectrodes with using  $\text{NH}_2$ -ssDNA probe (Fig. S6 a and b, supplementary data). This may be due to reduced number of negatively charged phosphate backbone of ftDNA onto nMgO-cMWCNTs/ITO electrode surface as compared to that of the dsDNA/nMgO-cMWCNTs/ITO bioelectrode.

The dsDNA/nMgO-cMWCNTs/ITO bioelectrode exhibits response time of 25 s after which the current is saturated (Fig. S7, supplementary data). The stability of the dsDNA/nMgO-cMWCNTs/ITO bioelectrode has been monitored by EIS response with respect to time; with a regular interval of 15 days for about 4 months (Fig. S8, supplementary data). After 2 months, the value of  $R_{ct}$  has reduced to 93.7% of its original value, which is marginally low. However, in the time span of 4 month, the  $R_{ct}$  value reached to 70 % of its original value indicating the significant change. This implies that better time to use the sensors is 2 months. This fabricated impedimetric genosensor shows good reproducibility with 4.51 % relative standard deviation (RSD) for different bioelectrodes ( $n = 5$ ; mean value 1.24  $\text{k}\Omega$ ) in 100  $\text{ng } \mu\text{L}^{-1}$ , ftDNA concentration (data not shown). The sensing characteristics of the dsDNA/nMgO-cMWCNTs/ITO bioelectrode based genosensor are summarized in Table S6 (supplementary data) along with those reported in the literature (Ho et al., 2006; Ligler et al., 2003).

### 3.5. Selectivity and interference studies

The selectivity studies of  $\text{NH}_2\text{-ssDNA/nMgO-cMWCNTs/ITO}$  bioelectrode have been conducted with various synthesized DNA sequences using EIS (Fig. 4(a)). The change in the  $R_{ct}$  value to 1.04 k $\Omega$  is observed after hybridization with complementary DNA (ncDNA) arises due to partial hybridization as shown in Fig. 4(a), curve (v). This bioelectrode exhibits hybridization with three bases mismatch DNA (mmDNA) (Fig. 4a, curve vi). In addition, the  $R_{ct}$  value after immobilization of complementary DNA (cpDNA) (Fig. 4(a), curve (vii)) on  $\text{NH}_2\text{-ssDNA/nMgO-cMWCNTs/ITO}$  electrode has been found to be 1.082 k $\Omega$ . Histogram in Fig. 4(b) shows the selectivity of various synthesized DNA sequence with change in hybridization signal ( $\Delta R_{ct}$ ) intensity. The interferences studies have been tested in the human blood/serum such as glucose (100 mg dL<sup>-1</sup>), cholesterol (5 mM), ascorbic acid (0.05 mM) and their mixture in normal concentration with dsDNA/nMgO-cMWCNTs/ITO bioelectrode (100 ng  $\mu\text{L}^{-1}$ ) (Fig. S9, supplementary data). It has been observed that the fabricated genosensor exhibits good selectivity even in the presence of interferences.

## 4. Conclusions

Nanostructured MgO (size < 10 nm) grafted cMWCNTs based impedimetric genosensor has been fabricated for the label free detection of *V. cholerae* (O1 gene) via functionalization of amino terminated single stranded DNA ( $\text{NH}_2\text{-ssDNA}$ ) probe. Raman and XPS studies confirm the functionalization of cMWCNTs and quantification of DNA molecules onto nMgO-cMWCNTs surface, respectively. XPS studies indicate that large amount of O-C=O group (10.22 %) is present on surface of nMgO-cMWCNTs, which has been utilized for binding of DNA molecules. In addition, the presence N1s peak confirms the DNA functionalization onto nMgO-cMWCNTs surface. The  $\text{NH}_2\text{-ssDNA/nMgO-cMWCNTs/ITO}$  bioelectrode exhibits linear response in the range

from 100 to 500 ng  $\mu\text{L}^{-1}$  with lower detection limit of 21.70 ng  $\mu\text{L}^{-1}$ . This fabricated genosensor exhibits high sensitivity of 3.87  $\Omega \text{ ng}^{-1} \text{ cm}^{-2}$  and fast response time (25 s) with regression coefficient of 0.993 for cholera detection. The fabricated genosensor exhibits specificity to complementary target DNA sequences in the presence of non-complementary strands and shows enormous potential for *V. cholerae* detection. Efforts should be made to explore the application of this interesting nMgO-cMWCNTs/ITO platform for the detection of typhoid, tuberculosis, dengue, and other infectious diseases.

### Acknowledgements

Authors thank Director, NPL, New Delhi, India to provide the research facilities. MKP, AA and SS are grateful to the CSIR, India for the award of Senior Research Fellowship. SGA acknowledges the financial support from CSIR and UGC, India for their major research projects. The financial support received from DST, India (Grant No. DST/TSG/ME/2008/18) and ICMR, India (Grant No. ICMR/5/3/8/91/GM/2010-RHN) is gratefully acknowledged. BDM thanks the Ministry of Education, Science and Technology (R32-20026) and Chungnam National University, Korea for visiting.

## References

- Abu-Salah, K.M., Alrokyan, S.A., Khan, M.N., Ansari, A.A., 2010. *Sensors* 10, 963-993.
- Bhatia, R., Prasad, V., 2010. *Solid State Communications* 150, 311-315.
- Bonanni, A., Pumera, M., 2011. *ACS Nano* 5, 2356-2361.
- Castaneda, M.T., Merkoci, A., Pumera, M., Alegret, S., 2007. *Biosensors and Bioelectronics* 22, 1961-1967.
- Datsyuk, V., Kalyva, M., Papagelis, K., Parthenios, J., Tasis, D., Siokou, A., Kallitsis, I., Galiotis, C., 2008. *Carbon* 46, 833-840.
- Ermini, M., Mariani, S., Scarano, S., Minunni, M., 2012. *Biosensors and Bioelectronics* 40, 193-199.
- Ferrari, B., Moreno, R., Sarkar, P., Nicholson, P.S., 2000. *Journal of the European Ceramic Society* 20, 99-106.
- Gooding, J.J., 2005. *Electrochimica Acta* 50, 3049-3060.
- Ho, J.-a.A., Wu, L.-C., Huang, M.-R., Lin, Y.-J., Baeumner, A.J., Durst, R.A., 2006. *Analytical Chemistry* 79, 246-250.
- Hu, C., Zhang, Y., Bao, G., Liu, M., Wang, Z.L., 2005. *The Journal of Physical Chemistry B* 109, 20072-20076.
- Hu, Y., Li, F., Bai, X., Li, D., Hua, S., Wang, K., Niu, L., 2011. *Chemical Communications* 47, 1743-1745.
- Huang, X., Yin, Z., Wu, S., Qi, X., He, Q., Zhang, Q., Yan, Q., Boey, F., Zhang, H., 2011. *Small* 7, 1876-1902.
- Hughes, M.E., Brandin, E., Golovchenko, J.A., 2007. *Nano Letters* 7, 1191-1194.
- Katz, E., Willner, I., 2003. *Electroanalysis* 15, 913-947.
- Kelly, P., 2011. *Medicine* 39, 201-206.
- Kong, R.M., Zhang, X.B., Chen, Z., Tan, W., 2011. *Small* 7, 2428-2436.
- Lazcka, O., Campo, F., Muñoz, F.X., 2007. *Biosensors and Bioelectronics* 22, 1205-1217.
- Ligler, F.S., Taitt, C.R., Shriver-Lake, L.C., Sapsford, K.E., Shubin, Y., Golden, J.P., 2003. *Analytical and Bioanalytical Chemistry* 377, 469-477.
- Liu, H., Ma, H., Zhou, W., Liu, W., Jie, Z., Li, X., 2012. *Applied Surface Science* 258, 1991-1994.
- Lu, G., Maragakis, P., Kaxiras, E., 2005. *Nano Letters* 5, 897-900.

- Moisel, M., de Mele, M.A.F.L., Müller, W.D., 2008. *Advanced Engineering Materials* 10, B33-B46.
- Park, J.S., Lee, J.M., Hwang, S.K., Lee, S.H., Lee, H.J., Lee, B.R., Park, H.I., Kim, J.S., Yoo, S., Song, M.H., Kim, S.O., 2012. *Journal of Materials Chemistry* 22, 12695-12700.
- Patel, M.K., Ali, M.A., Zafaryab, M., Agrawal, V.V., Rizvi, M.M.A., Ansari, Z.A., Ansari, S.G., Malhotra, B.D., 2013a. *Biosensors and Bioelectronics* 45, 181-188.
- Patel, M.K., Azahar Ali, M., Agrawal, V.V., Ansari, Z., Ansari, S., Malhotra, B., 2013b. *Applied Physics Letters* 102, 144106.
- Rath, S., Sarangi, S., Sahu, S., 2008. *Nanotechnology* 19, 115606.
- Shim, M., Shi Kam, N.W., Chen, R.J., Li, Y., Dai, H., 2002. *Nano Letters* 2, 285-288.
- Singh, S., Zack, J., Kumar, D., Srivastava, S., Saluja, D., Khan, M., Singh, P., 2010. *Thin Solid Films* 519, 1151-1155.
- Srivastava, S., Kumar, V., Ali, M.A., Solanki, P.R., Srivastava, A., Sumana, G., Saxena, P.S., Joshi, A.G., Malhotra, B.D., 2013. *Nanoscale* 5, 3043-3051.
- Tang, X., Bansaruntip, S., Nakayama, N., Yenilmez, E., Chang, Y.I., Wang, Q., 2006. *Nano Letters* 6, 1632-1636.
- Thiruppathiraja, C., Kamatchiammal, S., Adaikkappan, P., Santhosh, D.J., Alagar, M., 2011. *Analytical Biochemistry* 417, 73-79.
- Umar, A., Rahman, M., Hahn, Y.B., 2009. *Electrochemistry Communications* 11, 1353-1357.
- Yang, M., McGovern, M.E., Thompson, M., 1997. *Analytical Chimica Acta* 346, 259-275.
- Zhang, W.D., Xu, B., Jiang, L.C., 2010. *Journal Material Chemistry* 20, 6383-6391.
- Zhao, J., Park, H., Han, J., Lu, J.P., 2004. *The Journal of Physical Chemistry B* 108, 4227-4230.

## Figures captions

**Scheme 1.** The proposed mechanism of fabricated genosensor.

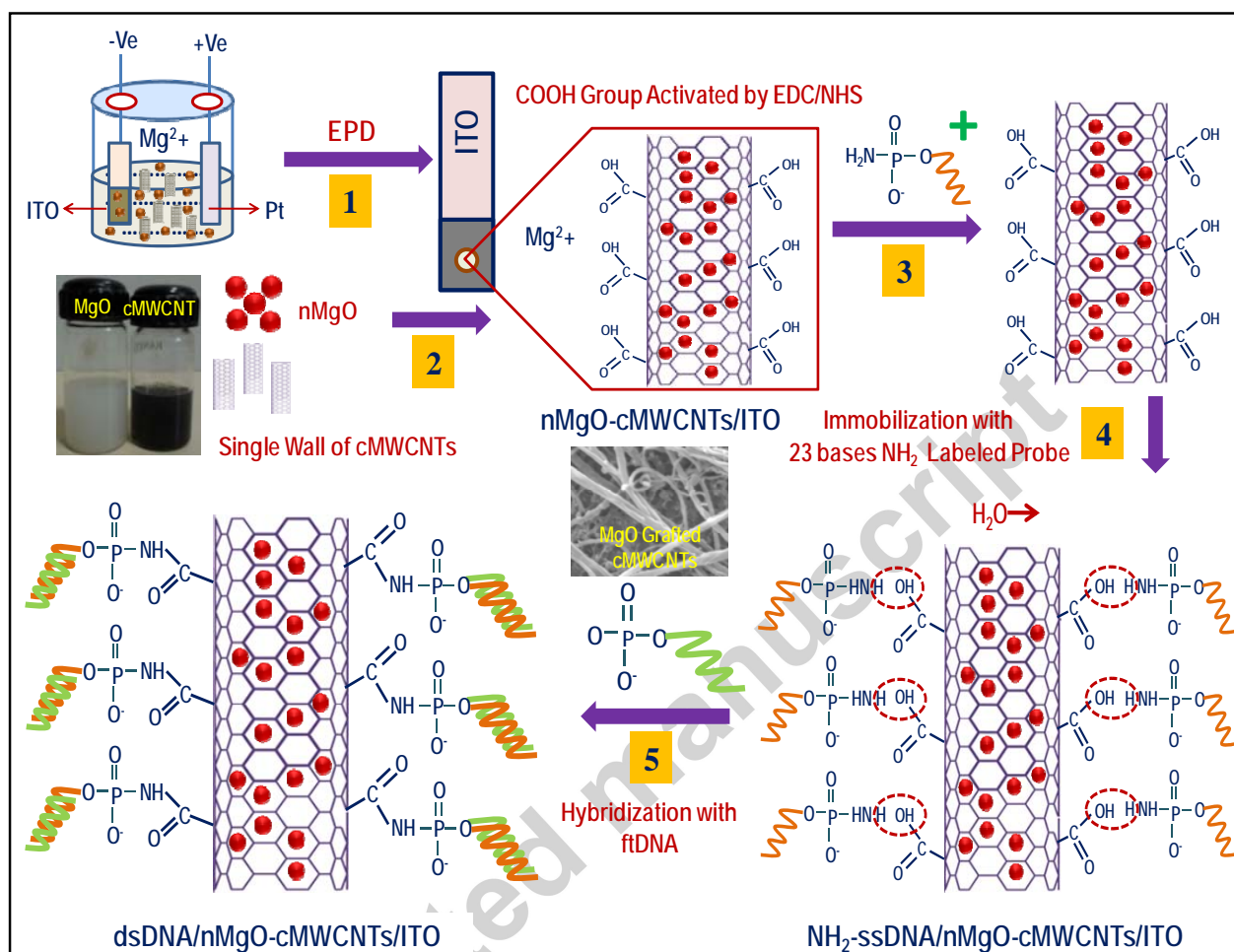
**Fig. 1.** (a) Survey scan XPS spectra of various films, (b) core level C1s spectra and (c) N1s core level spectra of nMgO-cMWCNTs/ITO and dsDNA/nMgO-cMWCNTs/ITO films. Dotted lines are the original data and solid lines are results of deconvolution.

**Fig. 2.** SEM images of (i) nMgO-cMWCNTs/ITO film and (ii) dsDNA/nMgO-cMWCNTs/ITO film with their elemental analysis (iii and iv)

**Fig. 3.** HR-TEM images of (i) nMgO-cMWCNTs, (ii) MgO particles (Inset: particle size distribution of MgO), (iii) nMgO grafted cMWCNTs and (iv-v) the average lattice spacing of nMgO grafted cMWCNTs.

**Fig. 4.** (a) EIS measurements of various electrodes in 50 mM PBS containing 1 mM  $[\text{Fe}(\text{CN})_6]^{3-/4-}$  at pH 7.0 (inset: equivalent circuit) and (b) histogram plot of comparative studies for various DNA electrodes using EIS technique,

**Fig.5.** EIS response studies of (a) dsDNA/nMgO-cMWCNTs bioelectrode with different ftDNA concentration range of 100 to 500 ng  $\mu\text{L}^{-1}$  and (b) calibration curve between charge transfer resistance of ftDNA concentration with respect to probe (inset: schematic representation of electronic transport mechanism of nMgO-cMWCNTs).



Scheme 1.



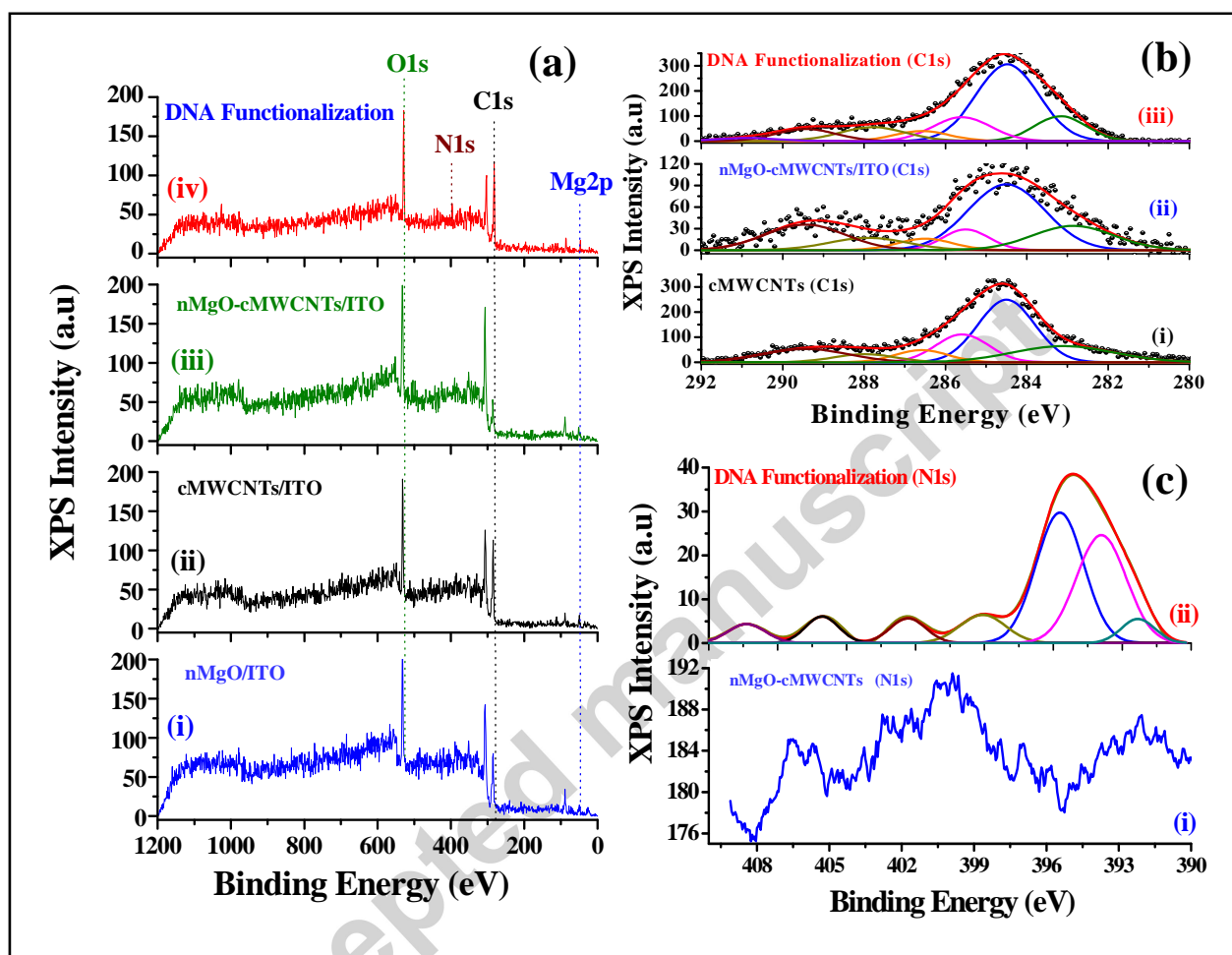


Fig. 1.

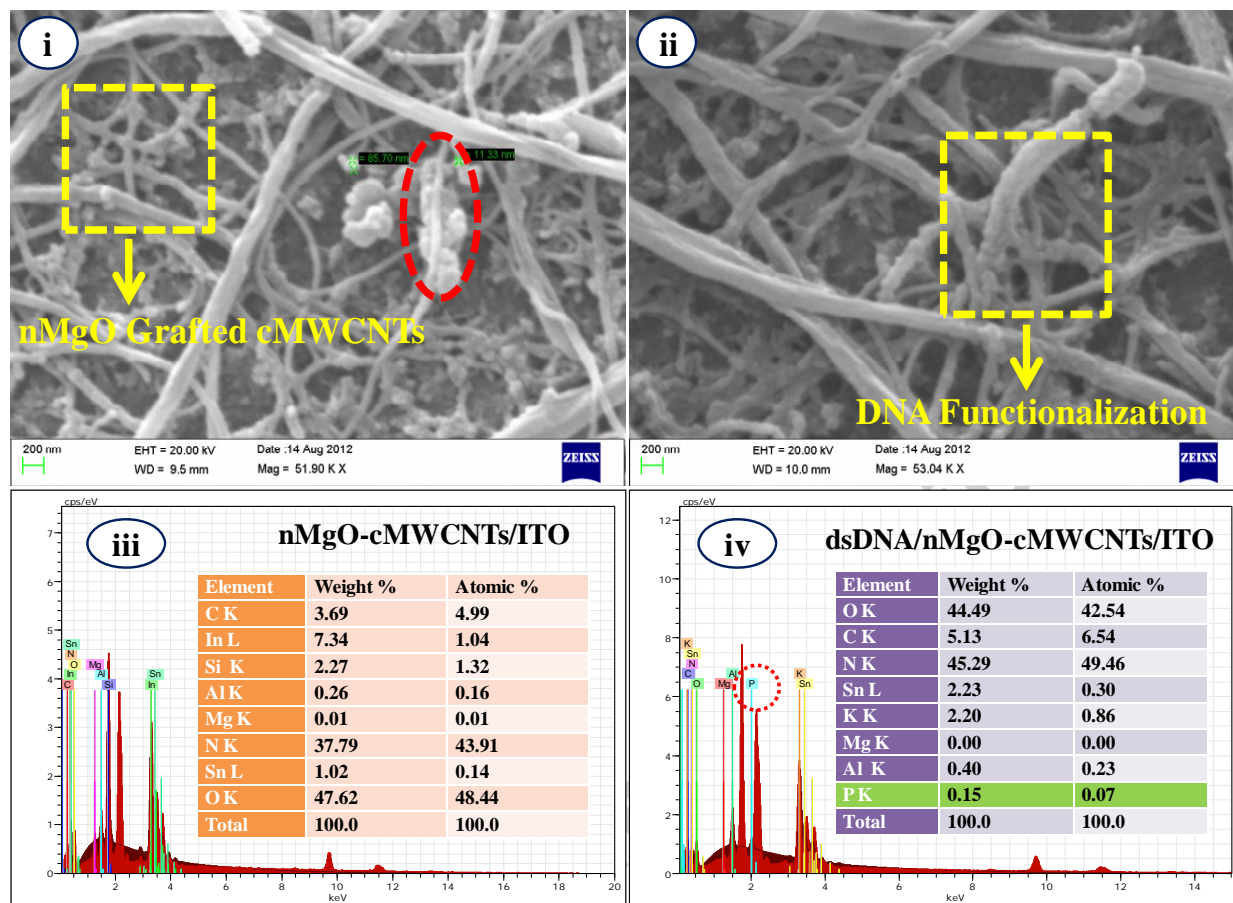
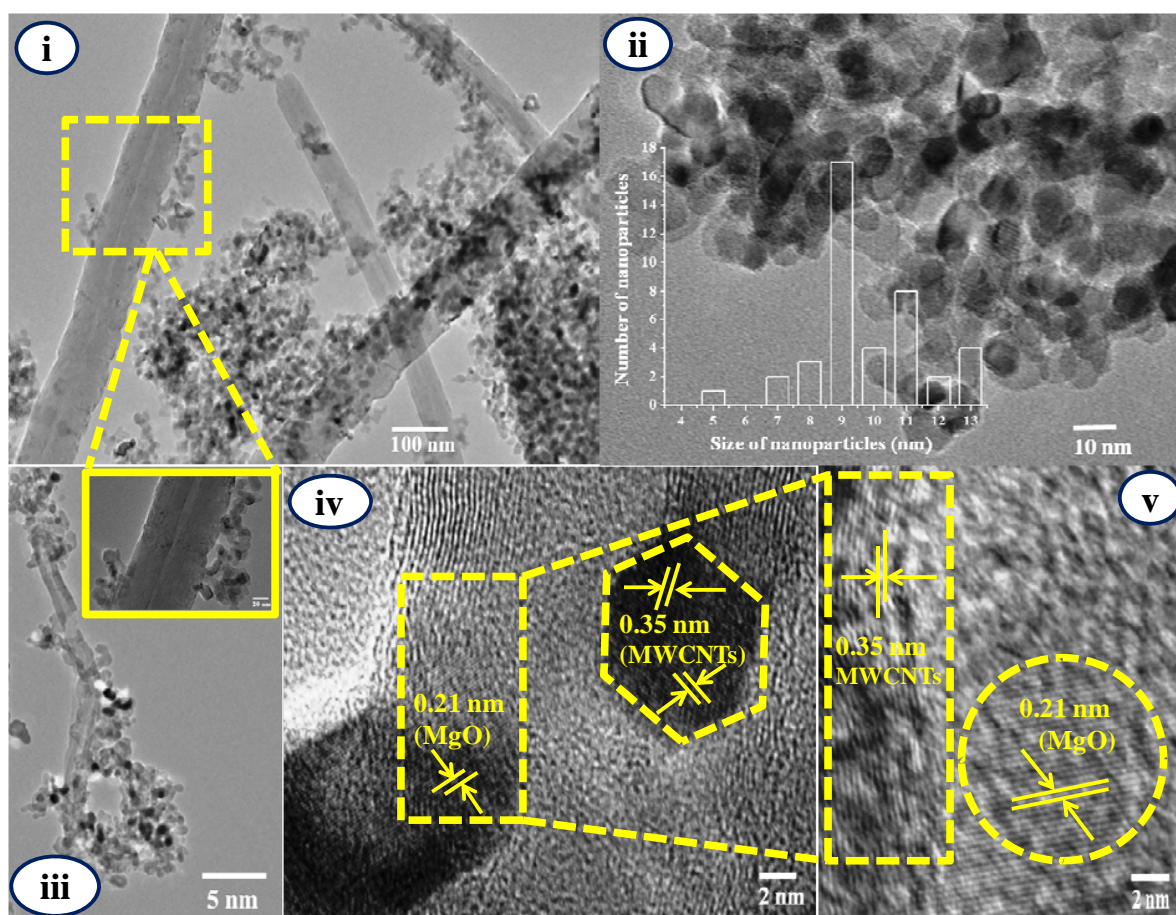


Fig. 2.

**Fig. 3.**

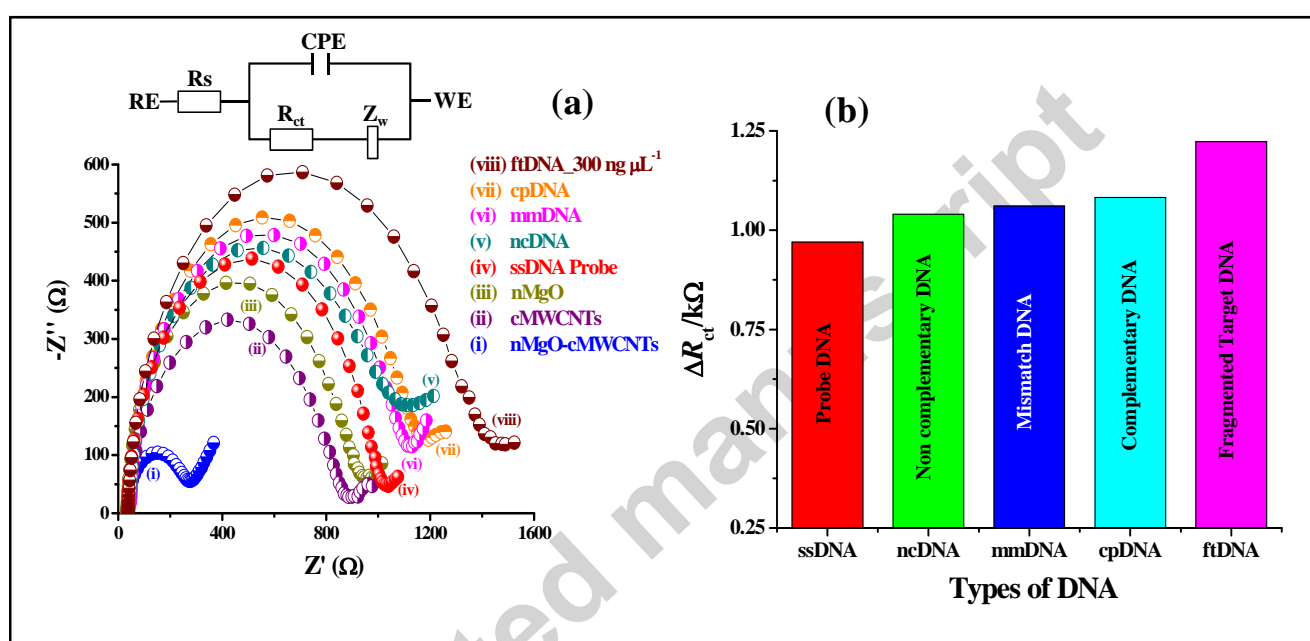


Fig.4.

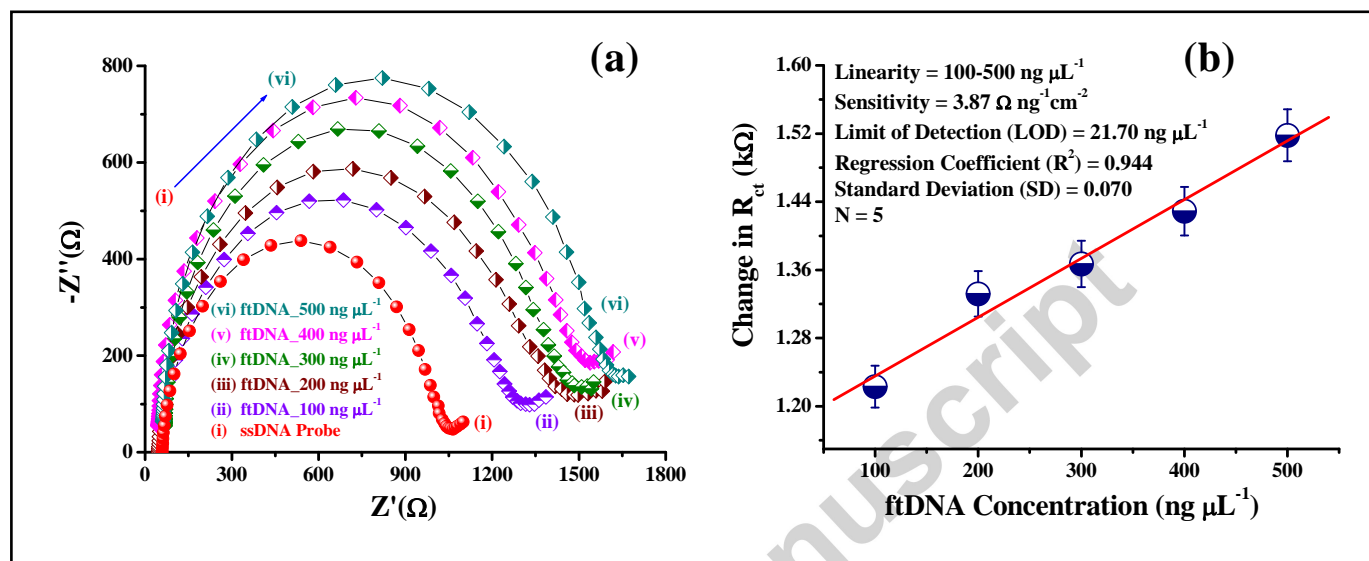


Fig.5.

**Highlights:**

- MgO-cMWCNT based impedimetric genosensor is highly efficient for the detection of *V. cholerae*.
- This genosensor provides rapid, low cost detection and more stability of about 120 days.
- Control experiment has been investigated the response of bioelectrode without hybridization.
- XPS studies reveal the quantification of DNA functionalization onto MgO-cMWCNT surface.

Accepted manuscript

# Modified Multi-Chaotic Systems that are Based on Pixel Shuffle for Image Encryption

Om Prakash Verma\*, Munazza Nizam\* and Musheer Ahmad\*\*

**Abstract**—Recently, a pixel-chaotic-shuffling (PCS) method has been proposed by Huang et al. for encrypting color images using multiple chaotic systems like the Henon, the Lorenz, the Chua, and the Rossler systems. All of which have great encryption performance. The authors claimed that their pixel-chaotic-shuffle (PCS) encryption method has high confidential security. However, the security analysis of the PCS method against the chosen-plaintext attack (CPA) and known-plaintext attack (KPA) performed by Solak et al. successfully breaks the PCS encryption scheme without knowing the secret key. In this paper we present an improved shuffling pattern for the plaintext image bits to make the cryptosystem proposed by Huang et al. resistant to chosen-plaintext attack and known-plaintext attack. The modifications in the existing PCS encryption method are proposed to improve its security performance against the potential attacks described above. The Number of Pixel Change Rate (NPCR), Unified Average Changed Intensity (UACI), information entropy, and correlation coefficient analysis are performed to evaluate the statistical performance of the modified PCS method. The simulation analysis reveals that the modified PCS method has better statistical features and is more resistant to attacks than Huang et al.'s PCS method.

**Keywords**—Chaotic Systems, Number of Pixel Change Rate, Unified Average Changed Intensity, Correlation Coefficient, Entropy

## 1. INTRODUCTION

With the rapid advancement in Internet and multimedia technologies, a number of researchers and scientists have made various attempts to solve the issue of data security and integrity by designing and deploying several encryption/decryption algorithms. Most important aspects of sensitive data are protection against fabrication, unauthorized access, and illegal usage. Encryption is the transformation of data such as text, images, audio, video, etc. into unintelligible forms that provides data confidentiality, integrity, authentication, and non-repudiation. The core idea behind encryption is to protect the valuable or sensitive data that can only be understood after decryption with correct secret key. A good encryption/decryption technique does not distort the original content and is resistant to conventional and other types of cryptographic attacks.

Traditional encryption techniques like Data Encryption Standard (DES), RSA, IDEA etc. are

---

Manuscript received November 13, 2012; accepted May 12, 2013.

**Corresponding Author: Munazza Nizam**

\* Dept. of Information Technology, Delhi Technological University, New Delhi, India ({munazzanizam23, opverma.dce}@gmail.com)

\*\* Dept. of Computer Engineering, JMI University, New Delhi, India (musheer.cse@gmail.com)



less efficient in encrypting the redundant and bulk-sized multimedia data like images [1-2].

To overcome this challenge, a number of image encryption techniques have been proposed in the literature on image security. Among them, chaos based techniques have gained special attention due to their intrinsic features like stochasticity, dynamic behavior, and sensitivity to initial conditions. A chaos based image encryption algorithm was first proposed by R. Matthews [3]. The highly sensitive response of chaotic system to the initial value conditions and to the variation in parameters makes the chaotic trajectory so unpredictable that a great number of researches implement chaotic sequences to perform encryption of images before transmitting them over an unsecure and open communication network.

## 2. RELATED WORK

In 2005, L. Zhang et al. [4] proposed a scheme to resist differential attacks by first analyzing the performance of discrete exponential chaotic map and then permuting the pixels of the image. A video encryption method that is based on chaotic maps in Discrete Cosine Transform (DCT) domain is presented in [5]. Two coupling chaotic maps were employed for scrambling the DCT coefficient of the original frame and for encrypting the DCT coefficients of the scrambled frame.

The one dimensional chaotic cryptosystem has drawbacks of small key space and weak security. Considering this point, Chong Fu et al. [6] proposed an image encryption technique based on 3D Lorenz chaotic system.

A new encryption scheme was presented in [7], which also employed 3D chaotic systems for bringing confusion and diffusion in encrypted image. It has the advantage of having large key space and low iteration time. In [8], an approach was designed to resist chosen-plaintext cryptanalysis and to protect the secrecy of digital images. The shuffling tables were generated by various logistic maps and the key space was governed by choosing the number of logistic maps. A random number, called 'nonce', was introduced to initialize the values of logistic maps. In [9], a scheme for encrypting color images was proposed to increase confusion and diffusion between pixels. It was based on chaotic maps and genetic operations as tools. The sequences were controlled by parameters and given initial values that were considered the key to the encryption technique. In [10], a cryptosystem is proposed that exploits the ergodic property of the simple low-dimensional and chaotic logistic map. However, there were certain drawbacks that were removed in [11] with adjustable sensitivity to initial conditions. A nonlinear chaotic algorithm (NCA) was proposed [12] to get over the drawbacks of one-dimensional linear logistic maps. The algorithm employed nonlinear functions, such as tangent function and power function with improved larger key space and high-level security. Many encryption algorithms have been proposed that use chaotic maps for encryption as their basic tool [13-18], as chaos based methods provide strong encryption strength, better statistical characteristics, and security.

### 2.1 Motivation

The cryptosystem proposed in [19] applied cipher block chaining (CBC) encryption and was penetrable to chosen-ciphertext attack (CCA) and chosen plaintext attack (CPA) since the keystream generated for every plaintext image was identical. This was cryptanalyzed by Rhouma [20] and in order to make the cryptosystem robust against CCA and CPA, the keystream was updated in a way so that every plaintext image has its own unique shuffling pattern for genera-

tion of ciphertext image. In 2009 C. K. Huang and H. H. Nien [21] proposed Pixel Chaotic Shuffle (PCS) encryption method, which is purely based on pixel shuffling using the chaotic sequences generated from 3D multiple chaotic systems. These sequences act as the key for the cryptosystem to perform vertical and horizontal shuffling of the plaintext image bits. However, Rhouma et al.[22] successfully broke the encryption scheme by cracking the sorting sequences that are the keys of the cryptosystem. This was due to the fact that the chaotic sequence used for shuffling the plaintext image bits neither depends on the plaintext image nor on the ciphertext image and the generated key was same for all plaintext images. By analyzing the plain/ciphered image pair, one can deduce the key sequences, and the scheme is prone to chosen-plaintext attack and known-plaintext attack. Thus, in order to make PCS cryptosystem robust against the aforesaid attacks, this paper presents modifications to make the keystream dependent on the plaintext image, which generates the chaotic sequence according to the information contained in the plaintext image. The proposed method generates different chaotic sequences for different plaintext images. The indices of the chaotic sequences are used for the encryption of RGB image by shuffling the bits of the three components column-wise and then row-wise into a pair of two bits.

## 2.2 Description of PCS cryptosystem

The PCS encryption scheme uses four three-dimensional chaotic systems for pixel shuffling. These chaotic systems are iterated to generate 12 random chaotic sequences. The indices of the sequences are used to map the plaintext image bits. The encryption is executed in two steps. In the first step, the bits of plaintext image are shuffled among themselves using column-wise shuffling. In the second step, the bits are rearranged within pixels of the image using row-wise shuffling. Each color component is shuffled separately using the chaotic sequences.

## 2.3 Weaknesses in PCS cryptosystem

The cryptanalysis performed in [22] on the cryptosystem [21] shows that the scheme is prone to two different attacks—namely, chosen-plaintext attack and known-plaintext attack. This weakness arises from the fact that same shuffling indices are used to shuffle the plaintext images without taking into account the plaintext image for sequence generation. Thus, the mapping of the pixel bits was same for all plaintext images. A slight change in the pixel values of original image produces negligible change in the respective encrypted image. This results in making the encrypted image easier to comprehend by analyzing the pairs of (plain/ciphered) images.

Another drawback of PCS encryption originates as the RGB components of the image are encrypted separately using the x, y, and z chaotic sequences of the maps, thereby decreasing the randomness of the bits in encrypted image. This facilitates the attacker to apply CPA and KPA to any of the color components of the RGB color image. The attacks are employed onto the 8-bit pixels of each of the color components of the image using the four chaotic sequences generated by the chaotic systems. Decoding the pixel values of color component individually needs lower computation and requires less time to carry out cryptanalysis of the method.

### 3. PROPOSED MODIFIED MULTI-CHAOTIC SYSTEMS THAT ARE BASED ON PIXEL SHUFFLE SCHEME

In this section we propose a modified version of the cryptosystem presented in [21] with a similar basic description and values of the parameters. The modification is performed to deal with the drawbacks mentioned in Section 2.3. The chaotic maps are generated by extracting the information from the plaintext image and are utilized to generate mapping sequences. Thus, an entirely different mapping sequence is used for shuffling each plaintext image. Furthermore, the bits of the RGB components are permuted to increase the randomness and confusion among pixels. Finally, column-wise and row-wise shuffling is performed to render the image totally unrecognizable and unpredictable. The flowchart of the proposed cryptosystem is shown in Fig. 1.

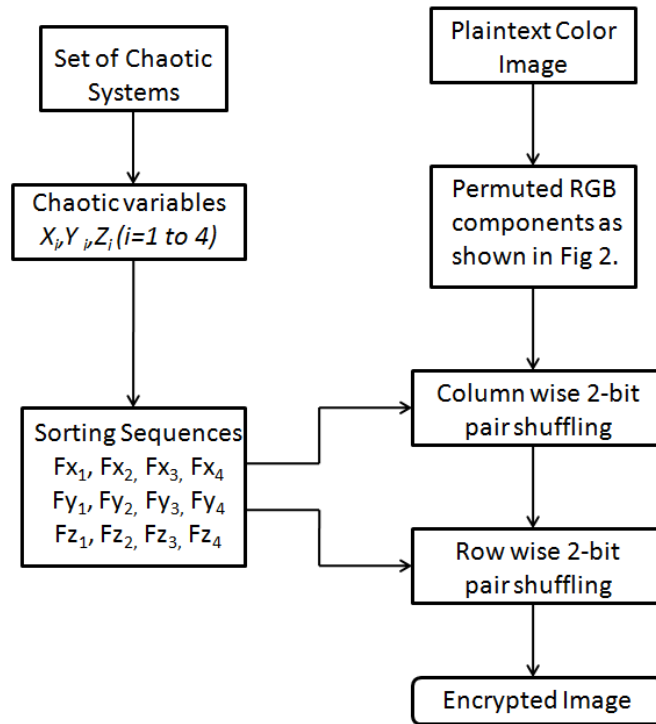


Fig. 1. Flowchart of the Modified Multi-Chaotic Image Encryption

#### 3.1 Plaintext Preparation

The plaintext is a color image of size  $m \times n$  where  $m$  and  $n$  are the number of rows and columns in the image respectively. Each pixel is represented as a byte. The plaintext image is first vectorized using row scan method to obtain an array of size  $N \times 1$ , where  $N = mn$ . The array of pixels is further split into its binary equivalents represented in 8-bit format. For example, a pixel with an intensity value of 125 is represented in 8-bit binary format by 01111101. Similarly, the pixel intensity of the color image is converted into its binary equivalent, forming an array of size  $N \times 8$  for each of the color components.

#### 3.2 Chaotic Map Generation

Let the size of image be  $m \times n$  where  $m$  and  $n$  are the number of rows and columns in the im-

age. To make the keystream dependent on the plaintext image, total number of  $I_s$  in binarized color image are calculated.

Let  $\omega$  be total number of  $I_s$  in the image. It plays the key role in generating different chaotic sequences for different plaintext images. The chaotic maps are evaluated iteratively and their iteration is controlled by:

$$\varphi = \omega + mn \quad (1)$$

Where  $\varphi$  is the total iterations of the chaotic maps. Two images differing from each other by just one pixel will also have entirely different sorting sequences. The chaotic sequence used for shuffling of plaintext image bits are  $x(k)$ ,  $y(k)$ , and  $z(k)$  where  $k$  varies from  $(\omega + 1)$  to  $\varphi$ .

The 3D chaotic maps with coordinates  $x$ ,  $y$ , and  $z$  used in the proposed cryptosystem are as follows [21]:

(1) Hénon map(discrete time):

$$x(k+1) = a - y^2(k) - bz(k) \quad (2a)$$

$$y(k+1) = x(k) \quad (2b)$$

$$z(k+1) = y(k) \quad (2c)$$

where  $a = 1.76$ ,  $b = 0.1$ .

(2) Lorenz (butterfly attractor):

$$\dot{x} = -\sigma x + \sigma y \quad (3a)$$

$$\dot{y} = -xz + \gamma y - y \quad (3b)$$

$$\dot{z} = xy - bz \quad (3c)$$

where  $\sigma = 16$ ,  $\gamma = 40$ ,  $b = 4$ .

(3) Chua (double scroll attractor):

$$\dot{x} = \alpha(y - x - h(x)) \quad (4a)$$

$$\dot{y} = x - y + z \quad (4b)$$

$$\dot{z} = -\beta y - \gamma z \quad (4c)$$

$$h(x) = m_1 x + 0.5(m_0 - m_1)(|x + 1| - |x - 1|)$$

where  $\alpha = 10$ ,  $\beta = 14.78$ ,  $\gamma = 0.0385$ ,  $m_0 = -1.27$  and  $m_1 = -0.68$ .

(4) Rössler (spiral attractor):

$$\dot{x} = -(y + z) \quad (5a)$$

$$\dot{y} = x + ay \quad (5b)$$

$$\dot{z} = b + z(x - c) \quad (5c)$$

where  $a = 0.2$ ,  $b = 0.2$  and  $c = 5.7$ .

### 3.3 Permutation of the Plaintext Image Bits

The data in the plaintext image have strong correlation among adjacent pixels. Therefore, the pixels of image are initially permuted amongst themselves in order to decrease the correlation and increase the confusion, as shown in Fig. 2. This increases the dependency of the color components on each other and increases the computation while decoding the information by any unauthorized individual.  $\Psi_{rgb} (mn \times 1)$  is the array of size  $mn \times 1$ , where each row consists of permuted 24 bits of RGB component.

Thus, the 8-bit RGB pixel that was shuffled individually [21] by 4 chaotic sequences  $X_1$  to  $X_4$ ,  $Y_1$  to  $Y_4$ , and  $Z_1$  to  $Z_4$ , respectively, are replaced by 24-bit shuffling of the RGB pixels using 12 chaotic sequences.

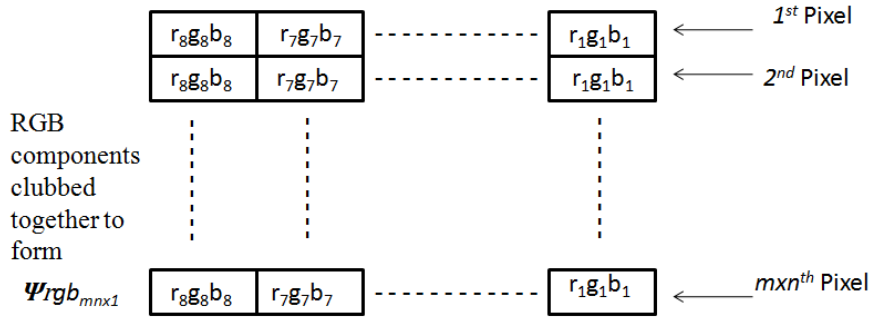


Fig. 2. Permutation of the RGB color components

### 3.4 Shuffling of the Plaintext Image Bits

**Step 1.** The chaotic sequences  $X_1$  to  $X_4$ ,  $Y_1$  to  $Y_4$ , and  $Z_1$  to  $Z_4$ , are generated as discussed in Section 3.2.

**Step 2.** Prepare the chaotic sequences  $X_{1(\mu,1)}$  to  $X_{4(\mu,1)}$ ,  $Y_{1(\mu,1)}$  to  $Y_{4(\mu,1)}$ , and  $Z_{1(\mu,1)}$  to  $Z_{4(\mu,1)}$ , which is generated from chaotic variable sets, and make the indexing sequences  $F_{x1}$  to  $F_{x4}$ ,  $F_{y1}$  to  $F_{y4}$ , and  $F_{z1}$  to  $F_{z4}$  that are :

$$F_{x1} = \text{sort}(X_{1(\mu,1)})$$

$$F_{x2} = \text{sort}(X_{2(\mu,1)})$$

$$F_{x3} = \text{sort}(X_{3(\mu,1)})$$

$$F_{x4} = \text{sort}(X_{4(\mu,1)})$$

for  $\mu = 1, 2, 3, \dots, m \times n$  where  $sort(\cdot)$  is the sequencing index function and  $m \times n$  is the dimension of the original plaintext image. Similarly, we will calculate the sequences  $F_{x1}$  to  $F_{x4}$ ,  $F_{y1}$  to  $F_{y4}$ , and  $F_{z1}$  to  $F_{z4}$ , respectively, as in [21, Section 2.2]

**Step 3.** Combine the original binarized R-level, G-level, and B-level matrixes to form  $\Psi rgb(m \times n)$ , as discussed in Section 3.3. Each row consists of 24-bits of the RGB image.

**Step 4.** Apply the shuffle function  $sq(\cdot)$  on the pixels of  $\Psi rgb$  for column indexing and shuffling, as shown in Fig. 3. The function  $sq(\cdot)$  shuffles and indexes the bits of each pixel by the indexing sequences. Thus, we have the encrypted column shuffled RGB-level matrix as:

$$\psi rgb = [\psi rgb_{\mu 1}, \psi rgb_{\mu 2}, \dots, \psi rgb_{\mu 24}]$$

Where,

$$\psi rgb_{\mu i} = \begin{cases} sq(\psi rgb_{\mu i}, F_{x1}), i = 1, 2 \\ sq(\psi rgb_{\mu i}, F_{x2}), i = 3, 4 \\ sq(\psi rgb_{\mu i}, F_{x3}), i = 5, 6 \\ sq(\psi rgb_{\mu i}, F_{x4}), i = 7, 8 \\ sq(\psi rgb_{\mu i}, F_{y1}), i = 9, 10 \\ sq(\psi rgb_{\mu i}, F_{y2}), i = 11, 12 \\ sq(\psi rgb_{\mu i}, F_{y3}), i = 13, 14 \\ sq(\psi rgb_{\mu i}, F_{y4}), i = 15, 16 \\ sq(\psi rgb_{\mu i}, F_{z1}), i = 17, 18 \\ sq(\psi rgb_{\mu i}, F_{z2}), i = 19, 20 \\ sq(\psi rgb_{\mu i}, F_{z3}), i = 21, 22 \\ sq(\psi rgb_{\mu i}, F_{z4}), i = 23, 24 \end{cases}$$

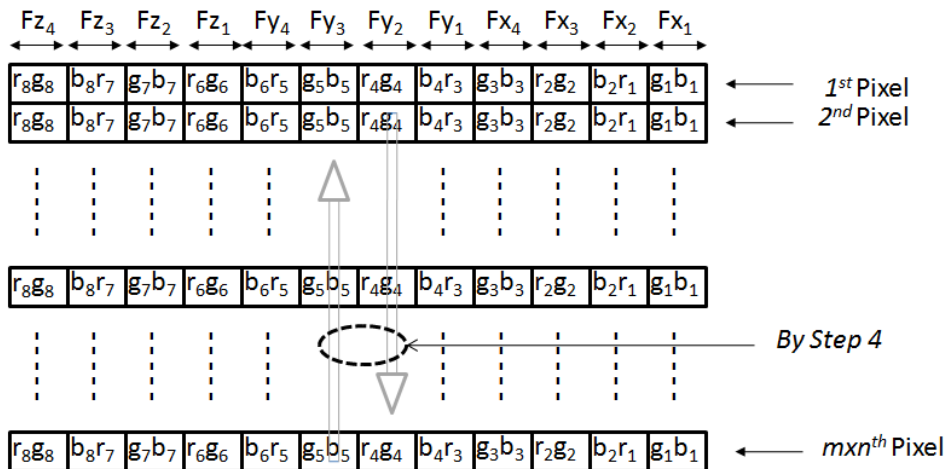


Fig. 3. Column-wise shuffling of the plaintext image bits

and  $\Psi_{rgb_{ul}}$  is the  $i$ th bit of the  $\mu$ th pixel of the original binary RGB-level matrix.

**Step 5.** Now, perform row-wise shuffling on the bits within each RGB block in pairs of 2-bits by using 12 sorted indices:  $F_{x1}$  to  $F_{x4}$ ,  $F_{y1}$  to  $F_{y4}$ , and  $F_{z1}$  to  $F_{z4}$ .

## 4. RESULTS

In this paper we have taken color images of Lena, Peppers, and Baboon in the size 256 x 256 as our test images to prove the security and robustness of the modified PCS method. The RGB components of the original image, *Lena*, and those obtained from [21] are shown in Fig. 4 and Fig. 5 respectively. The histogram levels show the distribution of pixel intensities in the image. Fig. 6 demonstrates the RGB levels in the encrypted image obtained by using proposed algorithm.

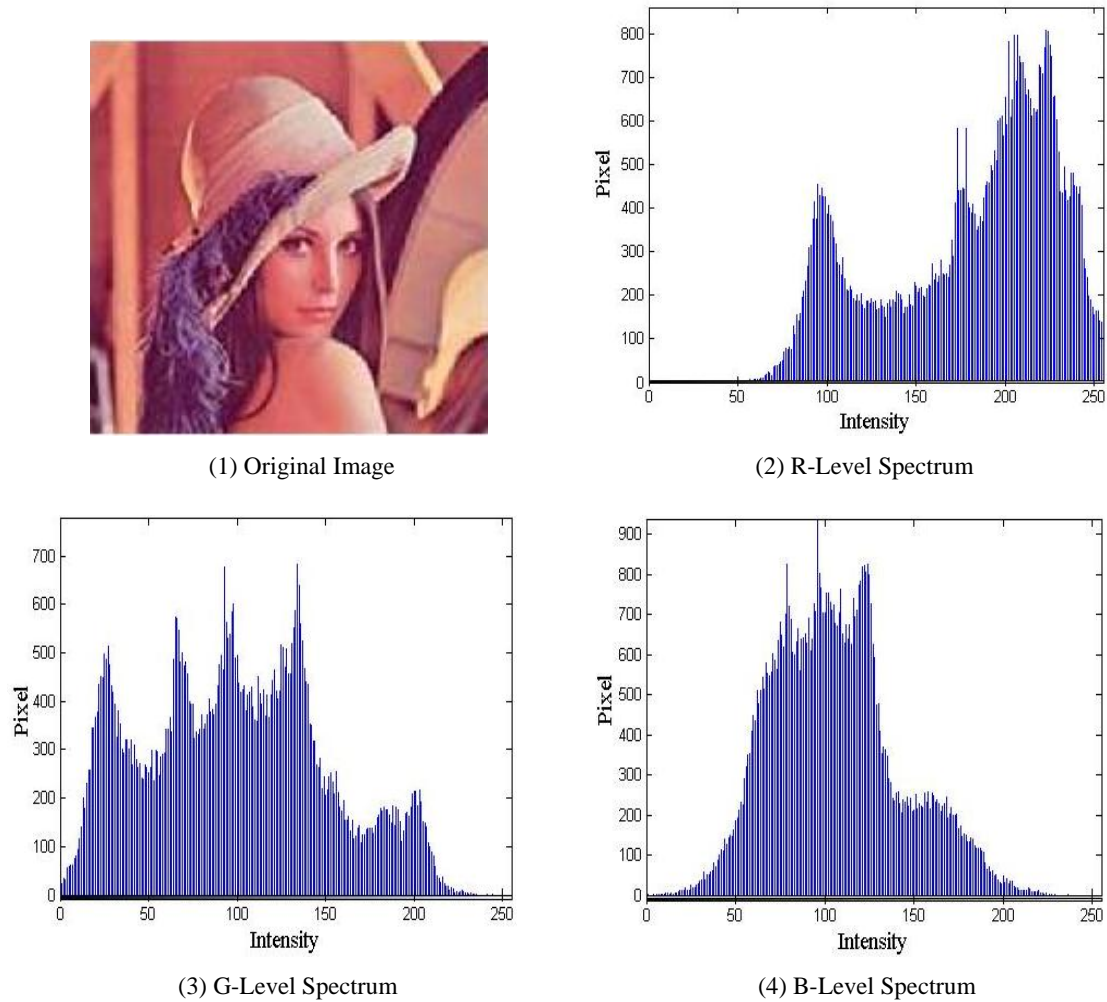


Fig. 4. Lena and its RGB-Level Spectrums



#### 4.1 Histogram Analysis

An image-histogram illustrates how pixels in an image are distributed by plotting the number of pixels of each color intensity level. The histogram obtained from the PCS technique shown in Fig. 5 has more number of peaks as compared to the proposed scheme. The image with flat histogram level is analogous to a noisy image and the ciphered image is indistinguishable when compared with the original image.

The histograms shown in Fig. 6 resembles that of a noisy image and do not reveal any information regarding pixel values of the plaintext image. We can observe that we obtain more flat and fairly uniform histogram using the proposed encryption scheme when compared with PCS cryptosystem.

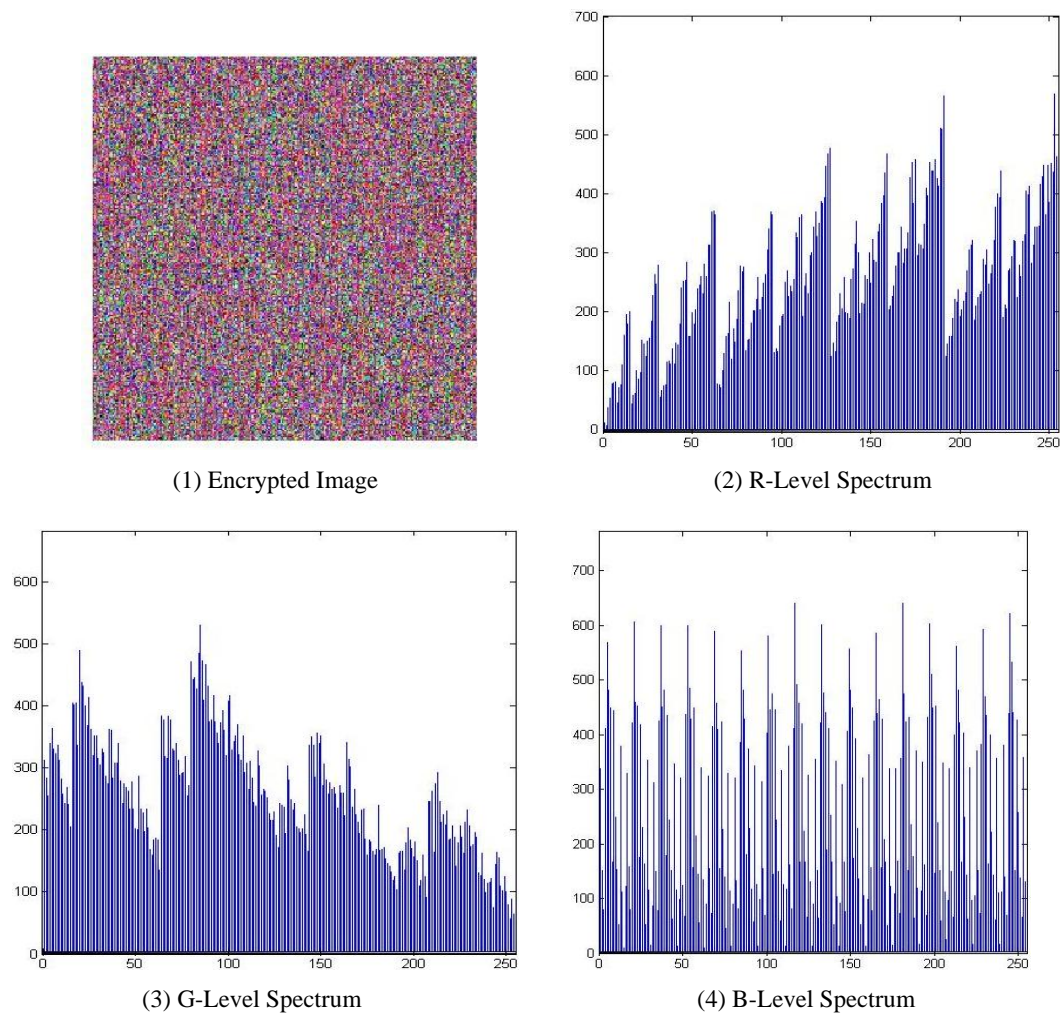


Fig. 5. The encrypted image of Lena using the PCS encryption scheme and its RGB-level spectrums

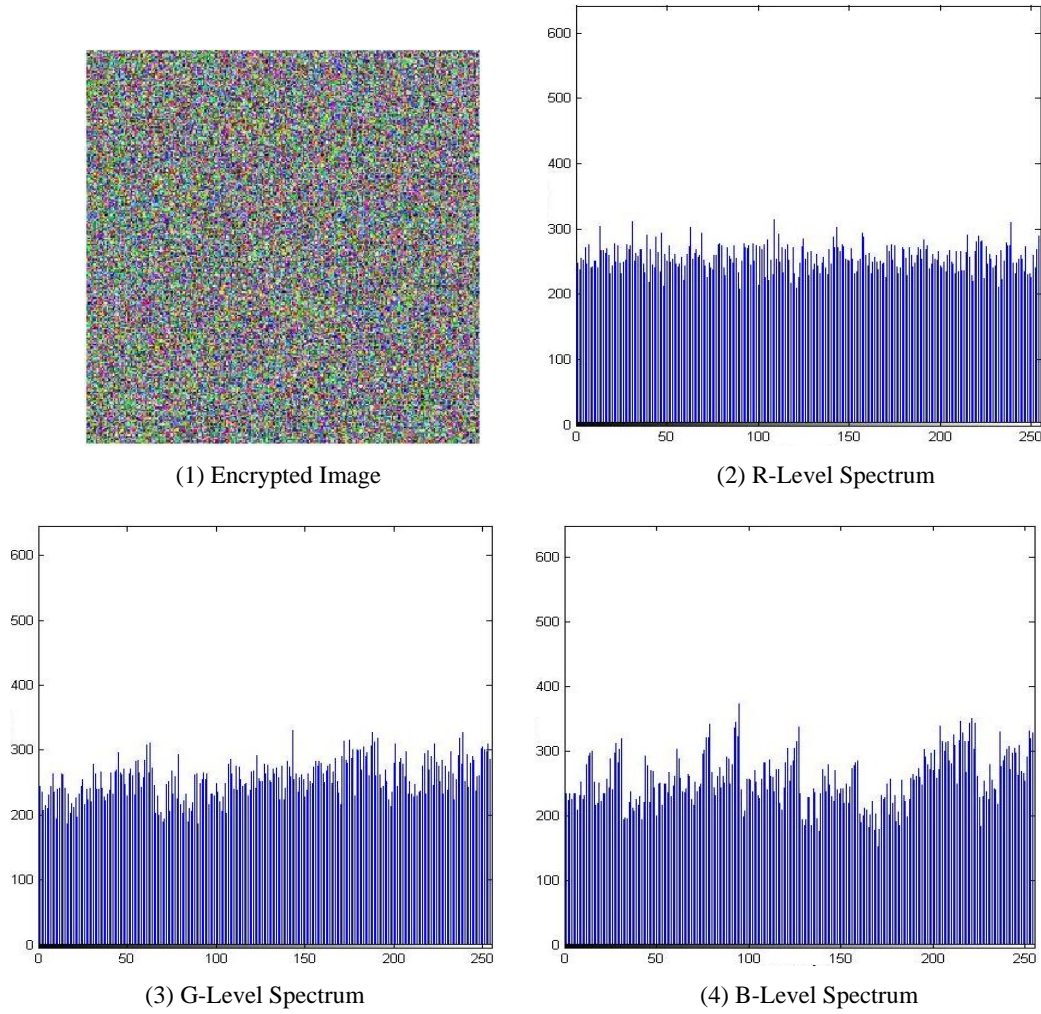


Fig. 6. The encrypted image of Lena using the proposed encryption scheme and its RGB-level spectrums

## 4.2 Entropy Analysis

The entropy of an image is a basic criterion used to depict the randomness of data and the distribution of the information. A greater value of information entropy shows a more uniform distribution of the gray value of the image. The entropy  $H$  of a symbol source  $S$  image can be computed by [23].

$$H(S) = \sum_{i=0}^{255} p(s_i) \log \left( \frac{1}{p(s_i)} \right) \quad (6)$$

Where  $p(s_i)$  represents the probability of symbol  $s_i$  and the entropy is expressed in bits. If the source  $S$  emits  $2^8$  symbols with equal probability (i.e.,  $S = \{S_0, S_1, \dots, S_{255}\}$ ) then the result of entropy is  $H(S) = 8$ , which corresponds to a true random source and represents the ideal value of entropy for message source.

Table 1. Information entropy for the original image and ciphered images

	Original Image	PCS Technique	Our Method
Lena	7.7847	7.6722	7.9838
Peppers	7.7242	7.5510	7.9628
Baboon	7.6310	7.5272	7.9798

If the entropy value tends to 8, then the predictability of the method decreases, which strengthens the image security. Table 1 shows that the entropy value of the proposed system is closer to ideal value of 8 than those computed from PCS encryption. Therefore, the leakage of information through entropy is lesser in the proposed encryption system when compared to PCS technique.

#### 4.3 NPCR and UACI Analysis

The NPCR and UACI are two most significant quantities that are used to evaluate the strength of image encryption algorithms/ciphers to resist different attacks. A sufficiently high NPCR/UACI score is usually considered to be a strong resistance against attacks. NPCR is the measure of absolute number of pixels change rate and UACI determines the averaged difference between two paired ciphertext images when the changes in plaintext images are subtle. In this section, NPCR and UACI values are computed as described below.

##### 4.3.1. NPCR and UACI between the ciphertext images before and after one pixel change

Let the plaintext image be  $P_1$  and the corresponding ciphertext image be  $C_1$ . Now, after altering a single pixel value in  $P_1$  we get changed plaintext image as  $P_2$ , and its ciphered image as  $C_2$ .

The NPCR and UACI value of the two ciphertext images,  $C_1$  and  $C_2$ , can be mathematically represented by equations (7) and (8), respectively, where  $T$  denotes the largest supported pixel value compatible with ciphertext image format,  $|\cdot|$  denotes absolute value function, and other symbols have their usual meanings[24].

$$\text{NPCR: } N(C_1, C_2) = \sum_{ij} \frac{D(i, j)}{m \times n} \times 100\% \quad (7)$$

$$\text{UACI: } U(C_1, C_2) = \frac{1}{m \times n} \sum_{ij} \frac{|C_1(i, j) - C_2(i, j)|}{T} \times 100\% \quad (8)$$

Where,

$$D(i, j) = \begin{cases} 0, & \text{if } C_1(i, j) = C_2(i, j) \\ 1, & \text{if } C_1(i, j) \neq C_2(i, j) \end{cases}$$

For example, the test image *Lena* shows that  $P_1$  is encrypted and ciphered image  $C_1$  has been obtained. To calculate NPCR/UACI, a pixel from the plaintext image  $P_1$  is randomly chosen ( $P_1(i, j)$ ,  $i = 40$ ,  $j = 56$ ) whose R color component is set to 0, while the value of the other two components remain the same. Let this new image be named  $P_2$  and its corresponding ciphered

Table 2. NPCR and UACI between  $C_1$  and  $C_2$  for *Lena*

Pixel value changed at position $P_1(i,j)$ here $i = 40, j = 56$		PCS Encryption Scheme		Proposed Encryption Scheme	
		NPCR%	UACI%	NPCR%	UACI%
$P_1(i, j, 1) = 0$	R	0.0156	0.0	99.51	33.44
	G	0.0	0.0	99.54	33.85
	B	0.0	0.0	99.57	33.89
$P_1(i, j, 2) = 0$	R	0.0	0.0	99.51	33.44
	G	0.0	0.0	99.54	33.85
	B	0.0	0.0	99.57	33.89
$P_1(i, j, 3) = 0$	R	0.0	0.0	99.52	33.10
	G	0.0	0.0	99.44	33.14
	B	0.0	0.0	99.38	33.47

image be  $C_2$ . The NPCR and UACI values for  $C_1$  and  $C_2$  are calculated for the proposed scheme and the original scheme and are listed in Table 2. Similarly, green and blue components are set to zero for the same pixel position ( $P_1(i,j)$ ,  $i = 40, j = 56$ ) and values of NPCR and UACI are evaluated. The results in Table 2 show that a small change in the plain image is reflected by a large difference in the ciphered image.

We can analyze from Table 2 that our scheme is significantly more sensitive towards initial conditions than PCS. The drastic variation in the values of NPCR and UACI arises from the fact that we employ dynamic chaotic maps that vary with varying plaintext images. On the other hand, a constant chaotic sequence for every plaintext image is being used in PCS and it shuffles the pixels to entirely same indices for all plaintext images. In PCS encryption, the two ciphered images obtained by changing one pixel in plaintext image differ from each other at utmost four pixel values, which correspond to the mapping done by the 4 chaotic sequences for the changed pixel value. The proposed technique changes the chaotic map completely and the two ciphered images differ entirely from each other, thus giving a higher score for NPCR and UACI.

#### 4.3.2 NPCR and UACI between the original image and the encrypted image

Let the plaintext image be denoted as  $P$  and the respective ciphered image obtained by applying proposed encryption algorithm is  $C$ . The formulae to calculate NPCR and UACI for the two images are represented by following equations:

$$\text{NPCR} : N(P, C) = \sum_{ij} \frac{D(i, j)}{m \times n} \times 100\% \quad (9)$$

$$\text{UACI} : U(P, C) = \frac{1}{m \times n} \sum_{ij} \frac{|P(i, j) - C(i, j)|}{T} \times 100\% \quad (10)$$

Where,

$$D(i, j) = \begin{cases} 0, & \text{if } P(i, j) = C(i, j) \\ 1, & \text{if } P(i, j) \neq C(i, j) \end{cases}$$

Table 3. NPCR and UACI between P and C for *Lena*

		PCS Encryption Scheme		Proposed Encryption Scheme	
		NPCR%	UACI%	NPCR%	UACI%
Lena	R	99.48	24.55	99.62	33.15
	G	99.55	27.51	99.60	30.67
	B	99.67	27.58	99.57	28.27

These values are calculated for the test image *Lena* and tabulated in Table 3. The NPCR and UACI scores determine the randomness between the plaintext image and its ciphertext image. We get a better UACI value for our system and NPCR score is also significantly good.

#### 4.4 Correlation Coefficient Analysis

To withstand statistical attack, the correlation between the adjacent pixels of the cipher image should be as low as possible. For evaluating correlation between pixels in the cipher image we randomly selected 5,000 pairs of adjacent pixels from an image (in horizontal, vertical, and diagonal direction). For precision these values were averaged for 100 iterations. Then, the correlation coefficient of each pair was calculated by [23].

$$\rho = \frac{N \sum_{i=1}^N (x_i \times y_i) - \sum_{i=1}^N x_i \times \sum_{i=1}^N y_i}{\sqrt{(N \sum_{i=1}^N x_i^2 - (\sum_{i=1}^N x_i)^2) \times (N \sum_{i=1}^N y_i^2 - (\sum_{i=1}^N y_i)^2)}} \quad (11)$$

where  $x$  and  $y$  are gray values of two adjacent pixels in an image and  $N$  is the total number of pairs of horizontally, vertically, or diagonally adjacent pixels. The values of correlation coefficients for the proposed algorithm and the PCS scheme are given in Table 4. According to the results, our proposed algorithm has a lesser value for correlation coefficient when compared to PCS scheme. Thus, our algorithm outperforms PCS encryption technique.

Table 4. Correlation coefficients for the test image *Lena*

	Original Image	PCS technique	Our Method
Horizontal	0.90795	0.08622	0.07457
Vertical	0.95298	0.19197	0.12074
Diagonal	0.85709	0.08429	0.08087

#### 4.5 Advantages of the Proposed Encryption Scheme

In the proposed version, the generation of shuffling sequences is made dependent on the pending image information in such a way that a tiny difference in the plaintext image results in distinct shuffling sequences, which in turn produces a totally different encrypted image. Moreover, the components of the pending image are processed collectively and dependently. These improvements make the attacks executed in [22] infeasible and impossible. So, the proposed updated version can resist the chosen-plaintext and known-plaintext attacks effectively.

## 5. CONCLUSION

In this paper a new way of image encryption that is robust against CPA and KPA has been proposed. The drawback of PCS technique is overcome by dynamically updating the chaotic map when the plaintext image changes. This ensures the robustness of the proposed algorithm against aforesaid attacks. It is achieved by giving weight to the total number of binary 1s in the plaintext image and using it in determining the key of the encryption scheme. To make the cipher image more robust against any attack, the color image is permuted before performing the actual column-wise and row-wise shuffling. The experimental values of NPCR and UACI show that the proposed encryption scheme is resistant to differential attacks. Thus, a cryptanalysis of plain/cipher image pair will not reveal the keystream. It is also shown that the ciphered image is very sensitive to a slight change in the bit values of the original image. If one pixel of the plaintext image is changed, then the corresponding cipher image obtained is altered completely in an unpredictable or pseudorandom manner. Several tests have been performed to evaluate the security of the proposed system. Namely, statistical analysis, which includes Histogram analysis; correlation analysis; NPCR and UACI analysis; and information entropy analysis. The experimental values that govern the proposed algorithm yield a very good performance over the existing PCS algorithm. Hence, this paper presents a cryptosystem that is highly secure against attacks and is useful for secure image encryption and transmission applications.

## REFERENCES

- [1] G. Chen, Y. Mao, C. Chui, "A symmetric image encryption scheme based on 3D chaotic cat maps", *Chaos, Solitons & Fractals*, Vol.21, Issue 3, 2004, pp.749–61.
- [2] F. Chiaraluce, L. Ciccarelli, "A new chaotic algorithm for video encryption," *IEEE Transactions on Consumer Electronics*, Vol.48, Issue 4, 2002, pp.838–44.
- [3] R. Matthews, "On the derivation of a chaotic encryption algorithm", *Cryptologia*, Vol.13, No. 1, Jan 1989, pp.29-41.
- [4] L. Zhang, X. Liao, X. Wang, "An image encryption approach based on chaotic maps," *Chaos Solitons Fractals*, Vol.24, Issue 3, 2005, pp.759 -765.
- [5] S. Yang, S. Sun, "A video encryption method based on chaotic maps in DCT domain", *Progress in Natural Science*; Vol.18, 2008, pp.1299–1304.
- [6] C. Fu, Z. Zhang, Y. Cao, "An improved image encryption algorithm based on chaotic maps," *Proceedings of the 3rd Int. Conf. on Natural Computation, (ICNC 2007)*: Haikou, Vol.3, pp.189-193.
- [7] K. Sakthidasan, B. V. K. Santhosh, "A New Chaotic Algorithm for Image Encryption and Decryption of Digital Color Images", *International Journal of Information and Education Technology*, Vol.1, No. 2, 2011, pp.137-141.
- [8] W. Li, N. Yu, "A Robust chaos based Image encryption scheme", *IEEE International Conference on Multimedia and Expo*: New York, 2009, pp.1034-1037.
- [9] M. El-Sayed, A. El-Alfy, Khaled, Al-Utaibi, "An Encryption Scheme for Color Images Based on-Chaotic Maps and Genetic Operators", *The Seventh International Conference on Networking and Services*, Venice/Mestre, Italy, 2011, pp.92-97.
- [10] M. S. Baptista, "Cryptography with chaos", *Phys Lett A*, Vol.240, Issue 1-2, 1998, pp.50–54.
- [11] P. L. de Oliveira Luiz, and S. Marcelo, "Cryptography with chaotic mixing" *Chaos, Solitons and Fractals*, Vol.35, Issue 3, 2008, pp.466–471.
- [12] H. Gao, Y. Zhang, S. Liang, D. Li, "A new chaotic algorithm for image encryption", *Chaos, Solitons and Fractals*, Vol.29, Issue 2, 2006, pp.393–399.
- [13] Y. Zhai, S. Lin, Q. Zhang, "Improving Image Encryption Using Multi-chaotic Map", Workshop on

- Power Electronics and Intelligent Transportation System (PEITS): Guangzhou, 2008, pp.143-148.
- [14] G. Xin, L. Fen-lin, L. Bin, W. Wei, C. Juan, "An Image Encryption Algorithm Based on Spatiotemporal Chaos in DCT Domain", *The 2<sup>nd</sup> International Conference on Information Management and Engineering(ICIME)*: Chengdu,2010, pp.267-270.
  - [15] H. H. Nien, C. K. Huang, S. K. Changchien, H. W. Shieh, C. T. Chen, Y. Y. Tuan, "Digital color image encoding and decoding using a novel chaotic random generator," *Chaos, Solitons and Fractals*, Vol.32, Issue 3, 2007, pp.1070-1080.
  - [16] K. Wang, W. Pei, L. Zou, A. Song, Z. He, "On the security of 3D Cat map based symmetric image encryption scheme," *Phys. Lett. A*, Vol.343, Issue 6, 2005, pp.432-439.
  - [17] Z. H. Guan, F. Huang, W. Guan, "Chaos-based image encryption algorithm," *Phys. Lett. A*, Vol.346, Issue 1-3, 2005, pp.153-157.
  - [18] T. G. Gao, Z.Q. Chen, "A new image encryption algorithm based on hyper-chaos," *Phys. Lett. A*, Vol.372, Issue 4, 2005, pp.394-400.
  - [19] S. Lian, "Efficient image or video encryption based on spatiotemporal chaos system", *Chaos Solitons Fractals*, Vol.40, Issue 5, 2009, pp.2509-2519.
  - [20] R. Rhouma, S. Belghith, "Cryptanalysis of a spatiotemporal chaotic image/video cryptosystem", *Phys. Lett. A*, Vol.372, Issue 36, 2008, pp.5790-5794.
  - [21] C. K. Huang, H. H. Nien, "Multi chaotic systems based pixel shuffle for image encryption," *Optics Communications*, Vol.282, Issue 11, 2009, pp.2123-2127.
  - [22] E. Solak, R. Rhouma, S. Belghith, "Cryptanalysis of a multi-chaotic systems based image cryptosystem", *Optics Communications*, Vol.283, Issue 2, 2010, pp.232-236.
  - [23] M. Ahmad, O. Farooq, "A Multi-Level Blocks Scrambling Based Chaotic Image Cipher", *Communications in Computer and Information Science*, Noida -India, Vol.94, Part 1, 2010, pp.171-182.
  - [24] Y. Wu, J. P. Noonan, S. Agaian, "NPCR and UACI Randomness Tests for Image Encryption", *Cyber Journals: Multidisciplinary Journals in Science and Technology, Journal of Selected Areas in Telecommunications (JSAT)*, April Edition, 2011, pp.31-38.



### Om Prakash Verma

Om Prakash Verma received his B.E. degree in Electronics and Communication Engineering from Malaviya National Institute of Technology, Jaipur, India, M. Tech. degree in Communication and Radar Engineering from Indian Institute of Technology (IIT), Delhi, India and Ph.D. degree from Delhi University. From 1992 to 1998 he was Assistant Professor in Department of Electronics & Communication Engineering, at Malaviya National Institute of Technology, Jaipur, India. He joined Department of Electronics & Communication Engineering, Delhi Technological University (Formerly Delhi College of Engineering), Delhi, India, as Associate Professor in 1998. Currently, he is Professor and Head of Department of Information Technology and Dean continuing education at Delhi Technological University Delhi. He has authored a book on Digital Signal Processing in 2003. His research interest includes Computer Vision and Image Processing, Application of Soft Computing techniques in Image Processing, Artificial Intelligent, Optimization techniques, Digital Signal Processing etc. He has published more than 30 research papers in International Journal and conference proceedings. He has guided 30 M. Tech. Students and presently 5 Ph.D. scholars are working under his supervision. He is Principal investigator of "Information Security Education Awareness" Project. This project is sponsored by Department of Information Technology, Ministry of MHRD, Govt. of India.



**Munazza Nizam**

Munazza Nizam received her B.Tech degree in Computer Engineering from Jamia Millia Islamia University, Delhi, India in 2010 and M.Tech degree in Information Systems from Delhi Technological University (Formerly Delhi College of Engineering), Delhi, India in 2012. She joined Deloitte Consulting India Pvt. Ltd in 2012 as Business Technology Analyst to develop ERP solutions. Currently she is working as Assistant Professor in Dept. of Computer Science and Engineering in Galgotias University, India. Her area of research includes Image Processing.

**Musheer Ahmad**

Musheer Ahmad received his B.Tech and M.Tech degrees from Department of Computer Engineering, ZH College of Engineering and Technology, AMU, India in 2004 and 2008, respectively. He joined the Department of Computer Engineering, AMU, India as a Faculty in 2006. Currently, he is with Department of Computer Engineering, Jamia Millia Islamia, New Delhi, India, as an Assistant Professor. He has published about 20 research papers in refereed academic journals and international conference proceedings. His areas of research interest include multimedia security, chaos-based cryptography, image processing and soft computing techniques.

# Multiband Microstrip Patch Antenna for Wireless Communication Systems.

Amit Kumar, Sachin Kumar, Prof.P.R.CHADHA

Dept.of ECE, Delhi Technological University, Delhi, INDIA, e-mail-amit2k11moc01@gmail.com

**Abstract**— In this paper a multiband microstrip patch antenna Design has been introduced which is a simple planer asymmetric C shaped microstrip patch. This patch antenna is designed on Sustrate of RT duroid having permittivity of 2.2. The thickness used for substrate is 0.25mm. The antenna is designed and all the results are plotted by using simulating software HFSS. Return loss, VSWR and field pattern of the designed one is plotted and found three band of operation having S11 less than -10dB and VSWR less than 2. The antenna designed antenna is having compact size and operation in WLAN, WiMAX and in ISM Band communication. Antenna is having very good polarization ratio and gain bandwidth. Operating band width is found around 300MHz.

**Index Terms**— Microstrip patch antenna, VSWR, Return Loss, Radiation Pattern, Gain, Bandwidth, WLAN, WiMAX and ISM Band.

## 1 INTRODUCTION

MICROSTRIP patches are an attractive type of antenna due to their low cost, conformability, and ease of manufacture. However, the primary barrier to implementing these antennas in many applications is their limited bandwidth which is only of the order of a few percent for a typical patch radiator. Because of this, much work has been devoted to increasing the bandwidth of microstrip antennas and 3 techniques that has been used is a near resonance aperture. This Paper also proposes a technique to enhance total available bandwidth of operation [1]. This paper proposes a patch antenna of multiband, resonating at three different frequencies, which can be used for multiple operations. The intrinsic disadvantages of patch antennas such as narrow band-width and non-uniform coverage are the reasons why this class of antenna has not been seriously considered for hand-held application[4].

The metallic patch essentially creates a resonant cavity, where the patch is the top of the cavity, the ground plane is the bottom of the cavity, and the edges of the patch form the sides of the cavity. The edges of the patch act approximately as an open-circuit boundary condition. Hence, the patch acts approximately as a cavity with perfect electric conductor on the top and bottom surfaces, and a perfect "magnetic conductor" on the sides[5][6].

Microstrip antenna is the ideal choice for such an application due to low profile, light weight, conformal shaping, low cost, simplicity of manufacturing and easy integration to circuit[1]. However, conventional microstrip patch antenna suffers from very narrow bandwidth, typically about 5% bandwidth with respect to the central frequency. There are numerous and well-known methods to increase the bandwidth of antennas, including increase of the substrate thickness, the use of a low dielectric substrate, the use of multiple resonators [2], [3].

The International standard of 3.5 GHz spectrum was the first to enjoy WiMAX products. The US license free spectrum at 5.8 GHz has a few WiMAX vendors building products. Licensed spectrum at 2.5 GHz used both domestically in the US and fairly widely abroad is the largest block in the US[7]. Also, in the US and in Korea products are shipping for the 2.3 GHz

spectrum range. Also in the US the 3.65 GHz band of frequencies now has WiMAX gear shipping to carriers. The most recent versions of both WiMAX standards in 802.16 cover spectrum ranges from at least the 2 GHz range through the 66 GHz range.

In this Paper a multiband Microstrip Patch antenna is introduced. The proposed patch is a planer structure having all the dimensions in mm. The proposed antenna is designed by using a substrate of R.D tm having thickness of mm. This proposed antenna is having three band of operation. Here Proposed antenna can be used in Wi-Max and in many more applications.

## 2 PROPOSED ANTENNA GEOMETRY

A modified c shaped microstrip patch antenna has been proposed here which is a multi band and multi operational antenna with very good impedance band width. The proposed antenna is designed with a substrate of Rogers RT/ duroid 5880(tm) having thickness of  $h=0.25\text{mm}$ . The substrate used is having dimension of  $W=40\text{mm}$  and  $L=35\text{mm}$ . Proposed antenna is having following new geometry.

1<sup>st</sup> The detailed dimensions are given in the table below all of which are calculated by using conventional relationship between W and L and all the material constants.

The Detailed dimensions are given in the below table, where all the dimensions are in mm.

L1	2mm
L2	7mm
L3	12mm
W1	6mm
W2	7mm
W3	1.5mm

**Table 1:** the detailed Dimensions of the modified C shaped patch.

The proposed geometry is given in below figure.

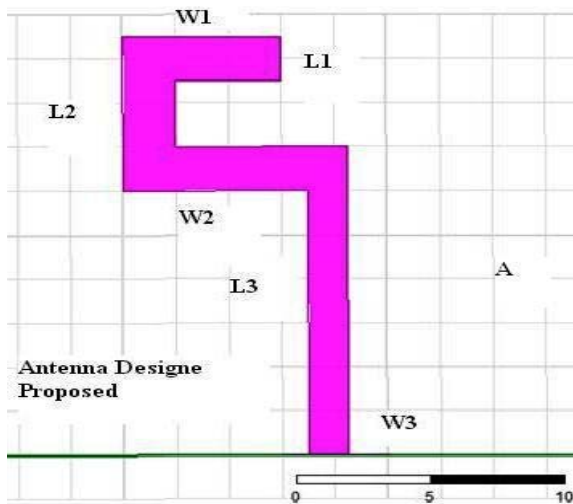


Fig no-1 Design of Proposed C shaped Patch.

The proposed shape is designed by using HFSS modular and the final result is obtained by simulating the same by using HFSS simulator .

### 3 RESULTS OF SIMULATION

When designed antenna is simulated in HFSS then following results were observed. Plote of returnloss and VSWR is given below. BY seaing the overall response of antenna for s11 parameter and VSWR.A multiband antenna has been designed. fig no-2

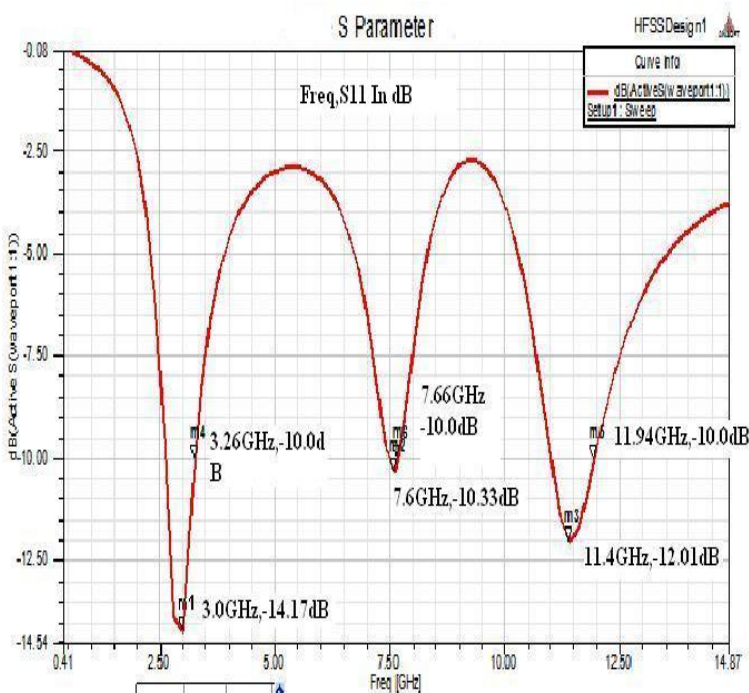


Fig no-2 S11 parameter

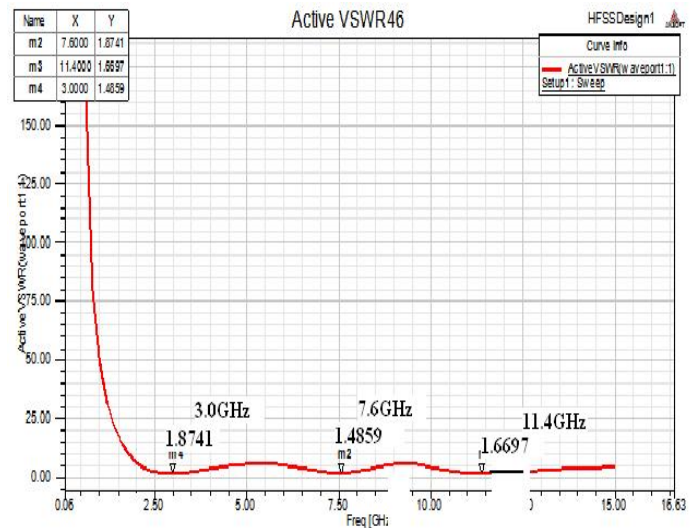


Fig 3 VSWR (Freq, VSWR)

From the above obtained results we can say that The de-signed antenna is having three band of operations which is having three band of operation.Obtained S11 parameter at all these frequencies is having values less then -10dB.Value of VSWR at all these three resonating frequency band is also less then 2 and greater then 1.So we can say that designed antenna is resonating at 3 different resonating frequencies.All these Frequency have it's own operation.The obtained result is also listed in the table below.

Frequency	S11	VSWR
3.0GHz	-14.17 dB	1.485
7.6GHz	-10.33 dB	1.8741
11.4GHz	-12.01 dB	1.669

Table 2: detailed designed simulation results.

Polarization and gain plot is also represented with radiation pattern for simple understanding.

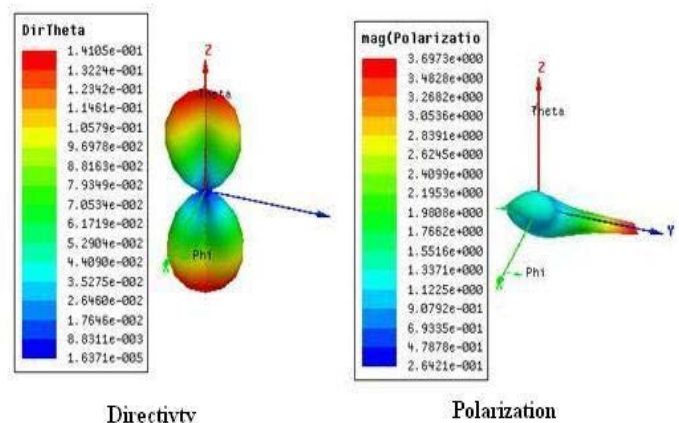


Fig no 3- Directivty and Polarization plot.

## 5 CONCLUSION

1<sup>st</sup> it is resonating at 3GHz which is near to ISM band and also the same band is applicable for lower WiMAX band application. The antenna is having return loss of -14.1772dB at 3GHz with impedance band width of approximately 300MHz. Similarly at 7.6GHz having S11 of -10.3361dB with band width of 300MHz and at 11.40 GHz S11 is -12.0183dB with band width of 300 MHz.

This designed antenna is the new one proposed and simulated on HFSS.

also results are checked mathematically, both results are approximately same.

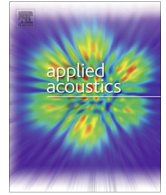
This antenna can be used in various ISM band communication, can be used as a fixed antenna service and as a satellite antenna at the same time. More no. of operations like WLAN, WiMAX, ISM band communication can be done by using same antenna system.

## ACKNOWLEDGMENT

The author wishes his thanks to Prof. Dr. Rajeev Kapoor (HOD-ECE) and Dr. N.S. Raghava, Associate Professor From Delhi Technological University for their sincere advice and support in the work. Author is also thanking to their parents and some friends for providing me such support during the work.

## REFERENCES

- [1] J. Ghalibafan and A. R. Attari, F. H. Kashani, "A NEW DUAL-BAND MICROSTRIP ANTENNA WITH U-SHAPED SLOT", *Progress In Electromagnetics Research C*, Vol. 12, 215(223, 2010.
- [2] Ka-Lam Lau, Kwai-Man Luk, and Kai-Fong Lee, "Design of a Circularly-Polarized Vertical Patch Antenna", *IEEE TRANSACTIONS ON ANTENNAS AND PROPAGATION*, VOL. 54, NO. 4, APRIL 2006.
- [3] AbuTarboush, H. S. Al-Raweshidy and R. Nilavalan, "Compact double U-Slots Patch Antenna for Mobile WiMAX Applications", *IEEE*
- [4] O. Hazila, S. A. Aljunid, Fareq Malek, A. Sahadah "Performance Comparison between Rectangular and Circular Patch Antenna Array" *Proceedings of 2010 IEEE Student Conference on Research and Development (SCoReD 2010)*, 13 - 14 Dec 2010, Putrajaya, Malaysia, pp 47-52.
- [5] Amit Kumar, P. R. Chadha, "Microstrip Antenna for WLAN Application Using Probe Feed", *IOSR-JECE*, Volume X, Issue X (Jan. - Feb. 2013)
- [6] Prof. P. R. Chadha, Amit Kumar, "Rectangular Microstrip Patch Antenna Design for WLAN Application Using Probe Feed", *IJETAE*, Volume 2, Issue 12, December 2012.
- [7] Wenkuan Chen, Yuanxin Li, Hongyan Jiang and Yunliang Long, "Design of novel tri-frequency microstrip patch antenna with arc slots", *ELECTRONICS LETTERS* 24th May 2012 Vol. 48 No. 11.



## Technical Note

## Parametric sensitivity analysis of factors affecting sound insulation of double glazing using Taguchi method

Naveen Garg<sup>a,b,\*</sup>, Anil Kumar<sup>a</sup>, Sagar Maji<sup>b</sup><sup>a</sup> Apex Level Standards and Industrial Metrology Division, CSIR – National Physical Laboratory, New Delhi 110 012, India<sup>b</sup> Department of Mechanical and Production Engineering, Delhi Technological University, Delhi 110 042, India

## ARTICLE INFO

## Article history:

Received 6 December 2012

Received in revised form 12 March 2013

Accepted 14 May 2013

## Keywords:

Sound transmission class (STC)

Spectrum adaptation terms ( $C$ ,  $C_{tr}$ )Weighted sound reduction index ( $R_w$ )Mass–air–mass frequency ( $m.a.m$ )

Taguchi method

 $L_9$  orthogonal array

## ABSTRACT

The paper presents application of Taguchi method in optimizing the sound transmission through double glazing in order to investigate the relative influence of the various parameters affecting the sound insulation characteristics for design of highly insulative facade constructions and windows for traffic noise abatement. The application of Taguchi method for optimizing sound transmission loss has been rarely reported. The present work uses the results analytically predicted using 'Insul' software for various double glazing configurations as desired by each experimental run in an  $L_9$  orthogonal array. The relative importance of the parameters on single number rating  $R_w$  ( $C$ ,  $C_{tr}$ ) was evaluated in terms of percentage contributions using Analysis of Variance (ANOVA). The analysis reveals that air-gap is a prominent factor in controlling the sound insulation characteristics of double glazing and thus regression equations correlating the single-number ratings with thickness of identical glass and air-gap in a double glazing is described.

© 2013 Elsevier Ltd. All rights reserved.

## 1. Introduction

The sound transmission through double glazing has always been a gray area of research for its applications in facades and windows in dwellings for outside noise abatement. Double glazing has been a preferred alternative for windows and also used widely in building facades. Although glass facades aesthetically prove to be the best alternative for facades, yet the sound insulation characteristics especially in noisy areas is a topic of concern. Triple glazing has been reported to have approximately the same performance as double window with the same total mass and thickness [1]. The complexity of triple glazing and economic constraints limits their applications in practical situations. Laminated glass created by bonding two or more layers of glass together with thin plastic inter-layers increases the damping of the bending waves in glass leading to increment in transmission loss ( $TL$ ) in the region of coincidence dip. Tadeu and Mateus [2] investigations on glazed solutions without frame reveal that double glazing only exhibits better insulation behavior than single panels if air chambers are close to or greater than 50 mm thick, or if air chambers are very small. Quirt investigations [3,4] reveal an increment of 6 dB in Sound transmission Class (STC) value for doubling of glass thickness in a double glazing, while an increment of 3 dB in STC value

is reported for doubling of inter-pane separation. Thus, it is imperative to analyze the relative influence of the parameters affecting the sound insulation properties of double glazing for design and applications for achieving the desired objectives. The major parameters affecting the sound insulation of double glazing have been assimilated in a cause-and-effect analysis diagram after exhaustive literature survey [5–14] as shown in Fig. 1.

Although the sound transmission loss in entire frequency range from 50 Hz to 5 kHz is important, yet dependence upon the single-number ratings has been a contemporary approach followed by manufacturers, engineers and even the acousticians too. The choice of appropriate single-number rating is however very important. The recent investigations pertaining to the consideration of single-number rating for building elements confirm the suitability of ISO 717-1 spectrum adaptation terms in sound regulation requirements for building elements [15,16]. Weighted standardized sound level difference of façades,  $D_{2m,nT,w} + C_{tr}$  rating has been recommended in some studies to be a suitable single-number quantity for building facades for evaluating the sound insulation towards traffic noise in some countries [17,18]. However, there is no threshold value prescribed for acoustic comfort criteria in dwellings. Some recent studies also recommend the use of Weighted Standardized Field Level Difference,  $D_{nT,w}$  in sound regulation requirements in dwellings [19,20]. The present study focuses on the laboratory sound insulation properties of the double glazing as laboratory experiments serves as a benchmark in design of improved constructions. The study analyzes the performance characteristic of double glazing in terms of  $R_w$  ( $C$ ,  $C_{tr}$ ) in frequency range

\* Corresponding author at: Apex Level Standards and Industrial Metrology Division, CSIR – National Physical Laboratory, New Delhi 110 012, India. Tel.: +91 9868377370; fax: +91 11 45608380.

E-mail address: [ngarg@mail.nplindia.ernet.in](mailto:ngarg@mail.nplindia.ernet.in) (N. Garg).



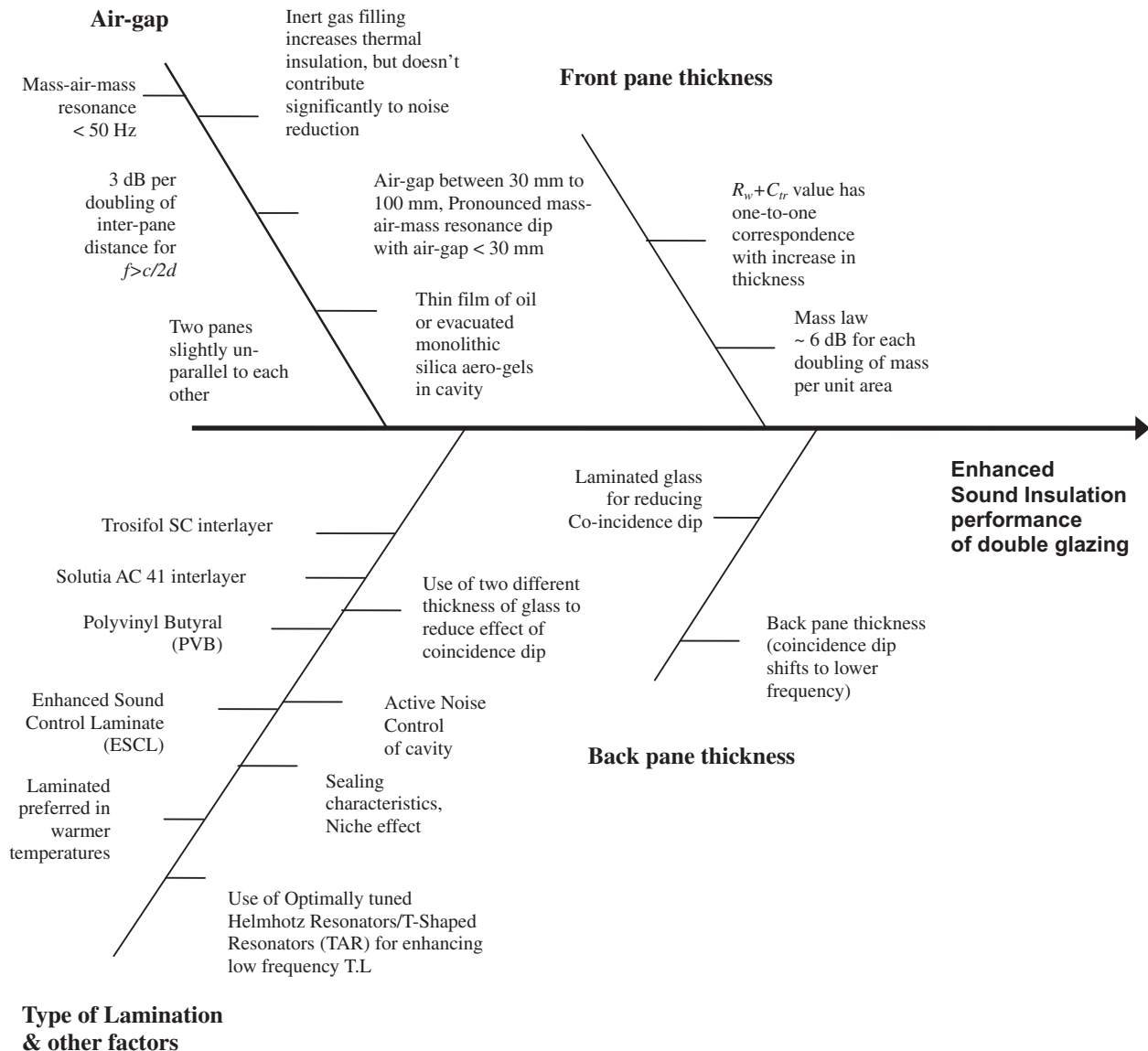


Fig. 1. Cause-and-effect analysis diagram for enhancing the sound transmission loss of double glazing.

100 Hz to 3.15 kHz and the *STC* rating. The relative importance of all these parameters on single-number rating is evaluated using Taguchi method, which is a well known method widely used in industrial engineering for optimization of process parameters. As the experimental results are practically cumbersome and expensive to perform, so a validated software '*Insul*' version 7.0.4 [21] was used to analytically predict the sound transmission and single number rating associated with various configurations. *Insul* software bases its calculations on model approaches suggested by Sharp, Cremer and others [21,22]. The size of the sample was taken as 2.7 m × 4 m. The recent investigations by Kurra [23] and development of a prediction model for multi-layered building elements confirm the compatibility of *Insul* model with experimental data although correlation coefficients are rather high. The standard deviation of difference of measured and *Insul* predicted data is observed to be 4.5 dB. Ballagh [24] investigations evidently reveals a mean difference in *STC/Rw* between measurement and theory less than 0.5 dB and 90% of results were found to lie within ±2.5 dB. These evidences confirm the suitability of the software for pursuing analytical studies pertaining to optimization of the performance characteristics of partition panels.

## 2. Taguchi method

The Taguchi method developed by Genuchi Taguchi is a statistical method used to improve the product quality and is commonly used in improving industrial product quality [25]. Taguchi designs experiments using specially constructed tables known as "orthogonal array" (OA). The method based on orthogonal arrays is widely used in industrial and research applications as in this approach fewer number of experiments are required to obtain optimum level of process parameters. An orthogonal array is a fractional factorial design used to ascertain the effects of multiple process variables on the performance characteristic while minimizing the number of test runs. The use of these tables makes the design of experiments very easy and consistent [26] and it requires relatively lesser number of experimental trials to study the entire parameter space. As a result, considerable savings in time, cost, and labour is achieved using this innovative technique. Taguchi recommends the use of the signal-to-noise (*S/N*) ratio to measure the quality characteristics deviating from the desired values. Usually, there are three categories of quality characteristic in the analysis of the *S/N* ratio, i.e. the-smaller-the-better, the-larger-

the-better, and the nominal-the-better. Furthermore, a statistical analysis of variance (ANOVA) is performed to investigate which process parameters are statistically significant.

The Taguchi technique includes the following steps:

- determine the control factors and their respective levels,
- select an appropriate orthogonal array,
- conduct the experiments as dictated by orthogonal array,
- analyze data using ANOVA and determine the optimal levels of control factors,
- investigate the relative influence of all these parameters
- perform the confirmation experiments and obtain the confidence interval,
- improve the quality characteristics through optimization.

The selection of an appropriate orthogonal array (OA) requires prior estimation of degrees of freedom. Basically the degree of freedom for an orthogonal array should be greater than or at least equal to those for the process parameters influencing the output [27]. The analysis of variance (ANOVA) is used to investigate the significance of design parameters significantly affecting the quality characteristic, which is accomplished by separating the total variability of the  $S/N$  ratios, measured by the sum of the squared deviations from the total mean  $S/N$  ratio, into contributions by each of the design parameters and the error. The total sum of squared deviations is decomposed into two parts: the sum of squared deviations due to each design parameter and the sum of squared error [28]. The percentage contribution by each of the design parameters is a ratio of the sum of squared deviations due to each design parameter to the total sum of squared deviations [27–30].  $F$ -ratio for each design parameter is the ratio of the mean of squared deviations to the mean of squared error and is used to statistically ascertain the significance of design variable. The methodology adopted for parametric sensitivity analysis using Taguchi method is shown in Fig. 2. The parametric sensitivity analysis is conducted using design of experiments based on  $S/N$  ratio and ANOVA analysis, wherein the significant parameters are analyzed in terms of main effects plot using  $S/N$  ratio and relative importance of the parameters on single number rating  $R_w$  ( $C$ ,  $C_{tr}$ ) is evaluated in terms of percentage contributions using Analysis of Variance (ANOVA). The final step in Taguchi method is to predict and confirm the quality characteristic using the determined optimal design parameters.

### 3. Application of Taguchi method

Selection of control factors and their levels are made on the basis of preliminary experimental investigations conducted in Reverberation chambers at Acoustics & Vibration division of National Physical Laboratory, India [31] and also from the literature review on the subject. Four control factors viz., front pane thickness, back pane thickness, air-gap and type of lamination are selected for the investigation. Each of the four factors is considered at three levels as shown in Table 1. The choice of three levels has been made because the effect of these factors on the performance characteristics may vary nonlinearly. The front pane thickness and back pane thickness is varied from 3 mm to 9 mm although for large thickness, coincidence dip may have its impact on the high frequency sound transmission loss of double glazing. The range of air-gap selected was 30 mm to 90 mm as previous investigations have shown that for an air-gap less than 30 mm, a pronounced mass-air-mass resonance dip is encountered seriously affecting the low frequency sound transmission loss [14]. The choice of lamination was challenging as there has been various commercial products developed. The PVB glazing is currently manufactured and marketed by a number of companies in various brands viz., 'S-Lec', 'Butacite', 'Solutia',

'Saflex', 'Trosifol' etc. The present study considers 'Trosifol' lamination as one of the parameters for analysis. The experiments were designed based on the orthogonal array technique. An  $L_9$  ( $3^4$ ) standard orthogonal array [28] as shown in Table 2 was used in present work. The array is most suitable to provide the minimum degrees of freedom as 9 [ $=1 + 4 \times (3 - 1)$ ] required for an experimental investigation.

Four control factors each identified at three levels viz.  $A_1$ ,  $A_2$ ,  $A_3$  etc. can be investigated using  $L_9$  orthogonal array, while the intersections are considered to be negligible. The array has 9 rows and 4 columns and each row represent an experimental run, while each column accommodates a specific process parameter. The factors investigated are identified as  $A$ ,  $B$ ,  $C$  and  $D$  and while conducting the experiment, all intersections amongst parameters  $A$ ,  $B$ ,  $C$  and  $D$  are ignored. The goal of the present work is to investigate about the double glazing configuration having maximum  $R_w + C_{tr}$  value. So, larger-the-better quality characteristic was implemented in this study. The equation for calculating signal-to-noise ratio ( $S/N$ ) for larger-the-better formulation is

$$S/N = -10 \log \left( \frac{1}{n} \sum_{i=1}^n \frac{1}{y_i^2} \right) \quad (1)$$

where  $n$  is number of tests in a trial and  $y_i$  is value of  $i$ th test in that trial. The results have been numerically predicted from the *Insul* software.

The variation in response was investigated using signal-to-noise ratio ( $S/N$ ) ratio judiciously chosen to accomplish the desired objective of maximizing the sound insulation. The average values of  $S/N$  ratios of four control factors at each level is shown in main effects plot in Fig. 3.

The optimum condition is examined to have that level corresponding to highest  $S/N$  ratio. It is evident from Fig. 2 that optimum levels are  $A_1$  (9 mm front pane thickness),  $B_3$  (9 mm back pane thickness),  $C_1$  (90 mm cavity depth) and  $D_3$  (Trosifol type lamination) respectively. The dotted line represents the mean value of  $S/N$  ratio.

### 4. Analysis and discussion

The analysis of variance (ANOVA) is also performed to investigate the relative influence of significant parameters. Table 3 shows the computed results for ANOVA analysis with 95% confidence level. The  $F$ -ratio and percentage contribution of the various single number rating  $R_w$  and  $R_w + C_{tr}$  are quantified in Table 3 and 4 at 95% confidence level

ANOVA usage in Taguchi methods can be seen as a two step procedure [32]. In the first stage, the variance due to the individual factors and all possible combinations of factors that were studied are computed. In the second stage, the variance due to any pair of factors (or combination) is compared. The analysis thus reveals the significant factors affecting the design output. The measure of relative significance is ascertained by an  $F$ -ratio, whereby the factors having high probability typically higher than 95% are confirmed as significant factors. Larger the  $F$ -ratio, the greater is the effect on the performance characteristic due to change of the process parameter. The inactive and smaller effects are added together to obtain a non-zero estimate of the error variance called 'pooling up' which can be used to combine factors or interaction effects with low magnitude of sum of squares [25,33]. These analysis thus ascertain the more robust design configuration. The ANOVA analysis for  $R_w$  value in Table 3 reveals the type of lamination does not play a significant role and thus contributes to the pooled error. Air-gap and back pane thickness evidently have a greater impact on the sound insulation performance of double glazing. A similar analysis was conducted for single-number rating  $R_w + C_{tr}$  as shown in Table 4. The type of lamination is also observed to be insignificant for  $R_w + C_{tr}$  rating. However, the ANOVA analysis shows that the



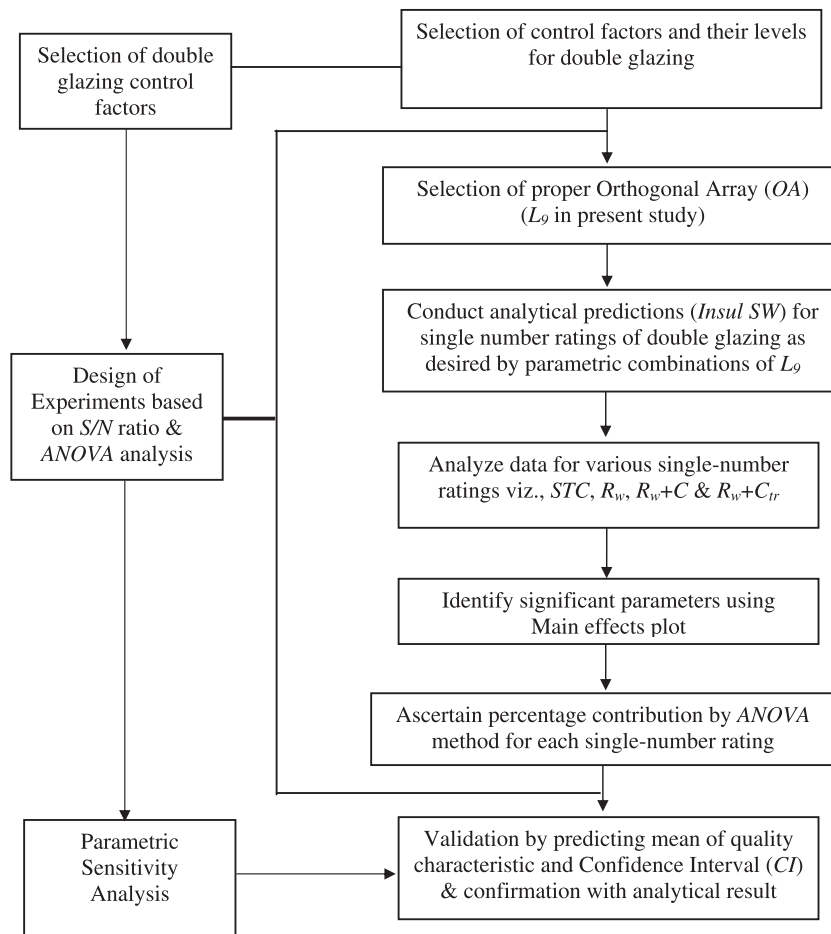


Fig. 2. Methodology adopted for parametric sensitivity analysis of factors affecting sound insulation of double glazing.

Table 1  
Selected parameters at different levels.

Parameter	Level 1 (mm)	Level 2 (mm)	Level 3
A Front pane thickness	9	6	3 mm
B Back pane thickness	3	6	9 mm
C Air-gap	90	60	30 mm
D Lamination type	PVB 0.38	PVB 0.76	Trosifol SC interlayer

Table 2  
 $L_9$  ( $3^4$ ) standard orthogonal array.

Expt. no.	Front pane thickness (mm) (A)	Back pane thickness (mm) (B)	Air-gap (mm) (C)	Lamination Type (D)
1	9	3	90	PVB 0.38
2	9	6	60	PVB 0.76
3	9	9	30	Trosifol SC interlayer
4	6	3	60	Trosifol SC interlayer
5	6	6	30	PVB 0.38
6	6	9	90	PVB 0.76
7	3	3	30	PVB 0.76
8	3	6	90	Trosifol SC interlayer
9	3	9	60	PVB 0.38

front pane thickness has slightly higher impact on the sound insulation performance. It may be noted here that these results do not contradict with the principle of reciprocity. The higher impact of back pane thickness in controlling  $R_w$  value and vice versa in case of  $R_w + C_{tr}$  rating needs further subtle investigations for analysis. There have been some experimental investigations reported [6] that confirm the prominent role of back pane thickness in controlling the coincidence dip. It has been observed that coincidence dip shifts towards low frequency as back pane thickness increases, while it is independent of inter-pane distance [6,7]. The slightly higher significance of front pane thickness in  $R_w + C_{tr}$  value may be attributed to the seriously affected low frequency sound insulation properties of front pane directly exposed to outside traffic noise.

The percentage analysis observed in ANOVA analysis has been shown in Fig. 4 for various single number rating  $R_w + C_{tr}$ ,  $R_w + C$ ,  $STC$  and  $R_w$ . It is evident that air-gap is the most significant factor followed by front pane thickness and back pane thickness. Only in case of  $R_w + C_{tr}$  rating, front pane is slightly more prominent, while in case of  $STC$ ,  $R_w$  and  $R_w + C$ , back pane thickness has more significance. The type of lamination has no statistical significance except in case of  $STC$  rating (5.3%). This may be attributed to the fact that laminated glass provide better sound control than regular glass, but the improvement occurs only in frequency range of coincidence effect [34].

These conclusions thus invite further analysis on the effect of these single-number ratings with changing the air gap. Consequently, an analysis is done on *Insul* software for predicting the  $R_w$  value and  $R_w + C_{tr}$  value for air-gap ranging from 10 mm to

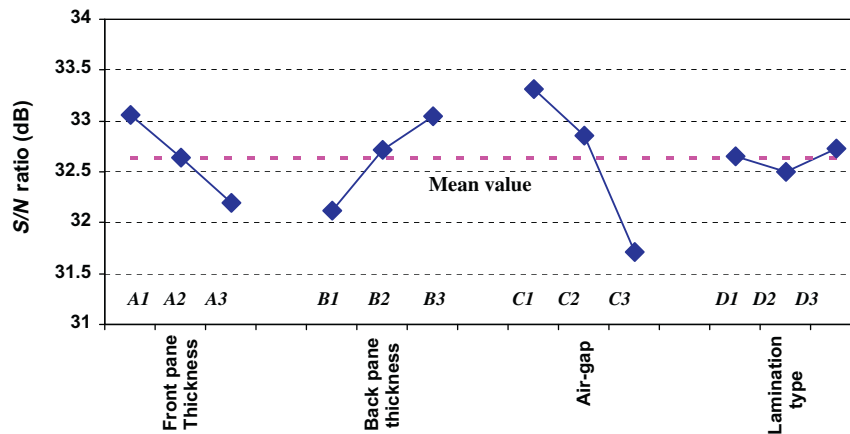


Fig. 3. Effect of parameters on average signal-to-noise (S/N) ratio for  $R_w + C_{tr}$  value of double glazing.

Table 3

Results of analysis of variance (ANOVA) for  $R_w$  of double glazing.

Parameter	Degree of freedom	Sum of squares (S)	Mean square	F-ratio	Contribution (%)
A Front pane thickness	2	24.00	12.00	35.77*	15.98
B Back Pane thickness	2	28.667	14.334	42.73*	19.18
C Air-gap	2	92.667	46.334	138.10*	63.01
Pooled error	2	0.667	0.336		1.83
Total	8	146.00			100.00

From F-Table,  $F_{0.05;1,2} = 18.5$ .

\* Factors are significant at 95% confidence level.

Table 4

Results of analysis of variance (ANOVA) for  $R_w + C_{tr}$  of double glazing.

Parameter	Degree of freedom	Sum of squares (S)	Mean square	F-ratio	Contribution (%)
A Front pane thickness	2	66.889	33.4445	42.99*	26.75
B Back Pane thickness	2	62.889	31.4445	40.42*	25.11
C Air-gap	2	112.889	56.4445	72.55*	45.59
Pooled error	2	1.556	0.778		2.55
Total	8	244.222			100.00

From F-Table,  $F_{0.05;1,2} = 18.5$ .

\* Factors are significant at 95% confidence level.

100 mm and with identical glasses in double glazing. Fig. 5 shows the effect of changing the air-gap on  $R_w$  value for various thicknesses. While designing the suitable glazing, the design factors are concentrated on shifting the mass-air-mass resonance frequency ( $m.a.m$ ) less than 50 Hz. The analytical predictions reveal that the design target for achieving the  $m.a.m$  resonance less than 50 Hz could be achieved with a double glazing with identical glasses of 9 mm thickness separated with 100 mm air-gap. The  $m.a.m$  frequency analytically predicted for identical 3 mm glazing on both sides is 84 Hz. For glazing with thickness ratio 1:2, the maximum  $m.a.m$  is calculated to be 73 Hz in case of double glazing comprising of 3 mm and 6 mm glass.

The regression fit for the single-number rating and variables air-gap ( $d$ ) and thickness ( $t$ ) of identical glass in a non-laminated double glazing is modelled as:

$$R_w = 0.75t + 0.0836d + 31.41; \quad r^2 = 0.89 \quad (2)$$

$$R_w + C_{tr} = 1.595t + 0.1107d + 18.29; \quad r^2 = 0.90 \quad (3)$$

$$R_w + C = 1.027t + 0.093d + 27.17; \quad r^2 = 0.88 \quad (4)$$

$$STC = 0.768t + 0.0949d + 30.60; \quad r^2 = 0.81 \quad (5)$$

The regression for the single-number rating and variables air-gap ( $d$ ) and thickness ( $t$ ) of identical glass in a laminated (PVB 0.76 mm) double glazing is modelled as:

$$R_w = 1.146t + 0.092d + 30.169; \quad r^2 = 0.92 \quad (6)$$

$$R_w + C_{tr} = 1.878t + 0.121d + 16.827; \quad r^2 = 0.92 \quad (7)$$

$$R_w + C = 1.458t + 0.105d + 25.31; \quad r^2 = 0.91 \quad (8)$$

$$STC = 1.182t + 0.101d + 29.57; \quad r^2 = 0.83 \quad (9)$$

These empirical formulations are valid for range  $30 \text{ mm} \leq d \leq 100 \text{ mm}$  and  $3 \text{ mm} \leq t \leq 10 \text{ mm}$  with coefficient of multiple determination ( $r^2$ ) in each case is greater than 0.80. It may be noted here that coefficient of multiple determination is a statistic that indicates the goodness of fit of model, whereby  $r^2 = 1$  indicates that regression line perfectly fits the data.

Fig. 6 shows the effect of air-gap on  $R_w + C_{tr}$  value of different double glazing of varied thickness. A 7 dB increment in  $R_w$  value is observed for 50 mm air-gap, while for an 100 mm air-gap, the increment observed is 5 dB in case of changing the thickness from 3 mm identical glasses to 10 mm. The increase in  $R_w + C_{tr}$  is 12 dB for 100 mm air-gap, while this increment is 13 dB for 50 mm air-gap. The predicted mean for quality characteristic ( $R_w + C_{tr}$  and  $R_w$ ) is computed as [25]:

$$(R_w + C_{tr})_{mp} = \bar{Y} + (\bar{A}_1 - \bar{Y}) + (\bar{B}_3 - \bar{Y}) + (\bar{C}_1 - \bar{Y}) + (\bar{D}_3 - \bar{Y}) \quad (10)$$

where  $\bar{Y}$  is the average of performance characteristic (sound transmission loss) corresponding to all nine experiments in Table 2. A 95% confidence interval (CI) for the predicted means of optimum quality characteristic ( $R_w + C_{tr}$  and  $R_w$ ) is estimated using the following equations [25]:

$$CI = \sqrt{F(\alpha, 1, f_e) V_e \left[ \frac{1}{N_{eff}} + \frac{1}{R} \right]} \quad (11)$$

where

$$N_{eff} = \frac{N}{1 + T_{DOF}} \quad (12)$$

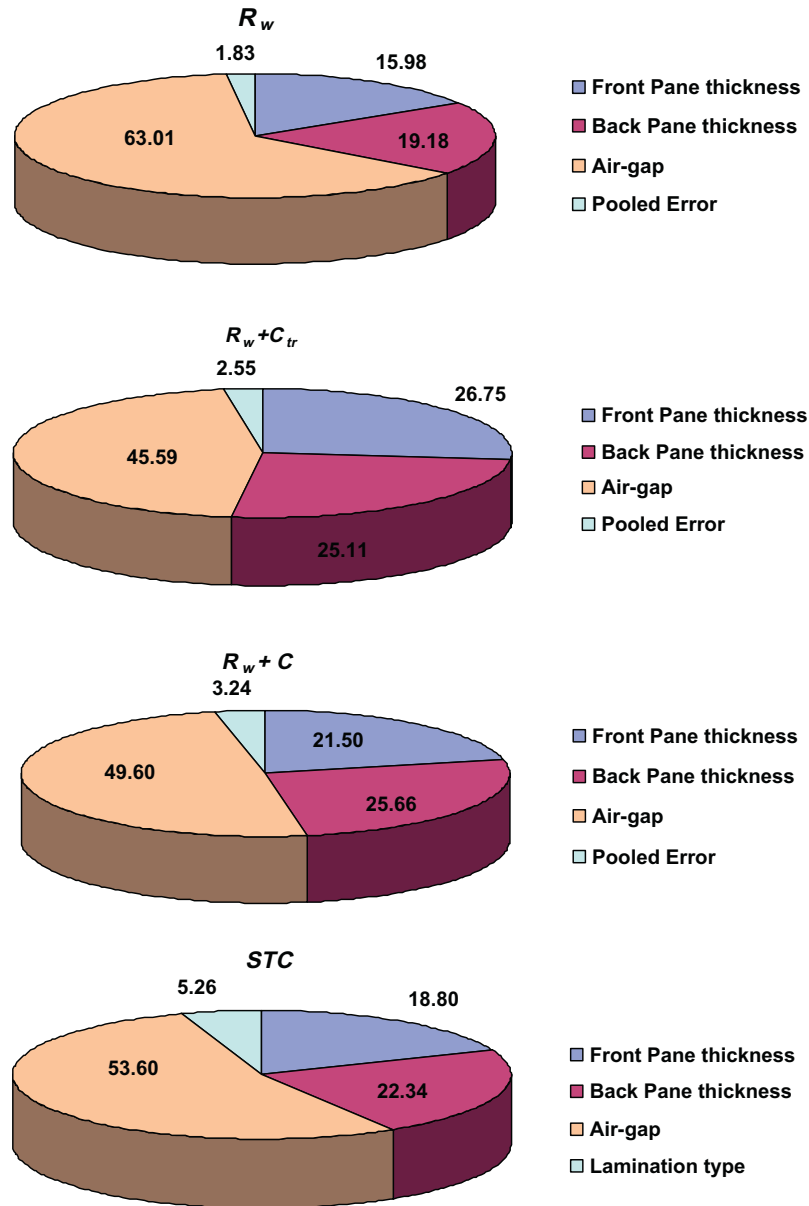


Fig. 4. Evaluation of percentage contribution using ANOVA of various parameters on single-number rating of double glazing.

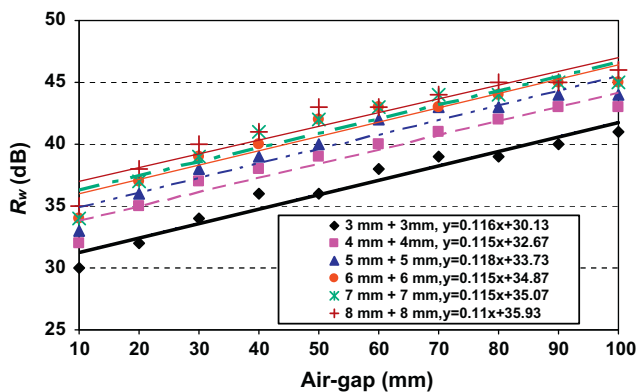


Fig. 5. Effect of air-gap on  $R_w$  of double glazing.

where  $F(\alpha, 1, f_e)$  is  $F$ -ratio required for 100  $(1 - \alpha)$  percent confidence interval,  $f_e$  is  $DOF$  for error,  $V_e$  is error variance (or Mean square error),  $R$  is number of repetitions for confirmation experiments ( $=1$ ) and  $N_{eff}$  is effective number of replications,  $N$  is total number of experiments ( $=9$ ) and  $T_{DOF}$  is total degrees of freedom ( $=8$ ) associated with estimate of mean optimum. From Tables 3 and 4, the values are:  $V_e = 0.336$  for  $R_w$  and  $V_e = 0.778$  for  $R_w + C_{tr}$ ,  $f_e = 2$  and from standard statistical table, the required  $F$ -ratio for  $\alpha = 0.05$  is  $F_{0.05;1,2} = 18.5$ . Substituting these values in Eqs. (11) and (12), the calculated  $CI$  is  $\pm 3.52$  for  $R_w$  and  $\pm 5.37$  for  $R_w + C_{tr}$  rating. Thus 95% confidence level of the predicted  $(R_w + C_{tr})_{mp}$  value is  $(46 \pm 5.4)$  dB and  $R_{w,mp}$  is  $(50 \pm 3.5)$  dB. The confirmation experiment was performed by analytically predicting the single-number rating for optimal configuration ( $A_1B_3C_1D_3$ ). The optimum configuration has  $R_w$  value of 49 and  $R_w + C_{tr}$  value of 44, which lies within the predicted range from Taguchi method.

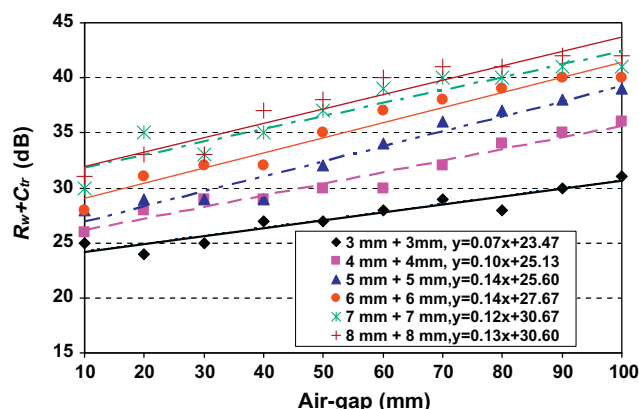


Fig. 6. Effect of air-gap on  $R_w + C_{tr}$  of double glazing.

## 5. Conclusions

The paper presents an application of well known Taguchi method in optimizing the sound transmission loss through double glazing for their applications as building facades and windows in dwellings. Taguchi's robust orthogonal array design method is suitable to analyze the sound transmission loss problem as described in this paper. Although the study considers the single-number ratings as the performance parameter which may sometimes not present the actual picture as the sound insulation in complete audio frequency range is equally important, yet the use of single-number quantities widely in sound regulation requirements and by manufacturers as well as acousticians necessitates such considerations. Also the use of spectrum adaptation terms recommended in ISO 717-1 and Scholl et al., 2011 investigations outlines the performance evaluation on the basis of single-number rating apart from comparison of sound insulation in the entire frequency range which is sometimes quite cumbersome. An  $L_9$  standard orthogonal array was used to accommodate four control factors each at three levels for adjudging their parametric sensitivity. The conclusions drawn from the present work are as follows:

- Air-gap plays a vital role in controlling the sound transmission of double glazing. The percentage contribution is 63% for  $R_w$  value, while it is 45.6% for  $R_w + C_{tr}$  value.
- The back pane thickness has higher percentage contribution in determination of single-number rating  $R_w$ ,  $R_w + C$  and  $STC$  value as compared to front pane thickness, while front pane thickness has slightly higher contribution in case of single number quantity  $R_w + C_{tr}$ . These investigations do not contradict with the reciprocity law as back pane thickness has been experimentally observed to be more sensitive in controlling the coincidence dip.
- The type of lamination has a very little role (<3%) which is statistically insignificant. However, in case of single number quantity  $STC$ , its percentage contribution is 5.3%.
- The optimal levels of process parameters are observed to be  $A_1$  (9 mm front pane thickness),  $B_3$  (9 mm back pane thickness),  $C_1$  (90 mm cavity depth) and  $D_3$  (Trosifol lamination) respectively. The mean value of  $R_w$  and  $R_w + C_{tr}$  corresponding to optimum condition was obtained as  $(50 \pm 3.5)$  dB and  $(46 \pm 5.4)$  dB. The actual value calculated from *Insul* software was 49 dB and 44 dB, which lies within the predicted range.
- A 5 dB increase in  $R_w$  value is analytically predicted by changing the thickness from 3 mm identical glasses to 10 mm in a double glazing. The increase in  $R_w + C_{tr}$  value is 12 dB from 100 mm air-gap and 13 dB for 50 mm air-gap in case of changing the

thickness from 3 mm identical glasses to 10 mm in a double glazing. The empirical formulations have been presented for various single-number ratings correlated with the air-gap and thickness of identical glass in non-laminated and laminated double glazing. The coefficient of multiple determination ( $r^2$ ) in each case is greater than 0.80. These formulations can serve as an easy guide for design of appropriate glazing configurations based on the noise level reduction required.

- A consideration on design target of  $R_w + C_{tr}$  value of 35 dB for window glazing, reveals that this value can be achieved with identical 4 mm glass with an 85 mm air-gap, while for an average gap of 50 mm, 6 mm identical glass on each side can accomplish the desired objective.

The present analytical investigations using validated *Insul* software can be thus instrumental in designing suitable double glazing for meeting the desired goals of sound insulation required. It may be noted that effect of window frame, sealing, installation etc. also plays an important role in the actual sound insulation provided by double glazing. Thus present study in conjunction with consideration of installation perspectives for double glazing can be very helpful in developing best constructions for traffic noise abatement.

## Acknowledgments

Authors thank Mr. Omkar Sharma and Dr. V. Mohanan for their valuable assistance and Mr. K. Ballagh of MDA, Auckland for procurement of *Insul* software. Authors thank the anonymous reviewers for their valuable comments and suggestions. Authors thank Prof. Dr. R.C. Budhani, Director, NPL & Dr. A.K. Bandyopadhyay, Head, *ALSIM* for sanctioning a special grant under *CSIR-MIST* Project for the upgradation of sound transmission loss measurement facility at NPL, India.

## References

- [1] A.C.C. Warnock and J.D. Quirt, Airborne sound insulation. Handbook of acoustical Measurements and Noise Control, 3rd ed.; 1991 [chapter 31].
- [2] Tadeu AJB, Mateus DMR. Sound transmission through single, double and triple glazing. Experimental evaluation. Appl Acoust 2001;62:307–25.
- [3] Quirt JD. Sound transmission through window I. Single and double glazing. J Acoust Soc Am 1982;72:834–44.
- [4] J.D. Quirt, Sound transmission through windows, Canadian Building Digest, CBD-240, 1988. <<http://www.nrc-cnrc.gc.ca/eng/ibp/irc/cbd/building-digest-240.html>>.
- [5] Brekke A. Calculation methods for the transmission loss of single. Double and triple partitions. Appl Acoust 1981;14:225–40.
- [6] Kim YT, Kim HC, Jung SS, Jho MJ, Suh SJ. Dependence of coincidence frequency in double-glazed window on glass thickness and inter-pane cavity. Appl Acoust 2002;63:927–36.
- [7] Quirt JD. Sound transmission through windows II. Double and triple glazing. J Acoust Soc Am 1983;74:534–42.
- [8] Yoshimura J, Kanazawa J. Influence of damping on the transmission loss of laminated glass. In: Proceedings internoise 84, vol. 1, pp. 589–592, December 1984.
- [9] Mao Q, Pietrzko S. Experimental study for sound control of sound transmission through double glazed window using optimally tuned Helmholtz resonators. Appl Acoust 2010;71:32–8.
- [10] Deyu Li, Xiao-Hong Z, Li C, Ganghua Y. Effectiveness of T-shaped acoustic resonators in low-frequency sound transmission control of a finite double-panel partition. J Sound Vib 2010;329:4740–55.
- [11] <http://www.fhwa.dot.gov/environment/audible/al4.htm>.
- [12] Vinokur R. Mechanism and calculation of niche effect in airborne sound transmission. J Acoust Soc Am 2006;119:2211–9.
- [13] Narang PP. A theoretical study of sound transmission through aerogel glazing systems. Appl Acoust 1991;34:249–59.
- [14] Garg N, Sharma O, Maji S. Design considerations for enhancing sound insulation characteristics of window glazing for traffic noise abatement. Build Acoust 2012;19:89–98.
- [15] ISO 717, Rating of sound insulation in buildings and of building elements, part 1; 1996.
- [16] Rasmussen B, Rindel JH. Sound insulation between dwellings-descriptors applied in building regulations in Europe. Appl Acoust 2010;71:171–80.

- [17] M. Fuente, E. Cagigal, S. Escudero, I. Flores, R + D for the integration of high acoustic-thermal performances in Spanish building products, *Acoustics* 08 Paris, June 29–July 4.
- [18] B. Ingelaere, M. Blasco, C. Crispin, G. Vermeir, Developing a new façade sound insulation requirement for dwellings: building solutions and their cost, *Inter-Noise* 2004, Czech Republic, 22–25 August.
- [19] Scholl W, Lang J, Wittstock V. Rating of sound insulation at present and in future. the revision of ISO 717. *Acta Acustica United Acustica* 2011;97:686–98.
- [20] Rasmussen B. Sound insulation between dwellings-requirements in building regulations in Europe. *Appl Acoust* 2010;71:373–85.
- [21] <http://www.insul.co.nz>.
- [22] J.E. Cambridge, An evaluation of various sound insulation programs and their use in the design of silent rooms, Master thesis, Chalmers University of Technology, Sweden; 2006. <[http://www.afconsult.com/upload/TJANSTER\\_SERVICES/Produkter/Foldrar/thesis.pdf](http://www.afconsult.com/upload/TJANSTER_SERVICES/Produkter/Foldrar/thesis.pdf)>.
- [23] Kurra S. Comparison of the models predicting sound insulation values of multi-layered building elements. *Appl Acoust* 2012;73:575–89.
- [24] K.O. Ballagh, Accuracy of prediction methods for sound transmission loss, *Inter-noise* 2004. <<http://www.insul.co.nz/download/Paper586BallaghNew.PDF>>.
- [25] Ross PJ. *Taguchi techniques for quality engineering*. New York: Mc Graw Hill; 1995.
- [26] Montgomery DC. *Design and analysis of experiments*. 4th ed. New York: John Wiley; 1997.
- [27] Yang WH, Tarn YS. Design optimization of cutting parameters for turning operations based on the Taguchi method. *J Mater Proc Technol* 1998;84:122–9.
- [28] Nalbant M, Gökkaya H, Sur G. Application of Taguchi method in the optimization of cutting parameters for surface roughness in turning. *Mater Des* 2007;28:1379–85.
- [29] Gopalsamy BM, Mondal B, Ghosh S. Taguchi method and ANOVA: an approach for process parameters optimization of hard machining while machining hardened steel. *J Sci Ind Res* 2009;68:686–95.
- [30] Chaulia PK, Das R. Process parameter optimization for fly ash brick by Taguchi method. *Mater Res* 2008;11:159–64.
- [31] Garg N, Sharma O, Maji S. Experimental investigations on sound insulation through single, double and triple window glazing for traffic noise abatement. *J Sci Ind Res* 2011;78:471–8.
- [32] <http://www.ielm.ust.hk/dfaculty/ajay/courses/ielm317/./robustdesign2.pdf>.
- [33] Lin CL. Use of the Taguchi method and grey relational analysis to optimize turning operations with multiple performance characteristics. *Mater Manuf Processes* 2004;19:209–20.
- [34] J.G. Lilly, Recent advances in acoustical glazing. <<http://www.sandv.com/downloads/0402lill.pdf>>.

# Sol-gel derived nanostructured zirconia for cholesterol detection

Ajeet Kaushik<sup>a,b,\*</sup>, Pratima R. Solanki<sup>a,c</sup>, Pandurang M. Chavhan<sup>a</sup>, Shekhar Bhansali<sup>b</sup>, Bansi D. Malhotra<sup>a,d,\*</sup>

<sup>a</sup> Biomedical Instrumentation Section, Materials Physics & Engineering Division, National Physical Laboratory (CSIR),  
Dr. K. S. Krishnan Marg, New Delhi 110012, India

<sup>b</sup> Department of Electrical and Computer Engineering, Florida International University,  
10555 West Flagler St. EC 3900, Miami, Florida FL 33174

<sup>c</sup> Amity Institute of Nanotechnology, Amity University Campus, Sector-125, Noida-201303, India

<sup>d</sup> Department of Biotechnology, Delhi Technological University, Shabad Daulatpur, Delhi-110047, India

\* Authors for correspondence: Bansi D. Malhotra, email: bansi.malhotra@gmail.com

Ajeet Kaushik, email: ajeet.npl@gmail.com

Received 21 Aug 2012; Accepted 27 Sep 2012; Available Online 27 Sep 2012

## Abstract

The sol-gel derived nanostructured zirconium oxide (nano-ZrO<sub>2</sub>) film has been fabricated onto indium-tin-oxide (ITO) coated glass to immobilize cholesterol oxidase (ChOx) to detect cholesterol. The oriented structural growth of nanoZrO<sub>2</sub> (with respect to 100 planes) has been confirmed using low angle X-ray diffraction (XRD) studies. The results of optical and electrochemical studies suggest that three dimensional cationic nanoZrO<sub>2</sub> platform provides an effective surface to ChOx resulting in enhanced electron transport to the bioelectrode. The low value of Michael-Mention ( $K_m$ ) constant suggests the good affinity of cholesterol to ChOx immobilized onto nanoZrO<sub>2</sub>/ITO electrode.

**Keywords:** Nanostructured ZrO<sub>2</sub>; Cholesterol oxidase; Electrochemical biosensor

## 1. Introduction

Nanostructured metal oxides (NMOs) such as zinc oxide (ZnO), iron oxide (Fe<sub>3</sub>O<sub>4</sub>), cerium oxide (CeO<sub>2</sub>), zirconium oxide (ZrO<sub>2</sub>) etc. with desired functionality, morphology, surface charge etc are known to provide effective surfaces for biomolecule immobilization wherein given biomolecules may retain desired conformations with high biological activities resulting in improved sensing characteristics [1-7]. The sensitivity, detection limit, and selectivity of a biosensor may perhaps be improved by tailoring NMO-biomolecule interface properties via engineering morphology, particle size, effective surface area, functionality, adsorption capability and electron transfer kinetics [3,4-10]. Besides this, it is possible to obtain improved direct electron transfer using a selective coating or a nanostructured electro-active surface platform via artificial mediator to achieve operation at lower potential of a desired biosensor.

Among the various NMOs, nano-ZrO<sub>2</sub> has aroused much interest due to its bio-compatibility, surface modification, easy preparation, non-toxicity, redox properties and affinity to oxygen atom of biomolecules can be used for development of an electrochemical biosensor. The high isoelectric point (IEP ~9.5) of nanoZrO<sub>2</sub> leads to high adsorption of biomolecules (low IEP ~4-5) via electrostatic interactions. In general biomolecules are known to bind with MO nanoparticles via physical adsorption and chemical binding [8-15]. The physical adsorption of biomolecules arising due to weak forces interaction (*van der Waals* interactions, electrostatic interactions) depends on the surface morphology, reaction medium and the net surface charge on MO [5]. In this context, sol-gel technique due to the simple preparation, tunable porosity, low temperature encapsulation, biodegradability and negligible swelling can be used to

fabricate nanoZrO<sub>2</sub> film for biosensing [8,9]. In this context, nano-ZrO<sub>2</sub> has been used to immobilize horseradish peroxidase, glucose oxidase and DNA as selective sorbents for organophosphate pesticides and nerve agents [9-13].

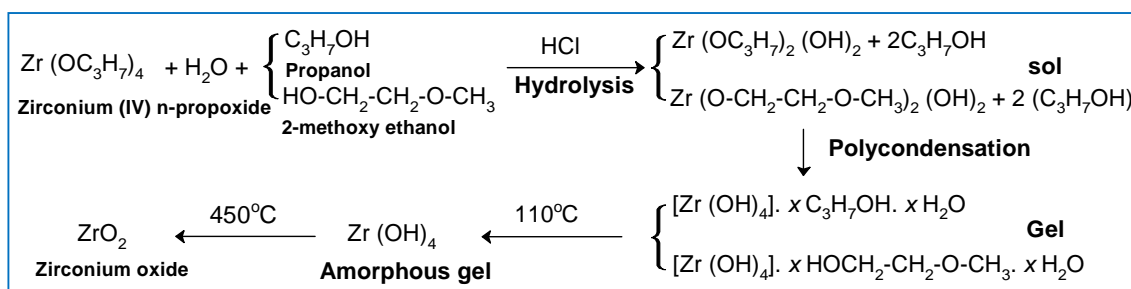
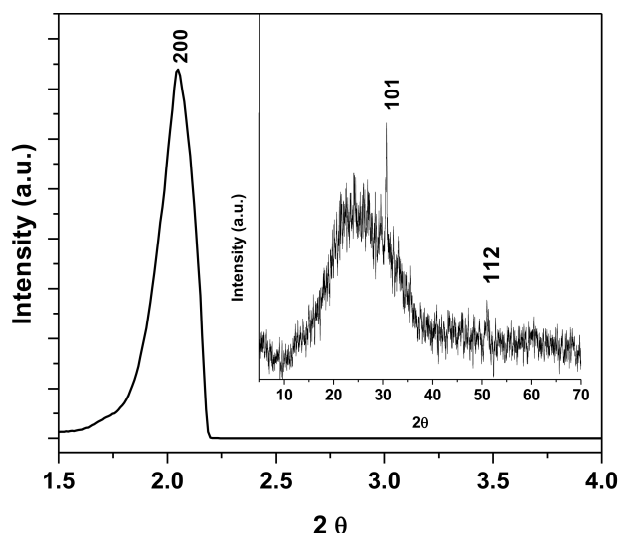
We report results of studies relating to the sol-gel derived three dimensional (3D) nanoZrO<sub>2</sub> film deposited onto indium-tin-oxide (ITO) substrate to immobilize ChOx via electrostatic interactions for cholesterol detection.

## 2. Experimental Details

All the chemicals have been purchased from Sigma-Aldrich and have been used without further purification. Zirconium (IV) n-propoxide (70 wt%) is diluted in propanol and 2-methoxy ethanol (50:50 vol%) and the resulting solution is hydrolyzed via drop wise addition of catalytic amount of H<sub>2</sub>O and hydrochloric acid under continuous stirring. After hydrolysis, the sol is continuously stirred (1h & 25°C) to polymerize the gel. The obtained transparent sol-gel solution is used to deposit film onto indium-tin-oxide (ITO, 0.25 cm<sup>2</sup>) coated glass substrate using dip coating method and is kept for drying at 110°C (1h) followed by annealing at 450°C (2h) in air atmosphere. The proposed reactions involved in the syntheses of ZrO<sub>2</sub> film using sol-gel technique are as shown Scheme 1.

10 µl of ChOx (1.0 mg/ml, in phosphate buffer PBS, 50 mM, pH 7.0) is immobilized onto nano-ZnO/ITO film via physisorption and is kept overnight for drying. XRD (Rigaku, miniflux 2) studies have been conducted to confirm formation of ZrO<sub>2</sub> nanostructure. The scanning electron microscope (SEM, LEO-440), Fourier transform infrared [FTIR, Perkin Elmer] spectrophotometer and Autolab [Potentiostat/Galvanostat] have been used to characterize desired electrodes and bioelectrode. Cyclic voltammetry (CV) and electrochemical impedance spectroscopy (EIS) studies



Scheme 1. Synthesis route to fabricate sol-gel derived nano-ZrO<sub>2</sub>.Figure 1. Low angle X-ray diffraction pattern of nano-ZrO<sub>2</sub>/ITO film, inset: wide angle X-ray diffraction pattern of nano-ZrO<sub>2</sub>/ITO film.

have been carried out in PBS [50 mM and 0.9% NaCl] containing 5 mM [Fe(CN)<sub>6</sub>]<sup>3-/4-</sup>.

### 3. Results and Discussion

The phase formation and purity of nano-ZrO<sub>2</sub> have been confirmed using low angle XRD studies (Figure 1). The observed well-resolved broad reflection plane (200) at  $2\theta = 2^\circ$  confirms the highly ordered structural growth of two dimensional hexagonal mesostructure of semi-crystalline ZrO<sub>2</sub> nanoparticles [14, 15]. However, the broadening of the peak is because of the small crystallite size. The average crystallite size calculated using Scherer formula is found to be ~30 nm. The observed reflection peak in the low angle XRD spectra is found at higher  $2\theta$  angle than that of reflection peak in ZrO<sub>2</sub> synthesized at low temperature (corresponds to inorganic/polymer mesostructure) suggests that mesoscopic order is preserved in the calcined ZrO<sub>2</sub>. The reflection plane at  $2\theta = \sim 28^\circ$  (corresponds to 101 reflection plane) and  $2\theta = \sim 50^\circ$  (corresponds to 112 reflection plane) in wide angle XRD studies (inset; Figure 1) of ZrO<sub>2</sub> film confirms crystallographic orientations during calcination that is limited to formation of nano-crystallite tetragonal phase of ZrO<sub>2</sub>. Thus prepared mesoporous nanostructured ZrO<sub>2</sub> platform exhibits high effective surface area and hence can be used for technological development of desired biosensors [15].

The effective MO-enzyme interface affects the electron transfer kinetics and helps a given enzyme to retain its biological activity due to biocompatible microenvironment provided by MO<sup>2-4</sup>. The SEM image of nano-ZrO<sub>2</sub>/ITO electrode (Figure 2A, image i) exhibits rough and dense flower like morphology wherein ZrO<sub>2</sub> is uniformly distributed over almost the entire surface. However, ZrO<sub>2</sub> nanoparticles are found to be agglomerated and interconnected indicating nanostructured like morphology (inset, image i) due to high surface charge and controlled slow hydrolysis process during the sol preparation. This 3D morphology of nano-ZrO<sub>2</sub> changes into another well-aligned regular morphology after the immobilization of ChOx (Figure 2A, image ii) reveals the immobilization via electrostatic binding due to the differences in IEP of ChOx (4.2) and ZrO<sub>2</sub> (9.5). This is because cationic dense cage-like inter connected nano-ZrO<sub>2</sub> with enhanced multiple charge sites provide friendly microenvironment for the immobilization of ChOx molecules to retain its desired conformation that may perhaps be responsible for enhanced electron transfer and hence sensing performance for cholesterol detection.

The presence of various functional groups associated with the nano-ZrO<sub>2</sub> and ChOx immobilized nano-ZrO<sub>2</sub> has been confirmed using FTIR in finger print region (Figure 2B). The band obtained at 580 cm<sup>-1</sup> in the FTIR spectra of nano-ZrO<sub>2</sub> film is due to Zr-O stretches and oxygen deficiency/vacancy defect complex [6]. The FTIR spectra of ChOx/nano-ZrO<sub>2</sub>/ITO bioelectrode exhibits IR bands corresponding to C-N stretching and N-H bending modes of amide I&II bands of ChOx at 1660 cm<sup>-1</sup> and 1230 cm<sup>-1</sup> (correlated with the FTIR spectra of ChOx, Figure 2C) [16] indicating immobilization of ChOx. The proposed scheme relating to the fabrication of biosensor and biochemical is shown in Figure 2D and well correlated with results explained on the basis of SEM and FTIR studies.

The stepwise fabrication of ChOx/nano-ZrO<sub>2</sub>/ITO bioelectrode has been investigated using electrochemical impedance spectroscopy (EIS, Figure 3A). The experimentally obtained data has been simulated using the electronic circuit {R<sub>s</sub>(C<sub>dl</sub>[R<sub>CT</sub> Z<sub>w</sub>])} where R<sub>s</sub> is the ohmic resistance of the electrolyte solution, R<sub>ct</sub> is electron charge transfer resistance (R<sub>CT</sub>), C<sub>dl</sub> is double layer capacitance and Z<sub>w</sub> is Warburg impedance. C<sub>dl</sub> and R<sub>CT</sub>, depend on the dielectric and insulating features at the electrode/electrolyte interface. The semicircle diameter of EIS spectra gives value of R<sub>CT</sub> that reveals electron-transfer kinetics of redox probe at the electrode interface. Moreover, R<sub>s</sub> and Warburg impedance (Z<sub>w</sub>) corresponding to bulk properties of the electrolyte solution and diffusion of applied redox probe are not affected by biochemical reaction occurring at the electrode interface [17].



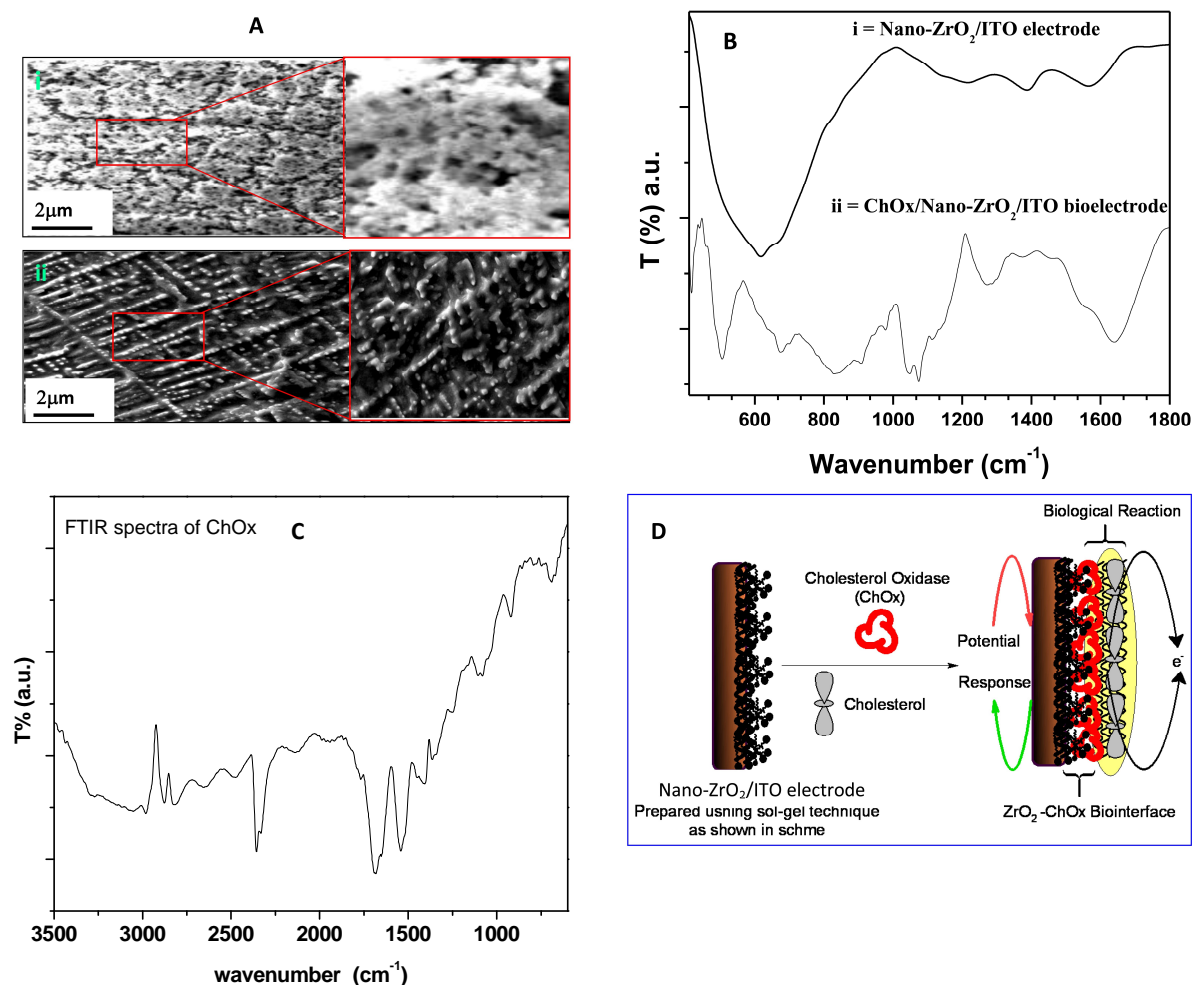


**Figure 2.** A) SEM image of nano-ZrO<sub>2</sub>/ITO electrode (image i) and ChOx/nano-ZrO<sub>2</sub>/ITO bioelectrode (image ii) B) FTIR spectra of nano-ZrO<sub>2</sub>/ITO electrode (i) and ChOx/nano-ZrO<sub>2</sub>/ITO bioelectrode (ii) C) FTIR spectra of ChOx D) Schematics for the fabrication of ChOx/nano-ZrO<sub>2</sub>/ITO biosensor.

In the Nyquist diagram, the value of  $R_{CT}$  obtained for nano-ZrO<sub>2</sub>/ITO electrode (curve ii) is lower (1.34 kΩ) than that of the bare ITO electrode ( $R_{CT}$  2.01 kΩ, curve i) indicating that nano-ZrO<sub>2</sub> increases effective electro-active surface area for diffusion of the redox species that help to improve the electron transport to electrode. The value of  $R_{CT}$  further decreases to 0.611 kΩ in case of ChOx/nano-ZrO<sub>2</sub>/ITO bioelectrode (curve iii) revealing that nanoZrO<sub>2</sub> provides effective microenvironment for ChOx immobilization resulting in improved electron transport.

The results of the CV (Figure 3B) studies reveal that magnitude of the current response of nano-ZrO<sub>2</sub>/ITO electrode (curve ii) is higher than that of bare ITO (curve i) due to increased concentration of electrons generated via Fe(II)/Fe(III) conversion resulting in higher electron transport between medium and electrode. The magnitude of response current obtained for nano-ZrO<sub>2</sub>/ITO electrode increases after immobilization of ChOx (curve iii) revealing that nanoZrO<sub>2</sub> film provides a desired environment for ChOx resulting in improved electron transport between mediator and electrode. Moreover, 3D arrangement of nanoZrO<sub>2</sub> favors direct and faster electron communication between ChOx and ITO surface. These results suggest that cationic nano-ZrO<sub>2</sub> platform has increased electro active surface area for the oriented immobilization of ChOx resulting in enhanced electron

transfer due to increased adsorption of the negatively charged ions [redox species, Fe(II)/Fe(III)] that appear to be responsible for enhanced electrochemical properties due to increased surface concentration. The surface concentration of the redox species onto nano-ZrO/ITO electrode and ChOx/nano-ZrO<sub>2</sub>/ITO bioelectrodes have been estimated using Equation 1 [18].

$$i_p = 0.227nFAC_0^*k^0 \exp\left[\frac{-\alpha n_a F}{RT}(E_p - E_0')\right] \quad (1)$$

where,  $i_p$  is the anodic peak current,  $n$  is the number of electrons transferred (1),  $F$  is the Faraday constant (96485.34 C mol<sup>-1</sup>),  $A$  is surface area (0.25 cm<sup>2</sup>),  $R$  is the gas constant (8.314 J mol<sup>-1</sup> K<sup>-1</sup>),  $C_0^*$  is surface concentration of the ionic species of film surface (mol cm<sup>-2</sup>),  $E_p$  is the peak potential and  $E_0$  is the formal potential.  $-\alpha n_a F/RT$  and  $k_0$  (rate constant) correspond to the slope and intercept of  $\ln(i_p)$  verses  $E_p - E_0$  curve at different scan rates.

It may be noted that the surface concentration of redox species onto nano-ZrO<sub>2</sub>/ITO bioelectrode (1.25 × 10<sup>-6</sup> mol cm<sup>-2</sup>) is higher than that of ITO (0.95 × 10<sup>-6</sup> mol cm<sup>-2</sup>). The increased surface concentration of redox species onto cationic

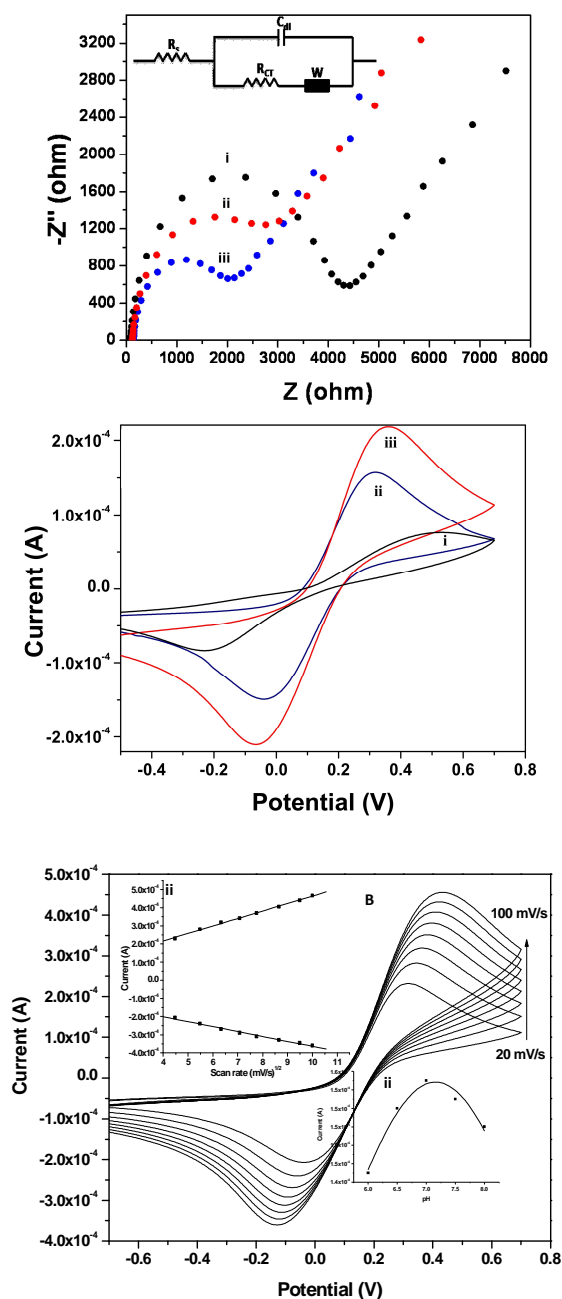


**Figure 3.** A) EIS studies of ITO electrode (i),  $\text{ZrO}_2/\text{ITO}$  electrode (ii) and  $\text{ChOx}/\text{nano-ZrO}_2/\text{ITO}$  bioelectrode (iii), B) CV studies of ITO electrode (curve i),  $\text{nano-ZrO}_2/\text{ITO}$  electrode (curve ii) and  $\text{ChOx}/\text{nano-ZrO}_2/\text{ITO}$  bioelectrode (iii), C) CV studies of  $\text{ChOx}/\text{nano-ZrO}_2/\text{ITO}$  bioelectrode as a function of scan rate (10–100 mV/s). *inset i*: current response as square root of scan rate, *inset ii*: CV studies of bioelectrode as function of pH in PBS [50 mM and 0.9 % NaCl] containing 5mM  $[\text{Fe}(\text{CN})_6]^{3-/4-}$ .

nanostructured  $\text{ZrO}_2$  electrode reveals that larger numbers of redox moieties are available for oxidation for leading to higher faradic current. After the immobilization of ChOx onto  $\text{nano-ZrO}_2/\text{ITO}$  electrode the surface concentration further increases ( $2.6 \times 10^{-6} \text{ mol cm}^{-2}$ ). This suggests that 3D cationic Nano- $\text{ZrO}_2$  provides electronically effective surface for ChOx immobilization (in the form of regular arrays) via electrostatic interactions due to difference in IEP that may be responsible for high adsorption of redox species for oxidation and hence improved electron transport leading to higher faradic current.

The CV studies (Figure 3 B) have been conducted  $\text{ChOx}/\text{nano-ZrO}_2/\text{ITO}$  bioelectrode obtained as a function of scan rate (10–100 mV/s). The magnitude of current for both the oxidation and reduction process increases linearly (inset i, Figure 3B) with square root of scan rate indicating controlled diffusion of redox species and obey Equations 2-3.

$$I_p[\text{A}]_{\text{ChOx}/\text{ZrO}_2/\text{ITO bioelectrode}} = 5.18 \times 10^{-5} (\text{A}) + 4.12 \times 10^{-5} [\text{As/V}] \times \text{scan rate (mV/s)}^{1/2}, R^2 = 0.999 \quad (2)$$

$$I_c[\text{A}]_{\text{ChOx}/\text{ZrO}_2/\text{ITO bioelectrode}} = -9.25 \times 10^{-5} (\text{A}) - 2.73 \times 10^{-5} [\text{As/V}] \times \text{scan rate (mV/s)}^{1/2}, R^2 = 0.999 \quad (3)$$

It has been shown that ChOx adsorbed onto  $\text{nano-ZrO}_2/\text{ITO}$  electrode undergoes reversible electron transfer with  $\text{nano-ZrO}_2/\text{ITO}$  film. It is found that cathodic ( $E_p$ ) and anodic ( $E_c$ ) peak potential difference also increases linearly as a function of scan rate (data not shown) revealing the facile electron transport.

The activity of  $\text{ChOx}/\text{nano-ZrO}_2/\text{ITO}$  bioelectrode has been investigated as a function of pH (inset ii, Figure 3B) using CV studies. The value of higher electrochemical current response is obtained at pH 7 and results are found to be repeatable and reproducible (~ 15 times). This suggests that bioelectrode shows maximum electron transfer kinetics at pH 7, wherein enzyme retain its natural structure with higher biological activity and is responsible for enhanced sensing parameters.

The electrochemical response of  $\text{ChOx}/\text{nano-ZrO}_2/\text{ITO}$  bioelectrode (Figure 4) has been investigated as a function of cholesterol concentration (10–400 mg/dL). The magnitude of electrochemical current response of  $\text{ChOx}/\text{nano-ZrO}_2/\text{ITO}$  bioelectrode increases as the concentration of cholesterol increases (inset i). This may be attributed to the fact that during the biochemical reaction the electrons generated via re-oxidation of ChOx directly are accepted by  $\text{nano-ZrO}_2$  and transferred to electrode. Thus  $\text{nano-ZrO}_2$  surface acts as electron transfer-accelerating layer for transfer of electrons and the observed response follows Equation 4.

$$I[\text{A}]_{\text{ChOx}/\text{ZrO}_2/\text{ITO bioelectrode}} = 2.19 \times 10^{-4} [\text{A}] + 2.74 \times 10^{-5} [\text{A}] [\text{dL/mg}] \times \text{Cholesterol Concn. [mg/dL]} \quad (4)$$

This  $\text{ChOx}/\text{nano-ZrO}_2/\text{ITO}$  biosensor exhibits low detection limit (5 mg/dL), fast response time (20s), high sensitivity ( $27 \mu\text{A}/\text{mg dL}^{-1}/\text{cm}^2$ ) and shelf-life (10 weeks). The value of the Michaelis–Menten constant ( $K_m$ ), that gives an indication of the enzyme–substrate kinetics, can be obtained using Lineweaver–Burke plot [26, 27]. The  $K_m$  value has been calculated using the graph between inverse of absorbance and inverse of cholesterol concentration and found to be 0.01 mM. The low  $K_m$  value (0.45 mg/dL) reveals that  $\text{nano-ZrO}_2$  matrix facilitates enzymatic reaction and helps the immobilized enzyme to achieve better conformation for faster enzymatic reaction resulting in enhanced enzymatic activity. This suggests that both morphology and charged surface provide a desired environment for higher loading of enzyme to achieve better conformation for faster enzymatic reaction resulting in enhanced enzymatic activity that is responsible for improved sensing parameters [1,2]. The conformational changes are known to affect a biochemical reaction at the bioelectrode resulting in increased interaction between the bio-substrate and the active site of ChOx.

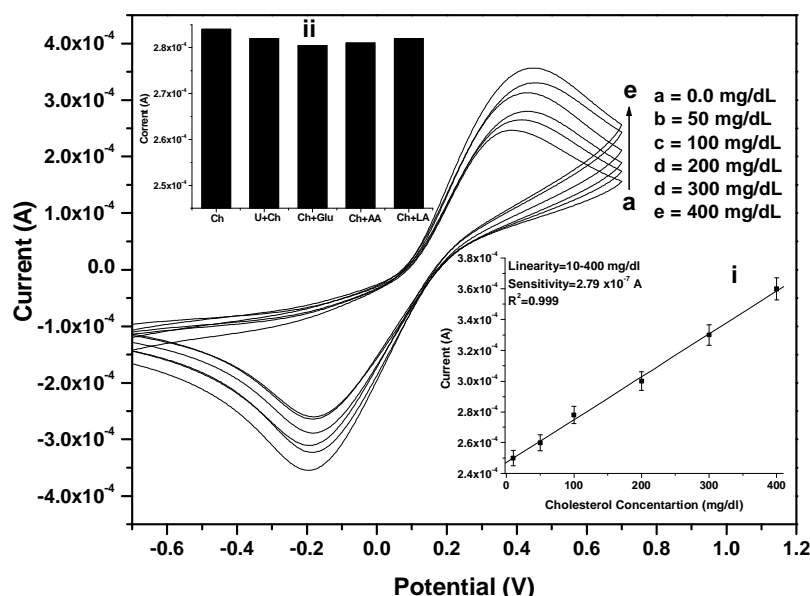


**Figure 4.** Electrochemical response of ChOx/nano-ZrO<sub>2</sub>/ITO bioelectrode as a function of cholesterol concentration, *inset (i)*: calibration curve, *inset (ii)*: interferences studies in PBS [50 mM and 0.9% NaCl]] containing 5 mM [Fe(CN)<sub>6</sub>]<sup>3-/4-</sup>.

The magnitude of electrochemical response current of ChOx/nano-ZrO<sub>2</sub>/ITO bioelectrode is not significantly affected due to the presence of interferences (inset ii) such as glucose (5 mM), ascorbic acid (0.05 mM), uric acid (0.1 mM), urea (5 mM) and lactic acid (5 mM). However, there is a decrease of about 5% in the case of ascorbic acid. It has been found that there is no significant change in response current of bioelectrode after using at least 15 times and the results are

found to be repeatable. Table 1 shows the characteristics of the ChOx/nano-ZrO<sub>2</sub>/ITO bioelectrode along with those reported for metal oxides based cholesterol sensors reported in literature [19-25]. This sensor exhibits wider detection range, low detection limit, long term stability, good sensitivity and obtained low  $K_m$  value reveals the higher affinity of ChOx immobilized onto ZrO<sub>2</sub> to the cholesterol.

**Table 1.** Characteristics of ChOx/nano-ZrO<sub>2</sub>/ITO bioelectrode along with those reported for metal oxides based cholesterol sensors reported in literature.

Electrode Immobilization and Transducers	Linear Range	Detection Limit	Sensitivity	$K_m$ value	Response time	Shelf life (days)	Ref.
ZnO/Au Physical/Electrochemical	0.65-10.34 mM		0.012 $\mu\text{A mM}^{-1} \text{cm}^{-2}$	2.1 mM	15s	70	19
ZnO/ITO Physical/Electrochemical	0.13-10.34 mM	0.013 mM	0.015 $\mu\text{A mM}^{-1} \text{cm}^{-2}$	0.025 mM	10s	85	20
Chitosan-ZnO/ITO Physical/Electrochemical	0.08-7.76 mM		0.015 $\mu\text{A mM}^{-1} \text{cm}^{-2}$	0.23 mM	15s	56	21
Chitosan-SnO <sub>2</sub> /ITO Physical/Electrochemical	0.13-10.34 mM	0.13 mM	0.897 $\mu\text{A mM}^{-1} \text{cm}^{-2}$	3.8 mM	5s	80	22
CeO <sub>2</sub> /ITO Physical/Electrochemical	0.26-10.34 mM	0.26 mM	-----	2.08 mM	15s	-----	23
Chitosan-CeO <sub>2</sub> /ITO Physical/Electrochemical	0.26-10.34 mM	0.13 mM	1.21 $\mu\text{A mM}^{-1} \text{cm}^{-2}$	0.08 mM	10s	60	24
Au Nanowire/MEMS	1-6 mM	-----	1.55 $\times 10^{-3} \mu\text{A mM}^{-1} \text{cm}^{-2}$		-----	10	25
Fe <sub>3</sub> O <sub>4</sub> nanoparticles Covalent/Spectroscopic	1.3-5.2 mM	----	-----	0.45 mM		15	16
nano-ZrO <sub>2</sub> /ITO Physical/Electrochemical	0.26-10.34 mM	0.01mM	0.70 $\mu\text{A mM}^{-1} \text{cm}^{-2}$	0.01 mM	20s	70	Present work

#### 4. Conclusions

3D cationic nano-ZrO<sub>2</sub> film has been found as an effective surface to immobilize ChOx resulting in faster electron transfer between medium to electrode with enhanced sensing characteristics. ChOx/nano-ZrO<sub>2</sub>/ITO biosensor exhibits detection limit (5 mg/dL), response time (20s), high sensitivity (27  $\mu\text{A}/\text{mgdL}^{-1}/\text{cm}^2$ ),  $K_m$  (0.45 mg/dL) and shelf life (10 weeks). This nano-ZrO<sub>2</sub> matrix with high structural order may be utilized for estimation of cholesterol in serum samples and for the fabrication of other biosensors to detect clinically important analytes including low density lipoproteins and triglycerides.

#### References

1. P. R. Solanki, A. Kaushik, V. Agrawal, B. D. Malhotra, NPG Asia Mater. 3 (2011) 14.
2. J. Wang, Analyst 130 (2005) 421.
3. J. Wang, Small 11 (2005) 1036.
4. M. M. Rahman, A. J. S. Ahammad, J. H. Jin, S. J. Ahn, J. J. Lee, Sensors 10 (2010) 4855.
5. A. E. Nell, L. Madler, D. Velegol, T. Xia, E. M. V. Hoek, P. Somasundaran, F. Klaessig, V. Castranova M. Thompson, Nat. Mater. 8 (2009) 543.
6. A. Liu, Biosens. Bioelectron. 24 (2008) 167.
7. A. Kaushik, P. R. Solanki, K. Kaneto, C. G. Kim, S. Ahmad, B. D. Malhotra, Electroanalysis 22 (2010) 1045.
8. M. Das, G. Sumana, R. Nagarajan, B. D. Malhotra, Appl. Phys. Lett. 96 (2010) 133703.
9. P. R. Solanki, A. Kaushik, P. M. Chavhan, S. N. Maheswari, B. D. Malhotra, Electrochem. Commun. 11 (2009) 2272.
10. N. Zhu, A. Zhang, Q. Wang, P. He, Y. Fang, Anal. Chim. Acta 510 (2004) 163.
11. B. Liu, Y. Cao, D. Chen, J. Kong, J. Deng, Anal. Chim. Acta 478 (2003) 59.
12. H. J. Kim, S. H. Yoon, H. N. Choi, Y. K. Lyu, W. Y. Lee, Bull. Korean Chem. Soc. 2003 (27) 65.
13. G. Liu, Y. Lin, Anal. Chem. 77 (2005) 5894.
14. E. L. Crepaldi, G. J. A. A. Soler-Illia, D. Grosso, C. Sanchez, New J. Chem. 27 (2003) 9.
15. P. Yang, D. Zhao, D. I. Margolese, B. F. Chmelka, G. D. Stucky, Nature 396 (1998) 152.
16. G. K. Kouassi, J. Irudayaraj, McCarty G., J. Nanobiotechnol. 3 (2005) 1.
17. A. J. Brad, L. R. Faulkner, Electrochemical Methods, Wiley, New York (2000).
18. Kaushik, P. R. Solanki, A. A. Ansari, G. Sumana, S. Ahmad, B. D. Malhotra, Sens. Actuat. B 138 (2009) 572.
19. S. P. Singh, S. K. Arya, P. Pandey, B. D. Malhotra, S. Saha, K. Sreenivas, V. Gupta, Appl. Phys. Lett. 91 (2007) 06390.
20. P. R. Solanki, A. Kaushik, A. A. Ansari, B. D. Malhotra, Appl. Phys. Lett. 94 (2009) 143901.
21. R. Khan, A. Kaushik, P. R. Solanki, A. A. Ansari, M. K. Pandey, B. D. Malhotra, Anal. Chim. Acta 616 (2008) 207.
22. A. A. Ansari, A. Kaushik, P. R. Solanki, B. D. Malhotra, Electroanalysis 21 (2009) 965.
23. A. Ansari, A. Kaushik, P. R. Solanki, B. D. Malhotra, Electrochem. Commun. 10 (2008) 1246.
24. B. D. Malhotra, A. Kaushik, Thin Solid Films 518 (2009) 614.
25. S. Aravamudhan, A. Kumar, S. Mohapatra, S. Bhansali, Biosens. Bioelectron. 22 (2007) 2289.
26. K. A. Johnson, R. S. Goody, Biochemistry 50 (2011) 8264.
27. R. A. Kamin, G. S. Wilson, Anal. Chem. 52 (1980) 1198.

#### Cite this article as:

Ajeet Kaushik *et al.*: Sol-gel derived nanostructured zirconia for cholesterol detection. *J. Nanosci. Lett.* 2013, 3: 23

# Performance and Emission Study of Linseed Oil as a Fuel for CI Engine

Ashutosh Kumar Rai, Naveen Kumar, and Bhupendra Singh Chauhan

**Abstract**—Increased energy demand and the concern about environment friendly technology, renewable bio-fuels are better alternative to petroleum products. In the present study linseed oil was used as alternative source for diesel engine fuel and the results were compared with baseline data of neat diesel. Performance parameters such as brake thermal efficiency (BTE) and brake specific fuel consumption (BSFC) and emissions parameters such as CO, unburned hydro carbon (UBHC), NO<sub>x</sub>, CO<sub>2</sub> and exhaust temperature were compared. BTE of the engine was lower and BSFC was higher when the engine was fueled with Linseed oil compared to diesel fuel. Emission characteristics are better than diesel fuel. NO<sub>x</sub> formation by using linseed oil during the experiment was lower than diesel fuel. Linseed oil is non edible oil, so it can be used as an extender of diesel fuel energy source for small and medium energy needs.

**Keywords**—Bio-fuel, exhaust emission, linseed oil, triglyceride.

## I. INTRODUCTION

THE world is moving towards a sustainable energy era with major emphasis on energy efficiency and use of renewable energy sources. Growing concerns on the long-term availability of diesel and its environmental disadvantage have necessitated the search for a renewable alternative to diesel fuel. Bio-fuels can provide a feasible solution to these problems; known liquid bio-fuels are fuels derived from alcohol and vegetable oils. However, modification, handling and transportation, ease of production, and investment cost are some of the important parameters that should be considered before using an alternative fuel in an existing diesel engine. The modification required in the engine design should be very minor to minimize the investment in engine modification [1]-[4]. Diesel engines are major source of energy for agricultural need. Linseed oil is a better option for small and medium capacity energy needs.

Oil seed crops can provide a fuel grade product using relatively simple extraction and processing technology which could be performed on individual farms. Vegetable oils are promising fuels, particularly for diesel engines. The practicality of vegetable oils as diesel fuels has been sufficiently demonstrated to warrant further investigation of

their effectiveness and to develop techniques that will permit their incorporation into agricultural operations, particularly in times of energy shortfall. The present work aims at comparative assessment of performance evaluation exhaust emissions of neat linseed oil with diesel fuel in a single cylinder diesel engine. Due to high viscosity and slight lower calorific value of Linseed oil it can be used with or without blending in diesel.

## II. LINSEED OIL AS A POTENTIAL FUEL FOR DIESEL ENGINE

Identification of alternative fuels for use in IC engines has been subjected to studies throughout the globe. Performance tests have shown suitability of variety of alternative fuels such as hydrogen, alcohols, biogas, producer gas and various types of edible and non edible oils. However, in Indian context, the bio-origin fuels like alcohols, vegetable oils, and biogas can contribute significantly towards the problems related to fuel crises. Petroleum based diesel fuels have different chemical structure than vegetable oil. The former contain only carbon and hydrogen atoms which are arranged in normal (straight chain) or branched chain structures as well as aromatic configurations. The normal structure is preferred for better ignition quality. Diesel fuel can contain both saturated and straight or unbranched chain unsaturated hydrocarbons, but the later are not present in large amounts to make oxidation a problem [5]-[7]. Vegetable oils consist of triglycerides to about 97%; the other 3% distribute among di and mono glycerides and further more 3 fatty acids and the fat accompanying which are mostly removed with refining [8]. Structurally, a triglyceride is a reaction product of one molecule of glycerol with three fatty acid molecules to yield three molecules of water and one molecule of triglyceride [9].

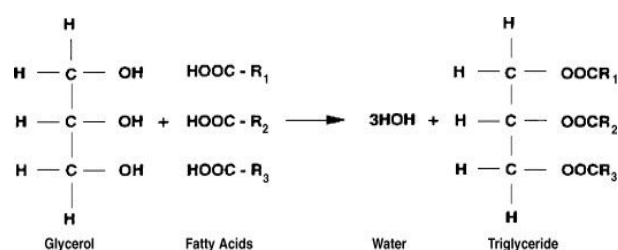


Fig. 1 Chemical structure of vegetable oils

where R<sub>1</sub>, R<sub>2</sub> and R<sub>3</sub> are the alkyl groups of different carbon chain lengths (varying between 12-18), and -COO- is an carboxyl group. Vegetable oils have different chemical structure as shown [10].

Ashutosh Kumar Rai is research scholar with the Department of Mechanical Engineering, Delhi Technological University, Delhi, India (phone: +91-9891161172; e-mail: ashu22sep@gmail.com).

Naveen Kumar is with the Department of Mechanical Engineering, Delhi Technological University, Delhi, India. (e-mail: naveenkumardce@gmail.com).

Bhupendra Singh Chauhan is with the Department of Mechanical Engineering, Delhi Technological University Delhi, India. (e-mail: bhupendradce@gmail.com).



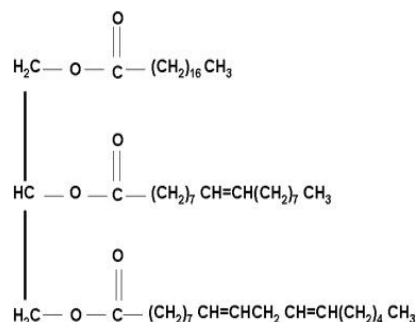


Fig. 2 Structure of a typical triglyceride molecule

The large size of the vegetable oil molecules and the presence of oxygen in the molecules suggest that some fuel properties of the vegetable oils would differ markedly from those of hydrocarbon fuels [8]. Linseed oil consists of primarily of the mixed glycerides of Oleic acid, Linoleic acid and Linolenic acid. The kinematic viscosity of Linseed oils varies in the range of 26-30 mm<sup>2</sup>/s at 40°C. The high viscosity is due to their larger molecular mass and chemical structure. Vegetable oils have high molecular weights of 600-900, which are three or more times higher than that of diesel fuel. The flash point of linseed oil is also very high (about 222°C). The auto-ignition temperature is about 343°C. Specific gravity is 0.93 and density 931 kg/m<sup>3</sup>. Calorific value is about 40 MJ/kg, comparatively lower than that of diesel fuels (about 45 MJ/kg). This is because the presence of chemically bonded oxygen in vegetable oils lowers the heating value by about 10%. The cetane number is in the range of 32-40, while the iodine value ranges from 0-200, depending on unsaturation. The cloud and pour point of vegetable oils is higher than that of diesel fuel [11]-[14].

### III. EXPERIMENTAL SETUP

A Kirloskar make, single cylinder, constant speed, air cooled, direct injection, CAF 8 model diesel engine was selected for the present research work, which is primarily used for agricultural activities and household electricity generations. It is a single cylinder, naturally aspirated, four stroke, vertical, air-cooled engine. It has a provision of loading electrically since it is coupled with single phase alternator through flexible coupling. The engine can be hand started using decompression lever and is provided with centrifugal speed governor. The lubrication system used in this engine is of wet sump type, and oil is delivered to the crankshaft and the big end by means of a pump mounted on the front cover of the engine and driven from the crankshaft. The inlet and exhaust valves are operated by an overhead camshaft driven from the crankshaft through two pairs of bevel gears. The fuel pump is driven from the end of camshaft.

A voltmeter, ammeter and wattmeter were connected between alternator and load bank. The thermocouples were mounted in the exhaust manifold to measure the exhaust temperature. The AVL 437 smoke meter and AVL Di-Gas Analyzer were also kept in proximity for the measurements

of various exhaust gas parameters. The engine was started at no load by pressing the exhaust valve with decompression lever and it was released suddenly when the engine was hand cranked at sufficient speed. Then feed control was adjusted so that engine attains rated speed and was allowed to run about half hour till the steady state condition was reached. With the fuel measuring unit and stop watch, the time elapsed for the consumption of 20cc of fuel was measured. Fuel consumption, RPM, exhaust temperature, smoke density, CO, NO<sub>x</sub>, HC, CO<sub>2</sub> and power output were also measured. The engine was loaded gradually keeping the speed within the permissible range and the observations of different parameters were evaluated. Short term performance tests were carried out on the engine with diesel to generate the base line data and subsequently Linseed Oil and Diesel was used to evaluate its suitability as a fuel. The performance and emission characteristics of Linseed Oil was evaluated and compared with diesel fuel.

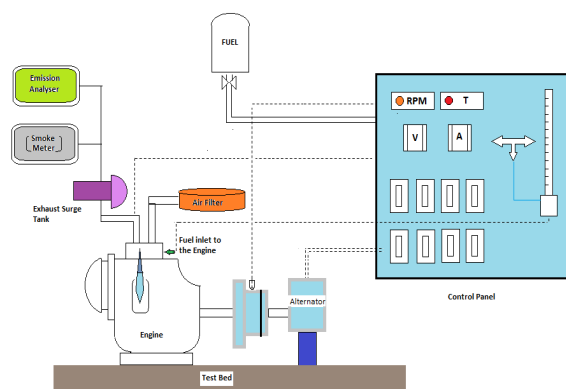


Fig. 3 Schematic diagram of experimental test rig

### IV. RESULT & DISCUSSION

The variation of the brake thermal efficiency (BTE) of the engine with linseed oil and diesel is shown in Fig. 4. With increasing brake power, the BTEs of vegetable oils and diesel also increased; however, they tended to decrease when further increase in brake power was observed. The BTEs of the linseed oil are lower than those of diesel fuel throughout the entire range, possibly due to the lower calorific value and the high viscosity of linseed oil compared with diesel fuel.

The brake-specific fuel consumptions (BSFC) were also higher in the case of linseed oil than in diesel fuel, as evident in Fig. 5. This is mainly due to the combined effects of the relative fuel density, viscosity, and heating value.

Within the experimental range, the CO emission from linseed oil is higher than neat diesel fuel, as seen in Fig. 6. This is possible due to the high viscosity of vegetable oils; the higher the viscosity, the more difficult it is to atomize vegetable oils. This resulted in locally rich mixtures in the engine.

The  $\text{CO}_2$  emissions are shown in Fig. 7. In the range of the whole engine load, the  $\text{CO}_2$  emissions of diesel fuel are higher than that of the other fuels because vegetable oil contains oxygen element. The carbon content is relatively lower in the same volume of fuel consumed at the same engine load, and consequently, the  $\text{CO}_2$  emissions from the vegetable oil and its blends are lower.

The value of unburned HC emission from the diesel engine in the case of straight vegetable oil is higher than that of diesel fuel, as seen in Fig. 8. HC emissions are lower at partial loads but tend to increase at higher loads for both fuels. This is due to the lack of oxygen, which is caused by engine operation at a higher equivalence ratio.

The  $\text{NO}_x$  emissions, shown in Fig. 9, increase along with the increasing engine load due to the higher combustion temperature. This proves that the most important factor for the emissions of  $\text{NO}_x$  is the combustion temperature in the engine cylinder and the local stoichiometry of the mixture. Within the  $\text{NO}_x$  emissions were reduced at full load, possibly due to the smaller calorific value of vegetable oils.

Fig. 10 shows that the exhaust gas temperature increases with the increase in brake power in all cases. This is due to the poor combustion characteristics of the linseed oil because of its high viscosity.

#### V. CONCLUSIONS

The results of the experiment showed that the performance of the engine on Linseed oil was slightly inferior to that on diesel fuel. The thermal efficiency of the engine was lower and the brake specific energy consumption of the engine was higher when the engine was fueled with Linseed oil compared to diesel fuel. The oxides of nitrogen from during the whole range of experiment were lower than diesel fuel. The Carbon monoxide, unburned hydrocarbon from the fuel was found higher than diesel fuel during the whole experimental range. The results from the experiments suggest that linseed oil is potentially good substitute fuel for diesel engine and performance and emissions characteristics were found to be comparable to diesel fuel.

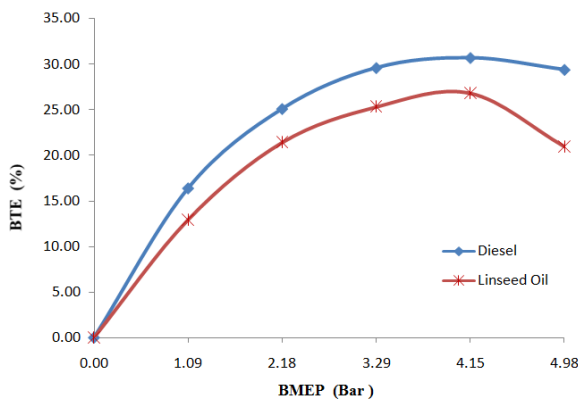


Fig. 4 Variation of brake thermal efficiency with brake means effective pressure

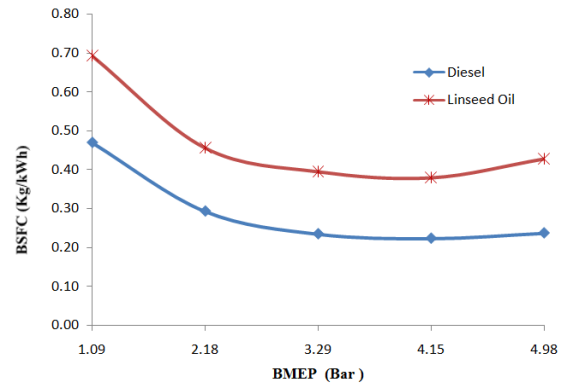


Fig. 5 Variation of brake specific fuel consumption with brake means effective pressure

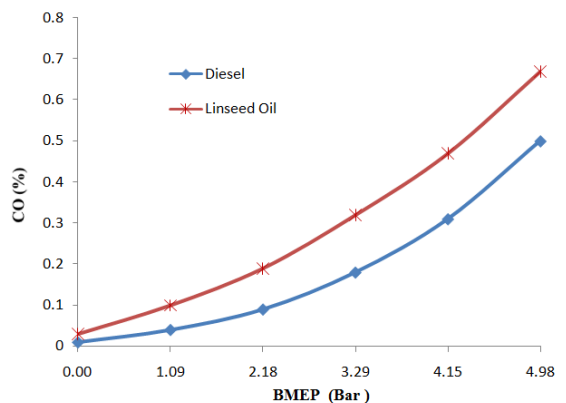


Fig. 6 Variation of carbon monoxide with brake means effective pressure

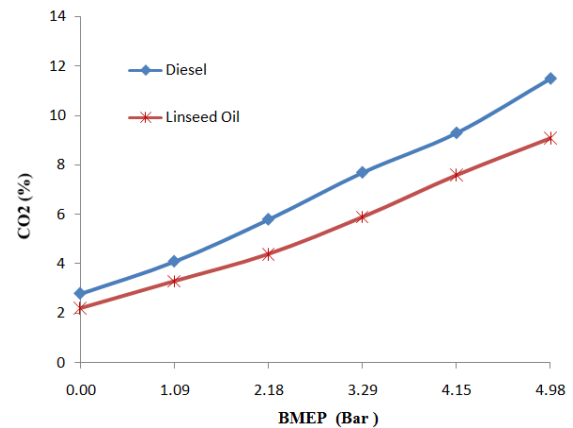


Fig. 7 Variation of carbon dioxide with brake means effective pressure



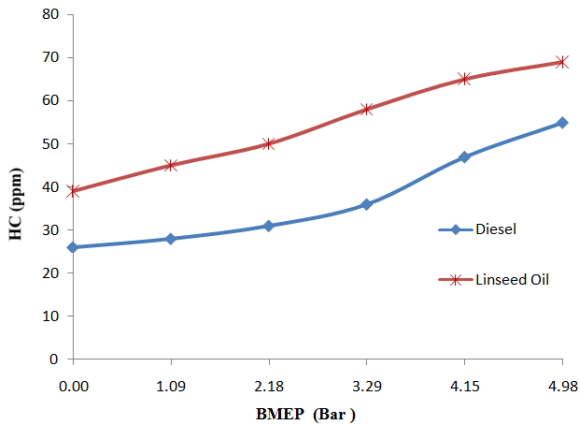


Fig. 8 Variation of unburned hydrocarbon with brake means effective pressure

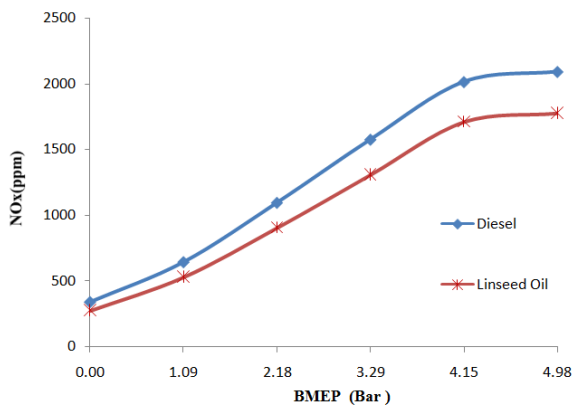


Fig. 9 Variation of oxides of nitrogen with brake means effective pressure

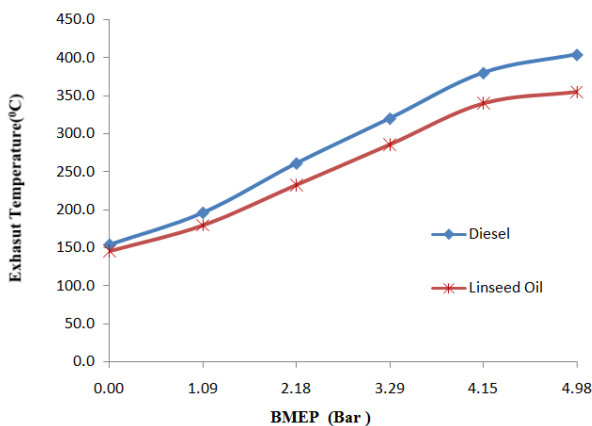


Fig. 10 Variation exhaust temperature with brake means effective pressure

#### REFERENCES

- [1] BS Chauhan, N Kumar, HM Cho. "A study on the performance and emission of a diesel engine fueled with Jatropha biodiesel oil and its blends," *Energy*; Vol. 37, pp. 616-622, 2012
- [2] BS Chauhan, N Kumar, YD Jun, KB Lee, "Performance and emission study of preheated Jatropha oil on medium capacity diesel engine," *Energy*, vol. 35, pp. 2484-92, 2010;

- [3] BS Chauhan, N Kumar, SS Pal, YD Jun, "Experimental studies on fumigation of ethanol in a small capacity diesel engine," *Energy*, vol. 36pp.1030-8, 2011.
- [4] BS Chauhan, N Kumar, HM Cho, "Performance and emission studies on an agriculture engine on neat Jatropha oil, *JMST* vol. 24(2), pp. 529-35, 2010.
- [5] A Srivastava, R Prasad, "Triglycerides-based diesel fuels" *Renewable and Sustainable Energy Reviews* vol. 4, pp.111-133, 2000.
- [6] JN Reddy, A Ramesh, "Parametric studies for improving the performance of a Jatropha oil-fuelled CI engine," *Renewable Energy* vol. 31, pp. 1994-2016, 2006.
- [7] BK Barnwal, MP Sharma, Prospects of biodiesel production from vegetable oils in India, *Renewable and Sustainable Energy Reviews*, vol. 9 pp. 363-378, 2005.
- [8] R. Narayan, "Biomass (renewable) resources for production of material," *Chemicals and Fuels*, vol 476 pp. 1-10, 1992.
- [9] A. Farsaie, J. V. Debarhte and W. J. Kenworthy, "Analysis of producing the vegetable oil as an alternate fuel" *Energy in Agriculture*, vol. 4, pp. 189-205, 1985.
- [10] Kemal, Yunus, Elcin, "Some Physical Properties of Linseed," *Biosystems Engineering* vol. 95 (4), pp. 607-612, 2006.
- [11] C. J. Abraham, "A solution to spontaneous combustion in linseed oil formulations," *Polymer Degradation and Stability*, vol. 5 4, pp.157-166, 1996.
- [12] Jutia et al, Oxidation reactions and spontaneous ignition of linseed oil, *Proceedings of the Combustion Institute* vol. 33 pp. 2625-2632, 2011.
- [13] V. Sharma et al, Spectroscopic characterization of linseed oil based polymer nano-composites, *Polymer Testing* vol. 27, pp. 916-923, 2008.
- [14] Sukumar et al, "Effect of injection pressure on performance, emission and combustion characteristics of high linolenic linseed oil methyl ester in a DI diesel engine," *Renewable Energy* vol. 34, pp. 1227-1233, 2009.

# Prevention Of DOS & DDOS Attack Using Count Based Filtering Method In Cloud Computing

R. K. Yadav

Delhi Technological University  
Computer Engineering Department  
Delhi, India

Daya Gupta

Delhi Technological University  
Computer Engineering Department  
Delhi, India

Devendra Dadoriya

Delhi Technological University  
Computer Engineering Department  
Delhi, India

## Abstract

*Cloud computing is a technology that provides services on-demand. Freedom, compliances, data security, data recovery, auditing and availability are the security issues in cloud computing. Denial of service (DOS) and Distributed denial of service (DDOS) attack affect availability issue. In the DOS and DDOS attack attacker sends large number of TCP ACK packets to victim. Victim does not process packets CPU exhaustion of the victim. Attacker sends large number of TCP SYN packets and connections open on different-2 port number then memory exhaustion of the victim. The count based filtering method handle these attacks using count number of packets and find within timestamp.*

**Index Terms**—Cloud Computing, Count Based Filtering, Distributed Denial of Service.

## 1. INTRODUCTION

Cloud computing is a recent technology, which is widely used for storing data remotely. It is used in educational and organizational both fields. Cloud computing provides services on software applications, programming platforms, infrastructure and data storage [1]. A user has a unique account for using each and every service on cloud and pay money according to using cloud services. It will distribute the resources to the user on the basis of need of the services. The Cloud Computing will do all the computation work for assign resources through software [2].

In the deployment model cloud have four types of cloud as follows: Public cloud, Private cloud, Hybrid cloud, and Community cloud [3]. Public cloud uses resources multiple customers and pay for service. It is public for all customers. It has less security because of publicly open. Private cloud uses some limited users. It is generally used managed data center [3]. It has more secure because of users are limited. Hybrid cloud is a combination of public cloud and private cloud. Community cloud creates by some set of organization and it has some standards and policies. Community cloud is operated by

one of the organization in the community or third party. All the organization has trust on third party [3].

The rest of the organization of the paper is follows, section II describe cloud computing security issues. DOS attack and DDOS attack is discuss in III section. Section IV discuss related work of this paper. Count based filtering method discuss in V section. Section VI discuss about performance analysis. Conclusion and future work discuss in VII section.

## 2. CLOUD COMPUTING SECURITY ISSUES

Recently, Cloud computing uses education and organizational areas. In the organization, cloud computing widely used for storing data on data centers and providing on-demand services. Data are storing globally then it has some security flaws. Users used services of cloud computing via internet through login id and password.

### 2.1 Data Security

In Cloud computing, where is the data more secure store in local machine or store in globally on data centers. If data store in local machine and machine does not connect to internet then it is secure. In the Berkeley paper's, If user want to store data on cloud then first user encrypt the data to own private key after that store data on cloud.

### 2.2 Freedom

In this issue, Cloud computing does not allow users to store data in its selected location. Cloud Service Provider (CSP) decides your data is storing which data centers [3]. Cloud computing allows users to retrieve data, store data and update data in cloud data centers.

### 2.3 Data Recovery

If customer lost the data due to some natural disaster, then customer ask to cloud service provider (CSP) how we recover data [4]. If CSP replicate the

data to another data centers then CSP provide data to other data centers. If CSP do not replicate data then ask to CSP how they provide data and it takes how much time.

## 2.4 Identification & Authentication

In Cloud computing, Identification is a process to identify user identity. Identify identity due to login id and password. Login id and password is valid for specific cloud. Cloud will allow services to user according to priority and permissions [5].

## 2.5 Availability

In present, Availability is a most popular security issue. In cloud computing SLAs defines server which types of services provide to customers. Availability means server will provide services all times. Availability can be affected temporarily or permanently. Denial of service attack affects the availability of cloud server [6].

## 2.6 Auditing

In the auditing check what happened in cloud. Auditing provides security of data and audit data periodically. Audit check store data is original data or modified data [7].

## 3. DOS & DDOS ATTACK

We are discussing aim of the attack and methods of the DOS and DDOS attack. DOS attack is one of the most famous attacks and DDOS attack is enhanced form of DOS attack. This attack has on end-systems.

### 3.1 Aim of DOS and DDOS attack

In the DOS attack, Attacker sends large number of packets over the network for consuming server resources and bandwidth. If any host sends a request to server for the resource but server does not entertained host and deny for the request. DOS attack has one-to-one mapping between attacker and victim and DDOS attack has many-to-one mapping between attacker and victim [8]. In the DOS attack, Attacker target to server memory, available CPU cycle, available disk space and maximum number of simultaneous connections [9].

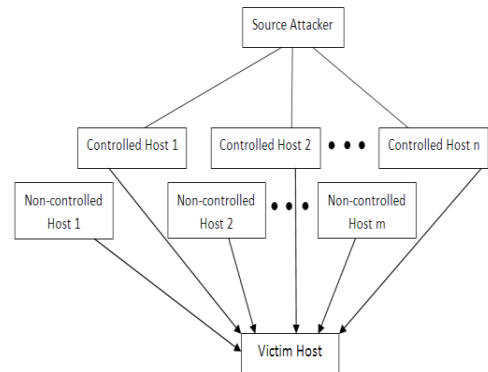


Figure 1. Architecture of DDOS attack [8]

In DDOS attack, Source attacker wants to DDOS attack to victim host. Source attacker control some specific number ( $n = \text{positive integer}$ ) of hosts and all  $n$  controlled hosts attack separately. Controlled hosts broadcast the packet for attack to victim host. Non-controlled hosts ( $m = \text{positive integer}$ ) have not necessary all the hosts send a packet.

### 3.2 Methods of DOS and DDOS attack

In the DOS and DDOS attack, we discuss method of attack. How attack is done to end-systems. This attack is use flood in the network. In the flooding, source broadcast the packet in the network and destination address in the packet is victim address. Due to flooding victim receives multiple copies of the packet and source target victims packet processing capability [10].

**3.2.1 TCP connection:** In this attack, Zombie hosts creates the more number of three way handshake TCP connection to victim. These connections are creating until memory or resources are not exhausted [8].

**3.2.2 TCP SYN flood attack:** In this attack, Attacker sends a large number of TCP SYN packets to victim. Victim receives the packet and reply TCP SYN+ACK packet to attacker. Attacker does not response to victim TCP SYN packet and victim is on TCP half-open state [9]. After timeout victim close the half-open connection. In this attack attacker target the memory exhaustion of the victim [9]. If attacker creates more TCP half-open connection before closing previous half-open connection by victim then memory exhaustion problem occur.

**3.2.3 TCP ACK flood attack:** An attacker sends large number of TCP ACK packets to victim. Victim process all the packets. This attack affects on CPU exhaustion [9]. Victim process large number of packet and CPU processing is slow. In this attack, Victim suffers from livelock [9]. Because incoming number of packets are increases and CPU does not do useful work due to more number of interrupts.

#### 4. RELATED WORK

In recent years, DOS and DDOS attack is a wide area of the research. This area have existed many successful solution. Filtering of the packets can be done on different-2 types like: victim-initiated, path-initiated, and source-initiated [11]. Victim-initiated reduce the incoming traffic of the packet. Path-initiated drop the packet if packet is not coming from appropriate router. In the source-initiated, source are responsible for incoming packets are attack free.

In other approach, DDOS defense using SOA-Based Traceback Approach (SBTA) [12]. SBTA is approach for identify true source of the packet in the cloud computing. SBTA placed on virtual machine in the cloud so that it is flexible and scalable. In cloud traceback (CTB) [13] main aim to apply service oriented architecture (SOA) for identify true source. CTB use deterministic packet marking (DPM) algorithm. DPM use some fields of IP packet and mark packet. Mark packet use for traceback the route.

Confidence based filtering (CBF) [14] is other method for prevent DDOS attack. In this method find the correlation pattern of the incoming packets. CBF method working on two periods: attacking period, Non-attacking period. If non-attack period, Nominal profile generate based on the fields of the packets and calculate confidence. If attack period, Nominal profile generate based on the fields of the occurrences of the packet and calculate confidence. According to confidence packet will be accept or discarded.

#### 5. COUNT BASED FILTERING METHOD

In this approach, we are trying to prevent DOS and DDOS attack to server. Firstly, we are discussing some keywords that using in this method. In this method we are maintaining four tables are table\_r, table\_q, and table\_p.

**Timestamp:** Timestamp is a positive integer value. It is a time in millisecond. In single timestamp, we are updating one table\_r. Timestamp value do not fix too small or vary large. If timestamp value is very small then most of the time of CPU taken computation work. If timestamp value is large then update in the rejection\_table is too late. Each timestamp creates one table. At the  $i^{\text{th}}$  timestamp three

table exist are  $i^{\text{th}}$  time (table\_r),  $(i-1)^{\text{th}}$  (table\_q) and  $(i-2)^{\text{th}}$  table\_p.

$$\text{Timestamp} \leq \text{cycle time}/3 \quad (1)$$

Cycle time: After this time sequence number will be repeat.

After first timestamp is field entry goes from table\_r to table\_q. Second timestamp is field entry goes from table\_q to table\_p and third timestamp is entry delete from table\_p and rejection\_table also.

**Table\_r, table\_q and table\_p:** Attributes of the table is source port number, destination port number, sequence number and count. Count is doing number of packets that contain remain three attributes are same.

**Rejection\_table:** This table contains attributes are source port number, destination port number, sequence number and count. This table contains all the entries of the table\_q and table\_p. If source port number, destination port number, sequence number are same in table\_q and table\_p then rejection\_table contain addition of the count of the both table.

**Field Attribute (FA) :** < source port number, destination port number, sequence number >

It is a combination of these attributes.

**Field<sub>(i)\_table\_name</sub> :** where i= tuple number of the specified table

**Count<sub>(i)\_table\_name</sub> :** where i= tuple number of the specified table that contain count

This method we are counting the number of packets per timestamp. According to its count packets will be accepted or rejected. rejection\_table will update after each timestamp. This algorithm works as follow:

```

1.  if ( ack_bit == 1 )
2.  {
3.      update ( Fieldpacket ) //update algorithm written
        in below
4.      if ( check( Fieldpacket ) ) //check algorithm
        written in below
5.          Process packet
6.      else
7.          Discard packet
8.  }
9.  else if ( syn_bit == 1 )
10. {
11.     update ( Fieldpacket ) //update algorithm written in
        below
12.     if ( check( Fieldpacket ) ) //check algorithm
        written in below
13.         Process packet
14.     else
15.         Discard packet
16. }
17. else
18.     process packet

```

After this algorithm, we are discussing update( Field<sub>packet</sub> ) algorithm. This algorithm updates the table<sub>r</sub>.

```

1  if ( Fieldpacket == Field(i)_table_r )
2      count(i)_table_r = count(i)_table_r + 1 (
    corresponding entry in the Fieldtable_r )
3  else
4      {
5          add new entry in the table_r
6          Count = 1 // corresponding entry
7      }

```

Now, we are discussing algorithm for check( Field<sub>packet</sub> ). This algorithm returns true if packet is processed otherwise return false.

```

1  if ( isEmpty ( rejection_table ) ) // return true if
    rejection_table is empty
2  {
3      if ( ( Fieldpacket == Field(i)_table_r ) && (
        count(i)_table_r > 1 ) )
4          return false
5      else
6          return true
7  }
8  else
9  {
10     if ( Fieldpacket == Field(i)_rejection_table )
11     {
12         if ( count(i)_rejection_table > 1 )
13             return false
14         else
15             return true
16     }
17     else
18     {
19         if ( ( Fieldpacket == Field(i)_table_r ) && (
            count(i)_table_r > 1 ) )
20             return false
21         else
22             return true
23     }
24 }

```

Finally, we are discussing algorithm for update rejection\_table. This table update after completion of each timestamp. All the update in the rejection\_table according to algorithm is as follows:

Algorithm for modify rejection\_table.

```

1  if ( isEmpty ( table_p ) ) //table_p is empty
2  {
3      if ( isEmpty ( table_q ) ) //table_q is empty
4          table_q = table_r
5      else //table_q is not empty
6      {
7          table_p = table_q

```

```

8          table_q = table_r
9      }
10     while ( ! isEmpty ( table_r ) ) // copy all the
        entry of table_r to rejection_table
11     {
12         if ( Field(i)_table_r == Field(j)_rejection_table )
13             count(j)_rejection_table =
                count(j)_rejection_table + count(i)_table_r
14         else
15             Add Field(i)_table_r and count(i)_table_r
                in the rejection_table
16         delete ith tuple in the table_r
17     }
18 }
19 else //table_p is not empty
20 {
21     while ( ! isEmpty ( table_p ) ) // delete all the
        entry in the rejection_table which is in the table_p
22     {
23         if ( Field(i)_table_p == Field(j)_rejection_table )
24             count(j)_rejection_table =
                count(j)_rejection_table - count(i)_table_p
25         {
26             if ( count(j)_rejection_table == 0 )
27                 delete jth tuple in the
                rejection_table
28         }
29         delete Field(i)_table_p in the table_p
30     }
31     table_p = table_q
32     table_q = table_r
33     while ( ! isEmpty ( table_r ) ) // copy all the
        entry of table_r to rejection_table
34     {
35         if ( Field(i)_table_r == Field(j)_rejection_table )
36             count(j)_rejection_table =
                count(j)_rejection_table + count(i)_table_r
37         else
38             Add Field(i)_table_r and count(i)_table_r
                in the rejection_table
39         delete ith tuple in the table_r
40     }
41 }

```

## 6. PERFORMANCE ANALYSIS

In this section, we are using some statistics to test this method results. We are testing this method in the environment of 2.66 GHz Intel core i5 processor and 4GB

memory. We are implementing this method in the cloud computing environment using cloudsim3.0.2 simulator. The cloudsim3.0.2 is a java library. For using this java library must have install jdk6.0 or above version and eclipse SDK. We are checking this method for denial of service attack and results calculated and compare these results to CBF method [14].

### 6.1 Simulation Conditions

In this paper, the average rate of arrival packets are 6000 to 7000 packets per second and arrival of packets rate is 22.33Mbps [14]. Sequence number contain 32 bit so that sequence space is  $2^{32}$ . According to [15] if data rate is 100Mbps then cycle time is 5.4 minutes and 22.33Mbps is much smaller than 100Mbps. We are using value of timestamp is 100ms. It means after every 100ms rejection\_table will be updated and table\_r will be empty. Timestamp value should not be large or small. If it is large then table size will be large and if it is small then increase cpu computation. Initially table\_p, table\_q, table\_r and rejection\_table are empty. In this simulation probability of arrival of attacking packets are 0.7 to 0.8.

TABLE1. NATURE OF THE ATTACK

Attack Intensity	Attack Packets	Legitimate Packets	Total no of Packets
1x	5,326	1,674	7,000
5x	25,326	9,674	35,000
10x	51,345	18,655	70,000
20x	1,02,929	37,071	1,40,000

### 6.2 Simulation results

In this section, we compare the count based filtering method and CBF method. Timestamp value is 100ms. Table2 denotes the comparison of both methods.

TABLE2. COMPARISON OF COUNT BASED FILTERING AND CBF METHOD

Attack Intensity	Process Time in Seconds	
	Count based filtering	CBF
1x	0.263	0.332
5x	0.758	1.073
10x	1.623	1.919
20x	3.179	3.661

We are improve the results because of count based filtering method does less computation work compare to CBF method.

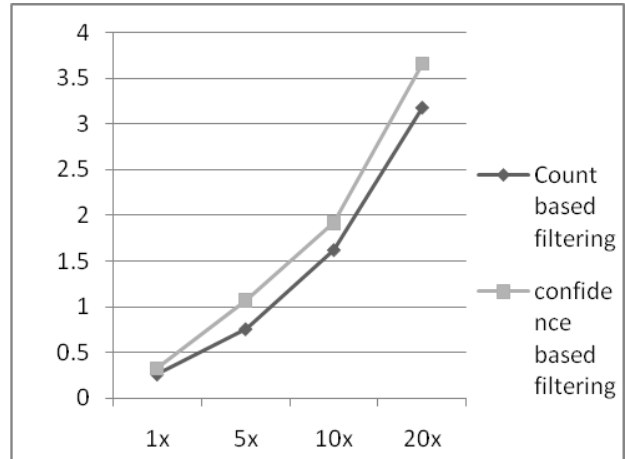


Figure 2. Comparison between confidence based filtering and count based filtering method

Result of count based filtering method may vary according to change the value of timestamp.

Since discarding or accepting a packet of CBF method first calculate confidence of packet and according to minconf packet will be accept or reject. Count based filtering method calculates count of packet and according to count packet will be accept or reject.

## 7. CONCLUSION AND FUTURE WORK

Cloud Computing is a recent technology that provides services remotely and users pay for service. Availability is a most important security problem. DOS and DDOS attack threats to availability. TCP SYN flood attack effect the memory exhaustion and TCP ACK flood attack effect the CPU exhaustion.

In this paper discuss count based filtering method. This method creates table and tables will be modify with the completion of timestamp and according to count of the same field packet will be processed or discarded. Performance of this method depends on the value of timestamp.

## REFERENCES

- [1] Dong Xu, "Cloud Computing: an Emerging Technology," in International Conference on Computer Design And Applications (ICDDA 2010) *IEEE*, vol. 1, pp. 100-104, 2010.
- [2] Shufen Zhang, Shuai Zhang, Xubin Chen, and Shangzhou Wu, "Analysis and Research of Cloud Computing System Instance," in International Conference on Future Networks (ICFN 2010) *IEEE*, pp. 88-92, 2010.
- [3] Jianfeng Yang, and Zhibin Chen, "Cloud Computing Research and Security Issues," *IEEE*, 2010.
- [4] Krešimir Popović, and Željko Hocenski, "Cloud Computing security issues and challenges," *IEEE*, pp. 344-349, May 24-28, 2010.



- [5] Ramgovind S, Eloff MM, and Smith E, "The Management of Security in Cloud Computing," *IEEE*, 2010.
- [6] Huaglory Tianfield, "Security Issues In Cloud Computing," in International Conference on Systems, Man, and Cybernetics *IEEE*, pp. 1082-1089, October 14-17, 2012.
- [7] Minqi Zhou, Rong Zhang, Wei Xie, Weining Qian, and Aoying Zhou, "Security and Privacy in Cloud Computing: A Survey," in International Conference on Semantics, Knowledge and Grids *IEEE*, pp. 105-112, 2010.
- [8] An Lei, and Zhu Youchen, "The Solution of DDOS attack based on Multi-agent," in International Conference on Educational and Information Technology (ICEIT 2010) *IEEE*, Vol. 2, pp. 530-532, 2010.
- [9] M. Handley, and E. Rescorla, "Internet Denial-of-Service Considerations," IETF, RFC 4732.
- [10] W. Eddy, "TCP SYN Flooding Attacks and Common Mitigations," IETF, RFC 4987.
- [11] Yoohwan Kim, Wing Cheong Lau, Mooi Choo Chuah, and Jonathan Chao, "PacketScore: A Statistics-Based Packet Filtering Scheme against Distributed Denial-of-Service Attack," in Transactions on dependable and secure computing *IEEE*, Vol. 3, No. 2, pp. 141-155, April-June 2006.
- [12] Lanjuan Yang, Tao Zhang, Jinyu Song, JinShuang Wang, and Ping Chen, "Defense of DDoS Attack for Cloud Computing," *IEEE*, pp. 626-629, 2012.
- [13] Bansidhar Joshi, A. Santhana Vijayan, and Bineet Kumar Joshi, "Securing Cloud Computing Environment Against DDoS Attacks," in International Conference on Computer Communication and Informatics (ICCCI-2012) *IEEE*, Jan. 10-12, 2012.
- [14] Qi Chen, Wenmin Lin, Wanchun Dou, and Shui Yu, "CBF: A Packet Filtering Method for DDoS Attack Defense in Cloud Environment," in Ninth International Conference on Dependable, Autonomic and Secure Computing, *IEEE*, pp. 427-434, 2011.
- [15] Jon Postel, "TRANSMISSION CONTROL PROTOCOL," IETF, RFC 793.



# Privacy & Security of Mobile Cloud Computing

Manmohan Chaturvedi<sup>\*,1</sup>, Sapna Malik<sup>2</sup>, Preeti Aggarwal<sup>3</sup> and Shilpa Bahl<sup>4</sup>

Ansal University, Sector 55, Gurgaon- 122011, India

<sup>1</sup>mmchaturvedi@ansaluniversity.edu.in <sup>2</sup>sapnadhankhar@gmail.com

<sup>3</sup>preetagarwal@gmail.com, <sup>4</sup>gerashilpa@gmail.com

## Abstract

The Indian government, like governments elsewhere in the world, has chosen mobile device as preferred platform to engage with citizens while offering various e-Governance services. Likewise there is huge market for mobile based e-Commerce applications across the globe. However uptake of these services is challenged by the security and privacy concerns of the end user. The limited processing power and memory of a mobile device dependent on inherently unreliable wireless channel for communication and battery for power leaves little scope for a reliable security layer. Thus there is a need for a lightweight secure framework that provides security with minimum communication and processing overhead on mobile devices. The security and privacy protection services can be achieved with the help of secure mobile-cloud application services. Taking support from a proximate cloud a security service could be devised for a mobile device which works as an interface and adaptively provides optimum security solutions based on communication channel capacity, available system resources both hardware and software and user-defined QoS parameters. We plan to explore and experiment with available options to recommend security and privacy enhancing approaches that may meet the security need for mobile application using automated sensing of the context.

**Key Words:** Mobile Security, Adaptive Security, m-governance, m-commerce, Privacy and Security

## 1. Introduction

Mobile Cloud Computing (MCC) is combination of two terms, mobile computing and cloud computing. Mobile computing is provision of applications on mobile devices. Cloud computing refers to getting paid services either in the form of infrastructure, platform or software through internet based cluster of distributed servers. Mobile cloud computing is provision of mobile applications using cloud to give more power to mobile devices towards computing, in spite of resource limitations in mobile devices. Mobile cloud computing is a concept that has been in use since 2009 and is still evolving.

There are various known challenges in the field of MCC viz. handover delay, bandwidth limitation, task division for offloading, reliability, integrity of data delivered, scalability of MCC without degradation in performance or change in infrastructure, security of data in mobile device within a cloud and in the communication channel, identity privacy, location privacy, etc. These challenges are the biggest obstacles in growth of mobile cloud computing. According to the literature [1,2] 74% of IT Executives and Chief Information Officers are not willing to adopt cloud services due to the risks associated with security and privacy. In MCC the security threats are likely in various segments viz. mobile device, communication channel or the cloud itself. So one has to provide protection from these threats by having secure cloud application services in mobile devices and cloud, secure routing protocols in communication channel and secure virtualization in cloud architecture. According to review of the current approaches in MCC [3], the security framework for MCC is divided into two categories; Data Security framework and Application Security Framework. Data Security frameworks are compared on the basis of their basic theory –mathematical principle or cryptographic principle, data protection –protection of data created or manipulate on device or data created or manipulate on cloud, data integrity, scalability, assumption of components-fully trusted, semi trusted or distrusted, data access automated or semi automated and authentication of originator of file. Application security framework can be compared on the basis of application type, security features like data security, integrity, identity privacy, location privacy, authentication, secure data access

---

\* Corresponding author : MM Chaturvedi (email :mmchaturvedi@ansaluniversity.edu.in , +919871078151 (m) )

management or secure routing, assumption of component trust levels, scalability of framework. Each security framework must be viewed with its security strength and resource usage. In security strength we take care of confidentiality, integrity, authentication parameters. In resource usage we consider memory usage, processing time and network overhead parameters [4].

In this paper, section 2 reviews the related literature on cloud computing, MCC and various security aspects of mobile and cloud computing. Section 3 deals with the overall architecture of the proposed plan elaborating on need of cloud computing in 3.1, features of mobile cloud computing in 3.2, objective in 3.3. Section 4 describes the possible validation approaches to test the design objective. Section 5 lists out the challenges involved in the research objectives whereas section 6 concludes the paper highlighting the possible outcome of this research work.

## 2. Related Work

Security and privacy issues of MCC have been discussed by many researchers. J. Oberheide et al [5] proposed Cloud AV platform, malware detection system for mobile device by moving detection capabilities to network service or cloud. Zhang et al [6] present security framework for elastic mobile application model by dividing an application into easily configurable weblets. Xiao and Gong [7] proposed scheme for mobile cloud environment to generate a dynamic credential for mobile user for their identity protection from hackers. Wang and Wang [8] have proposed privacy preserving framework for mobile devices while using location based scheme by spatial cloaking. Huan et al [9] presents framework –MobiCloud to enhance the functionality of MANET and cover security aspect in terms of risk management and secure routing. G. Portokalidis et al [10] proposed scheme for threat detection in a smart phone with Mobile Cloud Computing. H.Zhang and X Mingjun [11] proposed distributed spatial cloaking protocol for location privacy. P.Zou et al [12] propose Phosphor, a cloud based mobile digital right management scheme with Sim Card by designing License state word. R.Chow et al [13] present policy based cloud authentication platform using implicit authentication for solving privacy issues. Itani et al [14] proposed an energy efficient framework for mobile devices by using incremental message authentication code to ensure integrity of mobile users. Jia et al [15] presents proxy re-encryption (PRE) scheme and identity based encryption (IBE) scheme to achieve secure data service. Huang et al [16] proposed secure data processing framework for MobiCloud addressing issue of authentication on cloud. Hsueh et al [17] Proposed authentication mechanism to ensure security and integrity of mobile users files stored on cloud server. Yang et al [18] extended the public provable data possession scheme with Diffie Hellman Key Exchange, Bilinear mapping and Merkle Hash Tree (MHT). Chen et al [19] present security framework for location based grouped scheduling services for identity privacy and authentication. Ren et al [20] proposed three schemes; encryption based, coding based and sharing based to ensure the confidentiality and integrity of user's file stored at cloud. Zhou and Huang [21] proposed a privacy preserving framework by offloading the processing and storage intensive encryption and decryption on cloud based on Cipher text Policy attribute. Current research initiatives seem to address only one or two parameters of security from the comprehensive set of authentication, integrity, confidentiality and privacy. These research approaches favor static security algorithms without considering changing demand for security, quality of service, and resource usage of mobile users.

## 3. Architecture of the model proposed to be explored

### 3.1 Cloud Computing

The Cloud Computing is gaining popularity with its main advantage of reducing the computational burden of the client and thus reducing the complexity and other infrastructure requirements at the client end. However, it is important to realize that the market is still deprived of cloud service providers because of following important issues:

- Data replication
- Consistency
- Limited scalability
- Unreliability
- Unreliable availability of cloud resources
- Portability
- Trust
- Security
- Privacy

The commonly accepted definition of Cloud computing is an IT service being provided to users on demand and being paid for depending upon amount of usage. It can also be termed as a dynamic service being provided to users that can

add on to the available capacity and capabilities of user entity. Some of the key services of Cloud Computing as depicted in Figure 1 are:

- Infrastructure as a Service (IaaS)
- Data storage as a Service (DaaS)
- Communication as a Service (CaaS)
- Security as a Service (SecaaS)
- Hardware as a Service (HaaS)
- Software as a Service (SaaS)
- Business as a Service (BaaS)
- Platform as a Service (PaaS)
- Virtualization

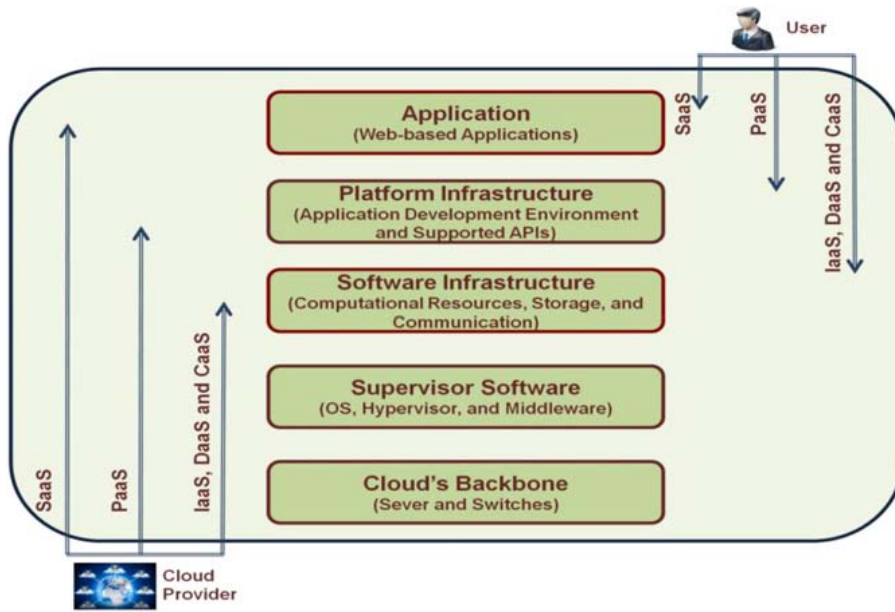


Fig. 1. Layered Architecture of Cloud Computing [3]

### 3.2 Mobile Cloud Computing

The application of cloud is possible in many domains. One of the domains of our current interest is that of mobiles. Hence, we will be focusing on utility of cloud computing environment for mobile usage and how can a cloud add value to the overall functionality and performance of mobile devices? According to Khan et al [3] as depicted in figure 2, MCC is a service that allows resource constrained mobile users to adaptively adjust processing and storage capabilities by transparently partitioning and offloading the computationally intensive and storage demanding jobs on traditional cloud resources by providing ubiquitous wireless access.

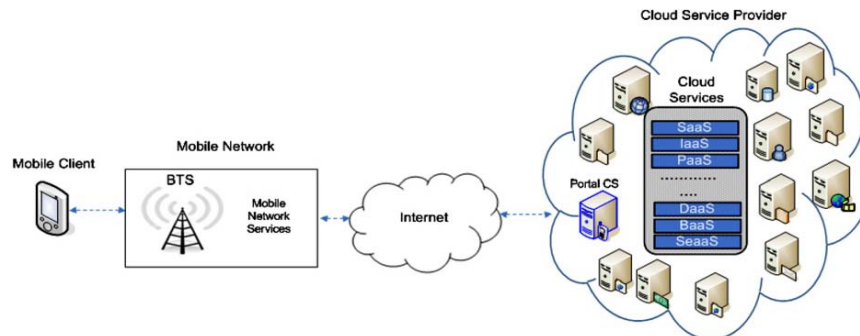


Fig. 2. Mobile Cloud Computing Architecture [3]

Some of the limitations of mobile devices which drive use of Cloud Computing for mobile devices are:

- Limited battery
- Limited processing power
- Low storage
- Less security
- Unpredictable Internet connectivity
- Less energy

### 3.3 Research Objective

Our research objective is to propose and develop a system in which security protocols can be decided for a mobile entity dynamically in a cloud. For this, we will be focusing on not just the mobile security parameters but also on the cloud security related issues and respective parameters. As suggested by Khan et al [3], the security and privacy protection services can be achieved with the help of secure cloud application services. Figure 3 describes the security services necessary at various layers of the supporting cloud. In addition to security and privacy, the secure cloud application services provide the user management, key management, encryption on demand, intrusion detection, authentication, and authorization services to mobile users. There is a need for a secure communication channel between cloud and the mobile device. The secure routing protocols can be used to protect the communication channel between the mobile device and cloud.

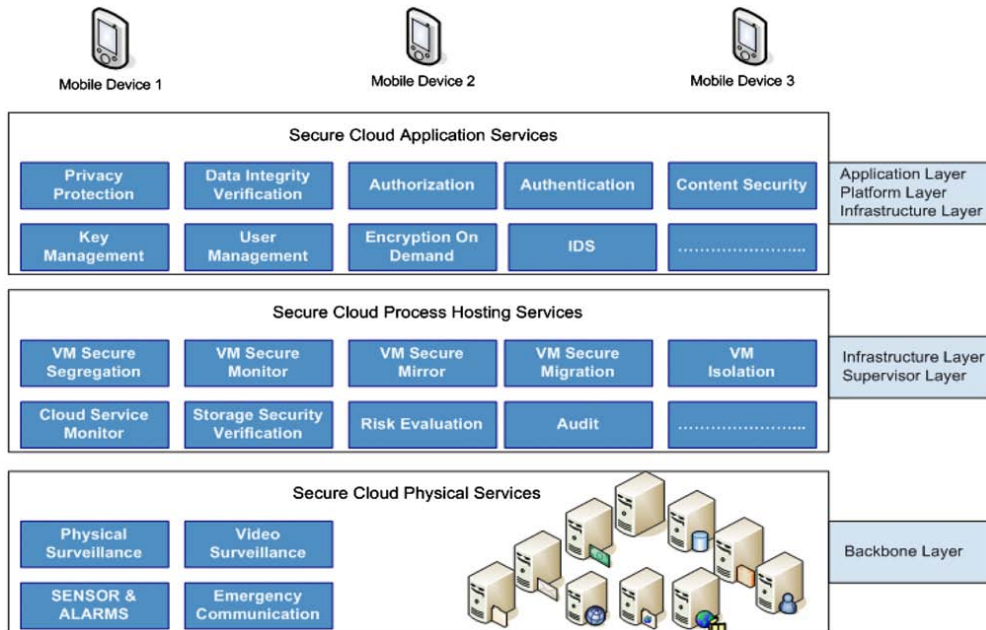


Fig. 3. Security services on different layers [3].

The key illustrative areas of proposed research are:

- Preparation of semantic data for security parameters
- Cloud Security attributes
- Mobile Security features and respective parameters
- Security protocols under different security requirements
- Platform Independent Security Architecture.

In the work of Khan et al [3], frameworks of various aspects of security features have been described in detail. As suggested by Rocha et al [4], a security service can be devised which works as a middleware with the ability to change the security protocols dynamically between two peers. In their work, domain is of independent mobile users.

We propose to expand this concept to a cloud where a number of mobile users will be acting as members of the cloud and will exchange information within the cloud. For this we need to define various levels of security. A mobile may require different levels of security at different times depending upon the service being used and the sensitivity of the data exchanged with the peer.

Broadly the proposed research could address following questions:

- a) What could be semantic data for mobile and cloud security?
- b) How the Protocol Selection Procedure can be made intelligent with option for static protocol selection when necessary?
- c) How workload could be partitioned between mobile and cloud after factoring various related issues?

The following options need to be evaluated to arrive at a possible mix to answer the framed research questions:

- a) As proposed by Zissis & Lekkas [22], a trusted third party could be tasked with assuring specific security characteristics within a cloud environment.
- b) Identification of appropriate security parameters for a mobile and cloud with their dependency matrix to suggest a security metric towards security of a mobile cloud computing application.
- c) Generation of semantic data which facilitates selection of the security protocol by the middleware. Intelligent protocol selection process would help conserve resources. This would permit use of already selected protocol if the semantic data values are unchanged.
- d) If the security requirement between two peers is same over a period of time, then repeated overhead of security parameter collection and protocol selection for every information exchange can be avoided by choosing the relevant security protocol for stipulated time duration before entering dynamic protocol selection mode as necessary.
- e) Security related work could be partitioned between the mobile and the cloud with computationally light tasks handled by the mobile itself and heavy tasks outsourced to the cloud.

#### 4. Proposed Validation approaches

Validation is done at the end of the development process and takes place after verifications are completed i.e. determining if the system complies with the requirements and performs functions for which it is intended and meets the stated goals and user needs [23].

The validation of the proposed research is to establish that it is adaptive in nature for several contexts and leads to benefits both in performance and ease to use and according to the type of user dependent data transfer. The designed software should permit the application to determine different semantic values for each part of the data to be transmitted, and thus addresses the main concern of the user viz. enhanced security.

##### *Cloud based Mobile Computing Testing practices:-*

It is important to take into consideration the additional time and/or personnel needed to perform exhaustive tests on all the devices eg according to Rocha & Costa[4] in the proposed middleware which is a system software responsible for managing the transparent execution and interaction among the jobs running on the cloud servers, it is mandatory to test these system software like OS and Hypervisor of the cloud .So the types of testing that is to be planned for the cloud system software are, Performance Testing, Capacity Testing, Fail-over Testing, Browser testing[24]

- **Application security testing.** This type of testing is done to secure application software that is running on or being developed in the cloud.
- **Governance Risk Compliance (GRC) testing.** Its main focus is to list threats, vulnerabilities and risks that are associated to all three parts of Cloud Computing – Infrastructure as a Service (IaaS), Platform as a Service (PaaS) & Software as a Service (SaaS) and suggest controls which have been assimilated from the best practices prevailing in the Industry.
- **Latency Testing.** Cloud testing is utilized to measure the latency between the action and the corresponding response for any application after deploying it in the cloud.

##### *Issues and Challenges in Cloud Testing*

There are a number of issues and challenges in testing clouds and cloud-based software. Here we discuss them from the following four areas.

- *On-demand test environment construction* – How to set up a testing environment systematically (or automatically) for on-demand testing services in a cloud? Although the current cloud technologies support automatic provision of required computing resources for each SaaS (or application) in a cloud, there are no supporting solutions to assist engineers to set up a required test environment in a cloud using a cost-effective way. It is necessary to provide an on-demand test environment for TaaS customers, IaaS customers, DaaS customers etc.
- *Scalability and performance testing* – Although many published papers discuss system performance testing and scalability evaluation in the past two decades, most of them address issues and solutions in conventional distributed software or web-based software systems. According to our recent literature survey on this subject, most existing papers focus on scalability evaluation metrics and frameworks for parallel and distributed systems.
- *Testing security and measurement in clouds* – Security testing has becoming a hot research subject with many open questions in current software testing community. Since security becomes a major concern inside clouds and security services become a necessary part in modern SaaS and cloud technology, engineers must deal with the issues and challenges in security validation and quality assurance for SaaS and clouds.

## 5. Key Challenges in the proposed research

The key challenges that we anticipate are:

- a) During experimentation the simulator being used should acquire necessary information from both the OS and through the wireless medium.
- b) Balance between security and maintaining communication quality and system performance.
- c) We should provide a single security layer for different contexts of hardware, software and communication modes.
- d) Need for the data semantics so as to determine different sensitivity levels of the data being transmitted, facilitating strong security mechanism only when they are actually needed rather than on the whole data.
- e) In the proposed approach the appropriate metrics and the parameters should be defined to facilitate objective evaluation of our approach.
- f) Design of a Platform Independent Security Architecture so that we can deploy lightweight part of security Framework on any Mobile device could pose interface issues.

## 6. Concluding Remarks

This paper has attempted literature review of various approaches for effective deployment of secure mobile cloud computing paradigm.

Challenges and possible options have been delineated while we try to explore and characterize an adaptable and dynamic framework providing configurable security interface at the application layer.

Issue connected with validation and testing of proposed solution have also been considered to help us formulate dependable testing and benchmarking of a security firmware in the context of mobile cloud computing.

The fallout of the proposed research is expected to be of interest to both E-governance and E-commerce applications. The challenges in this evolving field of research are many and we plan to proceed in phases with first phase attempting to characterize the problem in formal terms and propose a lightweight mobile interface having limited dynamic capability. Later phase may attempt expanded objectives.

## References

1. Subashini,S. ,Kavitha,V.: A survey on security issues in service delivery models of cloud computing, *Journal of Network and Computer Applications* 34 (1) 1–11 (2011).
2. Buyya,R.,Yeo C.S.,Venugopal,S., Broberg,J.,Brandic I.: Cloud computing and emerging IT platforms: vision, hype, and reality for delivering computing as the 5th utility, *Future Generation Computer Systems* 25 (6) (2009) 599–616
3. Khan,A.,N.,Mat Kiah,M.,L., Khan S.,U.,Madanic,S.A. :Towards secure mobile cloud computing: A survey, *Future Generation Computer Systems* 1-22 (2012)
4. Bruno P.S.Rocha,Daniel N.O.Costa,RandeA.Moreira,ristianoG.Rezende,Antonio A.F.Loureiro, Azzedine Boukerche : Adaptive security protocol selection for mobile computing, *Journal of Network and Computer Applications* (2012)
5. Oberheide,J., Veeraraghavan,K., Cooke, E., Flinn, J., and Jahanian, F.. :Virtualized in-cloud security services for mobile devices, in *Proceedings of the 1st Workshop on Virtualization in Mobile Computing (MobiVirt)*, pp. 31-35, (June 2008).
6. Zhang, X., Schiffman, J. , Gibbs ,S., Kunjithapatham, A., Jeong, S.: Securing elastic applications on mobile devices for cloud computing, in *Proceeding ACM workshop on Cloud computing security, CCSW '09, Chicago, IL, USA,( Nov. 2009.)*
7. Xiao, S., Gong, W.: Mobility can help: protect user identity with dynamic credential, in: *Proc. 11th Int. Conference on Mobile Data Management, MDM '10, Missouri, USA,(May 2010)*
8. Wang, S., Wang, X.S.: In-device spatial cloaking for mobile user privacy assisted by the cloud, in: *Proc. 11th Int. Conference on Mobile Data Management,MDM '10, Missouri, USA,( May 2010).*
9. Huan,D., Zhang, X., Kang ,M., Luo ,J.: MobiCloud: building secure cloud framework for mobile computing and communication, in: *Proc. 5th IEEE Int. Symposium on Service Oriented System Engineering, SOSE '10, Nanjing, China,(June 2010).*
10. Portokalidis,G.,Homburg,P.,Anagnostakis,K., Bos,H.: aranoid Android: versatile protection for smartphones, in *Proceedings of the 26th Annual Computer Security Application Conference (ACSAC)*, pp. 347-356, (September 2010).
11. Zhangwei ,H. and Mingjun ,X., : Distributed Spatial Cloaking Protocol for Location Privacy, in *Proceedings of the 2nd International Conference on Networks Security Wireless Communications and Trusted Computing (NSWCTC)*, vol. 2, pp. 468,( June 2010.)
12. Zou,P., Wang,C., Liu ,Z., and Bao ,D.,: Phosphor: A Cloud Based DRM Scheme with Sim Card, in *Proceedings of the 12th International Asia-Pacific on Web Conference (APWEB)*, pp. 459, (June 2010).
13. Chow, R., Jakobsson, M., Masuoka, R., Molina, J., Niu Y., Shi ,E., Song, Z. :Authentication in the clouds: a framework and its application to mobile users, in: *Proc. ACM Cloud Computing Security Workshop, CCSW '10, Chicago, USA,(Oct. 2010.)*
14. Itani,W., Kayssi,A., Chehab, A.: Energy-efficient incremental integrity for securing storage in mobile cloud computing, in: *Proc. Int. Conference on Energy Aware Computing, ICEAC '10, Cairo, Egypt, (Dec. 2010.)*
15. Jia,W., Zhu ,H., Cao, Z., Wei, L., Lin, X.,:SDSM: a secure data service mechanism in mobile cloud computing, in: *Proc. IEEE Conference on Computer Communications Workshops, INFOCOM WKSHPS, Shanghai, China,(Apr. 2011).*
16. Huang,D., Zhou,Z., Xu,L., Xing,T., Zhong,Y:Secure data processing framework for mobilecloud computing, in: *Proc. IEEE INFOCOM Workshop on Cloud Computing, INFOCOM '11, Shanghai, China, (June 2011.)*
17. Hsueh ,S.,C., Lin ,J.Y., Lin, M.Y.,: Secure cloud storage for conventional data archive of smart phones, in: *Proc. 15th IEEE Int. Symposium on Consumer Electronics,ISCE '11, Singapore, (June 2011.)*
18. Yang ,J., Wang, H., Wang, J., Tan, C., Yu1, D.: Provable data possession of resource constrained mobile devices in cloud computing, *Journal of Networks* 6 (7) 1033–1040 (2011).
19. Chen,Y.,J., Wang,L,C.: A security framework of group location-based mobile applications in cloud computing, in: *Proc. Int. Conference on Parallel Processing Workshops, ICPPW '11, Taipei, Taiwan, (Sep. 2011.)*
20. Ren,W., Yu,L., Gao,R., Xiong,F.: Lightweight and compromise resilient storage outsourcing with distributed secure accessibility in mobile cloud computing, *Journal of Tsinghua Science and Technology* 16 (5) 520–528 (2011).
21. Zhou,Z., Huang, D.: Efficient and secure data storage operations for mobile cloud computing, *IACR Cryptology ePrint Archive*: 185, (2011).
22. Dimitrios Zissis, Dimitrios Lekkas,: Addressing Cloud Computing Issues, *Future Generation Systems* (28) 583-592 (2012).
23. ISTQB Exam certification .com Webpage-<http://istqbexamcertification.com/what-is-validation-in-software-testing-or-what-is-software-validation/>
- 24.Belatrix cloud testing best practices, Belatrix Software Factory-White papers <http://www.belatrixsf.com/index.php/outsourcing-case-studies/131>



## About The Authors

**Manmohan Chaturvedi** is a retired Air Commodore from Indian Air Force with PhD in Information Security domain from IIT Delhi. He has about 35 years of experience in managing technology for IAF. An alumnus of National Defense College, New Delhi, he has held various appointments dealing with operational and policy dimensions of Information and Communication Technology. He graduated from Delhi College of Engineering and completed post graduation from IIT Delhi. Currently he is a Professor at School of Engineering and Technology, Ansal University with research interests in vulnerability of evolving ICT infrastructure and protection of Critical Information Infrastructure.

**Sapna Malik** is a Ph.D. candidate at the School of Engineering and Technology, Ansal University, India. She holds a M.Tech in IT from GGSIPU, New Delhi, India and B.Tech in CSE from Mayarishi Dayanand University, India. She is working as Assistant professor in department of Computer Science Engineering in Maharaja Surajmal Institute of technology, Delhi, India. Her Research interest includes Cloud computing, Network Security and Virtualization.

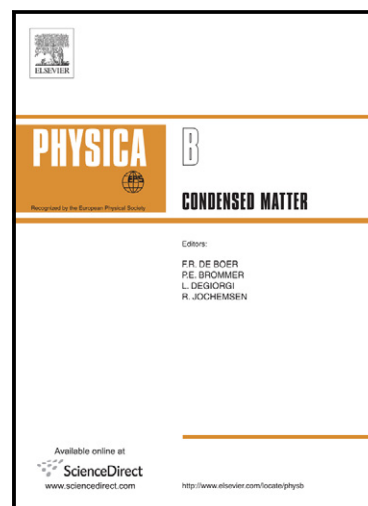
**Preeti Aggarwal** holds an M.Tech in IT from GGSIPU, New Delhi, an M.Sc in Informatics and a B.Sc (H) in Electronics from University Of Delhi and is currently pursuing Ph.D. in Data Mining and Information Security from Ansal university, Gurgaon. She is working as an Assistant Professor in department of Computer Science Engineering in KIIT College of Engineering, Gurgaon. She is also a member of Computer Society of India.

**Shilpa Bahl** holds M.Tech in IT from UIET, Krukshetra university, Kurukshetra and B.Tech in Electronics & communication From Kurukshetra university and is currently pursuing Ph.D. in Software testing and Information Security from Ansal university, Gurgaon. She is working as an Assistant Professor in department of Computer Science Engineering in KIIT College of Engineering, Gurgaon, having Six years of teaching experience in Computer Science department

# Author's Accepted Manuscript

Reddish-Orange emission from  $\text{Pr}^{3+}$  doped  
Zinc Alumino Bismuth Borate Glasses

Sk. Mahamuda, K. Swapna, A. Srinivasa Rao, T.  
Sasikala, L. Rama Moorthy



[www.elsevier.com/locate/physb](http://www.elsevier.com/locate/physb)

PII: S0921-4526(13)00428-6  
DOI: <http://dx.doi.org/10.1016/j.physb.2013.07.010>  
Reference: PHYSB307794

To appear in: *Physica B*

Received date: 4 May 2013  
Revised date: 7 July 2013  
Accepted date: 9 July 2013

Cite this article as: Sk. Mahamuda, K. Swapna, A. Srinivasa Rao, T. Sasikala, L. Rama Moorthy, Reddish-Orange emission from  $\text{Pr}^{3+}$  doped Zinc Alumino Bismuth Borate Glasses, *Physica B*, <http://dx.doi.org/10.1016/j.physb.2013.07.010>

This is a PDF file of an unedited manuscript that has been accepted for publication. As a service to our customers we are providing this early version of the manuscript. The manuscript will undergo copyediting, typesetting, and review of the resulting galley proof before it is published in its final citable form. Please note that during the production process errors may be discovered which could affect the content, and all legal disclaimers that apply to the journal pertain.

## Reddish-Orange emission from Pr<sup>3+</sup> doped Zinc Alumino Bismuth Borate Glasses

Sk.Mahamuda<sup>1</sup>, K.Swapna<sup>1</sup>, A.Srinivasa Rao<sup>\*1,2</sup>, T.Sasikala<sup>3</sup> and L.Rama Moorthy<sup>3</sup>

<sup>1</sup>Department of Physics, K L University, Green Fields, Vaddeswaram 522 502, A P, India

<sup>2</sup>Department of Applied Physics, Delhi Technological University, New Delhi-110 042, India.

<sup>3</sup>Department of Physics, S V University, Tirupathi 517 502, A P, India.

**\*Corresponding author: drsrallam@yahoo.co.in ., Tel: +91 85860 39007**

### Abstract

Praseodymium doped Zinc Alumino Bismuth Borate (ZnAlBiB) glasses were prepared by melt quenching technique and characterized by optical absorption and emission studies. The glassy nature of these glasses has been confirmed through XRD spectral measurements. From the absorption spectra, the Judd-Ofelt intensity parameters  $\Omega_\lambda$  ( $\lambda=2, 4$  and  $6$ ) and other radiative properties like transition probability ( $A_R$ ), radiative lifetimes ( $\tau_R$ ) and branching ratios ( $\beta_R$ ) have been evaluated. Emission spectra were measured for different concentrations of Pr<sup>3+</sup> ions doped glasses by exciting the glasses at 445 nm. The intensity of Pr<sup>3+</sup> emission spectra increases from 0.1 to 1 mol% and beyond 1 mol% concentration quenching is observed. The suitable concentration of Pr<sup>3+</sup> ions in ZnAlBiB glasses to act as a good lasing material at reddish-orange wavelength (604 nm) region has been discussed by measuring the emission cross-sections for the intense emission transition  $^1D_2 \rightarrow ^3H_4$ . The CIE chromaticity co-ordinates were also evaluated from the emission spectra for all the glasses to understand the suitability of these materials for reddish-orange emission. From the measured emission cross-sections and CIE chromaticity co-ordinates, it was found that 1 mol% of Pr<sup>3+</sup> is aptly suitable for the development of visible reddish-orange lasers.

**Key words:** Glasses, praseodymium, JO parameters, radiative properties, emission cross-section, colour co-ordinates.

## 1. Introduction

In quite recent years, rare earth doped glasses and crystals are playing an important role in the development of many opto-electronic devices such as lasers, light converters, sensors, hole burning high density memories, optical fiber amplifiers [1, 2]. The attractive feature of the rare earth ions is that they have a large number of energy levels in the infrared, visible and ultra violet spectral regions. These energy levels arising from the 4f electronic configurations of rare earth ions and are slightly influenced by the environment due to the screening effects produced by the completely filled outer 5s and 5p electronic shells. The optical properties of RE ions are strongly influenced by the ligand field surrounding them and on phonon energies of the host glass. In general, a host glass with low phonon energies can give high quantum efficiencies, which are useful to design lasers and optical fibre amplifiers [3]. Borate glasses are well known due to their high transparency, low melting point, high thermal stability and good rare earth ion solubility [4,5]. But these glasses cannot acts as good laser hosts due to their high phonon energies ( $\sim 1300\text{cm}^{-1}$ ). Such high phonon energies possessed by the borate glasses can be reduced by adding heavy metal oxides like  $\text{Bi}_2\text{O}_3$  to give high quantum efficiencies. Glasses based on heavy metal oxides such as  $\text{Bi}_2\text{O}_3$  possess high refractive index, high infrared transparency and high density. The presence of such heavy metal oxides can change the polarizabilities of the doped rare earth ions local background and will play a crucial role in photo excitations [6]. These glasses have wide applications in the field of glass ceramics, layers for optical and electronic devices, thermal and mechanical sensors and reflecting windows etc [7].  $\text{Bi}_2\text{O}_3$  cannot be considered as network former due to small field strengths of  $\text{Bi}^{3+}$  ions, but in combination with a good glass former like  $\text{B}_2\text{O}_3$  the glass formation is possible in a relatively large compositional range. The glasses based on  $\text{ZnO}$  have attracted many researchers because of its optical,

electrical and magnetic properties in combination with its non-toxicity, non-hygroscopic nature. The glasses containing ZnO have been used in the development of opto-electronic devices [8,9], solar energy converters [10], ultraviolet emitting lasers [11] and gas sensors [12]. The presence of  $\text{Al}_2\text{O}_3$  in a glass can increase the mechanical strength and thermal stability. Hence, for the present work we have prepared a glass with the chemical constituents  $\text{B}_2\text{O}_3$ ,  $\text{Bi}_2\text{O}_3$ , ZnO and  $\text{Al}_2\text{O}_3$ .

Among all the rare earth ions,  $\text{Pr}^{3+}$  activated amorphous materials have attracted many researchers because of their potential applications in the field of ultraviolet laser, scintillator and lamp phosphor [13-16]. The  $\text{Pr}^{3+}$  doped systems exhibit very rich emission spectra extending UV to infrared regions.  $\text{Pr}^{3+}$  ions doped glass fibres are currently used as the most promising candidates for 1.3 $\mu\text{m}$  communication window [17].  $\text{Pr}^{3+}$  systems are also interesting as short wavelength up-conversion laser materials [18]. One of the general features of some fluorescence levels of  $\text{Pr}^{3+}$  is that the emission is quenching when concentration increases.  $\text{Pr}^{3+}$  ions have the ability to show four level lasers action associated with the transitions from  $^3\text{P}_0$  state in certain host systems and are potentially active ions for visible laser generation [19]. Generally laser action has been observed for  $^1\text{D}_2 \rightarrow ^3\text{H}_4$  transition in  $\text{Pr}^{3+}$  doped glasses [20,21]. These applications can either be enhanced or optimized from systematic study of optical properties of  $\text{Pr}^{3+}$  ions in various environments. In the present work, Zinc Alumino Bismuth Borate glasses were prepared by varying  $\text{Pr}^{3+}$  concentration to study the suitability of these glasses for solid state laser devices and optical fiber amplifiers.

## 2. Experimental techniques

The glass samples used in the present work were prepared by conventional melt quenching technique with the following compositions.

**Glass A:**  $20\text{ZnO} - 10\text{Al}_2\text{O}_3 - 9.9\text{Bi}_2\text{O}_3 - 60\text{B}_2\text{O}_3 - 0.1\text{Pr}_6\text{O}_{11}$

**Glass B:**  $20\text{ZnO} - 10\text{Al}_2\text{O}_3 - 9.7\text{Bi}_2\text{O}_3 - 60\text{B}_2\text{O}_3 - 0.3\text{Pr}_6\text{O}_{11}$

**Glass C:**  $20\text{ZnO} - 10\text{Al}_2\text{O}_3 - 9.5\text{Bi}_2\text{O}_3 - 60\text{B}_2\text{O}_3 - 0.5\text{Pr}_6\text{O}_{11}$

**Glass D:**  $20\text{ZnO} - 10\text{Al}_2\text{O}_3 - 9.0\text{Bi}_2\text{O}_3 - 60\text{B}_2\text{O}_3 - 1.0\text{Pr}_6\text{O}_{11}$

**Glass E:**  $20\text{ZnO} - 10\text{Al}_2\text{O}_3 - 8.0\text{Bi}_2\text{O}_3 - 60\text{B}_2\text{O}_3 - 2.0\text{Pr}_6\text{O}_{11}$

Analytical reagents ZnO,  $\text{Al}_2\text{O}_3$ ,  $\text{Bi}_2\text{O}_3$ ,  $\text{B}_2\text{O}_3$  and  $\text{Pr}_6\text{O}_{11}$  were used as starting materials. About 10gm of batch compositions were crushed in an agate mortar to obtain homogeneous mixture. The homogeneous mixture was then taken into an alumina crucible and heated to  $1200^\circ\text{C}$  for 50 min in an electric furnace. The melt was thoroughly shaken at 5 min interval in order to ensure homogeneity. These melts were quenched between two preheated brass plates to obtain glass samples of uniform thickness. The glass samples thus prepared were annealed at  $400^\circ\text{C}$  for 4 hrs to remove thermal strains. After annealing, they were polished before measuring their optical properties.

The refractive indices of glass samples were measured at  $\lambda=650\text{nm}$  (He-Ne Laser) by using Brewster's method with an accuracy  $\pm 0.01$ . By classical Archimedes principle, the densities were determined with water as an immersion liquid with an accuracy  $\pm 0.01$ . The optical absorption spectra of the glasses were recorded using a double beam Varian Cary 5E UV-Vis-NIR spectrophotometer in the wavelength range 400-2200nm with a spectral resolution of 0.1nm. The emission spectra for all these glasses were recorded at room temperature by exciting the samples with 445nm wavelength using Hitachi F-3010 fluorescence spectrophotometer.

### 3. Results and Discussion

#### 3.1 XRD Spectral analysis

In order to check the amorphous nature of the prepared glasses, the XRD spectral measurement were taken for an undoped glass using Bruker X-ray diffractometer (model D8 Advance) at 40 KV and 40 mA current and is shown in Fig 1. The XRD spectrum shows a broad hump which is the characteristic of an amorphous material. Hence the prepared ZnAlBiB glasses have amorphous nature.

### 3.2 Physical properties

From the estimated values of density and refractive index, various other physical properties were calculated by using the relevant expressions available in literature [22] and are given in Table 1. From Table 1 it is observed that, the trend of inter atomic distance in the prepared glasses show a decrease of the available volume per atom. This implies that the atoms are more tightly packed as the  $\text{Pr}^{3+}$  ion concentration increases in the glass. But from the increasing values of mean atomic volume, it is expected that the substitution of boron atoms by rare earth ions with bigger radii such as praseodymium would result in an expansion of the rigid glass structure [23]. Moreover, the dopant ions break the bonds on the network, promoting the formation of non-bridging oxygen, thus resulting in a loosely packed structure [24]. The low field strength value observed for the present glasses indicates the high solubility of rare earth ions in the glass. Increasing values of optical basicity are the representation of increasing the ability of a glass to donate negative charges to the probe ion. Molecular electronic polarizability is related to many macro and microscopic physical and chemical properties such as optical UV absorption, ionic refraction, dielectric properties and chemical stability. From Table 1, it is also observed that these glasses possess low molecular electronic polarizability which makes them more stable. The light gathering capacity of an optical fibre i.e., numerical aperture ( $NA$ ) for the present glasses has been calculated using an expression given in literature [25] and are given in Table 1. The



typical range of  $NA$  is 0.13 to 0.50. Since the glasses under investigation are having good  $NA$  value (0.26), they are quite suitable as core material for an optical fibre as they can gather more light from the source.

### 3.3 Absorption spectral analysis

The absorption spectra of rare earth ions serve as a basis for understanding their radiative properties. The sharp absorption lines arising from the 4f-4f electronic transitions can be electric dipole, magnetic dipole or electric quadrupole in character. The absorption spectra at different concentrations of  $\text{Pr}^{3+}$  doped  $\text{ZnAlBiB}$  glasses in UV-Vis-NIR regions is shown Fig 2. Seven bands were observed for all the glasses at 446, 469, 482, 587, 1421 1518 and 1919 nm and are assigned to the transitions  $^3\text{H}_4 \rightarrow ^3\text{P}_2$ ,  $^3\text{P}_1$ ,  $^3\text{P}_0$ ,  $^1\text{D}_2$ ,  $^3\text{F}_4$ ,  $^3\text{F}_3$  and  $^3\text{F}_2$  respectively. The identification and assignment of energy levels are made by those determined by Carnall et.al [26]. For the observed band positions, the bonding parameters ( $\beta^G$ ,  $\delta$ ) for all  $\text{Pr}^{3+}$  doped glasses have been calculated using the expressions given in our previous paper [22]. For the present glasses, the bonding parameter for all the glasses is negative ( $A = -0.7798$ ,  $B = -0.5370$ ,  $C = -0.5183$ ,  $D = -0.5158$ ,  $E = -0.5136$ ) i.e., the prepared glasses possess ionic nature and the ionic nature decreases gradually as the  $\text{Pr}^{3+}$  ion concentration increases.

As shown in Fig 2, the absorption spectra consists a group of three overlapping bands corresponding to  $^3\text{H}_4 \rightarrow ^3\text{P}_{2,1,0}$  transitions in violet to blue regions, an isolated band corresponding to  $^3\text{H}_4 \rightarrow ^1\text{D}_2$  transition in the visible region and also three intense bands in the near infrared region associated to  $^3\text{H}_4 \rightarrow ^3\text{F}_{4,3,2}$  transitions. Among all these transitions, the transition  $^3\text{H}_4 \rightarrow ^3\text{P}_2$  is a hypersensitive transition and the position and intensities of the hypersensitive transitions are largely dependent on the local environment of the rare earth ion and in turn affects the magnitude of intensity parameters. From Fig 2 it is observed that, the peak wavelength of the hypersensitive transition shifts towards the shorter wavelength (449nm, 448nm, 447nm, 445nm and 444nm) with the increase of  $\text{Pr}^{3+}$  ion concentration. This shift is mainly because of nephelauxetic effect [27] which indicates that the degree of covalency of R-O bond decreases with increase of  $\text{Pr}^{3+}$

ion concentration. Hypersensitive transitions are governed by the selection rules  $|\Delta S|=0$ ,  $|\Delta L|\leq 2$ ,  $|\Delta J|\leq 2$  [28].

The experimental oscillator strengths ( $f_{exp}$ ) are determined by using the following expression and are given in Table 2.

$$f_{exp} = \frac{2.303mc^2}{N\pi e^2} \int \varepsilon(\vartheta) d\vartheta \quad \text{----- (1)}$$

m and e are mass and charge of an electron, c is the velocity of light, N is the Avogadro's number and  $\varepsilon(\vartheta)$  is the molar absorptivity of a band at a wave number  $\vartheta$  ( $\text{cm}^{-1}$ ). Using the experimental oscillator strengths ( $f_{exp}$ ), the host dependent JO intensity parameters ( $\Omega_2$ ,  $\Omega_4$  and  $\Omega_6$ ) and calculated oscillator strengths ( $f_{cal}$ ) for observed electric dipole transitions within the  $4f^2$  configuration have been determined using the following expression by least square fit procedure and are given in Table 2.

$$f_{cal} = \left[ \frac{8\pi^2 m c v}{3h(2J+1)} \right] \left[ \frac{(n^2+1)^2}{9n} \right] \sum_{\lambda=2,4,6} \Omega_{\lambda} (\psi_J \| U^{\lambda} \| \psi'_J)^2 \quad \text{----- (2)}$$

v is the wave number ( $\text{cm}^{-1}$ ) of the transition from ground state ( $\psi_J$ ) to excited state ( $\psi'_J$ ), c is the velocity of light in vacuum; m is the rest mass of an electron and  $\|U^{\lambda}\|^2$  doubly reduced matrix elements. The doubly reduced matrix elements were taken from the literature as they are insensitive to the environment of rare earth ions. The specific features of JO parameters may be distributed by the contributions of the phonon subsystem [29]. The quality of the fit is measured by root mean square deviation ( $\delta_{rms}$ ) between the experimental and calculated oscillator strengths by using the following expression and is given in Table 2.

$$\delta_{rms} = \left[ \frac{\sum (f_{exp} - f_{cal})^2}{p} \right]^{1/2} \quad \text{----- (3)}$$

p is the total number of energy levels included in the fitting procedure.

From Table 2 it is observed that, the evaluated values of root mean square deviation ( $\delta_{rms}$ ) are showing reasonably better agreement when the hypersensitive transition  $^3\text{H}_4 \rightarrow ^3\text{P}_2$  is excluded in the least square fit. However, there is no significant improvement observed in  $f_{cal}$  values by

including and excluding the hypersensitive transition  $^3\text{H}_4 \rightarrow ^3\text{P}_2$ . The JO intensity parameters have been calculated by including and excluding the hypersensitive transition  $^3\text{H}_4 \rightarrow ^3\text{P}_2$  and are given in Table 3 along with the values reported in the literature [30-37]. From Table 3, it is observed that the JO intensity parameters slightly increase when the hypersensitive transition  $^3\text{H}_4 \rightarrow ^3\text{P}_2$  is excluded keeping the JO parameters order same ( $\Omega_2 \square \Omega_6 \square \Omega_4$ ). The JO intensity parameter  $\Omega_2$  increases with the increase of concentration of  $\text{Pr}^{3+}$  from Glass A to Glass D and then decreases for Glass E. The  $\Omega_2$  parameter is higher for the present glasses in comparison to ZBP3, ZBP4, ZBP5, Phosphate, MgTP, LBTAF, oxy-fluoride, ZBLAN, and mixed halides and SASP [30-37]. The larger magnitude of  $\Omega_2$  observed for all glasses suggests that, the bonding of  $\text{Pr}^{3+}$  ions with the ligands is covalent in nature and the rare earth ion sites are having lower asymmetry in these host glasses. This indicates that the symmetry and covalency of  $\text{Pr}^{3+}$  doped ZnAlBiB glasses are stronger than those above mentioned glasses. Reisfeld and Jorgenson stated that [38] the magnitudes of  $\Omega_4$  and  $\Omega_6$  parameters are related to the bulk properties such as viscosity and rigidity of the medium in which the ions are situated. The intensity parameter  $\Omega_6$  is related to covalence of R-O bond increases with the increase in concentration of  $\text{Pr}^{3+}$  ions in ZnAlBiB glasses. This suggests that the covalence of the R-O bond increases with the increase of  $\text{Pr}^{3+}$  concentration which may be due to the tightening of structure with the formation of  $\text{BO}_4$  groups [39]. The ratio of ( $\Omega_4/\Omega_6$ ) parameters known as spectroscopic quality factor ( $\chi$ ) is used to predict the stimulated emission in a laser active medium [40]. The host materials with larger values of spectroscopic quality factors ( $\chi$ ) can have more potential stimulated emission. From Table 3 it is observed that, among all the prepared glasses, glass D (1 mol%  $\text{Pr}^{3+}$  doped ZnAlBiB Glass) possess highest spectroscopic quality factor ( $\chi$ ).

### 3.4 Emission spectra and Radiative properties

To analyse the emission spectra for the prepared glasses, it is necessary to know the excitation wavelengths of  $\text{Pr}^{3+}$  ions. For this purpose, we have recorded excitation spectra of  $\text{Pr}^{3+}$  doped ZnAlBiB glasses by fixing the emission at 607nm as shown in Fig 3. The excitation spectra recorded from 430-500 nm gives three emission bands at wavelengths approximately 445, 470 and 485 nm corresponding to the transitions  $^3\text{H}_4 \rightarrow ^3\text{P}_2$ ,  $^3\text{P}_1$  and  $^3\text{P}_0$  respectively. It is well known that the wavelength corresponding to the intense excitation band can give intense emissions. Among all the excitation bands, a band corresponding to the transition  $^3\text{H}_4 \rightarrow ^3\text{P}_2$  (445nm) is more intense and is used as an excitation wavelength to record the emission spectra for all the glasses under investigation. The room temperature emission spectra of different concentrations of  $\text{Pr}^{3+}$  doped ZnAlBiB glasses are shown in Fig 4. After excitation into the  $^3\text{P}_2$  excited level, appreciable radiative emissions took place from  $^3\text{P}_1$ ,  $^1\text{D}_2$  meta-stable levels. From Fig 4 it is observed that, the emission spectra of all the five glasses are found to be almost identical and show three emission lines at 530, 604 and 646 nm corresponding to  $^3\text{P}_1 \rightarrow ^3\text{H}_5$ ,  $^1\text{D}_2 \rightarrow ^3\text{H}_4$  and  $^3\text{P}_1 \rightarrow ^3\text{F}_3$  transitions respectively. Among all these transitions, the transition  $^1\text{D}_2 \rightarrow ^3\text{H}_4$  exhibits bright reddish-orange emission at 604nm and other two transitions  $^3\text{P}_1 \rightarrow ^3\text{H}_5$ ,  $^3\text{P}_1 \rightarrow ^3\text{F}_3$  are feeble. From Fig 4 it can be observed that emission quenching has been occurred at 1 mol% for all the peaks. Fig 5 shows the energy level diagram depicting the various lasing transitions of 1 mol% of  $\text{Pr}^{3+}$  ion in ZnAlBiB glass.

In order to predict the emission performance of  $\text{Pr}^{3+}$  doped ZnAlBiB glasses, the radiative parameters such as spontaneous transition probabilities ( $A_R$ ), total transition probabilities ( $A_T$ ), radiative lifetimes ( $\tau_R$ ) and luminescence branching ratios ( $\beta_R$ ) for all the emission transitions have been evaluated by using the JO parameters obtained from the absorption spectral measurements and are given in Table 4. In treating the fluorescence process, the radiative

transition probabilities ( $A_R$ ) for emission transitions can be evaluated by using the following expression [41]

$$A_R(a_J, b_{J'}) = \frac{64\pi^4 g}{3h(2J+1)} \left[ \frac{n(n^2+2)}{9} S_{ed}(a_J, b_{J'}) + n^3 S_{md}(a_J, b_{J'}) \right] \text{----- (4)}$$

The total transition probabilities ( $A_T$ ) for the emission transitions can be evaluated by using the following expression [41]

$$A_T = \sum_{b_{J'}} A_R(a_J, b_{J'}) \text{----- (5)}$$

The radiative lifetimes  $\tau_R(a_J, b_{J'})$  and the fluorescence branching ratios  $\beta_R(a_J, b_{J'})$  from an initial state  $a_J$  to a final state  $b_{J'}$  are [41]

$$\tau_R(a_J, b_{J'}) = \frac{1}{\sum_{b_{J'}} A_R(a_J, b_{J'})} \text{----- (6)}$$

$$\beta_R(a_J, b_{J'}) = A_R(a_J, b_{J'}) \cdot \tau_R(a_J, b_{J'}) \text{----- (7)}$$

The stimulated emission cross-section ( $\sigma_{se}$ ) is an important parameter and its value signifies the rate of energy extraction from the optical material. From the observed emission bands  $\sigma_{se}$  can be estimated by the following expression [41].

$$\sigma_{se}(a_J, b_{J'}) = \frac{\lambda_p^4}{8\pi c n^2 \Delta\lambda_p} A_R(a_J, b_{J'}) \text{----- (8)}$$

$\lambda_p$  is the emission peak wavelength and  $\Delta\lambda_p$  is the full width at half maximum which can be calculated by integrating the intensity at the peak wavelength [42].

Out of these parameters, the important parameters of interest for a laser designer are  $\Delta\lambda_p$ ,  $\sigma_{se}$ , gain band widths ( $\sigma_{se} \times \Delta\lambda_p$ ) and optical gain parameters ( $\sigma_{se} \times \tau_R$ ). Table 4 presents the various radiative parameters for  $^3P_1 \rightarrow ^3H_5$ ,  $^1D_2 \rightarrow ^3H_4$ ,  $^3P_1 \rightarrow ^3F_3$  emissions for different concentrations of  $Pr^{3+}$  doped ZnAlBiB glasses (glass A to E). The emission transitions with higher magnitude of  $\beta_R$  are more important for laser action originating from a given excited state. From Table 4 it is

observed that the  $\beta_R$  value of  $^1D_2 \rightarrow ^3H_4$  emission band decreases with the increase of  $Pr^{3+}$  concentration up to 0.5mol% and increases for 1mol% and again decreases for 2mol% of  $Pr^{3+}$  doped ZnAlBiB glasses. This may be due to the fluorescence quenching of  $^1D_2 \rightarrow ^3H_4$  emission. From Table 4 it is also observed that glass D possesses highest branching ratios ( $\beta_R$ ) which is an important parameter to decide the laser action. These  $\beta_R$  are in good agreement with the  $\beta_{exp}$  values. The large stimulated emission cross-sections ( $\sigma_{se}$ ) of a luminescence transition are one of the important parameter used to predict a laser active medium. From Table 5 it is observed that, the emission cross-section ( $\sigma_{se}$ ) is maximum for glass D for all the transitions. This stimulated emission cross-section is maximum for  $^3P_1 \rightarrow ^3H_5$ ,  $^3P_1 \rightarrow ^3F_3$  transitions and minimum for  $^1D_2 \rightarrow ^3H_4$  transition. This may be due to the variation of inhomogeneous line widths of the transitions. Hence among all the glasses glass D is suitable for laser host material.

The gain parameters ( $\sigma_{se} \times \tau_R$ ) are used to obtain a laser host material with the highest stability [43] and a glassy material doped with rare earth can act as a good optical fibre if the gain band width ( $\sigma_{se} \times \Delta\lambda_p$ ) and optical gain ( $\sigma_{se} \times \tau_R$ ) are having higher values. From Table 5 it is observed that glass D possesses highest gain band width ( $\sigma_{se} \times \Delta\lambda_p$ ) and optical gain ( $\sigma_{se} \times \tau_R$ ) for all the transitions. Hence glass D i.e. 1 mol% of  $Pr^{3+}$  doped ZnAlBiB glass can be recommended as a good host that can emit bright reddish-orange laser at 604nm and is suitable for optical amplification also.

### 3.5 CIE Chromaticity co-ordinates

The chromaticity co-ordinate values of  $Pr^{3+}$  doped ZnAlBiB glasses have been calculated from the fluorescence spectra using the Commission International de l'Eclairage France CIE system [44, 45] and are presented in Table 6. Fig 6 represents the CIE plot with colour co-ordinates calculated from the emission spectra for 1mol% of  $Pr^{3+}$  in ZnAlBiB glass (glass D) excited at 445nm wavelength. The emission spectra contain three parts. The first part is greenish to yellow, second part is orange to red and the third part is red. The CIE colour co-ordinates for all the samples were found to be in the orange red to red regions. Among all the glass samples, particularly glass D colour co-ordinates ( $x=0.6277$ ,  $y=0.3720$ ) falls in the bright reddish-orange region corresponding to  $^1D_2 \rightarrow ^3H_4$  transition. Hence glass D is suitable as a good host to give bright reddish-orange colour laser at 613 nm.

## Conclusion

Zinc Alumino Bismuth Borate (ZnAlBiB) glasses doped with different concentrations of  $\text{Pr}^{3+}$  ions were prepared using conventional melt quenching technique. The amorphous nature of these glasses has been confirmed by measuring an XRD spectrum. The bonding parameters measured from the absorption spectra confirms the ionic nature which decreases gradually with increase in  $\text{Pr}^{3+}$  concentration in these glasses. Shifting of peak wavelength of the hypersensitive transition towards the shorter wavelength in these glasses indicates the decrease in the degree of covalency of R-O bond with increase in  $\text{Pr}^{3+}$  ion concentration. From the absorption spectra of  $\text{Pr}^{3+}$  ions in ZnAlBiB glasses, the radiative properties such as transition probability, radiative lifetime and branching ratios are evaluated using Judd-Ofelt theory. The emission spectra recorded at different concentrations of  $\text{Pr}^{3+}$  ions show three emission bands one in yellow region ( $^3\text{P}_1 \rightarrow ^3\text{H}_5$ ), the second one in reddish-orange region ( $^1\text{D}_2 \rightarrow ^3\text{H}_4$ ) and the third one in red region ( $^3\text{P}_1 \rightarrow ^3\text{H}_5$ ). Among the three emission transitions observed,  $^1\text{D}_2 \rightarrow ^3\text{H}_4$  is more intense and is falling in reddish-orange region. Based on visible emission spectra, the high stimulated emission cross-section and branching ratios observed for  $^1\text{D}_2 \rightarrow ^3\text{H}_4$  transition for all these glasses suggest the feasibility of using these materials as lasers in reddish-orange visible region. The CIE chromaticity co-ordinates were also evaluated from the emission spectra for all the glasses by exciting them at 445nm to understand the feasibility of using of these materials for reddish-orange emission. From the measured emission cross-sections and CIE chromaticity co-ordinates, it was found that 1 mol% of  $\text{Pr}^{3+}$  (glass D) is aptly suitable for the development of visible reddish-orange lasers in principle from these ZnAlBiB glasses.

## Acknowledgements



One of the authors Mahamuda Shaik is very much thankful to Department of Science and Technology (DST), Government of India, New Delhi for awarding her with a Women Scientist's scheme under DST – WOS (A) programme (File No: SR/WOS-A/PS-53/2011).

## References

- [1] K.S.V.Sudhakar, M.Srinivasa Reddy, L.Srinivasa Rao, N.Veeraiah, J.Lumin.128 (2008) 1791-1798.
- [2] S.S.Sundari, K.Marimuthu, M.Sivraman, S.S.Babu, J.Lumin.130 (2010) 1313-1319.
- [3] Y.G. Choi, J.Heo, J.Non-Cryst.Solids 217 (1997)199-207.
- [4] N.Soga, K.Hauro, M.Yoshimoto, H.Yamamoto, J.Appl.Phys. 63 (1988) 4451-4454.
- [5] S.M.Kaczmarek, Opt.Mater. 19 (2002) 189-194.
- [6] T.Satyanarayana, M.G.Brik, N.Venkatramaiah, I.V.Kityk, K.J.Plucinski, V.Ravikumar, N.Veeraiah, J.Am.Ceram.Soc., 93(7) (2010) 2004-2011.
- [7] S.Sanghi, S.Duhan, A.Agarwal, P.Aghamkar, J.Alloy.Comp. 488 (2009) 454-458.
- [8] H. Yamasaki, K. Minato, D. Nezaki, T. Okamoto , A. Kawamoto,M. takata, Solid State Ionic 172 (2004) 349-352.
- [9] Y. I. Alivov, D.C Look , B.M. Ataev , M.V. Chukichev, V.V. Mamedov, V.I. Zineko, Y. A. Agafonov, A. N. Pustovit, Solid State Electron. 48 (2004) 2343-2346.

- [10] N. Saito , H. Haned , T. Skiguchi , N. Ohashi , I. Sakaguchi , K. Koumoto, Adv. Mater. 14 (2002) 418-421.
- [11] J. Ferber, J. Luther, Phys. Chem. B 105 (21) (2001) 4895-4903.
- [12] B.L. Zhu, C.S. Xie, D.W. Zeng, W.L. Song, A.H. Wang, Mater. Chem. Phys. 89 (1) (2005) 148-153.
- [13] Z.G.Nie, J.H.Zhang, X.Zhang, X.G.Ren, W.H.Di, G.B.Zhang, X.J.Wang, J.Phys.Condens.Matter 19 (2007) 076204.
- [14] S.Kuck, I.Sokolska, J.Phys.Condens.Matter 18(2006)5447-5458.
- [15] Z.G.Nie, J.H.Zhang, X.Zhang, X.G.Ren, Opt. Lett. 32 (2007) 991-993.
- [16] S.Kuck, I.Sokolska, Appl.Phys.A 77 (2003) 469-474.
- [17] K.Wei, D.P.machewirth, J.Wenzel, E.Snitzer, G.H.Sigel Jr., J.Non-Cryst.Solids 182 (1995)257-261.
- [18] G.Lakshminarayana, R.Vidya Sagar, S.Buddhudu, Physica B 403 (2008) 81-86.
- [19] K.Annapurna, R.Chakrabarthy, S.Buddhudu, J.Mater.Sci 42(2007)6755-6761.
- [20] F.Varsanyi, Appl.Phys.Lett. 19(1971)169-171.
- [21] J.Hegarty, D.L.Huber, W.M.Yen, Phys.Rev.B 25 (1982) 5638-5645.
- [22] A.S. Rao, Y.N. Ahammed, R.R. Reddy, T.V.R. Rao, Opt. Mater. 10 (1998) 245-252.
- [23] M.Subhadra, P.Kishtaiah, Physica B 406 (2011) 1501-1505.
- [24] Y.B.Saddek, L.A.E.Latif, Physica B, 348 (2004) 475-484.
- [25] G.Fuxi, Optical properties of glasses, Springer, Berlin, 1992.
- [26] W.T.Carnall, P.R.Fields, K.Rajnak, J.Chem.Phys. 49 (1968) 4424-4442.
- [27] M.B.Saisudha, J.Ramakrishna, Phys.Rev.B 53(1996)6186-6196.
- [28] S.Tanabe, T.Ohyagi, N.Soga, T.Hanada, Phys.Rev.B 46(1992)3305-3310.

- [29] A.Brenier, I.V.Kityk, J.Appl.Phys. 90 (2001) 232-236.
- [30] Inderpal, Ashish Agarwal, Sujata Sanghi, M.P.Aggarwal, J.Alloy.Comp. 509 (2011) 7625-7631.
- [31] Z.Mazurak, S.Bodyl, R.Lisiecki, J.Gabrys-Pisarska, M.Czaja, Opt.Mat. 32 (2010)547-553.
- [32] D.V.R.Murthy, B.C.Jamalaiah, T.Sasi Kala, L.Rama Moorthy, M.Jaya Simhadri, Kiwan Jang, Ho Sueb Lee, Soung Soo Yi, Jung Hyun Jeong, Physica B 405 (2010)1095-1100
- [33] B.C.Jamalaiah, J.Suresh Kumar, A.Mohan Babu, L.Rama Moorthy, Kiwan Jang, Ho Sueb Lee, M.Jaya Simhadri, Jung Hyun Jeong, Hyukjoon Choi, J.Lumin. 129(2009) 1023-1028.
- [34] R.T.Genova, I.R.Martin, U.R.R.Mendoza, F.Lahoz, A.D.L.Garrin, P.Nunez, J.G.Platas, V.Lavin, J.Alloys.Comp. 380(2004) 167-172.
- [35] D.R.Simons, A.J.Faber, H.De Wall, Opt.Lett. 20 (1995) 468-470.
- [36] M.A.Newhouse, R.F.Bartholomev, B.G.Aitken, L.J.Button, N.F.Borrelli, IEEE Photonic. Technol.Lett.6(1994)189-191.
- [37] S V J Lakhsman and A.Suresh Kumar J.Phys.Chem.Solids 49(1988) 807-811
- [38] S.Jiang, T.Luo, B.Hwang, F.Smekatala, K.Seneschal, J.Lucas, N.Phyghambarian, J.Non-Cryst. Solids 240 (1998)66-78.
- [39] K.Binnemans, R.Van Deun, C.Groller-Walrand, J.L.Adam, J.Non-Cryst. Solids 238 (1998) 11-29.
- [40] A.A.Kaminiskii, Laser Crystals, Springer, Berlin, 1990.
- [41] D.V.R.Murthy, B.C.Jamalaiah, T.Sasikala, L.Rama Moorthy, M.Jaya Simhadri, Kiwan Jang, Ho Sueb Lee, Soung Soo Yi, Jung Hyun Jeong, Physica B 405 (2010) 1095-1100.

- [42] B.Karthikeyan, S.Mohan, M.L.Baesso, Physica B 337(2003)249-254.
- [43] M. Liao, Z. Duan, L. Hu, Y. Fang, L. Wen, J. Lumin. 126 (2007) 139-144.
- [44] W.M.Yen, S.Shionoya, Phosphor Hand Book, CRC Press, New York, 1999, P.805.
- [45] F.W.Billmeyer, M.Saltzman Jr., Principles of color technology, Wiley, New York, 1981.

Accepted manuscript

**Table 1:**Various physical properties of  $\text{Pr}^{3+}$  doped ZnAlBiB glasses

Physical properties	Glass A	Glass B	Glass C	Glass D	Glass E
Refractive index, $n_d$	1.804	1.803	1.802	1.801	1.800
Density, $d$ (gm/cm <sup>3</sup> )	3.7719	3.7679	3.7639	3.7538	3.7336
Average molecular weight, $\bar{M}$ (g)	207.16	208.27	209.38	212.16	217.71
$\text{Pr}^{3+}$ ion concentration, $N$ ( $10^{21}$ ions/cm <sup>3</sup> )	1.0964	3.2700	5.4100	10.700	20.700
Mean atomic volume (g/cm <sup>3</sup> /atom)	12.314	12.393	12.472	12.672	13.074
Dielectric constant, $\epsilon$	3.2544	3.2508	3.2472	3.2436	3.2400
Optical dielectric constant	2.2544	2.2508	2.2472	2.2436	2.2400
Reflection losses, $R$ (%)	0.0822	0.0820	0.0819	0.0817	0.0816
Molar refraction, $R_m$ (cm <sup>-3</sup> )	23.564	23.694	23.823	24.182	24.926
Polaron radius, $R_p$ (Å)	1.8750	1.3000	1.1000	0.8790	0.7050
Interionic distance, $R_i$ (Å)	4.6524	3.2300	2.7300	2.1800	1.7500
Molecular electronic polarizability, $\alpha$ ( $10^{-23}$ cm <sup>3</sup> )	9.3464	3.1300	1.8900	0.9590	0.4940
Field strength, $F$ ( $10^{15}$ cm <sup>-2</sup> )	0.8533	1.7700	2.4700	3.8800	6.0300
Optical basicity, $\phi_{th}$	0.4400	0.4450	0.4490	0.4600	0.4770
Numerical aperture, $NA$	0.2550	0.2549	0.2548	0.2546	0.2545

**Table 2:**

Assignment of absorption bands, experimental oscillator strengths ( $f_{\text{exp}}$ )( $10^{-6}$ ), calculated oscillator strengths ( $f_{\text{cal}}$ )( $10^{-6}$ ) and  $\delta_{\text{rms}}$  deviations obtained by including and excluding the  $^3\text{H}_4 \rightarrow ^3\text{P}_2$  hypersensitive transition in  $\text{Pr}^{3+}$  doped  $\text{ZnAlBiB}$  glasses.

Transi tion	Ener gy ( $\text{cm}^{-1}$ )	Glass A			Glass B			Glass C			Glass D			Glass E		
		$f_{\text{ex}}$ p	$f_{\text{cal}}$	$f$ * cal	$f_{\text{ex}}$ p	$f_{\text{cal}}$	$f$ * cal	$f_{\text{ex}}$ p	$f_{\text{cal}}$	$f$ * cal	$f_{\text{ex}}$ p	$f_{\text{cal}}$	$f$ * cal	$f_{\text{ex}}$ p	$f_{\text{cal}}$	$f$ * cal
$^3\text{P}_2$	2240	3.	2.	-	3.	1.	-	4.	2.	-	7.	3.	-	5.	3.	-
	5	51	20		65	89		92	40		93	45		95	61	
$^3\text{P}_1$	2124	1.	0.	0.8	2.	1.	1.6	2.	1.	1.1	4.	3.	3.3	3.	2.	2.1
	1	42	87	9	04	67	9	51	15	7	89	28	2	74	09	2
$^3\text{P}_0$	2071	2.	0.	0.8	2.	1.	1.6	2.	1.	1.1	4.	3.	3.2	3.	2.	2.0
	5	19	86	8	99	65	7	02	14	6	20	21	7	60	06	9
$^1\text{D}_2$	1707	1.	0.	0.6	1.	0.	0.6	2.	0.	0.7	2.	1.	1.0	2.	1.	1.1
	0	07	69	8	26	61	0	63	78	7	94	12	8	04	14	2
$^3\text{F}_4$	7005	3.	2.	2.4	2.	1.	1.9	3.	2.	2.6	4.	3.	3.4	4.	3.	3.8
		04	46	2	49	99	3	35	70	5	23	57	3	86	90	3
$^3\text{F}_3$	6575	3.	3.	3.8	3.	3.	3.6	4.	4.	4.5	6.	6.	6.6	5.	6.	6.5
		47	92	8	27	71	4	02	58	3	09	83	6	88	66	8
$^3\text{F}_2$	5198	2.	2.	2.9	3.	3.	3.5	4.	4.	4.8	6.	6.	6.4	5.	5.	5.5
		98	94	5	56	52	3	82	88	7	47	41	3	63	57	8
$\delta_{\text{rms}}$		$\pm 0.7$		$\pm 0.$	$\pm 0.9$		$\pm 0.$	$\pm 1.1$		$\pm 1.$	$\pm 1.9$		$\pm 1.$	$\pm 1.3$		$\pm 1.$
( $10^{-6}$ )				6*			6*			0*			1*			1*

\* Values when hypersensitive transition  $^3\text{H}_4 \rightarrow ^3\text{P}_2$  is excluded in the fit

**Table 3:**

Comparison of JO parameters of ZnAlBiB glasses with the values reported for various Pr<sup>3+</sup> doped hosts.

System	$\Omega_2$	$\Omega_4$	$\Omega_6$	$\chi = \Omega_4 / \Omega_6$	Trend	Reference
Glass A	3.73	1.17	3.23	0.36	$\Omega_2 > \Omega_6 > \Omega_4$	Present work
Glass A*	3.74	1.20	3.16	0.37	$\Omega_2 > \Omega_6 > \Omega_4$	Present work
Glass B	4.13	2.24	3.33	0.92	$\Omega_2 > \Omega_6 > \Omega_4$	Present work
Glass B*	4.14	2.27	3.35	0.96	$\Omega_2 > \Omega_6 > \Omega_4$	Present work
Glass C	6.98	1.55	3.45	0.44	$\Omega_2 > \Omega_6 > \Omega_4$	Present work
Glass C*	6.99	1.58	3.37	0.46	$\Omega_2 > \Omega_6 > \Omega_4$	Present work
Glass D	7.33	4.39	4.39	1.00	$\Omega_2 > \Omega_6 > \Omega_4$	Present work
Glass D*	7.36	4.46	4.17	1.06	$\Omega_2 > \Omega_6 > \Omega_4$	Present work
Glass E	6.92	2.81	5.04	0.55	$\Omega_2 > \Omega_6 > \Omega_4$	Present work
Glass E*	6.93	2.85	4.93	0.57	$\Omega_2 > \Omega_6 > \Omega_4$	Present work
ZBP3	2.89	2.04	1.99	1.02	$\Omega_2 > \Omega_6 > \Omega_4$	[30]
ZBP4	3.23	1.88	2.03	0.92	$\Omega_2 > \Omega_6 > \Omega_4$	[30]
ZBP5	3.94	1.34	1.99	0.67	$\Omega_2 > \Omega_6 > \Omega_4$	[30]
Phosphate	4.19	4.29	6.40	0.67	$\Omega_6 > \Omega_4 > \Omega_2$	[31]



MgTP	2.69	11.8	8.39	1.40	$\Omega_4 > \Omega_6 > \Omega_2$	[32]
LBTAF	2.42	2.54	4.23	0.60	$\Omega_6 > \Omega_4 > \Omega_2$	[33]
Oxy-fluoride	0.13	4.09	6.33	0.64	$\Omega_6 > \Omega_4 > \Omega_2$	[34]
ZBLAN	2.9	6.40	5.50	1.16	$\Omega_4 > \Omega_6 > \Omega_2$	[35]
Mixed hallide	2.70	4.40	5.40	0.81	$\Omega_6 > \Omega_4 > \Omega_2$	[36]
SASP	12.0	2.1	8.5	0.24	$\Omega_2 > \Omega_6 > \Omega_4$	[37]

\*Values when hypersensitive transition  $^3H_4 \rightarrow ^3P_2$  is excluded in the fitting

**Table 4:**

Transition probabilities ( $A_R$ ) ( $s^{-1}$ ), measured and experimental branching ratios ( $\beta_R$  &  $\beta_{exp}$ ), radiative lifetimes ( $\tau_R$ ) ( $\mu s$ ) and total transition probability ( $A_T$ ) ( $s^{-1}$ ) for the observed emission transitions of  $Pr^{3+}$  doped ZnAlBiB glasses

Transition	$A_R$	$\beta_R$	$\beta_{exp}$	$\tau_R$	$A_T$
<b>Glass A</b>					
$^3P_1 \rightarrow ^3H_5$	5958	0.2097	0.0878	35	28406
$^1D_2 \rightarrow ^3H_4$	809	0.2218	0.2840	274	606
$^3P_1 \rightarrow ^3F_3$	10135	0.3568	0.0285	35	28406
<b>Glass B</b>					
$^3P_1 \rightarrow ^3H_5$	8168	0.2267	0.1140	27	36026
$^1D_2 \rightarrow ^3H_4$	711	0.1754	0.3440	246	4058
$^3P_1 \rightarrow ^3F_3$	12006	0.3333	0.1404	27	36026
<b>Glass C</b>					
$^3P_1 \rightarrow ^3H_5$	7143	0.1617	0.1492	22	44184
$^1D_2 \rightarrow ^3H_4$	903	0.1529	0.4580	169	5908
$^3P_1 \rightarrow ^3F_3$	18367	0.4157	0.1760	22	44184
<b>Glass D</b>					
$^3P_1 \rightarrow ^3H_5$	15607	0.2341	0.3750	15	66665

$^1D_2 \rightarrow ^3H_4$	1290	0.2764	0.5330	136	1017
$^3P_1 \rightarrow ^3F_3$	21584	0.4238	0.2660	15	66665
<b>Glass E</b>					
$^3P_1 \rightarrow ^3H_5$	11871	0.2157	0.2700	18	55036
$^1D_2 \rightarrow ^3H_4$	1331	0.1995	0.3540	149	6675
$^3P_1 \rightarrow ^3F_3$	19169	0.3483	0.1740	18	55036

**Table 5:**

Emission peak wavelength ( $\lambda_p$ )(nm), effective band widths ( $\Delta\lambda_p$ )(nm), stimulated emission cross-sections ( $\sigma_{se}$ ) ( $10^{-20}$ ) ( $cm^2$ ), gain band width( $\sigma_{se} \times \Delta\lambda_p$ ) ( $10^{-26}$ ) ( $cm^3$ ) and optical gain parameters ( $\sigma_{se} \times \tau_R$ ) ( $10^{-25}$ ) ( $cm^2 s$ ) for the emission transitions of  $Pr^{3+}$  doped ZnAlBiB glasses.

Spectral parameters	Glass A	Glass B	Glass C	Glass D	Glass E
$^3P_1 \rightarrow ^3H_5$					
$\lambda_p$	530	530	530	531	530
$\Delta\lambda_p$	24.5	23.6	22.7	16.4	17.3
$\sigma_{se}$	0.78	11.1	13.6	30.7	11.7
$\sigma_{se} \times \Delta\lambda_p$	1.92	2.63	2.95	5.04	2.03
$\sigma_{se} \times \tau_R$	2.74	29.9	30.1	46.1	21.1
$^1D_2 \rightarrow ^3H_4$					
$\lambda_p$	603	602	607	613	613
$\Delta\lambda_p$	28.2	26.4	24.5	22.7	27.3
$\sigma_{se}$	1.55	1.45	1.99	3.08	2.64
$\sigma_{se} \times \Delta\lambda_p$	0.43	0.38	0.48	0.69	0.72
$\sigma_{se} \times \tau_R$	42.4	35.8	33.7	41.8	37.8
$^3P_1 \rightarrow ^3F_3$					
$\lambda_p$	647	649	645	647	647

$\Delta\lambda_p$	10.08	8.18	7.27	5.45	6.37
$\sigma_{se}$	7.24	10.5	18.1	28.4	21.6
$\sigma_{se} \times \Delta\lambda_p$	7.24	8.59	13.2	15.5	13.8
$\sigma_{se} \times \tau_R$	25.3	28.3	39.8	42.6	38.9

**Table 6:**

The color co-ordinates of  $\text{Pr}^{3+}$  doped ZnAlBiB glasses.

Glass	CIE Co-ordinates	
	X- Co-ordinate	Y- Co-ordinate
A	0.5646	0.4097
B	0.5649	0.4347
C	0.5818	0.4178
D	0.6277	0.3720
E	0.5078	0.4823

### Figure captions

Fig 1. XRD spectrum for undoped ZnAlBiB glass

Fig 2. Absorption spectra of  $\text{Pr}^{3+}$  doped ZnAlBiB glasses

Fig 3. Excitation spectra of  $\text{Pr}^{3+}$  doped ZnAlBiB glass showing three excitation bands at 445, 470 and 485nm from the monitoring of red emission ( $^3\text{P}_0 \rightarrow ^3\text{H}_6$ ) at 607nm

Fig 4. Fluorescence spectra of  $\text{Pr}^{3+}$  doped ZnAlBiB glasses

Fig 5. Energy level diagram depicting the various lasing transitions of 1 mol% of  $\text{Pr}^{3+}$  ion in ZnAlBiB glass

Fig 6. CIE 1931 chromaticity diagram for 1 mol% of  $\text{Pr}^{3+}$  doped ZnAlBiB glass (glass D)

**Figures**

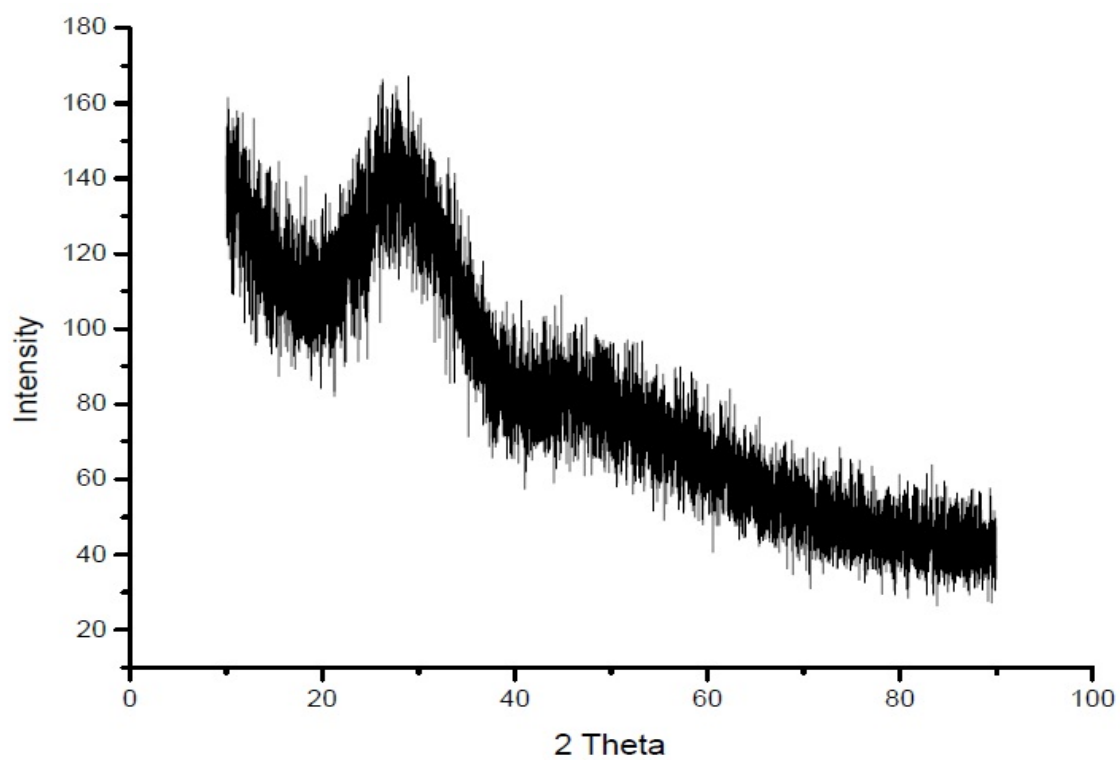


Fig 1

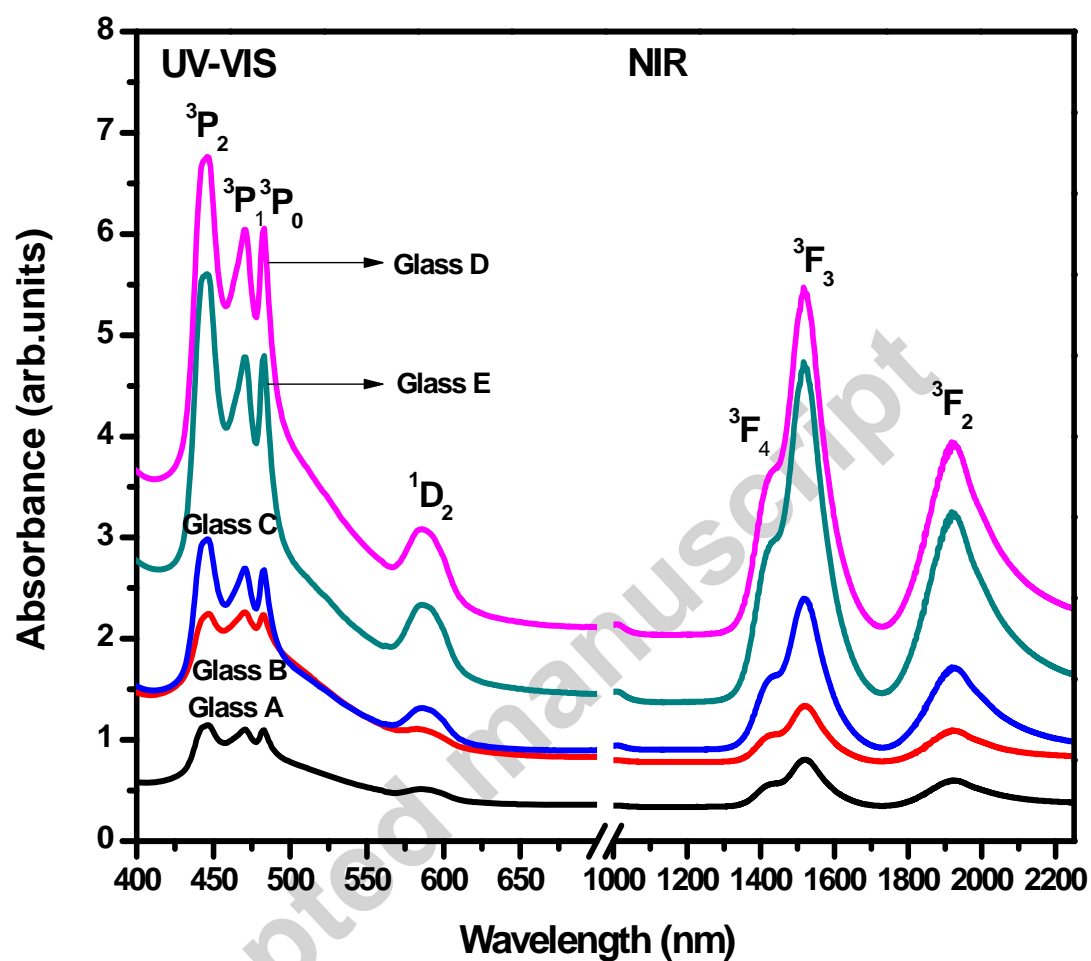


Fig 2

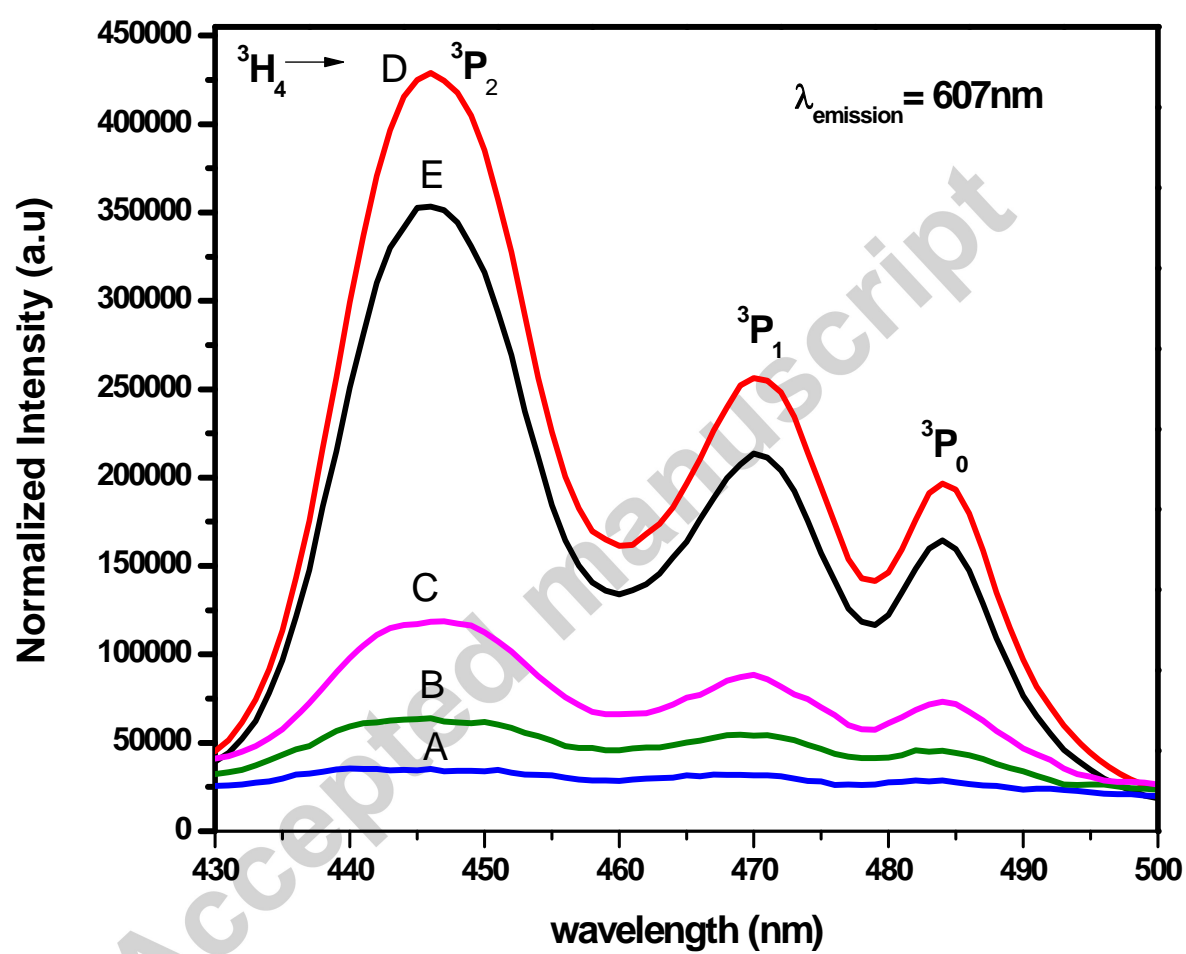


Fig 3



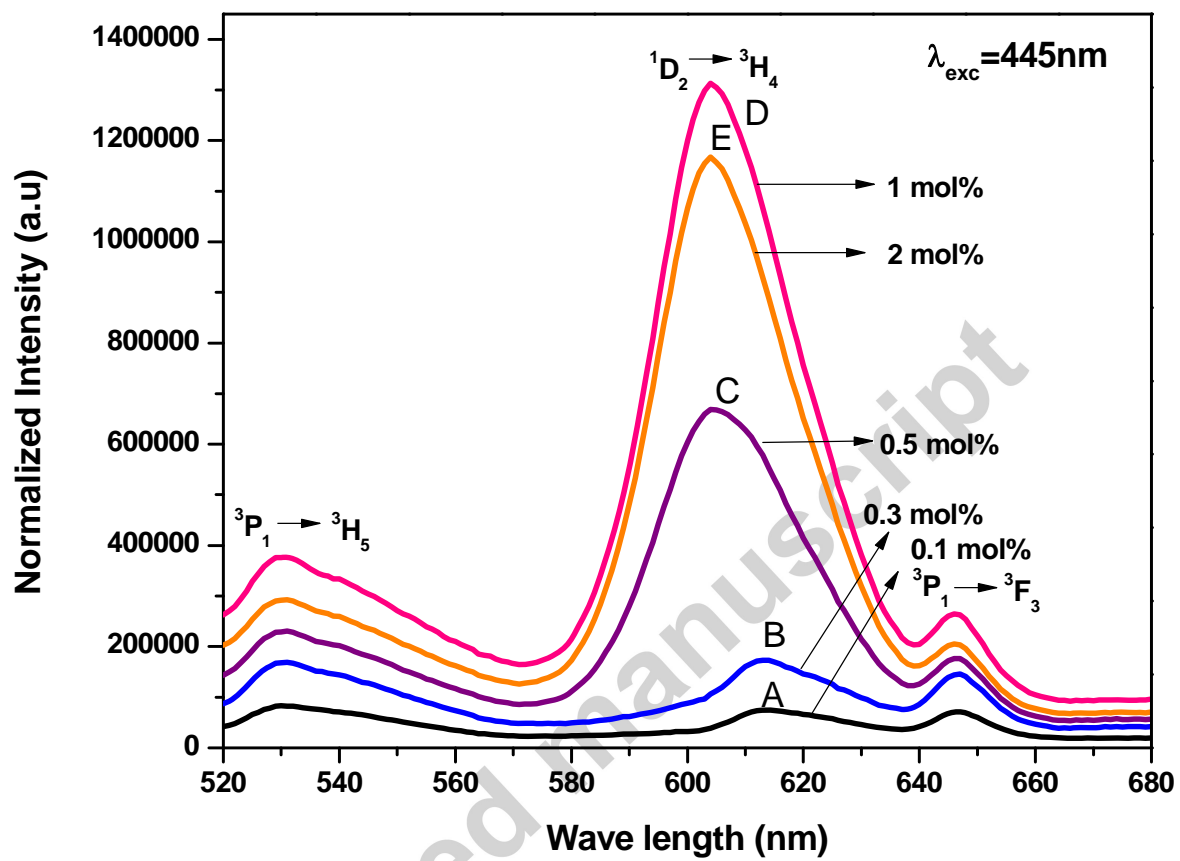


Fig 4

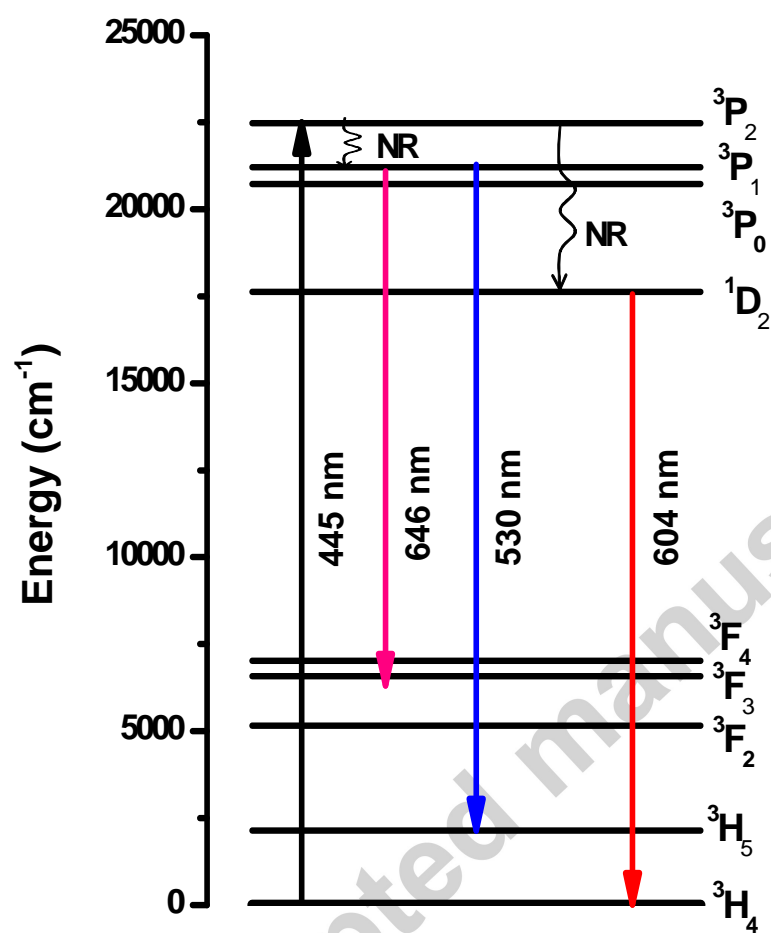


Fig 5

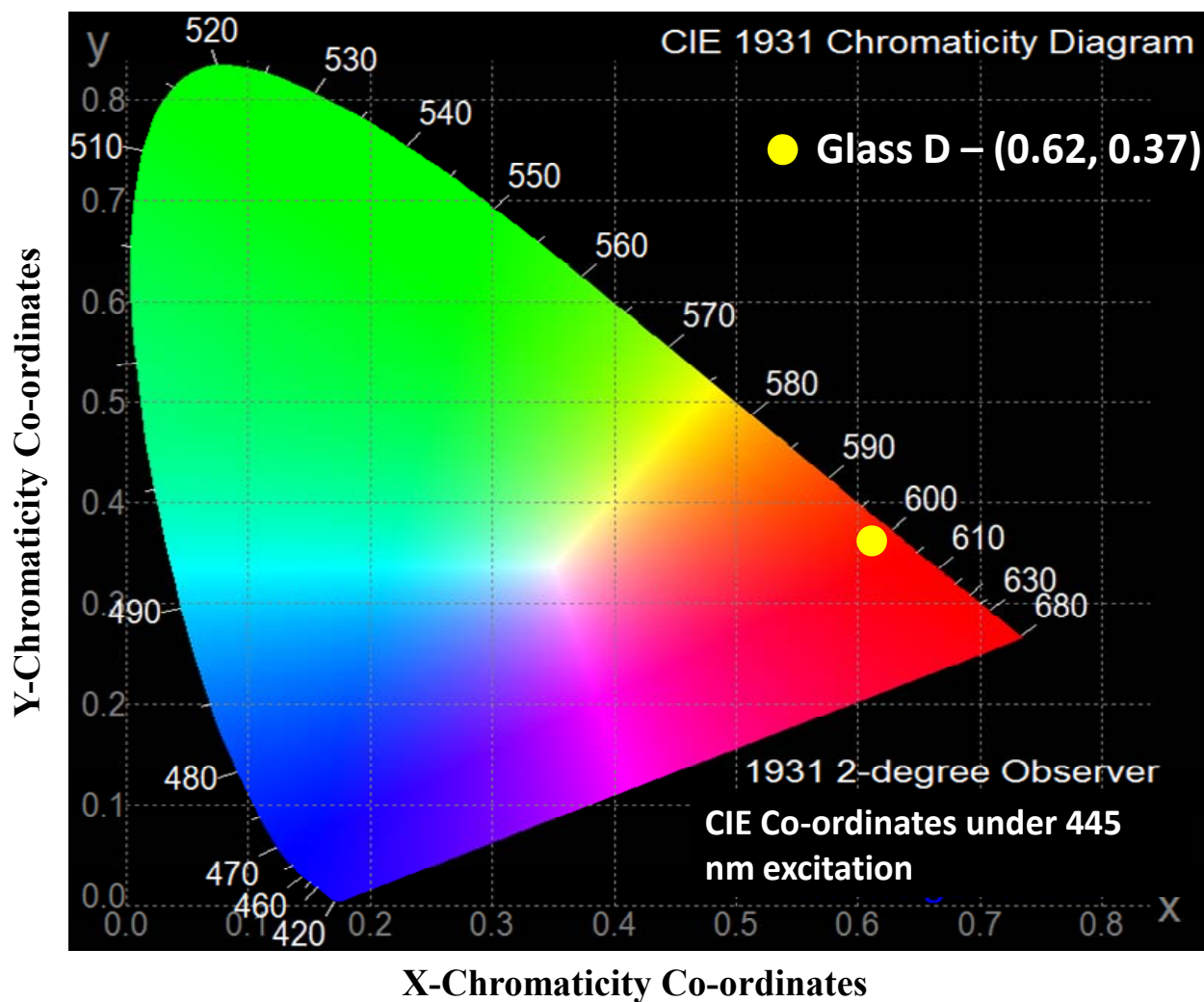
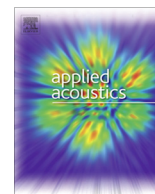


Fig 6



## Review

## Significance and implications of airborne sound insulation criteria in building elements for traffic noise abatement

Naveen Garg<sup>a,b,\*</sup>, Anil Kumar<sup>a</sup>, Sagar Maji<sup>b</sup><sup>a</sup> Apex Level Standards and Industrial Metrology Division, CSIR-National Physical Laboratory, New Delhi 110012, India<sup>b</sup> Department of Mechanical and Production & Industrial Engineering, Delhi Technological University, New Delhi 110042, India

## ARTICLE INFO

## Article history:

Received 23 November 2012

Received in revised form 12 March 2013

Accepted 17 May 2013

## Keywords:

Sound transmission Class (STC)

Spectrum adaptation terms ( $C$ ,  $C_{tr}$ )Weighted sound reduction index ( $R_w$ )Weighted apparent sound reduction index ( $R'_{w1}$ )

Weighted Standardized Field Level

Difference ( $D_{nT,w}$ )

## ABSTRACT

The paper extensively reviews the airborne sound insulation criteria followed in Europe and the sound descriptors used. The work focuses on significance and need of having modified sound insulation criteria in Indian dwellings for harmonization of sound descriptors with that followed in other countries for controlling the ever increasing traffic noise. Sound regulations in terms of prescriptive and verification criteria are proposed referring to regulations adopted in Europe and recent studies conducted by Rasmussen et al. [1] and Scholl et al. [6]. Practical implications of these regulations particularly related to material aspects w.r.t minimum and comfort class is also discussed. A study of laboratory sound transmission characteristics of dry wall constructions and massive concrete constructions to ascertain whether these criteria could be fulfilled easily or not reveals that the drywall constructions in conjunction with massive concrete constructions are suitable for achieving acoustic comfort in dwellings. It is envisaged that a clear definition, understanding and practical implementation of sound regulations criteria can be pivotal in controlling the outside traffic noise.

© 2013 Elsevier Ltd. All rights reserved.

## Contents

1. Introduction	1429
2. Selection of suitable sound descriptor	1431
3. Proposed sound regulations	1431
4. Implications	1432
5. Conclusions	1434
Acknowledgements	1434
References	1434

## 1. Introduction

Legal sound insulation requirements are very vital tool to fight against the ever increasing traffic noise. With increasing traffic noise and high vehicular density plying on the roads, introduction of elevated metro corridor and many other noise sources, there has been a significant increase in demand for high quality and comfort. In view of acoustic comfort, there has been a considerable research particularly in Europe for better sound insulation criteria to regulate the airborne and impact sound insulation between dwellings and airborne sound insulation of facades. Rasmussen [1,2] con-

ducted an extensive survey describing the main sound insulation requirements between dwellings in Europe which revealed a considerable differences not only in level of requirements, but also in terms of descriptors and frequency range applied. Also, meeting the legal requirements does not guarantee sufficient acoustic comfort and for this reason several countries in Europe have adopted classification schemes in a way of increasing order of better acoustic comfort which are further higher criteria than the legal requirements intended to provide the acoustic comfort. Studies on recommendation of facade performances in terms of traffic noise are very limited. Kurra and Dal [3] investigations reveal the required minimum noise reduction for facades exposed to traffic noise. The ISO standard 717-1 gives the spectrum adaptation terms ( $C$ ,  $C_{tr}$ ) applied to weighted sound reduction index,  $R_w$  when the representative spectrum i.e. pink noise or traffic noise is assumed

\* Corresponding author at: Apex Level Standards and Industrial Metrology Division, CSIR-National Physical Laboratory, New Delhi 110012, India.

E-mail address: [ngarg@mail.nplindia.ernet.in](mailto:ngarg@mail.nplindia.ernet.in) (N. Garg).

as loading noise [4]. The traditional frequency range for legal sound insulation was in range 100 Hz to 4 kHz in 1/3rd octave bands. However, in some countries with adaptation of light weight building practices, the need to include the low frequencies below 100 Hz become pertinent and thus frequency bands down to 50 Hz are applied in the regulatory requirements in Sweden [5]. The recent studies have recommended Standardized Field Level Difference ( $D_{nT,w}$ ) as the best single-number rating for describing the airborne sound insulation between dwellings [2,6]. The desire for improved acoustic comfort class intends to offer real acoustic comfort so that 90% of inhabitants are satisfied with the sound insulation. The condition  $D_{nT,w} \geq 54$  dB leads to an estimated 70% of the inhabitants satisfied with sound insulation [7]. In multi-storey dwellings, the requirement to obtain this has been specified to be  $D_{nT,w} \geq 58$  dB between dwellings. The requirement is increased by 4 dB when a living room is adjacent to a bedroom of another dwelling [8]. There have been many studies reported that focus on correlating the sound descriptors with subjective perception. Rindel [9] observations suggest that a change of 1 dB in sound insulation rating corresponds to a change of about 4% in the percentage of people disturbed by intruding noise.

In Indian perspectives, limited information prevails pertaining to the legal sound insulation criteria and sound descriptors use. Sound Transmission Class (STC) is the widely used single-number rating amongst manufacturers and testing laboratories. Although STC is a scientific rating and well defined method for describing the sound insulation properties of various acoustical materials, yet it suffers from the disadvantage wherein the low frequency sound transmission loss of material is poor and attributed to 8 dB rule, the STC value is seriously affected [10]. Also, it does not address frequency below 125 Hz which is another important issue to focus as low frequency noise plays a vital role in subjective perception. The EU Directive 49 urges to prepare the strategic noise maps and action plans amongst major transportation routes and major industrial premises [11]. Kurra and Dal [3] recent work in this regard describes a model to determine the required insulation performance for building external elements by using strategic noise maps. The European studies thus inculcate a need of contemporary study pertaining to sound regulations best suited in Indian

perspectives for adoption and strict implementation of revised sound regulations in combating the low frequency noise radiated by various transportation noise sources. It is thus vital to formulate a set of effective and practical sound regulation criteria based on scientific background and in line with the European studies e.g. COST Action TU 0901 and C12 on improving buildings structural quality by new technologies [12]. Fig. 1 shows the various features of the sound insulation regulations that should be accomplished for effective control of outside noise in dwellings for better acoustic comfort. The present standard followed however partially satisfies all these aspects with a major limitation in restriction of lower frequency range up to either 100 Hz or 125 Hz. Various studies have documented the domination of lower frequencies in transportation noise sources and low frequency resonances encountered in sandwich constructions further degrade the efficacy of materials in providing insulation from transportation noise although it may have high sound transmission loss in mid and high frequency range.

Correlation with subjective perception and A-weighting apart from reproducibility, along with the coverage of entire frequency range are essential desirables. Apart there needs to be harmonization with the international standards for global perspectives. The administrative and legal viability is a pertinent issue specifically in Indian conditions and thus sound regulations should be designed and formulated in such a way to provide analogous or complementary criteria's in conjunction with the in situ or field measurement criteria's. This will not only reduce the burden of Development Authorities for field/in situ testing in each case for type approval or compliance certifications, but also lay down more emphasis to laboratory testing in specialized reverberation chambers. The current international descriptors for evaluation of airborne sound insulation are described as per ISO 717:1996 [4] and the single-number quantities along with spectrum adaptation terms are derived from laboratory measurements in reverberation chambers according to ISO 140 [13]. Table 1 lists the descriptors used for sound insulation classes in some of European countries [14,15]. It is observed that there exists a difference of perception amongst the acousticians in choosing  $R'_w$  or  $D_{nT,w}$  for building sound regulations which has been however eliminated to a large extent by recent studies.

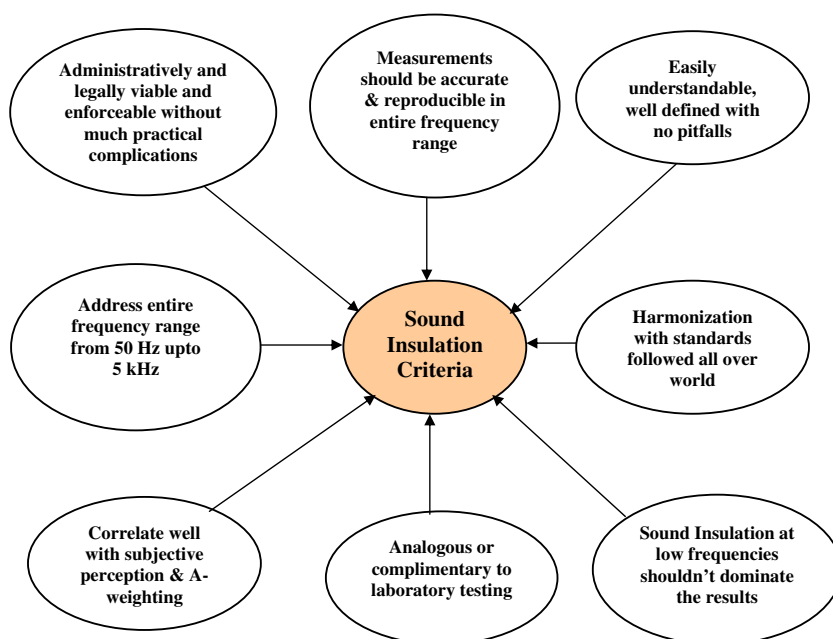


Fig. 1. Features of effective sound insulation criteria in building elements.

**Table 1**

Airborne sound insulation between dwellings. Main criteria in sound classification schemes in Europe [14,15].

Country	Class A NL: Class 1 DE: Class III FR: N/A	Class B NL: Class 2 DE: Class II FR: QLAC	Class C NL: Class 3 DE: Class I FR: QL	Class D NL: Class 4 DE: N/A FR: N/A	Class E NL: Class 5 DE: N/A FR: N/A
<i>Airborne sound insulation between dwellings – main class criteria in dB</i>					
Denmark	$R'_w + C_{50-3150} \geq 63$	$R'_w + C_{50-3150} \geq 58$	$R'_w \geq 55$	$R'_w \geq 50$	N/A
Finland	$R'_w + C_{50-3150} \geq 63$	$R'_w + C_{50-3150} \geq 58$	$R'_w \geq 55$	$R'_w \geq 49$	N/A
Iceland	$R'_w + C_{50-3150} \geq 63$	$R'_w + C_{50-3150} \geq 58$	$R'_w \geq 55^d$	$R'_w \geq 50$	N/A
Norway	$R'_w + C_{50-3150} \geq 63$	$R'_w + C_{50-3150} \geq 58$	$R'_w \geq 55^d$	$R'_w \geq 50$	N/A
Sweden	$R'_w + C_{50-3150} \geq 61$	$R'_w + C_{50-3150} \geq 57$	$R'_w + C_{50-3150} \geq 53$	$R'_w \geq 49$	N/A
Lithuania	$R'_w + C_{50-3150} \geq 63$ or $D_{nT,w} + C_{50-3150} \geq 63$	$R'_w + C_{50-3150} \geq 58$ or $D_{nT,w} + C_{50-3150} \geq 58$	$R'_w$ or $D_{nT,w} \geq 55^d$	$R'_w$ or $D_{nT,w} \geq 52$	$R'_w$ or $D_{nT,w} \geq 48$
Netherlands <sup>a</sup>	$D_{nT,w} + C \geq 62$	$D_{nT,w} + C \geq 57$	$D_{nT,w} + C \geq 52$	$D_{nT,w} + C \geq 47$	$D_{nT,w} + C \geq 42$
Germany <sup>b</sup> (multi storey housing)	$H : R'_w \geq 59$ $V : R'_w \geq 60$	$H : R'_w \geq 56$ $V : R'_w \geq 57$	$H : R'_w \geq 53$ $V : R'_w \geq 54$	N/A	N/A
Germany <sup>b</sup> (row housing)	$R'_w \geq 68$	$R'_w \geq 63$	$R'_w \geq 57$	N/A	N/A
France <sup>c</sup>	N/A	$D_{nT,w} + C \geq 56$	$D_{nT,w} + C \geq 53$	N/A	N/A

DE-Germany, FR-France, NL-Netherlands.

H = Horizontal; V = Vertical.

<sup>a</sup> Classes 1,2,3,4,5.<sup>b</sup> Classes III, II, I.<sup>c</sup> Classes QLAC, QL.<sup>d</sup> Use of  $C_{50-3150/5000}$  is recommended also in class C.

The present study is based on these recent findings reported and tries to assimilate the European concept and sound descriptors used for legal requirements and classification criteria for Indian dwellings for effective noise control. The study is however an independent study done by authors based on exhaustive literature survey and experience gained in laboratory testing in reverberation chambers and has nothing to do with any legal or government body sponsoring the work or accepting the conclusions of the present work.

## 2. Selection of suitable sound descriptor

The selection of suitable descriptor confirming to the guidelines in Fig. 1 is very vital in establishing the sound regulations. The conventional use of Sound Transmission Class (STC) in laboratory measurements has to be revised in present scenario owing to the limitation of frequency range up to 125 Hz and confusion observed due to 8 dB rule for constructions having low frequency sound transmission loss or wherein the mass-air-mass resonance is registered at low frequencies. Thus, it is imperative to adopt the sound regulations catering to the entire frequency range from 50 Hz to 5 kHz and having a subjective correlation with the sound insulation actually perceived by the receiver.

Scholl et al. [6] recommendations pertaining to the revision in current ISO 717-1 with addition of a speech sound reduction index,  $R_{speech}$  and introduction of traffic noise sound reduction index,  $R_{traffic}$ ; living noise sound reduction index,  $R_{living}$  and the corresponding field parameters shall be simpler and facilitates a clear identification and suitability w.r.t usage of single-number quantities for rating the sound insulation in building and of building elements and also harmonizes airborne sound insulation using sound reduction index,  $R$  as a common descriptor. The living noise sound reduction index  $R_{living}$  is the same as  $R_w + C_{50-5000}$  given in ISO 717-1. Table 2 incorporates all the pros and cons in terms of SWOT analysis (Strengths, Weaknesses, Opportunities and Threats) of the various single number ratings for field and in situ sound transmission loss measurements [1,2,6,16].  $D_{nT,w} + C$  has some inherent advantages owing to strong correlation observed with subjective response and its non dependency on room dimensions although there couldn't be a direct empirical formulation that could be developed for it in terms of the material properties for

theoretical predictions. The difference between  $R'_w$  and  $R_w$  is typically about 3 to 6 dB but can even exceed 20 dB if structure contains severe sound leaks. Thus, considering the flanking transmission,  $R_w$  is assumed to be of order of 5 dB higher than  $R'_w$ .

## 3. Proposed sound regulations

An exhaustive survey of sound insulation descriptors used in European continent in conjunction with subjective analysis has led to formulation of following criteria suggested by Rasmussen for airborne sound insulation between dwellings as [2]:

$$D_{nT,w} + C_{50-3150} \geq 55 \text{ dB} \quad (1)$$

The 2004 update of Building Codes of Australia [17] and UK Standard [18] adopts the use of  $C_{tr}$  adaptation terms for all situations including noise generated by building occupants, water pipe noise etc. There has been a varied opinion amongst researchers particularly on the inclusion of spectrum adaptation terms in sound regulations requirements attributed to  $C_{tr}$  emphasis on low frequencies [16]. Park and Bradley [19] investigations reveal that  $R_w$  values can be improved by addition of spectrum adaptation terms for music ( $R_w + C_{tr100-3150}$ ) and speech ( $R_w + C_{mod}$ ). Some studies [20] reveal that ( $R_w + C_{tr}$ ) gives the sound insulation values that are in middle of range of typical A-weighted sound insulation values for transportation noise. The prescriptive approach specified for deemed-to-satisfy provisions in Building Codes of Australia has been fixed to  $R_w + C_{tr}$  not less than 50 dB for walls between apartments when tested in laboratory and  $D_{nT,w} + C_{tr}$  not less than 45 dB when tested on-site [21].  $R_w$  not less than 50 dB for walls separating a dwelling from a plant room, lift shaft, stairway, public corridor, public lobby etc. and  $R_w + C_{tr}$  not less than 50 dB for floors between dwellings has been specified. The adoption of  $C_{tr}$  rating however may have legal and administrative implications for manufacturers owing to its significant dependence on low frequency sound insulation. The European classification system has defined four classes namely A, B, C and D for sound insulation requirements. Class C corresponds to minimum level that should be achieved in new buildings; while Class D applies to older buildings. Classes A and B enable better acoustical quality than required in building codes. There has been a varied approach in sound insulation requirements for facades in many countries.  $L_{Aeq,24h} \leq 20$  dB has been criteria set for facades in



**Table 2**  
SWOT analysis of different single number ratings for field/in situ sound transmission loss measurement.

Single number rating	Strengths	Weakness	Opportunities	Threats
Field Sound transmission Class (FSTC)	Simple and easy to calculate, widely used	8 dB rule sometimes create confusion, low frequency below 125 Hz not addressed	Widely used amongst manufacturers and architects	8 dB rule sometimes results in confusion especially wherein the low frequency mass-air-mass resonance is registered
Apparent living noise sound reduction index, $R'_{w} + C$	Spectrum adaptation term $C$ is analogous to A-weighting as it is calculated from A-weighting spectrum	Adversely affected for lightweight constructions and variations are large. $R'_{w}$ requires a common surface area of 10 m <sup>2</sup>	Used in sound regulation requirements in some countries	High measurement uncertainty associated with measurements down to 50 Hz. $C_{50-3150}$ is highly influenced by 50 Hz spectrum adaptation term
Standardized traffic noise level difference $D_{nT,w} + C_{tr}$ or Apparent traffic noise sound reduction index $R'_{w} + C_{tr}$	It is applicable for urban road traffic, railway traffic at low speeds, aircraft propeller driven, Jet aircraft, Disco music and factories emitting mainly low and medium frequency noise	It is not effective in dealing with normal living noise issues and generates too much emphasis at low frequencies	$D_{nT,w} + C_{tr}$ is used in sound regulation requirements in Australia and UK $D_{2m,nT,w} + C_{tr}$ is used for façade sound insulation criteria in some countries	High measurement uncertainty associated with measurements down to 50 Hz for measuring $D_{nT,w} + C_{tr}$ variation in measurements of 2–3 dB at lower frequencies can result a significant negative $C_{tr}$ correction value change from –5 to –12 dB
Standardized living noise level difference $D_{nT,w} + C$	Good correlation with subjective evaluation is realized. Room dimensions are not needed in calculation. Applicability to all type of field situations. Correction term 0.5 s corresponds to an average reverberation time of furnished rooms	No direct physical correlation can be established in prediction of $D_{nT,w}$ attributed to flanking transmission & its non-dependency on partition size	Recommended in recent studies conducted in past attributed to highest correlation with subjective response	Measurement accuracy associated with reverberation time measurements should be high especially in low frequencies and in practical situations wherein diffuse field conditions does not persists

Denmark, while in Norway and additional criteria of  $L_{pA,max23-07} - \leq 35$  dB is specified for facade insulation [22]. Some studies also state facade sound insulation in terms of weighted standardized sound level difference of facades,  $D_{2m,nT,w}$  and A-weighted sound level as [8,23]:

$$D_{2m,nT,w} + C_{tr,50-3150} \geq L_{1,2m,07h-23h} - 35 \text{ dB for day time and} \quad (2)$$

$$D_{2m,nT,w} + C_{tr,50-3150} \geq L_{1,2m,23h-07h} - 30 \text{ dB for night time.} \quad (3)$$

In all cases, the facade sound insulation should be at least  $D_{2m,nT,w} + C_{tr,50-3150} \geq 30$  dB even in quiet areas [23]. Fuente [24] enlists the current acoustical requirements in Spain building regulations as  $D_{2m,nT,w} + C_{tr,50-3150} \geq 42$  dB for  $70 < L_d \leq 75$  dB(A) and  $D_{2m,nT,w} + C_{tr,50-3150} \geq 47$  dB for  $L_d > 75$  dB(A). The importance of strengthening the facades can be realized from Norwegian investigations, wherein an average equivalent noise reduction inside the dwellings of 7 dB was obtained from the facade insulation which led to drop of % highly annoyed from 42% respondents before to 16% after the study [25].

Table 3 shows the proposed criteria and descriptors for building elements based on the exhaustive literature survey. The Weighted Standardized Field Level Difference is the descriptor used for the facade insulation and sound insulation requirements for doors and windows for uniformity and avoiding any confusion, although many studies report the use of  $D_{2m,nT,w}$ . The Class C refers to the minimum criteria that must be followed as chosen in other countries, while Class B is defined for the acoustic comfort having an average noise level reduction of the order of 35 dB. Class A represents the high acoustic comfort levels achieved through a noise level reduction of 40 dB. The  $R_w + C_{tr,50-3150} \geq 50$  dB criteria is chosen for Class A, when the outdoor noise level is within 70 dB(A) to 75 dB(A). The criteria is enhanced by 5 dB for an outdoor noise level more than 75 dB(A). The minimum criteria of weighted sound reduction index of 50 dB is judiciously chosen for new buildings for protection against external noise. In case of airborne sound insulation between dwellings, the spectrum adaptation term,  $C$  as recommended in many studies has been used in regulations for comfort criteria. An  $R_w + C_{50-3150} \geq 60$  dB presents an analogous criteria for the  $D_{nT,w} + C_{50-3150} \geq 55$  dB as reported

in various studies. The sound insulation of windows have been specified to follow  $R_w + C_{tr,50-3150} \geq 35$  dB for Class A level and further 5 dB relaxation is provided for the doors to compensate for higher area than windows in building facades. However, these criteria should be enhanced further by +5 dB in case the doors and windows occupy more than 25% of the area of total façade as reported in Wyle report [26]. Although the sound insulation criteria for weakest elements of building facades i.e. windows and doors is equally important to consider for accomplishing the desired targets for facade insulation, yet it introduces uncertainty also as difference in the field and laboratory results have been measured as great as 15 dB, and an average difference of 8 dB [27].

#### 4. Implications

Mixed building technology characterized by use of lightweight materials and adoption of fenestration areas can be instrumental not only considering the aesthetic, functional and economical terms but also in acoustical terms [28]. Guillen [29] observations revealed that masonry–air cavity–gypsum walls had higher sound reduction index than masonry–air cavity–brick ones. Although the sound insulation provided by plastered brick and masonry concrete walls is appreciably high, yet the low frequency sound insulation characteristics could be affected owing to flexural and mass-air-mass resonances encountered. The sound insulation provided by a 190 mm concrete block ( $R_w + C_{tr} = 53$  dB) and 9 in. (229 mm) brick wall ( $R_w + C_{tr} = 50$  dB) appears to be on the border-line of acoustic comfort criteria in dwellings and thus need further acoustic treatment for enhancing the sound insulation especially in dwellings situated near traffic intersections and busy roads. An investigation was conducted to evaluate the spectrum adaptation terms of ISO 717 for sandwich gypsum constructions. The experimental data published by Halliwell et al. [30] was used. The spectrum adaptation terms were calculated for transmission loss data documented in the report in frequency range 50 Hz to 3150 Hz. It can be observed from Fig. 2 that these spectrum adaptation terms are severely affected for sandwich gypsum constructions. The average value of spectrum adaptation terms for pink noise was observed to be –5.9 dB on averaging for 50 such

**Table 3**

Proposed criteria (in dB) and descriptors for building elements.

Building element	Prescriptive criteria (all values in dB)	Verification criteria (all values in dB)
Facades	Class A $R_w + C_{tr,50-3150} \geq 55$ when $L_d > 75$ dB(A)	Class A $D_{nT,w} + C_{tr,50-3150} \geq 50$ when $L_d > 75$ dB(A)
	Class B $R_w + C_{tr,50-3150} \geq 50$ when $70 \leq L_d \leq 75$ dB(A)	Class B $D_{nT,w} + C_{tr,50-3150} \geq 45$ when $70 \leq L_d \leq 75$ dB(A)
	Class C $R_w \geq 50$	Class C $D_{nT,w} \geq 45$
	Class D $R_w \geq 45$	Class D $D_{nT,w} \geq 40$
Between dwellings	Class A $R_w + C_{50-3150} \geq 60$	Class A $D_{nT,w} + C_{50-3150} \geq 55$
	Class B $R_w + C_{50-3150} \geq 55$	Class B $D_{nT,w} + C_{50-3150} \geq 50$
	Class C $R_w \geq 52$	Class C $D_{nT,w} \geq 47$
	Class D $R_w \geq 47$	Class D $D_{nT,w} \geq 42$
Rooms in dwelling units	$R_w \geq 40$	$D_{nT,w} \geq 35$
Classrooms, offices, kitchen & utility rooms	$R_w \geq 45$	$D_{nT,w} \geq 40$
Windows <sup>a</sup>	Class A $R_w + C_{tr,50-3150} \geq 35$	Class A $D_{nT,w} + C_{tr,50-3150} \geq 30$
	Class B $R_w + C_{tr,50-3150} \geq 30$	Class B $D_{nT,w} + C_{tr,50-3150} \geq 25$
	Class C $R_w \geq 30$	Class C $D_{nT,w} \geq 25$
	Class D $R_w \geq 25$	Class D $D_{nT,w} \geq 20$
Doors <sup>a</sup>	Class A $R_w + C_{tr,50-3150} \geq 30$	Class A $D_{nT,w} + C_{tr,50-3150} \geq 25$
	Class B $R_w + C_{tr,50-3150} \geq 25$	Class B $D_{nT,w} + C_{tr,50-3150} \geq 20$
	Class C $R_w \geq 25$	Class C $D_{nT,w} \geq 20$
	Class D $R_w \geq 20$	Class D $D_{nT,w} \geq 15$

<sup>a</sup> If the size of windows and doors are more than 25% the total area of façade, the criteria for each class is further enhanced by 5 dB.

sandwich constructions with a standard deviation of 1.81 dB. The average value spectrum adaptation term for traffic noise was observed to be  $-16.7$  dB with standard deviation of 4.04 dB.

A linear correlation fit was established between these single-number rating for sandwich gypsum constructions as:

$$R_w + C = 0.6893 \times STC + 10.704, \quad R^2 = 0.95 \quad (4)$$

$$R_w + C_{tr} = 0.4457 \times STC + 11.77, \quad R^2 = 0.83 \quad (5)$$

It can be inferred from above equations that for achieving acoustic comfort in dwellings considering the criteria  $R_w + C_{tr,50-3150} \geq 50$ , an STC of 86 is required for sandwich gypsum constructions, which is rather very large value. Thus, it is essential to consider the masonry constructions attached with the gypsum board to achieve the desired results. However, there is a lack of experimental data published on masonry materials. Warnock reports on sound transmission loss through concrete constructions along with gypsum board provide a large data base for referring to the sound insulation properties in frequency range 100 Hz to 4 kHz. A further investigation was carried out in calculating the spectrum adaptation terms for masonry concrete constructions along with gypsum board from the data available in Warnock report [31]. The average value of spectrum adaptation terms for pink noise was observed to be  $-2.6$  dB on averaging for 42 such sandwich constructions with a standard deviation of 1.1 dB. The average value spectrum adaptation term for traffic noise was observed to be  $-7.9$  dB with a standard deviation of 2.1 dB as shown in Fig. 3.

A linear correlation fit was established between the two single number ratings widely used viz.,  $R_w$  ( $C$ ,  $C_{tr}$ ) and STC for sandwich concrete and gypsum constructions as:

$$R_w + C = 0.9221 \times STC + 1.1326, \quad R^2 = 0.94 \quad (6)$$

$$R_w + C_{tr} = 0.8541 \times STC - 0.8765, \quad R^2 = 0.82 \quad (7)$$

These equations arrive at the following important conclusions as:

- The facade acoustic comfort can be achieved for sandwich concrete constructions with attached gypsum board having weighted sound insulation index,  $R_w$  of 58 dB considering the average spectrum adaptation term  $C_{tr}$  of these fabrications to be  $-8$  dB in frequency range 100 Hz to 3150 Hz. On correlating the  $R_w + C_{tr}$  rating required for acoustic comfort ( $R_w + C_{tr} = 50$  dB), the Sound Transmission Class value comes out to be 60. So, an STC value of 60 could be sufficient to provide acoustic comfort in case where the outdoor sound pressure levels are  $70 \leq L_d \leq 75$  dB(A).

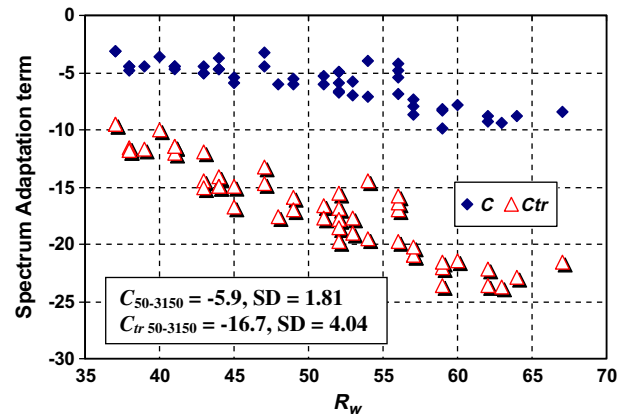


Fig. 2. Spectrum adaptation terms ( $C_{50-3150}$ ,  $C_{tr,50-3150}$ ) of ISO 717 for laboratory measurements of 50 Gypsum sandwich constructions [30].

- The acoustic comfort inside dwellings due to the neighboring dwellings could be achieved with constructions having  $R_w$  of 63 dB.
- While considering the spectrum adaptation term,  $C_{tr}$  in frequency range 50 Hz to 3150 Hz, the  $R_w + C_{tr}$  value further decrements on account of reduced low frequency sound transmission. It is thus imperative to consider an additional design factor of +3 to 5 dB for selecting the sandwich concrete constructions for façade insulation, which mean that  $R_w$  between 61 to 63 dB should be design target.

A clear cut definition and identification of single-number rating required shall be thus instrumental in selecting the appropriate material for accomplishing the desired objectives. There can be many suitable combinations designed based on theoretical predictions and validated by experimental investigations for their intended use in building facades. The stringent sound insulation criteria proposed for achieving the acoustic comfort thus makes it imperative for design and fabrications of improved sandwich constructions utilizing the drywall construction technology in conjunction with massive constructions. The design aspects w.r.t attachment of gypsum board via steel studs (staggered or double), resilient channels, stud spacing and inclusion of sound absorptive material in cavity arresting the low frequency mass-air-mass resonances has to be thus given utmost priority for satisfying the



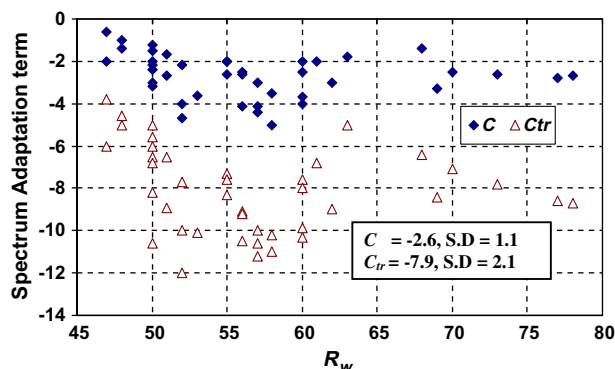


Fig. 3. Spectrum adaptation terms ( $C_{100-3150}$ ,  $C_{tr,100-3150}$ ) of ISO 717 for 42 concrete constructions with gypsum boards in laboratory measurements [31].

proposed criteria. Appropriate combinations incorporating structural breaks and added mass can significantly enhance the sound insulation characteristics as revealed by Bradley and Birta [32] investigations for wood stud exterior walls, wherein an increase in Outdoor Indoor Sound transmission Class (*OITC*) from 25 for base wall to 40 is shown. Evidently the low frequency field sound transmission characteristics [33] are experimentally observed to be better in case of 12 mm gypsum wall board mounted on resilient channels applied directly to 190 mm concrete block wall on each side ( $R'_w + C_{tr} = 49$  dB) as compared to 190 mm concrete block with 12 mm gypsum wall board cemented to each side ( $R'_w + C_{tr} = 45$  dB).

An air space greater than 60 mm for a single layer of wall board attached to concrete block wall [34] for encountering the low frequency mass-air-mass resonances, induction of absorptive material in cavity plays a prominent role in enhancing the sound insulation characteristics. A maximum increase in transmission loss of 15 dB is reported for cavity depths greater than 75 mm, wherein cavities are filled with sound absorbing material [35]. The validated theoretical models [36,37] on prediction of sound transmission characteristics of multilayered walls using the material physical properties can be helpful in devising the optimum configurations having very high sound insulation characteristics keeping in view the economic, structural and practical constraints. The sound insulation provided by the weakest façade elements i.e. windows and doors also plays a pivotal role in deciding the total façade insulation. Double glazing laminated windows with an optimum air-gap and steel doors with reduced interpanel connections are suitable for the meeting the proposed acoustic comfort criteria [38,39]. An optimum design of the front and back pane thickness in conjunction with proper selection of air-gap can be instrumental in controlling the sound transmission through double glazing. The laboratory values can be helpful for field of application of suitable glazings although a difference up to 15 dB has been reported between the field and laboratory values [27]. Sandwich door constructions with an absorptive material in cavity between two doors and proper sealing can meet the desired objectives.

The adoption of  $R_w$  and  $D_{nT,w}$  ratings for sound insulation have their legal implications also particularly in case of metro cities like Delhi wherein the multi-storey dwellings are rigorously expanding contemporary to the population density. The in situ measurements for verification of sound regulations are practically cumbersome in each case and thus the laboratory ratings of the sound insulation index could be relied directly to achieve the desired targets. Inculcating knowledge and information pertaining to building materials providing high sound insulation and exercising the sound regulation requirements at the very first stage of developing the housing plan could be instrumental in developing improved constructions. In France, there is a certification procedure known as 'Qualitel' in

which owner will first submit the drawing to a certified organism that will check whether the predictive acoustical performance will comply with requirements or not and satisfying these requirements will allow project to proceed further and allotment of funding [40]. These procedures can be easily exercised in Indian conditions at the initial stages of getting the housing plan approved from the Development Authority. The laboratory testing has also to be modified with precise measurements in the entire frequency range of 50 Hz to 5 kHz. Consequently, the diffusion characteristics of reverberation chambers have to be significantly enhanced and made conducive to comply with the relevant international standards.

## 5. Conclusions

The paper discusses the sound regulation requirements for traffic noise abatement in dwellings in terms of the single-number descriptors. The work extensively reviews the recent developments in adoption of the best single-number rating correlating with the subjective response for describing the sound regulation requirements. The introduction of the Standardized Living noise level difference,  $D_{nT,w}$  thus inculcates the highest precision and accuracy associated with reverberation time measurements at low frequencies. The material aspects particularly related to use of dry-wall constructions in conjunction with the massive constructions is thus highlighted for accomplishing the targets required for Class A criteria. The proposed sound insulation criteria will also create a harmonization with the descriptors used all over the world. Thus, it is imperative to design the best sandwich material configurations having high sound insulation to achieve the targets. It is also envisaged that a clarity in description of requirements for minimum insulation required and that for acoustic comforts along with freely available data on sound insulation characteristics of building materials can be very beneficial for architects and engineers for selection of best building materials. The conventional building technology of using plastered bricks and concrete structures has to be modified with dry wall constructions attached with steel studs to plastered bricks or concrete structures with sound absorbing material in the cavity and has to brought in wide usage for combating the low frequency transportation noise. Apart from the material aspects; administrative and legal aspects particularly related with the enforcement of sound regulation requirements and inculcating knowledge about strengthening the building facades shall be a vital step in fighting against the ever-increasing vehicular traffic noise.

## Acknowledgements

Authors would specially acknowledge the reports published by experts of *NRC Canada*, whose valuable data has been used in highlighting the sound transmission characteristics of masonry constructions. Authors also thank the anonymous reviewers for their comments and suggestions. Author shall appreciate any corrections, suggestions or updates of information.

## References

- [1] Rasmussen B, Rindel JH. Sound insulation between dwellings – descriptors applied in building regulations in Europe. *Appl Acoust* 2010;71:171–80.
- [2] Rasmussen B. Sound insulation between dwellings—requirements in building regulations in Europe. *Appl Acoust* 2010;71:373–85.
- [3] Kurra S, Dal L. Sound insulation design by using noise maps. *Build Environ* 2012;49:291–303.
- [4] ISO 717. Rating of sound insulation in buildings and of building elements, Part 1. 1996.
- [5] C. Simmons, Reliable building element sound insulation data for EN 12354 calculations facilitates analysis of Swedish dwelling houses. In: *Inter-noise* 2004, Prague, Czech Republic, August 22–25, 2004.

- [6] Scholl W, Lang J, Wittstock V. Rating of sound insulation at present and in future. The revision of ISO 717. *Acta Acustica united with Acustica* 2011;97:686–98.
- [7] J.H. Rindel, Acoustic quality and sound insulation between dwellings. In: Conference in building acoustic–acoustic performance of medium-rise timber buildings, Dublin; 1998.
- [8] Ingelaere B, Vermeir G, Damme MV. New Belgian requirements for dwellings. *Forum Acusticum* 2005.
- [9] J.H. Rindel, The relationship between sound insulation and acoustic quality in dwellings. In: *Inter-Noise 1998*, Christchurch, New Zealand; 1998.
- [10] Garg N, Kumar A, Maji S. Practical concerns associated with use of single number rating in measuring sound transmission loss properties of partition panels. *Archives of Acoustics* 2013;38:115–26.
- [11] Directive 2002/49/EC of the European parliament and of Council of 25 June 2002 relating to the assessment and management of environmental noise. *Official Journal of European Communities* 18.07.2002. L189/12 – 189/25.
- [12] Cost Action TU 0901. Integrating and Harmonizing sound insulation aspects in sustainable urban housing constructions. <<http://www.cost.esf.org>>.
- [13] ISO 140. Laboratory measurements of airborne sound insulation of building elements, Part 3. 1995.
- [14] B. Rasmussen, Convention nazionale del gruppo di acustica edilizia 11–12, March 2009. <[http://vbn.aau.dk/files/17156840/Sound\\_classification\\_of\\_dwellings.pdf](http://vbn.aau.dk/files/17156840/Sound_classification_of_dwellings.pdf)>.
- [15] B. Rasmussen, Sound classification of dwellings in the Nordic countries–differences and similarities between the five national schemes, In: *Joint Baltic-Nordic Acoustics Meeting*, Denmark, June 18–20, 2012.
- [16] S. Smith, R. MacKenzie, R. MacKenzie, T. Waters-Fuller, The implications of ISO 717 spectrum adaptation terms for residential buildings. In: *Proceedings of the institute of acoustics*, vol. 25; 2003. Pt. 5.
- [17] R.J. Fitzell, F.R. Fricke, Changes to the BCA—are they a step forward. In: *Proc. of acoustics 2004*, 3rd to 5th November, Australia: Gold Coast; 2004 151–157.
- [18] S. Smith, D. Baker, R. MacKenzie, J.B. Wood, P. Dunbavin, D. Panter, The development of robust details for sound insulation in new build attached dwellings. <<http://www.acousticconsultant.eu/Robust%20Details.pdf>>.
- [19] Park HK, Bradley JS. Evaluating standard airborne sound insulation measures in terms of annoyance, loudness and audibility ratings. *J Acoust Soc Am* 2009;126:208–19.
- [20] J.L. Davy, Insulating buildings against transportation noise. In: *Proceedings of annual conference of Australian acoustical society*, 3rd to 5th November, Australia: Gold Coast; 2004.
- [21] M.J. Patterson, Recent changes to the sound insulation provisions of the building code of Australia. In: *Proc. of acoustics*, 3rd to 5th November, Australia: Gold Coast; 2004.
- [22] B. Rasmussen, Façade sound insulation comfort criteria in European Classification schemes for dwellings, *Euronoise 2006*, 30th May to 1 June, 2006, Finland.
- [23] B. Ingelaere, M. Blasco, C. Crispin, G. Vermeir, Developing a new facade sound insulation requirement for dwellings: building solutions and their cost. In: *Inter-Noise*, Czech Republic, August 22–25, 2004.
- [24] M. Fuente, E. Cagigal, S. Escudero, I. Flores, R+D for the integration of high acoustic-thermal performances in Spanish building products. In: *Acoustics 2008*. Paris, June 29–July 4, 2008.
- [25] Amundsen AH, Klæboe R, Aasvang GM. The Norwegian Façade insulation study: the efficacy of facade insulation in reducing noise annoyance due to road traffic. *J Acoust Soc Am* 2011;129:1381–9.
- [26] Guidelines for sound insulation of residences exposed to aircraft operations. In: Deptt of Navy, Washington: Wyle Research and Consulting; 2005. <[http://www.fican.org/pdf/Wyle\\_Sound\\_Insulation.pdf](http://www.fican.org/pdf/Wyle_Sound_Insulation.pdf)>.
- [27] S. Olafsen, M.K. Strand, Field versus laboratory sound insulation of glass facades. In: *Inter-noise 2009*, Canada: Ottawa; August 23–26 2009.
- [28] Bragança L, Patrício J. Case study: comparison between the acoustic performance of a mixed building technology building and a conventional building. *Build Acoust* 2004;11:79–90.
- [29] Guillen I, Uris A, Estella H, Llinares J, Llopsi A. On the sound insulation of masonry wall facades. *Build Environ* 2008;43:523–9.
- [30] R.E. Halliwell, T.R.T. Nightingale, A.C.C. Warnock, J.A. Birta, Gypsum board walls: transmission loss data. NRC Canada, Report No. IRC-IR-761; 1998.
- [31] A.C.C. Warnock, Sound transmission loss measurement through 190 mm and 140 mm blocks with added dry wall and through cavity block walls. NRC Canada, Internal, Report No. 586; 1990.
- [32] Bradley JS, Birta JA. On the sound insulation of wood stud exterior walls. *J Acoust Soc Am* 2001;110:3086–96.
- [33] A.C.C. Warnock, Field sound transmission loss measurements. BRN 232, NRC Canada; 1985.
- [34] Warnock ACC. Factors affecting sound transmission loss. *Can Build Sci Insight CBD* 1985;239.
- [35] Bradley JS, Birta JA. A simple model of the sound insulation of gypsum board on resilient supports. *Noise Control Eng J* 2001;49:216–23.
- [36] K.O. Ballagh, Accuracy of prediction methods for sound transmission loss, In: *Internoise 2004*, Prague, Czech Republic, August 22–25, 2004.
- [37] Kurra S. Comparison of the models predicting sound insulation values of multi-layered building elements. *Appl Acoust* 2012;73:575–89.
- [38] Garg N, Sharma O, Maji S. Design considerations for enhancing sound insulation characteristics of window glazing for traffic noise abatement. *Build Acoust* 2012;19:89–98.
- [39] Hongisto V, Keränen J, Lindgren M. Sound insulation of doors-Part 2: Comparison between measurement results and prediction. *J Sound Vib* 2000;230:149–70.
- [40] Asselineau M. Noise control projects: the European experience. *International congress on sound and vibration, ICSV 14*. Australia: Cairns; 2007.